Transactions of the ASME®

Journal of Applied Mechanics

Published Bimonthly by The American Society of Mechanical Engineers

VOLUME 69 • NUMBER 5 • SEPTEMBER 2002

Transactions of the ASME, Journal of Applied Mechanics (ISSN 0021-8936) is published bimonthly (Jan., Mar., May, July, Sept., Nov.) The American Society of Mechanical Engineers, Three Park Avenue, New York, NY 10016. Periodicals postage paid at New York, NY and additional mailing office. POSTMASTER: Send address changes to Transactions of the ASME, Journal of Applied Mechanics, c/o THE AMERICAN SOCIETY OF MECHANICAL ENGINEERS, 22 Law Drive, Box 2300, Fairfield, NJ 07007-2300. **CHANGES OF ADDRESS** must be received at Society headquarters seven weeks before they are to be effective. Please send old label and new address. **STATEMENT from By-Laws.** The Society shall not be responsible for statements or opinions advanced in papers or . . . printed in its publications (B7.1, Para. 3).

TECHNICAL PAPERS

(Contents continued on inside back cover)

This journal is printed on acid-free paper, which exceeds the ANSI Z39.48-1992 specification for permanence of paper and library materials. ∞™
♻ 85% recycled content, including 10% post-consumer fibers.

Journal of Applied Mechanics Volume 69, Number 5 SEPTEMBER 2002

BRIEF NOTES

DISCUSSION

ERRATUM

ANNOUNCEMENTS AND SPECIAL NOTES

Journal of Applied Mechanics

Editorial

This editorial gives me an opportunity to introduce myself as the new editor of the *Journal of Applied Mechanics*. I succeed Lewis Wheeler who served almost ten years at the head of the Journal. On its behalf, I wish to extend thanks to him for his long service during which the *Journal of Applied Mechanics* has stayed at the forefront of its area and maintained its position as one of the leading periodicals in the fields of engineering.

During Professor Wheeler's term of service, important innovations were introduced. These changes will make it even more attractive for the applied mechanics community to publish its best work in the Journal. The length limit for papers has been increased to 9 journal pages, approximately 9,000 words. This increase from the previous level of 6 pages became effective some time ago and is applicable to any paper now submitted to the Journal. The board of Associate Editors and the Division of Applied Mechanics is convinced that this increase in the length limit will enable the journal to publish papers in a more effective format and to allow it to attract a greater diversity of excellent papers in areas where it was previously difficult to fit within the Journal's length constraints. Not least, the new length limit will enhance the Journal's ability to attract the best papers in the fields of applied mechanics and therefore will help maintain its leading position.

The Journal now publishes bimonthly and the time between the submission of a paper and its publication has improved dramatically. The Journal can now achieve publication of a paper in as little as 10 months after it has been first received at the editorial office, as can be confirmed by the submission dates in the May, 2002 issue. The bimonthly format also results in the Journal appearing on library shelves and on desks more frequently, commanding the attention of those working in the fields of applied mechanics more often each year. This publishing schedule makes the *Journal of Applied Mechanics* a more compelling habit on the part of its readers and a better vehicle for the publication of the best work in our field.

Another innovation that has been introduced is that special collections of papers will be assembled by editorial teams composed of Associate and Guest editors. The first of these on the nanomechanics of surfaces and interfaces, edited by Demitris Kouris and Huajian Gao, has already appeared in the July 2002 issue. These special collections will focus the attention of Journal readers on topical issues in applied mechanics and will be used to highlight important trends and developments in the fields relevant to the *Journal of Applied Mechanics*.

The typesetting, graphics and printing of the Journal have been improved. This has given the papers in the Journal a more professional appearance, so that authors can be better satisfied about how their work is being presented to the world. These benefits are not simply cosmetic; as a consequence of the changes, authors are now able to present information and data more clearly and with greater effectiveness in experimental papers and in the form of computer-generated graphics.

These improvements will encourage authors to continue to send their best work to the *Journal of Applied Mechanics*. In my period of being editor, I will endeavor to ensure that the Journal capitalizes on these changes and maintains its position as one of the leading periodicals in the field of applied mechanics. With advice from authors, the board of Associate Editors and the leadership and membership of the ASME Division of Applied Mechanics, I will seek further innovations in the Journal to improve its overall effectiveness, its attractiveness to potential authors and its significance and importance among its readership. This, I hope, will include a growth within the Journal of emerging areas of importance in applied mechanics and a broadening of the coverage of cross-disciplinary fields connected to them. We will also be considering improvements to the handling of manuscripts and reviews by electronic means to improve the efficiency of the process and to ease the work of authors, reviewers and Associate Editors while ensuring that the Journal remains the vehicle of choice for the best work in applied mechanics.

For me, it is a great honor to be appointed Editor of the *Journal of Applied Mechanics*. I follow in the footsteps of many distinguished individuals who have served before me in this position, such as the first Technical Editor, John Lessells, and his joint successors, Dan Drucker and Joe Kestin. It is my hope that I will succeed as well as my predecessors in my stewardship of the Journal and carry out my responsibilities as Editor in a way that makes the Journal stronger and more effective. In all this, though, the *Journal of Applied Mechanics*, the board of Associate Editors and I need the support of the community of applied mechanics in the form of the submission of its best papers and its willingness to carry out reviews of papers under consideration for publication. We hope that our efforts in the coming years will merit that support and together we can assure that the *Journal of Applied Mechanics* continues to be the leading publication for the field of applied mechanics.

Robert M. McMeeking

J. E. Bischoff
Department of Engineering Science,
University of Auckland,
Auckland, New Zealand
e-mail: j.bischoff@Auckland.ac.nz

E. A. Arruda[1]
Associate Professor,
Mem. ASME
e-mail: arruda@umich.edu

K. Grosh
Associate Professor,
Mem. ASME
e-mail: grosh@umich.edu

Department of Mechanical Engineering,
University of Michigan,
Ann Arbor, MI 48109-2125

A Microstructurally Based Orthotropic Hyperelastic Constitutive Law

A constitutive model is developed to characterize a general class of polymer and polymer-like materials that displays hyperelastic orthotropic mechanical behavior. The strain energy function is derived from the entropy change associated with the deformation of constituent macromolecules and the strain energy change associated with the deformation of a representative orthotropic unit cell. The ability of this model to predict nonlinear, orthotropic elastic behavior is examined by comparing the theory to experimental results in the literature. Simulations of more complicated boundary value problems are performed using the finite element method. [DOI: 10.1115/1.1485754]

1 Introduction

Many engineering materials such as wood and fiber-reinforced composites, as well as biological tissues such as cardiac tissue and skin, demonstrate anisotropic elasticity due to the presence of one or more preferred directions in the microstructure of the material. The degree of anisotropy is dependent on the preferred directions and can be orthotropic (for some biological tissues, for example) or transversely isotropic (fiber-reinforced composites) depending on the microstructural symmetries. Additionally, the anisotropy can vary within the material as the orientation of the fibers changes. Anisotropic materials that undergo small deformations can generally be modeled using conventional anisotropic linear elasticity. However, for rubbery elastic anisotropic materials such as collagenous biological tissues that can undergo large deformations and exhibit nonlinear elasticity, a different constitutive model must be used.

Attempts to model orthotropic hyperelasticity are primarily motivated by observed orthotropic, nonlinear behavior in human tissue, such as skin ([1,2]) and heart tissue ([3–6]). The load-deformation responses of each of these tissues show similar characteristics: an initial low-stiffness region, followed by a dramatically increased stiffness at higher stretches and a finite extensibility. Additionally, responses to deformation in each of the three principal material directions as determined from the fibrous structure differ in terms of the initial stiffness and the extensibility.

Early models of orthotropic hyperelasticity considered the strain energy function to be a polynomial function of suitable large strain measures, such as the components of the Lagrangian strain tensor ([3]). That is, for planar deformation,

$$W=W(E_{11},E_{22},E_{12})=\sum_{i,j,k} c_{ijk}E_{11}^{i}E_{22}^{j}E_{12}^{k} \tag{1}$$

where c_{ijk} are constants; *i*, *j*, and *k* sum over as large a range as necessary to capture the data; and E_{11}, E_{22}, and E_{12} are the in-plane components of the Lagrangian strain tensor. More recently, the polynomial function has been used as the argument Q in the strain energy function $W=c(\exp^{Q}-1)$ where c is a constant ([4]). In both cases, the strain energy function is strictly phenomenological. However, due to its simple analytic form, this model has been used as a basis for investigating other mechanical characteristics such as growth ([5]) and as the constitutive model in finite element analyses of structures such as blood vessels ([6]).

An example of a strain energy function that is more microstructurally based is one that sums an isotropic term that reflects the response of the isotropic ground substance and an anisotropic term that isolates the stretch along the principal material axis of the fibrous network and provides an increased stiffness to this component of the deformation ([7]). This decomposition can be represented as

$$W=W_1(I_1,I_2,I_3)+W_2(I_4,I_5) \tag{2}$$

where I_1, I_2, and I_3 are the invariants of the right Cauchy-Green tensor $\mathbf{C}$, $I_4=\mathbf{N}\cdot\mathbf{C}\cdot\mathbf{N}$, $I_5=\mathbf{N}\cdot\mathbf{C}^2\cdot\mathbf{N}$, and $\mathbf{N}$ is a unit vector that gives the orientation of the fibers through the continuum. More recently, investigators have reduced the number of invariants necessary to model tissue (for example, the dependence of the material response on the invariants I_2 and I_5 is generally weak and hence these invariants are not included in the strain energy function), as well as proposed forms of the functions W_1 and W_2 ([8]).

A microstructurally based model of a different form was first introduced by Lanir [2]. In his initially proposed model ([2]) and in subsequent refinements ([9–11]), the constituent fiber or fibers are treated as elastic fibers that can only maintain tensile loads. A distribution function for the unstretched lengths of the fibers in the continuum exists such that some fibers are slack in the undeformed configuration and can be distended without resistance. This distribution, coupled with a distribution of the orientation of the fibers within the planar section, allows for a bulk nonlinear response even when the constituent fibers themselves are modeled as linearly elastic. The strain energy function for such a model is

$$W=W(f_k(\lambda),R_k(\mathbf{n}),P_k(x)) \tag{3}$$

where $f_k(\lambda)$ is the response of an individual fiber of type k to a stretch λ along its length, $R_k(\mathbf{n})$ is the orientation distribution function for fibers of type k where $\mathbf{n}$ is a unit vector tangent to the fibers, and $P_k(x)$ is the probability that a fiber of type k first bears load at length x (that is, the fiber is fully uncrimped at a length x). These models have been successful in modeling both the nonlinear, locking behavior of tissue as well as the orthotropic mechanical response.

The model presented here uses a network microstructure to formulate a representative orthotropic unit cell. Unlike previous

[1]To whom correspondence should be addressed.

Contributed by the Applied Mechanics Division of THE AMERICAN SOCIETY OF MECHANICAL ENGINEERS for publication in the ASME JOURNAL OF APPLIED MECHANICS. Manuscript received by the ASME Applied Mechanics Division, January 15, 2001; final revision, September 11, 2001. Associate Editor: K. R. Rajagopal. Discussion on the paper should be addressed to the Editor, Professor Robert M. McMeeking, Department of Mechanical and Environmental Engineering University of California–Santa Barbara, Santa Barbara, CA 93106-5070, and will be accepted until four months after final publication of the paper itself in the ASME JOURNAL OF APPLIED MECHANICS.

models, the constituent fibers are treated from a statistical mechanics perspective such that the corresponding parameters possess physical meaning. Also, in contrast to other models involving an agglomeration of chains, here the fibers are connected in a network and thus *network* properties are also reflected in the model parameters. This paper will describe the development of the model, its predicted response to simple deformation states, and its response to inhomogeneous deformations using the finite element method.

2 Constitutive Model Development

To develop an orthotropic hyperelastic constitutive law based on the macromolecular microstructure of a material, a three-step process is employed: (1) model the constitutive response of a single macromolecule (chain); (2) develop the constitutive response for a representative unit cell composed of several chains; and (3) homogenize the unit cell into a three-dimensional, continuum constitutive model allowing for near incompressibility. The strain energy function W that results may be decomposed as

$$W = W_{\text{entropy}} + W_{\text{repulsion}} + W_{\text{bulk}} \tag{4}$$

where W_{entropy} is due to the configurational entropy of the unit cell, $W_{\text{repulsion}}$ is due to the interchain repulsive forces in the unit cell, and W_{bulk} is a bulk strain energy function used to enforce near incompressibility. The first two terms are attributed to the response of the underlying anisotropic fibrous network whereas W_{bulk} is attributed to the isotropic interstitial fluid or ground substance.

2.1 Mechanical Response of a Single Fiber. The mechanical response of various macromolecules, including biological molecules like titin ([12,13]), tenascin ([14]), and DNA ([9,15]), has been successfully modeled by using entropy-based constitutive laws. Additionally, the entropy changes associated with the deformation of a macromolecule have been the basis of several network models of rubber elasticity ([16–18]). For these reasons, an entropy-based constitutive law is used here to model the individual fibers in the unit cell.

Both Gaussian and non-Gaussian (Langevin) statistics have been used to develop models for elastic macromolecules by assuming they are freely jointed chains. Since large-deformation (non-Gaussian) behavior will be considered here, Langevin statistics will be used. Details about the use of statistical mechanics to model macromolecules can be found elsewhere ([10]); a summary will be presented here.

A macromolecule can be modeled as N freely jointed rigid links each of length l. (Note that the parameter N is a statistical quantity and its value will depend not only on the number of bonds in the backbone of the molecule but on the number of conformations available to the bonds as well. As such, N is not a parameter that can be measured directly, but it can be related to measurements of crosslink density and crosslink-to-crosslink chain length, for instance.) The increase in strain energy associated with deforming a molecule from its undeformed vector length $\mathbf{R}$ to its deformed vector length $\mathbf{r}$ (Fig. 1) can be calculated from the entropy difference between the two states. A molecule with one end fixed at the origin and the other end located in a volume dv at a location $\mathbf{r}$ has a configurational entropy proportional to the number of ways it can occupy space with its ends so fixed, given by $s = k\ln[p(\mathbf{r})dv]$ where $k = 1.38\cdot 10^{-23}$ J/K is Boltzmann's constant and $p(\mathbf{r})$ is the probability that the end of the chain is located in the volume dv at $\mathbf{r}$. The increase in strain energy associated with the deformation of the chain from an undeformed chain vector $\mathbf{R}$ to a deformed chain vector $\mathbf{r}$ is

$$\Delta w = -\Theta\Delta s = -k\Theta \ln\left[\frac{p(\mathbf{r})dv}{p(\mathbf{R})dV}\right] \tag{5}$$

where Θ is absolute temperature and dV is the volume initially occupied by the end of the chain.

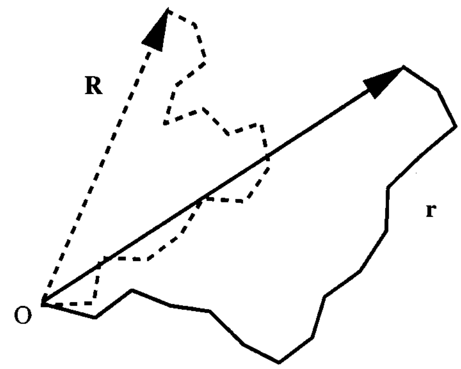

Fig. 1 The freely-jointed chain approximation of a macromolecule as a series of rigid links, with one end pinned at the origin *O* and the other end located by the chain vector R in its reference configuration and by the chain vector r in its deformed configuration

Following the method of Kuhn and Grün [11] for freely jointed chains, the non-Gaussian probability density function is given in logarithmic form by

$$\ln p(r) = p_0 - N\left(\frac{r}{Nl}\beta_r + \ln\frac{\beta_r}{\sinh\beta_r}\right) \tag{6}$$

where p_0 is a constant, $r = |\mathbf{r}|$, $\beta_r = \mathcal{L}^{-1}(r/Nl)$, and $\mathcal{L}(x) = \coth x - 1/x$ is the Langevin function. Assuming no volume change due to entropy such that $dv = dV$, the strain energy change accompanying deformation for a single chain is given by

$$\Delta w(r) = k\Theta N\left[\left(\frac{r}{Nl}\beta_r + \ln\frac{\beta_r}{\sinh\beta_r}\right) - \left(\frac{R}{Nl}\beta_R + \ln\frac{\beta_R}{\sinh\beta_R}\right)\right] \tag{7}$$

where $\beta_R = \mathcal{L}^{-1}(R/Nl)$ and $R = |\mathbf{R}|$. Treating the rigid link l as a characteristic length, Eq. (7) can be recast as

$$\Delta w(\rho) = k\Theta N\left[\left(\frac{\rho}{N}\beta_\rho + \ln\frac{\beta_\rho}{\sinh\beta_\rho}\right) - \left(\frac{P}{N}\beta_P + \ln\frac{\beta_P}{\sinh\beta_P}\right)\right] \tag{8}$$

where $\rho = r/l$ is the normalized deformed chain length, $\beta_\rho = \mathcal{L}^{-1}(\rho/N)$, $P = R/l$ is the normalized undeformed chain length, and $\beta_P = \mathcal{L}^{-1}(P/N)$. Normalization of length quantities by l will be consistently maintained throughout the remainder of this work and as such an explicit statement that length quantities introduced later are normalized by l will be dropped.

It is common practice in entropy-based models to assume the undeformed length of a chain to be equal to its root mean square (rms) length, such that $P/N = 1/\sqrt{N}$ ([19,20]). With this assumption, the nonlinear form of Δw as a function of ρ/N as given in Eq. (8) is shown in Fig. 2 for various values of N. Note that as N increases (from $N = 50$ to $N = 200$), the rms chain length decreases ($1/\sqrt{N} = 0.14$ to $1/\sqrt{N} = 0.07$). Negative values of Δw indicate that the strain energy decreases at lengths shorter than the rms (reference) length. The selection of a value of P/N different from the rms length would vertically shift the curves in Fig. 2 but negative values of Δw would still exist for $\rho/N < P/N$ and Δw would remain a monotonically increasing function of ρ/N. Since a chain is stress free at a length for which the strain energy is minimized, a chain at any nonzero length (including its assumed undeformed length P provided $P \neq 0$) will not be stress free, regardless of its reference length. Thus, it is not sufficient to develop a strain energy function based solely on the effects of isovolumetric entropy changes and additional contributions to the strain energy function are necessary.

The freely-jointed chain approximation, used to derive the strain energy change associated with the deformation of a single

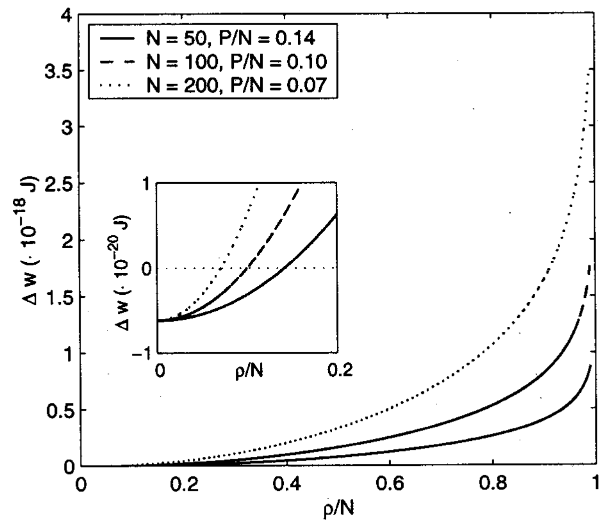

Fig. 2 The change in strain energy accompanying deformation of a single macromolecular chain from its rms length. Inset: a close-up of the curves near their respective rms lengths, showing that a decrease in chain length below the reference rms length results in a decrease in strain energy.

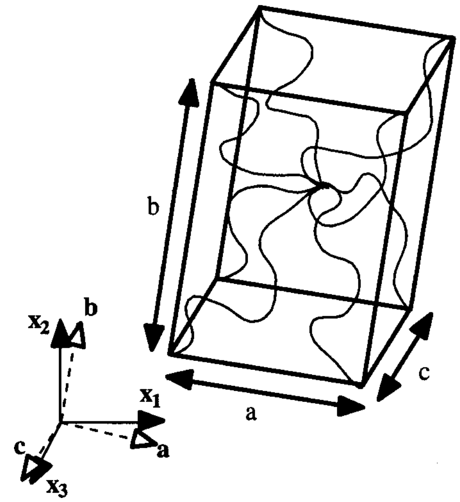

Fig. 3 Eight-chain, three-dimensional orthotropic unit cell. The eight curved lines in the unit cell represent the constituent macromolecules and the straight lines represent the boundaries of the unit cell. The cell has dimensions $a \times b \times c$ along the material axes a, b, c, respectively, oriented with respect to the reference coordinate system X_i.

chain given in Eq. (8), is one statistical representation of a macromolecule. However, other models exist that can similarly characterize the mechanics of single chains. For example the wormlike chain (WLC) model, another entropy-based constitutive model, has been successfully used to model long chain molecules like titin ([13]) and DNA ([9]). As such, other chain models such as the WLC model could be used in place of the freely-jointed chain approximation to develop the ensuing network constitutive law. However, provided the constitutive responses that are predicted from these chain models are similar to that of the freely-jointed chain model (which is true for the WLC model), the differences resulting from using these models versus the freely-jointed chain model in a network constitutive model will not be significant ([21]).

2.2 Orthotropic Unit Cell. Constitutive theories for initially isotropic rubbery materials have been developed using a variety of unit cells, including a three-chain model [22] a four-chain model [23], and the more recent eight-chain [16] model. These models allow for the rotation of the unit cell in space such that the principal stretches are applied along fixed cell directions. The orientation of the principal stresses and stretches, coupled with the geometry of the unit cells, insures isotropy of the initial mechanical response with respect to principal stretch space.

To incorporate the chain statistics into a unit cell that allows for the initial orthotropy of a network with a preferred fiber orientation, an eight-chain orthotropic unit cell is used as shown in Fig. 3. Orthotropy of the mechanical response of this unit cell results from two properties: the fixed orientation of the unit cell in space (as specified by the orthogonal principal material axes **a**, **b**, and **c** rotated relative to the reference coordinate system $\mathbf{X}_i$) and the "dimensions" a, b, and c along the axes **a**, **b**, and **c**, respectively (these "dimensions" are actually dimensionless as they have been normalized by l). Accordingly, the vector descriptions $\mathbf{P}^{(i)}$ of each of the chains in the undeformed unit cell where the superscript $i = 1 \ldots 8$ denotes the chain number are

$$\mathbf{P}^{(1)} = -\mathbf{P}^{(5)} = \frac{a}{2}\mathbf{a} + \frac{b}{2}\mathbf{b} + \frac{c}{2}\mathbf{c};$$

$$\mathbf{P}^{(2)} = -\mathbf{P}^{(6)} = \frac{a}{2}\mathbf{a} + \frac{b}{2}\mathbf{b} - \frac{c}{2}\mathbf{c};$$

$$\mathbf{P}^{(3)} = -\mathbf{P}^{(7)} = \frac{a}{2}\mathbf{a} - \frac{b}{2}\mathbf{b} + \frac{c}{2}\mathbf{c};$$

$$\mathbf{P}^{(4)} = -\mathbf{P}^{(8)} = \frac{a}{2}\mathbf{a} - \frac{b}{2}\mathbf{b} - \frac{c}{2}\mathbf{c}. \tag{9}$$

The length P of each undeformed chain is

$$P = \frac{1}{2}\sqrt{a^2 + b^2 + c^2}. \tag{10}$$

Because the undeformed lengths of each of the eight chains are equivalent and because it is assumed that the undeformed length of each chain is the rms length of the chain ($P = \sqrt{N}$), a constraint is established between the chain parameter N and the unit cell aspect ratios,

$$\sqrt{N} = \frac{1}{2}\sqrt{a^2 + b^2 + c^2}. \tag{11}$$

This constraint follows from a consistent normalization of all length quantities by l and means that larger values of a, b, and c necessarily reflect constituent chains with a larger number of rigid links.

Assuming an affine deformation, that is that the ends of the chains are fixed in the continuum and deform with the continuum (Lagrangian) strain field $\mathbf{E}$, the deformed lengths $\rho^{(i)}$ of the individual chains are

$$\rho^{(i)} = \sqrt{\mathbf{P}^{(i)T} \cdot \mathbf{C} \cdot \mathbf{P}^{(i)}} \tag{12}$$

where $\mathbf{C} = 2\mathbf{E} + \mathbf{I}$ is the right Cauchy-Green tensor and $\mathbf{I}$ is the identity tensor. Terms of this form satisfy material frame indifference on inspection since they are dependent on the deformation only through the Lagrangian strain tensor. Note that following Spencer [17], the invariants for a material with four families of reinforcing fibers oriented along the nonnormalized directions $\mathbf{P}^{(1)} - \mathbf{P}^{(4)}$ include $I_{\mathbf{P}^{(i)}\mathbf{P}^{(j)}} = \mathbf{P}^{(i)T} \cdot \mathbf{C} \cdot \mathbf{P}^{(j)} / P^2$ for $i, j = 1 \ldots 4$. The deformed lengths $\rho^{(i)}$ are functions of these invariants and thus satisfy the symmetry requirements given by Spencer [17].

The strain energy of the unit cell due to configurational entropy changes is the sum of the strain energies of the individual chains. Noting that from Eqs. (9) and (12) the deformed length of a chain $\mathbf{P}^{(1-4)}$ is equivalent to the deformed length of the corresponding chain $\mathbf{P}^{(5-8)}$, the strain energy w of the unit cell resulting from the entropy change associated with stretching the eight constituent chains is

$$w_{\text{entropy}}=w_0+2k\Theta N\sum_{i=1}^{4}\left[\frac{\rho^{(i)}}{N}\beta_\rho^{(i)}+\ln\frac{\beta_\rho^{(i)}}{\sinh\beta_\rho^{(i)}}\right] \tag{13}$$

where w_0 is a constant related to the nonzero entropy of the undeformed chains (thus allowing Eq. (13) to be written in terms of w_{entropy} as opposed to $\Delta w_{\text{entropy}}$) and $\beta_\rho^{(i)}=\mathcal{L}^{-1}[\rho^{(i)}/N]$. Because w_{entropy} is dependent on the deformation only through $\rho^{(i)}$, this strain energy function satisfies material frame indifference.

The strain energy function w_{entropy} is minimized when $\rho^{(i)}=0$, consistent with the previous discussion of Fig. 2, and thus the stress-free configuration of the unit cell when considering only the entropic contributions of the constituent chains to the strain energy is not the reference configuration. To enforce the previous assumption that the reference length of each constituent chain is equal to its rms length and establish a stress-free finite-volume unit cell composed of eight chains at their rms lengths, an additional term in the strain energy function is needed. This term is denoted $w_{\text{repulsion}}$ since it reflects a mutual repulsion of chains from each other that will prevent the entropic collapse of the unit cell while maintaining the orthotropic shape of the unit cell. A similar reasoning has been used previously to prevent the predicted entropic collapse of isotropic compressible rubbery elastic materials by including a term of the form $c_0 \ln \lambda_1\lambda_2\lambda_3$ in the strain energy function where c_0 is a constant and λ_i are the principal stretches ([18]). Accordingly, the orthotropic strain energy function here is augmented by the term

$$w_{\text{repulsion}}=-\frac{8k\Theta\sqrt{N}\beta_P}{a^2+b^2+c^2}\ln(\lambda_{\mathbf{a}}^{a^2}\lambda_{\mathbf{b}}^{b^2}\lambda_{\mathbf{c}}^{c^2}) \tag{14}$$

where $\lambda_{\mathbf{a}}=\sqrt{\mathbf{a}^T\cdot\mathbf{C}\cdot\mathbf{a}}$, $\lambda_{\mathbf{b}}=\sqrt{\mathbf{b}^T\cdot\mathbf{C}\cdot\mathbf{b}}$, and $\lambda_{\mathbf{c}}=\sqrt{\mathbf{c}^T\cdot\mathbf{C}\cdot\mathbf{c}}$ represent the stretches along the principal material axes. The coefficient in $w_{\text{repulsion}}$ allows for a finite-volume stress-free reference state while the functional dependence on $\lambda_{\mathbf{a}}^{a^2}\lambda_{\mathbf{b}}^{b^2}\lambda_{\mathbf{c}}^{c^2}$ allows for an orthotropic response of the unit cell. Note that $w_{\text{repulsion}}$ satisfies material frame indifference on inspection as it is dependent on the deformation through $\mathbf{E}$. Also, since the unit vectors $\mathbf{a}$, $\mathbf{b}$, and $\mathbf{c}$ can be written in terms of the fiber directions $\mathbf{P}^{(1)}-\mathbf{P}^{(4)}$ using Eq. (9), then $\lambda_{\mathbf{a}}$, $\lambda_{\mathbf{b}}$, and $\lambda_{\mathbf{c}}$ can be written in terms of the invariants $I_{\mathbf{P}^{(i)}\mathbf{P}^{(j)}}$ presented earlier and as proposed by Spencer [17] for materials reinforced by four classes of fibers. Finally, note that the effect of $w_{\text{repulsion}}$ on the total strain energy will be increasingly less significant as the material becomes more highly deformed as this is when the nonlinear strain hardening predicted by w_{entropy} is realized.

2.3 Homogenization and Bulk Compressibility. The unit cell above can be homogenized to form a macroscopic three-dimensional strain energy function. Assuming a fiber density per unit volume of n and noting there are eight chains per unit cell, the strain energy function per unit volume is

$$W(\mathbf{x})=\sum_{n/8} w(\mathbf{x})=\frac{n}{8}(w_{\text{entropy}}+w_{\text{repulsion}}). \tag{15}$$

Note that the parameters in the model (the chain density n and the unit cell dimensions a, b, and c) need not be constant but can vary with location $\mathbf{x}$.

The constitutive law above is overly compressible in practice. To allow for control over the compressibility of the material an isotropic bulk contribution

$$W_{\text{bulk}}=\frac{B}{\alpha^2}\{\cosh[\alpha(J-1)]-1\} \tag{16}$$

is appended to the strain energy function where $J=\det\mathbf{F}$ is the ratio of the deformed to the undeformed volume. This form of W_{bulk} was developed for modeling the compressibility of elastomers at finite deformations and was shown to capture the volume changes of several elastomers undergoing hydrostatic compression and uniaxial tension tests ([18]). There are two free parameters in this model, B and α; B controls the bulk compressibility near $J=1$ (no volume change) and α governs the curvature of the hydrostatic pressure versus volume curve for larger volume changes. As this term governs the bulk isotropic response of the material, it can be attributed to the response of the isotropic nearly incompressible ground substance that is present in orthotropic hyperelastic materials such as biological tissue.

The final form of the strain energy function is

$$W(\mathbf{x})=W_0+\frac{nk\Theta}{4}\left(N\sum_{i=1}^{4}\left[\frac{\rho^{(i)}}{N}\beta_\rho^{(i)}+\ln\frac{\beta_\rho^{(i)}}{\sinh\beta_\rho^{(i)}}\right]-\frac{\beta_P}{\sqrt{N}}\ln[\lambda_{\mathbf{a}}^{a^2}\lambda_{\mathbf{b}}^{b^2}\lambda_{\mathbf{c}}^{c^2}]\right)+\frac{B}{\alpha^2}\{\cosh[\alpha(J-1)]-1\} \tag{17}$$

where W_0 is a constant.

3 Continuum Mechanics Considerations

This constitutive law is developed consistent with the tenets of continuum mechanics as provided in detail elsewhere; conditions that must be met include material frame indifference and material symmetry ([24]). As stated previously, since the strain energy function is only dependent on the deformation state through the Lagrangian strain tensor $\mathbf{E}$ it satisfies objectivity (material frame indifference) on inspection. Additionally, it has been noted that the strain energy function W proposed here can be written as

$$W=\hat{W}(I_{\mathbf{P}^{(i)}\mathbf{P}^{(j)}},J) \tag{18}$$

where $(I_{\mathbf{P}^{(i)}\mathbf{P}^{(j)}},J)$ with i, $j=1\ldots4$ represents a subset of the invariants presented by Spencer for a material with four families of reinforcing fibers ([17]). However, this does not speak directly to the symmetry of materials for which this model is applicable as the symmetry is dependent on the relative orientations of the fiber families.

Towards this end, one approach that can be used to examine the implications of material symmetry has been developed by Smith and Rivlin, for example, ([25]) where orthogonal transformations of the material coordinate systems are considered. This approach is followed here, where the material coordinate system is defined by the principal material directions $\mathbf{a}$, $\mathbf{b}$, and $\mathbf{c}$.

Let $\mathbf{H}$ denote a coordinate transformation (such as rotation) that does not change the mathematical description of the microstructure of the material. For an isotropic material, this transformation could be any rotation. For the orthotropic material here defined by the material axes $\mathbf{a}$, $\mathbf{b}$, and $\mathbf{c}$, the set of symmetry transformations $\mathbf{H}_1$ is composed of any transformation that inverts one or several of the material axes such that

$$\mathbf{H}_1\begin{bmatrix}\mathbf{a}\\ \mathbf{b}\\ \mathbf{c}\end{bmatrix}=\begin{bmatrix}\pm\mathbf{a}\\ \pm\mathbf{b}\\ \pm\mathbf{c}\end{bmatrix}. \tag{19}$$

Note that a subset of these transformations includes 180-deg rotations about any of the three material axes. Also note that since $2\mathbf{P}^{(i)}=\pm a\mathbf{a}\pm b\mathbf{b}\pm c\mathbf{c}$, the set of invariants $I_{\mathbf{P}^{(i)}\mathbf{P}^{(j)}}$ with i, $j=1\ldots4$ that includes ten members can be reduced to a smaller set of invariants $I_{\mathbf{a}}=\mathbf{a}^T\cdot\mathbf{C}\cdot\mathbf{a}$, $I_{\mathbf{b}}=\mathbf{b}^T\cdot\mathbf{C}\cdot\mathbf{b}$, $I_{\mathbf{c}}=\mathbf{c}^T\cdot\mathbf{C}\cdot\mathbf{c}$, $I_{\mathbf{ab}}=\mathbf{a}^T\cdot\mathbf{C}\cdot\mathbf{b}$, $I_{\mathbf{ac}}=\mathbf{a}^T\cdot\mathbf{C}\cdot\mathbf{c}$, $I_{\mathbf{bc}}=\mathbf{b}^T\cdot\mathbf{C}\cdot\mathbf{c}$ that only has six members.

Since W_{bulk} is isotropic, its value is invariant to $\mathbf{H}_1$. On inspection $W_{\text{repulsion}}$ is also invariant to $\mathbf{H}_1$ because $W_{\text{repulsion}}=\hat{W}_{\text{repulsion}}(I_{\mathbf{a}},I_{\mathbf{b}},I_{\mathbf{c}})$ using the reduced set of invariants and $I_{\mathbf{a}}$, $I_{\mathbf{b}}$, and $I_{\mathbf{c}}$ are invariant to $\mathbf{H}_1$. To consider the effect on W_{entropy}, note that $\mathbf{H}_1$ effectively relabels the chains (1)–(4) given in Eq. (9). For example, the particular transformation $\mathbf{H}_1(\mathbf{a},\mathbf{b},\mathbf{c})$

$=(\mathbf{a},-\mathbf{b},\mathbf{c})$ relabels the chains as follows: $\mathbf{H}_1\mathbf{P}^{(1)}=\mathbf{P}^{(3)}$, $\mathbf{H}_1\mathbf{P}^{(2)}=\mathbf{P}^{(4)}$, $\mathbf{H}_1\mathbf{P}^{(3)}=\mathbf{P}^{(1)}$, $\mathbf{H}_1\mathbf{P}^{(4)}=\mathbf{P}^{(2)}$. Similar relations will hold for all other allowable transformations. Since W_{entropy} is dependent on each of the deformed chain lengths in the same way, the chains can be reordered without affecting W_{entropy}, and thus this term and the strain energy function W as a whole are invariant to $\mathbf{H}_1$. As such, this material model is applicable for *orthotropic* materials.

4 Examples

To explore the response of a material with the above constitutive law to various modes of deformation, the Cauchy stress tensor is calculated from the strain energy function. Towards this end, the second Piola-Kirchhoff stress tensor $\tilde{\mathbf{T}}=\partial W/\partial \mathbf{E}$ is given by

$$\tilde{T}_{jk}=\frac{nk\Theta}{4}\left[\sum_{i=1}^{4}\frac{P_j^{(i)}P_k^{(i)}}{\rho^{(i)}}\beta_\rho^{(i)}-\frac{\beta_P}{\sqrt{N}}\left(\frac{a^2}{\lambda_{\mathbf{a}}^2}a_j a_k+\frac{b^2}{\lambda_{\mathbf{b}}^2}b_j b_k+\frac{c^2}{\lambda_{\mathbf{c}}^2}c_j c_k\right)\right]+\frac{B}{\alpha}\sinh[\alpha(J-1)]\frac{\partial J}{\partial E_{jk}} \tag{20}$$

where

$$\frac{\partial J}{\partial E_{jk}}=\frac{\epsilon_{jyz}}{J}\delta_{1k}C_{y2}C_{z3}+\frac{\epsilon_{xjz}}{J}C_{x1}\delta_{2k}C_{z3}+\frac{\epsilon_{xyj}}{J}C_{x1}C_{y2}\delta_{3k}, \tag{21}$$

ϵ_{ijk} is a component of the permutation tensor, and δ_{ij} is a component of the second order identity tensor. The Cauchy stress tensor $\mathbf{T}$ can be calculated from the second Piola-Kirchhoff stress tensor as

$$\mathbf{T}=\frac{1}{J}\mathbf{F}\tilde{\mathbf{T}}\mathbf{F}^T \tag{22}$$

where $\mathbf{F}$ is the deformation gradient.

For the following analytic studies the principal material axes will be aligned with the coordinate axes $\mathbf{X}_1$, $\mathbf{X}_2$, and $\mathbf{X}_3$. Small volume changes will be assumed and thus α, the material parameter that governs the hydrostatic pressure versus volume curvature for large volume changes, is set equal to unity. Additionally, the deformations will all be triaxial deformation (no shear) such that the deformation gradient is

$$\mathbf{F}=\begin{bmatrix}\lambda_1 & 0 & 0\\ 0 & \lambda_2 & 0\\ 0 & 0 & \lambda_3\end{bmatrix}. \tag{23}$$

Accordingly, the Cauchy stresses are

$$T_{11}=\frac{nk\Theta a^2}{4J}\left[\frac{\lambda_1^2\beta_\rho}{\rho}-\frac{\beta_P}{\sqrt{N}}\right]+B\sinh(J-1)$$

$$T_{22}=\frac{nk\Theta b^2}{4J}\left[\frac{\lambda_2^2\beta_\rho}{\rho}-\frac{\beta_P}{\sqrt{N}}\right]+B\sinh(J-1)$$

$$T_{33}=\frac{nk\Theta c^2}{4J}\left[\frac{\lambda_3^2\beta_\rho}{\rho}-\frac{\beta_P}{\sqrt{N}}\right]+B\sinh(J-1) \tag{24}$$

where $\rho=\sqrt{a^2\lambda_1^2+b^2\lambda_2^2+c^2\lambda_3^2}/2$ and β_ρ and β_P are as defined before.

4.1 Uniaxial Deformation. The above equations can be used to predict the model's response in uniaxial tension by setting $T_{22}=T_{33}=0$ and solving those two coupled equations for the transverse stretches λ_2 and λ_3 given an applied stretch λ_1. An efficient way of solving for these stretches is to introduce two new variables,

$$X=b^2\lambda_2^2+c^2\lambda_3^2$$

$$Y=b^2\lambda_2^2-c^2\lambda_3^2. \tag{25}$$

The constitutive equations $T_{22}=0$ and $T_{33}=0$ from Eq. (24) can then be decoupled by taking $T_{22}+T_{33}=0$ and $T_{22}-T_{33}=0$, giving

$$T_{22}+T_{33}=\frac{nk\Theta}{4J}\left[\frac{X\beta_\rho}{\rho}-\frac{(b^2+c^2)\beta_P}{\sqrt{N}}\right]+2B\sinh(J-1)=0$$

$$T_{22}-T_{33}=\frac{Y\beta_\rho}{\rho}-\frac{(b^2-c^2)\beta_P}{\sqrt{N}}=0 \tag{26}$$

where $J=\lambda_1\sqrt{X^2-Y^2}/2bc$ and $\rho=\sqrt{a^2\lambda_1^2+X}/2$. The equation $T_{22}-T_{33}=0$ can be manipulated to give

$$Y(X)=\frac{\beta_P(b^2-c^2)\rho}{\beta_\rho\sqrt{N}} \tag{27}$$

and the equation $T_{22}+T_{33}=0$ can then be solved for X. The transverse stretches are calculated to be $\lambda_2=\sqrt{(X+Y)/2b^2}$ and $\lambda_3=\sqrt{(X-Y)/2c^2}$.

Using the above formulation, the predicted response of the constitutive law under uniaxial tension is shown in Fig. 4 for two different sets of aspect ratios: (1) $a=2$, $b=3$, $c=4$; and (2) $a=1.8$, $b=3.124$, $c=4$. Simulations were performed for uniaxial deformation along each of the three coordinate axes, denoted $\mathbf{X}_1$, $\mathbf{X}_2$, and $\mathbf{X}_3$ in the figure. All simulations were performed using $n=8\cdot 10^{24}/\text{m}^3$, $N=7.25$, and $B=1$ MPa. From this figure, it is apparent that nonunity aspect ratios give rise to an orthotropic response since for a given set of aspect ratios the deformation is stiffest along the direction with the longest dimension ($\mathbf{X}_3$ for these simulations) and most compliant along the direction with the smallest dimension ($\mathbf{X}_1$). Additionally, holding the locking stretch constant while increasing the value of one of the unit cell dimensions (a) stiffens the response of the material in that direction ($\mathbf{X}_1$) while making the response in the transverse direction ($\mathbf{X}_2$) whose dimension (b) was decreased more compliant. Since c was held constant for the two sets of simulations, the response in the $\mathbf{X}_3$ direction did not noticeably change.

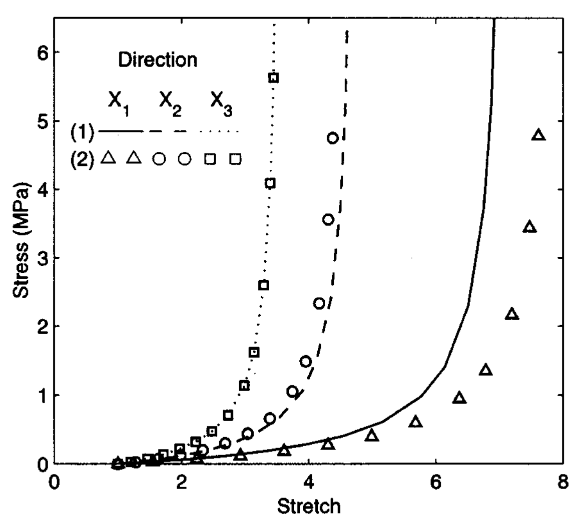

Fig. 4 Response of the orthotropic eight-chain model to uniaxial deformation in each of three directions ($\mathbf{X}_1$,$\mathbf{X}_2$,$\mathbf{X}_3$) for two sets of aspect ratios: (1) $a=2$, $b=3$, $c=4$, and (2) $a=1.8$, $b=3.124$, $c=4$. The material axes are mutually orthogonal and aligned with the coordinate axes. All simulations were performed using parameters $n=8\cdot 10^{24}/\text{m}^3$, $N=7.25$, and $B=1$ MPa.

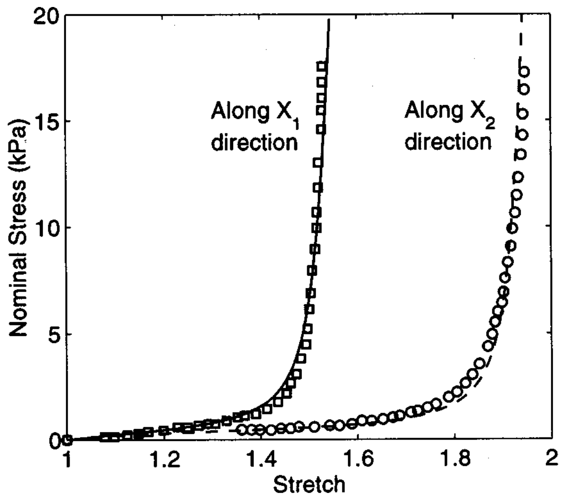

Fig. 5 Data from uniaxial tests on rabbit skin from Lanir and Fung [1] and the corresponding fits using the orthotropic model. Data are represented by symbols and the fits by solid lines. The parameters used to fit the data are $n=3.75\cdot10^{22}/\mathrm{m}^3$, $N=1.25$, $B=50$ kPa, $a=1.37$, $b=1.015$, and $c=1.447$.

The anisotropic hyperelastic mechanical response of biological soft tissue such as skin and heart tissue is often attributed to the underlying collagenous network in the tissue ([2,26,27]) and thus the microstructural model developed here is readily applicable to modeling the mechanical behavior of these materials. Accordingly, the model was used to fit data taken from in vitro uniaxial tests on rabbit skin in which lateral contraction was constrained ([1]), the results are shown in Fig. 5. The tests were performed along two mutually orthogonal material directions ($\mathbf{X}_1$ and $\mathbf{X}_2$). Prior to testing the specimens were allowed to completely relax ([1]) and thus the orthotropy of the response is solely due to material orthotropy. In the figure, data are represented by symbols and the theory by solid lines. The parameters used to fit the data are $n=3.75\cdot10^{22}/\mathrm{m}^3$, $N=1.25$, $B=50$ kPa, $a=1.37$, $b=1.015$, and $c=1.447$. Since $a>b$ the fibers are preferentially aligned along the $\mathbf{X}_1$-axis, resulting in a stiffer response and earlier locking in that direction as compared to the $\mathbf{X}_2$-direction.

4.2 Biaxial Deformation. Biaxial deformation analyses are conducted in which the material axes are aligned with the applied loads such that there are no shear stresses. Recent biaxial tests on aortic valve cusps ([28]) have been conducted at a constant ratio F_r of the applied forces in two mutually orthogonal material directions with no applied force in the third direction and this protocol will be followed here. The applied loads $F_1=T_{11}A_{23}^0\lambda_2\lambda_3$ and $F_2=T_{22}A_{13}^0\lambda_1\lambda_3$ (where A_{23}^0 and A_{13}^0 are the initial values of the corresponding cross-sectional areas) are controlled and related to each other by the ratio $F_r=F_2/F_1$ and the stretches λ_1 and λ_2 in the directions of the applied stresses as well as the out-of-plane stretch λ_3 must be calculated.

The three constitutive equations

$$f_1=\frac{nk\Theta a^2A_{23}^0}{4}\left[\frac{\beta\lambda_1^2}{\rho}-\frac{\beta_P}{\sqrt{N}}\right]+BJA_{23}^0\sinh(J-1)-F_1\lambda_1=0$$

$$f_2=\frac{nk\Theta b^2A_{13}^0}{4}\left[\frac{\beta\lambda_2^2}{\rho}-\frac{\beta_P}{\sqrt{N}}\right]+BJA_{13}^0\sinh(J-1)-F_rF_1\lambda_2=0$$

$$f_3=\frac{nk\Theta c^2A_{12}^0}{4}\left[\frac{\beta\lambda_3^2}{\rho}-\frac{\beta_P}{\sqrt{N}}\right]+BJA_{12}^0\sinh(J-1)=0 \quad (28)$$

are numerically solved simultaneously for the stretches λ_1, λ_2, and λ_3, given a value of F_1. A modified Newton-Raphson algorithm was used that requires the derivatives of λ_j with respect to f_i in order to estimate the stretches at each step according to the relations

$$\lambda_j^{(i+1)}=\lambda_j^{(i)}+\left(\frac{\partial\lambda_j}{\partial f_k}\right)^{(i)}[f_k^{(i+1)}-f_k^{(i)}]\epsilon \quad (29)$$

where $\epsilon<1$ is a relaxation parameter used to avoid overshoot.

The above algorithm was used to simulate load-controlled biaxial tension for various values of the stress ratio F_r assuming all initial cross-sectional areas to be equal to unity; results are shown in Fig. 6. All parameters other than F_r were held constant in the simulations: $n=8\cdot10^{24}/\mathrm{m}^3$, $N=2$, $B=40$ MPa, $a=1.2$, $b=1.5$, and $c=2.076$. Figure 6(a) shows the T_{11} versus λ_1 response and Fig. 6(b) shows the T_{22} versus λ_2 response for a given value of F_r. For larger values of F_r, the response in the $\mathbf{X}_2$-direction becomes more compliant and locks at a higher stretch whereas the response in the $\mathbf{X}_1$-direction stiffens and locks at a smaller stretch.

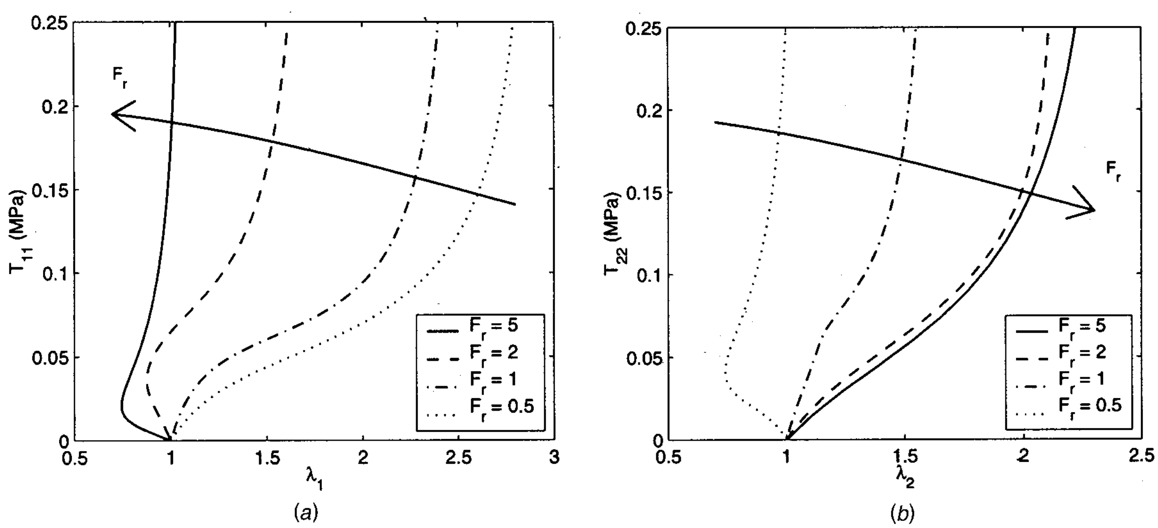

Fig. 6 Simulations of load-controlled biaxial tension for various values of the load ratio F_r. Other parameters in the simulations were fixed: $n=8\cdot10^{24}/\mathrm{m}^3$, $N=2$, $B=40$ MPa, $a=1.2$, $b=1.5$, and $c=2.076$. Figure 6(a) shows the T_{11} versus λ_1 response and Fig. 6(b) shows the T_{22} versus λ_2 response for a given value of F_r.

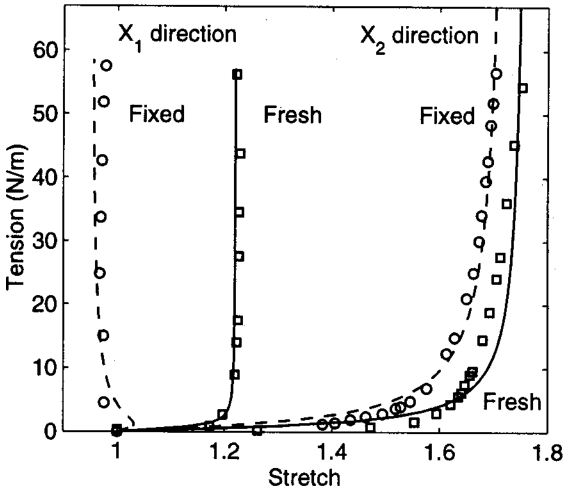

Fig. 7 Equibiaxial tension data from Billiar and Sacks [28] and corresponding fits using the orthotropic model. Data are plotted as symbols and represent the constitutive response for fresh and glutaraldehyde-fixed aortic valve cusp samples in the two material directions in which loads were applied. Fits are plotted as lines and were generated using the following parameters: for fresh tissue data, $n = 6 \cdot 10^{17}/m^3$, $N = 1.96$, $B = 100$ kPa, $a = 2.05$, $b = 1.7$, and $c = 0.865$; for fixed tissue data, $n = 7 \cdot 10^{17}/m^3$, $N = 1.48$, $B = 500$ kPa, $a = 1.85$, $b = 1.35$, and $c = 0.822$.

Of particular interest are the simulations for $F_r = 2$ and 5 where λ_1 initially decreases below unity, meaning the sample contracts in the $\mathbf{X}_1$-direction. However, as the stresses increase λ_1 begins to increase, reaching values greater than unity for larger stresses. This same phenomenon is observed in the $\mathbf{X}_2$-direction when $F_r = 0.5$ and is a consequence of the orthotropy of the material as an isotropic material would not show similar behavior.

The orthotropic behavior shown in Fig. 6 is qualitatively similar to data obtained from equibiaxial tension tests on fresh and glutaraldehyde-fixed aortic valve cusps performed by Billiar and Sacks [28]. This tissue is known to possess an anisotropic microstructure due to the preferred orientation of constituent fibers. Though the investigators attempted to align the test axes with the principal material axes, test results showed nontrivial shear strains which could be due to off-axis mounting ([28]) or material heterogeneity within the samples being tested. Nevertheless, the orthotropic model developed here was used to fit representative data from Billiar and Sacks assuming equibiaxial tension, homogeneity of the tissue samples, and perfect alignment of the test axes with the material axes. Data and fits are shown in Fig. 7 for fresh tissue and fixed tissue (data are shown with symbols and fits are shown with lines). Parameters used for the fits are as follows: for fresh tissue data, $n = 6 \cdot 10^{17}/\mathrm{m}^3$, $N = 1.96$, $B = 100$ kPa, $a = 2.05$, $b = 1.7$, and $c = 0.865$; for fixed tissue data, $n = 7 \cdot 10^{17}/\mathrm{m}^3$, $N = 1.48$, $B = 500$ kPa, $a = 1.85$, $b = 1.35$, and $c = 0.822$. Given the assumptions used to model the data, the qualitative agreement between the data and the theory is good; better results would likely be obtained with information about the shear strains present in the tests.

5 Finite Element Simulations

The constitutive law was incorporated into ABAQUS/Standard Version 5.8, a commercially available finite element software package produced by Hibbitt, Karlsson & Sorensen, Inc. [29], for simulation of more complex problems. A nonlinear orthotropic hyperelastic constitutive law can be incorporated into ABAQUS using the user subroutine UMAT, which allows the most flexibility in the material response. Needed in this subroutine are calculations for any given deformation gradient of the Cauchy stresses and the derivatives of the Cauchy stresses with respect to the Lagrangian strains. A 15-term series representation of the inverse Langevin function was used to save computational time in calculating these values and to avoid problems associated with the argument of the inverse Langevin function being greater than unity, for which values the inverse Langevin function is not defined.

To verify the incorporation of the constitutive law into ABAQUS (especially in view of possible convergence problems in the finite element code), single element simulations of uniaxial tension and biaxial tension were performed and compared to the numerical solutions. A single eight-noded three-dimensional linear brick element was used and the deformations were prescribed by assigning loads to individual nodes. Figure 8 shows comparisons between the finite element simulations and the numerical solutions for uniaxial tension using parameters $n = 2 \cdot 10^{24}/\mathrm{m}^3$, $N = 3$, $a = 2$, $b = 2.5$, $c = 1.32$, and $B = 1$ MPa. Figure 8*a* shows the stress-stretch response and Fig. 8(*b*) shows the variations of the trans-

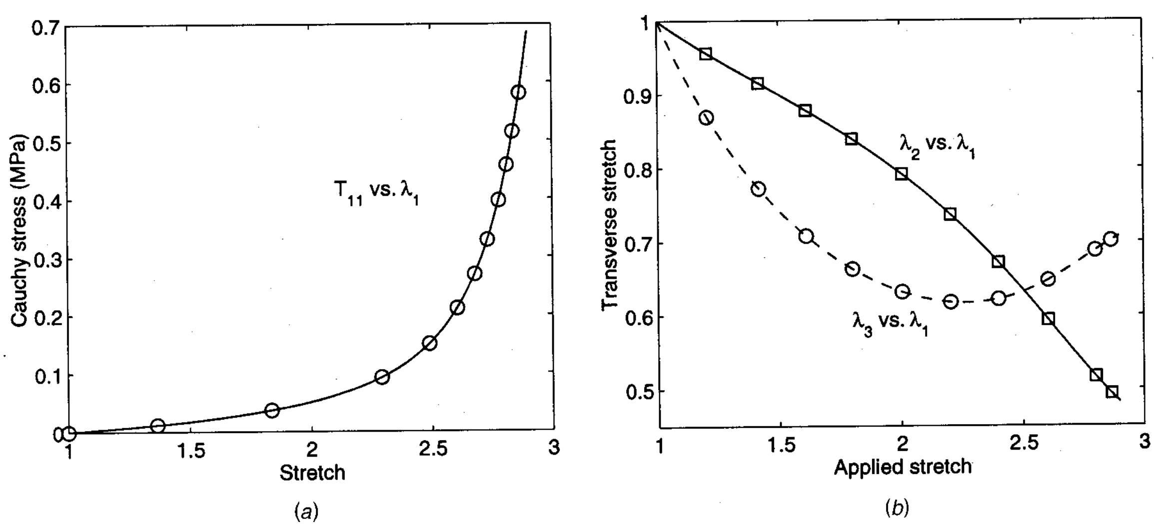

Fig. 8 Finite element simulations (using a single linear brick element) and numerical simulations of uniaxial tension. Parameters used for the simulations are $n = 2 \cdot 10^{24}/m^3$, $N = 3$, $a = 2$, $b = 2.5$, $c = 1.32$, and $B = 1$ MPa. Figure 8(*a*) shows the stress-stretch response in the direction of the applied load and Fig. 8(*b*) shows the variations of the transverse stretches λ_2 and λ_3 as functions of the applied stretch λ_1.

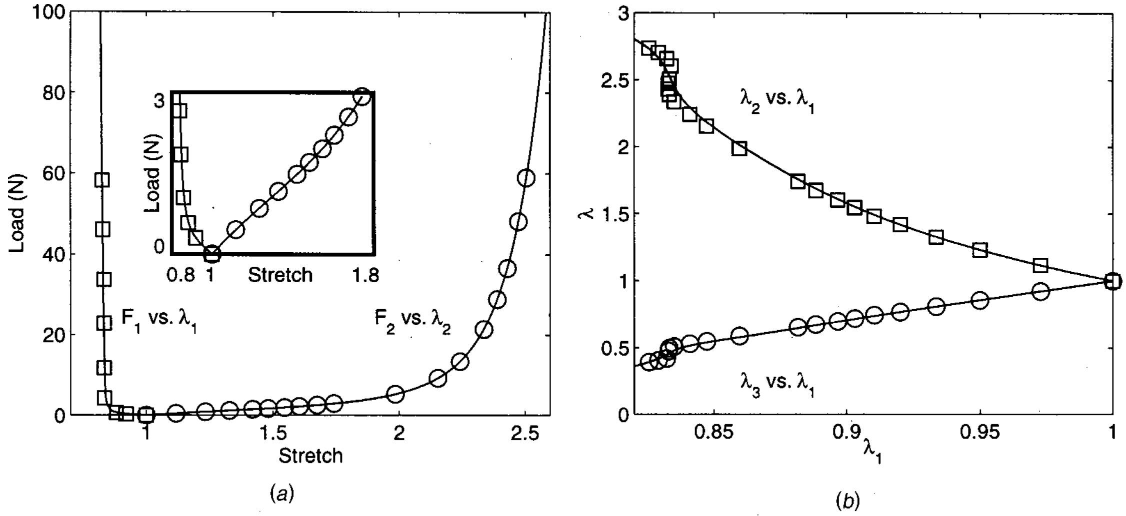

Fig. 9 Finite element simulation (using a single linear brick element) and numerical simulation of load-controlled biaxial tension. Parameters used for the simulations are $n=2\cdot10^{24}/\mathrm{m}^3$, $N=2.5$, $a=1.8$, $b=2$, $c=1.66$, and $B=1$ MPa. The ratio of the applied loads was fixed at $F_r=F_2/F_1=5$. Figure 9(a) shows the load-stretch responses in the directions of the applied loads and Fig. 9(b) shows the variation of the transverse stretch λ_3 as a function of the stretch λ_1. The inset in Fig. 9 shows the constitutive responses closer to zero deformation.

verse stretches with the stretch in the direction of the deformation. The finite element simulation for this deformation is very accurate at all values of the stretches.

A comparison of finite element simulations and numerical simulations of load-controlled biaxial tension is shown in Fig. 9. Parameters used for these simulations are $n=2\cdot10^{24}/\mathrm{m}^3$, $N=2.5$, $a=1.8$, $b=2$, $c=1.66$, and $B=1$ MPa. The ratio of the applied loads was fixed at $F_r=F_2/F_1=5$. Figure 9(a) shows the load-stretch responses in the directions of the applied loads and Fig. 9(b) shows the variation of the stretches λ_2 and λ_3 as functions of the stretch λ_1. The inset in Fig. 9 shows the constitutive responses closer to zero deformation. Excellent agreement between the finite element simulations and the numerical simulations is again seen throughout the deformation.

Though the ability of the finite element code to converge to the correct solution is excellent for the two cases described above, other simple homogeneous deformations can be problematic depending on the values of the parameters being used. For example, for a very large bulk modulus ($B \gg C_r$ where $C_r=nk\Theta$ is the rubbery modulus), convergence of the finite element code for simple homogeneous tests such as uniaxial tension required successive relaxations of the convergence criteria used by ABAQUS as the simulation progressed towards the strain hardening (locking) region. The accuracy of the uniaxial stress-strain response is not compromised for these simulations; however, the predictions by the finite element simulations of the transverse strains grew progressively worse as these strains affected the stresses only in a minor way. Similar results have been found when simulating hydrostatic compression; with orthotropic material parameters ($a \neq b \neq c$) a sample should deform orthotropically but this is not realized in finite element simulations because the orthotropic strains affect the hydrostatic stress in an insignificant way.

To test the ability of ABAQUS to simulate a more complex problem using the orthotropic hyperelastic constitutive law, a three-dimensional model was created with two distinct orientations of the principal material axes. The domain size is 50 mm×20 mm×0.1 mm with an element density of 49×7×1 eight-noded brick elements. Parameters used in the simulations are $n=2\cdot10^{24}/\mathrm{m}^3$, $N=1.1$, $a=1.4$, $b=1.0$, $c=1.2$, and $B=1$ MPa. The nodes at $X=0$ mm and $X=50$ mm were constrained from moving in the Y-direction and the nodes at $X=50$ mm were additionally given a displacement in the positive X-direction with the nodes at $X=0$ mm constrained from moving in the X-direction (constrained uniaxial extension). Two different orientations of the principal material axes were simulated: one in which **a** was fixed at a 30-deg orientation throughout the domain (Fig. 10(a)) and one in which a sinusoidal variation of the orientation of **a** was

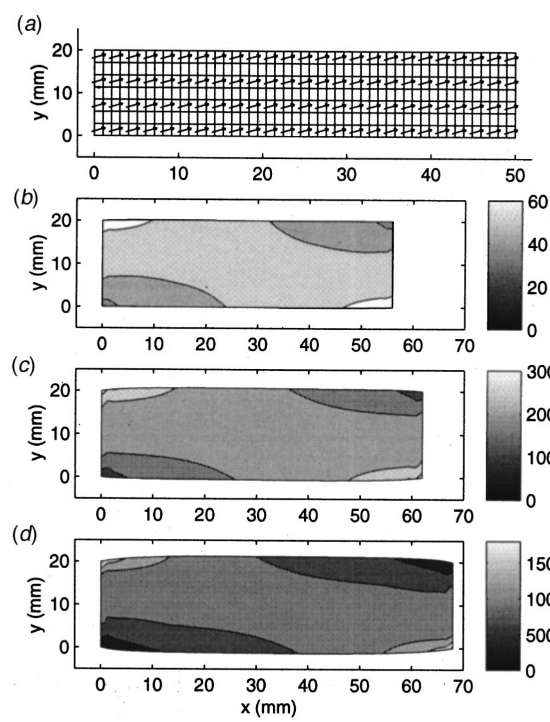

Fig. 10 Simulation of constrained uniaxial simulation in which a is initially fixed at a 30-deg orientation throughout the domain (Fig. 10(a)). Parameters used in the simulation are $n=2\cdot10^{24}/\mathrm{m}^3$, $N=1.1$, $a=1.4$, $b=1.0$, $c=1.2$, and $B=1$ MPa. Figures 10(b–d), corresponding to the global stress-stretch states marked (b)–(d), respectively, in Fig. 12, show deformed meshes with contours of the stress σ_{11} (kPa). Contour lines are shown in increments of 3 kPa, 10 kPa, and 15 kPa for Figs. 10(b), 10(c), and 10(d), respectively.

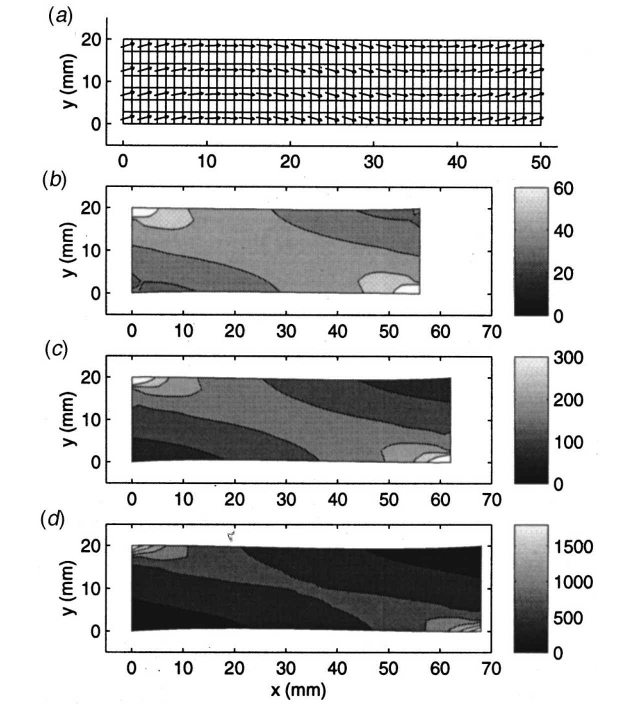

Fig. 11 Simulation of constrained uniaxial simulation in which the initial orientation of a varies sinusoidally with *X* (Fig. 11(*a*)). Parameters used in the simulation are the same as for the simulation in Fig. 10. In Figs. 11(*b–d*) the contour definitions and corresponding locations on the global stress-stretch curve (Fig. 12) are the same as for the simulation in Fig. 10.

prescribed such that the initial orientation at $X=0$ mm and $X=50$ mm is 30-deg and the initial orientation at $X=25$ mm is -30 deg (Fig. 11(a)). In both cases, the orientation of **b** was always locally orthogonal to **a** in the plane, and **c** was always oriented perpendicular to the plane. The condition of strong ellipticity was upheld throughout these simulations as the local Jacobian matrices extracted from the simulation results at various spatial locations and deformations were verified to be positive definite.

Figures 10(b–d) and 11(b–d) show deformed meshes with contour plots of σ_{11} (units of kPa) for the two simulations at the global stress-stretch states marked with filled symbols and labeled (b)–(d) in Fig. 12. Contour lines in Figs. 10(b–d) and 11(b–d) are shown in increments of 10 kPa, 50 kPa, and 300 kPa. All of the plots show nonsymmetric deformations and stress distributions about the vertical centerline initially located at $X=25$ mm. For simulations with constant fiber orientation the material is initially slightly drawn in in both the Y-direction and the Z-direction (results not shown here). At larger deformations the material expands in the Y-direction (Figs. 10(b–d)) while continuing to contract in the Z-direction. The expansion in the Y-direction is more pronounced on the left side of the top edge ($Y=20$ mm in the undeformed configuration) as compared to the right side; this is reversed on the lower edge ($Y=0$ mm in the undeformed configuration). This asymmetry is due to the constant skewed fiber orientation. In Figs. 11(b–d) there is contraction in the Y-direction (as well as in the Z-direction) at all deformations; along the top edge the material contracts to a greater degree near the right side of the sample as compared to the left side as a consequence of the fiber orientation.

At each of the three deformation states, the overall stress level in Figs. 11(b–d) is lower than that in the corresponding plot in Figs. 10(b–d). However, the peak stresses are higher in Figs. 11(b–d) than in Figs. 10(b–d) (in both cases the peak stresses are located in the upper left and lower right corners of the model). As a result, regions in Fig. 11 will lock at smaller values of the global

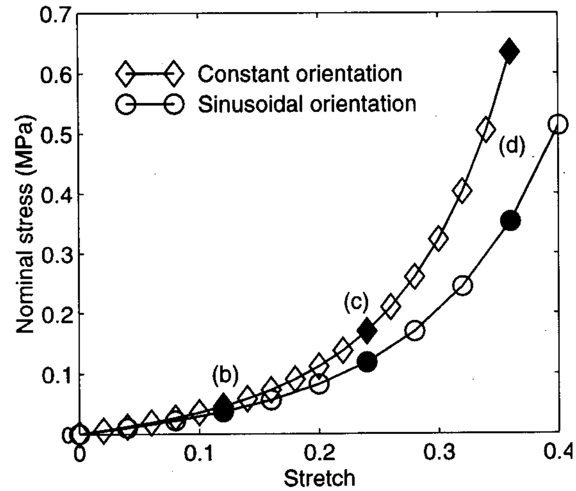

Fig. 12 Nominal stress (in the *X*-direction) versus stretch plots extracted from finite element simulations of constrained uniaxial extension with constant initial orientation of a and sinusoidally varying initial orientation of a as shown in Figs. 10(*a*) and 11(*a*).

stretch than the same regions in Fig. 10. Thus, a constant fiber orientation results in a globally stiffer material but one with smaller local peak stresses.

Figure 12 shows nominal stress (in the X-direction) versus stretch relations extracted from the simulation results. The filled symbols represent the deformation states at which contour plots are drawn in Figs. 10 and 11. Nominal stress was determined by summing the forces (in the X-direction) on the end nodes (at $X=0$ mm) and dividing by the initial cross-sectional area (2 mm^2); stretch was calculated by dividing the deformed length of the mesh by the undeformed length (50 mm). Though the same parameters were used for both simulations, the gross response of the simulation with constant fiber orientation was stiffer than that with varying fiber orientation. This supports what was previously seen in Figs. 10(b–d) and 11(b–d), that the overall stresses at a given stretch are higher in the simulation with constant fiber orientation than in the simulation with varying fiber orientation.

6 Conclusions

A finite deformation orthotropic hyperelastic constitutive law has been developed based on the statistical mechanics of macromolecules. In addition to the local orientation of the principal material axes, only five material parameters are necessary to use this model to characterize a nearly incompressible orthotropic material: density n of the constituent molecular chains, aspect ratios a, b, and c of the representative unit cell, and bulk modulus B. From the aspect ratios the locking stretch N of the constituent chains can be determined. The chain parameters and unit cell dimensions can be related to directly measurable physical properties such as the fiber length, density, and orientation. This model has been shown to successfully predict an orthotropic material response in uniaxial and biaxial tension and has been incorporated into ABAQUS for simulation of more complex boundary value problems.

References

[1] Lanir, Y., and Fung, Y. C., 1974, "Two-Dimensional Mechanical Properties of Rabbit Skin—II: Experimental Results," J. Biomech., **7**, pp. 171–182.
[2] Lanir, Y., 1979, "A Structural Theory for the Homogeneous Biaxial Stress-Strain Relationships in Flat Collagenous Tissues," J. Biomech., **12**, pp. 423–436.
[3] Lanir, Y., 1979, "Biaxial Stress-Strain Relationship in the Skin," Isr. J. Technol., **17**, pp. 78–85.
[4] Humphrey, J. D., Strumpf, R. K., and Yin, F. C. P., 1992, "A Constitutive

Theory for Biomembranes: Application to Epicardial Mechanics,'' ASME J. Biomech. Eng., **114**, pp. 461–466.
[5] Rodriguez, E. K., Hoger, A., and McCulloch, A. D., 1994, ''Stress-Dependent Finite Growth in Soft Elastic Tissues,'' J. Biomech., **27**(4), pp. 455–467.
[6] Holzapfel, G. A., Eberlein, R., Wriggers, P., and Weizsäcker, H. W., 1996, ''Large Strain Analysis of Soft Biological Membranes: Formulation and Finite Element Analysis,'' Comput. Methods Appl. Mech. Eng., **132**, pp. 45–61.
[7] Humphrey, J. D., and Yin, F. C. P., 1987, ''A New Approach for Describing Soft Tissue Behavior,'' *Proc. Thirteenth Annual NE Bioeng. Conf.*, IEEE, Piscataway, NJ, pp. 24–25.
[8] Humphrey, J. D., Strumpf, R. K., and Yin, F. C. P., 1990, ''Determination of a Constitutive Relation for Passive Myocardium—I: A New Functional Form,'' ASME J. Biomech. Eng., **112**, pp. 333–339.
[9] Baumann, C. G., Smith, S. B., Bloomfield, V. A., and Bustamente, C., 1997, ''Ionic Effects on the Elasticity of Single DNA Molecules,'' Proc. Natl. Acad. Sci. U.S.A., **94**, pp. 6185–6190.
[10] Treloar, L. R. G., 1975, *The Physics of Rubber Elasticity*, Clarendon Press. Oxford, UK.
[11] Kuhn, W., and Grün, F., 1942, ''Beziehungen Zwischen Elastischen Konstanten und Dehnungsdoppelbrechung Hochelastischer Stoffe,'' Kolloid-Z., **101**, pp. 248–271.
[12] Kellermayer, M. S. Z., Smith, S. B., Bustamente, C., and Granzier, H. L., 1998, ''Complete Unfolding of the Titin Molecule Under External Force,'' J. Struct. Biol., **122**, pp. 197–205.
[13] Trombitás, K., Greaser, M., Labeit, S., Jim, J.-P., Kellermayer, M., Helmes, M., and Granzier, H., 1998, ''Titin Extensibility in situ: Entropic Elasticity of Permanently Folded and Permanently Unfolded Molecular Segments,'' J. Cell Biol., **140**(4), pp. 853–859.
[14] Oberhauser, A. F., Marszalek, P. E., Erickson, H. P., and Fernandez, J. M., 1998, ''The Molecular Elasticity of the Extracellular Matrix Protein Tenascin,'' Nature (London), **393**, pp. 181–185.
[15] Hegner, M., Smith, S. B., and Bustamente, C., 1999, ''Polymerization and Mechanical Properties of Single RecA-DNA Filaments,'' Proc. Natl. Acad. Sci. U.S.A., **96**, pp. 10109–10114.
[16] Arruda, E. M., and Boyce, M. C., 1993, ''A Three-Dimensional Constitutive Model for the Large Stretch Behavior of Rubber Elastic Materials,'' J. Mech. Phys. Solids, **41**(2), pp. 389–412.
[17] Spencer, A. J. M., 1984, ''Constitutive Theory for Strongly Anisotropic Solids,'' CISM Courses and Lectures III, (282), pp. 1–32.
[18] Bischoff, J. E., Arruda, E. M., and Grosh, K., 2001, ''A New Constitutive Model for the Compressibility of Elastomers at Finite Deformations,'' Rubber Chem. Technol., **74**(4), pp. 0541–0559.
[19] Anand, L., 1996, ''A Constitutive Model for Compressible Elastomeric Solids,'' Comp. Mech., **18**, pp. 339–355.
[20] Treloar, L. R. G., and Riding, G., 1979, ''A Non-Gaussian Theory for Rubber in Biaxial Strain—I: Mechanical Properties,'' Proc. R. Soc. London, Ser. A, **369**, pp. 261–280.
[21] Bischoff, J. E., 2001, ''Constitutive Modeling and Testing of Biological Soft Tissue,'' Ph.D. thesis, University of Michigan.
[22] Wang, M. C., and Guth, E., 1952, ''Statistical Theory of Networks of Non-Gaussian Flexible Chains,'' J. Chem. Phys., **20**(7), pp. 1144–1157.
[23] Flory, P. J., and Rehner, J., Jr., 1943, ''Statistical Mechanics of Cross-Linked Polymer Networks,'' J. Chem. Phys., **11**, pp. 512–520.
[24] Malvern, L. E., 1969, *Introduction to the Mechanics of a Continuous Medium*, Prentice-Hall, Englewood Cliffs, NJ.
[25] Smith, G. F., and Rivlin, R. S., 1958, ''The Strain-Energy Function for Anisotropic Elastic Materials,'' Trans. Am. Math. Soc., **88**(1), pp. 175–193.
[26] Horowitz, A., Lanir, Y., Yin, F. C. P., Perl, M., Sheinman, I., and Strumpf, R. K., 1988, ''Structural Three-Dimensional Constitutive Law for the Passive Myocardium,'' ASME J. Biomech. Eng., **110**, pp. 200–207.
[27] Billiar, K. L., and Sacks, M. S., 2000, ''Biaxial Mechanical Properties of the Natural and Gluteraldehyde Treated Aortic Valve Cusp—Part II: A Structural Constitutive Model,'' ASME J. Biomech. Eng., **122**, pp. 1–9.
[28] Billiar, K. L., and Sacks, M. S., 2000, ''Biaxial Mechanical Properties of the Natural and Gluteraldehyde Treated Aortic Valve Cusp—Part I: Experimental Results,'' ASME J. Biomech. Eng., **122**, pp. 23–30.
[29] *ABAQUS/Standard User's Manual, Version 5.8*, 1999, Hibbitt, Karlsson & Sorensen, Inc., Pawtucket, RI.

A Surface Crack in a Graded Medium Under General Loading Conditions

S. Dag
Assoc. Mem. ASME

F. Erdogan
Fellow ASME

Department of Mechanical Engineering and Mechanics,
Lehigh University,
Bethlehem, PA 18015

In this study the problem of a surface crack in a semi-infinite elastic graded medium under general loading conditions is considered. It is assumed that first by solving the problem in the absence of a crack it is reduced to a local perturbation problem with arbitrary self-equilibrating crack surface tractions. The local problem is then solved by approximating the normal and shear tractions on the crack surfaces by polynomials and the normalized modes I and II stress intensity factors are given. As an example the results for a graded half-plane loaded by a sliding rigid circular stamp are presented.
[DOI: 10.1115/1.1488661]

1 Introduction

Graded materials, also known as *functionally graded materials* (FGMs) are generally multiphase composites with continuously varying thermomechanical properties. Used as coatings and interfacial zones they tend to reduce stresses resulting from the material property mismatch, increase the bonding strength, improve the surface properties and provide protection against severe thermal and chemical environments. Thus, the concept of grading the thermomechanical properties of materials provides the material scientists and engineers with an important tool to design new materials having highly favorable properties in certain specific applications ([1–6]).

To take full advantage of this new tool research is needed not only for developing efficient material processing and characterization techniques but also for carrying out basic studies relating to the safety and durability of FGM components. Typical current and potential applications for this new class of materials include thermal barrier coatings and abradable seals in gas turbines, preparation of wear-resistant surfaces in load transfer components such as gears, bearings, cams and machine tools, various interlayers in microlectronic and optoelectronic devices, high-speed graded index polymer optical fibers, impact resistant components, and thermoelectric cells (Miyamoto et al. [6]).

The primary interest in this study is in initiation and propagation of surface cracks in graded materials. Initially it is assumed that the conditions of crack initiation on the surface of the uncracked graded medium have been met and a surface crack has been initiatiated. Since the material on the surface of FGM is generally 100 percent ceramic and consequently rather brittle, this can be verified by applying a simple maximum tensile stress criterion. The main problem is, therefore, that of a surface crack subjected to general mixed-mode loading conditions. The corresponding mode I problem was considered by Erdogan and Wu [7,8]. The more general mode I problem of a graded layer bonded to a homogeneous substrate was studied by Kasmalkar [9]. The interface crack problem for graded coatings under antiplane shear loading is studied by Jin and Batra [10] by assuming an exponential variation in elastic properties. The power-law variation in the elastic properties of graded materials is considered by Wang et al. [11]. A moduli-perturbation approach is used by Gao [12] for the fracture analysis of nonhomogeneous materials. Wang et al. [13] and Nozaki and Shindo [14] developed a multilayered interfacial zone model to simulate the arbitrarily varying properties of FGMs. In addition to the references cited in [1–14], the review articles [15,16] may be of particular interest.

2 Formulation of the Problem

The geometry of the crack problem is shown in Fig. 1. The graded half-plane contains a surface crack of length d. The crack surfaces are assumed to be subjected to general mixed-mode loading. Because of the fact that main results of the crack problems in graded materials are rather insensitive to the variations in Poisson's ratio, in this study it is assumed that the elastic properties of the medium may be approximated by

$$\mu(x)=\mu_0 \exp(\gamma x), \tag{1a}$$

$$\kappa=\text{constant}, \tag{1b}$$

where μ is the shear modulus, γ is a nonhomogeneity parameter, $\kappa=3-4\nu$ for plane strain and $\kappa=(3-\nu)/(1+\nu)$ for generalized plane stress, ν being the Poisson's ratio. By using the Hooke's law

$$\sigma_{xx}(x,y)=\frac{\mu(x)}{\kappa-1}\left\{(\kappa+1)\frac{\partial u}{\partial x}+(3-\kappa)\frac{\partial v}{\partial y}\right\}, \tag{2a}$$

$$\sigma_{yy}(x,y)=\frac{\mu(x)}{\kappa-1}\left\{(\kappa+1)\frac{\partial v}{\partial y}+(3-\kappa)\frac{\partial u}{\partial x}\right\}, \tag{2b}$$

$$\sigma_{xy}(x,y)=\mu(x)\left\{\frac{\partial u}{\partial y}+\frac{\partial v}{\partial x}\right\} \tag{2c}$$

the equilibrium conditions $\sigma_{ij,j}=0$ can be expressed as

$$(\kappa+1)\frac{\partial^2 u}{\partial x^2}+(\kappa-1)\frac{\partial^2 u}{\partial y^2}+2\frac{\partial v}{\partial x\partial y}+\gamma(\kappa+1)\frac{\partial u}{\partial x}+\gamma(3-\kappa)\frac{\partial v}{\partial y}=0, \tag{3a}$$

$$(\kappa+1)\frac{\partial^2 v}{\partial y^2}+(\kappa-1)\frac{\partial^2 v}{\partial x^2}+2\frac{\partial^2 u}{\partial x\partial y}+\gamma(\kappa-1)\frac{\partial v}{\partial x}+\gamma(\kappa-1)\frac{\partial u}{\partial y}=0. \tag{3b}$$

Equations (3) must be solved under the following external loads:

$$\sigma_{xx}(0,y)=0,\quad \sigma_{xy}(0,y)=0,\quad -\infty<y<\infty, \tag{4a}$$

$$\sigma_{yy}(x,0)=-p(x),\quad \sigma_{xy}(x,0)=-q(x),\quad 0<x<d, \tag{4b}$$

$$\sigma_{ij}(x,y)\to 0\ \text{ as }\ (x^2+y^2)\to\infty,\ \ (i,j=x,y), \tag{4c}$$

Contributed by the Applied Mechanics Division of THE AMERICAN SOCIETY OF MECHANICAL ENGINEERS for publication in the ASME JOURNAL OF APPLIED MECHANICS. Manuscript received by the ASME Applied Mechanics Division, Apr. 2, 2001; final revision, Nov. 14, 2001. Associate Editor: H. Gao. Discussion on the paper should be addressed to the Editor, Prof. Robert M. McMeeking, Department of Mechanical and Environmental Engineering University of California–Santa Barbara, Santa Barbara, CA 93106-5070, and will be accepted until four months after final publication of the paper itself in the ASME JOURNAL OF APPLIED MECHANICS.

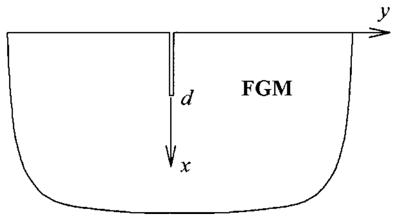

Fig. 1 Surface crack in a graded medium

where $p(x)$ and $q(x)$ are the crack surface tractions which are obtained from the solution of the original problem in the absence of the crack. We observe that the unknown functions that are convenient in this problem are the derivatives of the relative crack opening displacements defined by

$$\frac{2\mu_0}{\kappa+1}\frac{\partial}{\partial x}(v(x,+0)-v(x,-0))=f_1(x), \quad 0<x<d, \tag{5a}$$

$$\frac{2\mu_0}{\kappa+1}\frac{\partial}{\partial x}(u(x,+0)-u(x,-0))=f_2(x), \quad 0<x<d. \tag{5b}$$

2.1 The Opening Mode Problem. In the graded half-plane problem having a symmetry with respect to the $y=0$ plane in geometry and material property distribution, the mode I (or the opening mode) and mode II (or the sliding mode) problems turn out to be uncoupled. Therefore, the problems may be formulated separately. Furthermore, the solution to each problem may be expressed as the sum of two solutions, namely the infinite medium with a crack and a half-plane $x>0$ without a crack.

We consider first the infinite medium with a crack. Defining the displacements by

$$u_1^{(i)}(x,y)=\frac{1}{2\pi}\int_{-\infty}^{\infty}U_1^{(i)}(\omega,y)\exp(i\omega x)d\omega, \tag{6a}$$

$$v_1^{(i)}(x,y)=\frac{1}{2\pi}\int_{-\infty}^{\infty}V_1^{(i)}(\omega,y)\exp(i\omega x)d\omega, \tag{6b}$$

from Eq. (3) it follows that

$$(\kappa-1)\frac{d^2U_1^{(i)}}{dy^2}+(\kappa+1)(\gamma i\omega-\omega^2)U_1^{(i)}+(2i\omega+\gamma(3-\kappa))\frac{dV_1^{(i)}}{dy}=0, \tag{7a}$$

$$(2i\omega+\gamma(\kappa-1))\frac{dU_1^{(i)}}{dy}+(\kappa+1)\frac{d^2V_1^{(i)}}{dy^2}+(\kappa-1)(\gamma i\omega-\omega^2)V_1^{(i)}=0 \tag{7b}$$

where superscript i and subscript 1 refer to infinite medium and opening mode problem, respectively. Assuming the solution of Eq. (7) in the form $\exp(ny)$, the characteristic equation, its roots, and the displacements are found to be

$$(n^2-\delta_1 n+i\omega(\gamma+i\omega))(n^2+\delta_1 n+i\omega(\gamma+i\omega))=0, \tag{8a}$$

$$\delta_1=\gamma\sqrt{\frac{3-\kappa}{\kappa+1}}, \tag{8b}$$

$$n_1=-\frac{1}{2}\delta_1+\frac{1}{2}\sqrt{4\omega^2-4i\omega\gamma+\delta_1^2}, \quad \Re(n_1)>0, \tag{9a}$$

$$n_2=\frac{1}{2}\delta_1+\frac{1}{2}\sqrt{4\omega^2-4i\omega\gamma+\delta_1^2}, \quad \Re(n_2)>0, \tag{9b}$$

$$n_3=-\frac{1}{2}\delta_1-\frac{1}{2}\sqrt{4\omega^2-4i\omega\gamma+\delta_1^2}, \quad \Re(n_3)<0, \tag{9c}$$

$$n_4=\frac{1}{2}\delta_1-\frac{1}{2}\sqrt{4\omega^2-4i\omega\gamma+\delta_1^2}, \quad \Re(n_4)<0, \tag{9d}$$

$$u_1^{(i^-)}(x,y)=\frac{1}{2\pi}\int_{-\infty}^{\infty}\sum_{j=1}^{2}C_j(\omega)\exp(n_j y+i\omega x)d\omega, \tag{10a}$$

$$v_1^{(i^-)}(x,y)=\frac{1}{2\pi}\int_{-\infty}^{\infty}\sum_{j=1}^{2}C_j(\omega)A_j(\omega)\exp(n_j y+i\omega x)d\omega, \tag{10b}$$

for $y<0$, and

$$u_1^{(i^+)}(x,y)=\frac{1}{2\pi}\int_{-\infty}^{\infty}\sum_{j=3}^{4}C_j(\omega)\exp(n_j y+i\omega x)d\omega, \tag{11a}$$

$$v_1^{(i^+)}(x,y)=\frac{1}{2\pi}\int_{-\infty}^{\infty}\sum_{j=3}^{4}C_j(\omega)A_j(\omega)\exp(n_j y+i\omega x)d\omega, \tag{11b}$$

for $y>0$. In Eqs. (10) and (11) $C_j(\omega)$, $(j=1,2,3,4)$ are unknown and A_j are given by

$$A_j(\omega)=-\frac{n_j^2(\kappa-1)+(i\omega\gamma-\omega^2)(\kappa+1)}{n_j(2i\omega+\gamma(3-\kappa))}, \quad (j=1,2,3,4). \tag{12}$$

Consider now the half-plane problem for $x>0$ without the crack. By observing that the problem has a symmetry with respect to $y=0$ plane the solution may be expressed as

$$u_1^{(h)}(x,y)=\int_0^{\infty}U_1^{(h)}(x,\alpha)\cos(\alpha y)d\alpha, \tag{13a}$$

$$v_1^{(h)}(x,y)=\int_0^{\infty}V_1^{(h)}(x,\alpha)\sin(\alpha y)d\alpha, \tag{13b}$$

where superscript h and subscript 1 refer to the half-plane and the opening mode, respectively. From Eqs. (3) and (13) it follows that

$$(\kappa+1)\frac{d^2U_1^{(h)}}{dx^2}+\gamma(\kappa-1)\frac{dU_1^{(h)}}{dx}-\alpha^2(\kappa-1)U_1^{(h)}+2\alpha\frac{dV_1^{(h)}}{dx}+\gamma(3-\kappa)V_1^{(h)}=0, \tag{14a}$$

$$2\alpha\frac{dU_1^{(h)}}{dx}+\gamma\alpha(\kappa-1)U_1^{(h)}-(\kappa-1)\frac{d^2V_1^{(h)}}{dx^2}-\gamma(\kappa-1)\frac{dV_1^{(h)}}{dx}+\alpha^2(\kappa+1)V_1^{(h)}=0. \tag{14b}$$

Assuming the solution for Eq. (14) of the form $\exp(px)$, we find

$$(p^2+\gamma p-\alpha^2-i\alpha\delta_1)(p^2+\gamma p-\alpha^2+i\alpha\delta_1)=0, \tag{15}$$

$$p_1=-\frac{1}{2}\gamma+\frac{1}{2}\sqrt{\gamma^2+4\alpha^2+4i\alpha\delta_1}, \quad \Re(p_1)>0, \tag{16a}$$

$$p_2=-\frac{1}{2}\gamma+\frac{1}{2}\sqrt{\gamma^2+4\alpha^2-4i\alpha\delta_1}, \quad \Re(p_2)>0, \tag{16b}$$

$$p_3=-\frac{1}{2}\gamma-\frac{1}{2}\sqrt{\gamma^2+4\alpha^2+4i\alpha\delta_1}, \quad \Re(p_3)<0, \tag{16c}$$

$$p_4=-\frac{1}{2}\gamma-\frac{1}{2}\sqrt{\gamma^2+4\alpha^2-4i\alpha\delta_1}, \quad \Re(p_4)<0, \tag{16d}$$

$$u_1^{(h)}(x,y)=\int_0^{\infty}(B_3\exp(p_3 x)+B_4\exp(p_4 x))\cos(\alpha y)d\alpha, \tag{17a}$$

$$v_1^{(h)}(x,y)=\int_0^\infty (B_3D_3\exp(p_3x)+B_4D_4\exp(p_4x))\sin(\alpha y)d\alpha, \tag{17b}$$

$$D_j=-\frac{p_j^2(\kappa+1)+\alpha^2(1-\kappa)+\gamma p_j(1+\kappa)}{\alpha(2p_j+\gamma(3-\kappa))},\quad (j=3,4) \tag{18}$$

where δ_1 is given by Eq. (8*b*) and $B_3(\alpha)$ and $B_4(\alpha)$ are unknown functions. We now express the solution of the mode I problem as follows:

$$u_1(x,y)=u_1^{(i)}(x,y)+u_1^{(h)}(x,y), \tag{19a}$$

$$v_1(x,y)=v_1^{(i)}(x,y)+v_1^{(h)}(x,y), \tag{19b}$$

$$\sigma_{kj1}(x,y)=\sigma_{kj1}^{(i)}(x,y)+\sigma_{kj1}^{(h)}(x,y),\quad (k,j=x,y) \tag{19c}$$

where displacements are given in terms of six unknown functions $C_1,\ldots,C_4$, B_3, B_4 which are determined from the following six conditions:

$$\sigma_{xx1}(0,y)=0, \tag{20a}$$

$$\sigma_{xy1}(0,y)=0,\quad -\infty<y<\infty, \tag{20b}$$

$$\sigma_{yy1}(x,+0)=\sigma_{yy1}(x,-0), \tag{21a}$$

$$\sigma_{xy1}(x,+0)=\sigma_{xy1}(x,-0),\quad 0<x<\infty, \tag{21b}$$

$$u_1(x,+0)=u_1(x,-0),\quad 0<x<\infty, \tag{22}$$

$$\sigma_{yy1}(x,0)=-p(x),\quad 0<x<d, \tag{23a}$$

$$v_1(x,+0)=v_1(x,-0),\quad d<x<\infty. \tag{23b}$$

The homogeneous conditions (20)–(22) may be used to eliminate five of the unknown functions. The mixed boundary conditions (23) would then determine the sixth unknown.

By using the definitions given by Eq. (5), observing that for the mode I problem under consideration $f_2(x)=0$ and $q(x)=0$, replacing the condition (23*a*) by (5*a*), and substituting from (10), (11), (17), (19), and (2) into (20)–(23), we obtain the following expressions giving $C_1,\ldots,C_4$, B_3, B_4 in terms of $f_1(x)$:

$$C_j(\omega)=\frac{\kappa+1}{2\mu_0}P_j(\omega)\int_0^d f_1(t)\exp(-i\omega t)dt, \tag{24a}$$

$$\sum_{j=3}^{4}(i\omega(3-\kappa)+A_jn_j(1+\kappa))P_j(\omega)-\sum_{j=1}^{2}(i\omega(3-\kappa)+A_jn_j(1+\kappa))P_j(\omega)=0, \tag{24b}$$

$$\sum_{j=3}^{4}(n_j+i\omega A_j)P_j(\omega)-\sum_{j=1}^{2}(n_j+i\omega A_j)P_j(\omega)=0, \tag{24c}$$

$$i\omega\left\{\sum_{j=3}^{4}A_jP_j(\omega)-\sum_{j=1}^{2}A_jP_j(\omega)\right\}=1, \tag{24d}$$

$$P_4(\omega)+P_3(\omega)-P_2(\omega)-P_1(\omega)=0, \tag{24e}$$

$$\int_0^\infty\sum_{j=3}^{4}((\kappa+1)p_j+D_j\alpha(3-\kappa))B_j(\alpha)\cos(\alpha y)+\frac{1}{2\pi}\int_{-\infty}^{\infty}\sum_{j=3}^{4}(i\omega(\kappa+1)+A_jn_j(3-\kappa))C_j(\omega)\times\exp(n_jy)d\omega=0,\quad 0<y<\infty, \tag{25a}$$

$$\int_0^\infty\sum_{j=3}^{4}(D_jp_j-\alpha)B_j(\alpha)\sin(\alpha y)+\frac{1}{2\pi}\int_{-\infty}^{\infty}\sum_{j=3}^{4}(n_j+i\omega A_j)C_j(\omega)\exp(n_jy)d\omega=0,\quad 0<y<\infty \tag{25b}$$

where $f_1(x)$ is the new unknown function which is determined from Eq. (23*a*). Because of symmetry in this problem it is sufficient to consider $0<y<\infty$ only. Evaluating some of the integrals in closed form by using the theory of residues, Eqs. (25) may be reduced to

$$\sum_{j=3}^{4}((\kappa+1)p_j+D_j\alpha(3-\kappa))B_j^*(\alpha,t)=R_{xx1}(\alpha,t), \tag{26a}$$

$$\sum_{j=3}^{4}(D_jp_j-\alpha)B_j^*(\alpha,t)=R_{xy1}(\alpha,t), \tag{26b}$$

where

$$B_j(\alpha)=\frac{\kappa+1}{2\mu_0}\int_0^d B_j^*(\alpha,t)\exp\left(\left(\frac{\gamma}{2}-\lambda_1\right)t\right)f_1(t)dt, \tag{27}$$

and R_{xx1}, R_{xy1}, and λ_1 are given in Appendix A.

2.2 The Sliding Mode Problem. Referring to Fig. 1, in this section it is assumed that $y=0$ is a plane of antisymmetry. Consequently, in Eq. (4) $p(x)=0$ and in Eq. (5) $f_1(x)=0$. Thus, following a procedure similar to that of Section 2.1, the displacements for the graded infinite medium with a crack along the *x*-axis may be written as

$$u_2^{(i^-)}(x,y)=\frac{1}{2\pi}\int_{-\infty}^{\infty}\sum_{j=1}^{2}E_j(\omega)\exp(n_jy+i\omega x)d\omega, \tag{28a}$$

$$v_2^{(i^-)}(x,y)=\frac{1}{2\pi}\int_{-\infty}^{\infty}\sum_{j=1}^{2}E_j(\omega)A_j(\omega)\exp(n_jy+i\omega x)d\omega, \tag{28b}$$

for $y<0$ and

$$u_2^{(i^+)}(x,y)=\frac{1}{2\pi}\int_{-\infty}^{\infty}\sum_{j=3}^{4}E_j(\omega)\exp(n_jy+i\omega x)d\omega, \tag{29a}$$

$$v_2^{(i^+)}(x,y)=\frac{1}{2\pi}\int_{-\infty}^{\infty}\sum_{j=3}^{4}E_j(\omega)A_j(\omega)\exp(n_jy+i\omega x)d\omega, \tag{29b}$$

for $y>0$. In Eqs. (28) and (29) $E_1(\omega),\ldots,E_4(\omega)$ are unknown and n_j and A_j are given by Eqs. (9) and (12), respectively. Similarly, the general solution for the graded half-plane $x>0$ under antisymmetric loading conditions may be expressed as

$$u_2^{(h)}(x,y)=\int_0^\infty(G_3(\alpha)\exp(p_3x)+G_4(\alpha)\exp(p_4x))\sin(\alpha y)d\alpha, \tag{30a}$$

$$v_2^{(h)}(x,y)=\int_0^\infty(G_3(\alpha)H_3(\alpha)\exp(p_3x)+G_4(\alpha)H_4(\alpha)\exp(p_4x))\cos(\alpha y)d\alpha \tag{30b}$$

where $G_3(\alpha)$ and $G_4(\alpha)$ are unknown, the characteristic equation and its roots p_j, $(j=1,\ldots,4)$ are given by Eqs. (18) and (19) and $H_3(\alpha)$ and $H_4(\alpha)$ are

$$H_j(\alpha)=\frac{\gamma p_j(\kappa+1)+\alpha^2(1-\kappa)+p_j^2(\kappa+1)}{\alpha(2p_j+\gamma(3-\kappa))},\quad (j=3,4). \tag{31}$$

We now express the displacements and stresses in the cracked half-plane under antisymmetric loading in terms of the following sums:

$$u_2(x,y)=u_2^{(i)}(x,y)+u_2^{(h)}(x,y), \tag{32a}$$

$$v_2(x,y)=v_2^{(i)}(x,y)+v_2^{(h)}(x,y), \tag{32b}$$

$$\sigma_{kj2}(x,y)=\sigma_{kj2}^{(i)}(x,y)+\sigma_{kj2}^{(h)}(x,y), \quad (k,j=x,y). \tag{33}$$

In the surface crack problem under antisymmetric loading the solution given by Eqs. (32) and (33) must satisfy the following boundary and continuity conditions:

$$\sigma_{xx2}(0,y)=0, \quad \sigma_{xy2}(0,y)=0, \quad -\infty<y<\infty, \tag{34}$$

$$\sigma_{yy2}(x,+0)=\sigma_{yy2}(x,-0),$$

$$\sigma_{xy2}(x,+0)=\sigma_{xy2}(x,-0), \quad 0<x<\infty, \tag{35}$$

$$v_2(x,+0)=v_2(x,-0), \quad 0<x<\infty, \tag{36}$$

$$\sigma_{xy2}(x,0)=-q(x), \quad 0<x<d, \tag{37a}$$

$$u_2(x,+0)=u_2(x,-0), \quad d<x<\infty. \tag{37b}$$

Again, by replacing Eq. (37*a*) by Eq. (5*b*) and using the solution given by Eqs. (28)–(31), the conditions (34)–(37) may be reduced to a system of equations expressing the unknown functions $E_j(\omega)$, $(j=1,\ldots,4)$, $G_3(\alpha)$ and $G_4(\alpha)$ in terms of the new unknown function $f_2(x)$ as follows:

$$E_j(\omega)=\frac{\kappa+1}{2\mu_0}Z_j(\omega)\int_0^d f_2(t)\exp(-i\omega t)dt, \tag{38}$$

$$\sum_{j=3}^{4}(i\omega(3-\kappa)+A_jn_j(1+\kappa))Z_j(\omega) - \sum_{j=1}^{2}(i\omega(3-\kappa)+A_jn_j(1+\kappa))Z_j(\omega)=0, \tag{39a}$$

$$\sum_{j=3}^{4}(n_j+i\omega A_j)Z_j(\omega)-\sum_{j=1}^{2}(n_j+i\omega A_j)Z_j(\omega)=0, \tag{39b}$$

$$\sum_{j=3}^{4}A_jZ_j(\omega)-\sum_{j=1}^{2}A_jZ_j(\omega)=0, \tag{39c}$$

$$i\omega\{Z_4(\omega)+Z_3(\omega)-Z_2(\omega)-Z_1(\omega)\}=1. \tag{39d}$$

$$\int_0^\infty\sum_{j=3}^{4}((\kappa+1)p_j-H_j\alpha(3-\kappa))G_j(\alpha)\sin(\alpha y) + \frac{1}{2\pi}\int_{-\infty}^{\infty}\sum_{j=3}^{4}(i\omega(\kappa+1)+A_jn_j(3-\kappa))E_j(\omega) \times\exp(n_jy)d\omega=0, \quad 0<y<\infty, \tag{40a}$$

$$\int_0^\infty\sum_{j=3}^{4}(H_jp_j+\alpha)G_j(\alpha)\cos(\alpha y) + \frac{1}{2\pi}\int_{-\infty}^{\infty}\sum_{j=3}^{4}(n_j+i\omega A_j)E_j(\omega)\exp(n_jy)d\omega=0, \quad 0<y<\infty. \tag{40b}$$

In this problem, too, because of symmetry it is sufficient to consider $y>0$ half of the medium only. Also, by evaluating some of the integrals in closed form Eqs. (40a,b) may be reduced to

$$\sum_{j=3}^{4}((\kappa+1)p_j-H_j\alpha(3-\kappa))G_j^*(\alpha,t)=R_{xx2}(\alpha,t), \tag{41a}$$

$$\sum_{j=3}^{4}(H_jp_j+\alpha)G_j^*(\alpha,t)=R_{xy2}(\alpha,t), \tag{41b}$$

where

$$G_j(\alpha)=\frac{\kappa+1}{2\mu_0}\int_0^d G_j^*(\alpha,t)\exp\left(\left(\frac{\gamma}{2}-\lambda_1\right)t\right)f_2(t)dt, \tag{42}$$

and R_{xx2}, R_{xy2}, and λ_1 are given in Appendix A.

3 The Integral Equations

By using the solution developed in Section 2 all stress and displacement components can be expressed in terms of $f_1(x)$ and $f_2(x)$ with appropriate kernels. Specifically, observing that the problem is uncoupled, using Eqs. (22) and (36), the conditions (23*a*) and (37*a*) which are yet to be satisfied may be written as

$$\sigma_{yy}(x,0)=\lim_{y\to0}\int_0^d k_{11}(x,y,t)f_1(t)dt=-p(x), \quad 0<x<d, \tag{43}$$

$$\sigma_{xy}(x,0)=\lim_{y\to0}\int_0^d k_{22}(x,y,t)f_2(t)dt=-q(x), \quad 0<x<d, \tag{44}$$

where the kernels k_{11} and k_{22} are given in Appendix B. Note that unlike the homogeneous half-plane, in the graded medium with a surface crack $k_{11}(x,0,t)$ and $k_{22}(x,0,t)$ are not equal. The singular nature of the integral Eqs. (43) and (44) and that of the solutions f_1 and f_2 may be determined by examining the asymptotic behavior of the integrands $K_{ss}^{(r)}$, $(r=i,\ h;\ s=1,2)$ given in Appendix B. After performing the necessary analysis the integral Eqs. (43) and (44) may be reduced to

$$\int_0^d\left[\frac{1}{\pi}\frac{1}{t-x}+h_{11s}(x,t)+h_{11f}(x,t)\right]f_1(t)dt = -\exp(-\gamma x)p(x), \quad 0<x<d \tag{45a}$$

$$\int_0^d\left[\frac{1}{\pi}\frac{1}{t-x}+h_{22s}(x,t)+h_{22f}(x,t)\right]f_2(t)dt = -\exp(-\gamma x)q(x), \quad 0<x<d \tag{45b}$$

where h_{11s} and h_{22s} are generalized Cauchy kernels (of the order $1/t$) that become unbounded as the arguments x and t tend to the end point zero simultaneously. The limits of these singular kernels are found to be

$$\lim_{(x,t)\to0}h_{11s}(x,t)=\lim_{\gamma\to0}h_{11s}(x,t) = \lim_{(x,t)\to0}h_{22s}(x,t) = \lim_{\gamma\to0}h_{22s}(x,t) = \frac{1}{\pi}\left(\frac{1}{t+x}+\frac{2t}{(t+x)^2}-\frac{4t^2}{(t+x)^3}\right), \quad 0<(t,x)<d. \tag{46}$$

The expressions for h_{kks} and h_{kkf}, $(k=1,2)$ are given by Dag [17]. It may be observed that (46) is the standard expression found for edge cracks in homogeneous materials ([17]). Thus, the solution of the integral equations may be expressed as

$$f_1(x)=(d-x)^{-1/2}f_1^*(x), \quad 0<x<d, \tag{47a}$$

$$f_2(x)=(d-x)^{-1/2}f_2^*(x), \quad 0<x<d, \tag{47b}$$

where $f_1^*(x)$ and $f_2^*(x)$ are unknown bounded functions. Note that, there is no singularity at the crack mouth $x=0$, $y=0$ while the standard square-root singularity is retained at the crack tip.

4 On the Solution of the Integral Equations

The integral equations are solved by using a collocation technique. First the interval $(0,d)$ in (45) is normalized by defining

$$f_i(t)=\phi_i(r), \quad i=1,2, \quad -1<r<1, \tag{48a}$$

$$t=\frac{d}{2}r+\frac{d}{2}, \quad 0<t<d, \quad -1<r<1, \tag{48b}$$

$$x=\frac{d}{2}s+\frac{d}{2}, \quad 0<x<d, \quad -1<s<1. \tag{48c}$$

The solution may then be expressed as

$$\phi_1(r)=(1-r)^{-1/2}\sum_{n=0}^{\infty} A_{1n}P_n^{(-1/2,0)}(r), \tag{49a}$$

$$\phi_2(r)=(1-r)^{-1/2}\sum_{n=0}^{\infty} A_{2n}P_n^{(-1/2,0)}(r), \tag{49b}$$

where $P_n^{(-1/2,0)}(r)$, $-1<r<1$, are Jacobi polynomials. Substituting (49) in (45), truncating the infinite series at N and regularizing the singular terms, the integral equations become

$$\sum_{n=0}^{N}\left\{-\frac{\Gamma(-1/2)\Gamma(n+1)}{2^{1/2}\pi\Gamma(n+1/2)}F(n+1,-n+1/2;3/2;(1-s)/2) + m_{11n}(s)\right\}A_{1n}=-\exp(-\gamma d(1+s)/2)p(d(1+s)/2), \quad -1<s<1, \tag{50a}$$

$$\sum_{n=0}^{N}\left\{-\frac{\Gamma(-1/2)\Gamma(n+1)}{2^{1/2}\pi\Gamma(n+1/2)}F(n+1,-n+1/2;3/2;(1-s)/2) + m_{22n}(s)\right\}A_{2n}=-\exp(-\gamma d(1+s)/2)q(d(1+s)/2), \quad -1<s<1, \tag{50b}$$

where $\Gamma(\ )$ is the Gamma function and $F(\ )$ is the hypergeometric function. Expressions for $m_{kkn}(s)$, $(k=1,2)$ are given in Appendix B. Equations (50) are solved numerically using a collocation technique. The following roots of the Chebyshev polynomials are used as the collocation points:

$$s_j=\cos\left(\frac{\pi(2j-1)}{2(N+1)}\right), \quad j=1,\ldots,N+1. \tag{51}$$

After solving the integral equations for f_1 and f_2 stress intensity factors at the crack tip $(d,0)$ may be evaluated by using the results. The stress intensity factors are defined by and calculated from

$$k_1=\lim_{x\to d+0}\sqrt{2(x-d)}\sigma_{yy}(x,0) = -\lim_{x\to d-0}\frac{2\mu(x)}{\kappa+1}\sqrt{2(d-x)}\ \frac{\partial}{\partial x}(v(x,0^+)-v(x,0^-)), \tag{52a}$$

Table 1 Normalized mode I stress intensity factors

γd	$k_1/(\sigma_n d^{1/2})$				
	σ_0	$\sigma_1(x/d)$	$\sigma_2(x/d)^2$	$\sigma_3(x/d)^3$	$\sigma_4(x/d)^4$
-3.0	4.4345	1.9324	1.2148	0.8897	0.7076
-2.0	3.1238	1.4495	0.9525	0.7209	0.5879
-1.0	1.9846	1.0196	0.7152	0.5663	0.4774
-0.5	1.4988	0.8317	0.6099	0.4970	0.4274
-10^{-1}	1.1802	0.6690	0.5387	0.4498	0.3932
-10^{-2}	1.1259	0.6847	0.5265	0.4417	0.3873
-10^{-3}	1.1220	0.6831	0.5256	0.4410	0.3869
-10^{-4}	1.1215	0.6829	0.5255	0.4410	0.3868
0	1.1215	0.6829	0.5255	0.4410	0.3868
10^{-4}	1.1215	0.6829	0.5255	0.4410	0.3868
10^{-3}	1.1210	0.6827	0.5254	0.4409	0.3868
10^{-2}	1.1175	0.6812	0.5246	0.4404	0.3864
10^{-1}	1.0864	0.6690	0.5176	0.4358	0.3830
0.5	1.0225	0.6439	0.5035	0.4264	0.3763
1.0	0.9930	0.6328	0.4974	0.4225	0.3735
2.0	0.9807	0.6289	0.4956	0.4215	0.3729
3.0	0.9884	0.6329	0.4981	0.4233	0.3743

$$k_2=\lim_{x\to d+0}\sqrt{2(x-d)}\sigma_{xy}(x,0) = -\lim_{x\to d-0}\frac{2\mu(x)}{\kappa+1}\sqrt{2(d-x)}\ \frac{\partial}{\partial x}(u(x,0^+)-u(x,0^-)). \tag{52b}$$

From (49) and (52) it then follows that

$$k_1=-\exp(\gamma d)\sqrt{d}\ \sum_{n=0}^{N} A_{1n}P_n^{(-1/2,0)}(1), \tag{53a}$$

$$k_2=-\exp(\gamma d)\sqrt{d}\ \sum_{n=0}^{N} A_{2n}P_n^{(-1/2,0)}(1). \tag{53b}$$

5 Results and Discussion

The main results of this study are the variation of the stress intensity factors as functions of the material nonhomogeneity parameter γ. Some sample results are also obtained giving the crack opening displacements. Assuming that in practical applications the crack surface tractions for the perturbation problem would be sufficiently well-behaved continuous functions and may be approximated by fourth-degree polynomials with sufficient accuracy, the input functions may be expressed as

$$p(x)=\sum_{n=0}^{4}\ \sigma_n(x/d)^n, \tag{54a}$$

$$q(x)=\sum_{n=0}^{4}\ \tau_n(x/d)^n, \tag{54b}$$

where the coefficients σ_n and τ_n are known constants. To facilitate the application of the results, the normalized stress intensity factors are given in Tables 1 and 2 in tabular form. In the tables the numerical results for the limiting case of $\gamma d=0$ are obtained by solving the mixed mode surface crack problem in a homogeneous medium. As can be seen from the tables, for sufficiently small values of the nonhomogeneity parameter (i.e., $|\gamma d|=10^{-4}$) results obtained for a graded medium are in agreement with the results obtained from the homogeneous formulation up to the last significant digit calculated. In the special case of $p(x)=\sigma_0$ and $q(x)=\tau_0$ for $|\gamma d|\to 0$ the convergence of the stress intensity factors calculated for a graded medium to the known homogeneous results $k_1/(\sigma_0\sqrt{d})=k_2/(\tau_0\sqrt{d})=1.1215$ is shown in Fig. 2 as well as in the Tables 1 and 2. For $\gamma d\neq 0$ the problem does not have a

Table 2 Normalized mode II stress intensity factors

γd	$k_2/(\tau_n d^{1/2})$				
	τ_0	$\tau_1(x/d)$	$\tau_2(x/d)^2$	$\tau_3(x/d)^3$	$\tau_4(x/d)^4$
-3.0	1.6704	0.9273	0.6738	0.5437	0.4635
-2.0	1.4765	0.8398	0.6202	0.5063	0.4355
-1.0	1.2825	0.7534	0.5678	0.4700	0.4083
-0.5	1.1940	0.7144	0.5443	0.4539	0.3964
-10^{-1}	1.1347	0.6885	0.5288	0.4433	0.3885
-10^{-2}	1.1197	0.6825	0.5253	0.4409	0.3868
-10^{-3}	1.1212	0.6828	0.5254	0.4410	0.3868
-10^{-4}	1.1215	0.6829	0.5255	0.4410	0.3868
0	1.1215	0.6829	0.5255	0.4410	0.3868
10^{-4}	1.1215	0.6829	0.5255	0.4410	0.3868
10^{-3}	1.1216	0.6830	0.5255	0.4410	0.3868
10^{-2}	1.1233	0.6833	0.5256	0.4411	0.3869
10^{-1}	1.1094	0.6777	0.5224	0.4389	0.3853
0.5	1.0727	0.6620	0.5132	0.4327	0.3807
1.0	1.0429	0.6497	0.5062	0.4280	0.3773
2.0	1.0164	0.6397	0.5008	0.4245	0.3749
3.0	1.0128	0.6394	0.5011	0.4249	0.3753

closed-form solution and in the computer program one can not directly substitute $\gamma d = 0$. Thus, the results given in Tables 1 and 2 and Fig. 2 indicate that to calculate the stress intensity factor for the limiting case of $\gamma d = 0$ one can use $\gamma d = 10^{-4}$.

It should be pointed out that in a semi-infinite plane homogeneous elastic medium containing a surface crack of depth d and subjected to uniform tension parallel to the surface ($\sigma_{yy}(x, \mp\infty) = \sigma_0$, Fig. 1), the closed-form solution for the stress intensity factor $k_1(d)$ is given by Koiter [18] in terms of an infinite integral as follows:

$$\frac{k_1(d)}{\sigma_0\sqrt{d}} = \sqrt{\frac{2(B+1)}{\sqrt{\pi}A}}, \tag{55}$$

$$\log A = -\frac{1}{\pi}\int_0^\infty \frac{1}{1+\alpha^2}\log\left(\frac{\alpha\sinh(\pi\alpha)}{\sqrt{B^2+\alpha^2}(\cosh(\pi\alpha)-2\alpha^2-1)}\right)d\alpha \tag{56}$$

where B is an arbitrary real constant greater than 1 and the result is independent of the choice of B. The numerical evaluation of (55) and (56) show that (Kaya and Erdogan [19])

$$\frac{k_1(d)}{\sigma_0\sqrt{d}} = 1.12152226 \mp 10^{-8}. \tag{57}$$

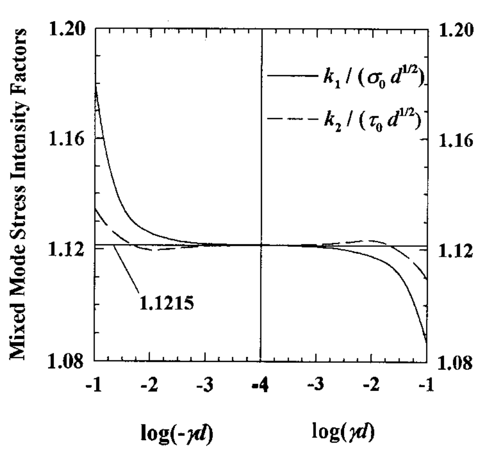

Fig. 2 Convergence of the numerical results for small values of the nonhomogeneity parameter

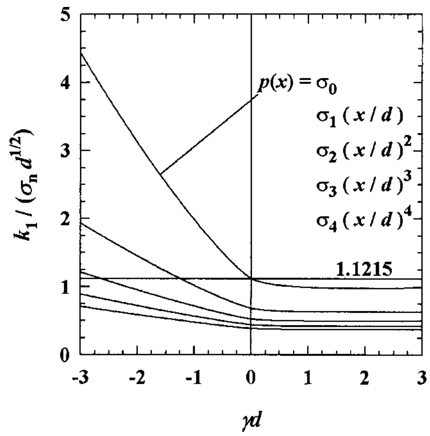

Fig. 3 Normalized mode I stress intensity factors, κ=2, $\mu(x) = \mu_0\exp(\gamma x)$

The result given by (57) was verified by Mahajan [20] by using an entirely different method.

The calculated stress intensity factors for crack surface tractions (54) are also shown in Figs. 3 and 4. The figures are self-explanatory: as the material nonhomogeneity parameter γ decreases, both k_1 and k_2 tend to increase, k_1 and k_2 are much more sensitive to the variations in γ for $\gamma<0$ (for the "softening" ma-

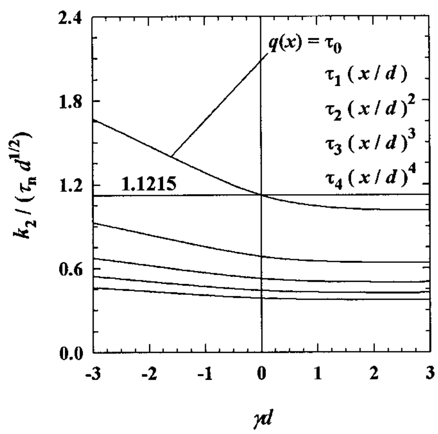

Fig. 4 Normalized mode II stress intensity factors, κ=2, $\mu(x) = \mu_0\exp(\gamma x)$

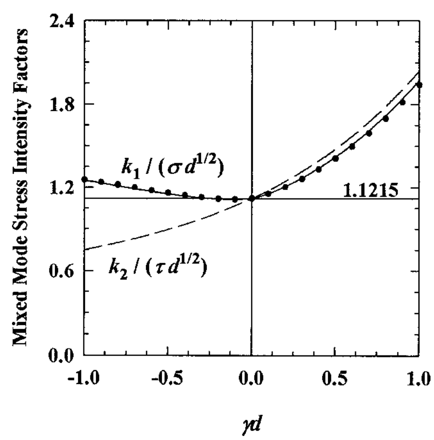

Fig. 5 Normalized modes I and II stress intensity factors for fixed grip tensile and shear loading, κ=1.8, $\mu(x) = \mu_0\exp(\gamma x)$, $\sigma = 8\mu_0\epsilon_0/(\kappa+1)$, $\tau = 8\mu_0\gamma_0/(\kappa+1)$

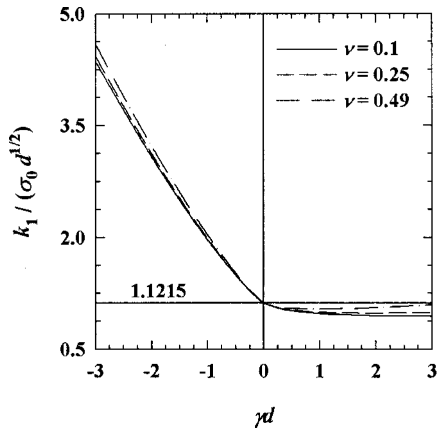

Fig. 6 The influence of Poisson's ratio on the normalized mode I stress intensity factor in a graded half-plane with a surface crack; the case of plane strain, $p(x)=\sigma_0$, $q(x)=0$, $\mu(x)=\mu_0 \exp(\gamma x)$

terial) than for $\gamma>0$, and generally for a given γ the amplitude of k_1 is greater than that of k_2. Figure 5 shows the results for fixed grip tensile ($\epsilon_{yy}(x,\mp\infty)=\epsilon_0$) and shear ($\gamma_{xy}(x,\mp\infty)=\gamma_0$) loading. Note that as the nonhomogeneity parameter γ increases, the normalized k_2 (dashed lines) monotonically increases, whereas k_1 goes through a minimum near $\gamma=0$. The figure also shows the mode I results for a graded half-plane under fixed grip loading ϵ_0 obtained by Kasmalkar [9] (full circles). Not only is the agreement quite good, also somewhat paradoxial result concerning the slight increase in k_1 for $\gamma<0$ is independently verified.

Figures 6 and 7 show the influence of the Poisson's ratio ν on the modes I and II stress intensity factors in a graded half-plane with a surface crack loaded by uniform crack surface tractions $p(x)=\sigma_0$ and $q(x)=\tau_0$, respectively. As shown in the previous studies, the effect of ν on k_1 does not seem to be significant. However, particularly for large values of γ, the influence of ν on k_2 could be significant.

Figures 8–11 show some sample results for the normalized crack opening displacement. It may be observed that in all cases as γ increases (or as the stiffness of the medium increases), the crack opening displacements decrease, the influence of γ on the crack opening displacement is more significant for $\gamma<0$ than for $\gamma>0$, and generally for $\gamma<0$ crack opening displacement under mode I loading (σ_0 and σ) is greater than that under mode II loading (τ_0 and τ). These are all intuitively expected results. From Figs. 8–11 it may be seen that for the homogeneous half-plane ($\gamma=0$) the calculated crack opening displacements in all four cases are identical. This may easily be shown analytically by using Eqs. (45) and (46). Figures 8–11 also show that the crack opening displacement for the homogeneous medium is bracketed by the results obtained for $\gamma<0$ and $\gamma>0$ and generally the crack opening displacements for the fixed grip loading (ϵ_0 and γ_0)

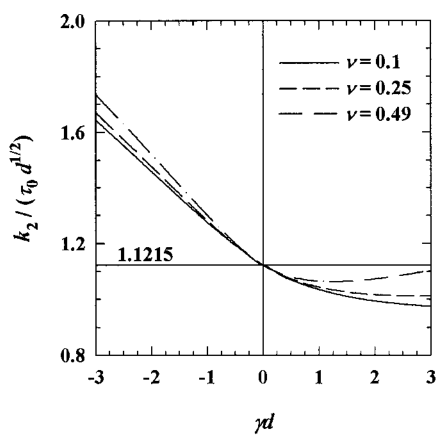

Fig. 7 The influence of Poisson's ratio on the normalized mode II stress intensity factor in a graded half-plane with a surface crack; the case of plane strain, $p(x)=0$, $q(x)=\tau_0$, $\mu(x)=\mu_0 \exp(\gamma x)$

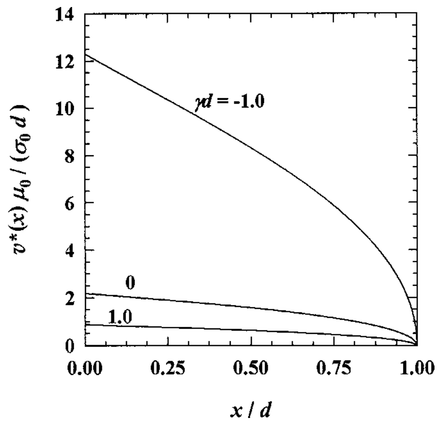

Fig. 8 Normal crack opening displacement, $v^*(x)=v(x,+0)-v(x,-0)$, $p(x)=\sigma_0$, $q(x)=0$, $\kappa=2$, $\mu=\mu_0 \exp(\gamma x)$

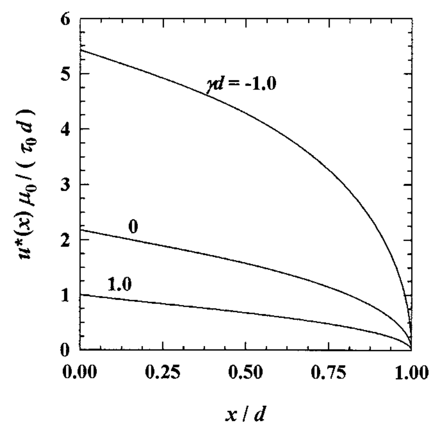

Fig. 9 Tangential crack opening displacement, $u^*(x)=u(x,+0)-u(x,-0)$, $p(x)=0$, $q(x)=\tau_0$, $\kappa=2$, $\mu=\mu_0 \exp(\gamma x)$

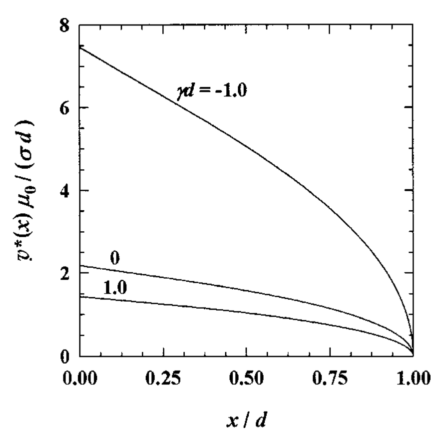

Fig. 10 Normal crack opening displacement for fixed grip loading, $v^*(x)=v(x,+0)-v(x,-0)$, $\sigma=8\mu_0\epsilon_0/(\kappa+1)$, $\kappa=2$, $\mu=\mu_0 \exp(\gamma x)$

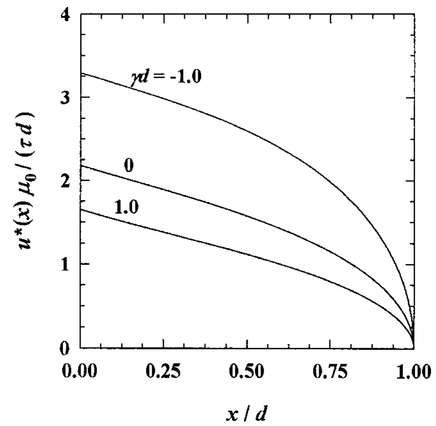

Fig. 11 Tangential crack opening displacement for fixed grip loading, $u^*(x)=u(x,+0)-u(x,-0)$, $\tau=8\mu_0\gamma_0/(\kappa+1)$, $\kappa=2$, $\mu(x)=\mu_0\exp(\gamma x)$

(Figs. 10 and 11) are closer to the homogeneous values than the crack opening displacements obtained from constant stresses (σ_0 and τ_0).

Figure 12 describes a sample problem concerning a graded half-plane with a surface crack loaded by a sliding rigid circular stamp. It is assumed that along the contact area $a<y<b$ the condition of Coulomb friction is valid with η as the coefficient of friction. For the geometry and the direction of loading shown, the results are given in Figs. 13–15. Figures 13 and 14 show the modes I and II stress intensity factors, respectively. Figure 15 shows the normalized force P for a given contact area ($(b-a)/R=0.1$) as a function of the stamp location. As expected, P increases with increasing material stiffness (or γ) and distance a. However, for $(a/R)>2$, P is very nearly constant. For details and extensive results see [17].

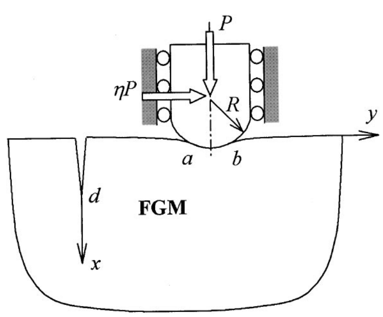

Fig. 12 A graded half-plane with a surface crack loaded by a sliding rigid circular stamp

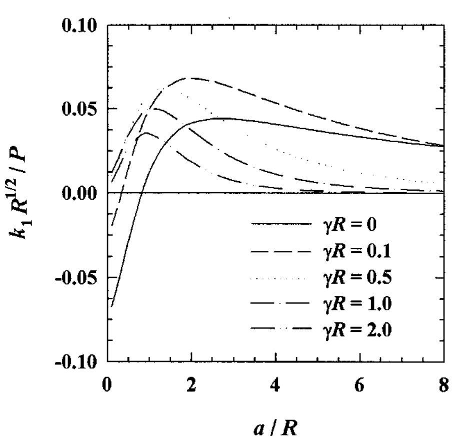

Fig. 13 Mode I stress intensity factors for a graded half-plane loaded by a sliding circular stamp as shown in Fig. 12, $(b-a)/R=0.1$, $d/R=0.1$, $\eta=0.4$, $\kappa=2$, $\mu(x)=\mu_0\exp(\gamma x)$

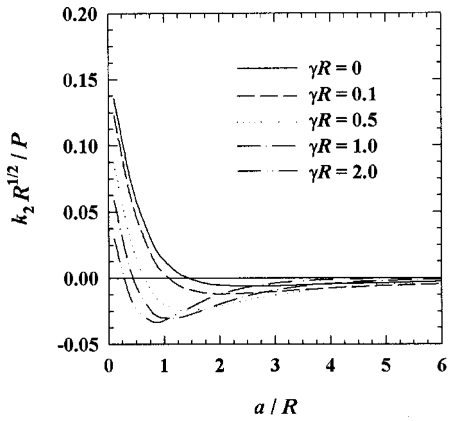

Fig. 14 Mode II stress intensity factors for a graded half-plane loaded by a sliding circular stamp as shown in Fig. 12, $(b-a)/R=0.1$, $d/R=0.1$, $\eta=0.4$, $\kappa=2$, $\mu(x)=\mu_0\exp(\gamma x)$

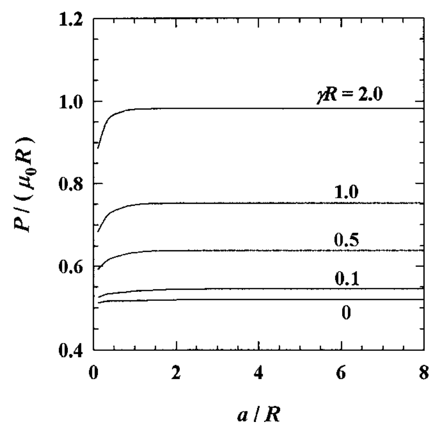

Fig. 15 Normalized force required for a given contact area $(b-a)/R=0.1$, $d/R=0.1$, $\eta=0.4$, $\kappa=2$, $\mu(x)=\mu_0\exp(\gamma x)$

It should be observed that since k_2 can be positive or negative there are no restrictions on the signs and relative magnitudes of shear loadings $\tau_0,\ldots,\tau_4$. However, $\sigma_0,\ldots,\sigma_4$ must be such that the resultant k_1 is positive. If k_1 is negative the results may still be useful in superposition with additional external loads giving a sufficiently high k_1 so that again final k_1 is positive. In the absence of such tensile loads the mode I problem has to be reconsidered as a crack closure or crack/contact problem in which near the crack tip the crack surfaces are partially closed and the contact region is determined by using $k_1(c)=0$ as closure criterion, where $c(0<c<d)$ is the end point of the contact region.

Thus, in the sliding contact problem considered in Fig. 12, the results given in Fig. 13 indicate that for small values of normalized material nonhomogeneity parameter γR and stamp distance a/R, k_1 is negative and, as they stand, the results are not valid. However, the results would be valid if the medium is subjected to for example, an additional in-plane tension.

Acknowledgment

This study was supported by AFOSR under the grant F49620-98-1-0028.

Appendix A

Various Functions Used in the Solution of the Mixed-Mode Crack Problem.

$$R_{xx1}(\alpha,t)=\frac{1}{\pi}\frac{\kappa-1}{\kappa+1}\frac{\alpha^2}{\lambda_1\lambda_2(\lambda_1^2+\lambda_2^2)}\{\gamma\lambda_2\cos(\lambda_2 t)+(\gamma\lambda_1-2(\lambda_1^2+\lambda_2^2)\sin(\lambda_2 t))\}, \quad (A1)$$

$$R_{xy1}(\alpha,t)=-\frac{2}{\pi}\frac{1}{\kappa+1}\frac{\alpha}{\lambda_1\lambda_2(\lambda_1^2+\lambda_2^2)}\{\lambda_2(\lambda_1^2+\lambda_2^2+\gamma^2/4)\times\cos(\lambda_2 t)-\lambda_1(\lambda_1^2+\lambda_2^2-\gamma^2/4)\sin(\lambda_2 t)\}, \quad (A2)$$

$$R_{xx2}(\alpha,t)=-\frac{2}{\pi}\frac{\kappa-1}{\kappa+1}\frac{\alpha^3}{\lambda_1\lambda_2(\lambda_1^2+\lambda_2^2)}\{\lambda_2\cos(\lambda_2 t)+\lambda_1\sin(\lambda_2 t)\}, \quad (A3)$$

$$R_{xy2}(\alpha,t)=-\frac{1}{\pi}\frac{1}{\kappa+1}\frac{\alpha^2}{\lambda_1\lambda_2(\lambda_1^2+\lambda_2^2)}\{\gamma\lambda_2\cos(\lambda_2 t)+(2(\lambda_1^2+\lambda_2^2)+\gamma\lambda_1)\sin(\lambda_2 t)\}, \quad (A4)$$

$$\lambda_1=\sqrt{\frac{R_1+R_2}{2}}, \quad (A5a)$$

$$\lambda_2=\sqrt{\frac{R_1-R_2}{2}}, \quad (A5b)$$

$$R_1=\sqrt{(\gamma^2/4+\alpha^2)^2+\alpha^2\gamma^2(3-\kappa)/(\kappa+1)}, \quad (A6)$$

$$R_2=\gamma^2/4+\alpha^2. \quad (A7)$$

Appendix B

Expressions for the kernels $k_{11}(x,y,t)$ and $k_{22}(x,y,t)$.

$$k_{11}(x,y,t)=k_{11}^{(i)}(x,y,t)+k_{11}^{(h)}(x,y,t), \quad (B1)$$

$$k_{22}(x,y,t)=k_{22}^{(i)}(x,y,t)+k_{22}^{(h)}(x,y,t), \quad (B2)$$

$$k_{11}^{(i)}(x,y,t)=\frac{\kappa+1}{\kappa-1}\frac{\exp(\gamma x)}{4\pi}\int_{-\infty}^{\infty}K_{11}^{(i)}(\omega,y)\exp(i\omega(x-t))d\omega, \quad (B3)$$

$$k_{11}^{(h)}(x,y,t)=\frac{\kappa+1}{\kappa-1}\frac{\exp(\gamma x)}{2}\int_{0}^{\infty}K_{11}^{(h)}(\alpha,t,x)\cos(\alpha y)d\alpha, \quad (B4)$$

$$k_{22}^{(i)}(x,y,t)=(\kappa+1)\frac{\exp(\gamma x)}{4\pi}\int_{-\infty}^{\infty}K_{22}^{(i)}(\omega,y)\exp(i\omega(x-t))d\omega, \quad (B5)$$

$$k_{22}^{(h)}(x,y,t)=(\kappa+1)\frac{\exp(\gamma x)}{2}\int_{0}^{\infty}K_{22}^{(h)}(\alpha,t,x)\cos(\alpha y)d\alpha, \quad (B6)$$

where the integrands are given as

$$K_{11}^{(i)}(\omega,y)=\sum_{j=3}^{4}(i\omega(3-\kappa)+A_j n_j(1+\kappa))P_j(\omega)\exp(n_j y), \quad (B7)$$

$$K_{22}^{(i)}(\omega,y)=\sum_{j=3}^{4}(n_j+i\omega A_j)Z_j(\omega)\exp(n_j y), \quad (B8)$$

$$K_{11}^{(h)}(\alpha,t,x)=\sum_{j=3}^{4}(p_j(3\text{-}\kappa)+D_j\alpha(1+\kappa))B_j^{*}(\alpha,t)\times\exp(p_j x+(\gamma/2-\lambda_1)t), \quad (B9)$$

$$K_{22}^{(h)}(\alpha,t,x)=\sum_{j=3}^{4}(\alpha+H_j p_j)G_j^{*}(\alpha,t)\exp(p_j x+(\gamma/2-\lambda_1)t). \quad (B10)$$

The terms used in Eq. (50) are in the following form:

$$m_{11n}(s)=\int_{-1}^{1}(1-r)^{-1/2}H_{11}(s,r)P_n^{(-1/2,0)}(r)dr, \quad (B11)$$

$$m_{22n}(s)=\int_{-1}^{1}(1-r)^{-1/2}H_{22}(s,r)P_n^{(-1/2,0)}(r)dr, \quad (B12)$$

$$H_{11}(s,r)=\frac{d}{2}\left\{h_{11s}\left(\frac{d}{2}s+\frac{d}{2},\frac{d}{2}r+\frac{d}{2}\right)+h_{11f}\left(\frac{d}{2}s+\frac{d}{2},\frac{d}{2}r+\frac{d}{2}\right)\right\}, \quad (B13)$$

$$H_{22}(s,r)=\frac{d}{2}\left\{h_{22s}\left(\frac{d}{2}s+\frac{d}{2},\frac{d}{2}r+\frac{d}{2}\right)+h_{22f}\left(\frac{d}{2}s+\frac{d}{2},\frac{d}{2}r+\frac{d}{2}\right)\right\}. \quad (B14)$$

References

[1] Yamanouchi, M., Koizumi, M., Hirai, T., and Shiota, I., eds., 1990, *FGM-90, Proc. 1st International Symposium on Functionally Gradient Materials*, Functionally Graded Materials Forum, Tokyo, Japan.

[2] Holt, J. B., Koizumi, M., Hirai, T., and Munir, Z. A., eds., 1993, *FGM-92, Proc. 2nd International Symposium on Functionally Gradient Materials*, The American Ceramic Society, Westerville, OH.

[3] Ilschner, B., and Cherradi, N., eds., 1995, *FGM-94, Proc. 3rd International Symposium on Structural and Functional Gradient Materials*, Presses Polytechniques et Universitaires Romandes, Lausanne, Switzerland.

[4] Shiota, I., and Miyamoto, Y., eds., 1997, *FGM-96, Proc. 4th International Symposium on Functionally Graded Materials*, Elsevier, Amsterdam.

[5] Kaysser, W. A., ed., 1999, *FGM-98, Proc. 5th International Symposium on Functionally Graded Materials*, Trans Tech Publications, NH.

[6] Miyamoto, M., Kaysser, W. A., Rabin, B. H., Kawasaki, A., and Ford, R. G., eds., 1999, *Functionally Graded Materials: Design, Processing and Applications*, Kluwer Academic Publishers, Norwell, MA.

[7] Erdogan, F., and Wu, B. H., 1997, "The Surface Crack Problem for a Plate With Functionally Graded Properties," ASME J. Appl. Mech., **64**, pp. 449–456.

[8] Erdogan, F., and Wu, B. H., 1996, "Crack Problems in FGM Layers under Thermal Stresses," J. Therm. Stresses, **19**, pp. 237–265.

[9] Kasmalkar M., 1997, "The Surface Crack Problem for a Functionally Graded Coating Bonded to a Homogeneous Layer," Ph.D. dissertation, Lehigh University, Bethlehem, PA.

[10] Jin, Z. H., and Batra, R. C., 1996, "Interface Cracking Between Functionally Graded Coatings and a Substrate Under Antiplane Shear," Int. J. Eng. Sci., **34**, pp. 1705–1716.

[11] Wang, X. Y., Wang, D., and Zou, Z. Z., 1996, "On the Griffith Crack in a Nonhomogeneous Interlayer of Adjoining Two Different Elastic Materials," Int. J. Fract., **79**, pp. R51–R56.

[12] Gao, H., 1991, "Fracture Analysis of Non-Homogeneous Materials via a Moduli Perturbation Approach," Int. J. Solids Struct., **27**, pp. 1663–1682.

[13] Wang, B. L., Han, J. C., and Du, S. Y., 2000, "Crack Problem for Non-Homogeneous Composite Material Subjected to Dynamic Loading," Int. J. Solids Struct., **37**, pp. 1251–1274.

[14] Nozaki, H., and Shindo, Y., 1998, "Effect of Interface Layers on Elastic Wave Propagation in a Fiber Reinforced Metal-Matrix Composite," Int. J. Eng. Sci., **36**, pp. 383–394.

[15] Erdogan, F., 1995, "Fracture Mechanics of Functionally Graded Materials," Composites Eng., **5**, pp. 753–770.

[16] Erdogan, F., 1998, "Crack Problems in Nonhomogeneous Materials," *Fracture, A Topical Encyclopedia of Current Knowledge*, G. P. Cherepanov, ed., Krieger Publishing Company, Malabar, FL, pp. 72–98.

[17] Dag, S., 2001, "Crack and Contact Problems in Graded Materials," Ph.D. dissertation, Lehigh University, Bethlehem, PA.

[18] Koiter, W. T., 1965, discussion of "Rectangular Tensile Sheet With Symmetrical Edge Cracks," Trans. ASME, J. Appl. Mech. **87**, pp. 237–238.

[19] Kaya, A. C., and Erdogan, F., 1987, "On the Solution of Integral Equations With Strongly Singular Kernels," Q. Appl. Math., **XLV**, pp. 105–122.

[20] Mahajan, R., 1991, "Crack Problems for an Elastic Film Bonded to an Orthotropic Substrate," Ph.D. dissertation, Lehigh University, Bethlehem, PA.

Vibration and Post-buckling of In-Plane Loaded Rectangular Plates Using a Multiterm Galerkin's Method

S. Ilanko
Department of Mechanical Engineering,
University of Canterbury,
Christchurch, New Zealand
e-mail: Ilanko@mech.canterbury.ac.nz

A procedure to calculate the natural frequencies of in-plane loaded, thin, slightly curved, simply supported rectangular plates is presented, with numerical results. This includes the solutions to von Karman's static equilibrium equation and the linear shell vibration equation using Galerkin's method. The compatibility equations are given in terms of Airy stress functions which satisfy the "shear free" and "constant normal displacement" in-plane edge conditions. This procedure is an extension to the method presented by Hui and Leissa, the difference being the use of a multiterm Fourier series representation for the initial imperfection, the static deflection and the vibratory modes.
[DOI: 10.1115/1.1489449]

1 Introduction

In an interesting article on the vibration of geometrically imperfect rectangular plates, Hui and Leissa [1] describe a single-term Galerkin's method to solve the nonlinear von Karman's equation for the static equilibrium state, and the linear shell vibration equation for the small amplitude vibratory motion, with the corresponding compatibility conditions expressed in terms of Airy stress functions, for simply supported plates subject to the following in-plane boundary conditions: all edges tangentially free (shear free), and constrained to move with constant displacement in the in-plane direction normal to the edges. For these conditions, the Airy stress functions derived in [1] satisfy the compatibility equation exactly, making this an ideal case for investigating the effect of geometric imperfections on the natural frequencies of in-plane stressed plates.

In [1], the initial imperfections, the static displacements and the transverse vibration modes were assumed to be of the same form as one of the vibration modes of the corresponding flat plate. The purpose of this paper is to extend this approach to permit the inclusion of a series of several vibration modes for the static and dynamic out-of-plane displacements. This method was first used by the author in a preliminary study to obtain the natural frequencies of slightly curved, unstressed plates, the results of which were subsequently verified by Harrington [2] in his undergraduate research project.

2 Static Analysis

Consider the static equilibrium of a simply supported rectangular plate with a small initial imperfection $z_0(x,y)$, thickness h, and edge dimensions a and b under biaxial normal in-plane loadings of intensity N_x and N_y. Let the out-of-plane static displacement measured from the plane containing the plate edges be $z(x,y)$, and the static Airy stress function be $F(x,y)$. The plate is made of an isotropic material having a density ρ, Poisson's ratio ν (taken as 0.3 in calculations), and an elastic modulus E. For convenience, the in-plane loading will be expressed nondimensionally in terms of the nominal lowest buckling load of a uniaxially loaded simply supported flat plate given by $N_{xc}=D\pi^2((1/a)^2+(1/b)^2)^2b^2$, where D is the plate flexural rigidity given by $D=Eh^3/(12(1-\nu^2))$. For simply supported plates, both z_0 and z may be expressed as Fourier sine series

$$z_0(x,y)=\sum_i \sum_j Z_{0i,j}\sin(i\pi x/a)\sin(j\pi y/b) \tag{1}$$

and

$$z(x,y)=\sum_i \sum_j Z_{i,j}\sin(i\pi x/a)\sin(j\pi y/b). \tag{2}$$

While any out-of-plane imperfection may be represented by an infinite series as in Eq. (1), computations are only done for a truncated series, with the number of functions in the x and y directions being n_x and n_y. The integers i and j would take odd values for symmetrical cases and even values for antisymmetrical cases.

The compatibility equation is

$$\nabla^4F=Eh((z_{,xy})^2-(z_{0,xy})^2-z_{,xx}z_{,yy}+z_{0,xx}z_{0,yy}). \tag{3}$$

The in-plane boundary conditions are

$$F_{xy}(0,y)=F_{xy}(a,y)=0;F_{yy}(0,y)=F_{yy}(a,y)=N_x;F_{xy}(x,0)=F_{xy}(x,b)=0;F_{xx}(x,0)=F_{xx}(x,b)=N_y. \tag{4}$$

Substituting Eqs. (1) and (2) into Eq. (3) and carrying out some algebraic, trigonometric and calculus operations leads to the following expression for F which also satisfies Eq. (4).

$$F=N_xy^2/2+N_yx^2/2+c_0\sum_i \sum_j \sum_k \sum_l (T_{1ijkl}+T_{2ijkl}+T_{3ijkl}+T_{4ijkl})(Z_{i,j}Z_{k,l}-Z_{0i,j}Z_{0k,l}). \tag{5}$$

Here

$$c_0=Eh/(4a^2b^2);T_{1ijkl}=c_1\cos((i-k)\pi x/a)\cos((j-l)\pi y/b);$$
$$T_{2ijkl}=c_2\cos((i-k)\pi x/a)\cos((j+l)\pi y/b);$$
$$T_{3ijkl}=c_3\cos((i+k)\pi x/a)\cos((j-l)\pi y/b);$$
$$T_{1ijkl}=c_4\cos((i+k)\pi x/a)\cos((j+l)\pi y/b),$$

Contributed by the Applied Mechanics Division of THE AMERICAN SOCIETY OF MECHANICAL ENGINEERS for publication in the ASME JOURNAL OF APPLIED MECHANICS. Manuscript received by the ASME Applied Mechanics Division, June 27, 2001; final revision, January 29, 2002. Associate Editor: N. C. Perkins. Discussion on the paper should be addressed to the Editor, Prof. Robert M. McMeeking, Department of Mechanical and Environmental Engineering University of California–Santa Barbara, Santa Barbara, CA 93106-5070, and will be accepted until four months after final publication of the paper itself in the ASME JOURNAL OF APPLIED MECHANICS.

in which

$$c_1=0 \text{ if } i=k \text{ and } j=l \text{ otherwise}$$
$$c_1=(ijkl-i^2l^2)/((i-k)^2/r+r(j-l)^2)^2;$$
$$c_2=(ijkl+i^2l^2)/((i-k)^2/r+r(j+l)^2)^2;$$
$$c_3=(ijkl+i^2l^2)/((i+k)^2/r+r(j-l)^2)^2;$$
$$c_4=(ijkl-i^2l^2)/((i+k)^2/r+r(j+l)^2)^2,$$

where the aspect ratio $r=a/b$.

The equilibrium equation for a rectangular plate is

$$D\nabla^4(z-z_0)=F_{,yy}z_{,xx}+F_{,xx}z_{,yy}-2F_{,xy}z_{,xy}. \quad (6)$$

Using Galerkin's method with a weighting function of the form $\sin(p\pi x/a)\sin(q\pi y/b)$ gives

$$D\pi^4((p/a)^2+(q/b)^2)^2(Z_{p,q}-Z_{0p,q})(ab/4)-\int_{x=0}^{a}\int_{y=0}^{b}(F_{,yy}z_{,xx}+F_{,xx}z_{,yy}-2F_{,xy}z_{,xy})\sin(p\pi x/a)\sin(q\pi y/b)\,dx\,dy=0. \quad (7)$$

For each choice of p and q, one nonlinear cubic equation is obtained, giving a total of $n_x\times n_y$ equations. These equations were solved using a Newton-Raphson iterative scheme and the results are discussed later.

3 Vibration Analysis

Let the dynamic out-of-plane displacement be

$$w(x,y,t)=W(x,y)\sin(\omega t+\phi)=\sum_m\sum_n H_{m,n}\sin(m\pi x/a)\sin(n\pi yy/b)\sin(\omega t+\phi). \quad (8)$$

The dynamic compatibility equation for small amplitude vibrations is

$$\nabla^4 f=Eh(2z_{,xy}w_{,xy}-z_{,yy}w_{,xx}-z_{,xx}w_{,yy}). \quad (9)$$

The in-plane boundary conditions are

$$f_{xy}(0,y)=f_{xy}(a,y)=f_{yy}(0,y)=f_{yy}(a,y)=f_{xy}(x,0)=f_{xy}(x,b)=f_{xx}(x,0)=f_{xx}(x,b)=0. \quad (10)$$

It can be shown that an Airy stress function that satisfies Eqs. (9) and (10) is

$$f=(Eh/4)\sum_i\sum_j\sum_k\sum_l(S_{1mnkl}+S_{2mnkl}+S_{3mnkl}+S_{4mnkl})\times(Z_{k,l}H_{m,n})\sin(\omega t+\phi) \quad (11)$$

where

$$S_{1mnkl}=c_5\cos((m-k)\pi x/a)\cos((n-l)\pi y/b);$$
$$S_{2mnkl}=c_6\cos((m-k)\pi x/a)\cos((n+l)\pi y/b);$$
$$S_{3mnkl}=c_7\cos((m+k)\pi x/a)\cos((n-l)\pi y/b);$$
$$S_{4mnkl}=c_8\cos((m+k)\pi x/a)\cos((n+l)\pi y/b)$$

in which

$$c_5=0 \text{ if } m=k \text{ and } n=l \text{ otherwise}$$
$$c_5=-(kn-ml)^2/((m-k)^2/r+r(n-l)^2)^2;$$
$$c_6=(kn+ml)^2/((m-k)^2/r+r(n+l)^2)^2;$$
$$c_7=(kn+ml)^2/((m+k)^2/r+r(n-l)^2)^2;$$
$$c_8=-(kn-ml)^2/((m+k)^2/r+r(n+l)^2)^2.$$

The equation of motion for small amplitude out-of-plane vibrations of a plate is

$$D\nabla^4 w-\rho h\omega^2 w-F_{,yy}w_{,xx}-F_{,xx}w_{,yy}+2F_{,xy}w_{,xy}-f_{,yy}z_{,xx}+f_{,xx}z_{,yy}+2f_{,xy}z_{,xy}=0.$$

On application of Galerkin's method, this yields

$$(D\pi^4((p/a)^2+(q/b)^2)^2-\rho h\omega^2)H_{p,q}(ab/4)\sin(\omega t+\phi)-\int_{x=0}^{a}\int_{y=0}^{b}(F_{,yy}w_{,xx}+F_{,xx}w_{,yy}-2F_{,xy}w_{,xy}+f_{,yy}z_{,xx}+f_{,xx}z_{,yy}-2f_{,xy}z_{,xy})\sin(p\pi x/a)\sin(q\pi y/b)\,dx\,dy=0. \quad (12)$$

Substituting Eqs. (5) and (11), and the values for $Z_{i,j}$ obtained from the static analysis into Eq. (12) and eliminating the common factor $\sin(\omega t+\phi)$ results in an eigenvalue equation of the form

$$[K]\{H\}=\omega^2[M]\{H\} \quad (13)$$

where $[K]$ and $[M]$ are the stiffness and mass matrices, respectively.

The solution to the above equation gives the natural frequencies.

4 Results and Discussion

Numerical solutions to Eqs. (7) and (13) were obtained for a square plate subject to uniaxial in-plane loading, for various values of load ratio ($\gamma=N_x/N_{xc}$) and initial imperfection. The results presented here are for an initial imperfection in the form of the fundamental vibration mode of a plate given by $z_0(x,y)=\mu_0 h\sin(\pi x/a)\sin(\pi y/b)$. The parameter μ_0 is a nondimensional initial imperfection. For the single term analyses, the function $\sin(\pi x/a)\sin(\pi y/b)$ was used for both w and z. For the four term analyses, the first two symmetrical sine functions were used in both x and y directions (i.e., $\sin(\pi x/a)$, $\sin(\pi x/a)$, $\sin(\pi y/b)$ and $\sin(3\pi y/b)$). The nine term analyses included the terms $\sin(5\pi x/a)$ and $\sin(5\pi y/b)$ also. The results are presented in terms of the following nondimensional parameters:

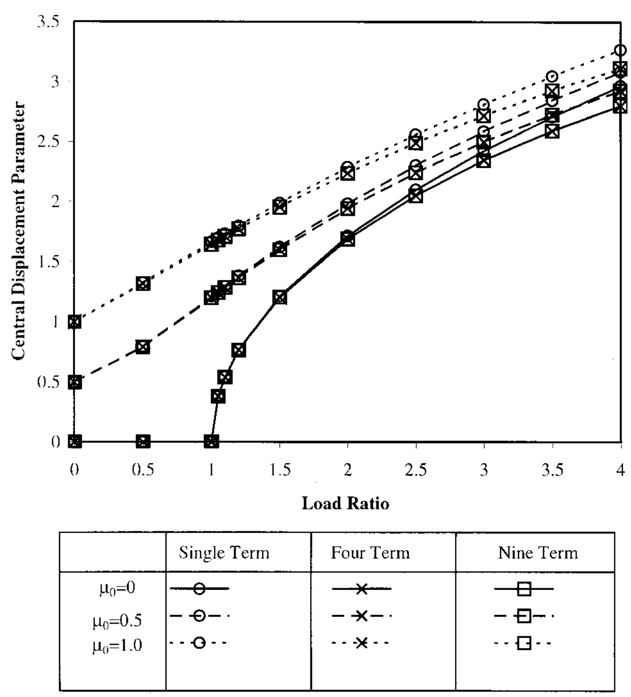

Fig. 1 Load-displacement relationship

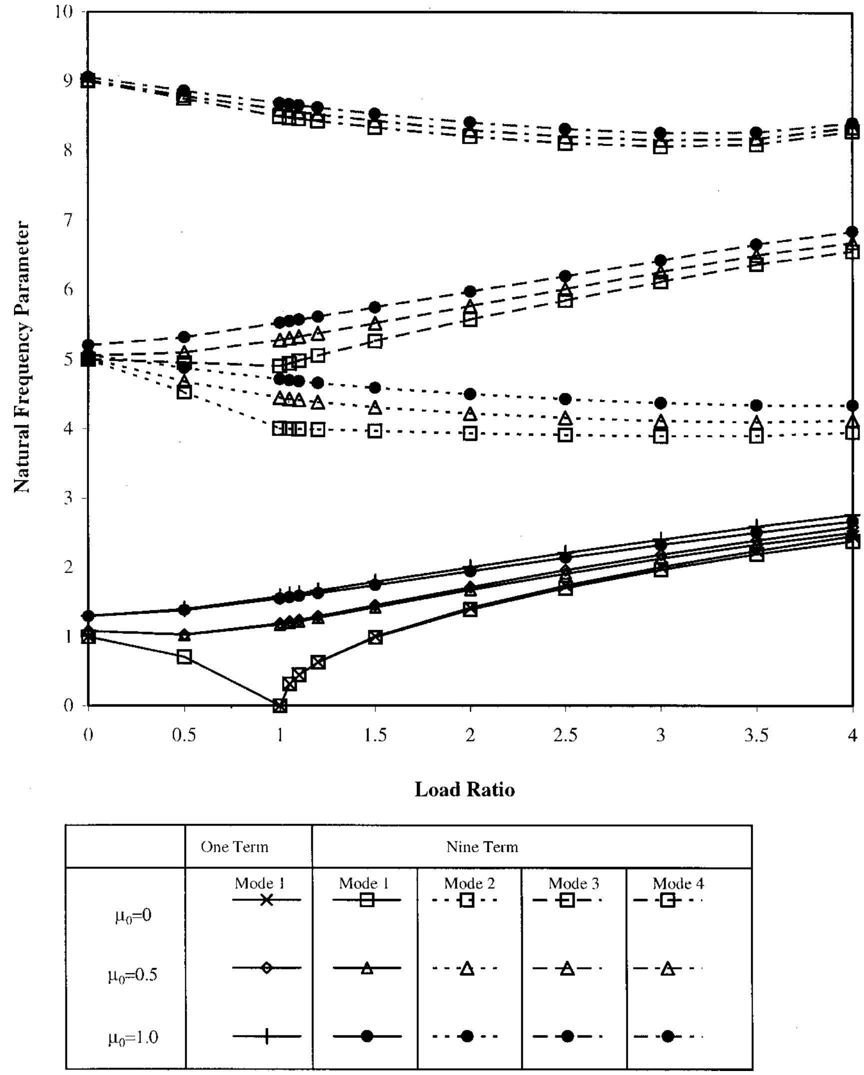

Fig. 2 Load-frequency relationship for the first four modes

central displacement parameter $\mu = z(0.5a, 0.5b)/h$ and natural frequency parameter $\lambda_n = \omega_n/\Omega_1$ where ω_n is the nth natural frequency of the loaded, deformed plate and Ω_1 is the fundamental natural frequency of the unstressed flat plate given by

$$\Omega_1 = \pi^2((1/a^2) + (1/b^2))\sqrt{D/(\rho h)}.$$

Figure 1 shows the variation of the central displacement parameter with load ratio, for initial imperfection values (μ_0) of zero (initially flat plate), 0.5, and 1.0. Figure 2 shows the variation of the natural frequency parameter with load. Some of the results are also given in numerical form in Table 1.

Computations were limited to the positive roots of the static displacement only. Vibration about the snap-through equilibrium configuration has not been considered here but these results may be generated using the computer program developed by the author currently available at ⟨http://www.geocities.ilanko/vibration.htm⟩.

From Table 1 and Fig. 1 it can be seen that the discrepancy between the four-term and nine-term solution for μ is very small, the worst being less than 1% for $\gamma = 4$ and $\mu_0 = 0$. However, the discrepancy between the single-term and nine-term results is noticeable, particularly for $\gamma > 1$, and reaches about 5.7% for $\gamma = 4$ and $\mu_0 = 0$.

From Fig. 2 it may be observed that for loadings below the

Table 1 Some numerical results

		μ			ω_1/Ω_1			ω_2/Ω_1		ω_3/Ω_1		ω_4/Ω_1	
μ_0	Load Ratio	Single Term	Four Term	Nine Term	Single Term	Four Term	Nine Term	Four Term	Nine Term	Four Term	Nine Term	Four Term	Nine Term
0	1.0	0.000	0.000	0.000	0.000	0.000	0.000	4.000	4.000	4.899	4.899	8.485	8.485
	4.0	2.965	2.802	2.804	2.449	2.388	2.377	3.958	3.941	6.552	6.544	8.289	8.279
1.0	1.0	1.662	1.643	1.643	1.577	1.547	1.547	4.708	4.707	5.521	5.520	8.685	8.680
	4.0	3.269	3.115	3.117	2.757	2.676	2.661	4.344	4.331	6.844	6.834	8.405	8.399

lowest nominal buckling load, the difference between the single-term results and the nine-term results for the fundamental frequency is not noticeable on the graph. This discrepancy becomes noticeable at higher loadings, and for $\gamma=4$ and $\mu_0=1.0$ it is about 3.6%. The effect of initial imperfection corresponding to the fundamental natural vibration mode of an unstressed flat plate on the higher natural frequencies is worth noting. For example, for $\gamma=4$, λ_2 changes from 3.941 for a flat plate to 4.331 for $\mu_0=1.0$, an increase of about 10%. This is comparable to the corresponding change in λ_1 which is about 12% which shows that in general a multiterm solution is desirable since any imperfection in practice is unlikely to be of a pure vibration mode.

Conclusions

The natural frequencies of in-plane loaded simply supported rectangular plates with initial out-of-plane geometric imperfection have been calculated using a multiterm Galerkin's method in which the Airy stress functions that exactly satisfy the compatibility equations for static and dynamic analyses were used. The results show that the discrepancy between the single-term results presented by Hui and Leissa [1] and the multiterm results, for the fundamental natural frequency of a square plate, is within about 3.6% for uniaxial loadings of up to about four times the nominal buckling load, for imperfections having the shape of the fundamental natural mode of vibration of the flat plate with a central deflection equal to the plate thickness. The determination of the effect of imperfections of arbitrary shapes would require a multiterm approach, as do the calculation of higher natural frequencies except when the imperfection is of the same shape as the mode under consideration.

Acknowledgment

The method presented here was first used by the author in a preliminary study of vibration of slightly curved unstressed plates during his doctoral studies at the University of Western Ontario, Canada. The author is thankful to his Ph.D. supervisor Emeritus Professor S. M. Dickinson for his advice and encouragement during this preliminary study.

References

[1] Hui, D., and Leissa, A. W., 1983, ''Effects of Geometrical Imperfections on Vibrations of Biaxially Compressed Rectangular Flat Plates,'' ASME J. Appl. Mech., **50**, pp. 750–756.

[2] Harrington, J. J., 1993, ''*The Small Amplitude Vibrations of Geometrically Imperfect, Simply Supported, Rectangular Plates*,'' BE Project Report No. 28, Department of Mechanical Engineering, University of Canterbury, New Zealand.

The Isotropic Ellipsoidal Inclusion With a Polynomial Distribution of Eigenstrain

M. Rahman
Daimler-Chrysler Corporation,
CIMS 484-14-01,
800 Chrysler Drive,
Auburn Hills, MI 48326-2757
e-mail: mr117@daimlerchrysler.com
Mem. ASME

We consider the problem of determining the elastic field in an infinite elastic solid induced by an ellipsoidal inclusion with a distribution of eigenstrains. The particular type of distribution considered in the article is characterized by a polynomial in the Cartesian coordinates of the points of the inclusion. Eshelby showed that in such a situation the induced strain field within the inclusion is also characterized by a polynomial of the same order. However, the explicit expression for this polynomial seems to have not yet been reported in the literature. The present study fills this gap. [DOI: 10.1115/1.1491270]

1 Introduction

The problem of an ellipsoidal inclusion undergoing a stress-free eigenstrain transformation (transformation strain) in the absence of the surrounding matrix, is by now a classical problem in linear elasticity. The presence of the surrounding material induces additional "constrained" strains in the inclusion. Eshelby [1–3] first considered this problem and showed that if the eigenstrain is given in the form of a polynomial of an arbitrary order in the Cartesian coordinates of the points of the inclusion, then the additional (induced) strain field in the inclusion is also characterized by a polynomial of the same order. We shall refer to this result as *Eshelby's polynomial conservation theorem*. Since the publication of Eshelby's work, considerable extent of research had been done over the past several decades on different aspects of this problem. Several authors, namely, Walpole [4], Kinoshita and Mura [5–7], and Asaro and Barnett [8] proved that this theorem also holds for an anisotropic medium. Mura [9,10], Nemat-Nasser and Hori [11], and Khachaturyan [12] have given exhaustive account of the available results in this area. Furthermore, it is Mura who is responsible for giving currency to the terminology "eigenstrain." Much of the recent interest in this area is due to Markenscoff and her co-workers ([13—16]), who were able to prove a conjecture of Eshelby's that ellipsoid is the only configuration having the remarkable property that the stress field inside an inclusion of uniform eigenstrain is constant.

Returning to Eshelby's polynomial conservation theorem, Mura [9] has outlined a general method, based on multipole expansion, of quantifying the additional strain field within the transformed ellipsoid with a polynomial distribution of eigenstrain. However, in practice, it is hardly possible to carry through his analysis beyond the first few terms. To the best of the writer's knowledge, no explicit expression for the polynomial characterizing the strain field within the transformed ellipsoid has yet been reported in the literature. The purpose of the present article is to fill this gap. Specifically, we deduce the explicit expression for this polynomial in terms of some integrals, which we call the potential integrals, and are able to concatenate the results into an algorithmic form usable for polynomials of arbitrary orders and especially suited for symbolic manipulation by computer. The method employed to deduce the results presented in the article is based on Ferrers—Dyson theorem ([17,18]) on the Newtonian potentials of heterogeneous ellipsoids and some of its further developments by Rahman [19].

Apart from the purely aesthetic appeal, the solution of the problem has considerable practical significance. For example, although in many practical applications, the eigenstrains may not be explicitly given in the form of a polynomial, but they can be *uniformly* approximated in the *bounded* domain of the ellipsoid by a polynomial, as long as the function characterizing the eigenstrains is *continuous*. The basis for this statement has its roots in a theorem in the theory of functions, known as Bernstein's theorem ([20]). To realize such an approximation practically, one can resort to some fairly well established algorithms, such as the least-squares and Marquardt-Levenberg methods. Thus, the solution of this problem is capable of extending our ability to analyze problems concerning ellipsoidal inclusions with nonuniform eigenstrains. Another area where the solution of the present problem might be useful is related to dynamically transforming ellipsoidal inclusions. It is well known that closed-form solutions of such problems can be developed only for a handful of configurations, such as, spherical ([21,22]) and cylindrical ([23]). It is probably not possible to derive a closed-form solution for the problem of a dynamically transforming ellipsoid with three unequal axes. However, for low frequency or short time ranges, the solution of the latter can be expanded as a formal power series in the wave number or time, with the zeroth-order term being the corresponding elastostatic one. The problem is thus reducible to a potential one so that the results of solution of the elastostatic counterpart of the problem for a polynomial distribution of eigenstrain can be applied to deduce an approximate analytical solution. Furthermore, by retaining a sufficient number of terms in such an expansion and using various perturbation series improvement techniques, such as, those based on exploiting the benefits of Domb-Sykes plot, as discussed by Van Dyke in a lucid article ([24]), it might be possible to improve the convergence of such a series solution of the problem up to a significant level to cover intermediate and even high-frequency/time regimes.

We begin by introducing the notation that we shall make use of. The symbol $\mathbf{x}$ is used in the article to mean the triplet of Cartesian coordinates (x_1, x_2, x_3) in the three-dimensional Euclidean space $\mathbf{R}^3$. Repeated indices are used to mean summation over 1, 2, 3, unless stated otherwise. The symbol ∂_i is used to mean the operation of differentiation with respect to x_i. The norm of the vector $\mathbf{x}$ is designated by $|\mathbf{x}|$.

2 The Derivation

It can be shown (see, for instance, [9]) that the displacement field in an infinite elastic solid caused by an eigenstrain $\varepsilon^*_{ij}(\mathbf{x})$ distributed within an inclusion occupying a domain $\Omega \in \mathbf{R}^3$ is given by the expression

Contributed by the Applied Mechanics Division of THE AMERICAN SOCIETY OF MECHANICAL ENGINEERS for publication in the ASME JOURNAL OF APPLIED MECHANICS. Manuscript received by the ASME Applied Mechanics Division, June 5, 2001; final revision, Dec. 10, 2001. Associate Editor: D. A. Kouris. Discussion on the paper should be addressed to the Editor, Prof. Robert M. McMeeking, Department of Mechanical and Environmental Engineering University of California–Santa Barbara, Santa Barbara, CA 93106-5070, and will be accepted until four months after final publication of the paper itself in the ASME JOURNAL OF APPLIED MECHANICS.

$$u_i(\mathbf{x}) = -C_{jkmn}\int_\Omega G_{ij,k}(\mathbf{x}-\mathbf{y})\varepsilon^*_{mn}(\mathbf{y})d\mathbf{y}, \tag{1}$$

where $G_{ij,k} = \partial_k G_{ij}$, $d\mathbf{y} = dy_1 dy_2 dy_3$, C_{jkmn} is the elasticity tensor and $G_{ij}(\mathbf{x}-\mathbf{y})$ is the elastostatic Green's function, which corresponds to the displacement response of an infinite elastic medium at the point $\mathbf{x}$, due to a point load applied at the point $\mathbf{y}$. The eigenstrain-tensor $\varepsilon^*_{mn}(\mathbf{x})$ is symmetric. In what follows, it will be assumed that Ω is an ellipsoid with three unequal axes $a_i (i = 1,2,3)(a_1 > a_2 > a_3)$, i.e.,

$$\Omega = \left\{ \mathbf{x}\in\mathbf{R}^3 \left| \sum_{i=1}^{3} x_i^2/a_i^2 \leqslant 1 \right.\right\}.$$

For a homogeneous isotropic material, we have

$$C_{jkmn} = \lambda\,\delta_{jk}\delta_{mn} + \mu\,\delta_{jm}\delta_{kn} + \mu\,\delta_{jn}\delta_{km},$$

$$G_{ij}(\mathbf{x}-\mathbf{y}) = \frac{1}{4\pi\mu}\frac{\delta_{ij}}{|\mathbf{x}-\mathbf{y}|} - \frac{1}{16\pi\mu(1-\nu)}\partial_i\partial_j|\mathbf{x}-\mathbf{y}|, \tag{2}$$

where δ_{ij} is Kronecker's delta, $\lambda = 2\nu\mu/(1-2\nu),\mu$ are the Lamé constants, and ν the Poisson's ratio of the material of the solid.

Putting (2) into (1), we obtain

$$u_i(\mathbf{x}) = \eta_1\partial_i\int_\Omega d\mathbf{y}\frac{\varepsilon^*_{mm}(\mathbf{y})}{|\mathbf{x}-\mathbf{y}|} - \eta_2\partial_j\int_\Omega d\mathbf{y}\frac{\varepsilon^*_{ij}(\mathbf{y})}{|\mathbf{x}-\mathbf{y}|} + \eta_3 x_k\partial_i\partial_j\int_\Omega d\mathbf{y}\frac{\varepsilon^*_{jk}(\mathbf{y})}{|\mathbf{x}-\mathbf{y}|} - \eta_3\partial_i\partial_j\int_\Omega d\mathbf{y}\frac{y_k\varepsilon^*_{jk}(\mathbf{y})}{|\mathbf{x}-\mathbf{y}|}, \tag{3}$$

where

$$\eta_1 = \frac{1-2\nu}{8\pi(1-\nu)}, \quad \eta_2 = \frac{3-4\nu}{8\pi(1-\nu)}, \quad \eta_3 = \frac{1}{8\pi(1-\nu)}. \tag{4}$$

In what follows, it is assumed that the eigenstrain $\varepsilon^*_{ij}(\mathbf{x})$ is given in the following form:

$$\varepsilon^*_{ij}(\mathbf{x}) = \sum_{p+q+r=0}^{N}\varepsilon^*_{ijpqr}\left(1-\sum_{n=1}^{3}\frac{x_n^2}{a_n^2}\right)^{l-1}\left(\frac{x_1}{a_1}\right)^p\left(\frac{x_2}{a_2}\right)^q\left(\frac{x_3}{a_3}\right)^r, \quad (l=1,2\cdots), \tag{5}$$

where ε^*_{ijpqr} are known dimensionless coefficients. Equation (5) represents a polynomial in $\mathbf{x}$ of order $N+2l-2$. Additionally, for $l = 2,3,4,\cdots$, this polynomial has the property that it vanishes at the bounding surface of the ellipsoid. It is worth mentioning in this context that the method employed (Ferrers-Dyson theorem) is also capable of taking into consideration the special case where $l=0$, in which case the eigenstrains are singular as the bounding surface of the ellipsoid is approached. It can be shown that this case leads to violation of compatibility of deformations and as such must be discarded.

Putting (5) into (3), we obtain

$$u_i(\mathbf{x}) = \eta_1\partial_i\Gamma^{N,l}_{mm} - \eta_2\partial_j\Gamma^{N,l}_{ij} + \eta_3 x_k\partial_i\partial_j\Gamma^{N,l}_{jk} - \eta_3 a_k\partial_i\partial_j\,{}^{(k)}\tilde{\Gamma}^{N,l}_{jk} \tag{6}$$

where the following notation is introduced:

$$\Gamma^{N,l}_{ij} = \sum_{p+q+r=0}^{N}\varepsilon^*_{ijpqr}\,{}^{(l)}V^{(\alpha)}_{pqr},$$

$${}^{(k)}\tilde{\Gamma}^{N,l}_{ij} = \sum_{p+q+r=0}^{N}\varepsilon^*_{ijpqr}\,{}^{(l)}V^{(\alpha)}_{p+\delta_{k1},q+\delta_{k2},r+\delta_{k3}} = \sum_{p+q+r=0}^{N+1}\varepsilon^*_{i,j,p-\delta_{k1},q-\delta_{k2},r-\delta_{k3}}\,{}^{(l)}V^{(\alpha)}_{pqr} \tag{7}$$

and

$${}^{(l)}V^{(\alpha)}_{pqr}(\mathbf{x}) = \int_\Omega\frac{d\mathbf{y}}{|\mathbf{x}-\mathbf{y}|}\left(1-\sum_{i=1}^{3}\frac{y_i^2}{a_i^2}\right)^{l-1}\left(\frac{y_1}{a_1}\right)^p\left(\frac{y_2}{a_2}\right)^q\left(\frac{y_3}{a_3}\right)^r. \tag{8}$$

In the second equation in (7), it should be assumed that $\varepsilon^*_{i,j,-1,k,l} = 0$, $\varepsilon^*_{i,j,k,-1,l} = 0$, $\varepsilon^*_{i,j,k,l,-1} = 0$, for $\forall(i,j = 1,2,3; k+l = 0\cdots N, k\geqslant 0, l\geqslant 0)$.

The reader would notice that Eq. (8) characterizes the Newtonian potential of a distribution of mass whose mass density is characterized by the function

$$\left(1-\sum_{i=1}^{3}\frac{x_i^2}{a_i^2}\right)^{l-1}\left(\frac{x_1}{a_1}\right)^p\left(\frac{x_2}{a_2}\right)^q\left(\frac{x_3}{a_3}\right)^r, \quad (l,p,q,r = 0,1,2\cdots). \tag{9}$$

This question was studied by Ferrers [17] and in complete generality by Dyson [18]. In particular, the latter showed that the matter distributed within an ellipsoid with three unequal semi-axes $a_i (i = 1,2,3)$ $(a_1 > a_2 > a_3)$ such that the mass density varies as

$$\sigma(\mathbf{x}) = \sigma_0\left(1-\sum_{i=1}^{3}\frac{x_i^2}{a_i^2}\right)^{\eta-1} f\left(\frac{x_1}{a_1},\frac{x_2}{a_2},\frac{x_3}{a_3}\right), \quad \eta > 0, \quad \sigma_0 \text{ is a constant}, \tag{10}$$

($f(\mathbf{x})$ is a sufficiently smooth function) produces outside the ellipsoid a harmonic potential $V(\mathbf{x})$:

$$V(\mathbf{x}) = \sigma_0\pi a\int_\alpha^\infty d\psi\frac{1}{\sqrt{\Delta}}\sum_{m=0}^{\infty}\frac{M^{m+\eta}\psi^m}{2^{2m}m!(\eta)_{m+1}} \times D^m f\left(\frac{a_1x_1}{a_1^2+\psi},\frac{a_2x_2}{a_2^2+\psi},\frac{a_3x_3}{a_3^2+\psi}\right), \tag{11}$$

where $a = a_1a_2a_3$, $(\eta)_{m+1} = \eta(\eta+1)(\eta+2)\ldots(\eta+m) = \Gamma(\eta+m+1)/\Gamma(\eta)$ ($\Gamma(\cdots)$ is the gamma function) is the Pochhammer's symbol, and

$$D = \sum_{i=1}^{3}\frac{a_i^2+\psi}{a_i^2}\frac{\partial^2}{\partial x_i^2}, \quad M = 1-\sum_{i=1}^{3}\frac{x_i^2}{a_i^2+\psi}, \quad \Delta = \prod_{i=1}^{3}(a_i^2+\psi), \tag{12}$$

and α is the positive root of the equation[1]

$$1-\sum_{i=1}^{3}\frac{x_i^2}{a_i^2+\alpha} = 0. \tag{13}$$

The potential in the interior of the ellipsoid can be found by putting $\alpha = 0$ in Eq. (11), which follows from Ivory's theorem. Equations (10) to (13) are also valid for $\eta = 0$, provided it is assumed that $(-1)! = 1$.

It can be easily seen from Eq. (11) that when the mass density is given by (9) and $\mathbf{x}\in\Omega$ (i.e., $\alpha = 0$), the infinite series in (11) conveniently terminates as a result of successive differentiation and reduces to a polynomial in $\mathbf{x}$ of order $p+q+r+2l$, implying that within the ellipsoid, $\Gamma^{N,l}_{ij}$, ${}^{(k)}\tilde{\Gamma}^{N,l}_{ij}$ reduce to polynomials in $\mathbf{x}$ of orders $N+2l$ and $N+2l+1$, respectively. Thus, it can be seen from Eq. (6) that the displacement field within the transformed ellipsoid is characterized by a polynomial in $\mathbf{x}$ of order $N+2l-1$, and hence the strain field by a polynomial in $\mathbf{x}$ of order $N+2l-2$. For the particular case where $l=1$, this leads to the conclusion that if the eigenstrains within ellipsoid are characterized by a polynomial in $\mathbf{x}$ of orders N, then the induced strain field within the transformed ellipsoid is also characterized by a polynomial in $\mathbf{x}$ of the same order. These were essentially the lines of arguments that led Eshelby to arrive at the polynomial conservation theorem.

[1]In fact, it can be shown (see, for instance, [25]) that for $\forall\mathbf{x}\in\mathbf{R}^3\backslash\Omega$, Eq. (13) has only *one real positive* root, the other two roots being complex conjugates.

Central to our derivation is the following result recently obtained by Rahman [19]:

$$
\begin{aligned}
{}^{(l)}V_{pqr}^{(\alpha)}(\mathbf{x}) = & \frac{\pi a p!q!r!(l-1)!}{2^{p+q+r}} \sum_{i+j+k=0}^{\beta} (-1)^{i+j+k} \frac{\Xi_{i+\delta(p)/2,j+\delta(q)/2,k+\delta(r)/2} x_1^{2i+\delta(p)} x_2^{2j+\delta(q)} x_3^{2k+\delta(r)}}{(\beta-i-j-k)!} \\
& \times \sum_{k'=0}^{[p/2]} \sum_{k''=0}^{[q/2]} \sum_{k'''=0}^{[r/2]} (-1)^{k'+k''+k'''} \frac{\Xi_{k'+\delta(p)/2,k''+\delta(q)/2,k'''+\delta(r)/2} a_1^{2k'+\delta(p)} a_2^{2k''+\delta(q)} a_3^{2k'''+\delta(r)}}{([p/2]-k')!([q/2]-k'')!([r/2]-k''')!} \\
& \times \Pi_{ijkk'k''k'''}^{pqr} I_{i+k'+\delta(p),j+k''+\delta(q),k+k'''+\delta(r)}^{(\alpha)}.
\end{aligned}
\tag{14}
$$

where $\beta = l+[p/2]+[q/2]+[r/2]$ ($[p/2]$ is equal to the integer part of $p/2$), and

$$
\Xi_{ijk} = \frac{1}{(2i)!(2j)!(2k)!},
$$

$$
\Pi_{ijklmn} = \frac{(2i+2l)!(2j+2m)!(2k+2n)!}{(i+l)!(j+m)!(k+n)!}, \tag{15}
$$

$$
\Pi_{ijklmn}^{pqr} \equiv \Pi_{i+\delta(p)/2,j+\delta(q)/2,k+\delta(r)/2,l+\delta(p)/2,m+\delta(q)/2,n+\delta(r)/2},
$$

and

$$
I_{ijk}^{(\alpha)} = \int_{\alpha}^{\infty} \frac{d\psi}{\sqrt{(a_1^2+\psi)^{2i+1}(a_2^2+\psi)^{2j+1}(a_3^2+\psi)^{2k+1}}}, \tag{16}
$$

and $\delta(i)$ is an integer-valued function such that $\delta(i)=0$ if i is zero or any even positive integer, and $\delta(i)=1$ if i is any odd positive integer. For points lying in the interior of the ellipsoid, α should be set equal to zero.

In [20], integrals (16) are defined as the *potential integrals of the ellipsoid*. Furthermore, they are defined as internal potential integrals and external potential integrals of the ellipsoid, depending on whether $\mathbf{x}\in\Omega$ (i.e., $\alpha=0$), or $\mathbf{x}\in\mathbf{R}^3\backslash\Omega$ (i.e., $\alpha\neq 0$). In the sequel, the interior potential integrals $I_{ijk}^{(0)}$ will be denoted simply by I_{ijk}. In Section 3, recurrence relations are given by means of which closed-form expressions for the potential integrals can be deduced for all $i,j,k=0,1,2,\cdots$, in terms of elliptic integrals of the first and second kinds.

An interesting feature of Eq. (14) is that each single term $x_1^p x_2^q x_3^r$ yields a polynomial in $\mathbf{x}$ of order $p+q+r+2l$. Furthermore, each individual power of x_1, x_2, x_3 in all the terms in the resulting polynomial is odd or even, depending on whether p,q,r are odd or even, respectively. For instance, the density characterized by the function $x_1^9 x_2^{10} x_3^7$ generates a potential characterized by a polynomial in $\mathbf{x}$ of order 28 in which the powers of x_1 and x_3 are only odd numbers, while that of x_2 is either zero or even numbers only. Specifically, the resulting polynomial would contain terms of the form $x_1^{2t_1+1} x_2^{2t_2} x_3^{2t_3+1}$, where $t_1+t_2+t_3=0,1,2,\cdots,13$.

Following the above arguments, Rahman [19] showed that for $\mathbf{x}\in\Omega$, equations in (7) can be reduced to the following explicit polynomial forms:

$$
\Gamma_{ij}^{N,l} = \sum_{p+q+r=0}^{N+2l} F_{pqr}^{ij,l} x_1^p x_2^q x_3^r,
$$

$$
{}^{(k)}\tilde{\Gamma}_{ij}^{N,l} = \sum_{p+q+r=0}^{N+2l+1} {}^{(k)}\tilde{F}_{pqr}^{ij,l} x_1^p x_2^q x_3^r, \tag{17}
$$

where

$$
\begin{aligned}
F_{pqr}^{ij,l} = & \frac{\pi a(l-1)!(-1)^{\beta_0}}{2^{\delta(p)+\delta(q)+\delta(r)} p!q!r!} \sum_{t_1+t_2+t_3=\tau}^{\gamma} \frac{[2t_1+\delta(p)]![2t_2+\delta(q)]![2t_3+\delta(r)]!}{4^{t_1+t_2+t_3}(t_1+t_2+t_3+l-\beta_0)!} \times \varepsilon_{i,j,\delta(p)+2t_1,\delta(q)+2t_2,\delta(r)+2t_3}^{*} \\
& \times \sum_{k'=0}^{t_1} \sum_{k''=0}^{t_2} \sum_{k'''=0}^{t_3} (-1)^{k'+k''+k'''} \frac{[p+2k'+\delta(p)]![q+2k''+\delta(q)]!}{(t_1-k')!(t_2-k'')!(t_3-k''')!} \\
& \times \frac{[r+2k'''+\delta(r)]!}{[2k'+\delta(p)]![2k''+\delta(q)]![2k'''+\delta(r)]![[p/2]+k'+\delta(p)]![[q/2]+k''+\delta(q)]![[r/2]+k'''+\delta(r)]!} \\
& \times a_1^{2k'+\delta(p)} a_2^{2k''+\delta(q)} a_3^{2k'''+\delta(r)} I_{(p+\delta(p))/2+k',(q+\delta(q))/2+k'',(r+\delta(r))/2+k'''}^{(0)}.
\end{aligned}
\tag{18}
$$

In Eq. (18), the following notation is introduced:

$$
\tau = \left\{ \begin{array}{ll} \beta_0 - l, \cdots \beta_0, \cdots, \gamma; & \text{if } \beta_0 \geqslant l \\ 0,1,\cdots,\gamma; & \text{if } \beta_0 \leqslant l \end{array} \right\}, \quad \beta_0 = \left[\frac{p}{2}\right] + \left[\frac{q}{2}\right] + \left[\frac{r}{2}\right],
$$

$$
\gamma = \left[\frac{N}{2}\right] - e_{pqr}^{N},
$$

$$
\begin{aligned}
e_{pqr}^{N} = & \frac{\delta(p+q+r+N)+\delta(p)+\delta(q)+\delta(r)-\delta(N)}{2} = \delta(p) \\
& + \delta(q)+\delta(r)-\delta(p)\,\delta(q)-\delta(q)\,\delta(r)-\delta(r)\,\delta(p) \\
& - \delta(N)\,\delta(p)-\delta(N)\,\delta(q)-\delta(N)\,\delta(r)+2\,\delta(p)\,\delta(q)\,\delta(N) \\
& + 2\,\delta(q)\,\delta(r)\,\delta(N)+2\,\delta(r)\,\delta(p)\,\delta(N)
\end{aligned}
\tag{19}
$$

Expression for ${}^{(k)}\tilde{F}_{pqr}^{ij,l}$ can be easily deduced from $F_{pqr}^{ij,l}$ by the following substitutions:

$$
\gamma \rightarrow \tilde{\gamma} = \left[\frac{N+1}{2}\right] - e_{pqr}^{N+1},
$$

$$
\varepsilon_{i,j,2t_1+\delta(p),2t_2+\delta(q),2t_3+\delta(r)}^{*} \rightarrow \varepsilon_{i,j,2t_1+\delta(p)-\delta_{k1},2t_2+\delta(q)-\delta_{k2},2t_3+\delta(r)-\delta_{k3}}^{*}.
$$

Putting (17) into (6), we obtain

$$
u_i(\mathbf{x}) = \sum_{p+q+r=0}^{N+2l-1} \Lambda_{pqr}^{i,l} x_1^p x_2^q x_3^r + x_k \sum_{p+q+r=0}^{N+2l-2} \Sigma_{pqr}^{ik,l} x_1^p x_2^q x_3^r, \tag{20}
$$

where

$$
\begin{aligned}
\Lambda_{pqr}^{i,l} = {} & \eta_1[(p+1)F_{p+1,q,r}^{mm,l}\delta_{i1}+(q+1)F_{p,q+1,r}^{mm,l}\delta_{i2}+(r+1)\\
& \times F_{p,q,r+1}^{mm,l}\delta_{i3}]-\eta_2[(p+1)F_{p+1,q,r}^{i1,l}+(q+1)F_{p,q+1,r}^{i2,l}+(r\\
& +1)F_{p,q,r+1}^{i3,l}]-\eta_3 a_k[(p+2)^{(k)}\tilde{F}_{p+2,q,r}^{1k,l}\\
& +(q+1)^{(k)}\tilde{F}_{p+1,q+1,r}^{2k,l}+(r+1)^{(k)}\tilde{F}_{p+1,q,r+1}^{3k,l}](p+1)\delta_{i1}\\
& -\eta_3 a_k[(p+1)^{(k)}\tilde{F}_{p+1,q+1,r}^{1k,l}+(q+2)^{(k)}\tilde{F}_{p,q+2,r}^{2k,l}\\
& +(r+1)^{(k)}\tilde{F}_{p,q+1,r+1}^{3k,l}](q+1)\delta_{i2}\\
& -\eta_3 a_k[(p+1)^{(k)}\tilde{F}_{p+1,q,r+1}^{1k,l}+(q+1)^{(k)}\tilde{F}_{p,q+1,r+1}^{2k,l}\\
& +(r+2)^{(k)}\tilde{F}_{p,q,r+2}^{3k,l}](r+1)\delta_{i3},
\end{aligned}
\tag{21}
$$

$$
\begin{aligned}
\Sigma_{pqr}^{ik,l} = {} & \eta_3[(p+2)F_{p+2,q,r}^{k1,l}+(q+1)F_{p+1,q+1,r}^{k2,l}\\
& +(r+1)F_{p+1,q,r+1}^{k3,l}](p+1)\delta_{i1}+\eta_3[(p+1)F_{p+1,q+1,r}^{k1,l}\\
& +(q+2)F_{p,q+2,r}^{k2,l}+(r+1)F_{p,q+1,r+1}^{k3,l}](q+1)\delta_{i2}\\
& +\eta_3[(p+1)F_{p+1,q,r+1}^{k1,l}+(q+1)F_{p,q+1,r+1}^{k2,l}\\
& +(r+2)F_{p,q,r+2}^{k3,l}](r+1)\delta_{i3}.
\end{aligned}
$$

Hence the strain field within the transformed ellipsoid is given by

$$
\begin{aligned}
2\varepsilon_{ij} = {} & \sum_{p+q+r=0}^{N+2l-2}[(\Lambda_{p+1,q,r}^{i,l}\delta_{j1}+\Lambda_{p+1,q,r}^{j,l}\delta_{i1})(p+1)+(\Lambda_{p,q+1,r}^{i,l}\delta_{j2}\\
& +\Lambda_{p,q+1,r}^{j,l}\delta_{i2})(q+1)+(\Lambda_{p,q,r+1}^{i,l}\delta_{j3}+\Lambda_{p,q,r+1}^{j,l}\delta_{i3})(r+1)\\
& +\Sigma_{pqr}^{ij,l}+\Sigma_{pqr}^{ji,l}]x_1^p x_2^q x_3^r + x_k\sum_{p+q+r=0}^{N+2l-3}[(\Sigma_{p+1,q,r}^{ik,l}\delta_{j1}\\
& +\Sigma_{p+1,q,r}^{jk,l}\delta_{i1})(p+1)+(\Sigma_{p,q+1,r}^{ik,l}\delta_{j2}+\Sigma_{p,q+1,r}^{jk,l}\delta_{i2})(q+1)\\
& +(\Sigma_{p,q,r+1}^{ik,l}\delta_{j1}+\Sigma_{p,q,r+1}^{jk,l}\delta_{i1})(r+1)]x_1^p x_2^q x_3^r.
\end{aligned}
\tag{22}
$$

In using Eq. (22), special attention should be paid to two possible circumstances. Specifically, if, in Eq. (18), it happens that $\gamma<0$ or $\gamma<\tau$, the corresponding $F_{pqr}^{ij,l}$s should be assumed equal to zero.

So far we have been concerned with the induced strain field within the transformed ellipsoid. It is also easy to calculate the strain field outside the ellipsoid using the present approach. This is based on the observation [19] that Eqs. (17) and (18) also valid for $\mathbf{x}\in\mathbf{R}^3\backslash\Omega$, provided the internal potential integrals

$$
I_{(p+\delta(p))/2+k',(q+\delta(q))/2+k'',(r+\delta(r))/2+k'''},
$$

are replaced by the corresponding external ones, i.e.,

$$
I_{(p+\delta(p))/2+k',(q+\delta(q))/2+k'',(r+\delta(r))/2+k'''}^{(\alpha)}.
$$

Putting then Eqs. (17) and (18) with these changes into (6), it is easy to calculate the displacement field and hence the strain field outside the ellipsoid. Care now should be taken of the situation that unlike the case where $\mathbf{x}\in\Omega$, the external potential integrals are dependent on $\mathbf{x}$ through α. Therefore, in applying the operator ∂_i, the following relation should be taken into view

$$
\begin{aligned}
& \partial_i(x_1^p x_2^q x_3^r I_{(p+\delta(p))/2+k',(q+\delta(q))/2+k'',(r+\delta(r))/2+k'''}^{(\alpha)})\\
& \quad =(p x_1^{p-1}x_2^q x_3^r\delta_{ip}+q x_1^p x_2^{q-1}x_3^r\delta_{iq}+r x_1^p x_2^q x_3^{r-1}\delta_{ir})I_{(p+\delta(p))/2+k',(q+\delta(q))/2+k'',(r+\delta(r))/2+k'''}^{(\alpha)}\\
& \qquad -\frac{x_1^p x_2^q x_3^r}{\sqrt{(a_1^2+\alpha)^{p+\delta(p)+2k'+1}(a_2^2+\alpha)^{q+\delta(q)+2k''+1}(a_3^2+\alpha)^{r+\delta(r)+2k'''+1}}}\partial_i\alpha.
\end{aligned}
$$

The resulting expressions for the displacement and strain fields outside the ellipsoid are therefore extremely involved. A full derivation is left to the interested reader as an exercise.

We close this section by considering the problem of a spherical inclusion with radius R_0. Solution of this problem can be easily deduced from the solution of the ellipsoidal inclusion by letting $a_i\rightarrow R_0$ in the relevant equations. The potential integrals (16) can be easily evaluated in closed form. Thus, for this case, the strain field within the transformed sphere is still given by Eqs. (21) and (22) with $F_{pqr}^{ij,l}$ given by

$$
\begin{aligned}
F_{pqr}^{ij,l} = {} & \frac{\pi R_0^2(l-1)!(-1)^{\beta_0}}{2^{\delta(p)+\delta(q)+\delta(r)}p!q!r!}\sum_{t_1+t_2+t_3=\tau}^{\gamma}\frac{[2t_1+\delta(p)]![2t_2+\delta(q)]![2t_3+\delta(r)]!}{4^{t_1+t_2+t_3}(t_1+t_2+t_3+l-\beta_0)!}\varepsilon_{i,j,\delta(p)+2t_1,\delta(q)+2t_2,\delta(r)+2t_3}^{*}\\
& \times\sum_{k'=0}^{t_1}\sum_{k''=0}^{t_2}\sum_{k'''=0}^{t_3}(-1)^{k'+k''+k'''}\frac{[p+2k'+\delta(p)]![q+2k''+\delta(q)]!}{(t_1-k')!(t_2-k'')!(t_3-k''')!}\\
& \times\frac{[r+2k'''+\delta(r)]!}{[2k'+\delta(p)]![2k''+\delta(q)]![2k'''+\delta(r)]![[p/2]+k'+\delta(p)]![[q/2]+k''+\delta(q)]![[r/2]+k'''+\delta(r)]!}\\
& \times\frac{1}{R_0^{p+q+r}(p+q+r+\delta(p)+\delta(q)+\delta(r)+2k'+2k''+2k''')}.
\end{aligned}
$$

3 Examples

3.1 Constant Eigenstrain. As the simplest application of the results obtained in this section, let us consider the case of constant eigenstrain, i.e., $N=0$, $l=1$. This case was studied by Eshelby [2]. Solution for this case can be obtained from our solution by putting

$$l=1, \quad \varepsilon^*_{ijpqr}=0 \quad (i,j=1,2,3 \text{ and } p+q+r\geqslant 1), \tag{23}$$

into the relevant equations.

Thus, using Eq. (22), we obtain

$$2\varepsilon_{ij}=\Lambda^{i,1}_{100}\delta_{j1}+\Lambda^{j,1}_{100}\delta_{i1}+\Lambda^{i,1}_{010}\delta_{j2}+\Lambda^{j,1}_{010}\delta_{i2}+\Lambda^{i,1}_{001}\delta_{j3}+\Lambda^{j,1}_{001}\delta_{i3} + \Sigma^{ij,1}_{000}+\Sigma^{ji,1}_{000}. \tag{24}$$

Writing Eq. (24) explicitly, we obtain

$$\begin{aligned}
&\varepsilon_{11}=\Lambda^{1,1}_{100}+\Sigma^{11,1}_{000}, \quad \varepsilon_{22}=\Lambda^{2,1}_{010}+\Sigma^{22,1}_{000}, \quad \varepsilon_{33}=\Lambda^{3,1}_{001}+\Sigma^{33,1}_{000},\\
&\varepsilon_{12}=\varepsilon_{21}=\frac{1}{2}(\Lambda^{2,1}_{100}+\Lambda^{1,1}_{010}+\Sigma^{12,1}_{000}+\Sigma^{21,1}_{000}),\\
&\varepsilon_{13}=\varepsilon_{31}=\frac{1}{2}(\Lambda^{3,1}_{100}+\Lambda^{1,1}_{001}+\Sigma^{13,1}_{000}+\Sigma^{31,1}_{000}),\\
&\varepsilon_{23}=\varepsilon_{32}=\frac{1}{2}(\Lambda^{3,1}_{010}+\Lambda^{2,1}_{001}+\Sigma^{23,1}_{000}+\Sigma^{32,1}_{000}),
\end{aligned} \tag{25}$$

where the relevant Λ's and Σ's, calculated as per Eqs. (21) and (18), are given by

$$\begin{aligned}
(2\pi a)^{-1}\Lambda^{1,1}_{100}=&-\eta_1\varepsilon^*_{mm000}I_{100}+\eta_2\varepsilon^*_{11000}I_{100}\\
&+\eta_3(3a_1^2\varepsilon^*_{11000}I_{200}+a_2^2\varepsilon^*_{22000}I_{110}+a_3^2\varepsilon^*_{33000}I_{101}),\\
(2\pi a)^{-1}\Sigma^{11,1}_{000}=&-\eta_3\varepsilon^*_{11000}I_{100},\\
(2\pi a)^{-1}\Lambda^{2,1}_{010}=&-\eta_1\varepsilon^*_{mm000}I_{010}+\eta_2\varepsilon^*_{22000}I_{010}\\
&+\eta_3(a_1^2\varepsilon^*_{11000}I_{110}+3a_2^2\varepsilon^*_{22000}I_{020}+a_3^2\varepsilon^*_{33000}I_{011}),\\
(2\pi a)^{-1}\Sigma^{22,1}_{000}=&-\eta_3\varepsilon^*_{22000}I_{010},\\
(2\pi a)^{-1}\Lambda^{3,1}_{001}=&-\eta_1\varepsilon^*_{mm000}I_{001}+\eta_2\varepsilon^*_{33000}I_{001}\\
&+\eta_3(a_1^2\varepsilon^*_{11000}I_{101}+a_2^2\varepsilon^*_{22000}I_{011}+3a_3^2\varepsilon^*_{33000}I_{002}),\\
(2\pi a)^{-1}\Sigma^{33,1}_{000}=&-\eta_3\varepsilon^*_{33000}I_{001},
\end{aligned} \tag{26}$$

$$\begin{aligned}
(2\pi a)^{-1}\Lambda^{2,1}_{100}&=\eta_2\varepsilon^*_{12000}I_{100}+\eta_3\varepsilon^*_{12000}(a_1^2+a_2^2)I_{110},\\
(2\pi a)^{-1}\Lambda^{1,1}_{010}&=\eta_2\varepsilon^*_{12000}I_{010}+\eta_3\varepsilon^*_{12000}(a_1^2+a_2^2)I_{110},\\
(2\pi a)^{-1}\Sigma^{12,1}_{000}&=-\eta_3\varepsilon^*_{12000}I_{100},\\
(2\pi a)^{-1}\Sigma^{21,1}_{000}&=-\eta_3\varepsilon^*_{12000}I_{010},\\
(2\pi a)^{-1}\Lambda^{3,1}_{100}&=\eta_2\varepsilon^*_{13000}I_{100}+\eta_3\varepsilon^*_{13000}(a_1^2+a_3^2)I_{101},\\
(2\pi a)^{-1}\Lambda^{1,1}_{001}&=\eta_2\varepsilon^*_{13000}I_{001}+\eta_3\varepsilon^*_{13000}(a_1^2+a_3^2)I_{101},\\
(2\pi a)^{-1}\Sigma^{13,1}_{000}&=-\eta_3\varepsilon^*_{13000}I_{100},\\
(2\pi a)^{-1}\Sigma^{31,1}_{000}&=-\eta_3\varepsilon^*_{13000}I_{001},\\
(2\pi a)^{-1}\Lambda^{3,1}_{010}&=\eta_2\varepsilon^*_{23000}I_{010}+\eta_3\varepsilon^*_{23000}(a_2^2+a_3^2)I_{011},\\
(2\pi a)^{-1}\Lambda^{2,1}_{001}&=\eta_2\varepsilon^*_{23000}I_{001}+\eta_3\varepsilon^*_{23000}(a_2^2+a_3^2)I_{011},\\
(2\pi a)^{-1}\Sigma^{23,1}_{000}&=-\eta_3\varepsilon^*_{23000}I_{010},\\
(2\pi a)^{-1}\Sigma^{32,1}_{000}&=-\eta_3\varepsilon^*_{23000}I_{001}.
\end{aligned}$$

Alternatively, Eqs. (25) and (26) can be cast into Eshelby's form:

$$\varepsilon_{ij}=S_{ijkl}\varepsilon^*_{kl000}, \tag{27}$$

where

$$\begin{aligned}
&S_{1111}=\frac{(1-2\nu)a}{4(1-\nu)}I_{100}+\frac{3aa_1^2}{4(1-\nu)}I_{200},\\
&S_{1112}=S_{1121}=S_{1113}=S_{1131}=0,\\
&S_{1122}=\frac{-(1-2\nu)a}{4(1-\nu)}I_{100}+\frac{aa_2^2}{4(1-\nu)}I_{110},\\
&S_{1133}=\frac{-(1-2\nu)a}{4(1-\nu)}I_{100}+\frac{aa_3^2}{4(1-\nu)}I_{101},\\
&S_{1212}=S_{1221}=\frac{(1-2\nu)a}{8(1-\nu)}(I_{100}+I_{010})+\frac{(a_1^2+a_2^2)a}{8(1-\nu)}I_{110},\\
&S_{1211}=S_{1213}=S_{1222}=S_{1223}=S_{1231}=S_{1232}=S_{1233}=0,\\
&S_{1313}=S_{1331}=\frac{(1-2\nu)a}{8(1-\nu)}(I_{100}+I_{001})+\frac{(a_1^2+a_3^2)a}{8(1-\nu)}I_{101},\\
&S_{1311}=S_{1312}=S_{1322}=S_{1323}=S_{1331}=S_{1332}=S_{1333}=0,\\
&S_{2323}=S_{2332}=\frac{(1-2\nu)a}{8(1-\nu)}(I_{010}+I_{001})+\frac{(a_2^2+a_3^2)a}{8(1-\nu)}I_{011},\\
&S_{2311}=S_{2312}=S_{2313}=S_{2321}=S_{2322}=S_{2331}=S_{2333}=0,\\
&S_{2211}=\frac{-(1-2\nu)a}{4(1-\nu)}I_{010}+\frac{aa_1^2}{4(1-\nu)}I_{110},\\
&S_{2222}=\frac{(1-2\nu)a}{4(1-\nu)}I_{010}+\frac{aa_2^2}{4(1-\nu)}I_{020},\\
&S_{2233}=\frac{-(1-2\nu)a}{4(1-\nu)}I_{010}+\frac{aa_3^2}{4(1-\nu)}I_{110},\\
&S_{2212}=S_{2221}=S_{2213}=S_{2231}=S_{2223}=S_{2232}=0,\\
&S_{3311}=\frac{-(1-2\nu)a}{4(1-\nu)}I_{001}+\frac{aa_1^2}{4(1-\nu)}I_{011},\\
&S_{3322}=\frac{-(1-2\nu)a}{4(1-\nu)}I_{001}+\frac{aa_2^2}{4(1-\nu)}I_{011},\\
&S_{3333}=\frac{(1-2\nu)a}{4(1-\nu)}I_{001}+\frac{aa_3^2}{4(1-\nu)}I_{011},\\
&S_{3312}=S_{3321}=S_{3313}=S_{3331}=S_{3323}=S_{3332}=0.
\end{aligned} \tag{28}$$

The elements of S_{ijkl} constitute a fourth-order tensor called the *Eshelby tensor*. All other components of this tensor not listed above may be found by using the obvious relations $S_{ijkl}=S_{jikl}$, $S_{ijkl}=S_{ijlk}$. Equations (28) coincide precisely with Eshelby's solution ([1–3,9]), and this renders credence to the correctness of our analysis.

3.2 Linear Eigenstrain. As the next example, let us consider the case of linear eigenstrain. Specifically, let us assume that $\varepsilon^*_{ijpqr}=0$ $(i,j=1,2,3)$, where $p+q+r\geqslant 2$. Furthermore, without loss in generality, we may assume that $\varepsilon^*_{ijpqr}=0$ $(i,j=1,2,3)$ for $p+q+r=0$, because this case corresponds to constant eigenstrain, which we have already treated.

Writing in explicit form, the induced strain field for this case can be written as

$$\varepsilon_{ij}=c_0^{ij}+c_1^{ij}x_1+c_2^{ij}x_2+c_3^{ij}x_3, \quad (i,j=1,2,3). \tag{29}$$

Here the coefficients c_0^{ij} are given by ε_{ij} in equations in (25) with the only difference that now in evaluating the relevant Λ's and Σ's, N should be put equal to 1. It turns out that $c_0^{ij}=0$. At the end of this section we will elaborate why $c_0^{ij}=0$ for this case. The other coefficients, namely $c_1^{ij}, c_2^{ij}, c_3^{ij}$, are given by

$$c_1^{11}=2(\Lambda_{200}^{1,1}+\Sigma_{100}^{11,1}),\quad c_2^{11}=\Lambda_{110}^{1,1}+\Sigma_{010}^{11,1}+\Sigma_{100}^{12,1},$$

$$c_3^{11}=\Lambda_{101}^{1,1}+\Sigma_{001}^{11,1}+\Sigma_{100}^{13,1},\quad c_1^{22}=\Lambda_{110}^{2,1}+\Sigma_{100}^{22,1}+\Sigma_{010}^{21,1},$$

$$c_2^{22}=2(\Lambda_{020}^{2,1}+\Sigma_{010}^{22,1}),\quad c_3^{22}=\Lambda_{011}^{2,1}+\Sigma_{001}^{22,1}+\Sigma_{010}^{23,1},$$

$$c_1^{33}=\Lambda_{101}^{3,1}+\Sigma_{100}^{33,1},\quad c_2^{33}=\Lambda_{011}^{3,1}+\Sigma_{010}^{33,1}+\Sigma_{001}^{32,1},$$

$$c_3^{33}=2(\Lambda_{002}^{3,1}+\Sigma_{001}^{33,1}),$$

$$c_1^{12}=\frac{1}{2}(2\Lambda_{200}^{2,1}+\Lambda_{110}^{1,1}+\Sigma_{100}^{12,1}+2\Sigma_{100}^{21,1}+\Sigma_{010}^{11,1}),$$

$$c_2^{12}=\frac{1}{2}(\Lambda_{100}^{2,1}+2\Lambda_{020}^{1,1}+2\Sigma_{010}^{12,1}+\Sigma_{010}^{21,1}+\Sigma_{100}^{22,1}),$$

$$c_3^{12}=\frac{1}{2}(\Lambda_{101}^{2,1}+\Lambda_{011}^{1,1}+\Sigma_{001}^{12,1}+\Sigma_{001}^{21,1}+\Sigma_{100}^{23,1}+\Sigma_{010}^{13}),\tag{30}$$

$$c_1^{13}=\frac{1}{2}(2\Lambda_{200}^{3,1}+\Lambda_{101}^{1,1}+\Sigma_{100}^{13,1}+2\Sigma_{100}^{31,1}+\Sigma_{001}^{11,1}),$$

$$c_2^{13}=\frac{1}{2}(\Lambda_{100}^{3,1}+\Lambda_{011}^{1,1}+\Sigma_{010}^{13,1}+\Sigma_{010}^{32,1}+\Sigma_{100}^{32,1}+\Sigma_{001}^{12,1}),$$

$$c_3^{13}=\frac{1}{2}(\Lambda_{101}^{3,1}+2\Lambda_{002}^{1,1}+2\Sigma_{001}^{13,1}+\Sigma_{001}^{31,1}+\Sigma_{100}^{33,1}),$$

$$c_1^{23}=\frac{1}{2}(\Lambda_{110}^{3,1}+\Lambda_{101}^{2,1}+\Sigma_{100}^{23,1}+\Sigma_{100}^{32,1}+\Sigma_{010}^{31,1}+\Sigma_{001}^{21,1}),$$

$$c_2^{23}=\frac{1}{2}(2\Lambda_{020}^{3,1}+\Lambda_{011}^{2,1}+\Sigma_{010}^{23,1}+2\Sigma_{010}^{32,1}+\Sigma_{001}^{22,1}),$$

$$c_3^{23}=\frac{1}{2}(\Lambda_{011}^{3,1}+2\Lambda_{002}^{2,1}+2\Sigma_{001}^{23,1}+\Sigma_{001}^{32,1}+\Sigma_{010}^{33,1}).$$

The relevant Λ's and Σ's entering into Eqs. (30), calculated using (21) and (18), are given by

$$\begin{aligned}
(\pi a)^{-1}\Lambda_{200}^{1,1}=&-3\eta_1 a_1\varepsilon_{mm100}^{*}I_{200}+\eta_2(3a_1\varepsilon_{11100}^{*}I_{200}\\
&+a_2\varepsilon_{12010}^{*}I_{110}+a_3\varepsilon_{13001}^{*}I_{101})\\
&-3\eta_3[(a_1\varepsilon_{11100}^{*}+a_2\varepsilon_{12010}^{*}+a_3\varepsilon_{13001}^{*})I_{200}\\
&-(5a_1^3\varepsilon_{11100}^{*}I_{300}+a_2^3\varepsilon_{12010}^{*}I_{210}+a_3^3\varepsilon_{13001}^{*}I_{201})]\\
&+3\eta_3 a_1a_2(a_1\varepsilon_{12010}^{*}+a_2\varepsilon_{22100}^{*})I_{210}\\
&+3\eta_3 a_1a_3(a_1\varepsilon_{13001}^{*}+a_3\varepsilon_{33100}^{*})I_{201},
\end{aligned}$$

$$(2\pi a)^{-1}\Sigma_{100}^{11,1}=-\eta_3(3a_1\varepsilon_{11100}^{*}I_{200}+a_2\varepsilon_{12010}^{*}I_{110}+a_3\varepsilon_{13001}^{*}I_{101}),$$

$$\begin{aligned}
(2\pi a)^{-1}\Lambda_{110}^{1,1}=&-a_2\eta_1\varepsilon_{mm010}^{*}I_{110}+\eta_2(a_1\varepsilon_{12100}^{*}+a_2\varepsilon_{11010}^{*})I_{110}\\
&+3a_1a_2\eta_3(a_1\varepsilon_{11010}^{*}+a_2\varepsilon_{12100}^{*})I_{210}\\
&-\eta_3[a_1\varepsilon_{21100}^{*}(I_{110}-3a_1^2I_{210})+a_2\varepsilon_{22010}^{*}\\
&\times(I_{110}-3a_2^2I_{120})+a_3\varepsilon_{23001}^{*}(I_{110}-a_3^2I_{110})]\\
&+\eta_3 a_2a_3(a_2\varepsilon_{23001}^{*}+a_3\varepsilon_{33010}^{*})I_{110},
\end{aligned}$$

$$(2\pi a)^{-1}\Sigma_{010}^{11,1}=-\eta_3(a_1\varepsilon_{12100}^{*}+a_2\varepsilon_{11010}^{*})I_{110},$$

$$(\pi a)^{-1}\Sigma_{100}^{12,1}=-\eta_3(3a_1\varepsilon_{12100}^{*}I_{200}+a_2\varepsilon_{22010}^{*}I_{110}+a_3\varepsilon_{23001}^{*}I_{101}),$$

$$\begin{aligned}
(2\pi a)^{-1}\Lambda_{101}^{1,1}=&-\eta_1 a_3\varepsilon_{mm001}^{*}I_{101}+\eta_2(a_1\varepsilon_{13100}^{*}+a_3\varepsilon_{11001}^{*})I_{101}\\
&+3\eta_3 a_1a_3(a_1\varepsilon_{11001}^{*}+a_3\varepsilon_{13100}^{*})I_{201}\\
&-\eta_3[a_1\varepsilon_{13100}^{*}(I_{101}-3a_1^2I_{201})+a_2\varepsilon_{32010}^{*}\\
&\times(I_{101}-a_2^2I_{111})+a_3\varepsilon_{33001}^{*}(I_{101}-3a_3^2I_{102})]\\
&+\eta_3 a_2a_3(a_2\varepsilon_{22001}^{*}+a_3\varepsilon_{23010}^{*})I_{111},
\end{aligned}$$

$$(2\pi a)^{-1}\Sigma_{001}^{11,1}=-\eta_3(a_1\varepsilon_{23100}^{*}+a_3\varepsilon_{11001}^{*})I_{101},$$

$$(2\pi a)^{-1}\Sigma_{100}^{13,1}=-\eta_3(3a_1\varepsilon_{13100}^{*}I_{200}+a_2\varepsilon_{23010}^{*}I_{110}+a_3\varepsilon_{33001}^{*}I_{101}),$$

$$\begin{aligned}
(2\pi a)^{-1}\Lambda_{110}^{2,1}=&-a_1\eta_1\varepsilon_{mm100}^{*}I_{110}+\eta_2(a_1\varepsilon_{22100}^{*}+a_2\varepsilon_{12010}^{*})I_{110}\\
&+3a_1a_2\eta_3(a_1\varepsilon_{12010}^{*}+a_2\varepsilon_{22100}^{*})I_{120}\\
&-\eta_3[a_1\varepsilon_{11100}^{*}(I_{110}-a_1^2I_{210})\\
&+a_2\varepsilon_{12010}^{*}(I_{110}-3a_2^2I_{120})+a_3\varepsilon_{13001}^{*}(I_{110}\\
&-3a_3^2I_{111})]+a_1a_3\eta_3(a_1\varepsilon_{12001}^{*}+a_3\varepsilon_{23100}^{*})I_{110},
\end{aligned}$$

$$(2\pi a)^{-1}\Sigma_{100}^{22,1}=-\eta_3(a_1\varepsilon_{22100}^{*}+a_2\varepsilon_{12010}^{*})I_{110},$$

$$(2\pi a)^{-1}\Sigma_{010}^{21,1}=-\eta_3(a_1\varepsilon_{11100}^{*}I_{110}+3a_2\varepsilon_{22010}^{*}I_{020}+a_3\varepsilon_{23001}^{*}I_{011}),$$

$$\begin{aligned}
(\pi a)^{-1}\Lambda_{020}^{2,1}=&-3\eta_1 a_2\varepsilon_{mm100}^{*}I_{020}+\eta_2(a_1\varepsilon_{12100}^{*}I_{110}\\
&+3a_2\varepsilon_{22100}^{*}I_{020}+a_3\varepsilon_{23001}^{*}I_{011})+3\eta_3 a_1a_2(a_1\varepsilon_{11010}^{*}\\
&+a_2\varepsilon_{12100}^{*})I_{120}-3\eta_3[a_1\varepsilon_{12100}^{*}(I_{020}-a_1^2I_{120})\\
&+a_2\varepsilon_{22010}^{*}(I_{020}-5a_2^2I_{030})+a_3\varepsilon_{23001}^{*}(I_{020}\\
&-3a_3^2I_{021})]+3\eta_3 a_2a_3(a_2\varepsilon_{23001}^{*}+a_3\varepsilon_{330010}^{*})I_{021},
\end{aligned}$$

$$(2\pi a)^{-1}\Sigma_{010}^{21,1}=-\eta_3(a_1\varepsilon_{12100}^{*}I_{110}+3a_2\varepsilon_{22010}^{*}I_{020}+a_3\varepsilon_{23001}^{*}I_{011}),$$

$$\begin{aligned}
(2\pi a)^{-1}\Lambda_{011}^{2,1}=&-\eta_1 a_3\varepsilon_{mm001}^{*}I_{011}+\eta_2(a_2\varepsilon_{23010}^{*}+a_3\varepsilon_{22001}^{*})I_{011}\\
&+\eta_3 a_1a_3(a_1\varepsilon_{11001}^{*}+a_2\varepsilon_{13100}^{*})I_{111}\\
&+3\eta_3 a_2a_3(a_2\varepsilon_{22001}^{*}+a_3\varepsilon_{23010}^{*})I_{021}\\
&-\eta_3[a_1\varepsilon_{13100}^{*}(I_{011}-a_1^2I_{111})+a_2\varepsilon_{23010}^{*}(I_{011}\\
&-3a_2^2I_{021})+a_3\varepsilon_{33001}^{*}(I_{011}-3a_3^2I_{012})]
\end{aligned}$$

$$(2\pi a)^{-1}\Sigma_{001}^{22,1}=-\eta_3(a_2\varepsilon_{23010}^{*}+a_3\varepsilon_{22001}^{*})I_{011},$$

$$(2\pi a)^{-1}\Sigma_{010}^{23,1}=-\eta_3(a_1\varepsilon_{13100}^{*}I_{110}+3a_2\varepsilon_{23010}^{*}I_{020}+a_3\varepsilon_{33001}^{*}I_{011}),$$

$$\begin{aligned}
(2\pi a)^{-1}\Lambda_{101}^{3,1}=&-\eta_1 a_3\varepsilon_{mm100}^{*}I_{101}+\eta_2(a_1\varepsilon_{33100}^{*}+a_3\varepsilon_{13001}^{*})I_{101}\\
&+3\eta_3 a_1a_3(a_1\varepsilon_{13001}^{*}+a_3\varepsilon_{33100}^{*})I_{102}\\
&-\eta_3[a_1\varepsilon_{11100}^{*}(I_{101}-3a_1^2I_{201})+a_2\varepsilon_{12010}^{*}(I_{101}\\
&-a_2^2I_{111})+a_3\varepsilon_{13001}^{*}(I_{101}-3a_3^2I_{102})]
\end{aligned}$$

$$(2\pi a)^{-1}\Sigma_{100}^{33,1}=-\eta_3(a_1\varepsilon_{23100}^{*}+a_3\varepsilon_{13001}^{*})I_{101},$$

$$\begin{aligned}
(2\pi a)^{-1}\Lambda_{011}^{3,1}=&-a_2\eta_1\varepsilon_{mm010}^{*}I_{011}+\eta_2(a_2\varepsilon_{33010}^{*}+a_3\varepsilon_{23001}^{*})I_{011}\\
&+\eta_3 a_1a_2(a_1\varepsilon_{11010}^{*}+a_2\varepsilon_{12100}^{*})I_{111}\\
&+\eta_3 a_2a_3(a_2\varepsilon_{23001}^{*}+a_3\varepsilon_{33010}^{*})I_{012}\\
&-\eta_3[a_1\varepsilon_{12100}^{*}(I_{011}-a_1^2I_{111})\\
&+a_2\varepsilon_{22010}^{*}(I_{011}-3a_2^2I_{021})\\
&+a_3\varepsilon_{23001}^{*}(I_{011}-3a_3^2I_{012})]\\
&+3\eta_3(a_2\varepsilon_{23001}^{*}+a_3\varepsilon_{33010}^{*})I_{012},
\end{aligned}\tag{31}$$

$$(2\pi a)^{-1}\Sigma_{010}^{33,1}=-\eta_3(a_2\varepsilon_{33010}^{*}+a_3\varepsilon_{23001}^{*})I_{011},$$

$$
\begin{aligned}
(2\pi a)^{-1}\Sigma^{32,1}_{001} &= -\eta_3(a_1\varepsilon^*_{12100}I_{101}+a_2\varepsilon^*_{22010}I_{011}+3a_3\varepsilon^*_{23001}I_{002}),\\
(\pi a)^{-1}\Lambda^{3,1}_{002} &= -3\eta_1 a_3\varepsilon^*_{mm001}I_{002}+\eta_2(a_1\varepsilon^*_{13100}I_{101}+a_2\varepsilon^*_{23010}I_{011}\\
&\quad +3a_3\varepsilon^*_{33001}I_{002})-3\eta_3[a_1\varepsilon^*_{13100}(I_{002}-a_1^2I_{102})\\
&\quad +a_2\varepsilon^*_{23010}(I_{002}-a_2^2I_{012})+a_3\varepsilon^*_{33001}(I_{002}-5a_3^2I_{003})]\\
&\quad +3\eta_3 a_1 a_3(a_1\varepsilon^*_{11001}+a_3\varepsilon^*_{13100})I_{102}\\
&\quad +3\eta_3 a_2 a_3(a_2\varepsilon^*_{22001}+a_3\varepsilon^*_{23010})I_{012},\\
(2\pi a)^{-1}\Sigma^{33,1}_{001} &= -\eta_3(a_1\varepsilon^*_{13100}I_{101}+a_2\varepsilon^*_{23010}I_{011}+a_3\varepsilon^*_{33001}I_{002}),\\
(\pi a)^{-1}\Lambda^{2,1}_{200} &= -\eta_1 a_2\varepsilon^*_{mm010}I_{110}+\eta_2(3a_1\varepsilon^*_{12100}I_{200}+a_2\varepsilon^*_{22010}I_{110}\\
&\quad +a_3\varepsilon^*_{23001}I_{101})+3\eta_3 a_1 a_2(a_1\varepsilon^*_{11010}+a_2\varepsilon^*_{12100})I_{210}\\
&\quad +\eta_3 a_2 a_3(a_2\varepsilon^*_{23001}+a_3\varepsilon^*_{33010})I_{111}\\
&\quad -\eta_3[a_1\varepsilon^*_{12100}(I_{110}-3a_1^2I_{210})+a_2\varepsilon^*_{22010}\\
&\quad \times(I_{110}-3a_2^2I_{120})+a_3\varepsilon^*_{23001}(I_{110}-a_3^2I_{111})]\\
(2\pi a)^{-1}\Lambda^{1,1}_{110} &= -\eta_1 a_2\varepsilon^*_{mm010}I_{110}+\eta_2(a_1\varepsilon^*_{12100}+a_2\varepsilon^*_{11010})I_{110}\\
&\quad +3\eta_3 a_1 a_2(a_1\varepsilon^*_{11010}+a_2\varepsilon^*_{12100})I_{210}\\
&\quad -\eta_3[a_1\varepsilon^*_{12100}(I_{110}-3a_1^2I_{210})+a_2\varepsilon^*_{22010}(I_{110}\\
&\quad -3a_2^2I_{120})+a_3\varepsilon^*_{23001}(I_{110}-a_3^2I_{111})]\\
&\quad -\eta_3[a_1\varepsilon^*_{13100}(I_{101}-3a_1^2I_{201})+a_2\varepsilon^*_{23010}(I_{101}\\
&\quad -a_2^2I_{111})+a_3\varepsilon^*_{33001}(I_{101}-a_3^2I_{102})]\\
(2\pi a)^{-1}\Sigma^{12,1}_{100} &= -\eta_3(3a_1\varepsilon^*_{12100}I_{200}+a_2\varepsilon^*_{22010}I_{110}+a_3\varepsilon^*_{23001}I_{101}),\\
(2\pi a)^{-1}\Sigma^{21,1}_{100} &= (2\pi a)^{-1}\Sigma^{11,1}_{010} = -\eta_3(a_1\varepsilon^*_{12100}+a_2\varepsilon^*_{11010})I_{110},\\
(2\pi a)^{-1}\Lambda^{2,1}_{110} &= -\eta_1 a_1\varepsilon^*_{mm100}I_{110}+\eta_2(a_1\varepsilon^*_{22100}+a_2\varepsilon^*_{12010})I_{110}\\
&\quad +3\eta_3 a_1 a_2(a_1\varepsilon^*_{12010}+a_2\varepsilon^*_{22100})I_{120}\\
&\quad +\eta_3 a_1 a_3(a_1\varepsilon^*_{13001}+a_3\varepsilon^*_{33100})I_{111}\\
&\quad -\eta_3[a_1\varepsilon^*_{11100}(I_{110}-3a_1^2I_{210})+a_2\varepsilon^*_{12010}\\
&\quad \times(I_{110}-3a_2^2I_{120})+a_3\varepsilon^*_{13001}(I_{110}-a_3^2I_{111})]\\
(\pi a)^{-1}\Lambda^{1,1}_{020} &= -3\eta_1 a_2\varepsilon^*_{mm010}I_{020}+\eta_2(a_1\varepsilon^*_{11100}I_{110}\\
&\quad +3a_2\varepsilon^*_{12010}I_{020}+a_3\varepsilon^*_{13001}I_{011})+3\eta_3 a_1 a_2(a_1\varepsilon^*_{12010}\\
&\quad +a_2\varepsilon^*_{22100})I_{120}+\eta_3 a_1 a_3(a_1\varepsilon^*_{13001}+a_3\varepsilon^*_{33100})I_{111}\\
&\quad -\eta_3[a_1\varepsilon^*_{11100}(I_{110}-3a_1^2I_{210})+a_2\varepsilon^*_{12010}\\
&\quad \times(I_{110}-3a_2^2I_{120})+a_3\varepsilon^*_{13001}(I_{110}-a_3^2I_{111})]\\
(2\pi a)^{-1}\Sigma^{12,1}_{010} &= -\eta_3(a_1\varepsilon^*_{22100}+a_2\varepsilon^*_{12010})I_{110},\\
(2\pi a)^{-1}\Sigma^{21,1}_{010} &= -\eta_3(a_1\varepsilon^*_{11100}I_{110}+3a_2\varepsilon^*_{12010}I_{020}+a_3\varepsilon^*_{13001}I_{011}),\\
(2\pi a)^{-1}\Sigma^{22,1}_{010} &= -\eta_3(a_1\varepsilon^*_{12100}I_{110}+3a_2\varepsilon^*_{22010}I_{020}+a_3\varepsilon^*_{23001}I_{011}),\\
(2\pi a)^{-1}\Lambda^{2,1}_{101} &= \eta_2(a_1\varepsilon^*_{23100}+a_3\varepsilon^*_{12001})I_{101}+\eta_3 a_2 a_3(a_2\varepsilon^*_{12001}\\
&\quad +a_3\varepsilon^*_{13010})I_{111}+\eta_3 a_1 a_3(a_1\varepsilon^*_{12001}+a_3\varepsilon^*_{23100})I_{111}\\
&\quad +\eta_3 a_1 a_2(a_1\varepsilon^*_{13010}+a_2\varepsilon^*_{23100})I_{111},\\
(2\pi a)^{-1}\Lambda^{1,1}_{011} &= \eta_2(a_2\varepsilon^*_{13010}+a_3\varepsilon^*_{12001})I_{011}+\eta_3 a_2 a_3(a_2\varepsilon^*_{12001}\\
&\quad +a_3\varepsilon^*_{13010})I_{111}+\eta_3 a_1 a_3(a_1\varepsilon^*_{12001}+a_3\varepsilon^*_{23100})I_{111}\\
&\quad +\eta_3 a_1 a_2(a_1\varepsilon^*_{13010}+a_2\varepsilon^*_{23100})I_{111},\\
(2\pi a)^{-1}\Sigma^{12,1}_{001} &= -\eta_3(a_1\varepsilon^*_{23100}+a_3\varepsilon^*_{12001})I_{101},\\
(2\pi a)^{-1}\Sigma^{21,1}_{001} &= -\eta_3(a_2\varepsilon^*_{13010}+a_3\varepsilon^*_{12001})I_{101},\\
(2\pi a)^{-1}\Sigma^{23,1}_{100} &= -\eta_3(a_1\varepsilon^*_{33100}+a_3\varepsilon^*_{13001})I_{101},\\
(2\pi a)^{-1}\Sigma^{13,1}_{010} &= -\eta_3(a_1\varepsilon^*_{23100}+a_2\varepsilon^*_{13010})I_{110},\\
(\pi a)^{-1}\Lambda^{3,1}_{200} &= -\eta_1 a_3\varepsilon^*_{mm001}I_{101}+\eta_2(3a_1\varepsilon^*_{13100}I_{200}+a_2\varepsilon^*_{23010}I_{110}\\
&\quad +a_3\varepsilon^*_{33001}I_{101})+3\eta_3 a_1 a_3(a_1\varepsilon^*_{11001}+a_3\varepsilon^*_{13100})I_{201}\\
&\quad +\eta_3 a_2 a_3(a_2\varepsilon^*_{22001}+a_3\varepsilon^*_{23010})I_{111}\\
&\quad -\eta_3[a_1\varepsilon^*_{13100}(I_{101}-3a_1^2I_{201})+a_2\varepsilon^*_{23010}\\
&\quad \times(I_{101}-a_2^2I_{111})+a_3\varepsilon^*_{33001}(I_{101}-3a_3^2I_{102})]\\
(2\pi a)^{-1}\Sigma^{31,1}_{100} &= -\eta_3(a_1\varepsilon^*_{13100}+a_3\varepsilon^*_{11001})I_{101},\\
(2\pi a)^{-1}\Lambda^{3,1}_{110} &= \eta_2(a_1\varepsilon^*_{23100}+a_2\varepsilon^*_{13010})I_{110}+\eta_3 a_2 a_3(a_2\varepsilon^*_{12001}\\
&\quad +a_3\varepsilon^*_{13010})I_{111}+\eta_3 a_1 a_3(a_1\varepsilon^*_{12001}+a_3\varepsilon^*_{23100})I_{111}\\
&\quad +\eta_3 a_1 a_2(a_1\varepsilon^*_{13010}+a_2\varepsilon^*_{23100})I_{111},\\
(2\pi a)^{-1}\Sigma^{32,1}_{010} &= -\eta_3(a_2\varepsilon^*_{23010}+a_3\varepsilon^*_{22001})I_{011},\\
(2\pi a)^{-1}\Sigma^{32,1}_{100} &= -\eta_3(a_1\varepsilon^*_{23100}+a_3\varepsilon^*_{12001})I_{101},\\
(\pi a)^{-1}\Lambda^{1,1}_{002} &= -\eta_1 a_1\varepsilon^*_{mm100}I_{101}+\eta_2(a_1\varepsilon^*_{11100}I_{101}+a_2\varepsilon^*_{12010}I_{011}\\
&\quad +3a_3\varepsilon^*_{13001}I_{002})+3\eta_3 a_1 a_3(a_1\varepsilon^*_{13001}\\
&\quad +a_3\varepsilon^*_{33100})I_{102}+\eta_3 a_1 a_2(a_1\varepsilon^*_{12010}+a_2\varepsilon^*_{22100})I_{111}\\
&\quad -\eta_3[a_1\varepsilon^*_{11100}(I_{101}-3a_1^2I_{201})+a_2\varepsilon^*_{12010}(I_{101}\\
&\quad -a_2^2I_{111})+a_3\varepsilon^*_{13001}(I_{101}-3a_3^2I_{102})]\\
(2\pi a)^{-1}\Sigma^{13,1}_{001} &= -\eta_3(a_1\varepsilon^*_{33100}+a_3\varepsilon^*_{13001})I_{101},\\
(2\pi a)^{-1}\Sigma^{31,1}_{001} &= -\eta_3(a_1\varepsilon^*_{11100}I_{101}+a_2\varepsilon^*_{12010}I_{011}+3a_3\varepsilon^*_{13001}I_{002}),\\
(2\pi a)^{-1}\Sigma^{31,1}_{010} &= -\eta_3(a_2\varepsilon^*_{13010}+a_3\varepsilon^*_{12001})I_{011},\\
(\pi a)^{-1}\Lambda^{3,1}_{020} &= -\eta_1 a_3\varepsilon^*_{mm001}I_{011}+\eta_2(a_1\varepsilon^*_{13100}I_{110}+3a_2\varepsilon^*_{23010}I_{020}\\
&\quad +a_3\varepsilon^*_{33001}I_{011})+\eta_3 a_1 a_3(a_1\varepsilon^*_{11001}+a_3\varepsilon^*_{13100})I_{111}\\
&\quad +3\eta_3 a_2 a_3(a_2\varepsilon^*_{22001}+a_3\varepsilon^*_{23010})I_{021}\\
&\quad -\eta_3[a_1\varepsilon^*_{13100}(I_{011}-a_1^2I_{111})+a_2\varepsilon^*_{23010}\\
&\quad \times(I_{011}-3a_2^2I_{021})+a_3\varepsilon^*_{33001}(I_{011}-3a_3^2I_{012})]\\
(\pi a)^{-1}\Lambda^{2,1}_{002} &= -\eta_1 a_2\varepsilon^*_{mm010}I_{011}+\eta_2(a_1\varepsilon^*_{12100}I_{101}+a_2\varepsilon^*_{22010}I_{011}\\
&\quad +3a_3\varepsilon^*_{23001}I_{002})+3\eta_3 a_2 a_3(a_2\varepsilon^*_{23001}\\
&\quad +a_3\varepsilon^*_{33010})I_{012}+\eta_3 a_1 a_2(a_1\varepsilon^*_{11010}+a_2\varepsilon^*_{12100})I_{111}\\
&\quad -\eta_3[a_1\varepsilon^*_{12100}(I_{011}-a_1^2I_{111})+a_2\varepsilon^*_{22010}\\
&\quad \times(I_{011}-3a_2^2I_{021})+a_3\varepsilon^*_{23001}(I_{011}-3a_3^2I_{012})]\\
(2\pi a)^{-1}\Sigma^{23,1}_{001} &= -\eta_3(a_2\varepsilon^*_{33010}+a_3\varepsilon^*_{23001})I_{011}.
\end{aligned}
$$

Closed-form expressions for all the potential integrals entering in Eq. (31) are given in the next section (see Eqs. (35), (36), and (37)). Equations (31) can also be cast in Eshelby's format. Calculations for eigenstrains characterized by higher order polynomials can be carried out in a similar fashion, although they are best done using different symbolic-numeric processors, such as, Matlab, Maple, and Mathematica. We close this section with two important observations. First, in the general case where the eigenstrains are given by quadratic or higher-order polynomials, it is not possible to represent the induced strain field in Eshelby's form. This can be easily illustrated by considering the case where the eigenstrains are given by a single term of the form

$$\varepsilon^*_{ijpqr}(x_1/a_1)^p(x_2/a_2)^q(x_3/a_3)^r(p+q+r\geqslant 2)$$
$$(\text{no summation on } p,q,r \text{ implied}).$$

The availability of the Eshelby tensor for this case would imply that the induced strain field is representable in the form

$$\varepsilon_{ij}=S_{ijkl}\varepsilon^*_{kl}$$
$$=S_{ijkl}\varepsilon^*_{klpqr}\left(\frac{x_1}{a_1}\right)^p\left(\frac{x_2}{a_2}\right)^q\left(\frac{x_3}{a_3}\right)^r$$
$$(\text{no summation on } p,q,r \text{ implied}).$$

However, as can be seen from Eq. (14), in this case the induced strain field is *not* characterized by just a single term of the form $(x_1/a_1)^p(x_2/a_2)^q(x_3/a_3)^r$, rather by an *entire* polynomial of order $p+q+r+2l$. Thus this observation leads us to the conclusion that in the general case of arbitrary order polynomials where the eigenstrains are neither constant nor linear, it is not possible to deduce an explicit expression for the Eshelby tensor.

The second observation is related to an interesting property of the polynomial characterizing the induced strain field within the ellipsoid. In order to lead the reader to this property, once again let us assume that the eigenstrains are given by a single term of the form $\varepsilon^*_{ijstu}(x_1/a_1)^s(x_2/a_2)^t(x_3/a_3)^u(s+t+u\geqslant 0)$ (no sum on s,t,u). Calculating the displacement gradient, we have

$$\partial_n u_i(\mathbf{x})=\eta_1\partial_i\partial_n\Gamma^{N,l}_{mm}-\eta_2\partial_i\partial_j\Gamma^{N,l}_{jn}+\eta_3\partial_i\partial_j\Gamma^{N,l}_{jr}+\eta_3 x_k\partial_i\partial_j\partial_n\Gamma^{N,l}_{jk}$$
$$-\eta_3\partial_i\partial_j\partial_n{}^{(k)}\tilde{\Gamma}^{N,l}_{jk}. \tag{32}$$

For this case, from Eqs. (7), we have

$$\Gamma^{N,l}_{ij}=\varepsilon^*_{ijstu}\,{}^{(l)}V^{(0)}_{stu},\ {}^{(k)}\tilde{\Gamma}^{N,l}_{ij}$$
$$=\varepsilon^*_{i,j,s-\delta_{k1},t-\delta_{k2},u-\delta_{k3}}\,{}^{(l)}V^{(0)}_{stu}\ (\text{no sum on } s,t,u).$$

Now, it can be easily seen from the Eqs. (32) and (14) that the polynomial characterizing the induced strain field in the ellipsoid (which is given by a polynomial of order $N+2l-2$) has the property that the sum of powers of x_1,x_2,x_3 in each individual term, $x_1^p x_2^q x_3^r$, in that polynomial (see Eq. (22)), i.e., $p+q+r$, must be even or odd, depending on whether $s+t+u$ is even or odd, respectively. Thus, in the linear eigenstrain case, the resulting polynomial will not have the zeroth-order term. This is why it turned out that in Eq. (29), $c_0^{ij}=0$. Further, if we consider the case of quadratic eigenstrains, i.e., $\varepsilon^*_{ij}=\varepsilon^*_{ijstu}(x_1/a_1)^s(x_2/a_2)^t(x_3/a_3)^u$ $(s+t+u=2)$, it will turn out that the resulting polynomial will not have the first-order terms. Similarly, for the case of cubic eigenstrains, the resulting polynomial will not have the zeroth-order and quadratic terms.

4 Recurrence Relations for the Potential Integrals

In this section we give a synopsis of the recurrence relations for the integral $I^{(\alpha)}_{ijk}$. Details of the derivation can be found in the writer's work [19].

$$I^{(\alpha)}_{l+1,m+1,n}=\frac{I^{(\alpha)}_{l,m+1,n}-I^{(\alpha)}_{l+1,m,n}}{a_1^2-a_2^2},$$
$$I^{(\alpha)}_{l+1,m,n+1}=\frac{I^{(\alpha)}_{l,m,n+1}-I^{(\alpha)}_{l+1,m,n}}{a_1^2-a_3^2},$$
$$I^{(\alpha)}_{l,m+1,n+1}=\frac{I^{(\alpha)}_{l,m,n+1}-I^{(\alpha)}_{l,m+1,n}}{a_2^2-a_3^2}. \tag{33}$$
$$(a_1^2+\alpha)(2l+1)I^{(\alpha)}_{l+1,m,n}+(a_2^2+\alpha)(2m+1)I^{(\alpha)}_{l,m+1,n}+(a_3^2+\alpha)(2n+1)I^{(\alpha)}_{l,m,n+1}=(2l+2m+2n+1)I^{(\alpha)}_{lmn}.$$

The starting values for the above recurrence relations are $I^{(\alpha)}_{000},I^{(\alpha)}_{100},I^{(\alpha)}_{010},I^{(\alpha)}_{001}$, which are given by the equations

$$I^{(\alpha)}_{000}=\frac{2}{\sqrt{a_1^2-a_3^2}}F(\theta,k),$$
$$I^{(\alpha)}_{100}=\frac{2}{(a_1^2-a_2^2)\sqrt{a_1^2-a_3^2}}[F(\theta,k)-E(\theta,k)],$$
$$I^{(\alpha)}_{010}=\frac{-2}{(a_1^2-a_2^2)\sqrt{a_1^2-a_3^2}}F(\theta,k)+\frac{2\sqrt{a_1^2-a_3^2}}{(a_1^2-a_2^2)(a_2^2-a_3^2)}E(\theta,k)$$
$$-\frac{2}{(a_2^2-a_3^2)}\sqrt{\frac{a_3^2+\alpha}{(a_1^2+\alpha)(a_2^2+\alpha)}}, \tag{34}$$
$$I^{(\lambda)}_{001}=\frac{-2}{(a_2^2-a_3^2)\sqrt{a_1^2-a_3^2}}E(\theta,k)+\frac{2}{(a_2^2-a_3^2)}\sqrt{\frac{a_2^2+\alpha}{(a_1^2+\alpha)(a_3^2+\alpha)}},$$

where $F(\theta,k)$, $E(\theta,k)$ are the incomplete elliptic integrals of the first and second kinds, respectively, and

$$\theta=\sin^{-1}\sqrt{\frac{a_1^2-a_3^2}{a_1^2+\alpha}},\quad k=\sqrt{\frac{a_1^2-a_2^2}{a_1^2-a_3^2}}. \tag{35}$$

The reader's attention should be brought to the fact that the first three equations in (33) are not applicable to those $I^{(\alpha)}_{ijk}$s, whose two of the three subscripts are simultaneously zero; such $I^{(\alpha)}_{ijk}$s need be modified using the fourth equation in (33), after which the first three equations can be utilized.

Equations (33) and (34) define a set of recurrence relations by means of which closed-form expressions for $I^{(\alpha)}_{ijk}$ can be deduced for all $i,j,k=0,1,2,\cdots$. For the case where $\mathbf{x}\in\Omega$, $\alpha=0$ and hence Eqs. (33), (34), and (35) simplify:

$$I_{000}=\frac{2}{\sqrt{a_1^2-a_3^2}}F(\theta_0,k),$$
$$I_{100}=\frac{2}{(a_1^2-a_2^2)\sqrt{a_1^2-a_3^2}}[F(\theta_0,k)-E(\theta_0,k)],$$
$$I_{010}=\frac{-2}{(a_1^2-a_2^2)\sqrt{a_1^2-a_3^2}}F(\theta_0,k)+\frac{2\sqrt{a_1^2-a_3^2}}{(a_1^2-a_2^2)(a_2^2-a_3^2)}E(\theta_0,k)$$
$$-\frac{2a_3}{a_1a_2(a_2^2-a_3^2)},$$
$$I_{001}=\frac{-2}{(a_2^2-a_3^2)\sqrt{a_1^2-a_3^2}}E(\theta_0,k)+\frac{2a_2}{a_1a_3(a_2^2-a_3^2)},$$
$$I_{l+1,m+1,n}=\frac{I_{l,m+1,n}-I_{l+1,m,n}}{a_1^2-a_2^2},$$
$$I_{l+1,m,n+1}=\frac{I_{l,m,n+1}-I_{l+1,m,n}}{a_1^2-a_3^2}, \tag{36}$$
$$I_{l,m+1,n+1}=\frac{I_{l,m,n+1}-I_{l,m+1,n}}{a_2^2-a_3^2},$$
$$a_1^2(2l+1)I_{l+1,m,n}+a_2^2(2m+1)I_{l,m+1,n}+a_3^2(2n+1)I_{l,m,n+1}$$
$$=(2l+2m+2n+1)I_{lmn},$$

where the expression for θ_0 can be deduced from that for θ by putting $\alpha=0$ into the first equation in (35), namely,

$$\theta_0=\sin^{-1}\frac{\sqrt{a_1^2-a_3^2}}{a_1}. \tag{37}$$

Note that there is an incorrect statement in Mura's book ([9], p. 93), implying that θ is equal to θ_0.

Thus, the following expressions are deduced using the recurrence relations (36):

$$I_{110}=\frac{I_{010}-I_{100}}{a_1^2-a_2^2},\quad I_{101}=\frac{I_{001}-I_{100}}{a_1^2-a_3^2},\quad I_{011}=\frac{I_{001}-I_{010}}{a_2^2-a_3^2},$$

$$I_{200}=\frac{3I_{100}-a_2^2I_{110}-a_3^2I_{101}}{3a_1^2},\quad I_{020}=\frac{3I_{010}-a_1^2I_{110}-a_3^2I_{011}}{3a_2^2},$$

$$I_{002}=\frac{3I_{001}-a_1^2I_{101}-a_2^2I_{011}}{3a_3^2},\quad I_{111}=\frac{I_{011}-I_{101}}{a_1^2-a_2^2}, \tag{38}$$

$$I_{201}=\frac{I_{101}-I_{200}}{a_1^2-a_3^2},\quad I_{210}=\frac{I_{110}-I_{200}}{a_1^2-a_2^2},\quad I_{012}=\frac{I_{002}-I_{011}}{a_2^2-a_3^2},$$

$$I_{021}=\frac{I_{011}-I_{020}}{a_2^2-a_3^2},\quad I_{102}=\frac{I_{002}-I_{101}}{a_1^2-a_3^2},\quad I_{120}=\frac{I_{020}-I_{110}}{a_1^2-a_2^2},$$

$$I_{300}=\frac{5I_{200}-a_2^2I_{210}-a_3^2I_{201}}{5a_1^2},\quad I_{030}=\frac{5I_{020}-a_1^2I_{120}-a_3^2I_{021}}{5a_2^2},$$

$$I_{003}=\frac{5I_{002}-a_1^2I_{102}-a_2^2I_{012}}{5a_3^2}.$$

5 Closure

The problem of determining the strain field within an isotropic ellipsoidal inclusion with eigenstrains characterized by an arbitrary order polynomial in the Cartesian coordinates of the points of the inclusion is considered in the present article. Ferrers-Dyson theorem on the Newtonian potential of a heterogeneous ellipsoid as well as some of its further development by the present writer are used to deduce an explicit expression for the polynomial characterizing the induced strain field within the transformed ellipsoid. Using a consistent notation, the results are organized into an algorithmic form especially suited for symbolic-numeric computation by computer. The results are capable of extending our ability to analyze various static and dynamic problems concerning ellipsoidal inclusions with nonuniform eigenstrains.

Acknowledgments

I dedicate the article to the memory of my mother. Also, I would like to thank Dr. D. M. Barnett (Stanford University) for his kind response to my queries on some aspects of the problem. Thanks are also due to my wife, Dr. Anisa Yasmin, whose comments were very valuable.

References

[1] Eshelby, J. D., 1957, "The Determination of the Elastic Field of an Ellipsoidal Inclusion, and Related Problems," Proc. R. Soc. London, Ser. A, **A241**, pp. 376–396.
[2] Eshelby, J. D., 1959, "The Elastic Field Outside an Ellipsoidal Inclusion," Proc. R. Soc. London, Ser. A, **A252**, pp. 561–569.
[3] Eshelby, J. D., 1960, "Elastic Inclusions and Inhomogeneities," *Progress in Solid Mechanics*, **2**, I. N. Sneddon and R. Hill, eds., North-Holland, Amsterdam, pp. 89–140.
[4] Walpole, L. J., 1967, "The Elastic Field of an Inclusion in an Anisotropic Medium," Proc. R. Soc. London, Ser. A, **300**, pp. 270–289.
[5] Kinoshita, N., and Mura, T., 1971, "Elastic Fields of Inclusions in Anisotropic Media," Phys. Status Solidi A, **5**, pp. 759–768.
[6] Kinoshita, N., and Mura, T., 1986, "An Ellipsoidal Inclusion With Polynomial Eigenstrains," Q. Appl. Math., **XLIV(1)**, pp. 195–199.
[7] Asaro, R. J., and Barnett, D. M., 1975, "The Non-uniform Transformation Strain Problem for an Anisotropic Ellipsoidal Inclusion," J. Mech. Phys. Solids, **23**, pp. 77–83.
[8] Mura, T., and Kinoshita, N., 1978, "The Polynomial Eigenstrain Problem for an Anisotropic Ellipsoidal Inclusion," Phys. Status Solidi A, **48**, pp. 447–450.
[9] Mura, T., 1987, *Micromechanics of Defects in Solids*, Martinus Nijhoff, The Hague.
[10] Mura, T., 1988, "Inclusion Problems," Appl. Mech. Rev., **41**(1), pp. 15–20.
[11] Nemat-Nasser, S., and Hori, M., 1999, *Micromechanics: Overall Properties of Heterogeneous Materials*, Elsevier, Amsterdam.
[12] Khachaturyan, A. G., 1983, *Theory of Structural Transformations in Solids*, John Wiley and Sons, New York.
[13] Markenscoff, X., 1998, "On the Shape of the Eshelby Inclusions," J. Elast., **44**, pp. 163–166.
[14] Markenscoff, X., 1998, "Inclusions With Constant Eigenstress," J. Mech. Phys. Solids, **46**, pp. 2297–2301.
[15] Markenscoff, X., 1998, "Inclusions of Uniform Eigenstrains and Constant or Other Stress Dependence," ASME J. Appl. Mech., **65**, pp. 863–866.
[16] Lubarda, V. A., and Markenscoff, X., 1998, "On the Absence of Eshelby Property for Non-ellipsoidal Inclusions," Int. J. Solids Struct., **35**, No. 25, pp. 3405–3411.
[17] Ferrers, N. M., 1877, "On the Potentials of Ellipsoids, Ellipsoidal Shells, Elliptic Laminae and Elliptic Rings of Variable Densities," Q. J. Pure Appl. Math., **14**(1), pp. 1–22.
[18] Dyson, F. D., 1891, "The Potentials of Ellipsoids of Variable Densities," Q. J. Pure Appl. Math., **XXV**, pp. 259–288.
[19] Rahman, M., 2001, "On the Newtonian Potentials of Heterogeneous Ellipsoids and Elliptic Discs," Proc. R. Soc. London, Ser. A, **A457**(2013), pp. 2227–2250.
[20] Natanson, I. P., 1967, *Theory of Functions of a Real Variable*, Frederick Ungar, New York.
[21] Mikata, Y., and Nemat-Nasser, S., 1990, "Elastic Field due to a Dynamically Transforming Spherical Inclusion," ASME J. Appl. Mech., **57**, pp. 845–849.
[22] Mikata, Y., and Nemat-Nasser, S., 1991, "Interaction of a Harmonic Wave With a Dynamically Transforming Inhomogeneity," J. Appl. Phys., **70**, pp. 2071–2078.
[23] Cheng, Z.-Q., and Batra, R. C., 1999, "Exact Eshelby Tensor for a Dynamic Circular Cylindrical Inclusion," ASME J. Appl. Mech., **66**, pp. 563–565.
[24] Van Dyke, M., 1974, "Analysis and Improvement of Perturbation Series," Q. J. Mech. Appl. Math., **XXVII**, Pt. 4, pp. 423–450.
[25] Bell, R. J. T., 1959, *An Elementary Treatise on Coordinate Geometry of Three Dimensions*, Macmillan, London.

A. S. Wineman[1]
Professor,
Fellow ASME
Mechanical Engineering,
The University of Michigan,
G042 Auto Lab,
Ann Arbor, MI 48109
e-mail: lardan@engin.umich.edu ASME

J. A. Shaw
Assistant Professor,
Assoc. Mem. ASME
Aerospace Engineering,
The University of Michigan,
1320 Beal Avenue,
Ann Arbor, MI 48109-2140
e-mail: jashaw@engin.umich.edu

Scission and Healing in a Spinning Elastomeric Cylinder at Elevated Temperature

When an elastomeric material is subject to sufficiently high temperature, macromolecular network junctions can undergo time-dependent scission and re-crosslinking (healing). The material system then consists of molecular networks with different reference states. A constitutive framework, based on the experimental work of Tobolsky, is used to determine the evolution of deformation of a solid rubber cylinder spinning at constant angular velocity at an elevated temperature. Responses based on underlying neo-Hookean, Mooney-Rivlin, and Arruda-Boyce models, were solved numerically and compared. Different amounts of healing were studied for each case. For neo-Hookean molecular networks, there may be a critical finite time when the radius grows infinitely fast and the cylinder "blows up." This time depends on the angular velocity and the rate of re-cross linking. In addition, no solution was possible for angular velocities above a critical value, even without the effects of scission. Such anomalous behavior does not occur for Mooney-Rivlin or Arruda-Boyce network response. [DOI: 10.1115/1.1485757]

1 Introduction

The general form of the constitutive equation for nonlinear thermoelasticity used to represent the response of elastomeric material is expressed in terms of a temperature-dependent strain energy density function. Implicit in the formulation is the usual assumption that material response is due to a macromolecular mechanism that does not change during the thermomechanical process being considered. Tobolsky [1] presented experimental results, however, indicating that when the temperature becomes high enough a change can occur in the macromolecular network. This mechanism consists of scission and subsequent re-cross linking of macromolecular network junctions. The process is time-dependent and can result in substantial changes in mechanical response and permanent set upon removal of applied loads.

Tobolsky's results show that the nonlinear theory of thermoelasticity applies provided the temperature is maintained below a critical value. When this temperature is exceeded, scission and re-cross linking of network junctions (referred to hereafter as 'healing') occur which requires the development of a new constitutive theory. In previous work, Wineman and Rajagopal [2] and Rajagopal and Wineman [3] developed a constitutive framework which applies when deformations are large enough to cause scission. By contrast, the present work uses this framework to express a constitutive theory that addresses temperature-induced scission and healing.

The problem of a rotating rubber cylinder has attracted the interest of a number of authors (see Horgan and Saccomandi [4] and Chadwick et al. [5]). A spinning rubber cylinder represents a very simple model of an automobile or aircraft tire, recognizing that the actual case likely involves nonuniform temperature fields which we will neglect here. Nevertheless, under certain operating conditions, these tires can experience a substantial increase in temperature. With recent events involving the failure of automobile and aircraft tires, it is natural to study the problem of a spinning rubber cylinder using a constitutive theory which allows for scission and healing at increased temperatures.

Section 2 begins with a presentation of the constitutive theory for the response of rubber that undergoes temperature-induced scission and re-cross linking. The problem of a rotating rubber cylinder is defined in Section 3, which reduces to an equation for the axial stretch ratio. The general constitutive framework of Section 2 allows the user to choose a specific underlying thermoelastic model. Responses based on neo-Hookean, Mooney-Rivlin, and Arruda-Boyce models, in turn, are studied for the spinning cylinder problem in Section 4. Results are illustrated with numerical examples, and comparisons are made for the different models.

2 Constitutive Framework

In the experiments conducted by Tobolsky [1], a rubber strip at room temperature was subjected to a fixed uniaxial stretch and then held at a higher fixed temperature for some time interval. At temperatures above T_{cr} (say 100°C), called the chemorheological temperature range, the stress was observed to decrease with time. At the end of the time interval, the stress was removed and the specimen was returned to its original temperature. Tests were carried out for different stretches, temperatures and time intervals. The decrease in tensile stress with time and the permanent stretch were measured. The data were analyzed assuming neo-Hookean behavior, for which the relation between tensile (Cauchy) stress $\sigma(t)$ and uniaxial stretch ratio λ is

$$\sigma(t)=2n(t)kT\left(\lambda^2-\frac{1}{\lambda}\right) \tag{1}$$

where T is the absolute temperature, k is the Boltzmann constant, and $n(t)$ is the current cross link density. It was concluded that the decrease in $\sigma(t)$ was due to scission of molecular network cross links, resulting in a decrease in $n(t)$. The permanent stretch was due to a new network which formed in the stretched state (healing). The stress-stretch relation for the system back at the original low temperature consisting of the two networks was assumed to be

$$\sigma(t)=2n_1kT\left(\lambda^2-\frac{1}{\lambda}\right)+2n_2kT\left[\left(\frac{\lambda}{\hat{\lambda}}\right)^2-\left(\frac{\hat{\lambda}}{\lambda}\right)\right] \tag{2}$$

[1]To whom correspondence should be addressed.

Contributed by the Applied Mechanics Division of THE AMERICAN SOCIETY OF MECHANICAL ENGINEERS for publication in the ASME JOURNAL OF APPLIED MECHANICS. Manuscript received by the ASME Applied Mechanics Division, April 5, 2001; final revision, February 5, 2002. Associate Editor: K. R. Rajagopal. Discussion on the paper should be addressed to the Editor, Prof. Robert M. McMeeking, Department of Mechanical and Environmental Engineering University of California–Santa Barbara, Santa Barbara, CA 93106-5070, and will be accepted until four months after final publication of the paper itself in the ASME JOURNAL OF APPLIED MECHANICS.

where $\hat{\lambda}$ is the stretch ratio of the original network held at the high temperature, n_1 is the cross link density of the original network at the end of the test, and n_2 is the cross link density of the new network. The second term in (2) expresses the assumption that the new network is formed stress free when the stretch ratio in the original network is $\hat{\lambda}$. Tobolsky's data also suggested that n_1 and n_2 are independent of the stretch ratio $\hat{\lambda}$ up to a stretch ratio of about 4. It was also assumed (Tobolsky [1], and Tobolsky et al. [6]) that all broken molecular cross links reform to produce a new network in a stress free state. That is, there is conservation of cross links, $n_1+n_2=n(0)$, which we hereafter refer to as complete healing. The validity of this assumption depends on the particular chemistry of the rubber being considered.

Neubert and Saunders [7] carried out tests similar to those of Tobolsky, but for a pure shear deformation. They measured permanent biaxial stretch after removal of stress and reduction of the temperature, and found that predictions based on a neo-Hookean model led to inaccurate predictions of permanent set. A Mooney-Rivlin material model led to better agreement with measured permanent biaxial stretch. Fong and Zapas [8] improved the agreement by using the Rivlin-Saunders model ([9]).

Using the uniaxial relations (1) and (2) as a guide, a three-dimensional constitutive framework is developed as follows. Consider a rubbery material in a stress free reference configuration at a low temperature T_0. It is assumed that there is a range of deformations and temperatures in which the material response is essentially incompressible, isotropic and nonlinearly elastic. If $\mathbf{x}$ is the position at current time t of a particle located at $\mathbf{X}$ in the reference configuration, the deformation gradient is defined as $\mathbf{F}=\partial\mathbf{x}/\partial\mathbf{X}$. The left Cauchy-Green tensor is $\mathbf{B}=\mathbf{F}\mathbf{F}^T$. The Cauchy stress $\boldsymbol{\sigma}$ is given by

$$\boldsymbol{\sigma}=-p^0\mathbf{I}+\boldsymbol{\sigma}^0(\mathbf{B},T)=-p^0\mathbf{I}+2W_1^0\mathbf{B}-2W_2^0\mathbf{B}^{-1} \tag{3}$$

where p^0 arises from the constraint that deformations are isochoric, I_1, I_2 are invariants of $\mathbf{B}$ and $W_1^0=\partial W^0/\partial I_1$ and $W_2^0=\partial W^0/\partial I_2$ are partial derivatives of the strain energy density $W^0(I_1,I_2,T)$ associated with the original material.

For low temperatures, $T<T_{cr}$, no scission occurs. All of the material has its original reference state and the total stress is given by (3). At time $t=0$ the temperature is increased to a high temperature, $T\geqslant T_{cr}$, and scission of the original microstructural network is assumed to occur continuously in time. A scalar-valued function $a(t)\geqslant 0$ is introduced, which represents the rate at which volume fraction of new network is formed at time t. Thus, $a(t)dt$ is interpreted as the volume fraction of new material that has formed during the time interval from t to $t+dt$. The volume fraction of original network remaining at time t is denoted as $b(t)$. $b(t)\in[0,1]$ and is a monotonically decreasing function of t. For the sake of simplicity and consistent with Tobolsky's observations, it is assumed that $a(t)$ and $b(t)$ do not depend on the deformation. He showed for experiments under uniaxial extension that this is reasonable provided the stretch remains less than 3 to 4. In addition, it is assumed that the rate of formation of new networks is given by

$$a(t)=-\eta\frac{db(t)}{dt}, \tag{4}$$

where $\eta\in[0,1]$ is a scalar parameter that depends on the particular rubber system being considered. Tobolsky's assumption of network conservation corresponds to complete healing, or $\eta=1$. Complete scission, by contrast, occurs with no new network formation and can be modeled with $\eta=0$. The work of Tobolsky does not address whether a time lag exists between scission and re-cross-linking. Accordingly, in the absence of experimental data on this point, Eq. (4) neglects any time lag between scission and healing.

Now consider an intermediate time $\hat{t}\in[0,t]$ and the corresponding deformed configuration of the original material. Due to the formation of new cross links, a network is formed in the interval from $\hat{t}$ to $\hat{t}+d\hat{t}$ whose reference configuration is the current configuration at time $\hat{t}$. As suggested by Tobolsky [1] and Tobolsky et al. [6], this is assumed to be an unstressed configuration for the newly formed network. Under subsequent deformation, the motion of the newly formed material network coincides with the motion of the original material network. Stress arises in this newly formed material network due to its deformation relative to its unstressed configuration at time $\hat{t}$. At the later time t, the material formed at earlier time $\hat{t}$ has the relative deformation gradient $\hat{\mathbf{F}}=\partial\mathbf{x}/\partial\hat{\mathbf{x}}$, where $\hat{\mathbf{x}}$ is the position of the particle in the configuration corresponding to time $\hat{t}$ and x is its position at time t.

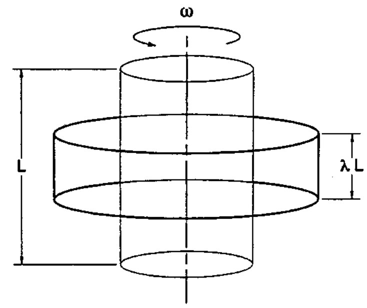

Fig. 1 Reference and current configuration for spinning cylinder

For simplicity, the new material network is also assumed to respond as an incompressible, isotropic, nonlinear elastic material. The left Cauchy-Green tensor $\hat{\mathbf{B}}=\hat{\mathbf{F}}\hat{\mathbf{F}}^T$ is introduced for relative deformations of this network. The constitutive equation for the network formed at time $\hat{t}$ is then given by

$$\overline{\boldsymbol{\sigma}}=-\hat{p}\mathbf{I}+\hat{\boldsymbol{\sigma}}(\hat{\mathbf{B}},T)=-\hat{p}\mathbf{I}+2\hat{W}_1\hat{\mathbf{B}}-2\hat{W}_2\hat{\mathbf{B}}^{-1} \tag{5}$$

where $\hat{p}$ arises from the constraint that deformations are isochoric, $\hat{I}_1,\hat{I}_2$ are invariants of $\hat{\mathbf{B}}$, and $\hat{W}_1=\partial\hat{W}/\partial\hat{I}_1$ and $\hat{W}_2=\partial\hat{W}/\partial\hat{I}_2$ are partial derivatives of energy density of the new network, $\hat{W}(\hat{I}_1,\hat{I}_2,T)$. In general, the energy density associated with the newly formed material can differ from that associated with the original material.

The total current stress in the material is taken as the superposition of the stress in the remaining material of the original network and the stress in new networks. Thus,

$$\boldsymbol{\sigma}=-p\mathbf{I}+b\boldsymbol{\sigma}^0(\mathbf{B},T)+\int_0^t a(\hat{t})\hat{\boldsymbol{\sigma}}(\hat{\mathbf{B}},T)d\hat{t} \tag{6}$$

where p, b, $\mathbf{B}$, T, $\boldsymbol{\sigma}$ are evaluated at the current time t. The term $-p\mathbf{I}$ incorporates the corresponding terms in (3) and (5). The stress in the original network, $\boldsymbol{\sigma}^0(\mathbf{B},T)$, is expressed in terms of $W^0(I_1,I_2,T)$ by (3), and the stress developed in any new networks, $\hat{\boldsymbol{\sigma}}(\hat{\mathbf{B}},T)$, is expressed in terms of $\hat{W}(\hat{I}_1,\hat{I}_2,T)$ by (5).

Although Tobolsky assumed the response of the original and newly formed networks to be neo-Hookean, Neubert and Sanders [7] and Fong and Zapas [8] considered other possibilities. Thus, $W^0(I_1,I_2,T)$ and $\hat{W}(\hat{I}_1,\hat{I}_2,T)$ are left, as yet, unspecified.

3 Boundary Value Problem Formulation

The boundary value problem consists of a solid cylinder of radius R_0, length L_0 in its undeformed configuration, and uniform mass density ρ, which is spinning about its central axis with a constant angular velocity ω (see Fig. 1). The temperature of the cylinder is changed at $t=0$ to a constant, uniform high temperature, $T>T_{cr}$, so that the material undergoes the scission-healing process. This chemically based relaxation process and the centrifugal loading cause the dimensions of the cylinder to change with time. The cylindrical coordinates of a point in the reference and current configurations, are denoted by (R,Θ,Z) and (r,θ,z), respectively. It is assumed that plane sections remain plane and cylindrical surfaces deform into cylindrical surfaces, resulting in a deformation described by

$$
\begin{aligned}
r&=r(R,t), \quad R\in[0,R_0],\\
\theta&=\Theta+\omega t, \quad \Theta\in[0,2\pi),\\
z&=\lambda(t)Z, \quad Z\in[0,L_0].
\end{aligned}
\tag{7}
$$

The material response is assumed to be isochoric. By considering the volume bounded by a radial surface and the ends of the cylinder in the reference and current configurations, it is found that

$$r(R,t)=\frac{R}{\sqrt{\lambda(t)}}, \tag{8}$$

where $\lambda(t)\in[0,1]$ is the axial stretch ratio. Accordingly, the current radius of the cylinder is

$$r_0=\frac{R_0}{\sqrt{\lambda(t)}}. \tag{9}$$

The physical components of the deformation gradient of the original network with respect to cylindrical coordinates are given by

$$
F(R,t)=\begin{bmatrix}\frac{\partial r}{\partial R}(R,t) & 0 & 0\\ 0 & \frac{r(R,t)}{R} & 0\\ 0 & 0 & \lambda(t)\end{bmatrix}
=\begin{bmatrix}\frac{1}{\sqrt{\lambda(t)}} & 0 & 0\\ 0 & \frac{1}{\sqrt{\lambda(t)}} & 0\\ 0 & 0 & \lambda(t)\end{bmatrix}. \tag{10}
$$

The reference configuration of any new formed network at time $\hat{t}$ is the configuration of the original network at time $\hat{t}$, and is defined by

$$
\begin{aligned}
\hat{r}&=r(R,\hat{t})=\frac{R}{\sqrt{\lambda(t)}}, \quad R\in[0,R_0]\\
\hat{\theta}&=\Theta+\omega\hat{t}, \quad \Theta\in[0,2\pi)\\
\hat{z}&=\lambda(\hat{t})Z, \quad Z\in[0,L_0].
\end{aligned}
\tag{11}
$$

The relation between the coordinates $(\hat{r},\hat{\theta},\hat{z})$ of a particle in the configuration at time $\hat{t}$ and its coordinates (r,θ,z) in the current configuration is found by eliminating (R,Θ,Z) in (7), (8), (11), giving

$$
\begin{aligned}
r&=\sqrt{\frac{\lambda(\hat{t})}{\lambda(t)}}\,\hat{r},\\
\theta&=\hat{\theta}+\omega(t-\hat{t}),\\
z&=\frac{\lambda(t)}{\lambda(\hat{t})}\hat{z}.
\end{aligned}
\tag{12}
$$

Since there is no relative motion between the network formed at time $\hat{t}$ and the original network, (12) describes the deformation of the network formed at time $\hat{t}$. The first equation of (12) arises from the condition that the volume of the newly formed network bounded by a radial surface and the ends of the cylinder at time $\hat{t}$ is the same as in the current configuration.

The physical components of the deformation gradient of the network formed at time $\hat{t}$ with respect to cylindrical coordinates are given by

$$
\hat{\mathbf{F}}(\hat{r},t)=\begin{bmatrix}\frac{\partial r}{\partial r}(\hat{r},t) & 0 & 0\\ 0 & \frac{r(\hat{r},t)}{\hat{r}} & 0\\ 0 & 0 & \lambda(t)\end{bmatrix}
=\begin{bmatrix}\sqrt{\frac{\lambda(\hat{t})}{\lambda(t)}} & 0 & 0\\ 0 & \sqrt{\frac{\lambda(\hat{t})}{\lambda(t)}} & 0\\ 0 & 0 & \lambda(t)/\lambda(\hat{t})\end{bmatrix}. \tag{13}
$$

Interestingly, $\mathbf{F}(R,t)$ and $\hat{\mathbf{F}}(\hat{r},t)$ are independent of radial position.

The stress components are found by calculating $\mathbf{B}(t)$ from (10) and $\hat{\mathbf{B}}(t)$ from (13) and substituting into the constitutive Eq. (6). Since $\mathbf{B}(t)$ and $\hat{\mathbf{B}}(t)$ are diagonal matrices, no shear stresses exist and the normal stresses can be written in the form

$$
\begin{aligned}
\sigma_{rr}&=\sigma_{\theta\theta}=-p+F_{rr},\\
\sigma_{zz}&=-p+F_{zz}.
\end{aligned}
\tag{14}
$$

In the subsequent analysis, only the expression for the difference $F_{rr}-F_{zz}$ appears, which can be written

$$
\begin{aligned}
F_{zz}-F_{rr}=&\,b(T,t)\left[\lambda(t)^2-\frac{1}{\lambda(t)}\right]\left(2W_1^0+\frac{1}{\lambda(t)}2W_2^0\right)+\int_0^t a(T,\hat{t})\\
&\times\left[\left(\frac{\lambda(t)}{\lambda(\hat{t})}\right)^2-\frac{\lambda(\hat{t})}{\lambda(t)}\right]\left(2\hat{W}_1+\frac{\lambda(\hat{t})}{\lambda(t)}2\hat{W}_2\right)d\hat{t}.
\end{aligned}
\tag{15}
$$

The scission-healing process is assumed to occur sufficiently slowly that inertia terms involving $\partial^2 r/\partial t^2$ and $\partial^2 z/\partial t^2$ can be neglected. Hence, in the expressions for the acceleration, these terms are neglected and only the centripetal term is considered. The axial and circumferential components of the equations of motion reduce to

$$\frac{\partial p}{\partial\theta}=\frac{\partial p}{\partial z}=0, \tag{16}$$

and the radial component becomes

$$\frac{\partial\sigma_{rr}}{\partial r}=-\rho\omega^2 r, \quad r\in[0,r_0(t)], \tag{17}$$

where use has been made of (14). Integrating (17) gives

$$\sigma_{rr}(r_0(t),t)-\sigma_{rr}(r,t)=-\frac{\rho\omega^2}{2}[r_0(t)^2-r^2]. \tag{18}$$

The outer surface is traction-free at each time, so (17) reduces to

$$\sigma_{rr}(r,t)=\frac{\rho\omega^2}{2}[r_0(t)^2-r^2]. \tag{19}$$

Combining (19) and (14) gives an expression for the scalar field p,

$$-p=\frac{\rho\omega^2}{2}[r_0(t)^2-r^2]-F_{rr}. \tag{20}$$

Substituting into (14) determines the axial normal stress,

$$\sigma_{zz}=\frac{\rho\omega^2}{2}[r_0(t)^2-r^2]+F_{zz}-F_{rr}. \tag{21}$$

Assuming that there is no resultant force on the ends of the cylinder leads to a boundary condition satisfied in the weak sense as

$$2\pi\int_0^{r_0(t)}\sigma_{zz}r\,dr=0. \tag{22}$$

Integrating the axial stress (21), then leads to the equation

$$F_{zz}-F_{rr}=-\frac{\rho\omega^2}{4}r_0(t)^2. \tag{23}$$

In view of (8), (23) reduces to

$$\lambda(t)[F_{zz}-F_{rr}]=-\frac{\rho\omega^2}{4}R_0^2. \tag{24}$$

Substituting from (15) leads to

$$b(T,t)\lambda(t)\left[\lambda(t)^2-\frac{1}{\lambda(t)}\right]\left(2W_1^0+\frac{1}{\lambda(t)}2W_2^0\right)+\lambda(t)\int_0^t a(T,\hat{t})\times\left[\left(\frac{\lambda(t)}{\lambda(\hat{t})}\right)^2-\frac{\lambda(\hat{t})}{\lambda(t)}\right]\left(2\hat{W}_1+\frac{\lambda(\hat{t})}{\lambda(t)}2\hat{W}_2\right)d\hat{t}=-\frac{\rho\omega^2}{4}R_0^2, \tag{25}$$

a nonlinear Volterra integral equation for the axial stretch ratio, $\lambda(t)$. Finally, dividing (25) by the shear modulus for infinitesimal deformations of the original network,

$$\mu(T)=2[W_1^0+W_2^0]_{I_1=I_2=3}, \tag{26}$$

produces the nondimensional equation

$$b(T,t)\lambda(t)\left[\lambda(t)^2-\frac{1}{\lambda(t)}\right]\left(w_1^0+\frac{1}{\lambda(t)}w_2^0\right)+\lambda(t)\int_0^t a(T,\hat{t})\times\left[\left(\frac{\lambda(t)}{\lambda(\hat{t})}\right)^2-\frac{\lambda(\hat{t})}{\lambda(t)}\right]\left(\hat{w}_1+\frac{\lambda(\hat{t})}{\lambda(t)}\hat{w}_2\right)d\hat{t}=-\Omega^2, \tag{27}$$

in which $\Omega=\omega/\omega_0(T)$, $\omega_0^2(T)=4\mu(T)/\rho R_0^2$, $w_\alpha^0=2W_\alpha^0/\mu$ and $\hat{w}_\alpha=2\hat{W}_\alpha/\mu$, $\alpha=1,2$.

Furthermore, a nondimensional temperature and nondimensional time can be defined as follows. According to Tobolsky [1], the rate of scission for many rubbery materials is given by

$$b(T,t)=\exp[-\alpha(T)t], \tag{28}$$

where

$$\alpha(T)=\frac{k}{h}T\exp\left[-\frac{E_{\mathrm{act}}}{RT}\right]. \tag{29}$$

In (29), k is Boltzmann's constant (1.38066×10^{-23} J/K), h is Planck's constant (6.62608×10^{-34} J-s), R is the gas constant, and E_{act} is an activation energy. For the particular material in Tobolsky's experiments, $E_{\mathrm{act}}=30.4$ kcal/mol (127.2 kJ/mol). In addition, Boltzmann's constant can be written as R/N_A, where $N_A=6.023\times10^{23}$/mol is Avogadro's number. Defining $\theta=RT/E_{\mathrm{act}}$ as a nondimensional temperature, allows (29) to be restated as

$$\alpha(\theta)=\frac{E_{\mathrm{act}}}{hN_A}\theta\exp\left[-\frac{1}{\theta}\right]. \tag{30}$$

Introducing a characteristic time for scission, $t_0=1/\alpha$, leads to the definition of a nondimensional time, $\tau=t/t_0=\alpha t$. According to (30), the characteristic time for scission is related to the nondimensional temperature as

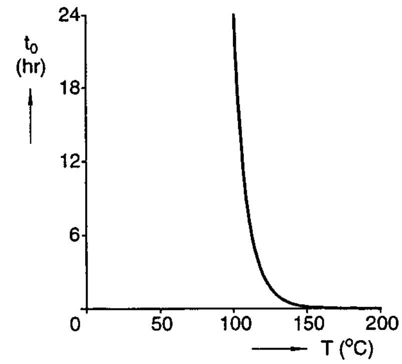

Fig. 2 Characteristic time for scission and healing for $E_{\mathrm{act}}=127.24$ kJ/mol

$$t_0=\frac{hN_A}{E_{\mathrm{act}}}\frac{\exp[1/\theta]}{\theta}. \tag{31}$$

This characteristic time is plotted versus actual temperature for Tobolsky's material in Fig. 2. Note the extreme temperature-dependence on this characteristic time. For example, the characteristic time is about 24 hrs for 100°C, but a 20°C increase gives a value of only 2.7 hrs, an order of magnitude reduction.

Finally, including the nondimensional time in (27) gives the governing equation

$$e^{-\tau}[\lambda(\tau)^3-1]\left(w_1^0+\frac{1}{\lambda(\tau)}w_2^0\right)+\eta\lambda(\tau)\times\int_0^\tau e^{-\hat{\tau}}\left[\left(\frac{\lambda(\tau)}{\lambda(\hat{\tau})}\right)^2-\frac{\lambda(\hat{\tau})}{\lambda(\tau)}\right]\left(\hat{w}_1+\frac{\lambda(\hat{\tau})}{\lambda(\tau)}\hat{w}_2\right)d\hat{\tau}=-\Omega^2. \tag{32}$$

4 Numerical Results

The response of the spinning cylinder to elevated temperature, for which scission-healing processes occur, is now investigated for three different material models, neo-Hookean, Mooney-Rivlin, and Arruda-Boyce. In the absence of experimental data to the contrary, we will assume that $w_0=\hat{w}$, i.e., the newly formed material has the same properties as the original material (this would be an interesting issue for further study). The nonlinear Volterra integral Eq. (32) for $\lambda(\tau)$ was solved numerically by discretizing the integral term in time using the trapezoidal rule and solving the resulting nonlinear algebraic equation by Newton iteration. The time increment was chosen sufficiently small such that the time evolution of $\lambda(\tau)$ had converged. A time increment of $\Delta\tau=1/100$ produced converged results. For each material model, the response was evaluated for three cases: no healing ($\eta=0$), partial healing ($\eta=0.5$), and complete healing ($\eta=1$).

4.1 Neo-Hookean Response. Consider first the response when both the original network and the newly formed networks are neo-Hookean. In this case, the shear modulus is constant, defined by $2W_1^0=\mu$, and $W_2^0=0$. Substituting the material parameters

$$w_1^0=\hat{w}_1=1,\quad w_2^0=\hat{w}_2=0 \tag{33}$$

into (32) gives the governing equation

$$\lambda(\tau)^3\left[e^{-\tau}+\eta\int_0^\tau e^{-\hat{\tau}}\lambda(\hat{\tau})^{-2}d\hat{\tau}\right]-\left[e^{-\tau}+\eta\int_0^\tau e^{-\hat{\tau}}\lambda(\hat{\tau})d\hat{\tau}\right]=-\Omega^2. \tag{34}$$

Before considering any numerical results, several deductions can be made regarding (34). It is instructive to first consider the case when $\eta=0$, that is, the original network undergoes scission but there is no subsequent cross linking. The governing Eq. (34) reduces to

$$\lambda(\tau)^3-1=e^{-\tau}\Omega^2. \tag{35}$$

At $\tau=0$, the axial stretch ratio is given by

$$\lambda(0)^3-1=-\Omega^2. \tag{36}$$

It is, therefore, assumed that

$$\Omega<1, \quad \text{or} \quad \omega^2<\frac{4\mu}{\rho R_0^2}, \tag{37}$$

a necessary and sufficient condition to ensure a physically meaningful solution ($\lambda(0)\in[0,1]$) for a neo-Hookean material. This observation was made previously by Horgan and Saccomandi [4] and Chadwick et al. [5]. Furthermore, there is a subsequent time τ_0^* given by

$$\tau_0^*=-2\ln\Omega, \tag{38}$$

when the length of the cylinder reduces to zero and the radius becomes infinite. It follows from (35) that $d\lambda/d\tau\rightarrow-\infty$ as $\tau\rightarrow\tau_0^*$. The radial increase becomes infinite according to (9), and time τ_0^* can be interpreted as a critical runaway time.

Next, let $0<\eta\leqslant1$, which allows for the formation of new networks. The right-hand equality represents the situation when the original network is completely transformed into new networks. It follows from (34) that

$$\lambda(\tau)^3=\frac{e^{-\tau}+\eta\int_0^{\tau}e^{-\hat{\tau}}\lambda(\hat{\tau})d\hat{\tau}-\Omega^2}{e^{-\tau}+\eta\int_0^{\tau}e^{-\hat{\tau}}\lambda(\hat{\tau})^{-2}d\hat{\tau}} \tag{39}$$

and

$$\frac{d\lambda(\tau)}{d\tau}=\frac{-e^{-\tau}[1-\lambda(\tau)^3]}{3\lambda(\tau)^2\left[e^{-\tau}+\eta\int_0^{\tau}\frac{e^{-\hat{\tau}}}{\lambda(\hat{\tau})^2}d\hat{\tau}\right]}. \tag{40}$$

At $\tau=0$, (39) reduces to (36). Equation (37) is still needed to ensure a physically meaningful solution. Since $\lambda(0)<1$ and (40) implies $d\lambda/d\tau<0$, $\lambda(\tau)<1$ and is monotonically decreasing. Next, consider the first two terms in the numerator of (39). Their time derivative is $[-1+\eta\lambda(\tau)]e^{-\tau}$. The inequality $0<\eta\leqslant1$, and the fact that $\lambda(\tau)<1$, indicates that $[-1+\eta\lambda(\tau)]e^{-\tau}\leqslant0$.

There are two cases to consider: Ω near unity and Ω near zero. First, if $\Omega\approx1$, the first two terms in the numerator will monotonically decrease and there may be a time, denoted τ_η^*, when the stretch ratio reaches zero. Consequently, τ_η^* satisfies

$$e^{-\tau_\eta^*}+\eta\int_0^{\tau_\eta^*}e^{-\hat{\tau}}\lambda(\hat{\tau})d\hat{\tau}-\Omega^2=0. \tag{41}$$

Combining (38) and (41), gives

$$e^{-\tau_\eta^*}=e^{-\tau_0^*}-\eta\int_0^{\tau_0^*}e^{-\hat{\tau}}\lambda(\hat{\tau})d\hat{\tau}. \tag{42}$$

The integral is positive, which implies

$$\tau_\eta^*>\tau_0^*. \tag{43}$$

Rewriting the denominator of (40) as

$$\lambda(\tau)^2e^{-\tau}+\eta\int_0^{\tau}e^{-\hat{\tau}}\frac{\lambda(\tau)^2}{\lambda(\hat{\tau})^2}d\hat{\tau}, \tag{44}$$

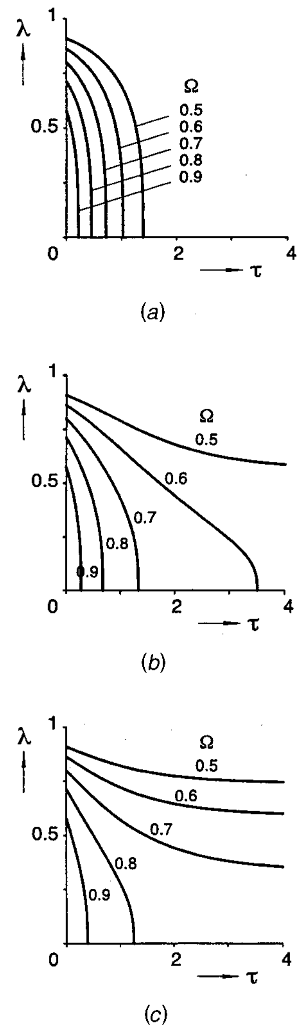

Fig. 3 Evolution of axial stretch for Neo-Hookean material: (*a*) no healing ($\eta=0$), (*b*) partial healing ($\eta=0.5$), (*c*) complete healing ($\eta=1$)

and taking the limit as $\tau\rightarrow\tau_\eta^*$, $\lambda(\tau)\rightarrow\lambda(\tau_\eta^*)=0$, the integral vanishes in the limit and the denominator approaches zero. It follows from (40) that $d\lambda/d\tau\rightarrow-\infty$ as $\tau\rightarrow\tau_\eta^*$. These results show that although new networks are formed, there may still be a critical runaway time τ_η^*. The consequence of the formation of new networks is to increase the critical runaway time τ_η^*. This implies that there is always a critical runaway time for any η for Ω approaching unity.

The other case is where the angular velocity is small ($\Omega\ll1$). In this case the numerator of (39) may not vanish, leaving $0<\lambda(\tau)<1$. Then, $d\lambda/d\tau\rightarrow0$ according to (40), and a finite steady-state value is possible, $\lambda(\tau)\rightarrow\lambda_\infty>0$.

Figure 3 shows the numerical results for the evolution of the axial stretch ratio $\lambda(\tau)$ for a neo-Hookean material undergoing scission healing. The case of no healing ($\eta=0$), or pure scission, is shown in Fig. 3(*a*) for different values of the nondimensional angular velocity Ω between 0.5 and 0.9. The axial stretch starts at an initial value less than one and then decreases monotonically to zero as expected, consistent with the above analysis. As Ω increases, τ_0^* decreases. The case of partial healing ($\eta=0.5$), where one half of network junctions that undergo scission reform, is shown in Fig. 3(*b*). For large values of Ω the axial stretch collapses to zero, but for small values (see $\Omega=0.5$) the axial stretch decreases but approaches a nonzero steady state value. The case of

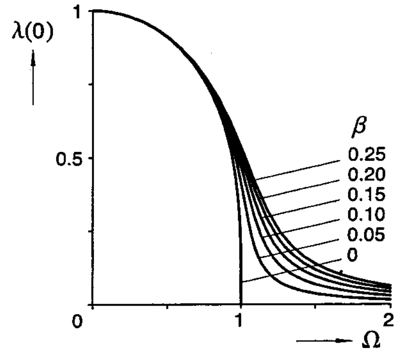

Fig. 4 Dependence of initial axial stretch for Mooney-Rivlin material with nondimensional angular velocity, Ω, for different ratios of MR constants, $\beta = W_2^0/W_1^0$

complete healing $(\eta = 1)$, where all network junctions that undergo scission reform, is shown in Fig. 3(c). The axial stretch collapses to zero for large Ω and approaches a steady state value for small Ω, but the limiting Ω between these two behaviors is larger (between 0.7 and 0.8) than for the partial healing case. For large angular velocity $(\Omega \approx 1)$, the critical collapse time (τ_η^*) gets smaller as Ω gets closer to unity.

It is interesting that a nonzero steady state value λ_∞ can be achieved even for moderate values of Ω. When $\lambda(\tau) \rightarrow \lambda_\infty$, (34) can be written as

$$\lambda_\infty^3 \int_0^\infty e^{-\hat{\tau}} \lambda(\hat{\tau})^{-2} d\hat{\tau} - \int_0^\infty e^{-\hat{\tau}} \lambda(\hat{\tau}) d\hat{\tau} = -\Omega^2/\eta, \qquad (45)$$

a cubic equation for λ_∞ akin to (36), once the integrals are known. Note that, since $0 < \lambda(\hat{\tau}) < 1$, the first integral is larger than the second one $(\int_0^\infty e^{-\hat{\tau}} \lambda(\hat{\tau})^{-2} d\hat{\tau} > \int_0^\infty e^{-\hat{\tau}} \lambda(\hat{\tau}) d\hat{\tau})$, which allows (45) to be satisfied for $0 < \lambda_\infty < 1$. This is a result of the assumption that no time lag exists between scission of original networks and formation of new networks and the assumption that new networks are not allowed to undergo scission again. These act to stabilize the material against structural collapse.

4.2 Mooney-Rivlin Response. Consider now the response when both the original network and the newly formed networks are Mooney-Rivlin materials. In this case, the initial shear modulus is defined by $2W_1^0 + 2W_2^0 = \mu$. W_1^0 and W_2^0 are independent of $\mathbf{B}$ and $\hat{W}_1$ and $\hat{W}_2$ are independent of $\hat{\mathbf{B}}$. The ratio of the two Mooney Rivlin constants is defined as $\beta = W_2^0/W_1^0$. Noting that $w_1^0 = 1/(1+\beta)$ and $w_2^0 = \beta/(1+\beta)$ allows (32) to be written as

$$e^{-\tau}[\lambda(\tau)^3 - 1]\left(1 + \frac{1}{\lambda(\tau)}\beta\right) + \eta\lambda(\tau) \times \int_0^\tau e^{-\hat{\tau}} \left[\left(\frac{\lambda(\tau)}{\lambda(\hat{\tau})}\right)^2 - \frac{\lambda(\hat{\tau})}{\lambda(\tau)}\right]\left(1 + \frac{\lambda(\hat{\tau})}{\lambda(\tau)}\beta\right) d\hat{\tau} = -\Omega^2(1+\beta). \qquad (46)$$

At $\tau = 0, \lambda(0)$ is the solution of

$$[1 - \lambda(0)^3]\left(1 + \frac{\beta}{\lambda(0)}\right) = \Omega^2(1+\beta). \qquad (47)$$

In contrast to (36), the left-hand side of (47) becomes unbounded as $\lambda(0) \rightarrow 0$ because of the nonzero constant W_2^0 in the Mooney-Rivlin response. Therefore, the solution $\lambda(0) = 0$ no longer exists. This can be seen in Fig. 4, which shows the initial axial stretch ratio for different angular velocities Ω and different values of β. Note that for $\beta = 0$, which is a neo-Hookean material, $\lambda(0) \rightarrow 0$ as $\Omega \rightarrow 1$. For nonzero β, however, $\lambda(0)$ never reaches zero for any Ω. Therefore, no restriction on Ω, such as (37), is needed to obtain physically meaningful results for a Mooney-Rivlin material.

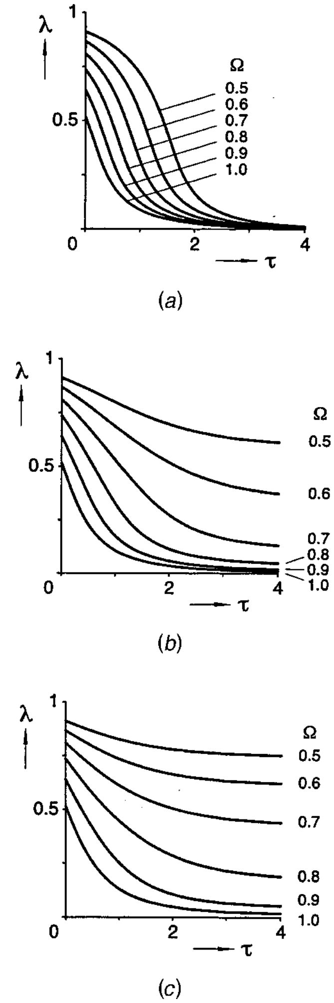

Fig. 5 Evolution of axial stretch for Mooney-Rivlin material with $\beta = 0.2$: (a) no healing $(\eta = 0)$, (b) partial healing $(\eta = 0.5)$, (c) complete healing $(\eta = 1)$

At each time, the left-hand side of (46) becomes unbounded as $\lambda(\tau) \rightarrow 0$ because of the terms containing β associated with Mooney-Rivlin response. A nonzero positive solution $\lambda(\tau)$ can be found without imposing restrictions of Ω^2. Accordingly, for Mooney-Rivlin response, there does not exist a finite time when the axial stretch vanishes and the radius becomes infinitely large.

Horgan and Saccomandi [4] considered the equivalent of (47) for the case of nonlinear elasticity when W_2^0 and W_1^0 depend on the first invariant of $\mathbf{B}$. They showed that for certain forms of W_1^0 (see Gent [10], determined from finite extensibility considerations, and Knowles [11], called the generalized neo-Hookean model) the axial stretch would always be nonzero. Thus, the nonphysical response found for neo-Hookean material does not occur for many other material models. This anomalous behavior seems to be a peculiarity of the neo-Hookean material model. It can be expected that there would not exist a finite time when the axial stretch vanishes if most any other model was used to represent the response of original and newly formed networks in a constitutive theory for scission healing.

Figure 5 shows the numerical results for the evolution of the axial stretch ratio $\lambda(\tau)$ for a Mooney-Rivlin material undergoing scission-healing. A typical value of $\beta = 0.2$ was used. The case of no healing $(\eta = 0)$, or pure scission, is shown in Fig. 5(a) for different values of the nondimensional angular velocity Ω be-

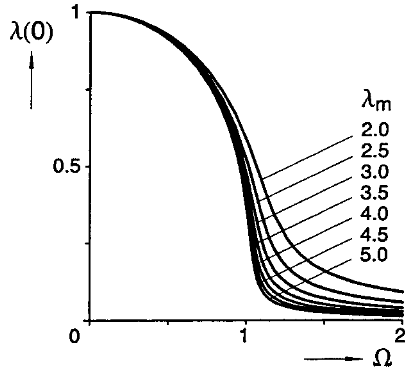

Fig. 6 Dependence of initial axial stretch for Arruda-Boyce material with nondimensional angular velocity, Ω, for different locking stretch ratios, λ_m

tween 0.5 and 1. The axial stretch starts at an initial value less than one and then decreases but only asymptotically approaches zero. The case of partial healing ($\eta=0.5$) is shown in Fig. 5(*b*). For large values of Ω the axial stretch approaches zero, but for small values the axial stretch approaches a nonzero steady-state value. The case of complete healing ($\eta=1$) is shown in Fig. 5(*c*). Again, the axial stretch approaches zero for large Ω and approaches a steady state nonzero value for small Ω, but the transition value of Ω is larger.

4.3 Arruda-Boyce Response. As a final case, the response when both the original network and the newly formed networks behave as Arruda-Boyce materials (see [12]) is considered. Assuming incompressibility, the strain energy density of a three-term Arruda-Boyce material is given by

$$W=\mu\left[\frac{1}{2}(I_1-3)+\frac{1}{20\lambda_m^2}(I_1^2-3^2)+\frac{11}{1050\lambda_m^4}(I_1^3-3^3)\right] \qquad (48)$$

where μ is the initial shear modulus and λ_m is the locking stretch ratio, a material parameter, both of which could be temperature-dependent. In this case, W_1^0 is not constant, but $W_2^0=0$. Substituting the material parameter

$$w_1^0=1+\frac{1}{5\lambda_m^2}I_1+\frac{11}{175\lambda_m^4}I_1^2 \qquad (49)$$

with $I_1=2/\lambda(\tau)+\lambda(\tau)^2$ and a similar expression for $\hat{w}_1$ with $\hat{I}_1=2\lambda(\hat{\tau})/\lambda(\tau)+[\lambda(\tau)/\lambda(\hat{\tau})]^2$ and then into (32), produces the governing equation.

The initial axial stretch solution $\lambda(0)$ is plotted in Fig. 6 as a function of angular velocities Ω for different values of λ_m. Similar to the Mooney-Rivlin case, $\lambda(0)$ is greater than zero for all values of Ω, although one can see that as the material parameter λ_m gets large $\lambda(0)$ approaches zero when $\Omega>1$.

Figure 7 shows the numerical results for the evolution of the axial stretch ratio $\lambda(\tau)$ for Arruda-Boyce material undergoing scission healing. A typical value of $\lambda_m=3$ was used. The case of no healing ($\eta=0$), or pure scission, is shown in Fig. 7(*a*) for different values of the nondimensional angular velocity Ω between 0.5 and 1. The axial stretch starts at an initial value less than one and then decreases, but only asymptotically approaches zero. Qualitatively, the response is similar to the Mooney-Rivlin case in Fig. 5(*a*). The cases of partial healing ($\eta=0.5$) and complete healing ($\eta=1$) are shown in Fig. 7(*b*) and Fig. 7(*c*). Again, the qualitative response is similar to that of the Mooney-Rivlin case, but the transition from a long time steady state behavior to a collapse behavior is more distinct in the Arruda-Boyce case. This case also confirms that the anomalous collapse behavior of the neo-Hookean case can be avoided by including a nonlinear polynomial dependence on I_1 in the energy density.

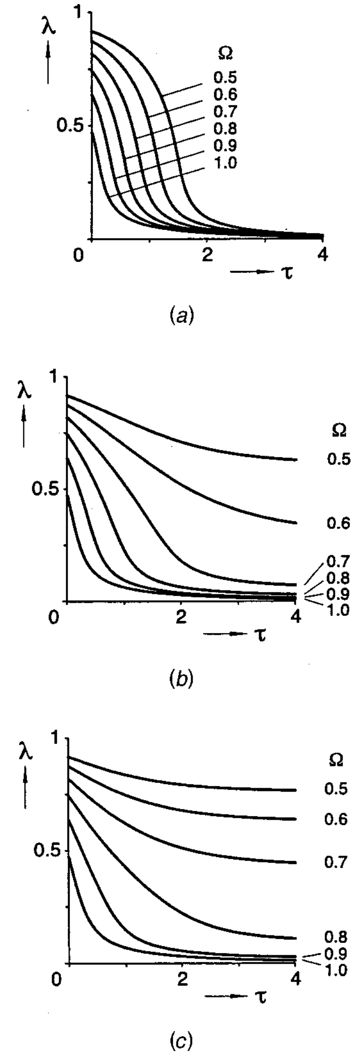

Fig. 7 Evolution of axial stretch for Arruda-Boyce material with $\lambda_m=3$: (*a*) no healing ($\eta=0$), (*b*) partial healing ($\eta=0.5$), (*c*) complete healing ($\eta=1$)

5 Summary and Conclusions

The boundary value problem of a spinning elastomeric cylinder undergoing temperature-induced scission and re-crosslinking was studied. The problem reduces to a nonlinear Volterra equation for the axial stretch ratio. The general constitutive framework allows the user to choose a specific underlying thermoelastic model for the original and healed microstructural material networks. Responses based on neo-Hookean, Mooney-Rivlin, and Arruda-Boyce models, were solved numerically and compared. Different amounts of re-crosslinking (healing) were studied for each case. Anomalous behavior was noted when using the neo-Hookean model, in that it was susceptible to premature and catastrophic collapse. In fact, no solution was possible for angular velocities above a critical value, even without the effects of scission. The Mooney-Rivlin and Arruda-Boyce cases, although quantitatively different, behaved qualitatively similar showing similar trends with angular velocity and healing rate. The study confirmed that the anomalous collapse behavior of the neo-Hookean case can be avoided by including a dependence on I_2 in the energy density, as in the Mooney-Rivlin case, or by including a nonlinear dependence on I_1, as in the Arruda-Boyce case.

Acknowledgments

The authors wish to express their gratitude to the National Science Foundation (NSF grant CTS-9908925) for their financial support. The help of Alan Jones in the preparation of the manuscript is also acknowledged with thanks.

References

[1] Tobolsky, A. V., 1960, *Properties and Structures of Polymers*, John Wiley and Sons, New York, Chap. 5, pp. 223–265.
[2] Wineman, A. S., and Rajagopal, K. R., 1990, ''On a Constitutive Theory for Materials Undergoing Microstructural Changes,'' Arch. Mech., **42**, pp. 53–74.
[3] Rajagopal, K. R., and Wineman, A. S., 1992, ''A Constitutive Equation for Non-linear Solids Which Undergo Deformation Induced Microstructural Changes,'' Int. J. Plast., **8**, pp. 385–395.
[4] Horgan, C. O., and Saccomandi, G., 2001, ''Large Deformations of a Rotating Solid Cylinder for Non-Gaussian Isotropic, Incompressible Hyperlastic Materials,'' ASME J. Appl. Mech., to appear.
[5] Chadwick, P., Creasy, C. F. M., and Hart, V. G., 1977, ''The Deformation of Rubber Cylinders and Tubes by Rotation,'' J. Austral. Math. Soc., **20** (Series 13), pp. 62–96.
[6] Tobolsky, A. V., Prettyman, I. B., and Dillon, J. H., 1944, ''Stress Relaxation of Natural and Synthetic Rubber Stocks,'' J. Appl. Phys., **15**, pp. 380–395.
[7] Neubert, D., and Saunders, D. W., 1944, ''Some Observations of the Permanent Set of Cross-Linked Natural Rubber Samples After Heating in a State of Pure Shear,'' Rheol. Acta, **1**, pp. 151–157.
[8] Fong, J. T., and Zapas, L. J., 1976, ''Chemorheology and the Mechanical Behavior of Vulcanized Rubber,'' Trans. Soc. Rheol., **20**, pp. 319–338.
[9] Rivlin, R. S., and Saunders, D. W., 1951, ''Large Elastic Deformations of Isotropic Materials. VII. Experiments on the Deformation of Rubber,'' Philos. Trans. R. Soc. London, Ser. A, **A243**, pp. 251–288.
[10] Gent, A. N., 1996, ''A New Constitutive Relation for rubber,'' Rubber Chem. Technol., **69**, pp. 59–61.
[11] Knowles, J. K., 1977, ''The Finite Anti-plane Shear Field Near the Tip of a Crack for a Class of Incompressible Elastic Solids,'' Int. J. Fract., **13**, pp. 611–639.
[12] Arruda, E. M., and Boyce, M. C., 1993, ''A Three Dimensional Constitutive Model for the Large Stretch Behavior of Rubber Elastic Materials,'' J. Mech. Phys. Solids, **41**, pp. 389–412.

Dynamic Condensation and Synthesis of Unsymmetric Structural Systems

G. Visweswara Rao
Engineering Mechanics Research India (P) Ltd.,
607/907 M. G. Road,
Bangalore 560001, India

In this paper model reduction of an unsymmetric and damped structural system is presented using a two-sided dynamic condensation technique. The method is an iterative one and essentially utilizes orthonormalized complex eigenvectors of the unsymmetric system. The eigensolution of the reduced order model with specified master degrees-of-freedom is obtained by Lanczos algorithm. The model reduction procedure is further utilized in substructure synthesis and eigenvalue analysis of large size unsymmetric systems. Application of the condensation technique is illustrated via two example problems of rotor bearing systems. [DOI: 10.1115/1.1432988]

1 Introduction

For eigensolution and response analysis of large structural systems, use of the complete analytical/discrete parameter model results in considerable computer run time and huge storage requirement as well. It is imperative that there is the need for reduced-order models to represent such large size systems especially from efficient use of available computer disk space. Dynamic condensation methods reported in literature ([1–3]) are essentially modified versions of the Guyan ([4]) reduction technique. Recent advancements in dynamic condensation approach are due to Suarez and Singh [5] and Qu and Fu [6]. The two approaches are iterative in nature. The initial approximation of the Guyan condensation matrix relating the chosen master degree-of-freedom and the slave degree-of-freedom is updated till desired convergence is achieved. While the iterative approach of Suarez and Singh is valid for standard eigenproblem, the method proposed by Qu and Fu is valid for general eigenproblem. All the above dynamic condensation methods are applicable only for handling undamped symmetric systems with symmetric mass and stiffness matrices. Kane and Torby [7] described a method to obtain a reduced-order model for unsymmetric systems such as rotating systems. However, the method suffers from the disadvantage of the necessity to have a prior eigensolution of the original system.

A computational procedure to effectively condense unsymmetric systems is presented in this paper. It is a two-sided procedure in that it implicitly utilizes both the left and right eigenvectors of the system. The procedure is iterative and avoids explicit derivation of the eigenvectors during the iteration process at each step. The method finally yields two condensation matrices that relate the master and slave degrees-of-freedom. Further, one important feature of the proposed method is that element matrices pertaining to any discrete springs/dampers present in the system initially remain out of the dynamic condensation technique and are attached to the reduced-order model matrices with due consideration to the boundary condition compatibility. This feature is further utilized in obtaining reduced-order models for complicated unsymmetric systems by substructure synthesis. Glasgow and Nelson [8] and Li and Gunter [9] have obtained reduced-order models for rotor-bearing systems using component mode synthesis. However, these methods invariably require an eigenvalue analysis of each component. Substructure synthesis as proposed in this paper condenses each substructure individually. Discrete/intermediate link elements, if any, that are present in the system are kept out of the condensation process initially. The use of the dynamic condensation technique and substructure synthesis procedure developed in this paper is illustrated via two example problems of rotor-bearing systems.

Contributed by the Applied Mechanics Division of THE AMERICAN SOCIETY OF MECHANICAL ENGINEERS for publication in the ASME JOURNAL OF APPLIED MECHANICS. Manuscript received by the ASME Applied Mechanics Division, October 7, 2000; final revision, August 10, 2001. Editor: N. C. Perkins. Discussion on the paper should be addressed to the Editor, Prof. Lewis T. Wheeler, Department of Mechanical Engineering, University of Houston, Houston, TX 77204-4792, and will be accepted until four months after final publication of the paper itself in the ASME JOURNAL OF APPLIED MECHANICS.

2 Unsymmetric Structural System and Discrete Parameter Model

A finite element model of a structural system with N degree-of-freedom is governed by the following equations of motion:

$$[M]\{\ddot{x}\}+[C]\{\dot{x}\}+[K]\{x\}=\{F(t)\} \tag{1}$$

where $\{F\}$ is the vector of external forces. $[M]$, $[C]$, and $[K]$ are the system mass, damping, and stiffness matrices of the order $N\times N$. These matrices may be symmetric, skew-symmetric, or unsymmetric. The standard/general eigenvalue problem ([5,6]) applies to undamped systems with symmetric matrices. On the other hand, unsymmetric systems are difficult to handle by the standard procedures. To obtain the eigensolution for such a unsymmetric system, one procedure is to recast Eq. (1) into first-order form in $2N\times 2N$ state space as

$$[\bar{M}]\{\dot{y}\}+[\bar{K}]\{y\}=\{0\} \tag{2}$$

where

$$[\bar{M}]=\begin{bmatrix}[0] & -[M]\\ [M] & [C]\end{bmatrix},$$

$$[\bar{K}]=\begin{bmatrix}[M] & [0]\\ [0] & [K]\end{bmatrix} \quad \text{and} \quad \{y\}=\{\dot{x},x\}^T.$$

The superscript T stands for transpose of a matrix.

The eigenvalue problem corresponding to Eq. (2) is now given by

$$[\bar{K}][\Phi^R]=[\bar{M}][\Phi^R][\lambda] \tag{3}$$

for right eigenvectors $[\Phi^R]$ and the adjoint eigenvalue problem by

$$[\Phi^L]^T[\bar{K}]=[\lambda][\Phi^L]^T[\bar{M}] \tag{4}$$

for left eigenvectors $[\Phi^L]$. $[\lambda]$ is the diagonal matrix of complex eigenvalues of the unsymmetric system.

An eigenvalue solver using, for example, a two-sided Lanczos algorithm ([10]) yields complex eigenvalues λ and the left and right complex eigenvectors $[\Phi^L]$ and $[\Phi^R]$. These eigenvectors satisfy the following bi-orthogonality relationships:

$$[\Phi^L]^T[\bar{M}][\Phi^R]=[I] \quad \text{and} \quad [\Phi^L]^T[\bar{K}][\Phi^R]=[\lambda]. \tag{5}$$

3 Dynamic Condensation

To start with the dynamic condensation, let the nodal displacement degree-of-freedom vector $\{x\}$ be partitioned into two groups. One is the master degree-of-freedom that are to be retained and the other, the slave degree-of-freedom to be eliminated during the condensation process. Let the number of master degree-of-freedom be "m." The number of the slave degree-of-freedom is hence N-m. Let the matrices $[M]$, $[C]$, and $[K]$ be partitioned according to these master and slave degrees-of-freedom. The vector $\{y\}$ is now ordered in the form $\{\dot{x}_m, x_m, \dot{x}_s, x_s\}$ with subscripts m and s indicating master and slave degrees-of-freedom, respectively. If the augmented matrices $[\bar{M}]$ and $[\bar{K}]$ are accordingly partitioned, keeping the master velocity and displacement degrees-of-freedom together, the eigenvalue problem in Eqs. (3) and (4) takes the form

$$\begin{bmatrix} \lfloor\bar{K}_{mm}\rfloor, & \lfloor\bar{K}_{ms}\rfloor \\ [\bar{K}_{sm}], & [\bar{K}_{ss}] \end{bmatrix} \begin{Bmatrix} [\Phi_m^R] \\ [\Phi_S^R] \end{Bmatrix} = \begin{bmatrix} \lfloor\bar{M}_{mm}\rfloor, & \lfloor\bar{M}_{ms}\rfloor \\ [\bar{M}_{sm}], & [\bar{M}_{ss}] \end{bmatrix} \begin{Bmatrix} [\Phi_m^R] \\ [\Phi_s^R] \end{Bmatrix} [\lambda] \tag{6}$$

$$\begin{bmatrix} [\bar{K}_{mm}], & [\bar{K}_{ms}] \\ [\bar{K}_{sm}], & [\bar{K}_{ss}] \end{bmatrix}^T \begin{Bmatrix} [\Phi_m^L] \\ [\Phi_s^L] \end{Bmatrix} = \begin{bmatrix} [\bar{M}_{mm}], & [\bar{M}_{ms}] \\ [\bar{M}_{sm}], & [\bar{M}_{ss}] \end{bmatrix}^T \begin{Bmatrix} [\Phi_m^L] \\ [\Phi_s^L] \end{Bmatrix} [\lambda]^T \tag{7}$$

where

$$[\bar{K}_{mm}] = \begin{bmatrix} \lfloor M_{mm}\rfloor, & [0] \\ [0], & [K_{mm}] \end{bmatrix}, \quad [\bar{K}_{ms}] = \begin{bmatrix} \lfloor M_{ms}\rfloor, & [0] \\ [0], & [K_{ms}] \end{bmatrix},$$

$$[\bar{K}_{sm}] = \begin{bmatrix} [M_{sm}], & [0] \\ [0], & [K_{sm}] \end{bmatrix} \text{ and } [\bar{K}_{ss}] = \begin{bmatrix} [M_{ss}], & [0] \\ [0], & [K_{ss}] \end{bmatrix} \tag{8}$$

$$[\bar{M}_{mm}] = \begin{bmatrix} [0], & \lfloor M_{mm}\rfloor \\ -[M_{mm}], & -[C_{mm}] \end{bmatrix},$$

$$[\bar{M}_{ms}] = \begin{bmatrix} [0], & \lfloor M_{ms}\rfloor \\ -[M_{ms}], & -[C_{ms}] \end{bmatrix},$$

$$[\bar{M}_{sm}] = \begin{bmatrix} [0], & [M_{sm}] \\ -[M_{sm}], & -[C_{sm}] \end{bmatrix} \text{ and}$$

$$[\bar{M}_{ss}] = \begin{bmatrix} [0], & [M_{ss}] \\ -[M_{ss}], & -[C_{ss}] \end{bmatrix}. \tag{9}$$

Expanding the lower part of the equations in Eq. (6) one obtains

$$[\bar{K}_{sm}][\Phi_m^R]+[\bar{K}_{ss}][\Phi_s{}^R]=[\bar{M}_{sm}][\Phi_m^R][\lambda]+[\bar{M}_{ss}][\Phi_s{}^R][\lambda]. \tag{10}$$

Similar expansion from Eq. (7) results in

$$[\bar{K}_{ms}]^T[\Phi_m{}^L]+[\bar{K}_{SS}]^T[\Phi_s{}^L]=[\bar{M}_{ms}]^T[\Phi_m{}^L][\lambda]^T + [\bar{M}_{ss}]^T[\Phi_s{}^L][\lambda]^T. \tag{11}$$

Let the slave part of the right and left eigenvectors $[\Phi_s{}^R]$ and $[\Phi_s{}^L]$ be expressed in terms of the corresponding master degree-of-freedom part of the right and left eigenvectors $[\Phi_m^R]$ and $[\Phi_m^L]$ as

$$[\Phi_s^R]=[R][\Phi_m^R] \quad \text{and} \quad [\Phi_s^L]=[S][\Phi_m^L]. \tag{12}$$

Using the transformation matrices $[R]$ and $[S]$ in Eqs. (10) and (11), one obtains the following equations for $[R]$ and $[S]$:

$$[R]=[\bar{K}_{ss}]^{-1}[([\bar{M}_{sm}]+[\bar{M}_{ss}][R])[\Phi_m^R][\lambda][\Phi_m^R]^{-1}-[\bar{K}_{sm}]] \tag{13}$$

$$[S]=[\bar{K}_{ss}^T]^{-1}[([\bar{M}_{ms}]^T+[\bar{M}_{ss}]^T[S])[\Phi_m^L][\lambda]^T[\Phi_m^L]^{-1}-[\bar{K}_{ms}^T]]. \tag{14}$$

Equations (13) and (14) contain the unknown matrices $[R]$ and $[S]$ implicitly. Once $[R]$ and $[S]$ are obtained, the bi-orthogonality relationships in Eq. (5) yield the reduced-order model for the given system in the following form of eigenvalue problem:

$$[K_R][\Phi_{mR}]=[M_R][\Phi_m^R][\lambda]$$

and

$$[\Phi_m^L]^T[K_R]=[\lambda][\Phi_m^L]^T[M_R]. \tag{15}$$

The reduced order $(2m\times 2m)$ stiffness and mass matrices $[K_R]$ and $[M_R]$ are given by

$$[K_R]=[\bar{K}_{mm}]+[\bar{K}_{ms}][R]+[S]^T[\bar{K}_{sm}]+[S]^T[\bar{K}_{ss}][R] \tag{16}$$

$$[M_R]=[\bar{M}_{mm}]+[\bar{M}_{ms}][R]+[S]^T[\bar{M}_{sm}]+[S]^T[\bar{M}_{ss}][R]. \tag{17}$$

The matrices $[K_R]$ and $[M_R]$ satisfy the orthogonality relationships given by

$$[\Phi_m^L]^T[M_R][\Phi_m^R]=[I] \quad \text{and} \quad [\Phi_m^L]^T[K_R][\Phi_m^R]=[\lambda]. \tag{18}$$

One can adopt an iterative procedure to first solve for $[R]$ and $[S]$ from Eqs. (13) and (14). The iterative procedure is started with initial approximation:

$$[R]=-[\bar{K}_{ss}]^{-1}[\bar{K}_{sm}] \text{ and } [S]=-[\bar{K}_{ss}^T]^{-1}[\bar{K}_{ms}]^T. \tag{19}$$

According to Eqs. (13) and (14) it is required that an eigenvalue solution is to be obtained at each iteration step. However, from the two orthogonality relationships in Eq. (18) the eigensolution can be avoided at each step if the following substitutions are effected in Eqs. (13) and (14):

$$[\Phi_m^R][\lambda][\Phi_m^R]^{-1}=[M_R]^{-1}[K_R] \quad \text{and} \quad [\Phi_m^L][\lambda]^T[\Phi_m^L]^{-1} = [M_R]^{-T}[K_R]^T. \tag{20}$$

With the above substitutions, the transformation matrices $[R]$ and $[S]$ and subsequently $[K_R]$ and $[M_R]$ are improved over a number of steps, which can be termed as one stage. At the end of a stage, the eigensolution with the use of the reduced-order model matrices $[K_R]$ and $[M_R]$, can be obtained from Eq. (15). The solution is compared with that obtained at a previous stage for testing the convergence. The criterion to terminate the iterative process is chosen to be

$$\frac{|\lambda_{i+1}-\lambda_i|}{\lambda_{i+1}}\leqslant \varepsilon \tag{21}$$

where ε is the convergence tolerance required and λ_{i+1} and λ_i are the eigenvalues obtained at ith and $i+1$th iteration.

4 Substructure Synthesis

The two-sided dynamic condensation technique as described above condenses the internal slave degree-of-freedom and in general can be considered as a part of substructuring approach. If the master degree-of-freedom are specified for each of the substructures that constitute a structural system (Fig. 1), the mass and stiffness matrices in Eqs. (16) and (17) define a corresponding reduced-order model.

The reduced-order matrices $[M_R]$ and $[K_R]$ of each substructure in Eqs. (16) and (17) are of order $2m\times 2m$. The corresponding master degree-of-freedom vector of order $2m$ includes the velocity degree-of-freedom also. Thus $[M_R]$ and $[K_R]$ are of the form

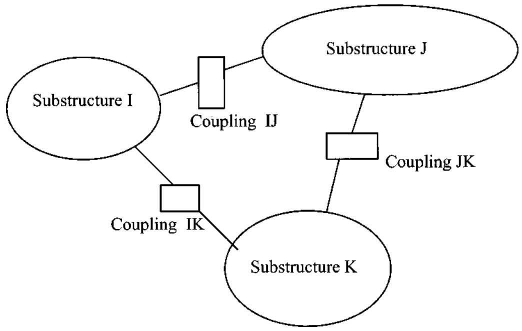

Fig. 1 Substructures and coupling elements

$$[M_R]=\begin{bmatrix}[0], & [M_{mmR}]\\ -[M_{mmR}], & -[C_{mmR}]\end{bmatrix} \text{ and }$$

$$[K_R]=\begin{bmatrix}[M_{mmR}], & [0]\\ [0], & [K_{mmR}]\end{bmatrix}. \tag{22}$$

In Eq. (22), $[M_{mmR}]$, $[C_{mmR}]$ and $[K_{mmR}]$ are the reduced-order mass, damping, and stiffness matrices of order $m\times m$. The matrices defining coupling elements, if any, (Fig. 1) can be assembled at this stage. For example, if the structural system consists of two substructures I and K and $[K_{IK}]$ represent the stiffness matrix relating the internal forces between the connecting degree-of-freedom of these substructures, the coupled equations of motion can be expressed as

$$\begin{bmatrix}[M^I_{mmR}], & [0]\\ [0], & [M^K_{mmR}]\end{bmatrix}\begin{Bmatrix}\{\ddot{x}^I_m\}\\ \{\ddot{x}^K_m\}\end{Bmatrix}+\begin{bmatrix}[C^I_{mmR}], & [0]\\ [0], & [C^K_{mmR}]\end{bmatrix}\begin{Bmatrix}\{\dot{x}^I_m\}\\ \{\dot{x}^K_m\}\end{Bmatrix}$$
$$+\left\{\begin{bmatrix}[K^I_{mmR}], & [0]\\ [0], & [K^K_{mmR}]\end{bmatrix}\begin{Bmatrix}\{x^I_m\}\\ \{x^K_m\}\end{Bmatrix}+[K_{IK}]\begin{Bmatrix}\{x^I{}_c\}\\ \{x^K_c\}\end{Bmatrix}\right\}=\{0\}. \tag{23}$$

In Eq. (23) the superscripts I and K stand for the Ith and Kth substructure, respectively. $\{x^I_m\}$ and $\{x^K{}_m\}$ represent the master degree-of-freedom vector of the two substructures. $\{x^I{}_c\}$ is the vector of common degree-of-freedom between the Ith substructure and the coupling element IK and is a subset of $\{x^I{}_m\}$ vector. In a similar fashion, $\{x^K{}_c\}$ is the vector of common degree-of-freedom between the Kth substructure and the coupling element IK and is a subset of $\{x^K{}_m\}$ vector. Equation (23) describes the usual displacement method of assembly for structural analysis. The assembly continues to cover all other link elements present in the system. The procedure is applicable in case these elements also possess mass and damping effects. The final assembled mass, damping, and stiffness matrices of the structural system is of the order given by the sum of the master degree-of-freedom of each substructure. These matrices are unsymmetric and are recast into the first-order form as in Eq. (2) to obtain the final eigensolution.

5 Some Implementation Issues

It is apt here to elaborate some of the implementation issues involved and adopted in the condensation technique. Especially when applied to large-order systems, it is important to avoid the direct matrix inversions in Eqs. (13) and (14). Moreover, the size of the matrices $\lfloor\overline{K}_{ss}\rfloor$ and $[\overline{K}_{ss}]^T$ is governed by the number of slave degree-of-freedom in the system/substructure and is large enough to require special storage techniques. In the present condensation algorithm these sparse, banded, and unsymmetric matrices are stored in blocks and the Crout decomposition method ([11–12]) is used to obtain the lower and upper triangular matrices. This blockwise storage and decomposition is accomplished

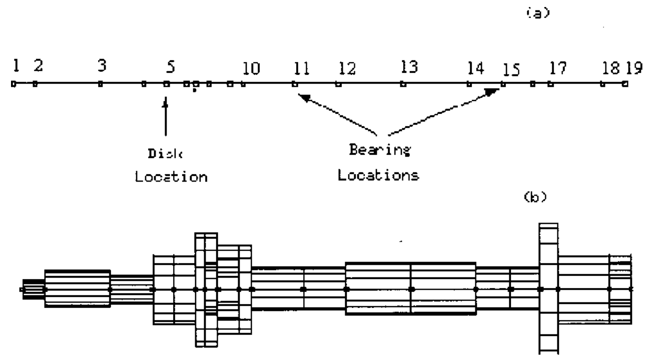

Fig. 2 Rotor bearing system and finite element model for Example Problem 1

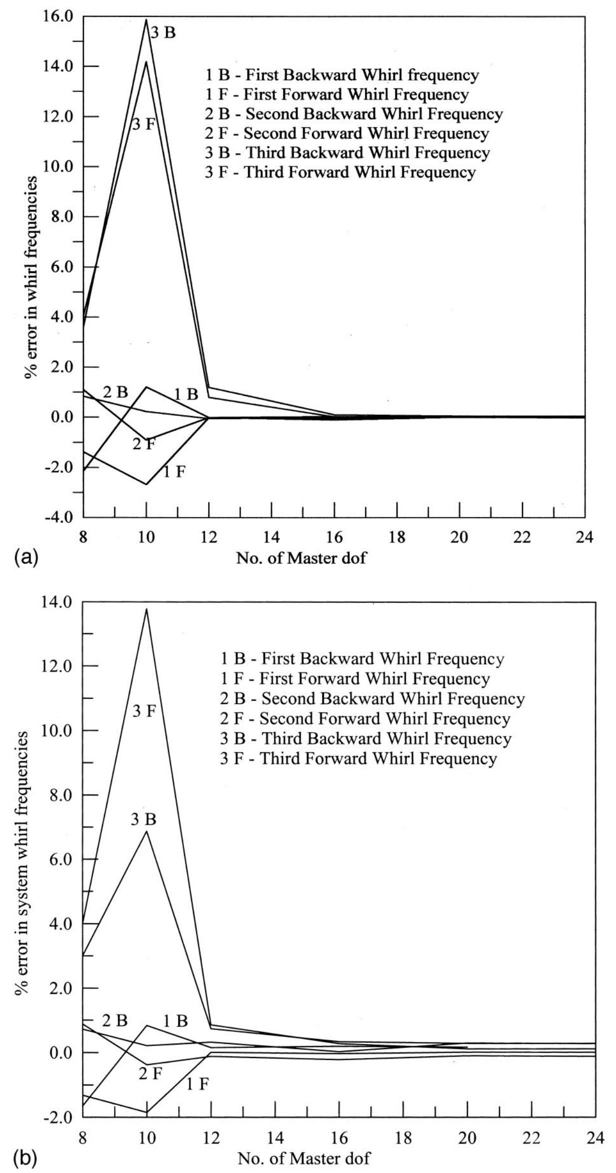

Fig. 3 (*a*) Example Problem 1. Percentage error between full and reduced-order model whirl frequencies. Case 1. System with isotropic bearings. (*b*) Example Problem 1. Percentage error between full and reduced-order model whirl frequencies. Case 2. System with orthotropic bearings.

Table 1 Configuration of the shaft in Example Problem 1

Node No.	Axial Distance From Shaft Left in m	Internal Diameter in m	Outer Diameter in m	Node No.	Axial Distance From Shaft Left in m	Internal Diameter in m	Outer Diameter in m
1	0.0	-	0.0051	11	0.1651	-	0.0127
2	0.0127	-	0.0102	12	0.1905	-	0.0152
3	0.0508	-	0.0076	13	0.2286	-	0.0152
4	0.0762	-	0.0203	14	0.2667	-	0.0127
5	0.0889	-	0.0203	15	0.2870	-	0.0127
6	0.1016	-	0.0330	16	0.3048	-	0.0381
7	0.1067	0.0152	0.0330	17	0.3150	-	0.0203
8	0.1143	0.0178	0.0254	18	0.3454	0.0152	0.0203
9	0.1270	-	0.0254	19	0.3581	0.0152	0.0203
10	0.1346	-	0.0127				

using out-of-core memory. It is required to factorize the matrices $[\bar{K}_{ss}]$ and $[\bar{K}_{ss}]^T$ only once and the factored matrices are used in solving Eqs. (13) and (14). A same block factorization procedure is uniformly adopted during the tridiagonalization involved in obtaining the eigensolution by Lanczos method ([10]).

6 Numerical Examples

Numerical results are obtained for two examples of rotor-bearing systems using the dynamic condensation procedure described above. Rotor-bearing systems are characterized by presence of gyroscopic terms that arise due to rotation and circulatory terms due to either orthotropic bearings or shaft damping ([13–15]).

The gyroscopic terms are skew-symmetric and the circulatory terms are unsymmetric. The size of the eigenvalue problem is large, as it is in general recast into first-order form of state-space variables (Eq. (2)). It is appropriate for one to resort to a dynamic condensation before a response analysis is performed on such complicated rotor-bearing systems.

The rotating shaft in the two example problems is mounted on hydrodynamic journal bearings. It is well known ([15]) that journal bearings are characterized by a 2×2 dynamic stiffness and 2×2 damping coefficients matrices. The bearing coefficients act in the two transverse degree-of-freedom of the rotating shaft according to the following equation:

$$\begin{bmatrix} C_{yy} & C_{yz} \\ C_{zy} & C_{zz} \end{bmatrix}\begin{Bmatrix} \dot{q}_y \\ \dot{q}_z \end{Bmatrix}+\begin{bmatrix} K_{yy} & K_{yz} \\ K_{zy} & K_{zz} \end{bmatrix}\begin{Bmatrix} q_y \\ q_z \end{Bmatrix}=\{F\}. \tag{24}$$

q_y and q_z are the transverse degree-of-freedom at the interface node on the shaft at which the bearing is located and are included in the master degrees-of-freedom vector. Thus a bearing element between two nodes is here represented by a 4×4 matrix given by

$$[K^b]=\begin{bmatrix} [K'] & -[K'] \\ -[K'] & [K'] \end{bmatrix} \quad \text{and}$$

$$[C^b]=\begin{bmatrix} [C'] & -[C'] \\ -[C'] & [C'] \end{bmatrix} \quad \text{where}$$

$$[K']=\begin{bmatrix} K_{yy} & K_{yz} \\ K_{zy} & K_{zz} \end{bmatrix} \quad \text{and} \quad [C']=\begin{bmatrix} C_{yy} & C_{yz} \\ C_{zy} & C_{zz} \end{bmatrix}. \tag{25}$$

Here, dynamic condensation can be conveniently performed on the system without regard to these link elements such as bearings

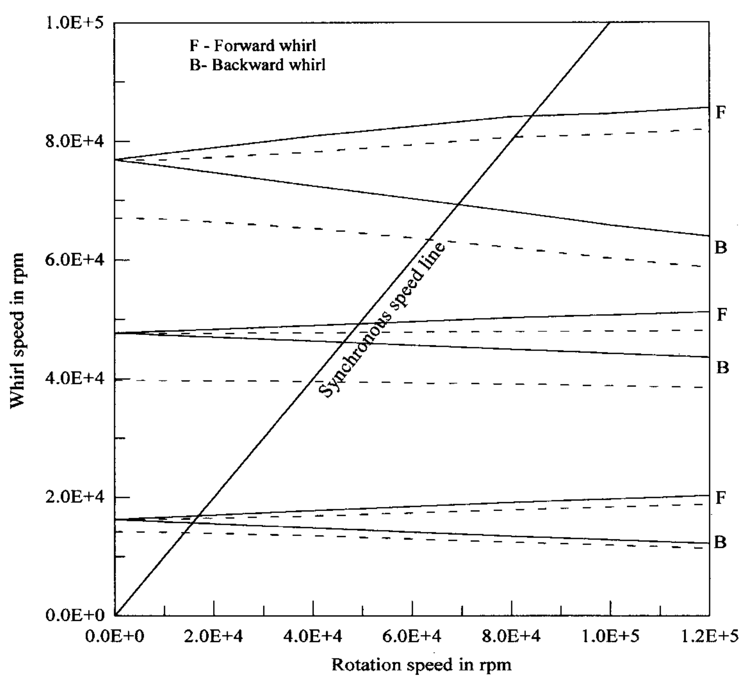

Fig. 4 Example Problem 1. Campbell diagram for rotor-bearing system after dynamic condensation with 12 master degrees-of-freedom. ——isotropic bearings, – – –orthotropic bearings.

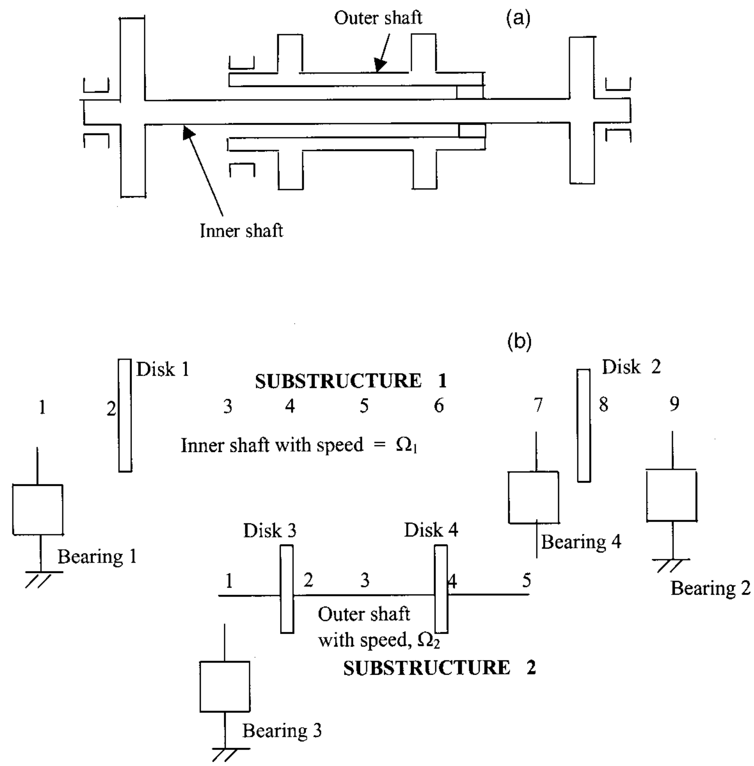

Fig. 5 Example Problem 2. (*a*) Dual rotor-bearing system. (*b*) Two substructures. Finite element model for the inner and outer shafts of dual rotor, disk, and bearings.

and any other coupling elements. One can integrate these elements with the final reduced-order model at the end of the iterative process with due consideration to the element connectivity.

Example 1. The first example refers to a rotor bearing system ([16]) with a nonuniform flexible shaft mounted on journal bearings (Fig. 2). The details of the shaft configuration are given in Table 1. Other shaft properties are: Young's modulus $= 2.078e+11\ \mathrm{N/m^2}$, and mass density $= 7806\ \mathrm{kg/m^3}$. The full model has 19 nodes and 18 beam elements with 76 degree-of-freedom. Thus each node is represented by two translatory and two rotational degree-of-freedom. The shaft carries a disk of mass $= 1.4$ Kg at node 5 and with polar moment of inertia $= 0.00203\ \mathrm{Kg\text{-}m^2}$ and diametrical moment of inertia $= 0.00136\ \mathrm{Kg\text{-}m^2}$. The bearing properties are:

Case 1 Isotropic—$K_{yy}=K_{zz}=4.378\mathrm{E}07$ N/m, $K_{yz}=K_{zy}=0.0$

Case 2 Orthotropic—$K_{yy}=K_{zz}=3.503\mathrm{E}07$ N/m, $K_{yz}=K_{zy}=-8.756\mathrm{E}06$ N/m.

The convergence of the reduced-order model is studied first with respect to a different number of master degree-of-freedom. The number of iterations over which the condensation matrices M_R and K_R are updated is kept at 10. At the end of each such stage the eigensolution is obtained and checked for convergence. The number of stages is taken to be 10 that is found to be enough for achieving a converged solution. Figure 3 shows the percentage error in the system eigenvalues versus the number of master degree-of-freedom. The error is with respect to the eigenvalues of the full model. The eigenvalues stand for the natural frequencies/whirl speeds of the rotor bearing system. The rotation speed is

Table 2 Critical speeds in rpm for rotor bearing system in Example Problem 1

			Reduced-Order Model With 12 Degrees-of-Freedom			
	Full Model		Isotropic Bearings			
	Backward Whirl	Forward Whirl	Backward Whirl		Forward Whirl	
Mode			Value	% Error	Value	% Error
1	15704	16883	15696	−0.051	16890	0.042
2	46152	49250	46118	−0.074	49288	0.077
2	68827	83580	69354	0.766	84210	0.754
	Full Model		Orthotropic Bearings			
	Backward Whirl	Forward Whirl	Backward Whirl		Forward Whirl	
Mode			Value	%Error	Value	% Error
1	14004	16396	14008	0.029	16418	0.013
2	39429	47802	39540	0.028	47754	−0.100
3	63106	80028	63424	0.504	80676	0.810

Table 3 Dynamic stiffness coefficients of bearings in Example Problem 2

Substructure No.	Node No.	K_{YY} N/m	K_{YZ} N/m	K_{ZY} N/m	K_{ZZ} N/m
1	1	2.62795e+07	0.0	0.0	2.62795e+07
1	9	1.7519e+07	0.0	0.0	1.7519e+07
1	7	8.7598e+06	0.0	0.0	8.7598e+06
2	1	1.7519e+07	0.0	0.0	1.7519e+07
2	5	8.7598e+06	0.0	0.0	8.7598e+06

Table 4 Properties of the disk elements in Example Problem 2

Substructure No.	Node No.	Mass in Kg	I_p in Kg-m^2	I_d in Kg-m^2
1	2	4.904	0.02712	0.01356
1	8	4.203	0.02034	0.01017
2	2	3.327	0.01469	0.00734
2	4	2.277	0.00972	0.00486

fixed at 10,000 rpm during the computations. Figure 3(*a*) corresponds to Case 1 of isotropic bearings and Fig. 3(*b*) to Case 2 of orthotropic bearings. Compared to the eigenvalues of full model, it can be observed that with the condensation technique described in this paper, a reduced-order model with 12 master degrees-of-freedom is sufficient enough to keep the percentage error of the first six predominant eigenvalues within 0.5 percent. These 12 degrees-of-freedom include the translational degrees-of-freedom corresponding to the disk node 5, the bearing nodes 11 and 15, and nodes 10, 13, and 17 (Fig. 2).

Figure 4 shows the Campbell diagram for the rotor bearing system. The Campbell diagram is a graph showing variation of shaft whirl speeds with respect to the rotation speed. The diagram helps in identifying the shaft critical speeds. For example, as shown in the Fig. 4, the critical speeds for synchronous vibration are obtained by the intersection of a unity slope line with the whirl speed curves. It is obvious that these speeds of rotation cause critical state of resonance due to inherent shaft/disk imbalance that generally exist in rotor bearing systems. Figure 4 includes whirl speed curves corresponding to both isotropic and orthotropic bearings. The nature of the whirl—forward or backward—is marked in the figure as per the displacements at node 5. The critical speeds for the rotor bearing system are given in Table 2. As can be observed form the values listed in the table, the percentage error between the reduced-order model and the full model is less than one percent. This is true for isotropic as well as the orthotropic bearings.

Example 2. This example refers to a dual rotor-bearing system ([8,17]) with two shafts of different rotating speeds. The system is shown in Fig. 5(*a*). The material properties for the two shafts are: Young's modulus $=2.069\text{e}+11$ N/m^2, and mass density $=8304$ kg/m^3. As shown in Fig. 5, the shafts are supported on journal bearings out of which one is an intershaft bearing. The bearings are isotropic and undamped. The dynamic stiffness coefficients for these bearing elements are given in Table 3.

The full finite element model has 15 nodes, 12 beam elements, and 60 degrees-of-freedom with two translational and two rotational degrees-of-freedom per node. The speed ratio is taken as 1.5 with inner shaft rotating at a lower speed. The two shafts are taken as two substructures for dynamic condensation as shown in Fig. 5(*b*). For the inner shaft, the number of master degrees-of-freedom is chosen to be 10 that include translational degrees-of-freedom corresponding to the two disk locations at nodes 2 and 8 and three bearing locations at nodes 1, 7, and 9 (Fig. 5(*b*)). The disk elements on the two substructures have the properties specified in Table 4.

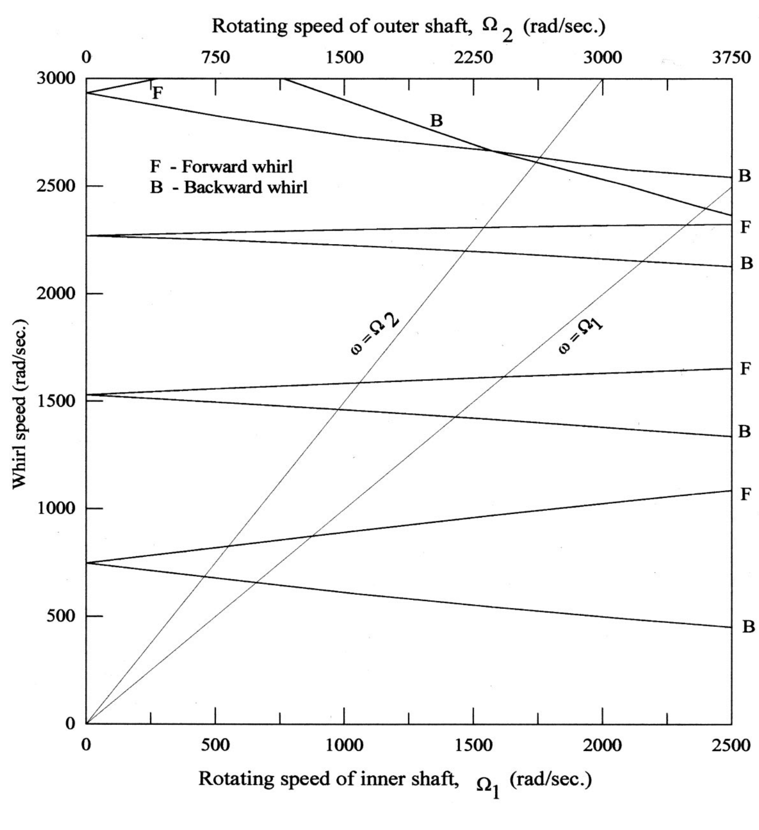

Fig. 6 Example Problem 2. Campbell diagram for dual rotor-bearing system after dynamic condensation (with undamped isotropic bearings).

Table 5 Critical speeds in rad/sec. for dual rotor-bearing system in Example Problem 2

	Inner Shaft, Ω_1					
	Full Model		Reduced-Order Model			
			Backward Whirl		Forward Whirl	
Mode	Backward whirl	Forward Whirl	Value	% Error	Value	% Error
1	660	863	657	−0.46	873	1.26
2	1425	1607	1428	0.21	1615	0.50
3	2125	2283	2153	1.32	2322	1.71
	Outer Shaft, $\Omega_2 = 1.5^*\Omega_1$					
			Backward Whirl		Forward Whirl	
Mode	Backward whirl	Forward Whirl	Value	% Error	Value	% Error
1	687	822	684	−0.44	827	0.61
2	1475	1590	1463	−0.81	1588	−0.13
3	2190	2290	2200	0.46	2309	0.83

The master degrees-of-freedom for the outer shaft is chosen to be 8 that includes translational degrees-of-freedom corresponding to the two disk locations at nodes 2 and 4 and two bearing locations at nodes 1 and 5 (Fig. 5(*b*)). Thus each node is represented by two translatory and two rotational degrees-of-freedom as in Example 1. Reduced-order models are obtained for the two shafts independently. With the chosen master degrees-of-freedom for the two substructures, the convergence of the individual reduced-order models is found to be satisfactory as in the case of Example Problem 1.

The final reduced-order model for the complete system is synthesized from the individual reduced-order models of the two substructures according to their connectivity at the interfaces. The element matrices of the link elements such as the bearings in the present example problem are integrated with the final reduced-order model as described in Section 4. Figure 6 shows the Campbell diagram obtained with the use of the final reduced-order model. The two shafts have different critical speeds as can be observed from the figure. The critical speeds as picked up from the Campbell diagram are listed in Table 5 and compare well with those obtained from the uncondensed model. The percentage error in the results is less than 1.7 percent, with number of stages in the iterative process being 10. The results are also in excellent agreement with those reported in Glasgow and Nelson [8] and Rao [17].

7 Conclusions

A new dynamic condensation procedure is presented in this paper to handle unsymmetric structural systems and to obtain reduced-order models. The efficiency of the procedure is shown with respect to the accuracy of the eigensolution. The two example problems considered in the paper have amply demonstrated the capability of the procedure in achieving the eigensolution within a percentage error of less than two percent.

The condensation technique is developed within the framework of finite element formulation and is iterative. The method implicitly uses the left as well as the right eigenvectors of the unsymmetric system in the iteration process and hence is termed as two-sided as compared to the techniques available in literature for symmetric systems. The method is developed is such a way to avoid the computation of the eigenvectors at each iteration of the iterative procedure.

As is the case with any condensation scheme, it is often the memory storage requirement that dominates the other requirements, especially when the total degrees-of-freedom in the structural system is too large for modern digital computer to handle economically. In this respect, the proposed dynamic condensation technique finds wider application in handling large-order unsymmetric systems via substructure synthesis.

Implementation issues such as the necessity to adopt blockwise storage and decomposition of the sparse, banded, and unsymmetric matrices using out-of-core memory are also highlighted in the paper. Further, while the effect of the number of master degrees-of-freedom on the convergence rate of the condensation procedure is illustrated, no special techniques are suggested in the selection of the particular master degrees-of-freedom. The issue needs further study that is beyond the scope of the present paper.

Acknowledgments

The author thanks Engineering Mechanics Research (India) Limited, Bangalore, India for the support and encouragement provided for the work.

References

[1] Kidder, R. L., 1973, "Reduction of Structural Frequency Equations," AIAA J., **11**, p. 892.
[2] Paz, M., 1982, "Practical Reduction of Structural Eigenproblems," J. Struct. Eng., **109**, pp. 2591–2599.
[3] Friswell, M. I., Garvey, S. D., and Penny, J. E. T., 1995, "Model Reduction Using Dynamic and Iterated IRS Techniques," J. Sound Vib., **186**, pp. 311–323.
[4] Guyan, R. J., 1965, "Reduction of Stiffness and Mass matrices," AIAA J., **3**, p. 380.
[5] Suarez, L. E., and Singh, M. P., 1992, "Dynamic Condensation Method for Structural Eigenvalue Analysis," AIAA J., **30**, pp. 1046–1054.
[6] Qu, Z. Q., and Fu, Z. F., 1998, "New Structural Dynamic Condensation Method for Finite Element Models," AIAA J., **36**, pp. 1320–1324.
[7] Kane, K., and Torby, B. J., 1991, "The Extended Modal Reduction Method Applied to Rotor Dynamic Problems," ASME J. Vibr. Acoust., **113**, pp. 79–84.
[8] Glasgow, D. A., and Nelson, H. D., 1980, "Stability Analysis of Rotor-Bearing Systems Using Component Mode Synthesis," ASME J. Mech. Des., **102**, pp. 352–359.
[9] Li, D. F., and Gunter, E. J., 1982, "Component Mode Synthesis of Large Rotor Systems," ASME J. Eng. Power, **104**, pp. 552–560.
[10] Rajakumar, C., and Rogers, C. R., 1991, "The Lanczos Algorithm Applied to Unsymmetric Generalized Eigenvalue Problems," Int. J. Numer. Methods Eng., **32**, pp. 1009–1026.
[11] Manoj, K. G., and Bhattacharya, S. K., 1997, "A Block Solver for Large, Unsymmetric, Sparse, Banded Matrices with Symmetric Profiles," Int. J. Numer. Methods Eng., **40**, pp. 3279–3295.
[12] Chapra, S. c., and Canale, R. P., 1989, *Numerical Methods for Engineers*, McGraw-Hill, London.
[13] Dimentberg, F. M., 1961, *Flexural Vibrations of Rotating Shafts*, Butterworths, London.
[14] Gunter, E. J., Jr., 1966, "Dynamic Stability of Rotor Bearing Systems," NASA SP-113.
[15] Zorzi, E. S., and Nelson, H. D., 1977, "Finite Element Simulation of Rotor-Bearing Systems With Internal Damping," ASME J. Turbines Power, **99**, Ser. A, pp. 71–76.
[16] Nelson, H. D., and McVaugh, J. M., 1976, "The Dynamics of Rotor-Bearing Systems Using Finite Elements," J. Eng. Ind., **98**, pp. 593–600.
[17] Rao, J. S., 1996, *Rotor Dynamics*, 3rd Ed., New Age International (p) Ltd., New Delhi.

M. De Angelis
Assistant Professor,
Dip. Ing. Strutt. e Geotecnica,
University di Roma "La Sapienza,"
Rome, Italy

H. Luş
Lecturer and Reseach Associate

R. Betti
Associate Professor

Department of Civil Engineering and
Engineering Mechanics,
Columbia University,
New York, NY 10027

R. W. Longman
Professor,
Department of Mechanical Engineering,
Columbia University,
New York, NY 10027
Mem. ASME

Extracting Physical Parameters of Mechanical Models From Identified State-Space Representations

In this study a new solution for the identification of physical parameters of mechanical systems from identified state space formulations is presented. With the proposed approach, the restriction of having a full set of sensors or a full set of actuators for a complete identification is relaxed, and it is shown that a solution can be achieved by utilizing mixed types of information. The methodology is validated through numerical examples, and conceptual comparisons of the proposed methodology with previously presented approaches are also discussed. [DOI: 10.1115/1.1483836]

1 Introduction

System identification, in the most general sense, can be described as the identification of the conditions and properties of mathematical models that aspire to represent real phenomena in an adequate fashion. The choice of such models is very much dependent on the type of application one considers. In finite element formulations, identification of physical parameters generally refers to the identification of the mass, damping, and stiffness parameters in the second order matrix differential equations. A possible approach is to identify these parameters directly from experimental dynamic data (see, for example, the works of Agbabian et al. [1] and Smyth et al. [2]). However, the most widely employed approach consists in identifying the modal parameters of the system, and to use them to update a pre-existing finite element model. Some of the noteworthy efforts and discussions in this direction are those of Ewins [3], Mottershead and Friswell [4], Berman [5], Baruch [6,7], and Beck and Katafygiotis [8].

The identification of the parameters in a first-order differential equation formulation has also received considerable attention, as evidenced by the works of Ibrahim and Mikulcik [9], Ibrahim [10], Vold et al. [11], Juang and Pappa [12], Juang et al. [13,14], and Luş et al. [15,16]. However, if one starts with a state-space model, and tries to identify the parameters of the second order model, issues such as nonuniqueness of the solution have to be considered, making such an ''inverse'' problem quite complex.

Usually, the modal parameters required for updating structural models are the undamped (normal) modal parameters, whereas when one works with the first-order formulation, the identified modal parameters are complex, and correspond, in some sense, to the damped modal parameters of the second-order formulation. Therefore, the retrieval of the undamped modal parameters from the identified complex modes also constitutes an important problem, and the study by Sestieri and Ibrahim [17] presents a well-documented discussion. One assumption often employed is that the vibrational modes of the second-order model are uncoupled (modal damping). In this case, arguably the most often employed method to retrieve the undamped modal parameters is the so-called standard technique (e.g., see Imregun and Ewins [18], Ibrahim [19], and Alvin [20]). It is well known, however, that this approximation loses its validity when the system under consideration is highly coupled. To overcome this limitation, many authors have focused their attention on how to retrieve the undamped modal parameters from complex modal parameters for the case of general damping. Some of the most noteworthy discussions include the works of Ibrahim [19], Alvin and Park [21], Zhang and Lallement [22], Yang and Yeh [23], Alvin et al. [24], Tseng et al. [25,26], Chen et al. [27], and Balmès [28].

Taking the inverse problem one step further, one might be interested in directly obtaining the parameters of the second-order model. When one tries to retrieve the second order parameters from the identified state-space model, various methodologies impose different restrictions on the number of sensors and actuators employed, assuming that all the modes of the structure have been successfully identified. The most restrictive requirement is that of having as many sensors and actuators as the number of identified modes, which was discussed by Yang and Yeh [23]. Later on (Alvin and Park [21]) this requirement was improved upon by requiring that only the number of sensors should be equal to the number of identified modes, with one co-located sensor–actuator pair. A further generalization was presented by Tseng et al. [25,26] for the case when the number of actuators is equal to the number of second-order modes, providing the most general solution available for a full set of actuators or sensors, with one co-located sensor–actuator pair.

In this study, we further improve on the requirement concerning the number of sensors and actuators. Based on some concepts previously discussed by Sestieri and Ibrahim [17], and Balmès [28], it is shown that the physical parameters of the second order model can be obtained by using the solution of a symmetric complex eigenvalue problem. The minimum requirement for the proposed methodology is that all the degrees-of-freedom should con-

Contributed by the Applied Mechanics Division of THE AMERICAN SOCIETY OF MECHANICAL ENGINEERS for publication in the ASME JOURNAL OF APPLIED MECHANICS. Manuscript received by the ASME Applied Mechanics Division, December 2, 2001; final revision, February 28, 2002. Associate Editor: R. C. Benson. Discussion on the paper should be addressed to the Editor, Professor Robert M. McMeeking, Department of Mechanical and Environmental Engineering University of California–Santa Barbara, Santa Barbara, CA 93106-5070, and will be accepted until four months after final publication of the paper itself in the ASME JOURNAL OF APPLIED MECHANICS.

tain *either* a sensor *or* an actuator, with at least one co-located sensor–actuator pair. It should be noted that this solution implicitly contains the solutions for the cases with full set of sensors and/or full set of actuators, and therefore, the approach discussed in this study provides a more general solution for the inverse problem.

2 Symmetric Formulation of a First-Order Dynamic Model

One of the most well-known linear time invariant models for dynamical systems is undoubtedly the matrix form of Newton's second law of motion written for discretized spatial domains, i.e.,

$$\mathcal{M}\ddot{\mathbf{q}}(t)+\mathcal{L}\dot{\mathbf{q}}(t)+\mathcal{K}\mathbf{q}(t)=\mathcal{B}\mathbf{u}(t)$$

$$\mathbf{y}(t)=\begin{bmatrix}\mathcal{C}_p\mathbf{q}(t)\\ \mathcal{C}_v\dot{\mathbf{q}}(t)\\ \mathcal{C}_a\ddot{\mathbf{q}}(t)\end{bmatrix} \tag{1}$$

where $\mathbf{q}(t)$ indicates the vector of the (generalized) nodal displacements, with $(\dot{\ })$ and $(\ddot{\ })$ representing, respectively, the first and second-order derivatives with respect to time. The vector $\mathbf{u}(t)$, of dimension $r\times 1$, is the input vector containing r external excitations acting on the system while $\mathbf{y}(t)$ represents the measurement vector, which may contain any combination of nodal displacements, velocities, and/or accelerations. For an N-degree-of-freedom system, $\mathcal{M}\in\Re^{N\times N}$, $\mathcal{L}\in\Re^{N\times N}$, and $\mathcal{K}\in\Re^{N\times N}$ are the symmetric positive definite mass, damping, and stiffness matrices, respectively, while $\mathcal{B}\in\Re^{N\times r}$ is the input matrix. The matrix $[\mathcal{C}_p^T\mathcal{C}_v^T\mathcal{C}_a^T]^T\in\Re^{m\times N}$ represents the output matrix that may incorporate position, velocity, and acceleration measurements, with m denoting the total number of outputs.

By defining a state vector $\mathbf{z}(t)=[\mathbf{q}(t)^T\dot{\mathbf{q}}(t)^T]^T$, the equations of motion in (1) can be conveniently written as

$$\begin{bmatrix}\mathcal{L} & \mathcal{M}\\ \mathcal{M} & \mathbf{0}\end{bmatrix}\dot{\mathbf{z}}(t)+\begin{bmatrix}\mathcal{K} & \mathbf{0}\\ \mathbf{0} & -\mathcal{M}\end{bmatrix}\mathbf{z}(t)=\begin{bmatrix}\mathcal{B}\\ \mathbf{0}\end{bmatrix}\mathbf{u}(t) \tag{2a}$$

$$\mathbf{y}(t)=[\mathcal{C}_p\ \ \mathbf{0}]\mathbf{z}(t) \tag{2b}$$

where, for ease of exposition, we have considered only position measurements in the output equation of Eqs. (2). However, the following results are true for any type of measurements (positions, velocities, or accelerations), and the generalization to velocity and acceleration measurements will be discussed in detail in a subsequent section. The advantage of rewriting Eqs. (1) into Eqs. (2) is that now the associated eigenvalue problem is kept symmetric and can be written in a matrix form as

$$\begin{bmatrix}\mathcal{L} & \mathcal{M}\\ \mathcal{M} & \mathbf{0}\end{bmatrix}\begin{bmatrix}\boldsymbol{\psi}\\ \boldsymbol{\psi}\boldsymbol{\Lambda}\end{bmatrix}\boldsymbol{\Lambda}=\begin{bmatrix}-\mathcal{K} & 0\\ \mathbf{0} & \mathcal{M}\end{bmatrix}\begin{bmatrix}\boldsymbol{\psi}\\ \boldsymbol{\psi}\boldsymbol{\Lambda}\end{bmatrix} \tag{3}$$

where $\boldsymbol{\psi}_{N\times 2N}=[\boldsymbol{\psi}_1\boldsymbol{\psi}_2\ldots\boldsymbol{\psi}_{2N}]$ is the matrix containing the eigenvectors of the complex eigenvalue problem

$$(\lambda_i^2\mathcal{M}+\lambda_i\mathcal{L}+\mathcal{K})\psi_i=0$$

and $\boldsymbol{\Lambda}_{2N\times 2N}$ is the diagonal matrix of the complex eigenvalues $\lambda_i=\sigma_i\pm j\omega_i$ (with $j=\sqrt{-1}$). When all the modes of the structure are underdamped, all the eigenvalues appear in complex conjugate pairs, i.e., they can be ordered such that $\lambda_{2i-1}=\lambda_{2i}^*$ with $i=1,2,\ldots,N$, where the superscript $(*)$ denotes complex conjugate. This implies that the complex eigenvectors have the similar property that $\psi_{2i-1}=\psi_{2i}^*$ for $i=1,2,\ldots,N$. In general, these eigenvectors can be arbitrarily scaled; however, if the scaling is chosen such that (see Sestieri and Ibrahim [17] and Balmès [28])

$$\boldsymbol{\psi}^T\mathcal{M}\boldsymbol{\psi}\boldsymbol{\Lambda}+\boldsymbol{\Lambda}\boldsymbol{\psi}^T\mathcal{M}\boldsymbol{\psi}+\boldsymbol{\psi}^T\mathcal{L}\boldsymbol{\psi}=\mathbf{I}$$

$$\boldsymbol{\Lambda}\boldsymbol{\psi}^T\mathcal{M}\boldsymbol{\psi}\boldsymbol{\Lambda}-\boldsymbol{\psi}^T\mathcal{K}\boldsymbol{\psi}=\boldsymbol{\Lambda}$$

or in matrix form

$$\begin{bmatrix}\boldsymbol{\psi}\\ \boldsymbol{\psi}\boldsymbol{\Lambda}\end{bmatrix}^T\begin{bmatrix}\mathcal{L} & \mathcal{M}\\ \mathcal{M} & \mathbf{0}\end{bmatrix}\begin{bmatrix}\boldsymbol{\psi}\\ \boldsymbol{\psi}\boldsymbol{\Lambda}\end{bmatrix}=\mathbf{I} \tag{4a}$$

$$\begin{bmatrix}\boldsymbol{\psi}\\ \boldsymbol{\psi}\boldsymbol{\Lambda}\end{bmatrix}^T\begin{bmatrix}\mathcal{K} & \mathbf{0}\\ \mathbf{0} & -\mathcal{M}\end{bmatrix}\begin{bmatrix}\boldsymbol{\psi}\\ \boldsymbol{\psi}\boldsymbol{\Lambda}\end{bmatrix}=-\boldsymbol{\Lambda} \tag{4b}$$

then, for a *proportionally damped system*, the real and imaginary parts of the components of these complex eigenvectors are equal in magnitude.

Once the symmetric eigenvalue problem (Eqs. (4)) has been solved, we can now conveniently rewrite Eqs. (2) by using the transformation $\mathbf{z}(t)=[\boldsymbol{\psi}^T(\boldsymbol{\psi}\boldsymbol{\Lambda})^T]^T\boldsymbol{\zeta}(t)$ so that

$$\dot{\boldsymbol{\zeta}}(t)=\boldsymbol{\Lambda}\boldsymbol{\zeta}(t)+\boldsymbol{\psi}^T\mathcal{B}\mathbf{u}(t) \tag{5a}$$

$$\mathbf{y}(t)=\mathcal{C}_p\boldsymbol{\psi}\boldsymbol{\zeta}(t). \tag{5b}$$

For ease of exposition, let us indicate with $\mathbf{M}(k,:)$ and $\mathbf{M}(:,l)$ the kth row and the ith column, respectively, of a generic matrix $\mathbf{M}$. The equations of motion rewritten in form (5) have the important property that, for a generic ith degree-of-freedom that contains a co-located sensor–actuator pair,

$$\mathcal{C}_p(i,:)\boldsymbol{\psi}=[\boldsymbol{\psi}^T\mathcal{B}(:,i)]^T, \tag{6}$$

and this property will be of great use (1) for determining and scaling the eigenvectors, and (2) for developing the concept of input-output equivalence, as presented in detail in Section 4.

3 Identification of the Physical Parameters of the System

The proposed identification algorithm consists of two well-defined phases: (1) the determination of a first-order model of the system, and (2) the transformation of such an identified model into a second-order model.

From general input-output data, it is possible to identify a state space realization in some arbitrary basis, and such a realization can be expressed as

$$\dot{\mathbf{x}}(t)=\mathbf{A}_C\mathbf{x}(t)+\mathbf{B}_C\mathbf{u}(t)$$

$$\mathbf{y}(t)=\mathbf{C}_C\mathbf{x}(t)+\mathbf{D}_C\mathbf{u}(t) \tag{7}$$

where now $\mathbf{A}_C\in\Re^{2N\times 2N}$, $\mathbf{B}_C\in\Re^{2N\times r}$, $\mathbf{C}_C\in\Re^{m\times 2N}$, and $\mathbf{D}_C\in\Re^{m\times r}$ are continuous time system matrices. In this study, an ERA/OKID based approach, as discussed by Juang et al. [13,14] and Luş et al. [15,16], was used for the identification of the discrete time system matrices (namely the matrices $\boldsymbol{\Phi}$, $\boldsymbol{\Gamma}$, $\mathbf{C}$, and $\mathbf{D}$), and these discrete time matrices were converted to their continuous time counterparts using the zero-order hold assumption. By considering the transformation $\mathbf{x}=\boldsymbol{\varphi}\boldsymbol{\theta}$, the continuous time system of Eqs. (7) can also be written in modal coordinates as

$$\dot{\boldsymbol{\theta}}(t)=\boldsymbol{\Lambda}\boldsymbol{\theta}(t)+\boldsymbol{\varphi}^{-1}\mathbf{B}_C\mathbf{u}(t) \tag{8a}$$

$$\mathbf{y}(t)=\mathbf{C}_C\boldsymbol{\varphi}\boldsymbol{\theta} \tag{8b}$$

where the matrix $\boldsymbol{\Lambda}$ contains the continuous time eigenvalues of the identified state space model, and $\boldsymbol{\varphi}$, of order $2N\times 2N$, is the matrix of the corresponding eigenvectors. The matrix $\mathbf{D}_C$ has been omitted in Eq. (8*b*) because it is independent of coordinate transformations. It is noteworthy that in the system of Eqs. (8), the products $\boldsymbol{\varphi}^{-1}\mathbf{B}_C$ and $\mathbf{C}_C\boldsymbol{\varphi}$ appear; these products impose a strong limitation on the order of the second-order model to be identified, whose dimensions are now constrained either by the number of actuators, or by the number of sensors (Tseng et al. [25,26]).

If the first-order system of Eqs. (7) was identified using data that actually came from the second-order model of Eq. (1), the models represented by Eqs. (5) and (8) are different models of the same system. Therefore, we look for a transformation matrix, $\mathcal{T}$, that relates these two representations, i.e.:

$$\mathcal{T}^{-1}\boldsymbol{\Lambda}\mathcal{T}=\boldsymbol{\Lambda} \tag{9a}$$

$$\mathcal{T}^{-1}\boldsymbol{\varphi}^{-1}\mathbf{B}_C=\boldsymbol{\psi}^T\mathcal{B} \tag{9b}$$

$$\mathbf{C}_C\boldsymbol{\varphi}\mathcal{T}=\mathcal{C}_p\boldsymbol{\psi}. \tag{9c}$$

If there are no repeated roots, it is easy to show that the transformation matrix is diagonal, i.e., $\mathcal{T}=\mathrm{diag}(t_1,t_2,\ldots,t_{2N})$ and its values are complex conjugate. By examining Eqs. (9), it is clear that the matrix $\mathcal{T}$ has a twofold effect: (1) to transform the eigenvectors from those of a nonsymmetric eigenvalue problem to those of a symmetric eigenvalue problem, and (2) to properly scale such eigenvectors. Here we discuss the identification of this transformation matrix $\mathcal{T}$ and the eigenvectors $\boldsymbol{\psi}$ when there are no repeated roots, and the input and output matrices ($\mathcal{B}$ and $\mathcal{C}_p$, respectively) of the finite element model are known. These input and output matrices are assumed to contain binary information, i.e., in the case of the input matrix $\mathcal{B}$, the coefficient in the ith row ($i=1,2,\ldots,N$) and jth column ($j=1,2,\ldots,r$) of $\mathcal{B}$ is 1 if the jth actuator is placed on the ith degree-of-freedom and this coefficient is 0 if the jth actuator is not placed on the ith degree-of-freedom. Similarly, the coefficient in the ith row ($i=1,2,\ldots,m$) and jth column ($j=1,2,\ldots,N$) of the output matrix $\mathcal{C}_p$ is 1 if the ith sensor is placed on the jth degree-of-freedom and this coefficient is 0 if the ith sensor is not placed on the jth degree-of-freedom.

To present the proposed methodology in a concise manner, let us assume that the input and output matrices of both representations (in Eqs. (9b) and (9c)) have been expanded to incorporate all the degrees-of-freedom. This is most easily achieved by incorporating columns of zeros in the input matrices ($\mathbf{B}_C$ and $\mathcal{B}$) and rows of zeros in the output matrices ($\mathbf{C}_C$ and $\mathcal{C}_p$) for the degrees-of-freedom that are either not excited or not measured. Furthermore, assume that these input and output matrices have been arranged so that the ith column of the input matrix corresponds to the ith degree-of-freedom (and hence there will be a column of zeros if there is no actuator placed on the ith degree-of-freedom), and similarly, the ith row of the output matrix corresponds to the ith degree-of-freedom (a row of zeros if there is no sensor on the ith degree-of-freedom). Now the previous transformation Eqs. (9) can be written in an "expanded" form as

$$\mathcal{T}^{-1}\boldsymbol{\Lambda}\mathcal{T}=\boldsymbol{\Lambda} \tag{10a}$$

$$\mathcal{T}^{-1}\boldsymbol{\varphi}^{-1}\mathbf{B}_C^E=\boldsymbol{\psi}^T\mathcal{B}^E \tag{10b}$$

$$\mathbf{C}_C^E\boldsymbol{\varphi}\mathcal{T}=\mathcal{C}_p^E\boldsymbol{\psi} \tag{10c}$$

where $\mathbf{B}_C^E$, $\mathcal{B}^E$, $\mathbf{C}_C^E$, and $\mathcal{C}_p^E$ are the expanded versions of the matrices $\mathbf{B}_C$, $\mathcal{B}$, $\mathbf{C}_C$, and $\mathcal{C}_p$, respectively.

The identification of the transformation matrix $\mathcal{T}$ and the properly scaled complex eigenvectors $\boldsymbol{\psi}$ can be investigated by studying a general limit case, since it can be shown that the case of full set of sensors and the case of full set of actuators are special cases of the general approach. Let us assume that each degree-of-freedom contains *either* an actuator *or* a sensor, with one degree-of-freedom containing a co-located sensor–actuator pair (hence $r+m=N+1$). With the notation introduced in Section 2, if the co-located sensor–actuator pair is at the ith degree-of-freedom the well-known co-location requirement can be written as

$$\mathcal{C}_p^E(i,:)\boldsymbol{\psi}=(\boldsymbol{\psi}^T\mathcal{B}^E(:,i))^T. \tag{11}$$

Using the co-location requirement, the transformation matrix $\mathcal{T}$ can be evaluated from Eqs. (10b), (10c), and Eq. (11) as

$$\begin{aligned}\mathbf{C}_C^E(i,:)\boldsymbol{\varphi}\mathcal{T}&=(\mathcal{T}^{-1}\boldsymbol{\varphi}^{-1}\mathbf{B}_C^E(:,i))^T;\\ \mathbf{C}_C^E(i,:)\boldsymbol{\varphi}\mathcal{T}^2&=(\boldsymbol{\varphi}^{-1}\mathbf{B}_C^E(:,i))^T.\end{aligned} \tag{12}$$

Since the matrix $\mathcal{T}$ is diagonal, each t_i ($i=1,2,\ldots,2N$) can be uniquely determined from Eq. (12). Once these scaling factors are obtained, what is left to be determined is the complex eigenvector matrix $\boldsymbol{\psi}$.

The information pertaining to a certain degree of freedom is embedded either in the input matrix or in the output matrix. Going back to Eqs. (10), the output matrices in Eq. (10c) essentially contain information about only m degree-of-freedom (with $m<N$). If there is a sensor at the kth degree-of-freedom then the kth row of the matrix $\boldsymbol{\psi}$ can be evaluated using Eq. (10c), i.e.,

$$\boldsymbol{\psi}(k,:)=\mathbf{C}_C^E(k,:)\boldsymbol{\varphi}\mathcal{T}. \tag{13}$$

On the other hand, if there is no sensor at the kth degree-of-freedom then $\mathcal{C}_p^E(k,:)\boldsymbol{\psi}=\mathbf{0}_{1\times 2N}$. However, if a degree-of-freedom is instrumented with either a sensor or an actuator, the kth row of the matrix $\boldsymbol{\psi}$ can be evaluated using Eq. (10b) as

$$\boldsymbol{\psi}(k,:)=(\mathcal{T}^{-1}\boldsymbol{\varphi}^{-1}\mathbf{B}_C^E(:,k))^T. \tag{14}$$

Clearly, this argument is valid for all the N degrees-of-freedom and so all the rows of the matrix $\boldsymbol{\psi}$ can be evaluated. It should be noted that, for the ith degree-of-freedom that contained the co-located sensor–actuator pair, one can use either Eq. (13) or Eq. (14), since they lead to the same result by the co-location requirement in Eq. (11).

If there is a full set of sensors (rank$(\mathcal{C}_p)=N$, $\mathcal{C}_p^E\equiv\mathcal{C}_p$, and $\mathbf{C}_C^E\equiv\mathbf{C}_C$), or a full set of actuators (rank$(\mathcal{B})=N$, $\mathcal{B}^E\equiv\mathcal{B}$, and $\mathbf{B}_C^E\equiv\mathbf{B}_C$), the scaling factors are still evaluated from Eq. (11). Once the scaling factors are evaluated, one can identify the complex eigenvector matrix $\boldsymbol{\psi}$ using

$$\mathcal{C}_p^{-1}\mathbf{C}_C\boldsymbol{\varphi}\mathcal{T}=\boldsymbol{\psi} \tag{15}$$

when there is a full set of sensors, or

$$\mathcal{T}^{-1}\boldsymbol{\varphi}^{-1}\mathbf{B}_C\mathcal{B}^{-1}=\boldsymbol{\psi}^T \tag{16}$$

when there is a full set of actuators. Clearly, these two cases can be regarded as special cases of the general formulation presented in this section.

Once the properly scaled eigenvector matrix $\boldsymbol{\psi}$ is evaluated, the mass, damping, and stiffness matrices of the finite element model can be obtained using the orthogonality conditions in Eqs. (4). As discussed in Balmès [28], algebraic manipulations on Eqs. (4) leads to the following identities:

$$\begin{aligned}\begin{bmatrix}\mathcal{L} & \mathcal{M}\\ \mathcal{M} & \mathbf{0}\end{bmatrix}^{-1}&=\begin{bmatrix}0 & \mathcal{M}^{-1}\\ \mathcal{M}^{-1} & -\mathcal{M}^{-1}\mathcal{L}\mathcal{M}^{-1}\end{bmatrix}\\ &=\begin{bmatrix}\boldsymbol{\psi}\\ \boldsymbol{\psi}\boldsymbol{\Lambda}\end{bmatrix}\begin{bmatrix}\boldsymbol{\psi}\\ \boldsymbol{\psi}\boldsymbol{\Lambda}\end{bmatrix}^T\\ &=\begin{bmatrix}\boldsymbol{\psi}\boldsymbol{\psi}^T & \boldsymbol{\psi}\boldsymbol{\Lambda}\boldsymbol{\psi}^T\\ \boldsymbol{\psi}\boldsymbol{\Lambda}\boldsymbol{\psi}^T & \boldsymbol{\psi}\boldsymbol{\Lambda}^2\boldsymbol{\psi}^T\end{bmatrix}\end{aligned} \tag{17a}$$

$$\begin{aligned}\begin{bmatrix}\mathcal{K} & \mathbf{0}\\ \mathbf{0} & -\mathcal{M}\end{bmatrix}^{-1}&=\begin{bmatrix}\mathcal{K}^{-1} & \mathbf{0}\\ \mathbf{0} & -\mathcal{M}^{-1}\end{bmatrix}\\ &=-\begin{bmatrix}\boldsymbol{\psi}\\ \boldsymbol{\psi}\boldsymbol{\Lambda}\end{bmatrix}\boldsymbol{\Lambda}^{-1}\begin{bmatrix}\boldsymbol{\psi}\\ \boldsymbol{\psi}\boldsymbol{\Lambda}\end{bmatrix}^T\\ &=-\begin{bmatrix}\boldsymbol{\psi}\boldsymbol{\Lambda}^{-1}\boldsymbol{\psi}^T & \boldsymbol{\psi}\boldsymbol{\psi}^T\\ \boldsymbol{\psi}\boldsymbol{\psi}^T & \boldsymbol{\psi}\boldsymbol{\Lambda}\boldsymbol{\psi}^T\end{bmatrix}.\end{aligned} \tag{17b}$$

In order for Eqs. (17) to be valid, it is necessary that

$$\mathcal{M}=(\boldsymbol{\psi}\boldsymbol{\Lambda}\boldsymbol{\psi}^T)^{-1},\quad \mathcal{L}=-\mathcal{M}\boldsymbol{\psi}\boldsymbol{\Lambda}^2\boldsymbol{\psi}^T\mathcal{M}, \tag{18a}$$

$$\mathcal{K}=-(\boldsymbol{\psi}\boldsymbol{\Lambda}^{-1}\psi^T)^{-1},\quad \boldsymbol{\psi}\boldsymbol{\psi}^T=\mathbf{0} \tag{18b}$$

and Eqs. (18) provide the required expressions for the mass, damping and stiffness matrices of the second-order model of the system.

3.1 Observations. There is a sign choice for the square roots when one solves for the scaling factors in $\mathcal{T}$ (see Eqs. (12)); however, this does not have any effect on the identified mass, damping, and stiffness matrices. To investigate this point, first let us note that a sign change in the scaling factor t_i causes a sign change in the ith complex mode $\boldsymbol{\psi}_i$. This sign change in $\boldsymbol{\psi}_i$ has no effect on the mass matrix, since the expression for the mass matrix can be written as

$$\begin{aligned}\mathcal{M}=(\boldsymbol{\psi}\boldsymbol{\lambda}\boldsymbol{\psi}^T)^{-1}&=(\lambda_1\boldsymbol{\psi}_1\boldsymbol{\psi}_1^T+\lambda_2\boldsymbol{\psi}_2\boldsymbol{\psi}_2^T+\ldots+\lambda_{2N}\boldsymbol{\psi}_{2N}\boldsymbol{\psi}_{2N}^T)^{-1}\\&=(\lambda_1(-\boldsymbol{\psi}_1)(-\boldsymbol{\psi}_1^T)+\lambda_2(-\boldsymbol{\psi}_2)(-\boldsymbol{\psi}_2^T)+\ldots\\&\quad+\lambda_{2N}(-\boldsymbol{\psi}_{2N})(-\boldsymbol{\psi}_{2N}^T))^{-1}\end{aligned}\tag{19}$$

and this expression is clearly invariant under a sign change for any of the complex eigenvectors. Analogous arguments can be used to show that the damping matrix $\mathcal{L}$ and the stiffness matrix $\mathcal{K}$ are also invariant under a sign change for the $\boldsymbol{\psi}_i$ ($i=1,2,\ldots,2N$).

On the other hand, a change in the ordering of the rows of the complex eigenvector matrix $\boldsymbol{\psi}$ changes the final form of the mass, damping, and stiffness matrices in the sense that two different ordering schemes lead to two different sets that differ only by the arrangement of rows and columns. In fact, if we consider the expression in Eq. (19) for the mass matrix, an interchange between the kth and lth rows of $\boldsymbol{\psi}$ clearly leads to an interchange between the kth and lth rows and columns of the mass matrix. However, this rearrangement also takes place in the damping and the stiffness matrices. In conclusion, this nonuniqueness is equivalent to the reordering of the degrees-of-freedom in the representation of Eq. (1).

In the foregoing discussion, it was assumed that there was only one co-located sensor–actuator pair, but in general, it is possible to have more co-located sensors and actuators. These extra conditions are redundant if the system is noise free, i.e., the scaling factors obtained by investigating one co-located sensor–actuator pair also satisfies the co-location requirement of any other co-located sensor–actuator pair. However, in the presence of noise, it might be best to proceed with a least-squares approach to obtain the entries of the matrix $\mathcal{T}$ (for a thorough investigation on the effects of noise on the proposed approach, the reader is referred to the work of Luş [29]).

If instead of displacement measurements one uses velocity or acceleration measurements, the output equation in Eqs. (5) can be rewritten as

- for velocity measurements:

$$\mathbf{y}(t)=[\mathbf{0}\ \ \mathcal{C}_v]\begin{bmatrix}\boldsymbol{\psi}\\ \boldsymbol{\psi}\boldsymbol{\Lambda}\end{bmatrix}\boldsymbol{\zeta}(t)=\mathcal{C}_v\boldsymbol{\psi}\boldsymbol{\Lambda}\boldsymbol{\zeta}(t)\tag{20}$$

- for acceleration measurements:

$$\mathbf{y}(t)=[\mathbf{0}\ \ \mathcal{C}_a]\begin{bmatrix}\boldsymbol{\psi}\\ \boldsymbol{\psi}\boldsymbol{\Lambda}\end{bmatrix}\boldsymbol{\zeta}(t)=\mathcal{C}_a\boldsymbol{\psi}\boldsymbol{\Lambda}^2\boldsymbol{\zeta}(t)+\mathcal{C}_a\boldsymbol{\psi}\boldsymbol{\Lambda}\boldsymbol{\psi}^T\mathcal{B}\mathbf{u}(t).\tag{21}$$

Clearly, these changes lead to some alterations in Eq. (9c), according to the type of measurements used:

$$\mathbf{C}_C\boldsymbol{\varphi}\mathcal{T}=\mathcal{C}_v\boldsymbol{\psi}\boldsymbol{\Lambda}\quad\text{for velocity measurements}$$

$$\mathbf{C}_C\boldsymbol{\varphi}\mathcal{T}=\mathcal{C}_a\boldsymbol{\psi}\boldsymbol{\Lambda}^2\quad\text{for acceleration measurements.}$$

Analogous to the output matrix $\mathcal{C}_p$, the output matrices $\mathcal{C}_v$ and $\mathcal{C}_a$ also contain binary information (as discussed in Section 3). Therefore, all we have to do to use the algorithms and discussions of Section 3 is to use $\mathbf{C}_C\boldsymbol{\varphi}\boldsymbol{\Lambda}^{-1}$ in Eq. (9c) for velocity measurements or $\mathbf{C}_C\boldsymbol{\varphi}\boldsymbol{\Lambda}^{-2}$ in the case of acceleration measurements. It is noteworthy that, in the case of acceleration measurements, only the first term enters in the identification process while the second term, independent of the transformation matrix, needs to be accounted only for simulation purposes.

In general, one can possibly use all types of measurements simultaneously, and in that case each row of the matrix $\mathbf{C}_C\boldsymbol{\varphi}$ must be handled separately with regards to the changes discussed above. Once appropriate alterations are made according to the type of sensor one uses, the formulations and discussions presented in Section 3 remain unchanged.

4 Concept of Input-Output Equivalence

The formulation presented in this study has one main advantage over previous studies, in the sense that the methodology presented here has more general theoretical implications about the number of sensors or actuators that can be used in dynamic testing. In order to clarify this point, let us consider an N degree-of-freedom system. By taking the Laplace transform of Eqs. (5) and by combining the two transformed equations, it is possible to obtain an expression that relates the input transform vector, $\mathbf{U}(s)$, and the output transform vector, $\mathbf{Y}(s)$, as

$$\mathbf{Y}(s)=\mathcal{C}_p\boldsymbol{\psi}[s\mathbf{I}-\boldsymbol{\Lambda}]^{-1}\boldsymbol{\psi}^T\mathcal{B}\mathbf{U}(s)=\mathcal{C}_p\mathbf{H}(s)\mathcal{B}\mathbf{U}(s)\tag{22}$$

where the matrix $\mathbf{H}(s)$, of dimension $N\times N$, represents the transfer function matrix of the system. The complete knowledge of $\mathbf{H}(s)$ would allow one to determine the response of the system at any point for an arbitrary input applied at any degree-of-freedom creating a complete predictive model of the system. Hence, the goal of any identification methodology should be the determination of the matrix $\mathbf{H}(s)$. For this purpose, the well-known property that $\mathbf{H}(s)$ is a symmetric matrix will be of great help. Again, for ease of presentation, we consider only displacement measurements but analogous formulations can be derived for velocity and acceleration measurements, as shown before.

Let us first consider the case where, in the identification process, we have N outputs and N inputs available ($m=N$ and $r=N$). This will correspond to the case of N co-located pairs of sensors and actuators. In the notation of Section 3, this case corresponds to having $\mathcal{C}_p\equiv\mathcal{C}_p^E$ and $\mathcal{B}\equiv\mathcal{B}^E$ and the matrix $\mathbf{H}(s)$ is directly determined.

If the system has been identified using N outputs and 1 input ($m=N$ and $r=1$) with the ith output co-located with the input, only the ith column of the transfer function matrix $\mathbf{H}(s)$ can be *directly* identified. This will be equivalent to knowing the matrix $\boldsymbol{\psi}$, since in Eqs. (22) the matrix $\mathcal{C}_p$ is the identity matrix, and, consequently, the entire transfer function matrix can be obtained. In this case (N outputs and 1 input), it is well known that the physical parameters of the second-order system of Eqs. (1) can be retrieved from the identified state-space model, as discussed previously by many authors (see, e.g., the works of Alvin and Park [21] or Tseng et al. [25,26]).

On the other hand, if the identified system has N inputs and 1 output ($m=1$ and $r=N$) with the ith input co-located with the ith output, only the ith row of the transfer function matrix $\mathbf{H}(s)$ can be *directly* identified. In this case, the matrix $\mathcal{B}$ in Eqs. (22) is the identity matrix, and analogous to the previous case, it is possible to completely determine the matrix $\mathbf{H}(s)$. A solution for this case was presented by Tseng et al. [25,26].

In system identification literature, these two previous cases are considered as the two limit cases. In fact, there is no methodology available that allows us to combine information coming from m outputs and r inputs, and the possibility of combining these two types of information is one of the innovations of the proposed approach. To present this generalization, let us identify an N degree-of-freedom system with m outputs and r inputs (with $m<N$ and $r<N$ and $m+r=N+1$), with one co-located sensor–actuator pair on the ith degree-of-freedom. At this point it is useful to remind the importance of having at least one pair of co-located sensor and actuator for the determination of the transformation matrix $\mathcal{T}$, which leads to the presence of $+1$ in the $m+r=N+1$ condition. What is noteworthy in this case is the fact that neither $\mathcal{C}_p$ nor $\mathcal{B}$ are square (identity) matrices and this implies that neither a column nor a row of $\mathbf{H}(s)$ is fully identified.

Due to the co-located sensor–actuator pair at the ith degree-of-freedom the entry at the ith row and ith column of $\mathbf{H}(s)$ ($H_{ii}(s)$) is identified. Now, if we consider an input on the lth degree-of-freedom and an output on the kth degree-of-freedom, we are capable of determining $H_{kl}(s)$, which represents the component of $\mathbf{H}(s)$ on the kth row and lth column. The main innovation in this study is that the formulations developed herein allow us to use the

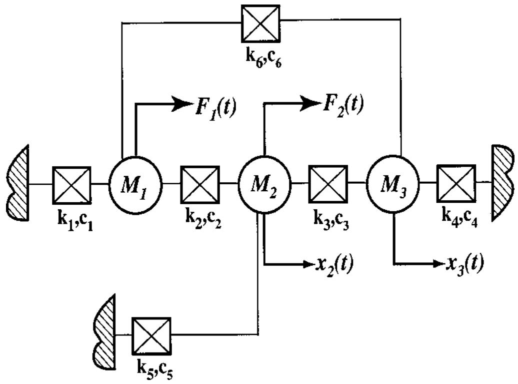

Fig. 1 Three-degree-of-freedom system considered for the application of the proposed approach

property that $\mathbf{H}(s)$ is symmetric, and hence even though we have not identified the component $H_{lk}(s)$, we can use $H_{kl}(s)$ instead. Therefore, if all the degrees-of-freedom have either an actuator or a sensor, the entire ith row and/or ith column of $\mathbf{H}(s)$ can be determined directly. This implies that it is possible to transform the general case of *m* sensors and *r* actuators to an equivalent case of a full set of sensors or of a full set of actuators. This has been possible because of the concept of "input–output equivalence," so that for this methodology, it is indifferent to have either an input or an output at each degree-of-freedom.

This concept of input–output equivalence is possible because of the particular eigenvector basis discussed, i.e., the eigenvectors for the symmetric eigenvalue problem of the system in Eqs. (2). On the other hand, if we were to use the eigenvectors of the nonsymmetric problem, the transpose of the eigenvector matrix in Eqs. (9*a*) would be replaced with the inverse of the matrix $\boldsymbol{\varphi}$ (dimension $2N\times 2N$), and hence, we would be limited to the case of either a full set of sensors (Alvin and Park [21] or Tseng et al. [25,26]) or a full set of actuators (Tseng et al. [25,26]).

5 Numerical Examples

To show the validity of the proposed approach, first a simple but general numerical example is presented. The system, shown in Fig. 1, has been previously studied by Agbabian et al. [1] and Koh and See [30]; the values for the mass and stiffness matrices used in this study are given in Table 1.

To consider the effects of the modal coupling on the structure of the eigenvectors, we consider two different damping matrices, as shown in Table 2. The first one leads to the more classical case of modal damping. The second matrix instead induces coupling of

Table 1 Mass and stiffness matrices used for the system of Fig. 1

Mass			Stiffness		
0.8	0.0	0.0	4.0	-1.0	-1.0
0.0	2.0	0.0	-1.0	4.0	-1.0
0.0	0.0	1.2	-1.0	-1.0	4.0

Table 2 Damping matrices leading to uncoupled and coupled second-order vibrational modes for the system of Fig. 1

uncoupled			coupled		
0.4	-0.1	-0.1	0.5	-0.1	-0.2
-0.1	0.4	-0.1	-0.1	0.7	-0.3
-0.1	-0.1	0.4	-0.2	-0.3	0.6

Table 3 Identified discrete time matrices of the state-space model for the uncoupled damping case

$\mathbf{\Phi}\times 10$

9.9520	0.0956	-0.6987	0.2243	0.0072	0.0178
-0.0761	9.8881	-0.5836	-0.6557	0.0264	0.0032
0.6886	0.5640	9.9450	-0.0075	-0.4241	-0.0190
-0.2833	0.7991	0.0135	9.8893	0.1779	-0.0022
0.1586	-0.0056	0.4669	-0.1255	9.6269	0.8757
0.0158	-0.0335	-0.0190	0.0679	-1.0219	9.9322

$\mathbf{C}\times 10$

1.6132	-1.2168	0.4631	-1.1516	0.1377	-0.0220
1.4748	0.6048	1.8841	0.2602	0.2798	-0.0377

$\mathbf{\Gamma}^T\times 10$

0.4917	0.0904	0.2763	0.0800	-2.5024	-0.4362
-0.4112	1.2005	0.2179	-1.2017	0.1888	0.3338

the second-order vibrational modes, and therefore, more conventional methods that employ the modal damping assumption are not applicable. Furthermore, we assume that the system is excited by only two actuators, located at the first and the second degrees-of-freedom and that accelerations are also measured only at two degrees-of-freedom (second and third degrees-of-freedom). With this particular setup, methodologies that require either a full set of sensors, or a full set of actuators, are also not applicable.

The state-space model is identified using the simulated pulse response data of the system (with a sampling time of $\Delta T = 0.05$ sec.), and by employing the ERA/DC algorithm (Juang et al. [13]). Using the identified state-space models for both the coupled and the uncoupled cases, the scaling factors in $\mathcal{T}$, the eigenvectors $\boldsymbol{\psi}$, and the mass, damping, and stiffness matrices of the second-order model ($\mathcal{M}$, $\mathcal{L}$, and $\mathcal{K}$, respectively) are retrieved using the methodology presented in this work.

5.1 Uncoupled Second-Order Modes. For this case, the identified system matrices for the discrete time state space model are presented in Table 3. Once these matrices have been obtained, they are converted to their continuous time counterparts, and the equations are written in the modal coordinates, as in Eqs. (8). At this point, it is possible to calculate the diagonal transformation matrix $\mathcal{T}$ using the information at the co-located sensor–actuator pair, leading to: $\mathrm{diag}(\mathcal{T}) = (2.966\mp j2.322,\ 8.996\mp j8.164,\ 6.449\mp j4.789)$, where $\mathrm{diag}(\mathcal{T})$ refers to the components on themain diagonal of the transformation matrix $\mathcal{T}$ (with all off-diagonal terms equal to zero). As expected, they appear in complex conjugate pairs.

Once these scaling factors have been evaluated, the eigenvector matrix $\boldsymbol{\psi}$ can be identified, as discussed in Section 3. The eigenvector matrix has the form $\boldsymbol{\psi} = [\boldsymbol{\psi}_1 \boldsymbol{\psi}_1^* \boldsymbol{\psi}_2 \boldsymbol{\psi}_2^* \boldsymbol{\psi}_3 \boldsymbol{\psi}_3^*]$ and for this case the identified complex eigenvectors $\boldsymbol{\psi}_1$, $\boldsymbol{\psi}_2$, and $\boldsymbol{\psi}_3$ are

$$\boldsymbol{\psi}_1 = \begin{bmatrix} -0.159 - j\ 0.159 \\ -0.276 - j\ 0.276 \\ -0.185 - j\ 0.185 \end{bmatrix}; \quad \boldsymbol{\psi}_2 = \begin{bmatrix} 0.109 + j\ 0.109 \\ -0.135 - j\ 0.135 \\ 0.274 + j\ 0.274 \end{bmatrix};$$

$$\boldsymbol{\psi}_3 = \begin{bmatrix} 0.334 + j\ 0.334 \\ -0.031 - j\ 0.031 \\ -0.114 - j\ 0.114 \end{bmatrix}.$$

As discussed in Section 2, for a proportionally damped system, the particular scaling choice employed in the proposed methodology leads to complex eigenvectors whose components have real and imaginary parts of equal magnitude. Once these eigenvectors

Table 4 Identified discrete time matrices of the state-space model for the coupled damping case

$\mathbf{\Phi} \times 10$

9.9461	0.3794	-0.5714	0.1773	0.0032	0.0157
-0.3310	9.8771	-0.5938	-0.6294	0.1211	0.0084
0.5782	0.4676	9.8825	-0.2419	-0.3919	-0.0220
-0.2784	0.8119	0.3483	9.8572	0.0833	-0.0785
0.1925	-0.1088	0.5346	0.0501	9.5282	0.9199
0.0117	-0.0764	-0.0880	0.1883	-0.9465	9.9287

$\mathbf{C} \times 10$

1.5236	-1.2545	0.2148	-0.8687	0.0960	-0.0348
1.3362	0.0325	1.5306	0.2360	0.2277	-0.0230

$\mathbf{\Gamma}^T \times 10$

0.5234	0.0030	0.6595	0.3176	-2.8212	0.0959
-0.5469	1.2525	1.0654	-1.3654	0.2666	0.6835

have been obtained, the mass, stiffness, and damping matrices can be evaluated using the expressions presented in Eq. (18)

$$\mathcal{M}=\begin{bmatrix} 0.8 & 0 & 0 \\ 0 & 2.0 & 0 \\ 0 & 0 & 1.2 \end{bmatrix}; \quad \mathcal{K}=\begin{bmatrix} 4.0 & -1.0 & -1.0 \\ -1.0 & 4.0 & -1.0 \\ -1.0 & -1.0 & 4.0 \end{bmatrix};$$

Table 5 Mean values of the identified samples for the mass, damping, and stiffness coefficients. The estimates for the coefficients are obtained at 5% RMS noise level.

Mass			Damping			Stiffness		
0.797	0.000	0.000	0.501	-0.099	-0.201	3.984	-0.998	-0.995
0.000	2.002	0.000	-0.099	0.702	-0.301	-0.998	4.003	-1.004
0.000	0.000	1.203	-0.201	-0.301	0.600	-0.995	-1.004	4.006

Table 6 Absolute values of the percentage errors in the mean values of the identified samples for the mass, damping, and stiffness coefficients. The estimates for the coefficients are obtained at 5% RMS noise level. The "-" entries in the tables correspond to coefficients for which the true values are 0.

Mass			Damping			Stiffness		
0.36	–	–	0.15	1.03	0.48	0.39	0.18	0.50
–	0.08	–	1.03	0.29	0.29	0.18	0.06	0.36
–	–	0.30	0.48	0.29	0.04	0.50	0.36	0.15

Table 7 Coefficients of variation (%) of the identified samples for the mass, damping, and stiffness coefficients. The estimates for the coefficients are identified at 5% RMS noise level, and the "-" entries in the tables correspond to coefficients for which the true values are 0.

Mass			Damping			Stiffness		
6.11	–	–	23.05	8.97	5.29	5.67	6.26	4.57
–	0.65	–	8.97	2.96	3.90	6.26	0.63	4.92
–	–	3.29	5.29	3.90	14.36	4.57	4.92	2.54

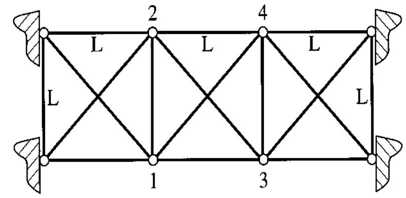

Fig. 2 Truss structure with eight unrestrained degrees-of-freedom (one horizontal and one vertical for each of the nodes denoted by 1, 2, 3, and 4)

$$\mathcal{L}=\begin{bmatrix} 0.4 & -0.1 & -0.1 \\ -0.1 & 0.4 & -0.1 \\ -0.1 & -0.1 & 0.4 \end{bmatrix}$$

which are exactly the system matrices we used to obtain the dynamic data. These matrices automatically come out as real, i.e., the imaginary components are of the order of 10^{-15} and therefore are numerical zeros for all purposes.

5.2 Coupled Second-Order Modes. The procedure for coupled systems are exactly the same as for uncoupled systems, only now the matrices we obtain at each step will look different than the ones obtained in the uncoupled case. In this case, the identified discrete time system matrices are presented in Table 4 while the diagonal entries of the matrix $\mathcal{T}$ are $\mathrm{diag}(\mathcal{T})=(0.256 \pm j4.218,\ 0.479 \mp j16.492,\ 9.980 \mp j0.754)$. The complex eigen-

Table 8 Mass, damping, and stiffness matrices for the truss system of Fig. 2. Only the unrestrained degrees-of-freedom are included in these matrices, and the order of the degrees-of-freedom are chosen as u_1, v_1, u_2 v_2, u_3, v_3, u_4, v_4.

Mass							
100	0	0	0	0	0	0	0
0	100	0.	0	0	0	0	0
0	0	100	0	0	0	0	0
0	0	0	100	0	0	0	0
0	0	0	0	100	0	0	0
0	0	0	0	0	100	0	0
0	0	0	0	0	0	100	0
0	0	0	0	0	0	0	100
Damping							
136.4	0.0	0.0	0.0	-50.0	0.0	-17.7	-17.7
0.0	86.4	0.0	-50.0	0.0	0.0	-17.7	-17.7
0.0	0.0	136.4	0.0	-17.7	17.7	-50.0	0.0
0.0	-50.0	0.0	86.4	17.7	-17.7	0.0	0.0
-50.0	0.0	-17.7	17.7	136.4	0.0	0.0	0.0
0.0	0.0	17.7	-17.7	0.0	86.4	0.0	-50.0
-17.7	-17.7	-50.0	0.0	0.0	0.0	136.4	0.0
-17.7	-17.7	0.0	0.0	0.0	-50.0	0.0	86.4
Stiffness							
27071.1	0.0	0.0	0.0	-10000.0	0.0	-3535.5	-3535.5
0.0	17071.1	0.0	-10000.0	0.0	0.0	-3535.5	-3535.5
0.0	0.0	27071.1	0.0	-3535.5	3535.5	-10000.0	0.0
0.0	-10000.0	0.0	17071.1	3535.5	-3535.5	0.0	0.0
-10000.0	0.0	-3535.5	3535.5	27071.1	0.0	0.0	0.0
0.0	0.0	3535.5	-3535.5	0.0	17071.1	0.0	-10000.0
-3535.5	-3535.5	-10000.0	0.0	0.0	0.0	27071.1	0.0
-3535.5	-3535.5	0.0	0.0	0.0	-10000.0	0.0	17071.1

Table 9 Properly scaled complex mode shapes (amplified by a factor of 100 for presentation) for the truss system of Fig. 2 identified with five sensors and four actuators via the proposed approach. Note that all the eigenvectors appear in complex conjugate pairs.

ψ_1, ψ_1^*	ψ_2, ψ_2^*	ψ_3, ψ_3^*	ψ_4, ψ_4^*
$-0.122 \mp -0.122j$	$-0.243 \mp -0.243j$	$-0.714 \mp -0.714j$	$0.621 \pm 0.621j$
$-1.050 \mp -1.050j$	$0.764 \pm 0.764j$	$-0.227 \mp -0.227j$	$0.197 \pm 0.197j$
$0.122 \pm 0.122j$	$0.243 \pm 0.243j$	$-0.714 \mp -0.714j$	$-0.621 \mp -0.621j$
$-1.050 \mp -1.050j$	$0.764 \pm 0.764j$	$0.227 \pm 0.227j$	$0.197 \pm 0.197j$
$0.122 \pm 0.122j$	$-0.243 \mp -0.243j$	$-0.714 \mp -0.714j$	$0.621 \pm 0.621j$
$-1.050 \mp -1.050j$	$-0.764 \mp -0.764j$	$0.227 \pm 0.227j$	$-0.197 \mp -0.197j$
$-0.122 \mp -0.122j$	$0.243 \pm 0.243j$	$-0.714 \mp -0.714j$	$-0.621 \mp -0.621j$
$-1.050 \mp -1.050j$	$-0.764 \mp -0.764j$	$-0.227 \mp -0.227j$	$-0.197 \mp -0.197j$
ψ_5, ψ_5^*	ψ_6, ψ_6^*	ψ_7, ψ_7^*	ψ_8, ψ_8^*
$0.191 \pm 0.191j$	$0.183 \pm 0.183j$	$-0.579 \mp -0.579j$	$-0.527 \mp -0.527j$
$-0.601 \mp -0.601j$	$-0.575 \mp -0.575j$	$0.067 \pm 0.067j$	$-0.168 \mp -0.168j$
$0.191 \pm 0.191j$	$0.183 \pm 0.183j$	$0.579 \pm 0.579j$	$-0.527 \mp -0.527j$
$0.601 \pm 0.601j$	$0.575 \pm 0.575j$	$0.067 \pm 0.067j$	$0.168 \pm 0.168j$
$0.191 \pm 0.191j$	$-0.183 \mp -0.183j$	$0.579 \pm 0.579j$	$0.527 \pm 0.527j$
$0.601 \pm 0.601j$	$-0.575 \mp -0.575j$	$0.067 \pm 0.067j$	$-0.168 \mp -0.168j$
$0.191 \pm 0.191j$	$-0.183 \mp -0.183j$	$-0.579 \mp -0.579j$	$0.527 \pm 0.527j$
$-0.601 \mp -0.601j$	$0.575 \pm 0.575j$	$0.067 \pm 0.067j$	$0.168 \pm 0.168j$

vector matrix $\boldsymbol{\psi}$ still has the same structure as in the previous case but now the identified complex eigenvectors $\boldsymbol{\psi}_1$, $\boldsymbol{\psi}_2$, and $\boldsymbol{\psi}_3$ are

$$\boldsymbol{\psi}_1 = \begin{bmatrix} 0.166 + j\ \ 0.154 \\ 0.266 + j\ \ 0.284 \\ 0.207 + j\ \ 0.171 \end{bmatrix}; \quad \boldsymbol{\psi}_2 = \begin{bmatrix} 0.127 + j\ \ 0.088 \\ -0.161 - j\ \ 0.120 \\ 0.251 + j\ \ 0.296 \end{bmatrix};$$

$$\boldsymbol{\psi}_3 = \begin{bmatrix} -0.327 - j\ \ 0.345 \\ 0.018 + j\ \ 0.045 \\ 0.139 + j\ \ 0.0093 \end{bmatrix}.$$

It is important to see that, since the system is not proportionally damped, the relation between the real and imaginary parts (that they are equal in magnitude in a proportionally damped system) is not valid anymore. However, this makes no difference on the rest of the procedure, and the identified physical parameters are

$$\mathcal{M} = \begin{bmatrix} 0.8 & 0 & 0 \\ 0 & 2.0 & 0 \\ 0 & 0 & 1.2 \end{bmatrix}; \quad \mathcal{K} = \begin{bmatrix} 4.0 & -1.0 & -1.0 \\ -1.0 & 4.0 & -1.0 \\ -1.0 & -1.0 & 4.0 \end{bmatrix};$$

$$\mathcal{L} = \begin{bmatrix} 0.5 & -0.1 & -0.2 \\ -0.1 & 0.7 & -0.3 \\ -0.2 & -0.3 & 0.6 \end{bmatrix}$$

which are identical to the initial second-order matrices.

5.3 Effects of Noise on Identified Parameters. In order to discuss, in a statistically meaningful framework, the effects of noise perturbations on the proposed approach, we perform Monte Carlo type simulations on the 3-degree-of-freedom system with nonproportional damping. Here we assume that a long duration pulse response data in the form of acceleration measurements is available at the second and the third masses, and that the response of the structure is due to unit pulses applied at degrees-of-freedom 1 and 2 only. The output data is then polluted with Gaussian, zero-mean, white noise sequences, whose root-mean-squared (RMS) values are adjusted to be 5% of the unpolluted time histories. We consider 200 different noise patterns, and each of the polluted time histories are used to identify a discrete time state-space model with ERA.

Tables 5, 6, and 7 concisely summarize the results of this study. It can be seen in Table 5 that the mean values of the identified samples are very close to the exact values; indeed Table 6 reveals that the maximum relative error (in the absolute value sense) in the identified mean values is about 1%. In addition, the coefficients of variation presented in Table 7 show that the scatters around the mean values for the mass and stiffness estimates are quite acceptable, especially for the degree-of-freedom with the co-located sensor–actuator pair (degree-of-freedom 2). The coefficients for the damping matrix, however, are generally larger than those of the mass and stiffness matrices. This could partially be attributed to the high sensitivity of the damping to the phase relations between the mode shape components which generically makes the identification of the damping matrix a harder task than the identification of the mass and stiffness matrices. Overall the results show that the proposed methodology provides extremely satisfactory results even in the presence of noise perturbations.

5.4 Identification of a Truss Structure. In order to present the applicability of the proposed methodology to a more complex case, we now consider a two-dimensional truss structure with limited number of sensors and actuators. This system, shown in Fig. 2, has a total number of eight nodes of which four are fully restrained, and hence the total number of active degrees-of-freedom

Table 10 Mass, damping, and stiffness matrices for the truss system of Fig. 2 identified with five sensors and four actuators via the proposed approach

Mass							
100	0	0	0	0	0	0	0
0	100	0	0	0	0	0	0
0	0	100	0	0	0	0	0
0	0	0	100	0	0	0	0
0	0	0	0	100	0	0	0
0	0	0	0	0	100	0	0
0	0	0	0	0	0	100	0
0	0	0	0	0	0	0	100
Damping							
136.4	0.0	0.0	0.0	-50.0	0.0	-17.7	-17.7
0.0	86.4	0.0	-50.0	0.0	0.0	-17.7	-17.7
0.0	0.0	136.4	0.0	-17.7	17.7	-50.0	0.0
0.0	-50.0	0.0	86.4	17.7	-17.7	0.0	0.0
-50.0	0.0	-17.7	17.7	136.4	0.0	0.0	0.0
0.0	0.0	17.7	-17.7	0.0	86.4	0.0	-50.0
-17.7	-17.7	-50.0	0.0	0.0	0.0	136.4	0.0
-17.7	-17.7	0.0	0.0	0.0	-50.0	0.0	86.4
Stiffness							
27071.1	0.0	0.0	0.0	-10000.0	0.0	-3535.5	-3535.5
0.0	17071.1	0.0	-10000.0	0.0	0.0	-3535.5	-3535.5
0.0	0.0	27071.1	0.0	-3535.5	3535.5	-10000.0	0.0
0.0	-10000.0	0.0	17071.1	3535.5	-3535.5	0.0	0.0
-10000.0	0.0	-3535.5	3535.5	27071.1	0.0	0.0	0.0
0.0	0.0	3535.5	-3535.5	0.0	17071.1	0.0	-10000.0
-3535.5	-3535.5	-10000.0	0.0	0.0	0.0	27071.1	0.0
-3535.5	-3535.5	0.0	0.0	0.0	-10000.0	0.0	17071.1

is 8 (one horizontal and one vertical per each node). The horizontal degrees-of-freedom are denoted by u_i and the vertical degrees-of-freedom are denoted by v_i, with the subscript referring to the node number (i.e., $i=1,2,3,4$). The mass, damping, and stiffness matrices for this system are presented in Table 8. Note that these second-order matrices contain the coefficients for only the unrestrained degrees-of-freedom and that these degrees-of-freedom are ordered such that the displacement vector can be written as $\mathbf{q}(t)=[u_1(t)v_1(t)\ \ldots\ u_4(t)v_4(t)]^T$.

The instrument scheme we consider is such that there are five output sensors and four actuators: u_1, v_1, v_2, v_3, and v_4 are instrumented with output sensors, the forces $f_2^u(t)$ and $f_3^u(t)$, are applied horizontally at degrees-of-freedom 2 and 3, whereas the other two, denoted by $f_1^v(t)$ and $f_4^v(t)$ are applied vertically at degrees-of-freedom 1 and 4, such that the force vector may be defined as $\mathbf{u}(t)=[f_1^v(t)f_2^u(t)f_3^u(t)f_4^v(t)]^T$. In this case the initial discrete time state-space model is identified from unpolluted general input/output data using the OKID/ERA approach.

The co-location requirement for this case can be written as $\mathcal{C}_p^E(2,:)\boldsymbol{\psi}=(\boldsymbol{\psi}^T\mathcal{B}^E(:,2))^T$, or equivalently

$$\mathbf{C}_C^E(2,:)\boldsymbol{\varphi}=(\boldsymbol{\varphi}^{-1}\mathbf{B}_C^E(:,2))^T\boldsymbol{\mathcal{T}}^2. \tag{23}$$

Once the transformation matrix is evaluated from Eq. (23), the rows of the eigenvector matrix $\boldsymbol{\psi}$ can be identified either from

$$\boldsymbol{\psi}(i,:)=\mathbf{C}_C^E(i,:)\boldsymbol{\varphi}\boldsymbol{\mathcal{T}}^{-1}\quad\text{for}\quad i=1,2,4,6,7 \tag{24}$$

for the rows corresponding to the degrees-of-freedom with output sensors, or from

$$\boldsymbol{\psi}(i,:)=(\boldsymbol{\mathcal{T}}\boldsymbol{\varphi}^{-1}\mathbf{B}_C^E(:,i))^T\quad\text{for}\quad i=2,3,5,8 \tag{25}$$

for the rows corresponding to the degrees-of-freedom with actuators (note that the row corresponding to v_1 can be identified from either (24) or (25) due to the co-location). Since all degrees-of-freedom of this structure are instrumented with either a sensor or an actuator, all the rows of the matrix $\boldsymbol{\psi}$ can be identified, and these eigenvectors are presented in Table 9. Analogous to the case of the 3-degrees-of-freedom system with proportional damping, also in this case the real and imaginary parts of the eigenvectors are equal to each other in magnitude since the damping matrix of the truss structure was constructed so as to lead to a classical damping case.

Using the identified complex eigenvector matrix ψ, the mass, damping, and stiffness matrices can once again be constructed via Eqs. (18), and these are presented in Table 10. All the identified quantities are exactly equal to those reported in Table 8 and so the proposed methodology has once again provided an exact solution.

6 Conclusions

In this study, a new methodology for the identification of second-order structural parameters from identified state-space representations was presented. It was shown that, with the formulation developed herein, it is possible to formulate the inverse problem as a problem of transforming the identified complex eigenvectors to a certain basis. The requirements for a successful transformation are that there should be a co-located sensor–actuator pair, and that all the degrees-of-freedom should contain *either* a sensor *or* an actuator. The numerical results included in this study emphasize the efficiency and generality of the proposed approach.

The main innovation in this study is that, with the proposed methodology, it is possible to utilize mixed types of information, thereby enabling one to treat the information from a sensor or an actuator in an analogous fashion. This conceptual "input–output equivalence" helps relaxing the necessity of having either a full set of sensors or a full set of actuators, allowing a more general sensor–actuator setup than those required in previously discussed approaches.

Acknowledgments

This research has been sponsored through a research grant by the National Science Foundation (CMS-9457305), whose support has been greatly appreciated.

References

[1] Agbabian, M. S., Masri, S. F., Miller, R. K., and Caughey, T. K., 1991, "System Identification Approach to Detection of Structural Changes," J. Eng. Mech., **117**(2), pp. 370–390.

[2] Smyth, A. W., Masri, S. F., Caughey, T. K., and Hunter, N. F., 2000, "Surveillance of Intricate Mechanical Systems on the Basis of Vibration Signature Analysis," ASME J. Appl. Mech., **67**(3), pp. 540–551.

[3] Ewins, D. J., 1984, *Modal Testing: Theory and Practice* Research Studies Press, Letchworth UK.

[4] Mottershead, J. E., and Friswell, M. I., 1993, "Model Updating in Structural Dynamics: A Survey," J. Sound Vib., **165**(2), pp. 347–375.

[5] Berman, A., 1979, "Mass Matrix Correction Using an Incomplete Set of Measured Modes," AIAA J., **17**(10), pp. 1147–1148.

[6] Baruch, M., 1982, "Optimal Correction of Mass and Stiffness Matrices Using Measured Modes," AIAA J., **20**(11), pp. 1623–1626.

[7] Baruch, M., 1997, "Modal Data are Insufficient for Identification of Both Mass and Stiffness Matrices," AIAA J., **35**(11), pp. 1797–1798.

[8] Beck, J. L., and Katafygiotis, L. S., 1998, "Updating Models and Their Uncertainties. I: Bayesian Statistical Framework," J. Eng. Mech., **124**(4), pp. 455–461.

[9] Ibrahim, S. R., and Mikulcik, E. C., 1997, "A Method for the Direct Identification of Vibration Parameters From the Free Response," Shock Vib. Bull., **47**, Part 4, pp. 183–198.

[10] Ibrahim, S. R., 1977, "Random Decrement Technique for Modal Identification of Structures," J. Spacecr. Rockets, **14**(11), pp. 696–700.

[11] Vold, H., Kundrat, J., Rocklin, G. T., and Russell, R., 1982, "A Multiple-Input Modal Estimation Algorithm for Mini Computers," SAE Trans., **91**(1), pp. 815–821.

[12] Juang, J. N., and Pappa, R. S., 1985, "An Eigensystem Realization Algorithm for Modal Parameter Identification and Model Reduction," J. Guid. Control Dyn., **8**(5), pp. 620–627.

[13] Juang, J. N., Cooper, J. E., and Wright, J. R., 1988, ''An Eigensystem Realization Algorithm Using Data Correlations (ERA/DC) for Modal Parameter Identification,'' Cont. Theor. Adv. Technol., **4**(1), pp. 5–14.

[14] Juang, J. N., Phan, M., Horta, L. G., and Longman, R. W., 1993, ''Identification of Observer/Kalman Filter Markov Parameters: Theory and Experiments,'' J. Guid. Control Dyn., **16**(2), pp. 320–329.

[15] Luş, H., Betti, R., and Longman, R. W., 1999, ''Identification of Linear Structural Systems Using Earthquake-Induced Vibration Data,'' Earthquake Eng. Struct. Dyn., **28**, pp. 1449–1467.

[16] Luş, H., Betti, R., and Longman, R. W., 2002, ''Obtaining Refined First-Order Predictive Models of Linear Structural Systems,''Earthquake Eng. Struct. Dyn., **31**, pp. 1413–1440.

[17] Sestieri, A., and Ibrahim, S. R., 1994, ''Analysis of Errors and Approximations in the Use of Modal Coordinates,'' J. Sound Vib., **177**(2), pp. 145–157.

[18] Imregun, M., and Ewins, D. J., 1993, ''Realization of Complex Modeshapes,'' *Proceedings of the 11th International Modal Analysis Conference*, Society for Experimental Mechanics, Bethel, CT, pp. 1303–1309.

[19] Ibrahim, S. R., 1983, ''Computation of Normal Modes From Identified Complex Modes,'' AIAA J., **21**(3), pp. 446–451.

[20] Alvin, K. F., 1993, ''Second-Order Structural Identification Via State Space Based System Realizations,'' Ph.D. Thesis, University of Colorado, Boulder, Co.

[21] Alvin, K. F., and Park, K. C., 1994, ''Second-Order Structural Identification Procedure Via State-Space-Based System Identification,'' AIAA J., **32**(2), pp. 397–406.

[22] Zhang, Q., and Lallement, G., 1987, ''Comparison of Normal Eigenmodes Calculation Methods Based on Identified Complex Eigenmodes,'' J. Spacecr. Rockets, **24**, pp. 69–73.

[23] Yang, C. D., and Yeh, F. B., 1990, ''Identification, Reduction, and Refinement of Model Parameters by the Eigensystem Realization Algorithm,'' J. Guid. Control Dyn., **13**(6), pp. 1051–1059.

[24] Alvin, K. F., Peterson, L. D., and Park, K. C., 1995, ''Method for Determining Minimum—Order Mass and Stiffness Matrices From Modal Test Data,'' AIAA J., **33**(1), pp. 128–135.

[25] Tseng, D.-H., Longman, R. W., and Juang, J. N., 1994, ''Identification of Gyroscopic and Nongyroscopic Second Order Mechanical Systems Including Repeated Problems,'' Adv. Astronaut. Sci., **87**, pp. 145–165.

[26] Tseng, D.-H., Longman, R. W., and Juang, J. N., 1994, ''Identification of the Structure of the Damping Matrix in Second Order Mechanical Systems,'' Adv. Astronaut. Sci., **87**, pp. 166–190.

[27] Chen, S. Y., Ju, M. S., and Tsuei, Y. G., 1996, ''Extraction of Normal Modes for Highly Coupled Incomplete Systems With General Damping,'' Mech. Syst. Signal Process., **10**(1), pp. 93–106.

[28] Balmès, E., 1997, ''New Results on the Identification of Normal Modes From Experimental Complex Modes,'' Mech. Syst. Signal Process., **11**(2), pp. 229–243.

[29] Luş, H. 2001, ''Control Theory Based System Identification,'' Ph.D. Thesis, Columbia University, New York.

[30] Koh, C. G., and See, L. M., 1993, ''Identification and Uncertainty Estimation of Structural Parameters,'' J. Eng. Mech., **120**(6), pp. 1219–1236.

Analysis of a Three-Dimensional Crack Terminating at an Interface Using a Hypersingular Integral Equation Method

T. Y. Qin
College of Engineering Science,
China Agricultural University,
Beijing 100083, P. R. China
e-mail: mech@maile.cau.edu.cn

N. A. Noda
Department of Mechanical Engineering,
Kyushu Institute of Technology,
Kitakyushu 804-8550, Japan

Using a body force method and the finite-part integral concepts, a set of hypersingular integral equations for a vertical crack terminating at an interface in a three-dimensional infinite bimaterial subjected to arbitrary loads are derived. The stress singularity orders and singular stress fields around the crack front terminating at the interface are obtained by the main-part analytical method of hypersingular integral equations. Then, a numerical method for the solution of the hypersingular integral equations in case of a rectangular crack is proposed, in which the crack displacement discontinuities are approximated by the product of basic density functions and polynomials. Numerical solutions for the stress intensity factors of some examples are given. [DOI: 10.1115/1.1488938]

1 Introduction

In recent decades, the use of new materials has been increasing in a wide range of engineering fields and the accurate evaluation of interface strength in dissimilar materials has become very important. Considerable research has been done to evaluate the stress intensity factors and crack-opening displacement for cracks in dissimilar materials ([1–4]). However, most of these works are on two-dimensional cases. Due to the mathematical difficulties, there are not any analytical methods for three-dimensional crack problems. However, several numerical methods are available ([5–8]). Lee and Keer [3] evaluated the stress intensity factors of a crack meeting the interface by a body force method, but they didn't give the singular stress field, and consider the singularity near the crack front at the interface in their numerical method. Noda et al. [9] studied mixed-mode stress intensity factors of an inclined semi-elliptical surface crack by a body force method, in which the unknown body force densities were approximated by the products of fundamental density functions and polynomials. This numerical method was applied by Wang and Noda [10] to investigate the stress intensity factors of a three-dimensional rectangular crack using the body force method.

In the present paper, the hypersingular integral equation method based on the body force method is applied to solve the problem of a three-dimensional vertical crack terminating at an interface, and the stress singularities and singular stress field around the crack front terminating at the interface are obtained by the main-part analytical method of singular integral equations. Based on these theoretical solutions, the numerical approach suggested by Noda and Kobayashi [9] will be used to obtain highly reliable numerical results of stress intensity factors.

2 General Solutions and the Hypersingular Integral Equation for a Planar Crack Meeting the Bimaterial Interface

A fixed rectangular Cartesian system x_i $(i=1,2,3)$ is used. Consider two dissimilar half-spaces bonded together along the x_1-x_3–plane. Suppose that the right half-space (x_2-plane) is occupied by an elastic medium with elastic constants (μ_1,ν_1) and the left half-space ($-x_2$-plane) is occupied by an elastic medium with elastic constants (μ_2,ν_2). The crack is assumed to be in a plane normal to the x_3-axis (Fig. 1). Based on the body force method ([3]), the displacements at a point $\mathbf{x}$ in the materials can be expressed as

$$u_k(\mathbf{x})=\int_S T_{ki}(\mathbf{x},\boldsymbol{\xi})\tilde{u}_i(\boldsymbol{\xi})ds(\boldsymbol{\xi}) \quad i,k=1,2,3 \tag{1}$$

where $\tilde{u}_i=u_i^+-u_i^-$ is the ith displacement discontinuity of the crack surface, and

$$T_{ki}(\mathbf{x},\boldsymbol{\xi})=\left\{\frac{2\mu_1\nu_1}{1-2\nu_1}\frac{\partial G_{kj}(\mathbf{x},\boldsymbol{\xi})}{\partial \xi_j}\delta_{3i}+\mu_1 \times\left[\frac{\partial G_{ki}(\mathbf{x},\boldsymbol{\xi})}{\partial \xi_3}+\frac{\partial G_{k3}(\mathbf{x},\boldsymbol{\xi})}{\partial \xi_i}\right]\right\}_{\xi_3=0} \quad j=1,2,3 \tag{2}$$

in which $G_{ij}(\mathbf{x},\boldsymbol{\xi})$ is the Green's function ([3,11]), which represents the x_i-direction displacement at point $\mathbf{x}$ produced by a unit load applied at point $\boldsymbol{\xi}$ in the x_j-direction. Then, the corresponding stress field can be obtained by use of the constitutive relations. The stresses at a point $\mathbf{x}$ outside of crack surface S are written as follows:

$$\sigma_{ij}(\mathbf{x})=\int_S S_{kij}(\mathbf{x},\boldsymbol{\xi})\tilde{u}_k(\boldsymbol{\xi})ds(\boldsymbol{\xi}) \tag{3}$$

where

$$S_{kij}(\mathbf{x},\boldsymbol{\xi})=\frac{2\mu_1\nu_1}{1-2\nu_1}\frac{\partial T_{lk}(\mathbf{x},\boldsymbol{\xi})}{\partial x_l}\delta_{ij}+\mu_1 \times\left[\frac{\partial T_{ik}(\mathbf{x},\boldsymbol{\xi})}{\partial x_j}+\frac{\partial T_{jk}(\mathbf{x},\boldsymbol{\xi})}{\partial x_i}\right] \quad l=1,2,3. \tag{4}$$

The traction boundary conditions of the crack surface are

$$\sigma_{3i}^+(\mathbf{x})=-p_i(\mathbf{x}) \quad \mathbf{x}\in S. \tag{5}$$

Contributed by the Applied Mechanics Division of THE AMERICAN SOCIETY OF MECHANICAL ENGINEERS for publication in the ASME JOURNAL OF APPLIED MECHANICS. Manuscript received by the Applied Mechanics Division, June 20, 2001; final revision, November 5, 2001. Associate Editor: J. R. Barber. Discussion on the paper should be addressed to the Editor, Prof. Robert M. McMeeking, Chair, Department of Mechanics and Environmental Engineering, University of California–Santa Barbara, Santa Barbara, CA 93106-5070, and will be accepted until four months after final publication in the paper itself in the ASME JOURNAL OF APPLIED MECHANICS.

Here the superscript + refers to the upper surface of the crack, and $p_i(\mathbf{x})$ represents the loading on the crack surface due to internal pressure or external loading, and it can obtained from the solution for the loading of the uncracked solid. Using boundary condition (5) and the finite-part integral concepts, the hypersingular integral equations for unknown displacement discontinuities can be obtained:

$$\frac{\mu_1}{\pi(\kappa_1+1)} \fint_S \left[\frac{\kappa_1-1}{2r_1^3}\delta_{\alpha\beta}+\frac{3(3-\kappa_1)}{4r_1^3}r_{1,\alpha}r_{1,\beta} + K_{\alpha\beta}(\mathbf{x},\boldsymbol{\xi})\right]\tilde{u}_\beta(\boldsymbol{\xi})ds(\boldsymbol{\xi})=-p_\alpha(\mathbf{x}) \quad \alpha,\beta=1,2 \quad \mathbf{x}\in S \tag{6}$$

$$\frac{\mu_1}{\pi(\kappa_1+1)} \fint_S \left[\frac{1}{r_1^3}+K_0(\mathbf{x},\boldsymbol{\xi})\right]\tilde{u}_3(\boldsymbol{\xi})ds(\boldsymbol{\xi})=-p_3(\mathbf{x}) \quad \mathbf{x}\in S \tag{7}$$

where $\fint$ is the symbol of the finite-part integral, r_1 is the distance from point $\mathbf{x}(x_1,x_2,0)$ to point $\boldsymbol{\xi}(\xi_1,\xi_2,0)$, r_2 is the distance from point $\mathbf{x}(x_1,x_2,0)$ to a symmetric point $(\xi_1,-\xi_2,0)$ of point $\boldsymbol{\xi}$, and

$$K_{11}(\mathbf{x},\boldsymbol{\xi})=\frac{2A\kappa_1(\kappa_1+6)+2B-5C}{4r_2^3}-\frac{24Ax_2\xi_2}{r_2^5} - \frac{3(4A\kappa_1-C)(x_2+\xi_2)^2}{4r_2^5}+\frac{30Ax_2\xi_2(x_2+\xi_2)^2}{r_2^7} - \frac{3(2A\kappa_1+A\kappa_1^2+B-2C)}{2r_2r_3^2} \tag{8}$$

$$K_{12}(\mathbf{x},\boldsymbol{\xi})=(x_1-\xi_1)\left[\frac{3C(x_2+\xi_2)}{4r_2^5}+\frac{30Ax_2\xi_2(x_2+\xi_2)}{r_2^7} + \frac{3A(\kappa_1-1)x_2}{r_2^5}+\frac{1}{2}(A\kappa_1+B-C) \times\left(\frac{1}{r_2^2r_3^2}+\frac{1}{r_2^3r_3}\right)\right] \tag{9}$$

$$K_{21}(\mathbf{x},\boldsymbol{\xi})=(x_1-\xi_1) \times\left[\frac{3(4A+4A\kappa_1-C)(x_2+\xi_2)}{4r_2^5}+\frac{3A(\kappa_1-1)x_2}{r_2^5} - \frac{30Ax_2\xi_2(x_2+\xi_2)}{r_2^7}-\frac{1}{2}(A\kappa_1+B-C) \times\left(\frac{1}{r_2^2r_3^2}+\frac{1}{r_2^3r_3}\right)\right] \tag{10}$$

$$K_{22}(\mathbf{x},\boldsymbol{\xi})=\frac{A+B-C}{2r_2^3}+\frac{3(C-4A)(x_2+\xi_2)^2}{4r_2^5}+\frac{24Ax_2\xi_2}{r_2^5} - \frac{30Ax_2\xi_2(x_1-\xi_1)^2}{r_2^7} \tag{11}$$

$$K_0(\mathbf{x},\boldsymbol{\xi})=\frac{2C-3A(\kappa_1^2-2\kappa_1+3)}{2r_2^3} + \frac{3A[12x_2\xi_2-(3-\kappa_1)(\kappa_1-1)(x_2+\xi_2)^2]}{2r_2^5} + \frac{3(2A\kappa_1+A\kappa_1^2+B-2C)}{2r_2r_3^2} \tag{12}$$

and

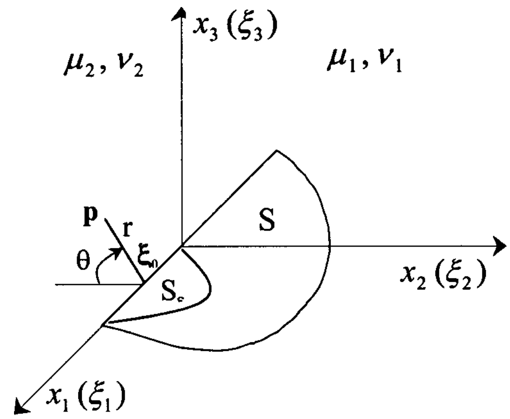

Fig. 1 Problem configuration

$$r_1=\sqrt{(x_1-\xi_1)^2+(x_2-\xi_2)^2}, \quad r_2=\sqrt{(x_1-\xi_1)^2+(x_2+\xi_2)^2},$$

$$r_3=r_2+x_2+\xi_2,$$

$$r_{1,\alpha}=(\xi_\alpha-x_\alpha)/r_1, \quad A=(\mu_1-\mu_2)/(\mu_1+\kappa_1\mu_2),$$

$$B=(\kappa_2\mu_1-\kappa_1\mu_2)/(\mu_2+\kappa_2\mu_1).$$

$$S=(\mu_1-\mu_2)/(\mu_1+\mu_2), \quad C=S(\kappa_1+1),$$

$$\kappa_1=3-4\nu_1, \quad \kappa_2=3-4\nu_2.$$

Equation (7) is the same as that given by Lee and Keer [3].

3 Stress Singularity Near the Crack Front at the Interface

According to the elastic theory [12], the displacement discontinuities of the crack surface near a point $\boldsymbol{\xi}_0$ at the interface can be assumed as

$$\tilde{u}_k(\boldsymbol{\xi})=D_k(\boldsymbol{\xi}_0)\xi_2^{\lambda_k} \quad 0<\mathrm{Re}(\lambda_k)<1 \quad k=1,2,3 \tag{13}$$

where $D_k(\boldsymbol{\xi}_0)$ is a nonzero constant related to point $\boldsymbol{\xi}_0$, and λ_k is the stress singular index near the crack front meeting the interface. Consider a small semicircle domain S_ε on the crack surface including point $\boldsymbol{\xi}_0$ as shown in Fig. 1. Let $t=\xi_2/x_2$, $\eta=\xi_1/x_2$, $x_1=x_2\mathrm{ctg}\varphi$, and $x_2\to 0$, and using the main-part analytical method ([12,13]), the following relations can be derived:

$$\fint_{S_\epsilon} \frac{\tilde{u}_1}{r_1^3}d\xi_1 d\xi_2=D_1(\boldsymbol{\xi}_0)x_2^{\lambda_1-1}\fint_0^\infty t^{\lambda_1}dt \times\int_{-\infty}^{\infty}\frac{d\eta}{[(\eta-\mathrm{ctg}\varphi)^2+(1-t)^2]^{3/2}} \cong -2\pi\lambda_1 D_1(\boldsymbol{\xi}_0)x_2^{\lambda_1-1}\cot(\lambda_1\pi) \tag{14}$$

$$\fint_{S_\epsilon} \frac{(x_1-\xi_1)^2}{r_1^5}\tilde{u}_1 d\xi_1 d\xi_2 \cong -\frac{2}{3}\pi\lambda_1 D_1(\boldsymbol{\xi}_0)x_2^{\lambda_1-1}\cot(\lambda_1\pi) \tag{15}$$

$$\int_{S_\varepsilon}\frac{\tilde{u}_2}{r_2^3}d\xi_1 d\xi_2 \cong 2\pi\lambda_2 D_2(\boldsymbol{\xi}_0)x_2^{\lambda_2-1}\frac{1}{\sin(\lambda_2\pi)} \tag{16}$$

$$\int_{S_\varepsilon}\frac{x_2\xi_2}{r_2^5}\tilde{u}_2 d\xi_1 d\xi_2 \cong \frac{2}{9}\pi\lambda_2(1-\lambda_2^2)D_2(\boldsymbol{\xi}_0)x_2^{\lambda_2-1}\frac{1}{\sin(\lambda_2\pi)} \tag{17}$$

$$\int_{S_\varepsilon}\frac{(x_2+\xi_2)^2}{r_2^5}\tilde{u}_2 d\xi_1 d\xi_2 \cong \frac{4}{3}\pi\lambda_2 D_2(\boldsymbol{\xi}_0)x_2^{\lambda_2-1}\frac{1}{\sin(\lambda_2\pi)} \tag{18}$$

$$\int_{S_\varepsilon}\frac{x_2\xi_2(x_1-\xi_1)^2}{r_2^7}\tilde{u}_2 d\xi_1 d\xi_2 \cong \frac{8}{45}\pi\lambda_2(1-\lambda_2^2)D_2(\boldsymbol{\xi}_0)x_2^{\lambda_2-1}\frac{1}{\sin(\lambda_2\pi)} \tag{19}$$

$$\int_{S_\varepsilon}\frac{x_2\xi_2(x_2+\xi_2)^2}{r_2^7}\tilde{u}_1 d\xi_1 d\xi_2 \cong \frac{2}{45}\pi\lambda_1(1-\lambda_1^2)D_1(\boldsymbol{\xi}_0)x_2^{\lambda_1-1}\frac{1}{\sin(\lambda_1\pi)} \tag{20}$$

$$\int_{S_\varepsilon}\frac{\tilde{u}_3}{r_2 r_3^2}d\xi_1 d\xi_2 \cong \frac{2}{3}\pi\lambda_3 D_3(\boldsymbol{\xi}_0)x_2^{\lambda_3-1}\frac{1}{\sin(\lambda_3\pi)}. \tag{21}$$

Using the above relations, from Eqs. (6) and (7), the stress singular index can be obtained. It can be shown than $\lambda_2=\lambda_3=\lambda$, and

$$4A\lambda^2+2\cos(\lambda\pi)-A-B=0 \tag{22}$$

$$\cos(\lambda_1\pi)=S. \tag{23}$$

The characteristic Eq. (22) is coincident with that for the two-dimensional case ([1,4]), and (23) is coincident with that for the antiplane case ([2]). The stress intensity factors at the crack front on the interface are defined by

$$K_1=\lim_{r\to 0}\sigma_{33}(r,\theta)_{|\theta=0}(2r)^{1-\lambda} \tag{24}$$

$$K_{11}=\lim_{r\to 0}\sigma_{23}(r,\theta)_{|\theta=0}(2r)^{1-\lambda} \tag{25}$$

$$K_{111}=\lim_{r\to 0}\sigma_{13}(r,\theta)_{|\theta=0}(2r)^{1-\lambda_1}. \tag{26}$$

4 Singular Stress Field Near the Crack Front at the Interface

Based on relation (13), the singular stress field around the crack front terminating at the interface can be obtained by the main-part analytical method. For a point **p** near the crack front in the material 1, using following relations:

$$\int_{S_\varepsilon}\left(\frac{1}{r_1^3}+\frac{6x_3^2}{r_1^5}-\frac{15x_3^4}{r_1^7}\right)\tilde{u}_3 d\xi_1 d\xi_2 \cong \frac{2\pi\lambda(1-\lambda)D_3(\boldsymbol{\xi}_0)r^{\lambda-1}}{\sin(\lambda\pi)}\times\sin\theta\sin(2-\lambda)\theta \tag{27}$$

$$\int_{S_\varepsilon}\frac{\tilde{u}_3}{r_2^3}d\xi_1 d\xi_2 \cong \frac{2\pi D_3(\boldsymbol{\xi}_0)r^{\lambda-1}\sin\lambda(\pi-\theta)}{\sin(\lambda\pi)\sin\theta} \tag{28}$$

$$\int_{S_\varepsilon}\frac{(x_2+\xi_2)^2\tilde{u}_3}{r_2^5}d\xi_1 d\xi_2 \cong \frac{2\pi D_3(\boldsymbol{\xi}_0)r^{\lambda-1}}{3\sin(\lambda\pi)\sin\theta}[\sin\lambda(\pi-\theta) - \lambda\sin\theta\cos(\lambda\pi+\theta-\lambda\theta)] \tag{29}$$

$$\int_{S_\varepsilon}\left(\frac{12x_3^2}{r_2^5}-\frac{15x_3^4}{r_2^7}-\frac{15(x_2+\xi_2)^2x_3^2}{r_2^7}\right)\tilde{u}_3 d\xi_1 d\xi_2 \cong 0 \tag{30}$$

$$\int_{S_\varepsilon}\left(\frac{18x_2\xi_2}{r_2^5}-\frac{180x_2\xi_2x_3^2}{r_2^7}+\frac{210x_2\xi_2x_2^4}{r_2^9}\right)\tilde{u}_3 d\xi_1 d\xi_2 \cong \frac{4\pi\lambda(1-\lambda^2)D_3(\boldsymbol{\xi}_0)r^{\lambda-1}\cos\theta\cos(\lambda\pi+2\theta-\lambda\theta)}{\sin(\lambda\pi)} \tag{31}$$

$$\int_{S_\varepsilon}\left(\frac{3}{r_2 r_3^2}-\frac{6x_3^2}{r_2^3 r_3^2}-\frac{12x_3^2}{r_2^2 r_3^3}+\frac{6x_3^4}{r_2^3 r_3^4}+\frac{6x_3^4}{r_2^4 r_3^3}+\frac{3x_3^4}{r_2^5 r_3^2}\right)\tilde{u}_3 d\xi_1 d\xi_2 \cong -\frac{2\pi\lambda D_3(\boldsymbol{\xi}_0)r^{\lambda-1}\cos(\lambda\pi+\theta-\lambda\theta)}{\sin\lambda\pi} \tag{32}$$

$$\int_{S_\varepsilon}(x_2-\xi_2)x_3\left(\frac{3}{r_1^5}-\frac{15x_3^2}{r_1^7}\right)\tilde{u}_2 d\xi_1 d\xi_2 \cong -\frac{2\pi\lambda(1-\lambda)D_2(\boldsymbol{\xi}_0)r^{\lambda-1}}{\sin(\lambda\pi)}\sin\theta\cos(2-\lambda)\theta \tag{33}$$

$$\int_{S_\varepsilon}\frac{(x_2+\xi_2)x_3\tilde{u}_2}{r_2^5}d\xi_1 d\xi_2 \cong \frac{2\pi\lambda D_2(\boldsymbol{\xi}_0)r^{\lambda-1}}{3\sin(\lambda\pi)}\sin(\lambda\pi+\theta-\lambda\theta) \tag{34}$$

$$\int_{S_\varepsilon}\frac{x_2x_3\tilde{u}_2}{r_2^5}d\xi_1 d\xi_2 \cong -\frac{2\pi\lambda D_2(\boldsymbol{\xi}_0)r^{\lambda-1}\cos\theta}{3\sin(\lambda\pi)\sin^2\theta}[\sin(\lambda\pi-\lambda\theta) + \lambda\sin\theta\cos(\lambda\pi+\theta-\lambda\theta)] \tag{35}$$

$$\int_{S_\varepsilon}\frac{x_2x_3^3\tilde{u}_2}{r_2^7}d\xi_1 d\xi_2 \cong -\frac{2\pi\lambda D_2(\boldsymbol{\xi}_0)r^{\lambda-1}\cos\theta}{3\sin(\lambda\pi)\sin^2\theta}[3\sin\lambda(\pi-\lambda\theta) + 3\lambda\sin\theta\cos(\lambda\pi+\theta-\lambda\theta) + \lambda(1-\lambda)\sin^2\theta\sin(\lambda\pi+2\theta-\lambda\theta)] \tag{36}$$

$$\int_{S_\varepsilon}\frac{x_3(x_2+\xi_2)^3\tilde{u}_2}{r_2^7}d\xi_1 d\xi_2 \cong \frac{2\pi\lambda D_2(\boldsymbol{\xi}_0)r^{\lambda-1}}{15\sin(\lambda\pi)}[3\sin(\lambda\pi+\theta -\lambda\theta)+(1-\lambda)\sin\theta\cos(\lambda\pi+2\theta -\lambda\theta)] \tag{37}$$

$$\int_{S_\varepsilon}x_2\xi_2(x_2+\xi_2)x_3\left(\frac{90}{r_2^7}-\frac{210x_3^2}{r_2^9}\right)\tilde{u}_2 d\xi_1 d\xi_2 \cong \frac{4\pi\lambda(1-\lambda^2)D_2(\boldsymbol{\xi}_0)r^{\lambda-1}\cos\theta\sin(\lambda\pi+2\theta-\lambda\theta)}{\sin(\lambda\pi)} \tag{38}$$

$$\int_{S_\varepsilon}\frac{1}{2}x_3\left(\frac{3}{r_2^2 r_3^2}+\frac{3}{r_2^3 r_3}-\frac{2x_3^2}{r_2^3 r_3^3}-\frac{3x_3^2}{r_2^4 r_3^2}-\frac{3x_3^2}{r_2^5 r_3}\right)\tilde{u}_2 d\xi_1 d\xi_2 \cong -\frac{2\pi\lambda D_2(\boldsymbol{\xi}_0)r^{\lambda-1}\cos(\lambda\pi+\theta-\lambda\theta)}{\sin\lambda\pi} \tag{39}$$

here r_1 is the distance from point $\mathbf{p}(x_1,x_2,x_3)$ to point $\boldsymbol{\xi}(\xi_1,\xi_2,0)$ and r_2 is the distance from point $\mathbf{p}(x_1,x_2,x_3)$ to the symmetric point $(\xi_1,-\xi_2,0)$ of point $\boldsymbol{\xi}(\xi_1,\xi_2,0)$, e.g., $r_1=\sqrt{(x_1-\xi_1)^2+(x_2-\xi_2)^2+x_3^2}$, $r_2=\sqrt{(x_1-\xi_1)^2+(x_2+\xi_2)^2+x_3^2}$, $r_3=r_2+x_2+\xi_2$, from (3), the singular stress can be expressed by

$$\sigma_{33}^1(\mathbf{p})=\frac{\mu_1\lambda\omega D_3(\boldsymbol{\xi}_0)}{(1+\kappa_1)\sin(\lambda\pi)r^{1-\lambda}}f_{331}^1(\theta) + \frac{\mu_1\lambda\omega D_2(\boldsymbol{\xi}_0)}{(1+\kappa_1)\sin(\lambda\pi)r^{1-\lambda}}f_{332}^1(\theta) \quad \pi/2\leqslant|\theta|\leqslant\pi \tag{40}$$

$$f_{331}^1(\theta)=\frac{1}{\omega}\{2\cos(1-\lambda)\theta+2(1-\lambda)\sin\theta\sin(2-\lambda)\theta +[A(1-2\lambda)(2+\lambda)+B]\cos(\lambda\pi+\theta-\lambda\theta)+A(1-\lambda) \times(1-2\lambda)\cos(\lambda\pi+3\theta-\lambda\theta)\} \tag{41}$$

$$f_{332}^{1}(\theta)=\frac{1}{\omega}\{-2(1-\lambda)\sin\theta\cos(2-\lambda)\theta+[2A\kappa_1-3A+B+2A\gamma(1+\lambda)+2A(1-\lambda)(2+\lambda)]\sin(\lambda\pi+\theta-\lambda\theta)+2A(1-\lambda)(2+\gamma+\lambda)\sin(\lambda\pi+3\theta-\lambda\theta)\} \tag{42}$$

and here $\omega=[2-A-B-2\lambda(A-B)]$, $\gamma=(3-\kappa_1)/2(\kappa_1-1)$. The superscript 1 refers to the material 1 marked in Fig. 1.

For a point $\mathbf{p}$ near the crack front in the material 2, using the following relations:

$$\int_{S_\varepsilon}\left(\frac{1}{r_1^3}-\frac{3x_3^2}{r_1^5}\right)\tilde{u}_3 d\xi_1 d\xi_2\cong\frac{2\pi\lambda D_3(\boldsymbol{\xi}_0)r^{\lambda-1}}{\sin(\lambda\pi)}\cos(1-\lambda)\theta \tag{43}$$

$$\int_{S_\varepsilon}\frac{1}{2}x_3\left(\frac{3}{r_1^2r_4^2}+\frac{3}{r_1^3r_4}-\frac{2x_3^2}{r_1^3r_4^3}-\frac{3x_3^2}{r_1^4r_4^2}-\frac{3x_3^2}{r_1^5r_4}\right)\tilde{u}_2 d\xi_1 d\xi_2\cong\frac{2\pi\lambda D_2(\boldsymbol{\xi}_0)r^{\lambda-1}\sin(1-\lambda)\theta}{\sin\lambda\pi} \tag{44}$$

$$\int_{S_\varepsilon}\left[\frac{3}{r_1r_4^2}-\frac{6x_3^2}{r_1^3r_4^2}-\frac{12x_3^2}{r_1^2r_4^3}+\frac{6x_3^4}{r_1^3r_4^4}+\frac{6x_3^4}{r_1^4r_4^3}+\frac{3x_3^4}{r_1^5r_4^2}\right]\tilde{u}_3 d\xi_1 d\xi_2\cong\frac{2\pi\lambda D_3(\boldsymbol{\xi}_0)r^{\lambda-1}\cos(1-\lambda)\theta}{\sin\lambda\pi} \tag{45}$$

$$\int_{S_\varepsilon}\left[\frac{3}{r_1^3r_4}+\frac{3}{r_1^2r_4^2}-\frac{18x_3^2}{r_1^5r_4}-\frac{18x_3^2}{r_1^4r_4^2}-\frac{12x_3^2}{r_1^3r_4^3}+\frac{15x_3^4}{r_1^7r_4}+\frac{15x_3^4}{r_1^6r_4^2}+\frac{12x_3^4}{r_1^5r_4^3}+\frac{6x_3^4}{r_1^4r_4^4}\right]\tilde{u}_3 d\xi_1 d\xi_2\cong-\frac{\pi\lambda(1-\lambda)D_3(\boldsymbol{\xi}_0)r^{\lambda-1}}{\sin\lambda\pi}[\cos(1-\lambda)\theta+\cos(3-\lambda)\theta] \tag{46}$$

$$\int_{S_\varepsilon}\frac{(x_2-\xi_2)x_3\tilde{u}_2}{r_1^5}d\xi_1 d\xi_2\cong-\frac{2\pi\lambda D_2(\boldsymbol{\xi}_0)r^{\lambda-1}}{3\sin(\lambda\pi)}\sin(1-\lambda)\theta \tag{47}$$

$$\int_{S_\varepsilon}\frac{(x_2-\xi_2)x_3^3}{r_1^7}\tilde{u}_2 d\xi_1 d\xi_2\cong\frac{\pi\lambda D_2(\boldsymbol{\xi}_0)r^{\lambda-1}}{15\sin(\lambda\pi)}[-(3-\lambda)\sin(1-\lambda)\theta+(1-\lambda)\sin(3-\lambda)\theta] \tag{48}$$

$$\int_{S_\varepsilon}x_3\left(\frac{3}{r_1^2r_4^2}+\frac{3}{r_1^3r_4}-\frac{2x_3^2}{r_1^3r_4^3}-\frac{3x_3^2}{r_1^4r_4^2}-\frac{3x_3^2}{r_1^5r_4}\right)\tilde{u}_2 d\xi_1 d\xi_2\cong\frac{2\pi\lambda D_2(\boldsymbol{\xi}_0)r^{\lambda-1}\sin(1-\lambda)\theta}{\sin\lambda\pi} \tag{49}$$

where $r_4=r_2-x_2+\xi_2$, the singular stresses can be expressed by

$$\sigma_{13}^2(\mathbf{p})=-\frac{\mu_1\mu_2\lambda_1D_1(\boldsymbol{\xi}_0)}{(\mu_1+\mu_2)\sin(\lambda_1\pi)r^{1-\lambda_1}}\cos(1-\lambda_1)\theta \quad -\pi/2<\theta\leqslant\pi/2 \tag{50}$$

$$\sigma_{23}^2(\mathbf{p})=\frac{\mu_1\lambda\omega D_3(\boldsymbol{\xi}_0)}{(1+\kappa_1)\sin(\lambda\pi)r^{1-\lambda}}f_{231}^2(\theta)+\frac{\mu_1\lambda\omega D_2(\boldsymbol{\xi}_0)}{(1+\kappa_1)\sin(\lambda\pi)r^{1-\lambda}}f_{232}^2(\theta) \quad -\pi/2<\theta\leqslant\pi/2 \tag{51}$$

$$\sigma_{33}^2(\mathbf{p})=\frac{\mu_1\lambda\omega D_3(\boldsymbol{\xi}_0)}{(1+\kappa_1)\sin(\lambda\pi)r^{1-\lambda}}f_{331}^2(\theta)+\frac{\mu_1\lambda\omega D_2(\boldsymbol{\xi}_0)}{(1+\kappa_1)\sin(\lambda\pi)r^{1-\lambda}}f_{332}^2(\theta) \quad -\pi/2<\theta\leqslant\pi/2 \tag{52}$$

$$f_{231}^2(\theta)=\frac{1}{\omega}\{[\Gamma(\kappa_1+B)-(1-A)(\kappa_1-1)-\lambda(1-2A+B)]\sin(1-\lambda)\theta-(1-\lambda)(1-B)\sin(3-\lambda)\theta\} \tag{53}$$

$$f_{232}^2(\theta)=-\frac{1}{\omega}2(1-\lambda)(1-B)\sin\theta\sin(2-\lambda)\theta+\cos(1-\lambda)\theta \tag{54}$$

$$f_{331}^2(\theta)=-\frac{1}{\omega}2(1-\lambda)(B-1)\sin\theta\sin(2-\lambda)\theta+\cos(1-\lambda)\theta \tag{55}$$

$$f_{332}^2(\theta)=\frac{1}{\omega}[(A-2B+1+2A\lambda-B\lambda-\lambda)\sin(1-\lambda)\theta-(1-B)(1-\lambda)\sin(3-\lambda)\theta]. \tag{56}$$

Here the superscript 2 refers to the material 2 marked in Fig. 1. Other singular stresses near point $\boldsymbol{\xi}_0$ can also be obtained by use of the above method. Using definitions (24)–(26), relation (13) and solutions (50)–(52), the stress intensity factors at the crack front on the interface can be written as

$$K_{\mathrm{I}}=\frac{2^{1-\lambda}\mu_1\lambda\omega D_3(\boldsymbol{\xi}_0)}{(1+\kappa_1)\sin(\lambda\pi)}=\lim_{\xi_2\to0}\frac{2^{1-\lambda}\lambda\mu_1\omega\tilde{u}_3}{(\kappa_1+1)\sin\lambda\pi\xi_2^{\lambda}} \tag{57}$$

$$K_{\mathrm{II}}=\frac{2^{1-\lambda}\mu_1\lambda\omega D_2(\boldsymbol{\xi}_0)}{(1+\kappa_1)\sin(\lambda\pi)}=\lim_{\xi_2\to0}\frac{2^{1-\lambda}\lambda\mu_1\omega\tilde{u}_2}{(\kappa_1+1)\sin\lambda\pi\xi_2^{\lambda}} \tag{58}$$

$$K_{\mathrm{III}}=\frac{2^{1-\lambda_1}\mu_1\mu_2\lambda_1D_1(\boldsymbol{\xi}_0)}{(\mu_1+\mu_2)\sin(\lambda_1\pi)}=\lim_{\xi_2\to0}\frac{2^{1-\lambda_1}\mu_1\mu_2\tilde{u}_1}{(\mu_1+\mu_2)\sin(\lambda_1\pi)\xi_2^{\lambda_1}}. \tag{59}$$

Using relations (56)–(59), the singular stresses solutions (40), (50)–(52) are expressed:

$$\sigma_{33}^1=\frac{K_{\mathrm{I}}}{(2r)^{1-\lambda}}f_{331}^1(\theta)+\frac{K_{\mathrm{II}}}{(2r)^{1-\lambda}}f_{332}^1(\theta) \quad \pi/2\leqslant|\theta|\leqslant\pi \tag{60}$$

$$\sigma_{13}^2=-\frac{K_{\mathrm{III}}}{(2r)^{1-\lambda_1}}\cos(1-\lambda_1)\theta \quad -\pi/2<\theta\leqslant\pi/2 \tag{61}$$

$$\sigma_{23}^2=\frac{K_{\mathrm{I}}}{(2r)^{1-\lambda}}f_{231}^2(\theta)+\frac{K_{\mathrm{II}}}{(2r)^{1-\lambda}}f_{232}^2(\theta) \quad -\pi/2<\theta\leqslant\pi/2 \tag{62}$$

$$\sigma_{33}^2=\frac{K_{\mathrm{I}}}{(2r)^{1-\lambda}}f_{331}^2(\theta)+\frac{K_{\mathrm{II}}}{(2r)^{1-\lambda}}f_{332}^2(\theta) \quad -\pi/2<\theta\leqslant\pi/2. \tag{63}$$

In the case of homogeneity, solutions (60)–(63) are the same as that given by Tang and Qin [13].

5 Numerical Procedure

Consider a rectangular crack meeting the interface in a three-dimensional infinite elastic solid under a normal load as shown in Fig. 2. Using its known behavior near the crack front and the fundamental solutions, the crack-opening displacement can be written as

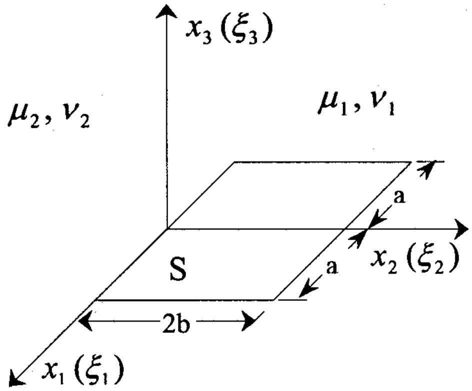

Fig. 2 A rectangular crack meeting the interface

$$\tilde{u}_3(\xi_1,\xi_2)=F_3(\xi_1,\xi_2)\xi_2^{\lambda}\sqrt{(a^2-\xi_1^2)(2b-\xi_2)}. \tag{64}$$

To numerically solve the unknown function $\tilde{u}_3$, the unknown function $F_i(\xi_1,\xi_2)$ is assumed as

$$F_3(\xi_1,\xi_2)=\sum_{n=1}^{N} a_{3n}G_n(\xi_1,\xi_2) \tag{65}$$

where a_{3n} is unknown constants $N=(K+1)(L+1)$, and

$$G_1(\xi_1,\xi_2)=1,\quad G_2(\xi_1,\xi_2)=\xi_1,\ \ldots,$$
$$G_{K+1}(\xi_1,\xi_2)=\xi_1^K,\quad G_{K+2}(\xi_1,\xi_2)=\xi_2,$$
$$G_{K+3}(\xi_1,\xi_2)=\xi_1\xi_2,\ \ldots,\quad G_{2K+2}(\xi_1,\xi_2)=\xi_1^K\xi_2,\ \ldots,$$
$$G_{(K+1)(L+1)}(\xi_1,\xi_2)=\xi_1^K\xi_2^L. \tag{66}$$

Substituting (64) and (65) into (7), a set of algebraic linear equations for unknown a_{3n} can be obtained:

$$\sum_{n=1}^{N} a_{3n}[I_{3n}^1(x_1,x_2)+I_{3n}^2(x_1,x_2)]=-\frac{\pi(\kappa_1+1)}{\mu_1}p_3(x_1,x_2) \tag{67}$$

where

$$I_{3n}^1(x_1,x_2)=\mathop{\,\,\,\int\!\!\!\!\!\!=}_S \frac{1}{r_1^3}\omega_2(\xi_1,\xi_2)d\xi_1 d\xi_2 \tag{68}$$

$$I_{3n}^2(x_1,x_2)=\int_S K_0(\mathbf{x},\boldsymbol{\xi})\omega_2(\xi_1,\xi_2)d\xi_1 d\xi_2 \tag{69}$$

in which

$$\omega_2(\xi_1,\xi_2)=\xi_2^{\lambda}\sqrt{(a^2-\xi_1^2)(2b-\xi_2)}G_n(\xi_1,\xi_2). \tag{70}$$

Integral (69) is general one, and can be numerically calculated. Integral (68) is hypersingular one, and must be treated before being numerically evaluated. Using the finite-part integral method ([14]) and the following relations

$$\xi_1=\chi_1+r_1\cos\theta_1\quad \xi_2=x_2+r_1\sin\theta_1 \tag{71}$$

$$\omega_2(\xi_1,\xi_2)=\omega_2(x_1,x_2)+D_{21}(x_1,x_2,\theta_1)r_1 + D_{22}(x_1,x_2,r_1,\theta_1)r_1^2, \tag{72}$$

the hypersingular integral (68) can be written as

$$I_{3n}^1(x_1,x_2)=\int_0^{2\pi}\Bigg[-\frac{\omega_2(x_1,x_2)}{R(\theta_1)}+D_{21}(x_1,x_2,\theta_1)\ln R(\theta_1) + \int_0^{R(\theta_1)} D_{22}(x_1,x_2,r_1,\theta_1)dr_1\Bigg]d\theta \tag{73}$$

where $D_{21}(x_1,x_2,\theta_1)$, and $D_{22}(x_1,x_2,r_1,\theta_1)$ are known functions, and can be derived by the Taylor expansion method. Now the integrals in (73) are generals, and can be calculated numerically. Using the above method, Eq. (6) can also be numerically solved.

6 Numerical Results

In order to verify the above method and illustrate its application, numerical results for a rectangular crack are presented in this section. Consider a rectangular crack meeting the interface in a three-dimensional infinite elastic solid under a uniform tension load σ_{33}^{∞} in infinity as shown in Fig. 2. The dimensionless stress intensity factor of the crack front for mode I is defined as

$$F_1=K_I/\sigma_{33}^{\infty}b^{1-\lambda}. \tag{74}$$

The collocation point number is taken as 20×20 for the present results. Before the results for the general cases are presented, two special cases of a square crack in homogenous materials and surface cracks are compared to other results. In the case of homogeneous materials, the numerical results of the stress intensity factor for a square crack are given in Table 1, and compared with those given by Wang and Noda [10]. It is shown that the results are convergent, and the polynomial exponents $K=L=9$ are enough for a satisfied result precision in this case, and these polynomial exponents will be taken for the following results.

A surface crack corresponds to the limiting case when $\mu_2/\mu_1=0$, and the values of the stress intensity factors at the crack front point (0, $2b$, 0) are given in Table 2. It is shown that present results agree with those by Noda and Wang [15] and Isida and Yoshida [16].

Numerical results for two typical examples are given below. Figure 3 gives the maximum dimensionless stress intensity factors at the center of the crack front on the interface varied with the ratio of μ_2/μ_1 for different ratios of a/b. Obviously, the variations of the stress intensity factors for the cracks with different ratios of a/b are similar, and more gently when $\mu_2/\mu_1\geqslant 20$. So the material 2 can be treated as a rigid medium when $\mu_2/\mu_1\geqslant 20$. The dimensionless stress intensity factors along the crack front at the interface are shown in Fig. 4 for different ratios of a/b ($\mu_2/\mu_1=0.5$) and compared with the two-dimensional case. It is shown that the stress intensity factor at the center of the crack front for the case of $a/b\geqslant 8$ is close to that of the two-dimensional case. This indicates that the stress intensity factor at the center of the crack front for the case of $a/b\geqslant 8$ can be calculated as the two-dimensional case.

7 Conclusion

A set of hypersingular integral equations of a flat crack terminating at a bimaterial interface in a three-dimensional infinite solid subjected to arbitrary loads is derived. The behaviors of the crack displacement discontinuities near the crack front meeting at the interface are analyzed by the main-part analytical method of hypersingular singular integral equations, and the singular orders are given. Then, the singular stress fields around the crack front terminating at the interface are obtained. Although the expressions of the displacements and stresses in the materials are complex in modality, the analytical solutions of singular stresses around the crack front are brief.

A numerical method for hypersingular integral equations of a rectangular crack terminating at the bimaterial interface is proposed, and the crack displacement discontinuities are approximated by products of a series of power polynomials and fundamental solutions, which exactly express the singularities of stresses near the crack front. This technique should be improved for other shape cracks in the future.

Highly reliable numerical results of stress intensity factors of mode I along the crack front are obtained. The numerical results show that this numerical technique for a rectangular crack is successful, and the solution precision is satisfied. From the numerical

Table 1 Convergence of stress intensity factor F_1 ($x_2=0$, $a/b=1$, $\mu_2/\mu_1=1$, $\nu_1=\nu_2=0.3$, $K=L$)

x_1/a	0/11	1/11	2/11	3/11	4/11	5/11	6/11	7/11	8/11	9/11	10/11
$K=6$	0.7522	0.7505	0.7468	0.7383	0.7260	0.7072	0.6821	0.6506	0.6085	0.5521	0.4446
$K=7$	0.7539	0.7534	0.7487	0.7391	0.7243	0.7046	0.6803	0.6508	0.6122	0.5528	0.4396
$K=8$	0.7512	0.7508	0.7474	0.7396	0.7260	0.7061	0.6803	0.6489	0.6102	0.5536	0.4451
$K=9$	0.7534	0.7512	0.7462	0.7379	0.7255	0.7072	0.6821	0.6497	0.6090	0.5521	0.4464
$K=10$	0.7534	0.7517	0.7465	0.7376	0.7245	0.7065	0.6827	0.6511	0.6088	0.5499	0.4523
$K=11$	0.7533	0.7517	0.7466	0.7377	0.7245	0.7064	0.6827	0.6514	0.6087	0.5491	0.4535
Wang	0.7534	0.7517	0.7465	0.7376	0.7245	0.7066	0.6828	0.6512	0.6086	0.5492	0.4536

Table 2 Dimensionless stress intensity factor F_1 for $\mu_2/\mu_1=0$, $\nu_1=0.3$ at $x_1=0$, $x_2=2b$

a/b	1	2	4	8	10	∞
Present	0.810	1.113	1.387	1.530	1.552	1586
Noda	0.810	1.112	1.386	1.529	1.550	-
Isida	0.803	1.069	1.318	1.481	-	1586

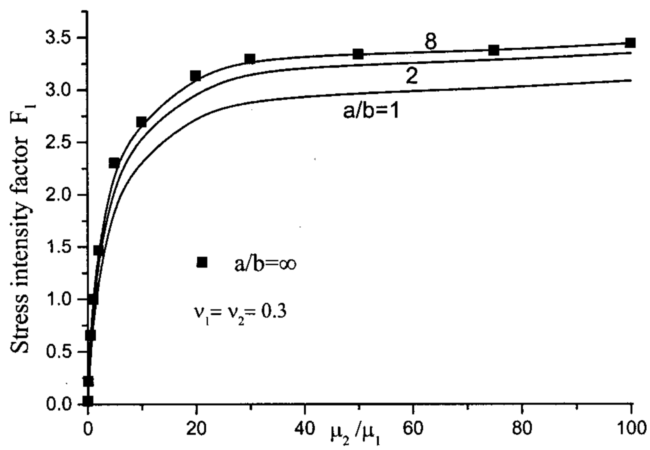

Fig. 3 Stress intensity factor F_1 at the center of the crack front on the interface ($x_2=0$)

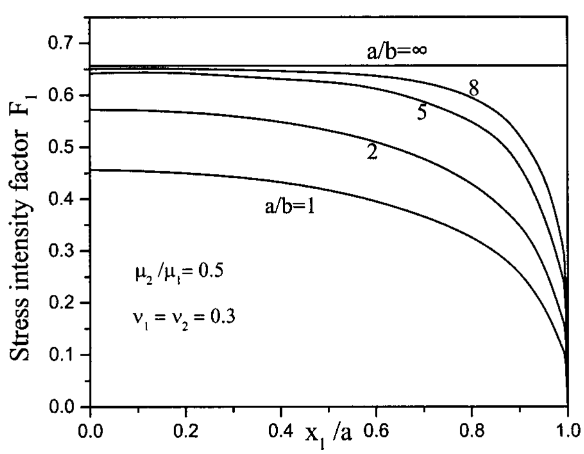

Fig. 4 Stress intensity factor F_1 along the crack front on the interface for $\mu_2/\mu_1=0.5$

solutions, it is shown that the stress intensity factors vary more gently when $\mu_2/\mu_1 \geqslant 20$, and the material 2 can be treated as a rigid medium in this case. Moreover, the stress intensity factor at the center of the crack front for the case of $a/b \geqslant 8$ is close to that of the two-dimensional case.

Acknowledgment

Financial supports from the Inoue Foundation for Science and the 75th Commemoration Fund of Kyushu Institute of Technology are gratefully acknowledged.

References

[1] Cook, T. S., and Erdogan, F., 1972, "Stresses in Bonded Materials With a Crack Perpendicular to the Interface," Int. J. Solids Struct., **10**, pp. 677–697.

[2] Erdogan, F., and Cook, T. S., 1974, "Antiplane Shear Crack Terminating at and Going Through a Bimaterial Interface," Int. J. Fract., **10**, pp. 227–240.

[3] Lee, J. C., and Keer, L. M., 1986, "Study of a Three-Dimensional Crack Terminating at an Interface," ASME J. Appl. Mech., **53**, pp. 311–316.

[4] Chen, D. H., and Nisitani, H., 1993, "Stress Intensity Factors of a Crack Meeting the Bimaterial Interface," Trans. Jpn. Soc. Mech. Eng., Ser. A, **59**, pp. 47–53 (in Japanese).

[5] Xu, G., and Ortiz, M., 1993, "A Variational Boundary Integral Method for the Analysis of 3-D Cracks of Arbitrary Geometry Modeled as Continuous Distributions of Dislocation Loops," Int. J. Numer. Methods Eng., **36**, pp. 3675–3701.

[6] Xu, Y., Moran, B., and Belytschko, T., 1997, "Self-Similar Crack Expansion Method for Three-Dimensional Crack Analysis," ASME J. Appl. Mech., **64**, pp. 729–737.

[7] Guo, Q., and Wang, J.-J., et al., 1995, "Elastic Analyses of Planar Cracks Arbitrary Shape," ASME J. Appl. Mech., **62**, pp. 108–115.

[8] Dai, D. N., Hills, D. A., and Nowell, D. N., 1997, "Modeling of Growth of Three-Dimensional Cracks by a Continuous Distribution of Dislocation Loops," Computational Mech., Berlin, **19**, pp. 538–544.

[9] Noda, N. A., Kobayashi, K., and Yagishita, M., 1999, "Variation of Mixed Modes Stress Intensity Factors of an Inclined Semi-Elliptical Surface Cracks," Int. J. Fract., **100**, pp. 207–225.

[10] Wang, Q., et al., 2000, "Solution of the Distribution of Stress Intensity Factor Along the Front of a 3D Rectangular Crack by Using a Singular Integral Equation Method," Trans. Jpn. Soc. Mech. Eng., Ser. A, **66**(650), pp. 1922–1927 (in Japanese).

[11] Chen, M. C., and Tang, R. J., 1997, "An Explicit Tensor Expression for the Fundamental Solutions of a Bimaterial Space Problem," Appl. Math. Mech., **18**(4), pp. 331–340.

[12] Erdogan F., 1978, "Mixed Boundary Value Problems," *Mechanics Today*, S. Nemat-Nasser ed., Pergamon Press, New York, **4**, pp. 1–86.

[13] Tang, R. J., and Qin, T. Y., 1993, "Method of Hypersingular Integral Equations in Three-Dimensional Fracture Mechanics," Acta Mech. Sin., **25**, pp. 665–675.

[14] Qin, T. Y., and Tang, R. J., 1993, "Finite-Part Integral and Boundary Element Method to Solve Embedded Planar Crack Problems," Int. J. Fract., **60**, pp. 191–202.

[15] Noda, N. A., and Wang, Q., 2000, "Application of Body Force Method to Fracture and Interface Mechanics of Composites," Research Report of the JSPS Postdoctoral Fellowship for Foreign Researchers, No. 98187.

[16] Isida, M., Yoshida, T., and Noguchi, H., 1991, "A Rectangular Crack in an Infinite Solid, a Semi-Infinite Solid and a Finite-Thickness Plate Subjected to Tension," Int. J. Fract., **52**, pp. 79–90.

Plane Thermal Stress Analysis of an Orthotropic Cylinder Subjected to an Arbitrary, Transient, Asymmetric Temperature Distribution

K.-C. Yee
Graduate Research Assistant
Department of Mechanical Engineering,
The University of Texas at Austin,
Austin, TX 78712-1063

T. J. Moon
Associate Professor,
Department of Mechanical Engineering
and Texas Materials Institute,
ETC II 5.160,
The University of Texas at Austin,
Austin, TX 78712-1063
Mem. ASME

A closed-form, analytical solution is presented for the transient, plane thermal stress analysis of a linearly elastic, homogeneously orthotropic hollow cylinder subjected to an arbitrary temperature distribution. The thermoelastic solution, obtained by a stress function approach, can be used as the basis for the corresponding thermoviscoelastic solution for thermorheologically simple viscoelastic materials by invoking the viscoelastic Correspondence Principle. This solution can also be directly extended to the class of weakly inhomogeneously orthotropic cylinders using perturbation methods. The transient asymmetric temperature field is characterized by Fourier-Bessel eigenfunction expansions. The analytically derived stress function satisfies a linear, fourth-order inhomogeneous partial differential equation and the Cesaro integral conditions, which assure the existence of a single-valued displacement field. The corresponding thermal stresses are then computed by the stress-stress function relations. A key feature of the analytical solution is that the hoop, radial, and shear stresses, due to the transient arbitrary temperature distribution, are expressed explicitly in terms of the scalar temperature field. A polymer composite example is presented to validate the current method and to qualitatively illustrate the distribution of thermal stresses due to an asymmetric temperature distribution. Numerical results are presented for the thermally driven hoop, radial and (interlaminar) shear stresses in a hollow, hoop-wound glass/epoxy cylinder. This analysis demonstrates that potentially debilitating interlaminar shear stresses can develop in laminated composites when subjected to an even modest transient asymmetric temperature distribution. Their magnitudes depend on the severity of the spatial and temporal thermal gradients in the circumferential direction. While still relatively low compared to the hoop stress, the shear stress may cause thermal failure due to the typically low interlaminar shear strengths of laminated composite materials. [DOI: 10.1115/1.1491268]

Introduction

Thermal stress analysis is an important issue for laminated materials. Laminated composite structures are being deployed in increasingly severe thermal environments, as well as being subjected to complex spatial and temporal thermal gradients during their manufacture. This issue is especially critical for laminated materials possessing relatively low interlaminar shear strengths as thermally induced shear stresses can initiate intra and interlaminar failure by delamination.

Generally, there are two kinds of thermal stress analyses in laminated materials: thermoelastic and thermoviscoelastic. Thermoelastic treatments assume that the material is elastic under thermal loading and thermal stresses are independent of temperature history. On the other hand, thermoviscoelastic treatments assume that the material is viscoelastic, hence greatly affected by temperature and thermal stresses that are generally history dependent. Thermoelasticity usually applies to solids at temperatures well below their glass-transition temperatures so that the material's viscoelastic behavior can be neglected, while thermoviscoelasticity applies to solids at temperatures close to and above their glass-transition temperature. For thermorheologically simple viscoelastic materials, the thermoviscoelastic solution can be obtained directly from the corresponding thermoelastic solution by invoking the viscoelastic Correspondence Principle ([1,2]); as a result, the thermoelastic solution is relevant to a wide variety of elastic and viscoelastic materials.

In thermoelastic problems, there are two major types of thermal stress analyses. The first type applies to linearly elastic, homogeneous domains such that an analytic solution can be derived using a displacement or stress formulation. Padovan [3] studied the effects of mechanical and thermal anisotropy on the thermoelastic field of laminated cylinders. Kalam and Tauchert [4] used an Airy stress function formulation to derive a closed-form solution for the thermal stresses in an orthotropic cylinder subject to a steady-state asymmetric temperature distribution. Iwaki [5] provided an analytical solution for the transient thermal stresses in fully and partly cooled circular rings. Experimental results using a photoelasticity technique were presented to compare with theoretical solutions. Good agreement was found between the numerical results and experimental data. Kardomateas [6,7] used a displacement formulation to derive the transient, axisymmetric thermal stresses in orthotropic hollow cylinders; Hankel asymptotic expansions of the Bessel functions of the first and second kind with small and large arguments were employed to obtain the solution for extremely short and long times. Sugano [8] presented an ana-

Contributed by the Applied Mechanics Division of THE AMERICAN SOCIETY OF MECHANICAL ENGINEERS for publication in the ASME JOURNAL OF APPLIED MECHANICS. Manuscript received by the ASME Applied Mechanics Division, August 24, 2001; final revision, February 28, 2002. Associate Editor: H. Gao. Discussion on the paper should be addressed to the Editor, Prof. Robert M. McMeeking, Department of Mechanical and Environmental Engineering University of California–Santa Barbara, Santa Barbara, CA 93106-5070, and will be accepted until four months after final publication of the paper itself in the ASME JOURNAL OF APPLIED MECHANICS.

lytical solution for an asymmetric plane thermal stress problem in an isotropic, inhomogeneous circular ring using the Airy stress function method. The Young's modulus and thermal conductivity were assumed to be power-law functions of the radial coordinate, while the coefficient of thermal expansion was assumed to be an arbitrary function of temperature. His numerical results showed that the temperature and thermal stresses were greatly affected by the degree of the material's nonlinearities. Zibdeh and Al Farran [9] presented a three-dimensional steady-state stress analysis of homogeneous hollow composite cylinders subjected to an asymmetric temperature distribution. In their analysis, a general displacement formulation was used in each ply with continuity conditions being imposed at each layer interface. Their results showed that the cylinder's stress response was sensitive to composite thickness, fiber orientation, and ply stacking sequence.

The second type thermoelastic stress analysis applies to inhomogeneous domains such that an analytical solution is intractable and therefore an approximate solution is sought. Hata and Atsumi [10] employed a perturbation method to study the axisymmetric transient thermal stresses in a transversely anisotropic hollow cylinder with temperature-dependent coefficient of thermal expansion and modulii. The applicability of their technique is quite general, except the solution procedure is mathematically tedious—in addition to being approximate. Tauchert [11] used the Rayleigh-Ritz method to analyze the plane stress/strain, axisymmetric thermal stresses in an inhomogeneous, anisotropic cylinder. The assumed displacement field was expanded by a polynomial series that satisfied the imposed kinematic boundary conditions. The coefficients of polynomial series were then determined by requiring the total potential energy be a minimum subject to prescribed boundary conditions using Lagrangian multipliers. Tauchert [12] further extended the Ritz method to solving a similar problem in an inhomogeneous, anisotropic, finite elastic cylinder. Both of Tauchert's analyses assume that the temperature and displacement fields can be approximated by power-series representations. Using the stress function formulation, Kalam [13] derived an approximate solution for the asymmetric thermoelastic analysis of an orthotropic cylinder. The cylinder's stiffness and coefficient of thermal expansion were assumed to depend on temperature in an arbitrary fashion. A complementary energy variational principle was used in the study to determine the coefficients of the approximate solution. To demonstrate the accuracy of the method, a finite element solution, as well as an exact solution, were presented to compare with the numerical results. Hyer and Cooper [14] employed a complementary virtual work principle to evaluate the thermal stresses in orthotropic composite tubes. A stress formulation was used in the study with the edge effect being ignored. Huang and Taucher [15] used an incremental analysis with large deformations to investigate the thermal stresses induced in nonlinear angle-ply composite laminates under a nonuniform temperature distribution. The displacement fields were expressed by series approximations that were determined by the principle of minimum potential energy.

The aim of the present work is to use a stress function approach to extend the work of Kalam and Tauchert [4] to present an analytical solution for a class of plane thermal stress boundary value problems having thermal boundary conditions and initial conditions being expressed by Fourier series representations.

Transient, Plane Temperature Distribution

The transient, plane temperature distribution $T(r,\theta,t)$ in an elastic, homogeneously orthotropic hollow cylinder (inner radius a, outer radius b) is governed by the following energy equation:

$$K_r\left(\frac{\partial^2 T}{\partial r^2}+\frac{1}{r}\frac{\partial T}{\partial r}\right)+K_\theta\frac{\partial^2 T}{\partial\theta^2}=\varrho c\frac{\partial T}{\partial t}+S(r,\theta,t) \tag{1}$$

where, respectively, r and θ are radial and circumferential coordinates measured relative to the cylinder's central axis, K_r and K_θ are the cylinder's radial and circumferential (hoop) thermal conductivities, and ρ and c are its mass density and specific heat. All properties are assumed to be independent of temperature, time, and position. The energy source (or sink) term, $S(r,\theta,t)$, may be due, for example, to a volumetric exothermic (or endothermic) chemical reaction or electromagnetic energy deposition. Without loss of generality, $T(r,\theta,t)$ can be interpreted as the temperature change relative to some reference temperature, say the "stress-free" temperature, T_{ref}. The Robin-type boundary conditions and initial condition considered here are

$$r=a,\quad L_{11}\frac{\partial T}{\partial r}+L_{12}T=0; \tag{2}$$

$$r=b,\quad L_{21}\frac{\partial T}{\partial r}+L_{22}T=0 \tag{3}$$

$$t=0,\quad T(r,\theta,0)=F(r,\theta) \tag{4}$$

where $L_{ij}, i,j=1,2$, are the thermal boundary condition coefficients and $F(r,\theta)$ is the initial temperature distribution.

Using an eigenfunction expansion, the general solution of (1) can be written

$$\begin{aligned}T(r,\theta,t)=&\sum_{i=1}^{\infty} a_{0i}R_0(\mu_{0i}r)e^{-\zeta\mu_{0i}^2 t}\\&+\sum_{n=1}^{\infty}\left(\sum_{i=1}^{\infty} a_{ni}R_{\kappa_n}(\mu_{ni}r)\cos(n\theta)\right.\\&\left.+\sum_{i=1}^{\infty} b_{ni}R_{\kappa_n}(\mu_{ni}r)\sin(n\theta)\right)e^{-\zeta\mu_{ni}^2 t}\end{aligned} \tag{5}$$

where the orthogonal eigenfunctions $R_{\kappa_n}(\mu_{ni}r)$ are defined by

$$\begin{aligned}R_{\kappa_n}(\mu_{ni}r)=&\frac{J_{\kappa_n}(\mu_{ni}r)}{L_{21}\mu_{ni}J'_{\kappa_n}(\mu_{ni}b)+L_{22}J_{\kappa_n}(\mu_{ni}b)}\\&-\frac{Y_{\kappa_n}(\mu_{ni}r)}{L_{21}\mu_{ni}Y'_{\kappa_n}(\mu_{ni}b)+L_{22}Y_{\kappa_n}(\mu_{ni}b)}\end{aligned} \tag{6}$$

whose norm $N(\mu_{ni}r,\kappa_n)$ is given by

$$N(\mu_{ni}r,\kappa_n)=\int_a^b rR_{\kappa_n}^2(\mu_{ni}r)dr. \tag{7}$$

The corresponding eigenvalues μ_{ni} satisfy the characteristic equations

$$\begin{aligned}&\left(L_{11}\left\{\mu_{ni}J_{\kappa_n-1}(\mu_{ni}a)-\frac{\kappa_n}{a}J_{\kappa_n}(\mu_{ni}a)\right\}+L_{12}J_{\kappa_n}(\mu_{ni}a)\right)\\&\quad*\left(L_{21}\left\{\mu_{ni}Y_{\kappa_n-1}(\mu_{ni}b)-\frac{\kappa_n}{b}Y_{\kappa_n}(\mu_{ni}b)\right\}+L_{22}Y_{\kappa_n}(\mu_{ni}b)\right)\\&\quad-\left(L_{11}\left\{\mu_{ni}Y_{\kappa_n-1}(\mu_{ni}a)-\frac{\kappa_n}{a}Y_{\kappa_n}(\mu_{ni}a)\right\}+L_{12}Y_{\kappa_n}(\mu_{ni}a)\right)\\&\quad*\left(L_{21}\left\{\mu_{ni}J_{\kappa_n-1}(\mu_{ni}b)-\frac{\kappa_n}{b}J_{\kappa_n}(\mu_{ni}b)\right\}+L_{22}J_{\kappa_n}(\mu_{ni}b)\right)\\&\quad=0,(n=0,1,2,\ldots\quad;i=1,2,3,\ldots\quad)\end{aligned} \tag{8}$$

where $\kappa_n=n\sqrt{K_\theta/K_r}$ depends upon the thermal orthotropy ratio and $\zeta=K_r/\rho c$ is the thermal diffusivity in the radial direction. Here, J_{κ_n} and Y_{κ_n} are (cylindrical) Bessel functions of the first and second kind, respectively, of order κ_n.

All unknowns a_{0i}, a_{ni}, and b_{ni} in (5) are determined by the initial condition

$$F(r,\theta)=\sum_{i=1}^{\infty} a_{0i}R_0(\mu_{0i}r)+\sum_{n=1}^{\infty}\left(\sum_{i=1}^{\infty} a_{ni}R_{\kappa_n}(\mu_{ni}r)\cos(n\theta)+\sum_{i=1}^{\infty} b_{ni}R_{\kappa_n}(\mu_{ni}r)\sin(n\theta)\right) \tag{9}$$

which, by Fourier series expansion, leads to

$$\sum_{i=1}^{\infty} a_{0i}R_0(\mu_{0i}r)=\frac{1}{2\pi}\int_0^{2\pi}F(r,\theta)d\theta \tag{10}$$

$$\sum_{i=1}^{\infty} a_{ni}R_{\kappa_n}(\mu_{ni}r)=\frac{1}{2\pi}\int_0^{2\pi}F(r,\theta)\cos(n\theta)d\theta \tag{11}$$

$$\sum_{i=1}^{\infty} b_{ni}R_{\kappa_n}(\mu_{ni}r)=\frac{1}{2\pi}\int_0^{2\pi}F(r,\theta)\sin(n\theta)d\theta. \tag{12}$$

Using Fourier-Bessel eigenfunction expansions (in conjunction with (6) and (7)), a_{0i}, a_{ni}, and b_{ni} can be written as

$$a_{0i}=\frac{1}{N(\mu_{0i}r,0)}\int_a^b rR_0(\mu_{0i}r)\left\{\frac{1}{2\pi}\int_0^{2\pi}F(r,\theta)d\theta\right\}dr \tag{13}$$

$$a_{ni}=\frac{1}{N(\mu_{ni}r,\kappa_n)}\int_a^b rR_{\kappa_n}(\mu_{ni}r)\left\{\frac{1}{2\pi}\int_0^{2\pi}F(r,\theta)\cos(n\theta)d\theta\right\}dr \tag{14}$$

$$b_{ni}=\frac{1}{N(\mu_{ni}r,\kappa_n)}\int_a^b rR_{\kappa_n}(\mu_{ni}r)\left\{\frac{1}{2\pi}\int_0^{2\pi}F(r,\theta)\sin(n\theta)d\theta\right\}dr. \tag{15}$$

Stress Formulation

Plane Stress Formulation. In a linearly elastic, homogeneously orthotropic solid, the associated stress-strain relations for a plane stress solid subjected to a temperature change $T(r,\theta,t)$ are

$$\varepsilon_{rr}=\frac{1}{E_r}\sigma_{rr}-\frac{\nu_{r\theta}}{E_r}\sigma_{\theta\theta}+\alpha_r T, \tag{16}$$

$$\varepsilon_{\theta\theta}=\frac{1}{E_\theta}\sigma_{\theta\theta}-\frac{\nu_{r\theta}}{E_r}\sigma_{rr}+\alpha_\theta T, \tag{17}$$

$$\varepsilon_{r\theta}=\frac{1}{2G_{r\theta}}\sigma_{r\theta} \tag{18}$$

where, respectively, ε_{rr}, $\varepsilon_{\theta\theta}$, $\varepsilon_{r\theta}$ and σ_{rr}, $\sigma_{\theta\theta}$, $\sigma_{r\theta}$ are the plane cylinderical strain and stress components; E_r and E_θ are the radial and circumferential elastic modulii; $G_{r\theta}$ is the in-plane, elastic shear modulus; α_r and α_θ are the radial and circumferential coefficients of thermal expansion; and $\nu_{r\theta}$ is the major Poisson's ratio.

In transient, plane elasticity problems, the stress components can be related to a single stress function $\Phi(r,\theta,t)$ by

$$\sigma_{rr}=\frac{1}{r}\frac{\partial\Phi}{\partial r}+\frac{1}{r^2}\frac{\partial^2\Phi}{\partial\theta^2}, \tag{19}$$

$$\sigma_{\theta\theta}=\frac{\partial^2\Phi}{\partial r^2}, \tag{20}$$

$$\sigma_{r\theta}=-\frac{1}{\partial r}\left(\frac{1}{r}\frac{\partial\Phi}{\partial\theta}\right). \tag{21}$$

In multiply connected regions, such as hollow cylinders, the necessary and sufficient conditions for a single-valued displacement field are: the compatibility equation

$$2\frac{\partial\varepsilon_{r\theta}}{\partial\theta}+2r\frac{\partial^2\varepsilon_{r\theta}}{\partial r\partial\theta}-2r\frac{\partial\varepsilon_{\theta\theta}}{\partial r}-r^2\frac{\partial^2\varepsilon_{\theta\theta}}{\partial r^2}-\frac{\partial^2\varepsilon_{rr}}{\partial\theta^2}+r\frac{\partial\varepsilon_{rr}}{\partial r}=0 \tag{22}$$

and the Cesaro integral conditions ([16])

$$\int_0^{2\pi}\left(\varepsilon_{rr}+2\frac{\partial\varepsilon_{r\theta}}{\partial\theta}-r\frac{\partial\varepsilon_{\theta\theta}}{\partial r}\right)r\sin\theta d\theta=0 \tag{23}$$

$$\int_0^{2\pi}\left(\varepsilon_{rr}+2\frac{\partial\varepsilon_{r\theta}}{\partial\theta}-r\frac{\partial\varepsilon_{\theta\theta}}{\partial r}\right)r\cos\theta d\theta=0 \tag{24}$$

$$\int_0^{2\pi}\left(\varepsilon_{rr}-\varepsilon_{\theta\theta}+\frac{\partial\varepsilon_{r\theta}}{\partial\theta}-r\frac{\partial\varepsilon_{\theta\theta}}{\partial r}\right)d\theta=0. \tag{25}$$

For simplicity, it is convenient to define the nondimensional ratios:

$$k=\sqrt{\frac{E_\theta}{E_r}},\quad m=\sqrt{\frac{E_\theta}{G_{r\theta}}},\quad M_\alpha=\frac{\alpha_\theta}{\alpha_r}. \tag{26}$$

Substituting (16)–(18) into (19)–(21) and further substituting those results into the compatibility Eq. (22) yields the compatibility equation in terms of the stress function $\Phi(r,\theta,t)$:

$$\begin{aligned}&\frac{\partial^4\Phi}{\partial r^4}+(m^2-2k^2\nu_{r\theta})\frac{1}{r^2}\frac{\partial^4\Phi}{\partial r^2\partial\theta^2}+\frac{k^2}{r^4}\frac{\partial^4\Phi}{\partial\theta^4}+\frac{2}{r}\frac{\partial^3\Phi}{\partial r^3}\\&-(m^2-2k^2\nu_{r\theta})\frac{1}{r^3}\frac{\partial^3\Phi}{\partial r\partial\theta^2}-\frac{k^2}{r^2}\frac{\partial^2\Phi}{\partial r^2}\\&+(2k^2(1-\nu_{r\theta})+m^2)\frac{1}{r^4}\frac{\partial^2\Phi}{\partial\theta^2}+\frac{k^2}{r^3}\frac{\partial\Phi}{\partial r}\\&=-E_\theta\alpha_\theta\left(\frac{\partial^2T}{\partial r^2}+\frac{2-M_\alpha}{r}\frac{\partial T}{\partial r}+\frac{M_\alpha}{r^2}\frac{\partial^2T}{\partial\theta^2}\right).\end{aligned} \tag{27}$$

Similarly, the Cesaro integral conditions expressed in terms of the stress function $\Phi(r,\theta,t)$ are

$$\begin{aligned}&\int_0^{2\pi}\left(-r\frac{\partial^3\Phi}{\partial r^3}+\frac{(1-\nu_{r\theta})k^2}{r}\frac{\partial\Phi}{\partial r}+\frac{(1-2\nu_{r\theta})k^2+m^2}{r^2}\frac{\partial^2\Phi}{\partial\theta^2}\right.\\&\left.+\frac{m^2-\nu_{r\theta}k^2}{r}\frac{\partial^3\Phi}{\partial r\partial\theta^2}\right)r\sin\theta d\theta\\&=-E_\theta\alpha_\theta\int_0^{2\pi}\left(M_\alpha T-r\frac{\partial T}{\partial r}\right)r\sin\theta d\theta\end{aligned} \tag{28}$$

$$\begin{aligned}&\int_0^{2\pi}\left(-r\frac{\partial^3\Phi}{\partial r^3}+\frac{(1-\nu_{r\theta})k^2}{r}\frac{\partial\Phi}{\partial r}+\frac{(1-2\nu_{r\theta})k^2+m^2}{r^2}\frac{\partial^2\Phi}{\partial\theta^2}\right.\\&\left.+\frac{m^2-\nu_{r\theta}k^2}{r}\frac{\partial^3\Phi}{\partial r\partial\theta^2}\right)r\cos\theta d\theta\\&=-E_\theta\alpha_\theta\int_0^{2\pi}\left(M_\alpha T-r\frac{\partial T}{\partial r}\right)r\cos\theta d\theta\end{aligned} \tag{29}$$

$$\begin{aligned}&\int_0^{2\pi}\left(-r\frac{\partial^3\Phi}{\partial r^3}-\frac{\partial^2\Phi}{\partial r^2}+\frac{k^2}{r}\frac{\partial\Phi}{\partial r}+\frac{2(1-nu_{r\theta})k^2+m^2}{2r^2}\frac{\partial^2\Phi}{\partial\theta^2}\right.\\&\left.-\frac{m^2-2\nu_{r\theta}k^2}{2r}\frac{\partial^3\Phi}{\partial r\partial\theta^2}\right)d\theta\\&=-E_\theta\alpha_\theta\int_0^{2\pi}\left((M_\alpha-1)T-r\frac{\partial T}{\partial r}\right)d\theta.\end{aligned} \tag{30}$$

Stress Function Solution. For notational convenience, the transient temperature field can be expressed in the form

$$T(r,\theta,t)=f_0(r,t)+\sum_{n=1}^{\infty} f_n(r,t)\cos n\theta+\sum_{n=1}^{\infty} g_n(r,t)\sin n\theta. \tag{31}$$

The time-independent, homogeneous solution $\Phi_h(r,\theta)$ of (27) is

$$\begin{aligned}\Phi_h(r,\theta)=&A_0+B_0r^2+C_0r^{1-k}+D_0r^{1+k}+\Big(A_0'+B_0'r^2+C_0'r^{(1-k)}\\&+D_0'r^{(1+k)}\Big)\theta+H_1r\theta\sin\theta+[A_1r+B_1r\ln r+C_1r^{1-\beta}\\&+D_1r^{1+\beta}]\cos\theta+H_1'r\theta\cos\theta+[A_1'r+B_1'r\ln r\\&+C_1'r^{1-\beta}+D_1'r^{1+\beta}]\sin\theta+\sum_{n=2}^{\infty}\left[\left(\sum_{i=1}^{4}A_{ni}r^{\lambda_{ni}}\right)\cos n\theta\right.\\&\left.+\left(\sum_{i=1}^{4}B_{ni}r^{\lambda_{ni}}\right)\sin n\theta\right]\end{aligned} \tag{32}$$

where A_0, B_0, C_0, D_0, A_0', B_0', C_0', D_0', H_1, H_1', A_1, B_1, C_1, D_1, A_1', B_1', C_1', D_1', A_{ni}, and B_{ni} are arbitrary coefficients and

$$\beta=\sqrt{1+(1-2\nu_{r\theta})k^2+m^2} \tag{33}$$

$$\lambda_{n1}=1+\sqrt{1-\frac{1}{2}[I_1(n)+I_2(n)]} \tag{34}$$

$$\lambda_{n2}=1+\sqrt{1-\frac{1}{2}[I_1(n)-I_2(n)]} \tag{35}$$

$$\lambda_{n3}=1-\sqrt{1-\frac{1}{2}[I_1(n)+I_2(n)]} \tag{36}$$

$$\lambda_{n4}=1-\sqrt{1-\frac{1}{2}[I_1(n)-I_2(n)]} \tag{37}$$

where

$$I_1(n)=1-(1-2n^2\nu_{r\theta})k^2-n^2m^2 \tag{38}$$

$$I_2(n)=\sqrt{[1+n^2m^2+((1-2n^2\nu_{r\theta})k^2)]^2-[2k(n^2-1)]^2}. \tag{39}$$

Moreover, the fact that when $n=0$, $\lambda_{0i}=0,1,1-k,1+k$, and when $n=1$, $\lambda_{1i}=1,1,1+\beta,1-\beta$ $(i=1,2,3,4)$ has been incorporated.

Next, substituting (32) into (27) and using the orthogonal property of $\cos n\theta$ and $\sin n\theta$ over the interval $(0,2\pi)$, the time-dependent particular solution $\Phi_p(r,\theta,t)$ of (27) is found to be

$$\begin{aligned}\Phi_p(r,\theta,t)=&\sum_{i=1}^{4}\Pi_i^0r^{\lambda_{0i}}\int_a^r\rho^{3-\lambda_{0i}}\vartheta_0^c(\rho,t)d\rho\\&+\left[\frac{r}{\beta}\int_a^r\rho^2\ln r\,\vartheta_1^c(\rho,t)d\rho-\frac{r\ln r}{\beta}\int_a^r\rho^2\vartheta_1^c(\rho,t)d\rho\right.\\&-\frac{r^{1-\beta}}{2\beta^3}\int_a^r\rho^{2+\beta}\vartheta_1^c(\rho,t)d\rho\\&\left.+\frac{r^{1+\beta}}{2\beta^3}\int_a^r\rho^{2-\beta}\vartheta_1^c(\rho,t)d\rho\right]\\&\times\cos\theta\left[\frac{r}{\beta}\int_a^r\rho^2\ln r\,\vartheta_1^s(\rho,t)d\rho\right.\\&-\frac{r\ln r}{\beta}\int_a^r\rho^2\vartheta_1^s(\rho,t)d\rho-\frac{r^{1-\beta}}{2\beta^3}\int_a^r\rho^{2+\beta}\vartheta_1^s(\rho,t)d\rho\\&\left.+\frac{r^{1+\beta}}{2\beta^3}\int_a^r\rho^{2-\beta}\vartheta_1^s(\rho,t)d\rho\right]\sin\theta\\&+\sum_{n=2}^{\infty}\left[\sum_{i=1}^{4}\Pi_i^nr^{\lambda_{ni}}\int_a^r\rho^{3-\lambda_{ni}}\vartheta_n^c(\rho,t)d\rho\right]\cos n\theta\\&+\sum_{n=2}^{\infty}\left[\sum_{i=1}^{4}\Pi_i^nr^{\lambda_{ni}}\int_a^r\rho^{3-\lambda_{ni}}\vartheta_n^s(\rho,t)d\rho\right]\sin n\theta\end{aligned} \tag{40}$$

where

$$\Pi_1^n=\frac{1}{(\lambda_{n2}-\lambda_{n1})(\lambda_{n3}-\lambda_{n1})(\lambda_{n4}-\lambda_{n1})} \tag{41}$$

$$\Pi_2^n=\frac{1}{(\lambda_{n1}-\lambda_{n2})(\lambda_{n3}-\lambda_{n2})(\lambda_{n4}-\lambda_{n2})} \tag{42}$$

$$\Pi_3^n=\frac{1}{(\lambda_{n1}-\lambda_{n3})(\lambda_{n2}-\lambda_{n3})(\lambda_{n4}-\lambda_{n3})} \tag{43}$$

$$\Pi_4^n=\frac{1}{(\lambda_{n1}-\lambda_{n4})(\lambda_{n2}-\lambda_{n4})(\lambda_{n3}-\lambda_{n4})} \tag{44}$$

for $n=0,2,3,\ldots$ $(n\neq 1)$ and

$$\vartheta_0^c(\rho,t)=-E_\theta\alpha_\theta\left(\frac{\partial^2f_0}{\partial r^2}+\frac{2-M_\alpha}{r}\frac{\partial f_0}{\partial r}\right) \tag{45}$$

$$\vartheta_n^c(\rho,t)=-E_\theta\alpha_\theta\left(\frac{\partial^2f_n}{\partial r^2}+\frac{2-M_\alpha}{r}\frac{\partial f_n}{\partial r}-\frac{n^2M_\alpha}{r^2}f_n\right) \tag{46}$$

$$\vartheta_n^s(\rho,t)=-E_\theta\alpha_\theta\left(\frac{\partial^2g_n}{\partial r^2}+\frac{2-M_\alpha}{r}\frac{\partial g_n}{\partial r}-\frac{n^2M_\alpha}{r^2}g_n\right) \tag{47}$$

where $n=1,2,\ldots$. By the principle of linear superposition, the general solution of (27) is then

$$\Phi(r,\theta,t)=\Phi_h(r,\theta)+\Phi_p(r,\theta,t). \tag{48}$$

Stress Field. Substituting the stress function (48) into (19)–(21), the corresponding stress components can be determined. They must, however, simultaneously satisfy the Cesaro integral conditions that assure a single-valued displacement in a multiply connected domain; they require

$$B_0=0, \tag{49}$$

$$H_1=-\frac{\beta^2}{2(1-\nu_{r\theta})k^2}B_1, \tag{50}$$

$$H_2=-\frac{\beta^2}{2(1-\nu_{r\theta})k^2}B_1'. \tag{51}$$

It should be noted that in (32), the term $(A_0'+B_0'r^2+C_0'r^{(1-k)}+D_0'r^{1+k})\theta$ corresponds to a pure shear deformation that cannot exist in a thermoelastic problem and thus is excluded from the stress field.

After integration by parts, the thermal stresses can be written as

$$\begin{aligned}\sigma_{rr}=&\left[C_3+\frac{(M_\alpha-k)E_\theta\alpha_\theta}{2k}\int_a^r\rho^{-k}f_0(\rho,t)d\rho\right]r^{k-1}\\&+\left[C_4+\frac{(M_\alpha+k)E_\theta\alpha_\theta}{2k}\int_a^r\rho^kf_0(\rho,t)d\rho\right]r^{-(k+1)}\\&+\left[\frac{B_1+2H_1}{r}-\beta C_1r^{-(\beta+1)}+\beta D_1r^{(\beta-1)}\right.\\&+\frac{(M_\alpha+1-\beta)E_\theta\alpha_\theta r^{\beta-1}}{2\beta}\int_a^r\rho^{-\beta}f_1(\rho,t)d\rho\\&\left.-\frac{(M_\alpha+1+\beta)E_\theta\alpha_\theta r^{-(\beta+1)}}{2\beta}\int_a^r\rho^\beta f_1(\rho,t)d\rho\right]\cos\theta\end{aligned}$$

$$
+\left[\frac{B_1'+2H_1'}{r}-\beta C_1' r^{-(\beta+1)}+\beta D_1' r^{(\beta-1)}\right.
+\frac{(M_\alpha+1-\beta)E_\theta\alpha_\theta r^{\beta-1}}{2\beta}\int_a^r \rho^{-\beta} g_1(\rho,t)d\rho
\left.-\frac{(M_\alpha+1+\beta)E_\theta\alpha_\theta r^{-(\beta+1)}}{2\beta}\int_a^r \rho^{\beta} g_1(\rho,t)d\rho\right]\sin\theta
+\sum_{n=2}^{\infty}\left\{\sum_{i=1}^{4}(\lambda_{ni}-n^2)r^{\lambda_{ni}-2}\left[A_{ni}+\Pi_i^n E_\theta\alpha_\theta((\lambda_{ni}-M_\alpha-1)\right.\right.
\left.\left.\times(2-\lambda_{ni})+n^2M_\alpha)\int_a^r \rho^{1-\lambda_{ni}} f_n(\rho,t)d\rho\right]\right\}\cos n\theta
+\sum_{n=2}^{\infty}\left\{\sum_{i=1}^{4}(\lambda_{ni}-n^2)r^{\lambda_{ni}-2}\left[B_{ni}+\Pi_i^n E_\theta\alpha_\theta((\lambda_{ni}-M_\alpha-1)\right.\right.
\left.\left.\times(2-\lambda_{ni})+n^2M_\alpha)\int_a^r \rho^{1-\lambda_{ni}} g_n(\rho,t)d\rho\right]\right\}\sin n\theta \tag{52}
$$

$$
\sigma_{\theta\theta}=\left[C_3k+\frac{(M_\alpha-k)E_\theta\alpha_\theta}{2}\int_a^r \rho^{-k} f_0(\rho,t)d\rho\right]r^{k-1}
-\left[C_4k+\frac{(M_\alpha+k)E_\theta\alpha_\theta}{2}\int_a^r \rho^{k} f_0(\rho,t)d\rho\right]r^{-(k+1)}
-E_\theta\alpha_\theta f_0+\left[\frac{B_1}{r}+\beta(\beta-1)C_1r^{-(\beta+1)}+\beta(\beta+1)D_1r^{(\beta-1)}\right.
+\frac{(M_\alpha+1-\beta)(\beta+1)E_\theta\alpha_\theta r^{\beta-1}}{2\beta}\int_a^r \rho^{-\beta} f_1(\rho,t)d\rho
+\frac{(M_\alpha+1+\beta)(\beta-1)E_\theta\alpha_\theta r^{-(\beta+1)}}{2\beta}\int_a^r \rho^{\beta} f_1(\rho,t)d\rho
\left.-E_\theta\alpha_\theta f_1\right]\cos\theta+\left[\frac{B_1'}{r}+\beta(\beta-1)C_1' r^{-(\beta+1)}\right.
+\beta(\beta+1)D_1' r^{(\beta-1)}
+\frac{(M_\alpha+1-\beta)(\beta+1)E_\theta\alpha_\theta r^{\beta-1}(\beta-1)}{2\beta}\int_a^r \rho^{-\beta} g_1(\rho,t)d\rho
-\frac{(M_\alpha+1+\beta)E_\theta\alpha_\theta r^{-(\beta+1)}}{2\beta}\int_a^r \rho^{\beta} g_1(\rho,t)d\rho
\left.-E_\theta\alpha_\theta g_1\right]\sin\theta+\sum_{n=2}^{\infty}\left\{\sum_{i=1}^{4}\lambda_{ni}(\lambda_{ni}-1)r^{\lambda_{ni}-2}\left[A_{ni}\right.\right.
+\Pi_i^n E_\theta\alpha_\theta((\lambda_{ni}-M_\alpha-1)(2-\lambda_{ni})
\left.\left.+n^2M_\alpha)\int_a^r \rho^{1-\lambda_{ni}} f_n(\rho,t)d\rho\right]-E_\theta\alpha_\theta f_n\right\}\cos n\theta
+\sum_{n=2}^{\infty}\left\{\sum_{i=1}^{4}\lambda_{ni}(\lambda_{ni}-1)r^{\lambda_{ni}-2}\left[B_{ni}+\Pi_i^n E_\theta\alpha_\theta((\lambda_{ni}-M_\alpha\right.\right.
\left.-1)(2-\lambda_{ni})+n^2M_\alpha)\int_a^r \rho^{1-\lambda_{ni}} g_n(\rho,t)d\rho\right]
\left.-E_\theta\alpha_\theta g_n\right\}\sin n\theta \tag{53}
$$

$$
\sigma_{r\theta}=\left[\frac{B_1}{r}-\beta C_1r^{-(\beta+1)}+\beta D_1r^{(\beta-1)}\right.
+\frac{(M_\alpha+1-\beta)E_\theta\alpha_\theta r^{\beta-1}}{2\beta}\int_a^r \rho^{-\beta} f_1(\rho,t)d\rho
\left.-\frac{(M_\alpha+1+\beta)E_\theta\alpha_\theta r^{-(\beta+1)}}{2\beta}\int_a^r \rho^{\beta} f_1(\rho,t)d\rho\right]\sin\theta
-\left[\frac{B_1'}{r}-\beta C_1' r^{-(\beta+1)}+\beta D_1' r^{(\beta-1)}\right.
+\frac{(M_\alpha+1-\beta)E_\theta\alpha_\theta r^{\beta-1}(\beta-1)}{2\beta}\int_a^r \rho^{-\beta} g_1(\rho,t)d\rho
\left.-\frac{(M_\alpha+1+\beta)E_\theta\alpha_\theta r^{-(\beta+1)}}{2\beta}\int_a^r \rho^{\beta} g_1(\rho,t)d\rho\right]\cos\theta
+\sum_{n=2}^{\infty}\left\{\sum_{i=1}^{4}n(\lambda_{ni}-1)r^{\lambda_{ni}-2}\left[A_{ni}+\Pi_i^n E_\theta\alpha_\theta((\lambda_{ni}-M_\alpha-1)\right.\right.
\left.\left.\times(2-\lambda_{ni})+n^2M_\alpha)\int_a^r \rho^{1-\lambda_{ni}} f_n(\rho,t)d\rho\right]\right\}\sin n\theta
+\sum_{n=2}^{\infty}\left\{\sum_{i=1}^{4}n(\lambda_{ni}-1)r^{\lambda_{ni}-2}\left[B_{ni}+\Pi_i^n E_\theta\alpha_\theta((\lambda_{ni}-M_\alpha-1)\right.\right.
\left.\left.\times(2-\lambda_{ni})+n^2M_\alpha)\int_a^r \rho^{1-\lambda_{ni}} g_n(\rho,t)d\rho\right]\right\}\cos n\theta. \tag{54}
$$

Boundary Conditions. In a pure thermoelastic problem, the stress-free boundary conditions at the inner and outer surfaces are

$$r=a,\quad \sigma_{rr}=\sigma_{r\theta}=0; \tag{55}$$

$$r=b,\quad \sigma_{rr}=\sigma_{r\theta}=0. \tag{56}$$

Plane-Strain Formulation. The plane-strain solution is obtained directly from the plane stress solution by replacing the plane-stress compliances S_{11}, S_{22}, S_{12} by the corresponding plane-strain compliances S_{11}', S_{22}', S_{12}' where

$$S_{ij}'=S_{ij}-\frac{S_{i3}S_{j3}}{S_{33}},\quad i,j=1,2 \tag{57}$$

$$S_{11}=\frac{1}{E_r},\quad S_{22}=\frac{1}{E_\theta},\quad S_{12}=-\frac{\nu_{r\theta}}{E_r} \tag{58}$$

$$S_{13}=S_{13}'=\frac{1}{G_{rz}},\quad S_{23}=S_{23}'=\frac{1}{G_{\theta z}},\quad S_{33}=S_{33}'=\frac{1}{E_z}. \tag{59}$$

The subscript 3 denotes the axial (z) direction. Likewise, the coefficients of thermal expansion are related through

$$\alpha_r'=\alpha_r+\nu_{zr}\alpha_z, \tag{60}$$

$$\alpha_\theta'=\alpha_\theta+\nu_{z\theta}\alpha_z. \tag{61}$$

Also,

$$k'=\sqrt{\frac{S_{11}'}{S_{22}'}},\quad m'=\sqrt{\frac{1}{G_{r\theta}S_{22}'}},\quad M_\alpha'=\frac{\alpha_r'}{\alpha_\theta'},\quad \nu_{r\theta}'=\frac{\nu_{r\theta}(1+\nu_{z\theta})}{S_{11}'E_r}. \tag{62}$$

Polymer Composite Example and Discussion

To illustrate the use of the analysis, an orthotropic cylinder (Fig. 1) having an insulated inner boundary, a convective outer boundary and two halves initially at two different, uniform tem-

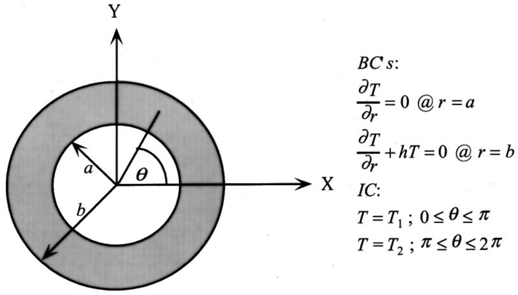

Fig. 1 Example orthotropic cylinder with imposed boundary conditions and initial condition

peratures is considered. The cylinder is not otherwise being heated, so that $S(r,\theta,t)=0$. The assumed cylinder dimensions and thermal boundary condition coefficents are: $a=0.05$ m, $b=0.1$ m, $L_{11}=1$, $L_{12}=0$, $L_{21}=1$, $L_{22}=10$. The initial temperature distribution is: $F(r,\theta)=T_1$, $0\leqslant\theta\leqslant\pi$; $F(r,\theta)=T_2$, $\pi\leqslant\theta\leqslant 2\pi$. The material properties are taken to be $E_\theta=44$ GPa, $E_r=11$ GPa, $\zeta=5\times10^{-7}$ m^2/s, $\alpha_r=60\times10^{-6}$/°C, $\alpha_\theta=5\times10^{-6}$/°C, $K_r=1$ W/m°C, $K_\theta=9$ W/m°C, which are typical values for a 60% fiber-volume-fraction hoop-wound E-glass/epoxy composite. The thermal stresses are nondimensionalized using $\overline{\sigma_{rr}}=\sigma_{rr}/E_\theta\alpha_\theta\overline{T}$, $\overline{\sigma_{\theta\theta}}=\sigma_{\theta\theta}/E_\theta\alpha_\theta\overline{T}$, $\overline{\sigma_{r\theta}}=\sigma_{r\theta}/E_\theta\alpha_\theta\overline{T}$, where $\overline{T}=(T_1+T_2)/2$ is the axisymmetric part of the initial temperature.

In the example problem, the initial condition can be expressed as $F(r,\theta)=\overline{T}+(T_1-T_2)/2$, $0\leqslant\theta\leqslant\pi$, $F(r,\theta)=\overline{T}-(T_1-T_2)/2$, $\pi\leqslant\theta\leqslant 2\pi$ so that the principle of linear superposition can be applied to add the axisymmetric thermal stresses caused by an initial axisymmetric temperature field ($\overline{T}$) to the asymmetric thermal stresses caused by an initial asymmetric temperature distribution ($(T_1-T_2)/2$, $0\leqslant\theta\leqslant\pi$; $-(T_1-T_2)/2$, $\pi\leqslant\theta\leqslant 2\pi$). In the following plots, $T_1=100$°C and $T_2=80$°C; the dimensionless time, $\tau=\zeta t/a^2$, is chosen to be $\tau=0$, $\tau=0.36$ and $\tau=0.72$, corresponding to $t=0$, $t=1800$, and $t=3600$ seconds, respectively. Computationally, the asymmetric part of the initial condition is expanded by a Fourier Sine series: $4(T_1-T_2)\Sigma_{n=1,3,5,..}^{\infty}\sin n\theta/n$. To obtain sufficiently convergent results, the number of eigenvalues in the temperature distribution is taken to be $i=10$ and $n=11$. All integral terms in (52)–(54) are evaluated numerically by a Gaussian quadrature rule using 30 Gauss integration points.

The transient, surface temperature histories at three circumferential directions ($\theta=-\pi/2,0,\pi/2$) are illustrated in Fig. 2. As τ increases, the temperature at $\theta=-\pi/2$ increases gradually and asymptotically converges to that at $\theta=\pi/2$ due to the initial temperature gradient. In the current example, the temperature history at an arbitrary position is bounded by a horn-shape evolution.

Figure 3 demonstrates the transient, radial temperature variation

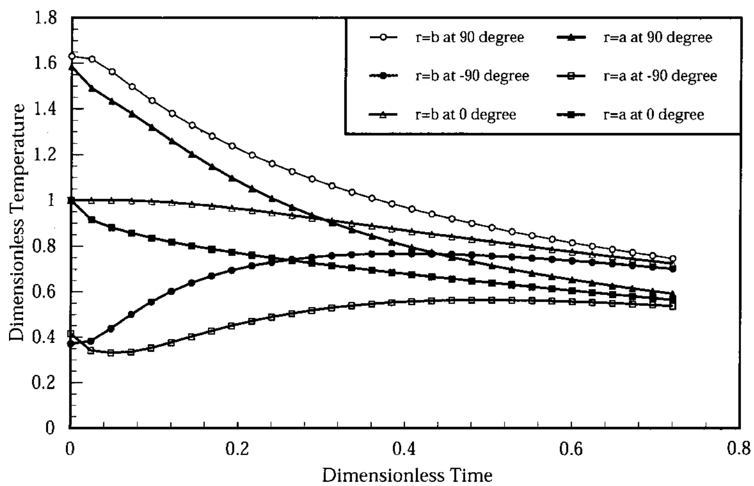

Fig. 2 Surface temperature history for $\theta=-\pi/2,0,\pi/2$

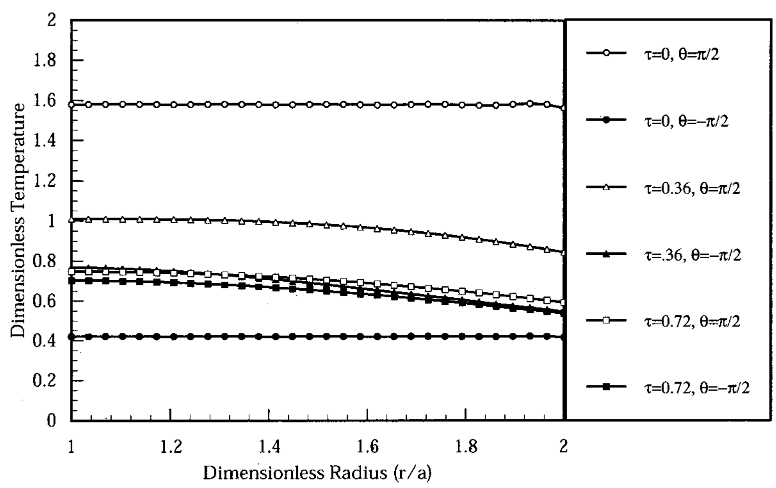

Fig. 3 Transient temperature distribution in the radial direction for $\theta=-\pi/2,\pi/2$

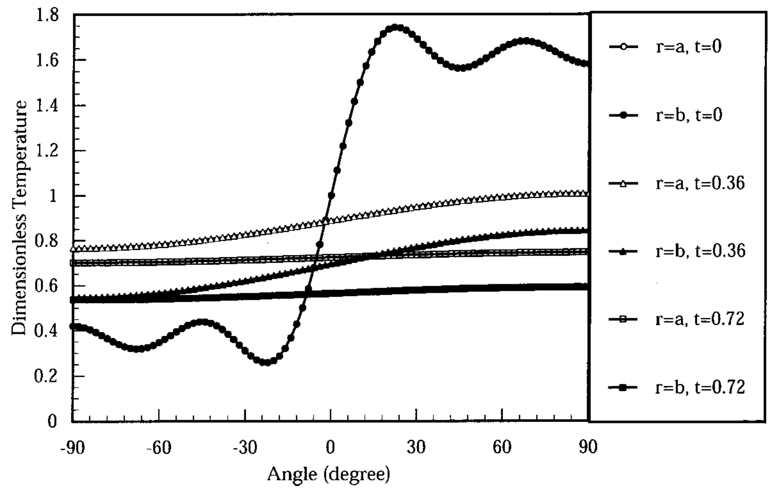

Fig. 4 Transient, surface temperature distribution in the circumferential direction

at $\theta=-\pi/2,\pi/2$. As expected, the numerical results reveal that the initial temperature difference between the two diametrically opposite positions diminishes as τ increases.

Figure 4 depicts the transient, circumferential temperature variation at $r=a,b$. At $\tau=0$, the temperature distribution at the cylinder's inner and outer surfaces coincide due to the initial uniform distribution of temperature; the circumferential oscillations are the result of using a finite number of terms in the Fourier series to represent the abrupt, step change in temperature at $\theta=\pi,2\pi$. As τ increases, the temperature gradient in the circumferential direction decays as the cylinder approaches an axisymmetric, thermal steady state.

Figure 5 shows the surface hoop stress history in three circumferential directions. Since the maximum hoop stress occurs at either the cylinder's inner or outer surface, the hoop stress for any intermediate radial position again falls into a horn-shape evolution. As the spatial and temporal temperature gradients decay, the hoop stresses converge asymptotically to a steady-state value.

Figure 6 illustrates the transient hoop-stress variation at $r=a,b$ in the circumferential direction. As expected, the numerical results show that at $\tau=0$ the maximum tensile hoop stress occurs at $r=b$, $\theta=\pi/2$ and the maximum compressive hoop stress occurs at $r=a$, $\theta=\pi/4$. Meanwhile, it is informative to note that the hoop stress is tensile and compressive at the outer and inner surfaces, respectively.

Figure 7 depicts the transient hoop stress in the radial direction for $\theta=-\pi/2,\pi/2$. The maximum compressive hoop stress ($r=a$, $\theta=\pi/2$) decreases to two-thirds its initial value by $\tau=0.36$; in the same period, the maximum tensile hoop stress ($r=b$, $\theta=-\pi/2$) drops to less than half its original value. Often, a composite cylinder's tensile strength is significantly higher than its compressive strength due to defects (e.g., residual stresses, microcracks, fiber waveness) generated during the manufacturing process. As a result, when considering the failure of a composite cylinder under thermal loading, both the magnitude and sign are important.

Figure 8 shows the transient radial stress along the radial direction at $\theta=-\pi/2,\pi/2$. The compressive radial stress suggests that interlaminar delaminations and/or microcracks in the fiber direction will not open further under this particular thermal loading.

Figure 9 displays the transient shear stress in the radial direction at $\theta=0,\pi$. Due to the symmetric temperature distribution with respect to the Y-axis, the shear stress is necessarily zero at $\theta=-\pi/2,\pi/2$. As the resulting shear stress is antisymmetric, the shear stress for any intermediate radial position is bounded by the envelope spanning from $\theta=0,\pi$. Clearly, the shear stress eventually diminishes as τ increases, which can be seen from the temperature distribution discussed earlier in Fig. 4. In the present problem, the maximum shear stress is only about 3% of the maximum hoop stress; however, thermal stresses may initiate failure by

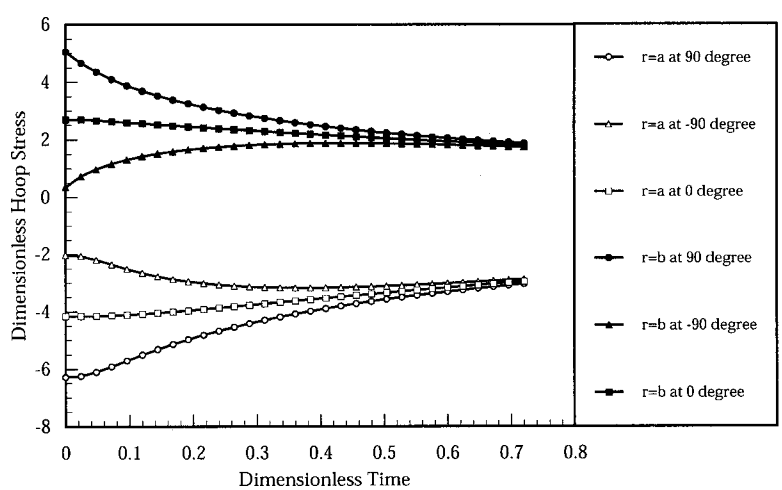

Fig. 5 Surface hoop-stress history for $\theta=-\pi/2,0,\pi/2$

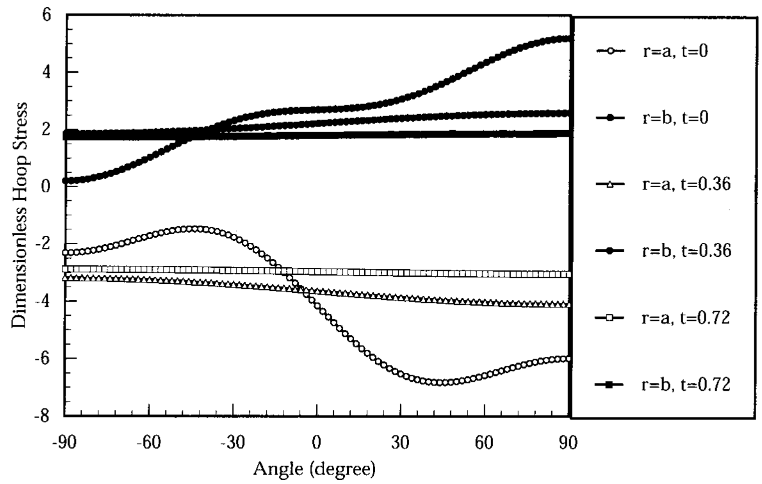

Fig. 6 **Transient, surface hoop-stress distribution in the circumferential direction**

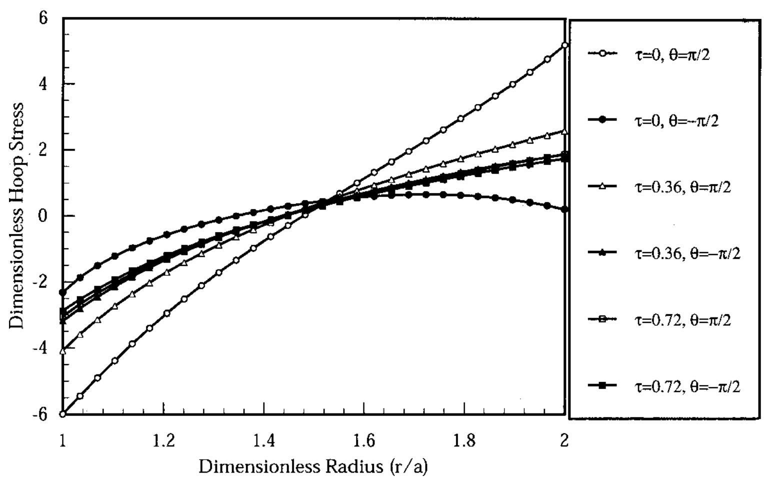

Fig. 7 **Transient, hoop-stress distribution in the radial direction for $\theta=-\pi/2,\pi/2$**

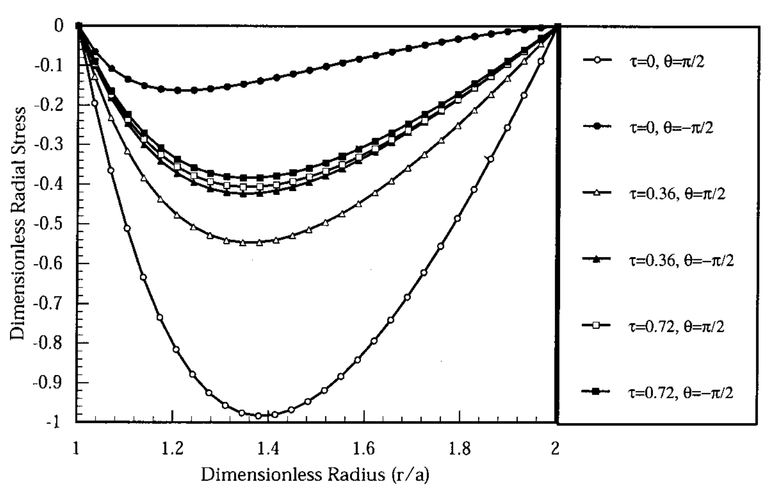

Fig. 8 **Transient, radial-stress distribution in the radial direction for $\theta=-\pi/2,\pi/2$**

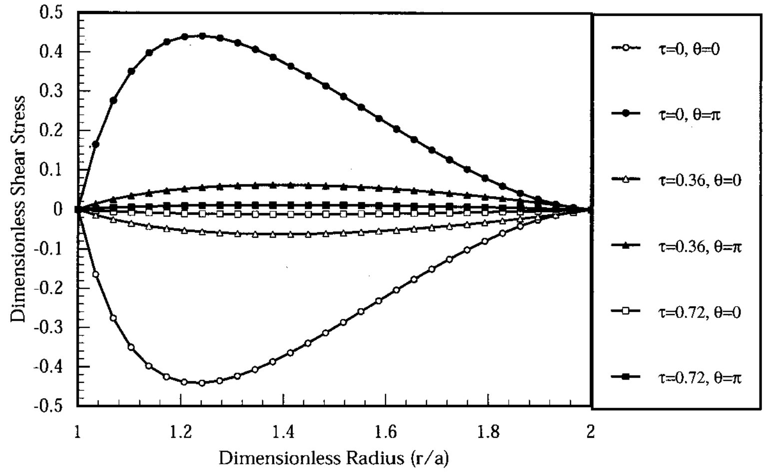

Fig. 9 Transient, shear-stress distribution in the radial direction for $\theta=0,\pi$

the action of shear stresses—not hoop stresses—due to the often low, interlaminar shear strengths in composite structures.

Conclusions

This paper presents a closed-form analytical solution for the transient, plane thermal stress analysis of a linearly elastic, homogeneously orthotropic hollow cylinder subjected to an arbitrary, asymmetric temperature distribution. The hoop, radial, and shear stresses, due to the transient arbitrary temperature distribution, are expressed explicitly in terms of the scalar temperature field. The current analysis is compact, straightforward; it does not require complicated mathematical operations using the Hankel asymptotic expansions of the Bessel functions to tackle the difficulty caused by the limiting cases of extremely short and long times ([6,7]).

The current thermoelastic stress analysis assumes that the cylinder's mechanical and thermal properties are homogeneously distributed; however, using perturbation techniques, this solution can be directly extended to include weakly inhomogeneously orthotropic cylinders. Moreover, using the viscoelastic Correspondence Principle, the thermoelastic solution also immediately yields the thermoviscoelastic solution for thermorheologically simple viscoelastic materials.

Representative numerical results for the thermally driven hoop, radial, and shear stresses in a hollow hoop-wound glass/epoxy cylinder reveal that

- asymmetric spatial and temporal thermal gradients induce potentially debilitating shear stresses, which can initiate intra or interlaminar failure in orthotropic laminated materials—prior to the onset of tensile/compressive failure.
- the thermal stress distributions are greatly affected by the thermal boundary (and initial) conditions. In the example, the cylinder's thermal boundary conditions—and hence steady state—were homogenous and independent of the circumferential position; as a direct result, the cylinder had only a transient shear stress, which decayed to zero with the thermal gradients. However, spatially varying thermal boundary conditions imposed on a homogeneously orthotropic hollow cylinder can induce nonzero shear stresses, which will not necessarily decay to zero with the thermal gradients.
- for homogeneously orthotropic hollow cylinders exposed to asymmetric temperature gradients, but axisymmetric thermal boundary conditions and no internal heating, the asymmetric thermal stress analysis exhibits maximum stress envelopes, which provide useful information on how the maximum thermal stresses evolve during the transient state.

Acknowledgments

Support from Dr. Yapa Rajapakse of the U.S. Office of Naval Research through grant number ONR-N00014-92-J-1470 is gratefully acknowledged, as is the support provided by Dr. Bruce Kramer of the National Science Foundation through grant numbers DDM-9109592, DDM-9258413, and DDM-9311241. Additional equipment support was provided through the Texas Advanced Technology Program, grant number 1993-003658-359. Finally, the support from the University of Texas at Austin's Bureau of Engineering Research is also acknowledged.

References

[1] Biot, M., 1958, "Linear Thermodynamics and the Mechanics of Solids," *Proc. 3rd U.S. National Congress of Applied Mechanics*, ASME, New York, pp. 1–18.
[2] Schapery, R. A., 1962, "Approximate Methods of Transform Inversion for Visocelastic Stress Analysis," *Proc. 4th U.S. National Congress of Applied Mechanics*, ASME, New York, pp. 1075–1084.
[3] Padovan, N. J., 1976, "Thermoelasticity of Cylindrically Anisotropic Generally Laminated Cylinders," ASME J. Appl. Mech., **43**, pp. 124–130.
[4] Kalam, M. A., and Tauchert, T. R., 1978, "Stresses in an Orthotropic Elastic Cylinder due to a Plane Temperature Distribution $T(r\cdot\theta)$," J. Therm. Stresses, **1**, pp. 13–24.
[5] Iwaki, T., 1986, "Transient Thermal Stresses in Fully and Partially Cooled Circular Rings," Exp. Mech., **25**, pp. 163–168.
[6] Kardomateas, G. A., 1989, "Transient Thermal Stresses in Cylindrically Orthotropic Composite Tubes," ASME J. Appl. Mech., **56**, pp. 411–417.
[7] Kardomateas, G. A., 1990, "The Initial Phase of Transient Thermal Stresses due to General Boundary Thermal Loads in Orthotropic Hollow Cylinders," ASME J. Appl. Mech., **57**, pp. 719–724.
[8] Sugano, Y., 1990, "An Analytical Solutions for a Plane Thermal Stress Problem in Nonhomogeneous Multiply Connected Regions," JSME Int. J., **33**, pp. 136–144.
[9] Zibdeh, H. S., and Al Farran, J. M., 1995, "Stress Analysis in Composite Hollow Cylinders due to an Asymmetric Temperature Distribution," ASME J. Pressure Vessel Technol., **117**, pp. 59–65.
[10] Hata, T., and Atsumi, A., 1968, "Transient Thermoelastic Problem for a Transversely Anisotropic Hollow Cylinder With Temperature-Dependent Properties," Bull. JSME, **11**, pp. 404–412.
[11] Tauchert, T. R., 1976, "Ritz Solution for Thermoelastic Cylinders," J. Eng. Mech. Div., **102**(EM5), pp. 825–836.
[12] Tauchert, T. R., 1978, "Ritz Solutions for Axisymmetric Temperature and Stress Fields in Finite Elastic Cylinders," Int. J. Numer. Methods Eng., **12**, pp. 567–572.
[13] Kalam, M. A., 1981, "Modified Rayleigh-Ritz Method in Nonaxisymmetric Thermoelastic Analysis of an Orthotropic Cylinder," J. Therm. Stresses, **4**, pp. 31–38.
[14] Hyer, M. W., and Cooper, D. E., 1988, "Thermal Stresses in Composite Tubes Using Complementary Virtual Work," J. Therm. Stresses, **11**, pp. 93–113.
[15] Huang, N. N., and Taucher, T. R., 1988, "Large Deformation of Antisymmetric Angle-Ply Laminates Resulting From Nonuniform Temperature Loadings," J. Therm. Stresses, **11**, pp. 287–297.
[16] Irving, A. C., and Francis, H. S., 1992, *Elastic and Inelastic Stress Analysis*, Prentice-Hall, Englewood Cliffs, NJ.

D. N. Robinson
Professor Emeritus
Department of Civil Engineering,
University of Akron,
Akron, OH 44325

K. J. Kim

J. L. White
Director

Institute of Polymer Engineering,
University of Akron,
Akron, OH 44325

Constitutive Model of a Transversely Isotropic Bingham Fluid

A constitutive theory is presented for a transversely isotropic, viscoplastic (Bingham) fluid. The theory accounts for threshold (yield) and viscous flow characteristics through inclusion of a potential function serving the dual role of a threshold function and a viscous flow potential. The arguments and form of the potential function derive from the theory of tensorial invariants. The model reduces to a transversely isotropic model of perfect plasticity in the limit of vanishing viscosity. In the limit of isotropy, it reduces to the Hohenemser-Prager generalization of Bingham's model. A characterization procedure is prescribed based on correlation with experiments conducted under simple states of stress. Application is made to polymer melts filled with talc particles.
[DOI: 10.1115/1.1483831]

1 Introduction

Concentrated suspensions of small particles in various matrices including polymer melts are known to exhibit a threshold or yield stress, i.e., a stress below which no flow occurs. This behavior is well documented in shear flow experiments, e.g., Chapman and Lee [1], Vinogradov et al. [2], Suetsugu and White [3], and Osanaiye et al. [4]. Evidence of such behavior also exists in uniaxial elongational flow, cf., Toki and White [5], Montes and White [6], Suetsugu and White [3], and Kim and White [7].

There is a long history of effort to develop constitutive equations for particle filled suspensions. A simple shear model of a fluid that is rigid below a threshold stress and exhibits linear viscous flow above was proposed by Bingham [8]. Multiaxial extensions of Bingham's model were made over the following two decades by Hohenemser and Prager [9] and Oldroyd [10]. Prager [11] in his monograph examines and generalizes this earlier work and makes application to some simple classical flows. More recently, White [12] and White and Lobe [13] developed a multiaxial plastic/viscoelastic model. In each of the multiaxial models cited, the features of plasticity are based on the von Mises (J_2) yield criterion of isotropic perfectly plastic solids.

The investigations addressed above are directed to suspensions where the effect of the dispersed particles results in viscoplastic behavior that is essentially isotropic. However, fibrous or disk-like (talc, mica, etc.) particles used as fillers in some industrial compounds often result in anisotropy. It is observed that such particles tend to orient during flow or processing, resulting in material properties that have a preferential direction and are thus transversely isotropic. Ericksen [14] was the first to develop a theory of anisotropic fluids. A theory of transversely isotropic plastic-viscoelastic fluids applicable to polymer melts has been developed by White and Suh [15]. Their model makes use of an anisotropic yield criterion due to Hill [16–18]. A recent paper by White et al. [19] considers an alternate model of a transversely isotropic plastic-viscoelastic fluid in which the anisotropic yield criterion of Hill is replaced by one based on the theory of tensorial invariants following Spencer [20–23].

Contributed by the Applied Mechanics Division of THE AMERICAN SOCIETY OF MECHANICAL ENGINEERS for publication in the ASME JOURNAL OF APPLIED MECHANICS. Manuscript received by the ASME Applied Mechanics Division, January 3, 2000; final revision, December 14, 2001. Associate Editor: D. A. Siginer. Discussion on the paper should be addressed to the Editor, Prof. Robert M. McMeeking, Department of Mechanical and Environmental Engineering, University of California–Santa Barbara, Santa Barbara, CA 93106-5070, and will be accepted until four months after final publication of the paper itself in the ASME JOURNAL OF APPLIED MECHANICS.

In this paper, we propose a constitutive theory of a transversely isotropic viscoplastic fluid based on a potential function that plays the dual role of a threshold function and a viscous flow potential. The potential implies a form of path-independence and limits the representation to fluids whose viscosity is independent of deformation history (e.g., excluding thixotropy). We develop the transversely isotropic constitutive theory and examine some limiting cases. Application is made to PS polymer melts filled with 20%V and 40%V of talc particles.

2 Constitutive Model

Consider a non-Newtonian viscous material (fluid) under isothermal conditions represented by

$$\mathbf{V}=\frac{\partial\Omega}{\partial\boldsymbol{\sigma}} \tag{1}$$

in which $\mathbf{V}$ = the rate of deformation, $\boldsymbol{\sigma}$ = the Cauchy stress, and Ω = a viscous dissipation potential function. Equation (1) expresses normality of the rate of deformation $\mathbf{V}$ to surfaces of $\Omega(\boldsymbol{\sigma})$ = const. in a combined rate of deformation /stress space, cf., Appendix A. Convexity of the surfaces $\Omega(\boldsymbol{\sigma})$ = const. in that space ensures that the representation is dissipative.

For an anisotropic fluid Ω must depend not only on stress but also on the local material orientation, cf., Appendix B. In the case of transverse isotropy, the local preferred orientation can be designated by a unit vector $\mathbf{d}$. As the sense of $\mathbf{d}$ has no special significance, we take the dyadic self product of $\mathbf{d}$ defining a symmetric orientation tensor $\mathbf{D}=\mathbf{d}\otimes\mathbf{d}$ with $tr\mathbf{D}=1$. Assuming the fluid response to be independent of hydrostatic stress, we take the stress dependence on the deviatoric stress $\mathbf{s}$. Thus, the viscous potential $\Omega(\mathbf{s},\mathbf{D})$ depends on two symmetric, second rank tensors.

Following Spencer [20–23], objectivity of (1) requires that Ω depends on an irreducible integrity basis comprised of invariants and joint invariants of its arguments $\mathbf{s}$ and $\mathbf{D}$. Included in the integrity basis is the subset of quadratic invariants:

$$\begin{aligned} J_2&=\frac{1}{2}tr\mathbf{s}^2\\ I_0^2&=(tr\mathbf{Ds})^2\\ I&=tr\mathbf{Ds}^2 \end{aligned} \tag{2}$$

Thus, we may take

$$\Omega(J_2,I_0^2,I). \tag{3}$$

Instead, we are guided by Lance and Robinson [24] and Robinson and Duffy [25] and make use of a physically based set of invariants that are combinations of (2), i.e.,

$$
\begin{aligned}
I_1 &= J_2 - I + \frac{1}{4} I_0^2 \\
I_2 &= I - I_0^2 \\
I_3 &= \left(\frac{3}{2} I_0\right)^2
\end{aligned}
\tag{4}
$$

and we take

$$\Omega(I_1, I_2, I_3). \tag{5}$$

I_1 in (4) specifies the square of the maximum transverse shear stress at a material (fluid) element, i.e., the maximum shear stress on planes containing the local preferential direction **d** and perpendicular to it. I_2 is the square of the maximum longitudinal shear stress on planes containing **d** and parallel to **d**. I_3 gives the square of the normal stress on a plane perpendicular to **d**, i.e., on the plane of isotropy.

We introduce an intermediate function Φ that incorporates a polynomial of the invariants (4), i.e.,

$$\Omega(\Phi) \tag{6}$$

$$\Phi = I_1 + \alpha^2 I_2 + \beta^2 I_3 \tag{7}$$

in which $\alpha > 0$ and $\beta > 0$ are material constants. We note from (7) that Φ is a quadratic, convex function of stress. Similarly, Ω is convex in stress, ensuring that the representation is dissipative (cf., Appendix A).

Using (1) and (6) we write

$$\mathbf{V} = \frac{\partial \Omega}{\partial \boldsymbol{\sigma}} = \frac{d\Omega}{d\Phi} \frac{\partial \Phi}{\partial \boldsymbol{\sigma}} \tag{8}$$

and calculate, from (4) and (7)

$$\frac{\partial \Phi}{\partial \boldsymbol{\sigma}} = \mathbf{\Gamma} = \mathbf{s} + (\alpha^2 - 1)(\mathbf{sD} + \mathbf{Ds} - 2 I_0 \mathbf{D}) + (3\beta^2 - 1)\frac{I_0}{2}(3\mathbf{D} - \mathbf{I}). \tag{9}$$

It is readily shown from (9) that $tr\mathbf{\Gamma} = 0$. Then, from (8) we have $tr\mathbf{V} = 0$ indicating incompressibility.

We need to specify the function $d\Omega/d\Phi$ in (8) for a particular fluid. Following Hohenemser and Prager [9] and Prager [11] we adopt a simple power-law form

$$\frac{d\Omega}{d\Phi} = \frac{F^n}{2\mu} \quad \text{where} \quad F = 1 - \frac{K}{\sqrt{\Phi}} \tag{10}$$

in which $n \geqslant 1$, μ and K are material constants.

As our interest is in a representation of a viscoplastic material that is essentially a viscous fluid but can sustain shear stress in a state of rest, we state the constitutive theory in the form (again guided by Hohenemser and Prager [9] and Prager [11]):

$$2\mu \mathbf{V} = \begin{cases} 0 & \text{for} \quad F < 0 \\ F^n \mathbf{\Gamma} & \text{for} \quad F \geqslant 0 \end{cases} \tag{11}$$

$$F = 1 - \frac{K}{\sqrt{\Phi}} \qquad \Phi = I_1 + \alpha^2 I_2 + \beta^2 I_3$$

$$\mathbf{\Gamma} = \mathbf{s} + (\alpha^2 - 1)(\mathbf{sD} + \mathbf{Ds} - 2 I_0 \mathbf{D}) + (3\beta^2 - 1)\frac{I_0}{2}(3\mathbf{D} - \mathbf{I}) \tag{12}$$

where (7), (9), and (10) are repeated for convenience.

This completes the representation of a transversely isotropic, non-Newtonian visco-plastic fluid. Its full specification includes (2), (4), and (9)–(12). Application to a particular fluid requires the determination of the material parameters

$$K, \mu, n, \alpha, \text{ and } \beta. \tag{13}$$

K has units of stress, μ has the units of viscosity (stress-time), and the remaining parameters are dimensionless.

The second Eq. (11) can be transposed as

$$2\bar{\mu}\mathbf{V} = \mathbf{\Gamma} \tag{14}$$

where

$$\bar{\mu} = \mu F^{-n} \tag{15}$$

is a transversely isotropic viscosity. We note that (cf., Appendix A). $\Omega = $const. surfaces in stress space are surfaces of $F = $const., and by (15), $\bar{\mu} = $const. In particular, the threshold surface $F = 0$ corresponds to $\bar{\mu} = \infty$.

The anisotropy parameters α and β and the threshold stress K in (11) and (12) are material constants relating to a fixed degree of anisotropy and stress threshold. This is consistent with steady-state flow where the oriented filler particles have fully aligned with the flow (as the talc particles in the subsequent application). Under transient conditions where the filler particles (fibers) may be initially randomly orientated and convect with the flow, the scalars α, β, and K need to be considered state variables each having an evolutionary equation coupled with the flow equations, for example with forms $\dot{\alpha}(\boldsymbol{\sigma}, \mathbf{D}, \mathbf{V})$, $\dot{\beta}(\boldsymbol{\sigma}, \mathbf{D}, \mathbf{V})$, and $\dot{K}(\boldsymbol{\sigma}, \mathbf{D}, \mathbf{V})$, cf., Poitou, Chinesta, and Bernier [26] and Advani [27].

Definition of the evolutionary equations is left as a topic of future research.

3 Some Limiting Conditions

The second Eq. (11) or (14) can be written as

$$\mathbf{\Gamma} = \left[(2\mu)^{1/n} + \frac{K}{\sqrt{\Phi}} \left(\frac{tr\mathbf{\Gamma}^2}{tr\mathbf{V}^2} \right)^{1/2n} \right]^n \mathbf{V}. \tag{16}$$

Equation (16), of course, holds only if the rate of deformation is nonzero.

Taking the trace of each side of (16) multiplied by itself gives

$$tr\mathbf{\Gamma}^2 = \left[(2\mu)^{1/n} + \frac{K}{\sqrt{\Phi}} \left(\frac{tr\mathbf{\Gamma}^2}{tr\mathbf{V}^2} \right)^{1/2n} \right]^{2n} tr\mathbf{V}^2. \tag{17}$$

For $\mu \to 0$ in (17) there results

$$\frac{K^{2n}}{\Phi^n} = 1 \quad \text{or} \quad \Phi = K^2. \tag{18}$$

Equation (18) serves as a transversely isotropic yield condition that is satisfied whenever the rate of deformation is not zero.

Under the same limit $\mu \to 0$, (16) reduces to

$$\mathbf{\Gamma} = \sqrt{\frac{tr\mathbf{\Gamma}^2}{tr\mathbf{V}^2}}\mathbf{V} \quad \text{or} \quad \mathbf{V} = \lambda \mathbf{\Gamma}; \quad \lambda > 0. \tag{19}$$

The yield condition (18) and the flow law (19) are supplemented by the condition

$$\Phi < K^2 \tag{20}$$

corresponding to zero deformation rate. Thus, the viscoplastic constitutive model expressed in (9)–(12) reduces to a transversely isotropic perfect plasticity model (18)–(20) in the limit of zero viscosity $\mu \to 0$. This anisotropic plasticity model was employed earlier in Robinson and Pastor [28].

Further, we consider another limiting case, i.e., the isotropic limit $\alpha \to 1$, $\beta \to 1/\sqrt{3}$ with $n = 1$. Under this limit (2), (4), (7), and (9) give $\Phi = 1/2\, tr\mathbf{s}^2 = J_2$ and $\mathbf{\Gamma} = \mathbf{s}$ and the viscoplasticity model (9)–(12) becomes

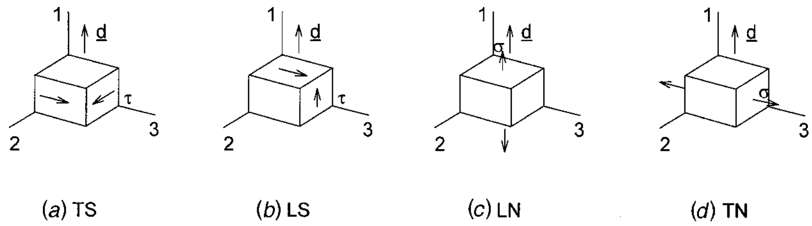

Fig. 1 "Natural" stress states

$$2\mu\mathbf{V}=\begin{cases}0 & \text{for} \quad F<0\\ F\mathbf{s} & \text{for} \quad F\geqslant 0\end{cases} \tag{21}$$

$$F=1-\frac{K}{\sqrt{J_2}} \tag{22}$$

which is recognized as the multiaxial generalization of Bingham's model proposed by Hohenemser and Prager [9] and Prager [11].

The isotropic limit of the anisotropic perfect plasticity model (18)–(20) is

$$J_2=K^2 \tag{23}$$

replacing the yield condition (18). The flow law (19) becomes

$$\mathbf{V}=\lambda\mathbf{s} \tag{24}$$

and (20) is replaced by

$$J_2<K^2. \tag{25}$$

The isotropic perfect plasticity model specified in (23)–(25) is that first considered by von Mises [29].

4 Response to Simple Stress States

Natural Stress States. We now calculate the response of the viscoplastic model (9)–(12) under some simple stress states, referred to as "natural" stress states for the model. These are illustrated in Fig. 1. We choose coordinate directions as shown, with the preferential direction along the x_1-axis. Thus, the orientation tensor $\mathbf{D}$ has components $D_{11}=1$ with all others zero.

Transverse shear (TS) is depicted in Fig. 1(a). The relevant stress components are $\sigma_{23}=\sigma_{32}=\tau$, all others are zero. Calculating the pertinent invariants using (2) and (4) and substitution into (7) and (9) yields $\Phi=\tau^2$ and $\Gamma_{23}=\tau$. At the threshold $F=0$, we have

$$\tau=\pm K. \tag{26}$$

Thus, the material parameter K introduced in (10) represents the threshold stress in transverse shear (TS).

Using (11) and denoting $\dot{\gamma}_{23}\equiv 2V_{23}$, we obtain an expression for transverse shear (TS) flow:

$$\dot{\gamma}_{23}=\frac{1}{\mu}\left(1-\frac{K}{|\tau|}\right)^n\tau \qquad |\tau|\geqslant K. \tag{27}$$

Next, we consider longitudinal shear (LS) as illustrated in Fig. 1(b). Now the relevant stress components are $\sigma_{13}=\sigma_{31}=\tau$, all others zero. Again, calculating the pertinent invariants using (2) and (4) and substitution into (7) and (9) yields $\Phi=\alpha^2\tau^2$ and $\Gamma_{13}=\alpha^2\tau$. At the threshold $F=0$

$$\tau=\pm\frac{K}{\alpha}=\pm K_L \tag{28}$$

where K_L is the threshold stress in longitudinal shear and

$$\alpha=\frac{K}{K_L} \tag{29}$$

defines the material parameter α.

Using (11) and taking $\dot{\gamma}_{13}\equiv 2V_{13}$, we obtain the longitudinal shear (LS) flow

$$\dot{\gamma}_{13}=\frac{\alpha^2}{\mu}\left(1-\frac{K_L}{|\tau|}\right)^n\tau \qquad |\tau|\geqslant K_L. \tag{30}$$

Now we consider a third simple stress state, i.e., longitudinal normal (LN) stress as depicted in Fig. 1(c). Here, the single nonzero stress component is $\sigma_{11}=\sigma$. Using (2), (4), (7), and (9) we get $\Phi=\beta^2\sigma^2$ and $\Gamma_{11}=2\beta^2\sigma$. At the threshold stress $F=0$ we have

$$\sigma=\pm\frac{K}{\beta}=\pm Y_L \tag{31}$$

where Y_L is the threshold under longitudinal normal (LN) stress and

$$\beta=\frac{K}{Y_L} \tag{32}$$

defines the parameter β.

From (11) with $\dot{\varepsilon}_{11}\equiv V_{11}$ we have elongational (LN) flow

$$\dot{\varepsilon}_{11}=\frac{\beta^2}{\mu}\left(1-\frac{Y_L}{|\sigma|}\right)^n\sigma \qquad |\sigma|\geqslant Y_L. \tag{33}$$

The fourth natural stress state illustrated in Fig. 1(d) is that of transverse normal (TN) stress. Here, the only nonzero stress component is $\sigma_{33}=\sigma$. Again from (2), (4), (7), and (9) we have $\Phi=[(1+\beta^2)/4]\sigma^2$ and $\Gamma_{33}=[(1+\beta^2)/2]\sigma$. At the threshold $F=0$

$$\sigma=\pm\sqrt{4/(1+\beta^2)}K=\pm Y_T \tag{34}$$

or

$$\frac{K}{Y_T}=\sqrt{(1+\beta^2)/4}. \tag{35}$$

Again, from (11) with $\dot{\varepsilon}_{33}\equiv V_{33}$, we get an expression for the transverse normal (TN) flow

$$\dot{\varepsilon}_{33}=\frac{(1+\beta^2)/4}{\mu}\left(1-\frac{Y_T}{|\sigma|}\right)^n\sigma \qquad |\sigma|\geqslant Y_T. \tag{36}$$

Comparing (32) and (35), we observe that with the transverse shear threshold K known, determination of either Y_L or Y_T provides the parameter β. Evidently, Y_L and Y_T are not independent. This is because the theory developed here does not include the full integrity basis of invariants for transverse isotropy. This situation is analogous to that of the isotropic von Mises (J_2) theory of perfect plasticity (23)–(25), which is similarly based on an incomplete basis of invariants. There, with the shear yield stress K known, the uniaxial yield Y is not independent but determined as $Y=\sqrt{3}K$.

Combined Normal and Shear Stress. Before specifying a characterization procedure based on the natural stress states, we consider the response under combined normal and shear stress as

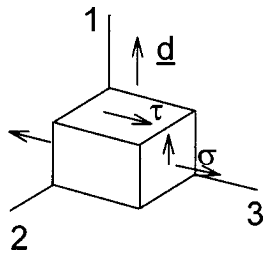

Fig. 2 Combined shear stress (LS) and normal stress (TN)

indicated in Fig. 2. In terms of the natural stress states the stress state of Fig. 2 is combined (LS) and (TN). The preferential direction is again taken along the x_1-coordinate direction; thus, again, the orientation tensor has components $D_{11}=1$ with all others zero. The nonzero stress components are $\sigma_{13}=\sigma_{31}=\tau$ and $\sigma_{33}=\sigma$.

Calculating the pertinent invariants using (2) and (4) and substitution into (7) yields

$$\Phi=\frac{1+\beta^2}{4}\sigma^2+\alpha^2\tau^2. \tag{37}$$

At the threshold $F=0$, using (29) and (35) and normalizing by K_L, we write

$$\frac{K_L^2}{Y_T^2}\left(\frac{\sigma}{K_L}\right)^2+\left(\frac{\tau}{K_L}\right)^2=1. \tag{38}$$

The threshold curve (surface) (38) is illustrated in the σ/K_L, τ/K_L space of Fig. 3. Varying degrees of anisotropy are specified by values of K_L/Y_T. Evidently, the shape of the threshold surfaces directly reflect the degree of anisotropy. The dotted curve relates to isotropy with $K_L/Y_T=1/\sqrt{3}=0.577$. That labeled 0.474 relates to a subsequent application to a filled PS/TALC 40V% melt.

Figure 4 shows the same stress space and includes the threshold surface designated as $K_L/Y_T=0.474$ in Fig. 3. Also shown is a family of surfaces $\Phi=$const. (or equivalently, $F=$const., $\bar{\mu}$ $=$const.). Stress points inside the threshold $F=0$ ($\bar{\mu}=\infty$), i.e., in

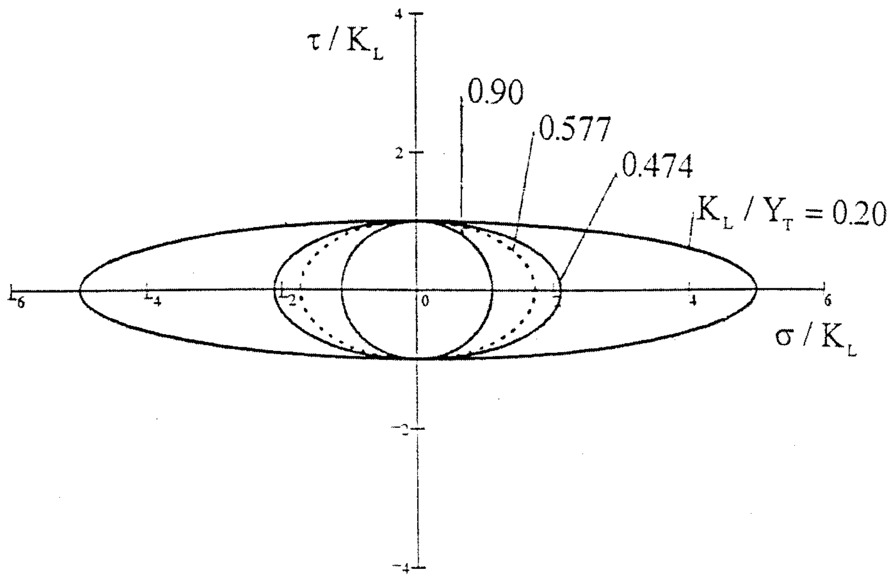

Fig. 3 Threshold curves in normalized σ/K_L, τ/K_L space. PS/TALC 40V%–0.474, Isotropic–0.577.

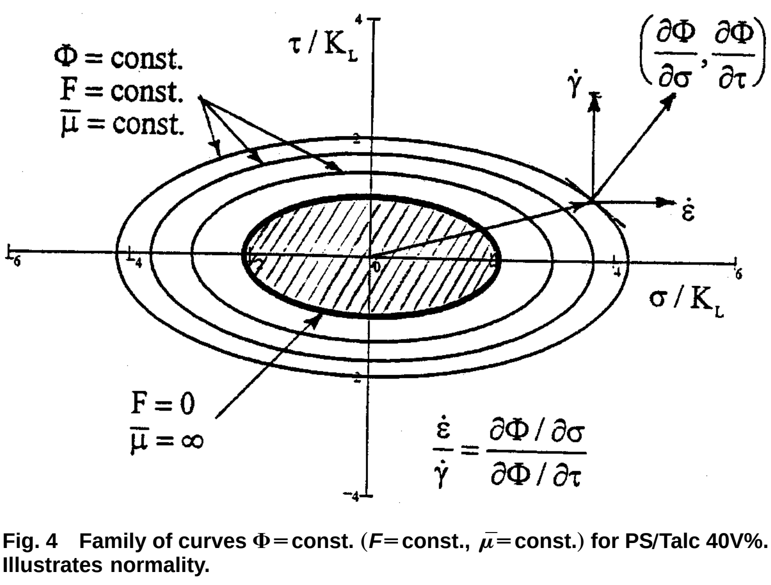

Fig. 4 Family of curves $\Phi=$const. ($F=$const., $\bar{\mu}=$const.) for PS/Talc 40V%. Illustrates normality.

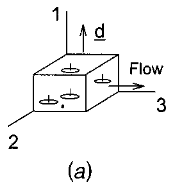

Fig. 5 Fluid elements showing preferential and flow directions; (*a*) disk-like filler particles, (*b*) elongated fiber filler particles

the shaded region, do not cause viscous flow; stress points outside $F=0$ ($\overline{\mu}=\infty$) produce flow with viscosity equal to the value of $\overline{\mu}=$const. passing through that stress point.

Flow under the combined σ,τ stress is calculated using (11). Denoting as earlier $\dot{\gamma}_{13}\equiv 2V_{13}$ and $\dot{\varepsilon}_{33}\equiv V_{33}$ and using (37) we have

$$\dot{\gamma}_{13}=\frac{\alpha^2}{\mu}\left(1-\frac{K}{\sqrt{\Phi}}\right)^n\tau \quad \Phi\geqslant K^2 \tag{39}$$

for the shear flow, and

$$\dot{\varepsilon}_{33}=\frac{(1+\beta^2)/4}{\mu}\left(1-\frac{K}{\sqrt{\Phi}}\right)^n\sigma \quad \Phi\geqslant K^2 \tag{40}$$

for the elongational flow.

Computing the ratio $\dot{\varepsilon}_{33}/\dot{\gamma}_{13}$,

$$\frac{\dot{\varepsilon}_{33}}{\dot{\gamma}_{13}}=\left(\frac{K_L}{Y_T}\right)^2\frac{\sigma}{\tau}=\frac{\partial\Phi/\partial\sigma}{\partial\Phi/\partial\tau}, \tag{41}$$

we see that it is equal to the ratio of components of the gradient vector (Fig. 4) computed using (37). The gradient vector is directed normal to the $\Phi=$const. curve passing through a particular stress point. This further illustrates the concept of normality as discussed in Appendix A. Clearly, the nature of the flow is influenced by the shapes of the $\Phi=$const. ($F=$const., $\overline{\mu}=$const.) curves, which, in turn, are dictated by the degree of anisotropy.

5 Characterization/Determination of Material Parameters

We now outline a characterization procedure for representing a particular fluid, i.e., a procedure for determining the material parameters (13). Hypothetically, experiments are conducted under the "natural" stress states (Fig. 1); the parameters are determined by correlating calculations based on results of the previous section and the measured responses. If we assume that the independent threshold stresses K,K_L and Y_L (or Y_T) are measurable, α and β are then determined through (29) and (32) (or (35)). Further, if shear and/or elongational flow data are available from experiments under any of the natural stress states (TS), (LS), (LN), or (TN), these data can be correlated with the respective predictions (27), (30), (33), or (36) to determine least-squares fits of the flow parameters μ and n. In principle, this completes the specification of the material parameters (13), i.e., K,μ,n,α and β.

In practice, not all experiments relating to the "natural" stress states can be performed. Rheological properties (yield and flow) are typically measured using rheometers, such as a sandwich rheometer for shear properties and a uniaxial elongational rheometer for elongational properties, cf., Kim and White [7]. Observe the two fluid elements of Figs. 5(a) and 5(b) corresponding to two types and configurations of filler particles under flow. The flow indicated in Fig. 5 is shear flow relating to a shear rheometer and extensional flow for an elongational rheometer The element in Fig. 5(a) shows disk-like particles having their disk normals oriented at right angles to the flow. Figure 5(b) shows elongated fibrous particles oriented with the flow direction. The material element of Fig. 5(a) is representative of the talc-filled PS melts considered in the next section.

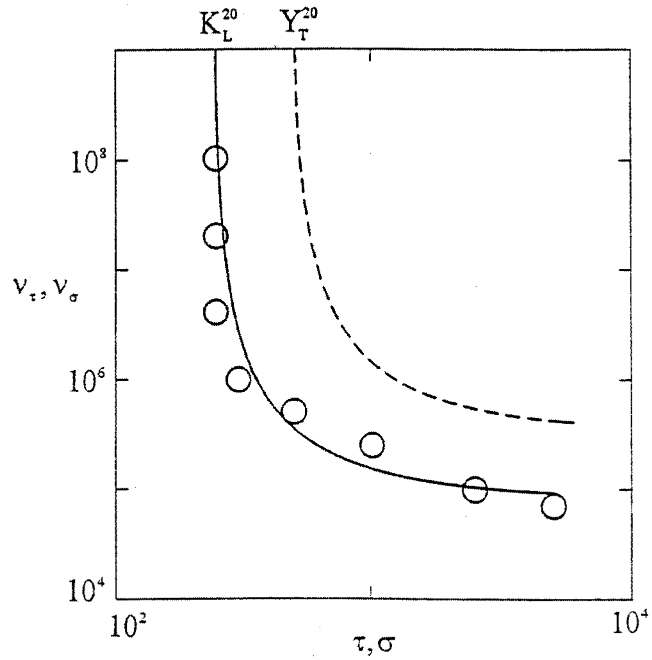

Fig. 6 Apparent viscosity (Pa-S) versus stress (Pa) for PS/TALC 20% (symbols). Correlation of shear flow (LS)–(solid curve). Prediction of elongational flow (TN)–(dashed curve).

Shear flow of the element in Fig. 5(a) is identified as longitudinal shear (LS) in accordance with the previous section (Fig. 1(b)). The corresponding threshold shear stress is K_L. Extensional flow of the same element is recognized as (TN) flow (Fig. 1(d)) with threshold stress Y_T. These flow and yield features are directly measurable using shear and elongational rheometry but do not allow a complete specification of the material parameters (13). Additional measurements are necessary for a full specification, e.g., measurments of transverse shear flow (TS) and/or the threshold stress K. However, these are not readily obtained for the class of fluids of interest.

A partial characterization useful in processing applications is found for talc-filled PS melts in the following section. This is based on rheometric measurments of Kim and White [7].

6 Application to Talc-Filled Polymer Melts

Application of the model is made to polymer melts containing disk-like talc particles (Fig. 5(a)). We suppose that a fluid element contains a large number of these particles oriented with their disk normals at right angles to the flow direction, cf., White and Suh [15] and White et al. [19].

As indicated in Fig. 5(a) we adopt a coordinate system with the axis x_1 aligned with $\mathbf{d}$, the local preferential direction. As earlier, the orientation tensor has the only nonzero component $D_{11}=1$. The flow direction is x_3.

The polymer melts of interest are PS/TALC 20 V% and PS/TALC 40 V % at 200°C. Figures 6 and 7 show experimental data (symbols) taken from Kim and White [7] and plotted as viscosity versus stress. As discussed earlier, the stress state under which these flow measurements were made is that of longitudinal shear (LS) as in Fig. 1(b). The measured longitudinal threshold shear stresses K_L are indicated in Figs. 6 and 7 (and Table 1) as $K_L^{20}\approx 245$ Pa for 20 V% TALC and $K_L^{40}\approx 5120$ Pa for 40 V % TALC.

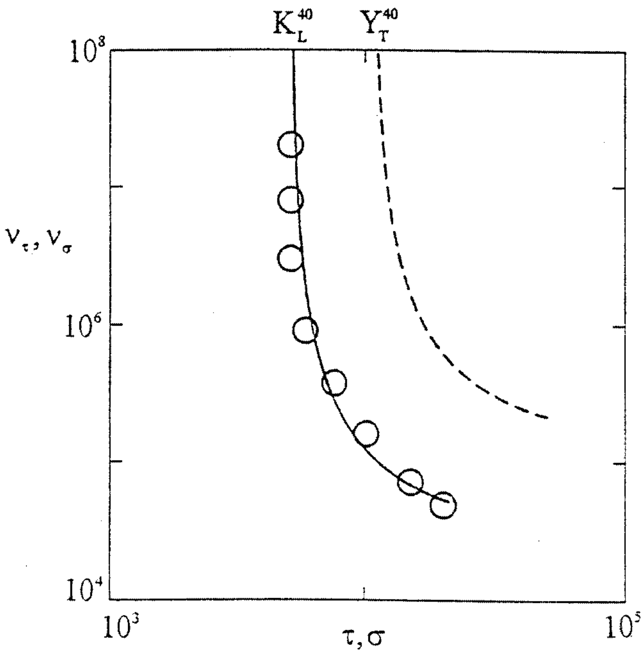

Fig. 7 Apparent viscosity (Pa-S) versus stress (Pa) for PS/TALC 40% (symbols). Correlation of shear flow (LS)–(solid curve). Prediction of elongational flow (TN)–(dashed curve).

As the flow data relates to longitudinal shear (LS), it should correlate with the flow prediction (30). However, first we rewrite (30) in terms of apparent shear viscosity ν_τ, i.e.,

$$\nu_\tau = \frac{\tau}{\dot{\gamma}_{13}} = \mu' \left(1 - \frac{K_L}{|\tau|}\right)^{-n} \qquad |\tau| \geq K_L \tag{42}$$

where we have denoted $\mu' = \mu/\alpha^2$. With K_L known and flow data recorded in the form of data pairs (τ, ν_τ), best fits of the parameters μ' and n can be found. This has been done for PS/TALC 20 V% and PS/TALC 40 V % using curve fitting software in Mathematica. The results are listed in the following table.

The threshold stresses K_L and Y_T have the units Pa, μ' has units Pa x S. The solid curves in Figs. 6 and 7 are curve fits[1], i.e., plots of (42) with the optimal values of μ' and n from Table 1.

Although elongational flow data (TN) are not available in Kim and White [7], measurements of the normal stress thresholds Y_T were made using an elongational rheometer. These are indicated in Figs. 6 and 7 (and Table 1) as $Y_T^{20} \approx 489$ Pa and $Y_T^{40} \approx 10800$ Pa.

As discussed in the previous section, data including K_L, Y_T and (LS) flow data providing optimal fits of n and $\mu' = \mu/\alpha^2$ are not sufficient in themselves for a complete characterization of the model. With K_L and Y_T known, we write from (29) and (35)

$$\frac{K_L}{Y_T} = \sqrt{\frac{1+\beta^2}{4\alpha^2}}. \tag{43}$$

If, in addition, a measurement of the transverse shear threshold K were possible, α would then be known from (29) and β from (43). Finally, with $\mu = \mu' \alpha^2$ a complete specification of the material parameters would be realized.

[1]Observe that the correlations in Figs. 6 and 7 are good over the limited stress range considered (i.e., one or two orders of magnitude above the threshold stress). Practically, this range of stress is sufficient in most polymer processing calculations. However, we observe from (42), or more generally from (11) and (12), that in the limit of large stress, the proposed model predicts Newtonian response. For applications that require modeling over a large stress range and the behavior is non-Newtonian at high stress, the form of F in (12) may not be appropriate and would need to be replaced by a more suitable form.

Table 1

	K_L	Y_T	μ'	n	K_L/Y_T
PS/TALC 20 V%	245	489	8.30×10^4	2.15	0.501
PS/TALC 40 V%	5120	10 800	2.98×10^4	1.98	0.474

In the absence of additional data for a complete characterization, nevertheless we can predict the elongational (TN) flow response. Using (36) and (43) we write

$$\nu_\sigma = \frac{\sigma}{\dot{\varepsilon}_{33}} = \frac{\mu'}{(K_L/Y_T)^2}\left(1 - \frac{Y_T}{|\sigma|}\right)^{-n} \qquad |\sigma| \geq Y_T \tag{44}$$

for the apparent elongational viscosity ν_σ.

Predictions using (44) for PS/TALC 20 V% and PS/TALC 40 V % are plotted as dashed lines in Figs. 6 and 7. If elongational viscosity data (σ, ν_σ) for these melts become available, a comparison with these predictions would furnish a definitive assessment of the proposed model.

Recall that the predicted threshold curve for PS/TALC 40V% under combined σ, τ stress was shown in the normalized stress space $(\sigma/K_L, \tau/K_L)$ of Fig. 3. It is identified there as $K_L/Y_T = 0.474$ (cf., Table 1). The comparable threshold for an isotropic fluid is also illustrated in Fig. 3; it is labeled 0.577.

The same threshold curve for PS/TALC 40V% is included in Fig. 4, labeled $F=0$ $(\bar{\mu}=\infty)$. The model predicts no viscous flow for PS/TALC 40V% associated with stress points σ, τ inside this threshold curve (shaded region); stress points outside cause flow with finite viscosity, corresponding to the calculated $\bar{\mu}=$const. curve passing through the given stress point. In particular, the ratio of elongational flow rate $\dot{\varepsilon}_{33}$ to shear flow rate $\dot{\gamma}_{13}$ for PS/TALC 40V% under the combined stress σ, τ is calculated by (41) as

$$\frac{\dot{\varepsilon}_{33}}{\dot{\gamma}_{13}} \approx 0.225\frac{\sigma}{\tau}. \tag{45}$$

This ratio is $\sigma/3\tau$ for an isotropic fluid.

7 Summary and Conclusions

A constitutive theory is proposed for a transversely isotropic, viscoplastic (Bingham) fluid. The model treats threshold and flow characteristics as having essentially the same physical origin, i.e., the impedance of molecular reptation by the presence of small suspended, oriented filler particles. The theory incorporates a potential function serving the dual role of a threshold (yield) function and a viscous flow potential. The arguments of the potential consist of a subset of the integrity basis of invariants for transverse isotropy; the resulting representation is objective and dissipative.

The anisotropy parameters α and β and the threshold stress K are considered material constants in the proposed model corresponding to a fixed degree of anisotropy and stress threshold. This is consistent with steady-state flow as in the present application to talc-filled polymers where the oriented filler particles have fully aligned with the flow. In transient flow where the filler particles may be initially randomly orientated and convect with the flow, the scalars α, β, and K must be considered state variables, each with a specified evolutionary equation that is coupled with the flow field equations, cf., Poitou, Chinesta, and Bernier [26] and Advani [27]. Definition of the equations of evolution is left as a topic of future research.

The proposed viscoplasticity model reduces to a transversely isotropic perfect plasticity model in the limit of zero viscosity. In the limit of isotropy the proposed theory reduces to the multiaxial generalization of Bingham's theory by Hohenemser and Prager.

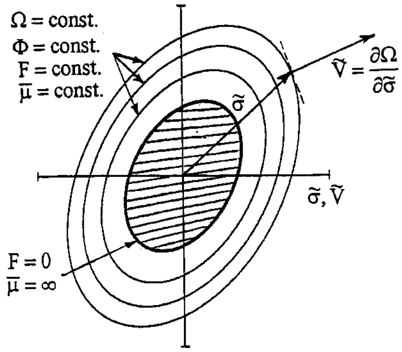

Fig. 8 Convex Ω=const. surfaces in $\boldsymbol{\sigma}$, V space. Threshold surface F=0 ($\bar{\mu}=\infty$). Illustrates normality.

A simple characterization procedure is outlined based on calculated and measured responses under fundamental (natural) states of stress. Although experiments under all the natural stress states are not always attainable, the stated procedure serves as a framework for determining the material parameters.

Application of the model is made to PS polymer melts containing disk-like talc particles of 20 V% and 40V% at 200°C. The data set for each melt consists of measured threshold stresses K_L and Y_T and shear flow measurements corresponding to the natural stress state of longitudinal shear (LS). These data do not constitute a complete set for full characterization. Nevertheless, good correlation of the model with the (LS) data is obtained over one or two decades of stress above the threshold K_L. The correlation with the (LS) data and the measurement of Y_T allows a prediction of transverse elongational flow (TN). If (TN) flow data were to become available for these melts, a comparison with the prediction would provide a definitive assessment of the model.

It is noted that the present model shows Newtonian response asymptotically as the stress becomes large relative to the stress threshold. Application to transversely isotropic fluids for which the flow is non-Newtonian at high stress can be represented by the same theoretical framework with different choices of the functional forms, cf., Perzyna [30].

The proposed constitutive theory is limited to isothermal conditions and is not applicable to hereditary fluids whose viscosity is dependent on deformation history (e.g., thixotropic fluids). Extension to nonisothermal conditions can be achieved by appropriately including Arrhenius (or WLF) forms and conducting experiments under the natural stress states at other temperatures. Extension to hereditary fluids is left for future study.

Appendix A

Figure 8 shows a superimposed (six-dimensional) stress $\boldsymbol{\sigma}$ and rate of deformation **V** space. The state of stress and rate of deformation at a fluid element are represented as points (or vectors) in this space. We see from (6), (10), and (15) that the (hyper) surfaces $\Omega(\boldsymbol{\sigma})$=const. in stress space are equivalently surfaces of $\Phi(\boldsymbol{\sigma})$=const., $F(\boldsymbol{\sigma})$=const. and $\overline{\mu}(\boldsymbol{\sigma})$=const. The latter are surfaces of constant viscosity (15).

From (10) and (15) we identify the surface $F=0$ ($\overline{\mu}=\infty$) as the threshold (or yield) surface. Stress points inside this surface (in the shaded area of Fig. 8) produce no viscous flow. Stress points outside the threshold cause flow with finite viscosity.

From geometry, we recognize $\partial\Omega/\partial\boldsymbol{\sigma}$ as a gradient vector. At a stress point $\boldsymbol{\sigma}$ on the surface $\Omega(\boldsymbol{\sigma})$=const. (Fig. 8), the associated gradient vector lies along the outward normal to that surface. According to (1), the rate of deformation **V** coincides with the gradient vector $\partial\Omega/\partial\boldsymbol{\sigma}$ and is thus similarly directed (in the combined **V**, $\boldsymbol{\sigma}$ space) normal to $\Omega(\boldsymbol{\sigma})$=const., cf., Drucker [31,32]. This concept of normality is a principal feature in classical plasticity theory. Evidently, the rate of deformation produced by a given stress depends critically on the shape of the Ω=const. (F=const.) surfaces. In turn, these shapes are strongly dependent on the nature and degree of anisotropy, cf., Figs. 3 and 4.

We further observe from Fig. 8 that the surfaces Ω=const. enclose the origin of the stress space and, provided they are convex, the scalar product

$$\boldsymbol{\sigma}\mathbf{V} \geqslant 0 \tag{A1}$$

i.e., the viscous dissipation rate is non-negative.

As always, the existence of a potential as in (1) implies a form of path independence. Here, this is manifest in the calculation of complementary viscous dissipation over a generic path in stress space from $\boldsymbol{\sigma}^A$ to $\boldsymbol{\sigma}^B$, i.e.,

$$\int_{\boldsymbol{\sigma}^A}^{\boldsymbol{\sigma}^B} \mathbf{V}d\boldsymbol{\sigma} = \Omega(\boldsymbol{\sigma}^B) - \Omega(\boldsymbol{\sigma}^A) \tag{A2}$$

($A2$) shows independence of path between $\boldsymbol{\sigma}^A$ and $\boldsymbol{\sigma}^B$. Such path independence excludes application of the present development to thixotropic fluids, or more generally, to fluids whose viscosity is dependent on deformation history.

For incremental changes in $\boldsymbol{\sigma}$ and **V**, we have from (1), in component form

$$dV_{ij} = \frac{\partial^2\Omega}{\partial\sigma_{ij}\partial\sigma_{kl}} d\sigma_{kl} = L_{ijkl} d\sigma_{kl} \tag{A3}$$

with

$$L_{ijkl} = L_{klij} \tag{A4}$$

relating to Onsager's Principle for a Newtonian fluid, cf., Drucker [32], Ziegler [33].

Appendix B

The general (component) form of (1) for an anisotropic viscous material (fluid) is

$$V_{ij} = M_{ijkl} \frac{\partial\Omega}{\partial\sigma_{kl}}. \tag{B1}$$

Following Betten [34], who addresses the plastic behavior of anisotropic solids, we express ($B1$) as

$$V_{ij} = \frac{\partial\Omega}{\partial\sigma_{ij}} + \xi m_{ijkl} \frac{\partial\Omega}{\partial D_{kl}} \tag{B2}$$

for a transversely isotropic fluid with a viscous potential $\Omega(\boldsymbol{\sigma},\mathbf{D})$. Betten [34] identifies the second term in ($B2$) as being of second-order relating to the plastic potential of an anisotropic plastic solid; he derives its specific form using representation theory of tensor functions. As our objective is to formulate a simple constitutive law, applicable in processing calculations, we ignore the second term in ($B2$), arguing that it is likewise of second order for the viscous potential of a transversely isotropic fluid. Thus, we contend that (1) provides a first-order representation of a transversely isotropic fluid with viscous potential $\Omega(\boldsymbol{\sigma},\mathbf{D})$.

The relative importance of the second term in ($B2$) for a transversely isotropic viscous material (fluid) must ultimately be determined through experiment, e.g., through experiments mapping surfaces Ω=const., measuring the appropriate components of flow rate and thereby assessing the concept of normality (cf., Appendix A). Experiments of this type have been conducted on transversely isotropic viscous (creeping) solids in the form of reinforced thin-walled polymeric tubes, cf., Robinson, Binienda, and Ruggles [35]. The results support the concept of normality and suggest that the second term in ($B2$) is negligible for a transversely isotropic viscous material.

References

[1] Chapman, F. M., and Lee, T. S., 1970, ''Effect of Talc Filler on the Melt Rheology of Polypropylene,'' SPE J., **26**, pp. 37–40.

[2] Vinogradov, G. V., Malkin, A. Y., Plotnikova, E. P., Sabsai, O. Y., and Nikolayeva, N. E., 1972, ''Viscoelastic Properties of Filled Polymers,'' Int. J. Polym. Mat., **2**, pp. 1–27.

[3] Suetsugu, Y., and White, J. L., 1983, ''The Influence of Particle Size and Surface Coating of Calcium Carbonate on the Rheological Properties of Its Suspensions in Molten Polystyrene,'' J. Appl. Polym. Sci., **28**, pp. 1481–1501.

[4] Osanaiye, G., Leonov, A. I., and White, J. L., 1993, ''Investigations of the Rheological Behavior of Rubber Carbon-Black Compounds Over a Wide-Range of Stresses Including Very-Low Stresses,'' J. Non-Newtonian Fluid Mech., **49**, pp. 87–101.

[5] Toki, S., and White, J. L., 1982, ''Rheological and Solid Boundary Condition Characterization of Unvulcanized Elastomers and Their Compounds,'' J. Appl. Polym. Sci., **27**, pp. 3171–3184.

[6] Montes, S., and White, J. L., 1982, ''A Comparative Rheological Investigation of Natural and Systhetic Cis-1,4 Polyisoprenes and Their Carbon Black Compounds,'' Rubber Chem. Technol., **55**, pp. 1354–1369.

[7] Kim, K. J., and White, J. L., 1999, ''Rheological Investigations of Suspensions of Talc, Calcium Carbonate and Their Mixtures in a Polystyrene Melt,'' Polym. Eng. Sci., **39**, pp. 2189–2198.

[8] Bingham, E. C., 1922, *Fluidity and Plasticity*, McGraw-Hill, New York.

[9] Hohenemser, K., and Prager, W., 1932, ''Über die ansätze der mechanik isotroper kontinua,'' Z. Angew. Math. Mech., **12**, pp. 216–226.

[10] Oldroyd, J. G., 1947, ''A Rational Formulation of the Equations of Plastic Flow for a Bingham Solid,'' Proc. Cambridge Philos. Soc., **43**, pp. 100–105.

[11] Prager, W., 1961, *Introduction to Mechanics of Continua*, Ginn and Co., Boston.

[12] White, J. L., 1979, ''A Plastic-Viscoelastic Constitutive Equation to Represent the Rheological Behavior of Concentrated Suspensions of Small Particles in Polymer Melts,'' J. Non-Newtonian Fluid Mech., **5**, pp. 177–190.

[13] White, J. L., and Lobe, V. M., 1982, ''Comparison of the Prediction of Viscoelastic and Plastic-Viscoelastic Fluid Model to the Rheological Behavior of Polystyrene and Polystyrene-Carbon Black Compounds,'' Rheol. Acta, **21**, pp. 167–175.

[14] Ericksen, J. L., 1961, ''Poiseuille Flow of Certain Anisotropic Fluids,'' Arch. Ration. Mech. Anal., **8**, pp. 1–8.

[15] White, J. L., and Suh, C. H., 1997, ''A Theory of Transversely Isotropic Plastic Viscoelastic Fluids to Represent the Flow of Talc and Similar Disc-Like Particle Suspensions in Thermoplastics,'' J. Non-Newtonian Fluid Mech., **69**, pp. 15–27.

[16] Hill, R., 1949, ''A Theory of the Yielding and Plastic Flow of Anisotropic Metals,'' Proc. R. Soc. London, Ser. A, **A193**, pp. 281–428.

[17] Hill, R., 1949, ''The Theory of Plane Plastic Strain for Anisotropic Metals,'' Proc. R. Soc. London, Ser. A, **A193**, pp. 428–437.

[18] Hill, R., 1950, *The Mathematical Theory of Plasticity*, Oxford University Press, Oxford, UK.

[19] White, J. L., Kim, K. J., and Robinson, D. N., 1999, ''Alternate Models for a Transversely Isotropic Plastic Viscoelastic Fluid,'' J. Non-Newtonian Fluid Mech., **83**, pp. 19–32.

[20] Spencer, A. J. M., 1971, *Continuum Physics*, A. C. Eringen, ed., Academic Press, San Diego, CA.

[21] Spencer, A. J. M., 1972, *Deformations of Fiber-Reinforced Materials*, Clarendon Press, Oxford, England.

[22] Spencer, A. J. M., 1984, *Continuum Theory of Fiber-Reinforced Composites*, Springer-Verlag, New York.

[23] Spencer, A. J. M., 1992, ''Plasticity Theory for Fiber-Reinforced Composites,'' J. Eng. Math., **26**, pp. 107–118.

[24] Lance, R. H., and Robinson, D. N., 1971, ''A Maximum Shear Stress Theory of Plastic Failure for Fiber-Reinforced Materials,'' J. Mech. Phys. Solids, **19**, pp. 49–60.

[25] Robinson, D. N., and Duffy, S. F., 1990, ''Continuum Deformation Theory for High Temperature Metallic Composites,'' J. Eng. Mech., **116**(4), pp. 832–844.

[26] Poitou, A., Chinesta, F., and Bernier, G., 2001, ''Orienting Fibers by Extrusion in Reactive Powder Concrete,'' J. Eng. Mech., **127**(6), pp. 593–598.

[27] Advani, S. G., 1994, *Flow and Rheology in Polymer Composites Manufacturing*, Elsevier Science, Amsterdam.

[28] Robinson, D. N., and Pastor, M. S., 1992, ''Limit Pressure of a Circumferentially Reinforced SiC/Ti Ring,'' Composites Eng., **2**(4), pp. 229–238.

[29] von Mises, R., 1928, ''Mechanik der plastischen formänderung von kristallen,'' Z. Angew. Math. Mech., **8**, pp. 161–185.

[30] Perzyna, P., 1966, ''Fundamental Problems in Viscoplasticity,'' Adv. Appl. Mech., **9**, pp. 243–377.

[31] Drucker, D. C., 1959, ''A Definition of Stable Inelastic Material,'' ASME J. Appl. Mech., **26**, pp. 101–106.

[32] Drucker, D. C., 1962, ''Stress-Strain-Time Relations and Irreversible Thermodynamics,'' *Proc. of the International Symposium on Second Order Effects in Elasticity, Plasticity and Fluid Mechanics*, Haifa, Pergamon, London, pp. 331–351.

[33] Ziegler, H., 1958, ''An Attempt to Generalize Onsager's Principle,'' Z. Angew. Math. Phys., **9b**, pp. 748–763.

[34] Betten, J., 1981, ''On the Representation of the Plastic Potential of Anisotropic Solids,'' *Plastic Behavior of Anisotropic Solids, Proc. CNRS Internat. Colloquium*, J. P. Boehler, ed., Villard-de-Lans, Editions du Centre National de la Recherche Scientifique, pp. 213–228.

[35] Robinson, D. N., Bininda, W. K., and Ruggles, M. B., 2001, ''Creep of Polymer Matrix Composites (PMC), Norton/Bailey Creep Law for Transverse Isotropy,'' submitted for publication.

The Proportional-Damping Matrix of Arbitrarily Damped Linear Mechanical Systems

J. Angeles
e-mail: angeles@cim.mcgill.ca

S. Ostrovskaya
e-mail: svetlana@cim.mcgill.ca

Department of Mechanical Engineering and Centre for Intelligent Machines, McGill University, 817 Sherbrooke Street, West, Montreal, PQ H3A 2K6, Canada

The vibration of linear mechanical systems with arbitrary damping is known to pose challenging problems to the analyst, for these systems cannot be analyzed with the techniques pertaining to their undamped counterparts. It is also known that a class of damped systems, called proportionally damped, can be analyzed with the same techniques, which mimic faithfully those of single-degree-of-freedom systems. For this reason, in many instances the system at hand is assumed to be proportionally damped. Nevertheless, this assumption is difficult to justify on physical grounds in many practical applications. What this assumption brings about is a damping matrix that admits a simultaneous diagonalization with the stiffness matrix. Proposed in this paper is a decomposition of the damping matrix of an arbitrarily damped system allowing the extraction of the proportionally damped component, which, moreover, approximates optimally the original damping matrix in the least-square sense. Finally, we show with examples that conclusions drawn from the proportionally damped approximation of an arbitrarily damped system can be dangerously misleading. [DOI: 10.1115/1.1483832]

1 Introduction

While the theory of linear systems with constant coefficients, termed *linear time-invariant systems*, is well established, its application to the analysis and identification of mechanical systems with arbitrary damping is still a subject of research ([1–6]). Indeed, the modal analysis of linear, constant-coefficient mechanical systems has focused on systems with *proportional damping*, which allows the simultaneous diagonalization of the damping and the stiffness matrices. Such a diagonalization, in turn, leads to a decoupling of the system under study into a set of uncoupled single-degree-of-freedom systems, thereby allowing for their study with the classical techniques developed for these systems. To be sure, systems with arbitrary damping can be analyzed within the framework of state-variable models ([7]), but these models lack the transparency of the usual second-order models, and hence, have not found their way into the daily engineering practice.

Proportional damping occurs naturally in the discretization of linear viscoelastic structures, but seldom occurs in the presence of lumped damping. The need to optimize structures and machines that comprise damping elements such as shock absorbers calls for a thorough analysis of systems with arbitrary damping. The authors proposed recently a novel approach along these lines ([8]).

Engineers, however, feel more comfortable when working with proportionally damped systems, and hence, resort to a proportionally damped model whenever the need arises. Nevertheless, guidelines as to how to derive a proportionally damped model for a system that is known to have nonproportional damping are not fully developed, although some progress has been reported ([6,9]). The subject of this paper is a procedure whereby the proportional component of an arbitrary damping matrix is computed, that best approximates the latter in the least-square sense. The method is robust, for it is *direct*, as opposed to *iterative*, while preserving the numerical conditioning of the matrices involved. Moreover, the method is applicable to n-degree-of-freedom systems, for any integer n.

A word of caution is in order: Results drawn from the proportional-damping approximation of an arbitrarily damped system can be dangerously misleading, even in the presence of the best approximation. We illustrate this claim with an example.

2 Nomenclature and Definitions

The mathematical model of linear, time-invariant mechanical systems takes the form

$$\mathbf{M}\ddot{\mathbf{x}}+\mathbf{C}\dot{\mathbf{x}}+\mathbf{K}\mathbf{x}=\mathbf{f}(t), \quad \mathbf{x}(0)=\mathbf{x}_0, \quad \dot{\mathbf{x}}(0)=\mathbf{v}_0, \tag{1}$$

in which
$\mathbf{M}$: $n\times n$ positive-definite *mass* matrix;
$\mathbf{C}$: $n\times n$ positive-semidefinite *damping* matrix;
$\mathbf{K}$: $n\times n$ positive-semidefinite *stiffness* matrix;
$\mathbf{x}(t)$: n-dimensional vector of generalized coordinates;
$\mathbf{f}(t)$: n-dimensional vector of generalized external forces.

It is known that proportional damping occurs when the damping matrix is a linear combination of the mass and stiffness matrices. A commonly accepted form of the damping matrix $\mathbf{C}_p$ of a proportionally damped system is, thus,

$$\mathbf{C}_p=\alpha\mathbf{M}+\beta\mathbf{K} \tag{2}$$

where α and β are real parameters that are chosen by the analyst. In formulating the eigenvalue problem of the system (1), both sides of the governing equation are premultiplied by $\mathbf{M}^{-1}$, which is also done with Eq. (2), to yield

$$\mathbf{M}^{-1}\mathbf{C}_p=\alpha\mathbf{1}+\beta\mathbf{M}^{-1}\mathbf{K}, \tag{3}$$

thereby making apparent that the foregoing damping leads to a linear combination of what is known as the *dynamic matrix* $\mathbf{M}^{-1}\mathbf{K}$ and the $n\times n$ identity matrix $\mathbf{1}$. Therefore, matrices $\mathbf{M}^{-1}\mathbf{C}_p$ and $\mathbf{M}^{-1}\mathbf{K}$ share the same set of eigenvectors, which explains why, under form (2), the mathematical model at hand can be *decoupled*, i.e., transformed into a system of n uncoupled second-order ordinary differential equations. However, notice that form (2) is only one instance of a damping matrix leading to proportional damping. Indeed, adding a linear combination of powers of the dynamic matrix to the right-hand side of Eq. (3)

Contributed by the Applied Mechanics Division of THE AMERICAN SOCIETY OF MECHANICAL ENGINEERS for publication in the ASME JOURNAL OF APPLIED MECHANICS. Manuscript received by the ASME Applied Mechanics Division, December 17, 1999; final revision, February 28, 2002. Associate Editor: V. K. Kinra. Discussion on the paper should be addressed to the Editor, Professor Robert M. McMeeking, Department of Mechanical and Environmental Engineering, University of California–Santa Barbara, Santa Barbara, CA 93106-5070, and will be accepted until four months after final publication of the paper itself in the ASME JOURNAL OF APPLIED MECHANICS.

yields a new matrix that still shares the same eigenvectors with the dynamic matrix. Such generalizations of the $\mathbf{C}_p$ matrix have been proposed ([9]).

Now, since $\mathbf{M}$ is positive-definite, it admits the factoring

$$\mathbf{M}=\mathbf{N}^T\mathbf{N} \tag{4}$$

where $\mathbf{N}$ is a nonsingular matrix. One candidate to define $\mathbf{N}$ can be derived from the Cholesky decomposition ([10]) of $\mathbf{M}$, but other means exist, for example, *any* square root of $\mathbf{M}$ can also work.

Upon introduction of the above factoring in the mathematical model, Eq. (1), we can transform this model into a form in which the coefficient of the highest-order derivative is the $n\times n$ identity matrix $\mathbf{1}$, namely,

$$\ddot{\mathbf{y}}+\mathbf{\Delta}\dot{\mathbf{y}}+\mathbf{\Omega}^2\mathbf{y}=\mathbf{g}(t),\quad \mathbf{y}(0)=\mathbf{y}_0=\mathbf{N}\mathbf{x}_0,\quad \dot{\mathbf{y}}(0)=\mathbf{w}_0=\mathbf{N}\mathbf{v}_0 \tag{5}$$

with the definitions

$$\mathbf{y}\equiv\mathbf{N}\mathbf{x},\quad \mathbf{\Delta}\equiv\mathbf{N}^{-T}\mathbf{C}\mathbf{N}^{-1},\quad \mathbf{\Omega}^2\equiv\mathbf{N}^{-T}\mathbf{K}\mathbf{N}^{-1},\quad \mathbf{g}\equiv\mathbf{N}^{-T}\mathbf{f}. \tag{6}$$

As we proposed in [8], we shall refer henceforth to form (5) as the *monic representation* of the mathematical model of Eq. (1). Note that, in this representation, (a) the new variable, $\mathbf{y}$, has units of generalized coordinate times square root of generalized mass, which means that the units of $\mathbf{y}$ are those of the *modal vectors* of the associated undamped system, i.e., the columns of the *modal matrix* of this system ([7]); (b) the "inversion" of $\mathbf{N}$ is safer than that of $\mathbf{M}$, for the condition number ([10]) of the former is *exactly* the square root of the condition number of the latter, when the condition number is defined over the Frobenius norm; and (c) all coefficient matrices are symmetric. Also note that the two new matrices, $\mathbf{\Delta}$ and $\mathbf{\Omega}$, have units of frequency; moreover, they are positive-semidefinite as well. Henceforth, we shall call the latter the *frequency matrix*; the former will be called the *dissipation matrix*, in order to avoid confusion with the original damping matrix $\mathbf{C}$.

Now it is apparent that proportional damping, which leads to a damping matrix of the form displayed in Eq. (2), implies that the dissipation matrix takes a special form $\mathbf{\Delta}_p$ that is a linear combination of $\mathbf{1}$ and $\mathbf{\Omega}^2$, or of $\mathbf{1}$ and $\mathbf{\Omega}$, for that matter, i.e., scalar factors α and β exist so that

$$\mathbf{\Delta}_p=\alpha\mathbf{1}+\beta\mathbf{\Omega}. \tag{7}$$

The generalization of Eq. (7) is, then,

$$\mathbf{\Delta}_p=\sum_0^{n-1}\alpha_k\mathbf{\Omega}^k. \tag{8}$$

By virtue of the Cayley-Hamilton Theorem ([11]), the right-hand side of the above expansion represents, upon a suitable choice of the real coefficients $\{\alpha_k\}_0^{n-1}$, *any* analytic function of the frequency matrix. Below we discuss a choice of the above coefficients that produces the *closest proportional* approximation of a given damping matrix in the least-square sense.

3 The Co-spectral Space of Matrices Commuting With the Frequency Matrix

Two matrices that share the same set of eigenvectors will be termed henceforth *co-spectral*. A simple test to decide whether two given matrices are co-spectral is to verify whether these matrices commute under multiplication. If they do, then they are co-spectral; otherwise, they are not.

A central concept is recalled below:

Lemma 3.1 *Any square matrix is co-spectral with any of its integer powers.*

The proof of the foregoing lemma is straightforward, and hence, can be skipped. Moreover,

Lemma 3.2 *The set of co-spectral matrices of a given square matrix is a vector space over the complex field.*

Proof: Assume that an $n\times n$ matrix $\mathbf{A}$ is given, and that $\mathbf{B}$ and $\mathbf{C}$ are co-spectral with $\mathbf{A}$. It is apparent that

(i) the $n\times n$ zero matrix is co-spectral with $\mathbf{A}$;

(ii) $\mathbf{B}+\mathbf{C}$ is co-spectral with $\mathbf{A}$;

(iii) given any complex β, $\beta\,\mathbf{B}$ is co-spectral with $\mathbf{A}$.

Moreover, the operations of addition and scalar multiplication, defined for these matrices, obviously satisfy the standard laws for a vector space, thereby completing the proof.

Now, by virtue of the Cayley-Hamilton theorem and the above result, we have

Lemma 3.3 *Given an $n\times n$ matrix* $\mathbf{A}$ *with a* complete set *of eigenvectors, the linearly independent set $\{\mathbf{A}^k\}_0^{\nu-1}$, with $\nu\leq n$, spans the space of matrices that are co-spectral with* $\mathbf{A}$. *This set is then a basis for the said space. For symmetric matrices, $\nu=n$.*

We will limit the discussion below to only symmetric, positive-semidefinite (or definite) matrices. We are interested in *projecting* the dissipation matrix $\mathbf{\Delta}$ onto the space $\mathcal{O}$ of matrices that are co-spectral with $\mathbf{\Omega}$—we use caligraphic fonts for spaces and sets; in the absence of a caligraphic $\mathbf{\Omega}$, we use the caligraphic font of its Latin counterpart. We term $\mathcal{O}$ the *co-spectral space* of $\mathbf{\Omega}$. By analogy with Cartesian vectors, whereby a projection onto a coordinate axis is obtained from the inner product of the given vector with the unit vector associated with that axis, we shall define the projection of a matrix onto a space in terms of the *inner product* of the matrices involved. More specifically, we need a basis for the co-spectral space $\mathcal{O}$ of $\mathbf{\Omega}$. While any basis will do, it is most comfortable to work with an orthonormal basis $\mathcal{E}$. Such a basis can be readily obtained from the set $\{\mathbf{\Omega}^k\}_0^{n-1}$ by means of the Gram-Schmidt procedure ([10]). To this end, the orthonormal basis is defined as $\mathcal{E}\equiv\{\mathbf{E}_k\}_0^{n-1}$. We describe below how to define each of the basis matrices $\mathbf{E}_k$.

The inner product of two $n\times n$ matrices $\mathbf{A}$ and $\mathbf{B}$, which will be needed in the sequel, is defined as

$$(\mathbf{A},\mathbf{B})\equiv\mathrm{tr}(\mathbf{A}\mathbf{W}\mathbf{B}^T)$$

where $\mathbf{W}$ is a positive-definite weighting matrix that is defined according to the user's needs. Note that the *Frobenius norm* of any $n\times n$ matrix now becomes, under the above inner-product definition,

$$\|\mathbf{A}\|=\sqrt{\mathrm{tr}(\mathbf{A}\mathbf{W}\mathbf{A}^T)}.$$

It is thus apparent that, if we want the $n\times n$ identity matrix $\mathbf{1}$ to have a unit Frobenius norm, we have to define $\mathbf{W}$ as

$$\mathbf{W}\equiv\frac{1}{n}\mathbf{1},$$

and hence, the inner product becomes

$$(\mathbf{A},\mathbf{B})\equiv\frac{1}{n}\mathrm{tr}(\mathbf{A}\mathbf{B}^T) \tag{9}$$

while the Frobenius norm takes the form

$$\|\mathbf{A}\|=\sqrt{\frac{1}{n}\mathrm{tr}(\mathbf{A}\mathbf{A}^T)}. \tag{10}$$

Now we have

$$\mathbf{E}_0=\mathbf{\Omega}^0=\mathbf{1}$$

which is, by definition, of unit norm. Moreover, the projection of $\mathbf{\Delta}$ onto $\mathbf{E}_0$ is simply

$$(\mathbf{\Delta},\mathbf{E}_0)=\frac{1}{n}\,\mathrm{tr}(\mathbf{\Delta}\mathbf{E}_0^T)=\frac{1}{n}\mathrm{tr}(\mathbf{\Delta}).$$

Furthermore, the component $\mathbf{\Delta}_0$ of $\mathbf{\Delta}$ onto $\mathbf{E}_0$ is

$$\mathbf{\Delta}_0=\frac{1}{n}\mathrm{tr}(\mathbf{\Delta})\mathbf{1}.$$

Likewise, the component $\boldsymbol{\Delta}_k$ of $\boldsymbol{\Delta}$ onto $\mathbf{E}_k$ is given by

$$\boldsymbol{\Delta}_k=\frac{1}{n}\,\mathrm{tr}(\boldsymbol{\Delta}\mathbf{E}_k^T)\mathbf{E}_k\,.$$

Therefore, the component $\boldsymbol{\Delta}_{01}$ of $\boldsymbol{\Delta}$ onto the subspace spanned by $\mathbf{E}_0$ and $\mathbf{E}_1$ is simply

$$\boldsymbol{\Delta}_{01}\equiv\frac{1}{n}\,\mathrm{tr}(\boldsymbol{\Delta})\mathbf{1}+\frac{1}{n}\,\mathrm{tr}(\boldsymbol{\Delta}\mathbf{E}_1)\mathbf{E}_1$$

where we have recalled the symmetry of $\mathbf{E}_k$, for $k=0,\ldots,n-1$. By extension, the component of the same matrix $\boldsymbol{\Delta}$ onto the subspace spanned by $\{\mathbf{E}_k\}_0^l$ is denoted by $\boldsymbol{\Delta}_{01\cdots l}$ and is defined, for $l=1,\cdots,n-1$, as

$$\boldsymbol{\Delta}_{01\cdots l}\equiv\frac{1}{n}\left[\,\mathrm{tr}(\boldsymbol{\Delta})\mathbf{1}+\mathrm{tr}(\boldsymbol{\Delta}\mathbf{E}_1)\mathbf{E}_1+\cdots+\mathrm{tr}(\boldsymbol{\Delta}\mathbf{E}_l)\mathbf{E}_l\right].$$

Now it is apparent that the component $\boldsymbol{\Delta}_{\mathcal{O}}$ of $\boldsymbol{\Delta}$ onto the space $\mathcal{O}$ is

$$\boldsymbol{\Delta}_{\mathcal{O}}=\frac{1}{n}\sum_{0}^{n-1}\,\mathrm{tr}(\boldsymbol{\Delta}\mathbf{E}_l^T)\mathbf{E}_l\,. \tag{11}$$

Thus, all we need to obtain the foregoing projection is the orthonormal basis $\mathcal{E}$. This basis can be found by means of the Gram-Schmidt orthogonalization procedure:

$$\mathbf{E}_0=\boldsymbol{\Omega}^0\equiv\mathbf{1},$$

$$\mathbf{E}_1=\frac{\boldsymbol{\Omega}-(1/n)\mathrm{tr}(\boldsymbol{\Omega})\mathbf{1}}{\|\boldsymbol{\Omega}-(1/n)\mathrm{tr}(\boldsymbol{\Omega})\mathbf{1}\|},$$

$$\mathbf{E}_2=\frac{\boldsymbol{\Omega}^2-(1/n)[\,\mathrm{tr}(\boldsymbol{\Omega}^2)\mathbf{1}+\mathrm{tr}(\boldsymbol{\Omega}^2\mathbf{E}_1)\mathbf{E}_1]}{\|\boldsymbol{\Omega}^2-(1/n)[\,\mathrm{tr}(\boldsymbol{\Omega}^2)\mathbf{1}+\mathrm{tr}(\boldsymbol{\Omega}^2\mathbf{E}_1)\mathbf{E}_1]\|},$$

$$\vdots$$

$$\mathbf{E}_{n-1}=\frac{\boldsymbol{\Omega}^{n-1}-(1/n)\Sigma_0^{n-2}\mathrm{tr}(\boldsymbol{\Omega}^{n-1}\mathbf{E}_{n-2})\mathbf{E}_{n-2}}{\left\|\boldsymbol{\Omega}^{n-1}-(1/n)\Sigma_0^{n-2}\mathrm{tr}(\boldsymbol{\Omega}^{n-1}\mathbf{E}_{n-2})\mathbf{E}_{n-2}\right\|}.$$

4 The Orthogonal Decomposition of the Damping Matrix

Based on the foregoing background, we have a decomposition of the dissipation matrix in the form

$$\boldsymbol{\Delta}=\boldsymbol{\Delta}_{\mathcal{O}}+\boldsymbol{\Delta}_{\perp}\,, \tag{12}$$

where $\boldsymbol{\Delta}_{\perp}$—read *delta-perp*—is the component of $\boldsymbol{\Delta}$ lying outside of the space spanned by $\mathcal{E}$, and hence, it is the *error* in the approximation of the dissipation matrix with $\boldsymbol{\Delta}_{\mathcal{O}}$. By virtue of the definition of the foregoing approximation, moreover, the two components of the decomposition (12) are mutually orthogonal, a relation that is made apparent below.

First, we calculate the inner product of the two foregoing components:

$$\mathrm{tr}(\boldsymbol{\Delta}_{\mathcal{O}}\boldsymbol{\Delta}_{\perp})=\mathrm{tr}(\boldsymbol{\Delta}_{\mathcal{O}}\boldsymbol{\Delta})-\mathrm{tr}(\boldsymbol{\Delta}_{\mathcal{O}}^2).$$

Furthermore, the first term of the expression appearing in the right-hand side of the above equation is readily computed, recalling Eq. (11), as

$$\mathrm{tr}(\boldsymbol{\Delta}_{\mathcal{O}}\boldsymbol{\Delta})=\frac{1}{n}\sum_{0}^{n-1}\,\mathrm{tr}^2(\boldsymbol{\Delta}\mathbf{E}_l). \tag{13a}$$

The second term of the same expression is expanded, in turn, as

$$\mathrm{tr}(\boldsymbol{\Delta}_{\mathcal{O}}^2)=\frac{1}{n^2}\,\mathrm{tr}\{[\,\mathrm{tr}(\boldsymbol{\Delta})\mathbf{1}+\mathrm{tr}(\boldsymbol{\Delta}\mathbf{E}_1)\mathbf{E}_1+\cdots+\mathrm{tr}(\boldsymbol{\Delta}\mathbf{E}_{n-1})\mathbf{E}_{n-1}]^2\}$$

or, upon further expansion,

$$\begin{aligned}\mathrm{tr}(\boldsymbol{\Delta}_{\mathcal{O}}^2)=&\frac{\mathrm{tr}(\boldsymbol{\Delta})}{n^2}\,\mathrm{tr}\{\mathbf{1}[\,\mathrm{tr}(\boldsymbol{\Delta})\mathbf{1}+\mathrm{tr}(\boldsymbol{\Delta}\mathbf{E}_1)\mathbf{E}_1+\cdots+\mathrm{tr}(\boldsymbol{\Delta}\mathbf{E}_{n-1})\mathbf{E}_{n-1}]\}\\&+\frac{\mathrm{tr}(\boldsymbol{\Delta}\mathbf{E}_1)}{n^2}\mathrm{tr}\{\mathbf{E}_1[\,\mathrm{tr}(\boldsymbol{\Delta})\mathbf{1}+\mathrm{tr}(\boldsymbol{\Delta}\mathbf{E}_1)\mathbf{E}_1+\cdots\\&+\mathrm{tr}(\boldsymbol{\Delta}\mathbf{E}_{n-1})\mathbf{E}_{n-1}]\}\\&\vdots\\&+\frac{\mathrm{tr}(\boldsymbol{\Delta}\mathbf{E}_{n-1})}{n^2}\,\mathrm{tr}\{\mathbf{E}_{n-1}[\,\mathrm{tr}(\boldsymbol{\Delta})\mathbf{1}+\mathrm{tr}(\boldsymbol{\Delta}\mathbf{E}_1)\mathbf{E}_1+\cdots\\&+\mathrm{tr}(\boldsymbol{\Delta}\mathbf{E}_{n-1})\mathbf{E}_{n-1}]\}.\end{aligned}$$

Now, if we recall the orthonormality of $\mathcal{E}$, the above expression simplifies to

$$\mathrm{tr}(\boldsymbol{\Delta}_{\mathcal{O}}^2)=\frac{1}{n}\sum_{0}^{n-1}\,\mathrm{tr}^2(\boldsymbol{\Delta}\mathbf{E}_l). \tag{13b}$$

Upon comparison of expressions (13*a*) and (13*b*), we obtain

$$\mathrm{tr}(\boldsymbol{\Delta}_{\mathcal{O}}\boldsymbol{\Delta}_{\perp})=0 \tag{14}$$

and hence, the two components $\boldsymbol{\Delta}_{\mathcal{O}}$ and $\boldsymbol{\Delta}_{\perp}$ are orthogonal to each other. Moreover, the relative error e of the foregoing approximation is readily computed as

$$e=\frac{\|\boldsymbol{\Delta}_{\perp}\|}{\|\boldsymbol{\Delta}\|}=\sqrt{\frac{\mathrm{tr}(\boldsymbol{\Delta}_{\perp}^2)/n}{\mathrm{tr}(\boldsymbol{\Delta}^2)/n}}=\sqrt{\frac{\mathrm{tr}(\boldsymbol{\Delta}_{\perp}^2)}{\mathrm{tr}(\boldsymbol{\Delta}^2)}}. \tag{15}$$

Let us now recall the definitions (6), which allow us to obtain a decomposition of $\mathbf{C}$ similar to that of Eq. (12), namely,

$$\mathbf{C}\equiv\mathbf{C}_{\mathcal{O}}+\mathbf{C}_{\perp}$$

where, apparently,

$$\mathbf{C}_{\mathcal{O}}\equiv\mathbf{N}^T\boldsymbol{\Delta}_{\mathcal{O}}\mathbf{N},\quad \mathbf{C}_{\perp}\equiv\mathbf{N}^T\boldsymbol{\Delta}_{\perp}\mathbf{N}$$

and hence,

$$\boldsymbol{\Delta}_{\mathcal{O}}=\mathbf{N}^{-T}\mathbf{C}_{\mathcal{O}}\mathbf{N}^{-1},\quad \boldsymbol{\Delta}_{\perp}=\mathbf{N}^{-T}\mathbf{C}_{\perp}\mathbf{N}^{-1}.$$

Upon substitution of the foregoing relations into Eq. (14), we obtain

$$\mathrm{tr}(\mathbf{N}^{-T}\mathbf{C}_{\mathcal{O}}\mathbf{N}^{-1}\mathbf{N}^{-T}\mathbf{C}_{\perp}\mathbf{N}^{-1})\equiv\mathrm{tr}(\mathbf{N}^{-T}\mathbf{C}_{\mathcal{O}}\mathbf{M}^{-1}\mathbf{C}_{\perp}\mathbf{N}^{-1})=0$$

and, if we recall that the trace of a product is invariant under a cyclic permutation of its factors, then

$$\mathrm{tr}(\mathbf{M}^{-1}\mathbf{C}_{\mathcal{O}}\mathbf{M}^{-1}\mathbf{C}_{\perp})=0$$

or

$$\mathrm{tr}[\mathbf{M}^{-1}\mathbf{C}_{\mathcal{O}}(\mathbf{C}_{\perp}\mathbf{M}^{-1})^T]=0.$$

That is: *the product* $\mathbf{C}_{\perp}\mathbf{M}^{-1}$ *is orthogonal to the product* $\mathbf{M}^{-1}\mathbf{C}_{\mathcal{O}}$. It is thus apparent that the orthogonal decomposition of the dissipation matrix $\boldsymbol{\Delta}$ does not lead to an orthogonal decomposition of the damping matrix $\mathbf{C}$ as such, but rather of a linear transformation of it. This is not surprising at all, for the transformation of Eqs. (6) is not isometric, i.e., it does not preserve the inner product of the space at hand. Nevertheless, the component $\mathbf{C}_{\mathcal{O}}$ of the damping matrix $\mathbf{C}$ is guaranteed to lead to a decouplable system, namely,

$$\mathbf{M}\ddot{\mathbf{x}}+\mathbf{C}_{\mathcal{O}}\dot{\mathbf{x}}+\mathbf{K}\mathbf{x}=\mathbf{f}(t),\quad \mathbf{x}(0)=\mathbf{x}_0,\quad \dot{\mathbf{x}}(0)=\mathbf{v}_0, \tag{16}$$

and hence, the damping represented by matrix $\mathbf{C}_{\mathcal{O}}$ is *proportional*. Moreover, the foregoing matrix $\mathbf{C}_{\mathcal{O}}$ is closest to the original matrix $\mathbf{C}$ in the least-square sense.

4.1 The Least-Square Approximation of the Damping Matrix. The above results show that the proportional-damping matrix of an arbitrarily damped system cannot be obtained directly from the given mathematical model, Eq. (1). That is, the projection of $\mathbf{C}$ onto the co-spectral space of $\mathbf{K}$ does not lead to the least-square approximation of $\mathbf{C}$ with a proportional-damping matrix.

Kujath [9] proposed a proportional-damping matrix $\mathbf{D}$ derived from $\mathbf{\Delta}$ in the form

$$\mathbf{\Delta}' \equiv \mathbf{E}^T\mathbf{\Delta}\mathbf{E} = \mathbf{D} + \mathbf{G}$$

where $\mathbf{E}$ is defined as

$$\mathbf{E} = [\mathbf{e}_1 \ \ \mathbf{e}_2 \ \ \cdots \ \ \mathbf{e}_n]$$

with $\mathbf{e}_i$ being the ith (unit) eigenvector of $\mathbf{\Omega}$, and hence, $\mathbf{E}$ is orthogonal, while $\mathbf{D}$ is defined as

$$\mathbf{D} \equiv \mathrm{diag}(\delta'_{11}\delta'_{22}\cdots\delta'_{nn})$$

and δ'_{ii} is the ith diagonal entry of $\mathbf{\Delta}'$. Notice that $\mathbf{\Delta}'$ is diagonal only if the system is proportionally damped. Apparently, the diagonal entries of $\mathbf{G}$ are all zero, and hence, $\mathrm{tr}(\mathbf{G}) = 0$; moreover,

$$\mathrm{tr}(\mathbf{\Delta}_\perp) = \mathrm{tr}(\mathbf{EGE}^T) = \mathrm{tr}(\mathbf{E}^T\mathbf{EG}) = \mathrm{tr}(\mathbf{G}) = 0, \tag{17}$$

i.e.,

$$\mathrm{tr}(\mathbf{\Delta}_{\mathcal{O}}) = \mathrm{tr}(\mathbf{\Delta}) = \mathrm{tr}(\mathbf{\Delta}'). \tag{18}$$

We prove below that $\mathbf{D}$ is nothing but the least-square approximation $\mathbf{E}^T\mathbf{\Delta}_{\mathcal{O}}\mathbf{E}$ defined above.

To this end, we show first that the two matrices $\mathbf{\Delta}_{\mathcal{O}}$ and $\mathbf{\Delta}'$, or their counterparts $\mathbf{E}^T\mathbf{\Delta}_{\mathcal{O}}\mathbf{E}$ and $\mathbf{D}$, have the same projections along a set of n linearly independent vectors spanning $\mathcal{O}$. Let us choose, for convenience, this set as $\mathcal{B} = \{\mathbf{\Omega}^k\}_0^{n-1}$. Moreover, since $\mathbf{\Delta}'$ is the dissipation matrix expressed in the basis $\{\mathbf{e}_i\}_1^n$, we also need $\mathbf{\Omega}$ in this basis. Let $\mathbf{\Omega}_d$ be the representation of $\mathbf{\Omega}$ in this basis, i.e.,

$$\mathbf{\Omega}_d = \mathbf{E}^T\mathbf{\Omega}\mathbf{E} = \mathrm{diag}(\omega_1, \omega_2, \cdots, \omega_n)$$

where $\{\boldsymbol{\omega}_i\}_1^n$ is the set of eigenvalues of $\mathbf{\Omega}$. Hence,

$$\mathbf{\Omega}_d^k = \mathrm{diag}(\omega_1^k, \omega_2^k, \cdots, \omega_n^k).$$

Now,

$$(\mathbf{D}, \mathbf{\Omega}_d^0) = \frac{1}{n}\mathrm{tr}(\mathbf{D1}) = \frac{1}{n}\mathrm{tr}(\mathbf{D}) = \frac{1}{n}\sum_1^n \delta'_{ii} = \frac{1}{n}\mathrm{tr}(\mathbf{\Delta}')$$

$$= \frac{1}{n}\mathrm{tr}(\mathbf{\Delta}_{\mathcal{O}}) = (\mathbf{\Delta}, \mathbf{\Omega}_d^0),$$

where we have recalled Eq. (18). Likewise, for $k = 2, \cdots, n-1$,

$$(\mathbf{D}, \mathbf{\Omega}_d^k) = \frac{1}{n}\mathrm{tr}(\mathbf{D\Omega}_d^k) = \frac{1}{n}\sum_1^n \delta'_{ii}\omega_i^k = (\mathbf{\Delta}, \mathbf{\Omega}_d^k) = \frac{1}{n}\mathrm{tr}(\mathbf{\Delta\Omega}_d^k)$$

$$= (\mathbf{\Delta}_{\mathcal{O}}, \mathbf{\Omega}_d^k),$$

thereby proving that $\mathbf{D} = \mathbf{E}^T\mathbf{\Delta}_{\mathcal{O}}\mathbf{E}$. Note that $\mathbf{D}$ is apparently positive-definite and hence, $\mathbf{\Delta}_{\mathcal{O}}$ is positive-definite as well.

We illustrate now the foregoing concepts with three examples.

5 Examples

In the examples below, reference is made to the damping ratio of a mode. In order to define a *modal damping ratio*, the characteristic equation of an n-degree-of-freedom system is represented as a product of $2n$ linear factors, namely,

$$P(s) = (s-s_1)(s-\overline{s_1})(s-s_2)(s-\overline{s_2})\cdots(s-s_c)(s-\overline{s_c}) \times (s-s_{c+1})\cdots(s-s_{2n}) \tag{19}$$

where we have assumed c pairs of complex-conjugate eigenvalues and $r \equiv 2(n-c)$ real eigenvalues. Every pair of complex-conjugate factors leads to a quadratic factor of the form $(s-s_i)\times(s-\overline{s_i}) = s^2 + 2\zeta_i\omega_i s + \omega_i^2$, where $0 < \zeta_i < 1$ plays the role of the damping ratio of the ith underdamped mode and ω_i that of the natural frequency of the same mode. However, similar quadratic terms are not directly available for real eigenvalues, since the r last linear factors of the product of Eq. (19) can give rise to up to $r!/[2(r-2)!]$ quadratic factors. We will not dwell on how to pair the $2(n-c)$ real eigenvalues to yield the damping ratios of the overdamped systems. In the examples below, $r = 2$ at most, and all linear factors yield one unique quadratic factor.

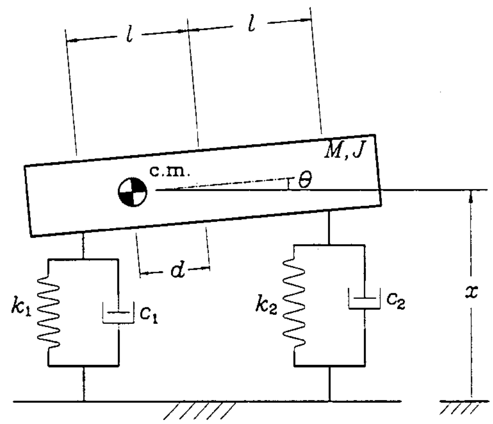

Fig. 1 A two-degree-of-freedom model of a suspension

5.1 A Two-Degree-of-Freedom Model of the Suspension of a Terrestial Vehicle. A model of the suspension of a terrestrial vehicle is shown in Fig. 1. The model consists of a body with mass M, supported by two spring-dashpot arrays. The stiffness k_i and the dashpot coefficient c_i, for $i = 1,2$, of the two arrays are not necessarily the same. Moreover, the center of mass (c.m.) of the body is located a distance d from its geometric center and the mass moment of inertia of the body about its c.m. is denoted by J. We will consider only two types of motion for the system, namely, (a) up-and-down translational motion of the body along the x-axis and (b) small angular motion of the body about an axis perpendicular to the plane of the figure. The mathematical model takes on the form of Eq. (1), with $\mathbf{x} = [x \ \ \theta]^T$ and coefficient matrices

$$\mathbf{M} \equiv \begin{bmatrix} M & 0 \\ 0 & J \end{bmatrix},$$

$$\mathbf{C} \equiv \begin{bmatrix} c_1 + c_2 & c_2(l+d) - c_1(l-d) \\ c_2(l+d) - c_1(l-d) & c_1(l-d)^2 + c_2(l+d)^2 \end{bmatrix},$$

and

$$\mathbf{K} \equiv \begin{bmatrix} k_1 + k_2 & k_2(l+d) - k_1(l-d) \\ k_2(l+d) - k_1(l-d) & k_1(l-d)^2 + k_2(l+d)^2 \end{bmatrix}.$$

Now, we choose matrix $\mathbf{N}$ as

$$\mathbf{N} = \begin{bmatrix} \sqrt{M} & 0 \\ 0 & \sqrt{I} \end{bmatrix},$$

the mathematical model of the system at hand in monic form (5) then following. In order to ease the ensuing calculations, we assume the relations

$$c_1 = c, \quad c_2 = 2c, \quad k_1 = 2k, \quad k_2 = k, \quad d = \frac{l}{2}, \quad I = Mr^2$$

with r denoting the radius of gyration of the block. With the foregoing relations, the system matrices now become

$$\mathbf{M}=M\begin{bmatrix}1 & 0\\ 0 & r^2\end{bmatrix},\quad \mathbf{C}=c\begin{bmatrix}3 & 5l/2\\ 5l/2 & 19(l/2)^2\end{bmatrix},$$

$$\mathbf{K}=k\begin{bmatrix}3 & l/2\\ l/2 & 11(l/2)^2\end{bmatrix},$$

whence

$$\mathbf{N}=\sqrt{M}\begin{bmatrix}1 & 0\\ 0 & r\end{bmatrix}.$$

Moreover, we introduce the notation

$$\lambda=\frac{l}{r},\quad \sigma=\frac{c}{M},\quad \omega^2=\frac{k}{M}.$$

Then, the two matrices $\mathbf{\Omega}^2$ and $\mathbf{\Delta}$ are readily computed as

$$\mathbf{\Omega}^2=\omega^2\begin{bmatrix}3 & \lambda/2\\ \lambda/2 & 11(\lambda/2)^2\end{bmatrix},\quad \mathbf{\Delta}=\sigma\begin{bmatrix}3 & 5\lambda/2\\ 5\lambda/2 & 19(\lambda/2)^2\end{bmatrix}.$$

It is now apparent that $\mathbf{\Delta}$ and $\mathbf{\Omega}^2$ do not commute under multiplication, and hence, the system at hand is not proportionally damped. Assuming the numerical values

$$\lambda=2\sqrt{3},\quad \omega=1\ \text{rad/s},\quad M=1\ \text{ton},$$

$$\text{and}\quad l=1\ \text{m},\quad \sigma=1\ \text{ton/s},$$

we obtain the system matrices displayed below[1]:

$$\mathbf{M}=\begin{bmatrix}1 & 0\\ 0 & 1/12\end{bmatrix},\quad \mathbf{C}=\begin{bmatrix}3 & 5/2\\ 5/2 & 19/4\end{bmatrix},\quad \mathbf{K}=\begin{bmatrix}3 & 1/2\\ 1/2 & 11/4\end{bmatrix}.$$

Therefore,

$$\mathbf{\Omega}^2=\begin{bmatrix}3 & \sqrt{3}\\ \sqrt{3} & 33\end{bmatrix},\quad \mathbf{\Delta}=\begin{bmatrix}3 & 5\sqrt{3}\\ 5\sqrt{3} & 57\end{bmatrix},$$

while the orthonormal basis $\mathcal{E}$ comprises two matrices, namely,

$$\mathbf{E}_0=\begin{bmatrix}1 & 0\\ 0 & 1\end{bmatrix},\quad \mathbf{E}_1=\begin{bmatrix}-0.993399 & 0.114708\\ 0.114708 & 0.993399\end{bmatrix},$$

whence

$$\mathbf{\Delta}_{\mathcal{O}}=\begin{bmatrix}2.368421 & 3.190620\\ 3.190620 & 57.631578\end{bmatrix}$$

and

$$\mathbf{\Delta}_{\perp}=\mathbf{\Delta}-\mathbf{\Delta}_{\mathcal{O}}=\begin{bmatrix}0.631578966 & 5.469634129\\ 5.469634129 & -0.63157897\end{bmatrix}.$$

The eigenvalues of $\mathbf{\Omega}$ are, moreover,

$$\omega_1=1.703035858,\quad \omega_2=5.753231170,$$

while its eigenvectors are stored columnwise in matrix $\mathbf{E}$:

$$\mathbf{E}=\begin{bmatrix}0.05744881285 & 0.9983484531\\ 0.9983484531 & -0.05744881285\end{bmatrix}.$$

Now,

$$\mathbf{\Delta}'=\mathbf{E}^T\mathbf{\Delta}\mathbf{E}=\begin{bmatrix}2.1848205012 & 5.505977615\\ 5.505977616 & 57.81517949\end{bmatrix}$$

and hence,

$$\mathbf{D}=\begin{bmatrix}2.1848205012 & 0\\ 0 & 57.81517949\end{bmatrix},$$

$$\mathbf{G}=\begin{bmatrix}0 & 5.505977615\\ 5.505977616 & 0\end{bmatrix}$$

As the reader can readily verify, $\mathbf{D}=\mathbf{E}^T\mathbf{\Delta}_{\mathcal{O}}\mathbf{E}$ and $\mathbf{G}=\mathbf{E}^T\mathbf{\Delta}_{\perp}\mathbf{E}$. The Frobenius norm of the error in the approximation of the dissipation matrix with $\mathbf{\Delta}_{\mathcal{O}}$ is computed from Eq. (15), which yields about 13%.

The mathematical model of the same system in decoupled form thus becomes

$$\ddot{z}_2+2.184205\dot{z}_2+2.900331z_2=h_2(t)$$

$$\ddot{z}_1+57.815179\dot{z}_1+33.099669z_1=h_1(t)$$

where z_1 and z_2 are the normal coordinates of the proportionally damped system, and $h_1(t)$, $h_2(t)$ are the projections of the generalized force of the given system in monic form onto the normal coordinates. Moreover, the projection $\mathbf{C}_{\mathcal{O}}$ of the damping matrix $\mathbf{C}$ onto the space $\mathcal{O}$ is calculated as

$$\mathbf{C}_{\mathcal{O}}=\begin{bmatrix}2.368421 & 0.9210526\\ 0.9210526 & 4.802632\end{bmatrix}$$

The computed eigenvalues of the given system and its proportionally damped approximation are displayed in Table 1. It is apparent from Table 1 that the given system and its proportionally damped approximation have two complex and two real eigenvalues, that are quite close to each other. Moreover, these eigenvalues indicate one underdamped and one overdamped modes. The natural frequencies and the damping ratios for the two systems are, correspondingly, slightly different, as illustrated in Table 2. Note that the natural frequencies of the proportionally damped system underestimate those of the given system. However, the proportionally damped system overestimates the damping ratio of the first mode but underestimates that of the second mode.

Table 1 Eigenvalues of the given system and its proportionally damped approximation

Given System	Proportionally Damped System
$-0.8512987042\pm j1.590887366$	$-1.092410247\pm j1.306510995$
-0.5102756076	-0.5782926128
-57.78712698	-57.23688690

5.2 A Three-Degree-of-Freedom Model for the Vertical Vibration of Mass-Transit Cars. The *mechanical model* of one-half of a subway car with pneumatic tires is shown in Fig. 2. The car is mounted on two *bogies*, each carrying two wheel axles. The above model consists of an H-shaped structural element, which is for this reason termed *the H* in the subway jargon. Moreover, the suspension itself consists of two parts, the *primary* and the *secondary* suspensions. The primary suspension is composed, in turn, of eight identical springs of stiffness k_1 and four more of stiffness k_2, where k_1 accounts for the coupling of the chassis to the axle and k_2 for the support of the motor-differential bridge. The car body is coupled to the chassis via a secondary suspension, com-

Table 2 Modal parameters of the given system and its proportionally damped approximation

Given System	Proportionally Damped System
$\omega_1=1.804337024\ \text{s}^{-1}$	$\omega_1=1.703035856\ \text{s}^{-1}$
$\zeta_1=0.4998712741$	$\zeta_1=0.6414487666$
$\omega_2=5.430226637\ \text{s}^{-1}$	$\omega_2=5.753231170\ \text{s}^{-1}$
$\zeta_2=5.367860910$	$\zeta_2=5.024583385$

[1]The units of $\mathbf{M}$, $\mathbf{C}$ and $\mathbf{K}$ are ton, ton s^{-1}, and ton s^{-2}, respectively, those of $\mathbf{\Delta}$ and $\mathbf{\Omega}$ being s^{-1}.

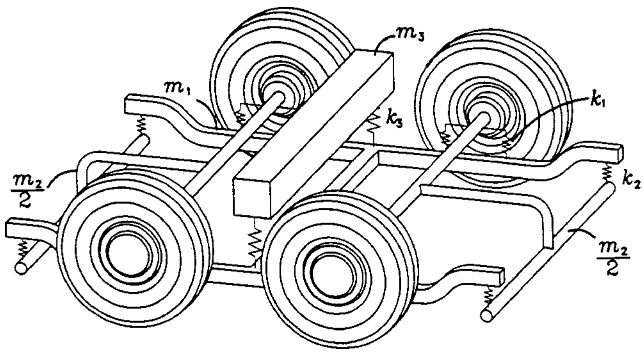

Fig. 2 Layout of the suspension system

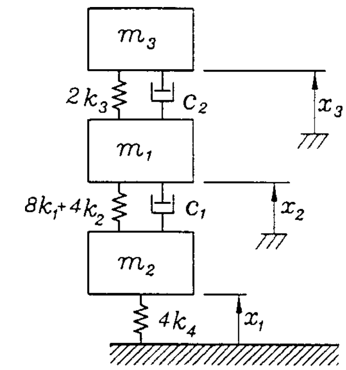

Fig. 3 The iconic model of the suspension of subway cars

posed of two identical springs of stiffness k_3. Furthermore, the spring stiffness of the rubber wheels is k_4. Except for the internal damping of the rubber in which the springs are cast, and for that of the tires, the system is undamped. Referring to Fig. 2, we have the definitions below:

m_1: mass of the chassis;
$m_2/2$: mass of each motor-differential bridge;
m_3: one-half the mass of the car body.

In an attempt to damp the vibrations observed when the cars run at speeds higher than 80 km/h, a study was conducted to determine suitable values of dashpot coefficients c_1 and c_2 for the primary and secondary suspensions, respectively ([12]).

The iconic model corresponding to the layout of Fig. 2 with added shock absorbers is shown in Fig. 3, where we neglect the damping of the tires. In deriving the mathematical model of the system appearing in this figure, we define now the three-dimensional vector of generalized coordinates $\mathbf{x}$ as $\mathbf{x} = [x_1 \;\; x_2 \;\; x_3]^T$ where all three components are measured from the equilibrium configuration.

The mathematical model corresponding to Fig. 3 takes the form of Eq. (1), with matrices $\mathbf{M}$, $\mathbf{C}$, and $\mathbf{K}$ given by

$$\mathbf{M}=\begin{bmatrix} m_2 & 0 & 0 \\ 0 & m_1 & 0 \\ 0 & 0 & m_3 \end{bmatrix}, \quad \mathbf{C}=\begin{bmatrix} c_1 & -c_1 & 0 \\ -c_1 & c_1+c_2 & -c_2 \\ 0 & -c_2 & c_2 \end{bmatrix},$$

$$\mathbf{K}=\begin{bmatrix} k_{11} & k_{12} & 0 \\ k_{12} & k_{22} & k_{23} \\ 0 & k_{23} & k_{33} \end{bmatrix}$$

where $k_{11}=8k_1+4k_2+4k_4$, $k_{12}=-8k_1-4k_2$, $k_{22}=8k_1+4k_2+2k_3$, $k_{23}=-k_{33}=-2k_3$. Moreover, the manufacturer provides the numerical values given below[2]:

$$k_1=4900, \quad k_2=3430, \quad k_3=837, \quad k_4=1783$$

$$m_1=1.971, \quad m_2=3.256, \quad m_3=15.78$$

where the value of m_3 is given under full load, i.e., when the cars are fully packed with people. Furthermore, the values of the dashpot coefficients that best damp the system were found in [12] as

$$c_1=156.9, \quad c_2=247.1. \tag{20}$$

Using the foregoing data, the system matrices are readily calculated as

$$\mathbf{M}=\begin{bmatrix} 3.256 & 0 & 0 \\ 0 & 1.971 & 0 \\ 0 & 0 & 15.78 \end{bmatrix},$$

$$\mathbf{C}=\begin{bmatrix} 156.9 & -156.9 & 0 \\ -156.9 & 404.0 & -247.1 \\ 0 & -247.1 & 247.1 \end{bmatrix},$$

$$\mathbf{K}=\begin{bmatrix} 60052000 & -52920000 & 0 \\ -52920000 & 54594000 & -1674000 \\ 0 & -1674000 & 1674000 \end{bmatrix},$$

whence the two matrices $\mathbf{\Omega}^2$ and $\mathbf{\Delta}$ are given by

$$\mathbf{\Omega}^2=\begin{bmatrix} 18443.48893 & -20889.8021 & 0 \\ -20889.8021 & 27698.63011 & -300.1640260 \\ 0 & -300.1640260 & 106.836501 \end{bmatrix},$$

$$\mathbf{\Delta}=\begin{bmatrix} 48.187961 & -61.935184 & 0 \\ -61.935184 & 204.972096 & -140.112194 \\ 0 & -140.112194 & 156.590621 \end{bmatrix}.$$

It can be shown that these two matrices do not commute under multiplication, and hence, this system, like the previous one, is not proportionally damped. Using the same procedure as for the first example, we find the projection $\mathbf{\Delta}_{\mathcal{O}}$ of $\mathbf{\Delta}$ onto the space $\mathcal{O}$ as

$$\mathbf{\Delta}_{\mathcal{O}}=\begin{bmatrix} 158.432273 & -40.325342 & -34.744055 \\ -40.325342 & 174.719532 & -30.743266 \\ -34.744055 & -30.743266 & 76.598872 \end{bmatrix},$$

while its complement $\mathbf{\Delta}_{\perp}$ is given by

$$\mathbf{\Delta}_{\perp}=\begin{bmatrix} -110.2443123 & -21.60984227 & 34.74405632 \\ -21.60984229 & 30.2525629 & -109.3689278 \\ 34.74405632 & -109.3689278 & 79.99174968 \end{bmatrix}.$$

The eigenvalues of $\mathbf{\Omega}$ are, in turn,

$$\omega_1=9.092542549\,\mathrm{s}^{-1}, \quad 41.19482359\,\mathrm{s}^{-1}, \quad 210.8755911\,\mathrm{s}^{-1}$$

and its eigenvectors are stored columnwise in matrix $\mathbf{E}$:

$$\mathbf{E}=\begin{bmatrix} -0.7748604459 & 0.6259605113 & 0.08811769568 \\ -0.6211730188 & -0.7798369042 & 0.07744988086 \\ 0.1171979980 & 0.005276513996 & 0.9930945517 \end{bmatrix}.$$

Then

[2]The units used in this example are the same as those of Example 1.

Table 3 Eigenvalues of the given system and its proportionally damped approximation

Given System	Proportionally Damped System
$-96.88268863\pm j168.2682971$	$-102.1831157\pm j184.4644295$
$-30.66301121\pm j10.35129840$	$-27.53342017\pm j30.64187108$
$-6.863859157\pm j10.53039184$	$-4.693023040\pm j7.787802295$

$$\mathbf{\Delta}'=\mathbf{E}^T\mathbf{\Delta}\mathbf{E}=\begin{bmatrix}55.06684058 & 66.77996143 & 22.70847441\\ 66.77996143 & 204.3662317 & 25.90924029\\ 22.70847441 & 25.90924030 & 9.386045683\end{bmatrix}$$

while

$$\mathbf{D}=\begin{bmatrix}55.06684058 & 0 & 0\\ 0 & 204.3662317 & 0\\ 0 & 0 & 9.386045683\end{bmatrix},$$

and

$$\mathbf{G}=\begin{bmatrix}0 & 66.77996143 & 22.70847441\\ 66.77996143 & 0 & 25.90924029\\ 22.70847441 & 25.90924030 & 0\end{bmatrix}.$$

The error in this approximation, computed with the aid of Eq. (15), gives about 45%. The mathematical model of the closest proportionally damped system in decoupled form then becomes

$$\ddot{z}_1+55.06684034\dot{z}_1+1697.013489z_1=h_1(t)$$

$$\ddot{z}_2+204.3662314\dot{z}_2+44468.51488z_2=h_2(t)$$

$$\ddot{z}_3+9.386046082\dot{z}_3+82.67432986z_3=h_3(t)$$

where $\{z_i\}_1^3$ is the set of normal coordinates of the proportionally damped system at hand, while $\{h_i(t)\}_1^3$ are the projections of the generalized force of the said system onto the normal coordinates. Moreover, the projection $\mathbf{C}_{\mathcal{O}}$ of the damping matrix $\mathbf{C}$ onto the space $\mathcal{O}$ is

$$\mathbf{C}_{\mathcal{O}}=\begin{bmatrix}368.6169970 & -185.4163721 & -25.11919552\\ -185.4163721 & 286.9551152 & -23.02098903\\ -25.11919552 & -23.02098902 & 158.0985150\end{bmatrix}$$

which thus leads to the closest proportionally damped system in the form of Eq. (16). The computed eigenvalues of the given system and its proportionally damped approximation are displayed in Table 3.

It is again apparent that the given system and its proportionally damped approximation observe the same modal behavior: three underdamped modes. Notice, however, from Table 4, that now the differences between the corresponding modal parameters of the two systems are more pronounced. Also notice that the proportionally damped system shows a first natural frequency lower then that of the given system, but the second and third frequencies observe the reverse relation. Moreover, the three damping ratios of the proportionally damped system underestimate those of the given system. In particular, the second damping ratio of the proportional system underestimates the actual one by about 30%.

An important feature of this example is that it illustrates that properties of a single-degree-of-freedom systems, or of proportionally damped systems for that matter, cannot be extrapolated to arbitrarily damped multi-degree-of-freedom systems. While the model of Fig. 3 may lead one to conclude that this system has one undamped mode, namely, one motion under which $x_1=x_2=x_3$, the fact of the matter is, as Table 4 shows, that all three modes of this model are damped.

Table 4 Modal parameters of the given system and its proportionally damped approximation

Given System	Proportionally Damped System
$\omega_1=12.56987330\ \mathrm{s}^{-1}$	$\omega_1=9.092542540\ \mathrm{s}^{-1}$
$\omega_2=32.36309063\ \mathrm{s}^{-1}$	$\omega_2=41.19482358\ \mathrm{s}^{-1}$
$\omega_3=194.1661020\ \mathrm{s}^{-1}$	$\omega_3=210.8755910\ \mathrm{s}^{-1}$
$\zeta_1=0.5460563518$	$\zeta_1=0.5161397947$
$\zeta_2=0.9474685703$	$\zeta_2=0.6683708723$
$\zeta_3=0.4989680878$	$\zeta_3=0.4845658770$

5.3 A Three-Degree-of-Freedom System With One Overdamped Mode. We include this example to show the dramatic differences that can occur in the modal behavior of the given system and its proportionally damped approximation. To this end, we use the same parameters of the system of Fig. 3, but with a different damping matrix $\mathbf{M}$ whose third diagonal entry is one order of the magnitude smaller than its counterpart in Example 2:

$$\mathbf{M}=\begin{bmatrix}3.256 & 0 & 0\\ 0 & 1.971 & 0\\ 0 & 0 & 1.578\end{bmatrix}.$$

Then, the original system and its proportionally damped approximation have two underdamped and one overdamped modes, while the eigenvalues are now substantially different, as can be seen from Tables 5 and 6. Furthermore, while the second underdamped mode of the given system is slightly damped, with $\zeta_2<3\%$, its proportionally damped counterpart is heavily damped, with $\zeta_2>92\%$. As to the third mode, note that the damping ratio of the given system is about two times as big as that of its proportionally damped approximation.

Our analysis then shows that design conclusions drawn from a proportional-damping approximation can be dangerously wrong: a mode of the proportionally damped system derived using a least-square approximation can appear heavily damped, and not needing any active control, when this mode is, in fact, slightly damped,

Table 5 Eigenvalues of the given system and its proportionally damped approximation

Given System	Proportionally Damped System
$-67.41861484\pm j168.1615288$	$-103.8729329\pm j183.5492179$
$-0.8578582497\pm j31.72446644$	$-24.30331859\pm j9.960961556$
-266.1058354	-138.7439747
-7.091895084	-14.65419970

Table 6 Modal parameters of the given system and its proportionally damped approximation

Given System	Proportionally Damped System
$\omega_1=181.1727612\ \mathrm{s}^{-1}$	$\omega_1=210.9025879\ \mathrm{s}^{-1}$
$\omega_2=31.73606296\ \mathrm{s}^{-1}$	$\omega_2=26.26541547\ \mathrm{s}^{-1}$
$\omega_3=43.44185385\ \mathrm{s}^{-1}$	$\omega_3=45.09081849\ \mathrm{s}^{-1}$
$\zeta_1=0.3721233501$	$\zeta_1=0.4925161608$
$\zeta_2=0.0270310230$	$\zeta_2=0.9252973218$
$\zeta_3=3.144406906$	$\zeta_3=1.700991239$

and needing active control. Even the proportionally damped system best approximated with the method proposed here in the least-square sense can be dangerously misleading.

6 Conclusions

The decomposition of the damping matrix of arbitrarily damped linear mechanical systems into two orthogonal components was the subject of this paper. One of these components, the best approximation of the given damping matrix in the least-square sense, leads to proportional damping. Upon a linear transformation given by the factors of the mass matrix of the system, the two components of the damping matrix are orthogonal, which justifies the above claim on the least-square approximation of the damping matrix. The concept was illustrated with three examples. Apparently, even the best proportionally damped approximation to an arbitrarily damped system can be misleading in that it can yield a heavily damped mode, while the actual mode can be slightly damped. We have also shown, with Examples 2 and 3, that properties of single-degree-of-freedom systems, or of proportionally damped systems for that matter, cannot be extrapolated to arbitrarily-damped systems.

Finally, we have shown that the proportional-damping matrix that best approximates the nonproportional-damping matrix is positive-definite if the latter is; else, it is positive-semidefinite.

We have also shown that the least-square approximation of the nonproportional damping matrix with a proportional-damping matrix can be computed from the same similarity transformation of the dissipation matrix that renders the frequency matrix diagonal, as proposed elsewhere.

Acknowledgments

The research work reported here was made possible under NSERC (Natural Sciences and Engineering Research Council, of Canada) Grant A4532. Discussions held with Prof. M. Kujath, Dalhousie University, Halifax (Nova Scotia, Canada), while on sabbatical at McGill University, motivated the work reported in this paper. The authors wish to express their most sincere appreciation to Prof. Kujath for the insight with which he contributed in these discussions. The first author completed this work while on a Visiting Professorship at Nanyang Technological University (NTU), Singapore. The support of NTU, especially of its School of Mechanical and Production Engineering, is highly acknowledged.

References

[1] Prater, G., and Singh, R., 1986, ''Quantification of the Extend of Non-proportional Viscous Damping in Discrete Vibratory Systems,'' J. Sound Vib., **104**(1), pp. 109–125.
[2] Minas, C., and Inman, D. J., 1991, ''Identification of Nonproportional Damping Matrix From Incomplete Modal Information,'' ASME J. Vibr. Acoust., **113**, pp. 219–224.
[3] Roemer, M. J., and Mook, D. J., 1992, ''Mass, Stiffness and Damping: An Integrated Approach,'' ASME J. Vibr. Acoust., **114**, pp. 358–363.
[4] Gladwell, G. M. L., 1993, *Inverse Problems in Scattering: An Introduction*, Kluwer Academic Publishers, Dordrecht, The Netherlands.
[5] Abrahamsson, T., 1994, ''Modal Parameter Extraction for Nonproportionally Damped Linear Systems,'' Proc. 12 International Modal Analysis Conference.
[6] Kujath, M. R., Liu, K., and Akpan, D., 1998, ''Analysis of Complex Modes Influence on Modal Correlation of Space Structures,'' Technical Report, Canadian Space Agency, St.-Hubert, Quebec, Canada.
[7] Meirovitch, L., 2001, *Fundamentals of Vibrations*, McGraw-Hill, New York.
[8] Angeles, J., Zanganeh, K. E., and Ostrovskaya, S., 1999, ''The Analysis of Arbitrarily-Damped Linear Mechanical Systems,'' Arch. Appl. Mech., **69**(8), pp. 529–541.
[9] Kujath, M. R., 1999, ''Proportional vs. Non-proportional Damping,'' Technical Memorandum, Dalhousie University.
[10] Golub, G., and Loan, F. V., 1983, *Matrix Computations*, The John Hopkins University Press, Baltimore, MD.
[11] Kaye, R., and Wilson, R., 1998, *Linear Algebra*, Oxford University Press, New York.
[12] Angeles, J., and Espinosa, I., 1981, ''Suspension-System Synthesis for Mass Transport Vehicles With Prescribed Dynamic Behavior,'' ASME Paper No. 81-DET-44.

L. Kogut
e-mail: mekogut@tx.technion.ac.il

I. Etsion
e-mail: etsion@tx.technion.ac.il
Fellow ASME

Department of Mechanical Engineering,
Technion,
Haifa 32000, Israel

Elastic-Plastic Contact Analysis of a Sphere and a Rigid Flat

An elastic-plastic finite element model for the frictionless contact of a deformable sphere pressed by a rigid flat is presented. The evolution of the elastic-plastic contact with increasing interference is analyzed revealing three distinct stages that range from fully elastic through elastic-plastic to fully plastic contact interface. The model provides dimensionless expressions for the contact load, contact area, and mean contact pressure, covering a large range of interference values from yielding inception to fully plastic regime of the spherical contact zone. Comparison with previous elastic-plastic models that were based on some arbitrary assumptions is made showing large differences.
[DOI: 10.1115/1.1490373]

Introduction

The elastic-plastic contact of a sphere and a flat is a fundamental problem in contact mechanics. It is applicable, for example, in problems such as particle handling ([1]), or sealing, friction, wear, and thermal and electrical conductivity between contacting rough surfaces. Indeed, an impressive number of works on the contact of rough surfaces, that were published so far (see review by Liu et al. [2]), are based on the contact behavior of a single spherical asperity (Bhushan [3]) in a statistical model of multiple asperity contact (Bhushan [4]). Some of these works are restricted to mainly pure elastic deformation of the contacting sphere, e.g., the pioneering work of Greenwood and Williamson [5], which is based on the Hertz solution for a single elastic sphere (e.g., Timoshenko and Goodier [6]). Other works are restricted to pure plastic deformation of the contacting sphere, based on the model of Abbott and Firestone [7], which neglects volume conservation of the plastically deformed sphere.

The works on either pure elastic or pure plastic deformation of the contacting sphere overlook a wide intermediate range of interest where elastic-plastic contact prevails. An attempt to bridge this gap was made by Chang et al. [8] (CEB model). In this model the sphere remains in elastic Hertzian contact until a critical interference is reached, above which volume conservation of the sphere tip is imposed. The contact pressure distribution for the plastically deformed sphere was assumed to be rectangular and equal to the maximum Hertzian pressure at the critical interference. The CEB model suffers from a discontinuity in the contact load as well as in the first derivatives of both the contact load and the contact area at the transition from the elastic to the elastic-plastic regime. These deficiencies triggered several modifications by other researchers. Evseev et al. [9] suggested a uniform pressure distribution, equal to the maximum Hertzian pressure at the critical interference, in the central portion of the contact area, and an elliptical Hertzian distribution outside this portion starting from the maximum pressure and approaching zero at the contact boundary. The authors concluded their paper with a recommendation to find a more general model for the elastic-plastic regime. Chang [10] used an approximate linear interpolation for the elastic-plastic regime by connecting the value of the contact load at yielding inception to that at the beginning of the fully plastic regime. Zhao et al. [11] used mathematical manipulation to smooth the transition of the contact load and contact area expressions between the elastic and elastic-plastic deformation regimes. Kucharski et al. [12] solved the contact problem of a deformed sphere by the finite element method (FEM) and developed empirical proportional expressions for the contact load and the contact area. Although the authors intended to describe elastic-plastic contact, their results concentrated on the behavior of the sphere deep into the plastic regime. Surprisingly, the mean contact pressure in [12] was, in some cases, higher than the indentation hardness and therefore unreasonable.

The work in [1] employed the finite element method to analyze the contact of two identical spheres, which by symmetry is equivalent to that of one sphere in contact with a frictionless rigid plane. The analysis in [1] was restricted to an aluminum sphere of radius $R=0.1$ m loaded with a mean contact pressure that never exceeded 2.3 times the material's yield strength.

As can be seen from the literature survey, accurate general solutions for the elastic-plastic contact of a deformable sphere and a rigid flat are still missing. The existing elastic-plastic solutions suffer from several deficiencies caused mainly by assuming some arbitrary contact pressure distribution or an arbitrary evolution of the plastic region inside the sphere. The few existing finite element method solutions are too restricted in terms of materials, geometry, and loading.

It should be noticed here that much research has also been done (mostly by utilizing the finite element method) on the indentation problem of a half-space by a rigid sphere, e.g., [13–16]. However, from the results provided by Mesarovic and Fleck [17] for both a sphere pressed by a rigid flat and a half-space indented by a rigid sphere, deep into the fully plastic regime, it seems that the behavior of these two cases is different. Intuitively, one can see that in the indentation case the radius of the rigid spherical indenter remains constant whereas the curvature of a deformable sphere changes continuously during the deformation. Moreover, the displaced material in the indented half-space is confined by the rigid indenter and the elastic bulk of the half-space. This is quite different from the situation where the displaced material of the deformable sphere is free to expand radially as shown schematically in Fig. 1.

The present research offers an accurate finite element method solution for the elastic-plastic contact of a deformable sphere and a rigid flat by using constitutive laws appropriate to any mode of deformation, be it elastic or plastic. It also offers a general dimensionless solution not restricted to a specific material or geometry.

Theoretical Background

Figure 1 presents a deformable hemisphere, with a radius R, pressed by a rigid flat. The solid and dashed lines show the situ-

Contributed by the Applied Mechanics Division of THE AMERICAN SOCIETY OF MECHANICAL ENGINEERS for publication in the ASME JOURNAL OF APPLIED MECHANICS. Manuscript received by the ASME Applied Mechanics Division, August 6, 2001; final revision, December 14, 2001. Associate Editor: E. Arruda. Discussion on the paper should be addressed to the Editor, Prof. Robert M. McMeeking, Department of Mechanical and Environmental Engineering University of California–Santa Barbara, Santa Barbara, CA 93106-5070, and will be accepted until four months after final publication of the paper itself in the ASME JOURNAL OF APPLIED MECHANICS.

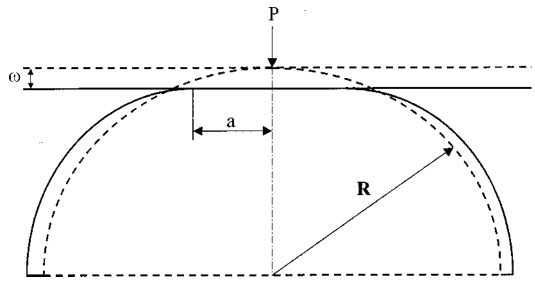

Fig. 1 A deformable sphere pressed by a rigid flat

ation after and before the deformation, respectively. The interference, ω, and contact area with a radius, a, (see Fig. 1) correspond to a contact load, P.

The critical interference, ω_c, that marks the transition from the elastic to the elastic-plastic deformation regime (i.e., yielding inception) is given by (e.g., Chang et al. [8])

$$\omega_c = \left(\frac{\pi K H}{2E}\right)^2 R. \tag{1}$$

The hardness, H, of the sphere is related to its yield strength by $H=2.8Y$ ([18]). The hardness coefficient, K, is related to the Poisson ratio of the sphere by (Chang et al. [19]) $K=0.454+0.41\nu$. E is the Hertz elastic modulus defined as

$$\frac{1}{E} = \frac{1-\nu_1^2}{E_1} + \frac{1-\nu_2^2}{E_2}$$

where E_1, E_2 and ν_1, ν_2 are Young's moduli and Poisson's ratios of the two materials, respectively. In the case of the rigid flat $E_2 \to \infty$.

The Hertz solution for the elastic contact of a sphere and a flat provides the contact load, P_e, and contact area, A_e, for $\omega \leqslant \omega_c$ in the form

$$P_e = \frac{4}{3} E R^{1/2} \omega^{3/2} = P_c \left(\frac{\omega}{\omega_c}\right)^{3/2} \tag{2}$$

$$A_e = \pi R \omega = A_c \frac{\omega}{\omega_c} \tag{3}$$

where P_c and A_c are the contact load and contact area, respectively, at $\omega = \omega_c$. Note that P_e and A_e can be normalized by P_c and A_c, respectively, to obtain simple exponential functions of the dimensionless interference, ω/ω_c. These functions are independent of the material properties and sphere radius.

Using Eqs. (1)–(3) the mean contact pressure, $p_e = P_e/A_e$, for $\omega \leqslant \omega_c$ is

$$p_e = \frac{2}{3} K H \left(\frac{\omega}{\omega_c}\right)^{1/2} = p_c \left(\frac{\omega}{\omega_c}\right)^{1/2} \tag{4}$$

where p_c is the mean contact pressure at $\omega = \omega_c$.

For $\omega > \omega_c$ the contact is elastic-plastic and a numerical solution is required to find the relation between ω/ω_c, the contact load, contact area, and mean contact pressure. The finite element method (for example, Refs. [20] and [21]) is commonly used for such a numerical solution where the contact between the sphere and the flat is detected by special contact elements ([22]). A yielding criterion should be adopted in solving elastic-plastic problems. In the present analysis the von Mises criterion, which correlates well with experiments (see Bhushan [3]) was selected as the preferred criterion. A recent example for the finite element method solution to an elastic-plastic contact problem can be found in Liu et al. [23].

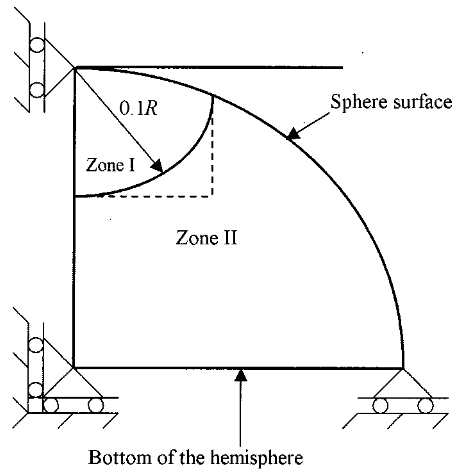

Fig. 2 Model description

Finite Element Model (FEM)

A commercial ANSYS 5.7 package was used to solve the contact problem. The hemisphere, shown in Fig. 2, was modeled by a quarter of a circle, due to its axisymmetry. The rigid flat was modeled by a line. The material of the sphere was assumed elastic-perfectly plastic with identical behavior in tension and compression. Although the model can easily accommodate strain hardening the simpler behavior was selected to allow comparison with existing previous models. A static, small-deformation analysis type was used and justified by comparison with the results of a large-deformation analysis. The von Mises yielding criterion was used to detect local transition from elastic to plastic deformation.

The finite element method numerical solution requires as an input some specific material properties and sphere radius (see [1], for example). However, in order to generalize the present solution and eliminate the need for a specific input, the numerical results were normalized with respect to their corresponding critical values at yielding inception, ω_c, similar to Eqs. (2) and (3). The normalization of the mean contact pressure, p, was done with respect to the yield strength, Y, of the sphere material. The validity of this normalization was tested by solving the problem for several different material properties $(100<E/Y<1000, \nu=0.3)$ and sphere radii $(0.1\text{ mm}<R<10\text{ mm})$. The dimensionless results of P/P_c, A/A_c, and p/Y versus the dimensionless interference, ω/ω_c, were always the same regardless of the selection of material properties and sphere radius.

The finite element mesh consisted of 225 eight-node quadrilateral axisymmetric elements comprising a total of 714 nodes. High-order elements were selected to better fit the curvature of the sphere. The sphere was divided into two different mesh density zones. Zone I, within a $0.1R$ distance from the sphere tip (see Fig. 2), contained 87% of the nodes and had extremely fine mesh to better handle the high stress gradients in this zone and to achieve good discretization for accurate detection of the contact area radius, a. For this reason the typical mesh size was $0.03a_c$ where $a_c = (R\omega_c)^{1/2}$. Zone II, outside the $0.1R$ distance, had gradual coarser mesh at increasing distance from the sphere tip. The model also contained a single two-dimensional target element laying on the flat and 16 two-dimensional surface-to-surface contact elements on the sphere surface in zone I.

The boundary conditions are presented in Fig. 2. The nodes on the axis of symmetry of the hemisphere cannot move in the radial direction. Likewise the nodes on the bottom of the hemisphere cannot move in the axial direction due to symmetry. Restricting also the radial motion of these nodes did not affect the results of

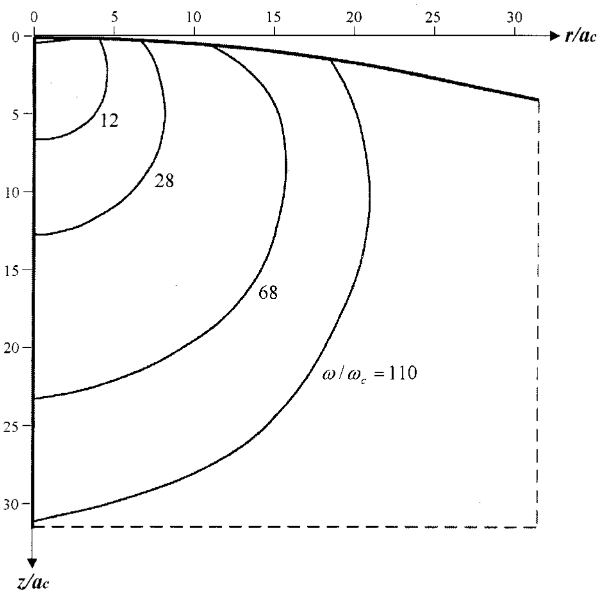

Fig. 3 Evolution of the plastic region in the sphere tip for 12 $\leqslant \omega/\omega_c \leqslant 110$

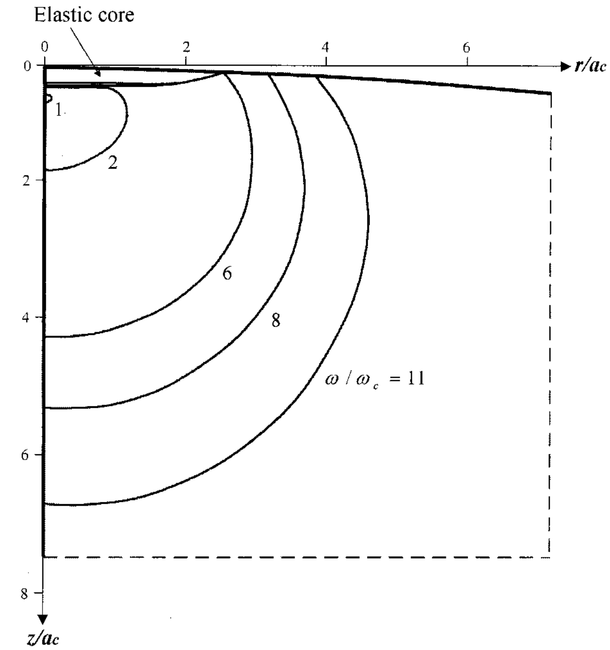

Fig. 4 Evolution of the plastic region in the sphere tip for 1 $\leqslant \omega/\omega_c \leqslant 11$

the finite element analysis (FEA) since this boundary is very far away from the contact zone and therefore has very little effect on the contact results.

The numerical model was first verified by comparing its output with the analytical results of the Hertz solution in the elastic regime, i.e., for $\omega < \omega_c$. The verification included the contact load, contact area radius, and stress distribution in the contact area and along the axis of symmetry. The difference between the numerical and analytical results was always less than 2.8%. Another verification of the model was done in the elastic-plastic regime (for $1 < \omega/\omega_c < 110$) by increasing the mesh density to 2944 nodes and comparing the results with these obtained with the original 714 nodes. The largest differences in the contact load and contact area were only 1% and 3%, respectively. These two verifications establish the validity of the numerical model with the original mesh to study the behavior of the sphere in the elastic-plastic regime.

Results and Discussion

Figure 3 presents the evolution of the plastic region inside the sphere (within the dashed line frame shown in Fig. 2) for increasing interference values up to $\omega/\omega_c = 110$. The elastic-plastic boundary at each interference is determined by all the nodes with equivalent total strain larger than the yield strain, ε_Y. The axial and radial coordinates in Fig. 3 are normalized by the critical contact radius, a_c. It is interesting to note the larger axial penetration of the plastic region compared to its radial spread. At $\omega/\omega_c = 110$, for example, the plastic region penetrates about $32a_c$ below the contact surface and reaches only about $18a_c$ on the sphere surface.

The evolution of the plastic region at its earlier stages, $\omega/\omega_c \leqslant 11$, is shown in more details in Fig. 4. Up to $\omega/\omega_c = 6$ the plastic region is completely surrounded by elastic material. At $\omega/\omega_c = 6$ the plastic region first reaches the sphere surface at a radius of about $2.7a_c$. At this point an elastic core remains locked between the plastic region and the sphere surface. As the interference increases above $\omega/\omega_c = 6$ and the plastic region grow, the elastic core gradually shrinks as shown in Fig. 5. The shrinkage rate is very small below $\omega/\omega_c = 30$ and rapidly increases thereafter. The surface of the sphere at the contact region is now divided into three subregions as follows: (I) an inner circular elastic subregion extending radially from the center of the contact until the edge of the elastic core; (II) an intermediate annular plastic subregion between the edge of the elastic core and the outer front of the plastic region, and (III) an outer elastic subregion thereafter. The evolution of these three subregions on the sphere surface for $\omega/\omega_c \geqslant 6$ is demonstrated in Fig. 6 that shows the radial locations of the inner and outer elastic-plastic boundaries normalized by the contact area radius, a, as a function of the dimensionless interference ω/ω_c. The horizontal dashed line at $r/a = 1$ indicates the circular boundary of the contact area. From the figure it can be easily seen that below $\omega/\omega_c = 6$ the sphere surface is fully elastic. At $\omega/\omega_c = 6$ the plastic region reaches the sphere surface for the

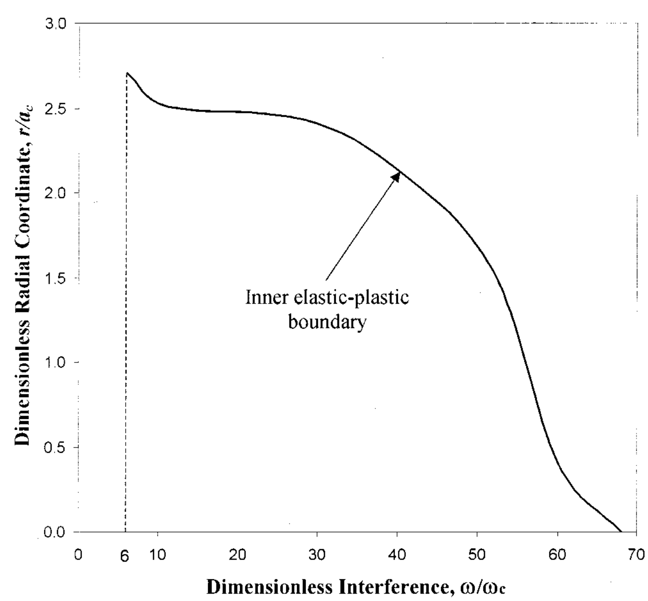

Fig. 5 Dimensionless radial location, r/ac_c, of the inner elastic-plastic boundary on the sphere surface showing its shrinkage for $6 \leqslant \omega/\omega_c \leqslant 68$

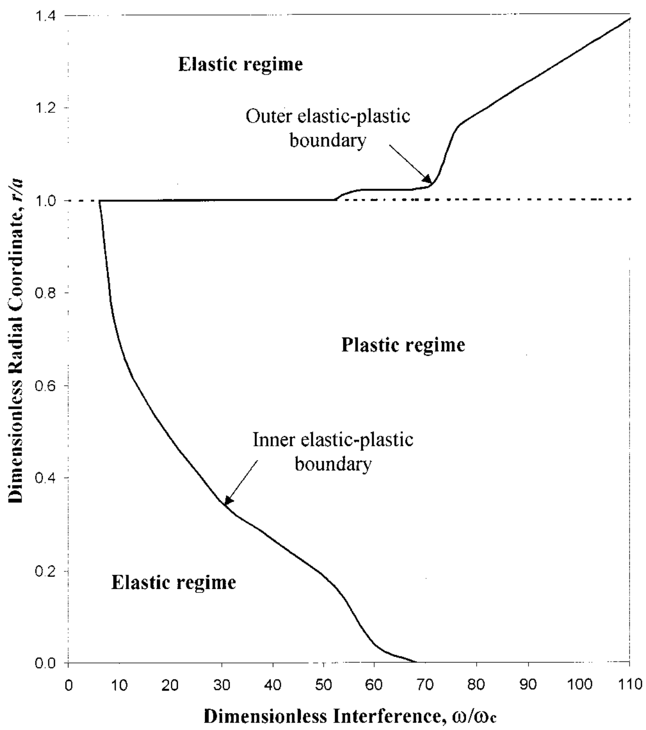

Fig. 6 Radial location of inner and outer elastic-plastic boundaries on the sphere surface for $6 \leqslant \omega/\omega_c \leqslant 110$

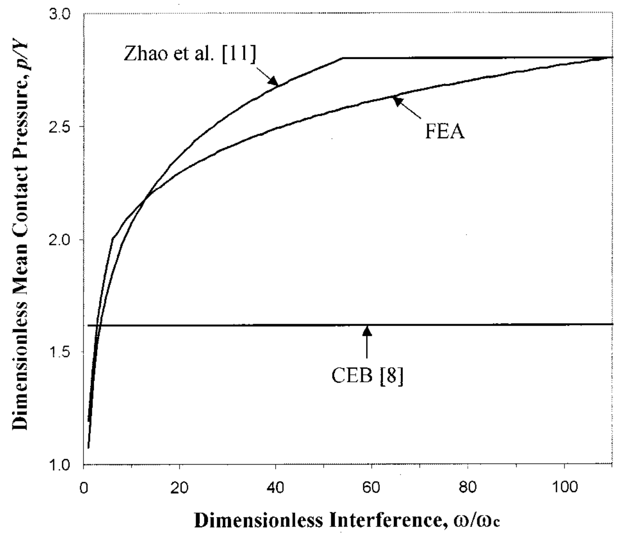

Fig. 7 Dimensionless mean contact pressure, p/Y, as a function of the dimensionless interference, ω/ω_c, in the elastic-plastic regime

first time. This occurs very close to the boundary of the contact area, at $r/a = 0.94$. For $6 \leqslant \omega/\omega_c \leqslant 56$ the annular plastic subregion remains within the contact area. Its outer boundary, which first reaches the edge of the contact area at $\omega/\omega_c = 6.2$, coincides with that of the contact area while its inner boundary gradually moves towards the contact center as the elastic core shown in Fig. 4 shrinks. For $\omega/\omega_c > 56$ the outer boundary of the annular plastic subregion somewhat exceeds the boundary of the contact area while the inner elastic core continues to shrink and disappears completely at $\omega/\omega_c = 68$. From there on the entire contact zone is plastic and the rate of its radial expansion increases substantially.

From the above discussion it can be seen that the evolution of the elastic-plastic contact can be divided into three distinct stages. The first one for $1 \leqslant \omega/\omega_c \leqslant 6$ where the plastic region develops below the sphere surface and the entire contact area is elastic. The second one for $6 \leqslant \omega/\omega_c \leqslant 68$ where the contact area is elastic-plastic containing an annular plastic subregion confined by inner and outer elastic ones. The third stage for $\omega/\omega_c > 68$ corresponds to a fully plastic contact area.

Figure 7 presents the results of the mean contact pressure p/Y as a function of the interference, ω/ω_c, that were obtained by the present finite element analysis along with the results from the CEB model ([8]) and from Zhao et al. [11]. When the discrete numerical results of the finite element analysis were curve fitted it became evident that a distinct transition point exists at $\omega/\omega_c = 6$. This is clearly observed in Fig. 7 by the discontinuity in the slope of the finite element analysis results at $\omega/\omega_c = 6$. Apparently, the transition from fully elastic to elastic-plastic contact area, which occurs when the expanding plastic region first reaches the sphere surface, changes the behavior of the mean contact pressure. No similar transition or change was found at $\omega/\omega_c = 68$ that marks the inception of fully plastic contact area when the central elastic core is completely eliminated. The empirical expressions obtained from the curve fitting for the mean contact pressure in the stages that were discussed above are

$$\left(\frac{p}{Y}\right)_1 = 1.19\left(\frac{\omega}{\omega_c}\right)^{0.289} \quad \text{for } 1 \leqslant \omega/\omega_c \leqslant 6 \tag{5}$$

$$\left(\frac{p}{Y}\right)_2 = 1.61\left(\frac{\omega}{\omega_c}\right)^{0.117} \quad \text{for } 6 \leqslant \omega/\omega_c \leqslant 110. \tag{6}$$

From Fig. 7 it can be seen that the dimensionless mean contact pressure of the finite element analysis at $\omega/\omega_c = 110$ approaches the value $p/Y = 2.8$. This is identical to the ratio between the hardness and yield strength found experimentally for many materials as indicated by Tabor [18]. Hence, the value of p at this point is that of the material hardness, H, and, hence, $\omega/\omega_c = 110$ marks the inception of the fully plastic regime where the mean contact pressure assumes a constant value equals to the material hardness.

The CEB model ([8]) predicts a constant mean contact pressure, which largely underestimates the finite element analysis results except for a small range, $\omega/\omega_c \leqslant 3$, where it largely overestimates the finite element analysis results. This is one of the limitations of this model as discussed by Evseev et al. [9].

Zhao et al. model [11] predicts p/Y values that are fairly close to the finite element analysis results. The largest deviation of about 9% occurs at $\omega/\omega_c = 54$, which was selected in Ref. [11], based on the work of Johnson [24], as the lowest possible inception of fully plastic regime where $p/Y = 2.8$. Actually the fully plastic regime starts at $\omega/\omega_c = 110$ as can be seen from the finite element analysis results in Fig. 7.

The results obtained by Kucharski et al. [12] cover the range of $175 \leqslant \omega/\omega_c \leqslant 2800$ that is very deep into the fully plastic regime and therefore outside the range of interest of the present analysis.

The change in the slope of the mean contact pressure at the transition point $\omega/\omega_c = 6$ is somewhat similar to a typical stress strain curve where a change of slope occurs at the elastic limit. In the spherical contact problem the value $\omega/\omega_c = 6$ is analogous to the critical strain, which corresponds to yielding inception. This point marks the elastic limit of the spherical contact interface. From there on the resistance of the material to increasing strain decreases and eventually disappears at $\omega/\omega_c = 110$.

The finite element analysis results for the dimensionless contact area and contact load are presented in Figs. 8 and 9, respectively, along with the results of Refs. [8] and [11]. The corresponding empirical expressions obtained from curve fitting of the finite element analysis numerical results in the various stages of the evolution of the elastic-plastic contact are

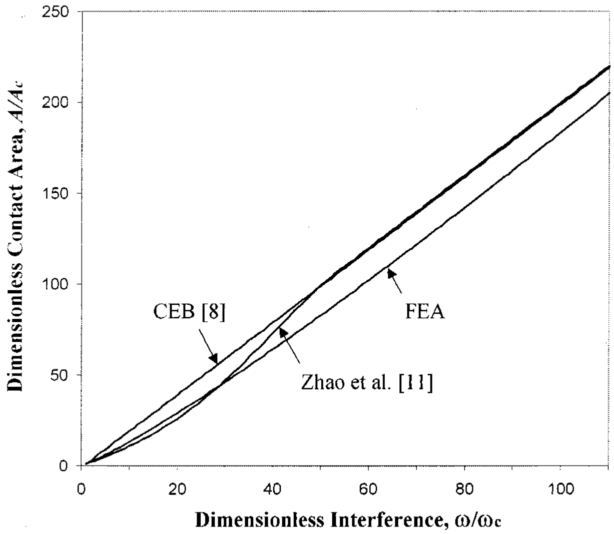

Fig. 8 Dimensionless contact area, A/A_c, as a function of the dimensionless interference, ω/ω_c, in the elastic-plastic regime

$$\left(\frac{P}{P_c}\right)_1 = 1.03\left(\frac{\omega}{\omega_c}\right)^{1.425}$$

$$\left(\frac{A}{A_c}\right)_1 = 0.93\left(\frac{\omega}{\omega_c}\right)^{1.136} \quad \text{for } 1 \leqslant \omega/\omega_c \leqslant 6 \qquad (7)$$

$$\left(\frac{P}{P_c}\right)_2 = 1.40\left(\frac{\omega}{\omega_c}\right)^{1.263}$$

$$\left(\frac{A}{A_c}\right)_2 = 0.94\left(\frac{\omega}{\omega_c}\right)^{1.146} \quad \text{for } 6 \leqslant \omega/\omega_c \leqslant 110. \qquad (8)$$

The accuracy of the curve fitting for Eqs. (7) and (8) was better than 97% throughout the range of ω/ω_c.

From Fig. 8 it is clear that the contact area obtained by the CEB model ([8]) overestimates the finite element analysis results. The largest difference is 56% at $\omega/\omega_c = 4$. This difference diminishes as the interference increases and for $\omega/\omega_c = 110$ it becomes less than 7%. The reason for the larger deviation at smaller interferences is that the CEB model assumes volume conservation of the entire sphere tip for $\omega/\omega_c \geqslant 1$. This in fact is equivalent to assuming fully plastic regime of the entire sphere tip as soon as the critical interference is reached. From Fig. 3 it is clear that the plastic region develops gradually with increasing interference and only for very large interferences the entire asperity tip is plastically deformed.

The Zhao et al. [11] results underestimate the finite element analysis ones by up to 18% at $\omega/\omega_c = 10$ and overestimate them by up to 20% at $\omega/\omega_c = 51$. The Zhao et al. model assumes fully plastic sphere tip at $\omega/\omega_c = 54$. From this point on the contact area is calculated from the geometrical intersection of the flat with the original profile of the sphere according to Abbott and Firestone [7]. This is also true for the CEB model, which therefore predicts the same results at large interferences.

At $\omega/\omega_c = 110$ the contact area based on the Abbott and Firestone approximate calculation is only 7% higher than the more accurate result of the finite element analysis. It seems therefore, that the Abbott and Firestone model is a relatively fair approximation for the contact area in the fully plastic regime.

Figure 9 presents the contact load P/P_c versus the interference ω/ω_c. The contact load obtained by the CEB model ([8]) clearly differs from the finite element analysis results. It overestimates the finite element analysis results at small interferences, by up to 62% at $\omega/\omega_c = 2$, and underestimates these results by up to 38% at $\omega/\omega_c = 110$. This is due to a combination of the very inaccurate assumption of constant mean pressure and too large contact area in [8] as shown in Figs. 7 and 8. Contrary to the CEB model, the contact load obtained by Zhao et al. underestimates the finite element analysis results at small interferences (21% at $\omega/\omega_c = 7$) and overestimates these results at large interferences (about 30% at $\omega/\omega_c = 52$).

Since the model is general enough to accommodate material behavior other than elastic-perfectly plastic, various levels of linear isotropic strain hardening were also investigated. In the extreme case of a very large tangent modulus that is $0.1E$, the difference in the results, compared to the present elastic-perfectly plastic case, was less than 20%. In fact for $\omega/\omega_c \leqslant 20$ the maximum difference was less than 4.5%. For most practical materials the tangent modulus is less than $0.05E$ hence, the difference in the results is much smaller and the present case can be considered a general elastic plastic one.

It is interesting to compare some features of the present contact problem of a deformable sphere and a rigid flat with these of the half-space indented by a rigid sphere. The fully plastic regime in indentation starts at $A/A_c = 113.2$ according to Francis [25], and at $P/P_c \cong 360$ according to Johnson [24]. The corresponding finite element analysis results for fully plastic deformable sphere at $\omega/\omega_c = 110$ are $A/A_c = 205$ and $P/P_c = 534$. Clearly the two problems exhibit different behavior. The indented half-space yields more easily than the pressed sphere. This is probably due to the greater resistance to radial expansion that is imposed on the deflected material in the case of the indented half-space as compared to the case of the deformable sphere.

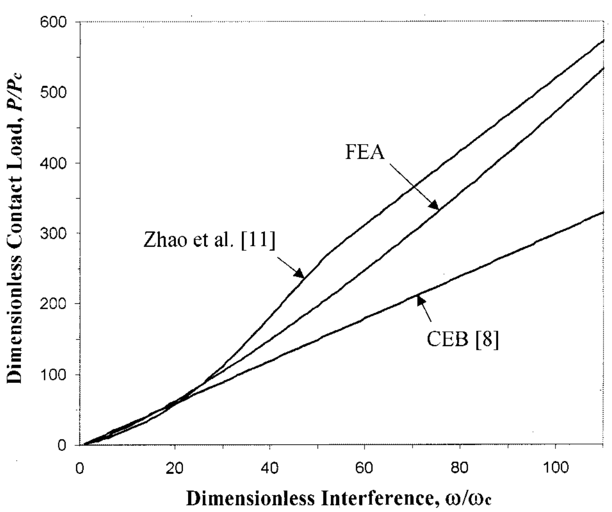

Fig. 9 Dimensionless contact load, P/P_c, as a function of the dimensionless interference, ω/ω_c, in the elastic-plastic regime

Conclusion

The elastic-plastic contact problem of a deformable sphere and a rigid flat was solved by the finite element method considering the actual constitutive laws for the relevant regime of deformation. Hence, the present model is much more accurate than previous ones that relied on unrealistic assumptions regarding the contact pressure distribution or evolution of the plastic region above the critical interference. By properly normalizing the contact load, contact area, and mean contact pressure, the present model provides simple analytical expressions that extend the classical Hertz solution up to a fully plastic contact.

It was found that the evolution of the elastic-plastic contact can be divided into three distinct stages. The first one for $1 \leqslant \omega/\omega_c$

$\leqslant 6$ where the plastic region develops below the sphere surface and the entire contact area is elastic. The second one for $6 \leqslant \omega/\omega_c \leqslant 68$ where the contact area is elastic-plastic, and the third stage for $\omega/\omega_c > 68$ corresponds to a fully plastic contact area.

The numerical results of the present finite element analysis were normalized in a way that allowed a general solution that is independent of specific material and radius of the sphere. Dimensionless expressions for the mean contact pressure, contact load and contact area were derived for a large range of interference values up to $\omega/\omega_c = 110$.

A change in the behavior of the mean contact pressure was observed at $\omega/\omega_c = 6$, which marks the elastic limit of the contact area. The interference $\omega/\omega_c = 110$ marks the inception of fully plastic regime where the mean contact pressure becomes equal to the material hardness.

A comparison of the present results with the results of previous elastic-plastic models as well as with these of indentation models showed substantial differences.

Acknowledgment

This research was supported in parts by the Fund for the Promotion of Research at the Technion and by the German-Israeli Project Cooperation (DIP).

Nomenclature

- a = radius of contact area
- A = contact area
- E = Hertz elastic modulus
- $E_{1,2}$ = Young's moduli
- H = hardness of the sphere
- K = hardness factor, $0.454 + 0.41\nu$
- P = contact load
- p = mean contact pressure, P/A
- R = radius of the sphere
- Y = yield strength of the sphere
- ν = Poisson's ratio of the sphere
- $\nu_{1,2}$ = Poisson's ratio
- ω = interference

Subscripts

- c = critical values
- e = elastic contact

References

[1] Vu-Quoc, L., Zhang, X., and Lesburg, L., 2000, "A Normal Force-Displacement Model for Contacting Spheres Accounting for Plastic Deformation: Force-Driven Formulation," ASME J. Appl. Mech., **67**, pp. 363–371.

[2] Liu, G., Wang, Q. J., and Lin, C., 1999, "A Survey of Current Models for Simulating the Contact between Rough Surfaces," Tribol. Trans., **42**, pp. 581–591.

[3] Bhushan, B., 1996, "Contact Mechanics of Rough Surfaces in Tribology: Single Asperity Contact," Appl. Mech. Rev., **49**, pp. 275–298.

[4] Bhushan, B., 1998, "Contact Mechanics of Rough Surfaces in Tribology: Multiple Asperity Contact," Tribol. Lett., **4**, pp. 1–35.

[5] Greenwood, J. A., and Williamson, J. B. P., 1966, "Contact of Nominally Flat Surfaces," Proc. R. Soc. London, Ser. A, **295**, pp. 300–319.

[6] Timoshenko, S. P., and Goodier, J. N., 1970, *Theory of Elasticity*, 3rd Ed., McGraw-Hill, New York.

[7] Abbott, E. J., and Firestone, F. A., 1933, "Specifying Surface Quality—A Method Based on Accurate Measurement and Comparison," Mech. Eng. (Am. Soc. Mech. Eng.), **55**, p. 569.

[8] Chang, W. R., Etsion, I., and Bogy, D. B., 1987, "An Elastic-Plastic Model for the Contact of Rough Surfaces," ASME J. Tribol., **109**, pp. 257–263.

[9] Evseev, D. G., Medvedev, B. M., and Grigoriyan, G. G., 1991, "Modification of the Elastic-Plastic Model for the Contact of Rough Surfaces," Wear, **150**, pp. 79–88.

[10] Chang, W. R., 1997, "An Elastic-Plastic Contact Model for a Rough Surface With an Ion-Plated Soft Metallic Coating," Wear, **212**, pp. 229–237.

[11] Zhao, Y., Maietta, D. M., and Chang, L., 2000, "An Asperity Microcontact Model Incorporating the Transition From Elastic Deformation to Fully Plastic Flow," ASME J. Tribol., **122**, pp. 86–93.

[12] Kucharski, S., Klimczak, T., Polijaniuk, A., and Kaczmarek, J., 1994, "Finite-Elements Model for the Contact of Rough Surfaces," Wear, **177**, pp. 1–13.

[13] Hardy, C., Baronet, C. N., and Tordion, G. V., 1971, "The Elasto-Plastic Indentation of a Half-Space by a Rigid Sphere," Int. J. Numer. Methods Eng., **3**, pp. 451–462.

[14] Kral, E. R., Komvopoulos, K., and Bogy, D. B., 1993, "Elastic-Plastic Finite Element Analysis of Repeated Indentation of a Half-Space by a Rigid Sphere," ASME J. Appl. Mech., **60**, pp. 829–841.

[15] Komvopoulos, K., and Ye, N., 2001, "Three-Dimensional Contact Analysis of Elastic-Plastic Layered Media with Fractal Surface Topographies," ASME J. Tribol., **123**, pp. 632–640.

[16] Giannakopoulos, A. E., 2000, "Strength Analysis of Spherical Indentation of Piezoelectric Materials," ASME J. Appl. Mech., **67**, pp. 409–416.

[17] Mesarovic, S. D., and Fleck, N. A., 2000, "Frictionless Indentation of Dissimilar Elastic-Plastic Spheres," Int. J. Solids Struct., **37**, pp. 7071–7091.

[18] Tabor, D., 1951, *The Hardness of Metals*, Clarendon Press, Oxford, UK.

[19] Chang, W. R., Etsion, I., and Bogy, D. B., 1988, "Static Friction Coefficient Model for Metallic Rough Surfaces," ASME J. Tribol., **110**, pp. 57–63.

[20] Reddy, J. N., 1993, *An Introduction to the Finite Element Method*, 2nd Ed., McGraw-Hill, New York.

[21] Owen, D. R. J., and Hinton, E., 1980, *Finite Elements in Plasticity: Theory and Practice*, Pineridge Press, Swansea, UK.

[22] Zhong, Z. H., 1993, *Finite Element Procedures for Contact Impact Problems*, Oxford University Press, New York.

[23] Liu, G., Zhu, J., Yu, L., and Wang, Q. J., 2001, "Elasto-Plastic Contact of Rough Surfaces," Tribol. Trans., **44**, pp. 437–443.

[24] Johnson, K. L., 1985, *Contact Mechanics*, Cambridge University Press, Cambridge, UK.

[25] Francis, H. A., 1976, "Phenomenological Analysis of Plastic Spherical Indentation," ASME J. Eng. Mater. Technol., **98**, pp. 272–281.

Dynamic Shear Fracture at Subsonic and Transonic Speeds in a Compressible Neo-Hookean Material Under Compressive Prestress

L. M. Brock
Department of Mechanical Engineering,
University of Kentucky,
Lexington, KY 40506
e-mail: brock@engr.uky.edu
Fellow ASME

A crack driven by shear forces translating on its surfaces grows in an isotropic compressible neo-Hookean material that is initially in uniform compression. The material replicates a linear isotropic solid at small deformations, and preserves as a limit case for all deformations the incompressibility that occurs in the linear case when Poisson's ratio becomes 1/2. A plane-strain steady state is assumed such that the crack and surface forces move at the same constant speed, whether subsonic, transonic, or supersonic. An exact analysis is performed based on superposition of infinitesimal deformations upon large, both for frictionless crack surface slip, and slip resisted by friction. The pre-stress induces anisotropy and increases the Rayleigh, rotational and dilatational wave speeds from their classical values. A positive finite fracture energy release rate arises for crack speeds below the Rayleight value and at two transonic speeds. In contrast, the transonic range in a purely linear analysis exhibits only one speed. It is found that friction enhances fracture energy release rate, and that compressive pre-stress enhances the rates for small crack speeds, but decreases it for speeds near the Rayleigh value. [DOI: 10.1115/1.1490374]

Introduction

Rapid crack growth in shear (mode II) is an important model for material failure. Because the fracture energy release rate becomes negative there, the Rayleigh wave speed often serves as the theoretical limit for subsonic planar nonbranching growth ([1]). It is known ([1–4]) however, that a positive energy release rate also occurs in the transonic (intersonic) range at the value $\sqrt{2}v_r$, where v_r is the rotational wave speed ([5]). Analyses of both the subsonic and transonic cases generally treat linear elastic isotropic or orthotropic ([6]) solids and assume that wave speeds and other material properties do not themselves change. However, large ambient compressive stresses could alter these values, and leave the material in an initial state of large elastic deformation.

This study, therefore, considers mode II shear crack growth in an unbounded highly elastic solid initially in a state of uniform compressive pre-stress. For purposes of illustration, a compressible neo-Hookean material that, at small deformations replicates a standard isotropic linear elastic solid ([7]), is treated. The material preserves as a limit case for all deformations the incompressibility that occurs in a linear solid when Poisson's ratio $\nu=1/2$. The crack is a semi-infinite slit driven by shear loads that translate on its surfaces. A plane-strain dynamic steady state is assumed, in which the crack and loads move at the same speed. The speed can be any constant value—subsonic, transonic, supersonic. The frictionless crack is treated in detail, and the case of crack surfaces subject to Coulomb sliding friction is obtained by simple quadrature of the frictionless results. The analysis is exact, and after ([8,9]) based on the superposition of infinitesimal deformations upon large.

Contributed by the Applied Mechanics Division of THE AMERICAN SOCIETY OF MECHANICAL ENGINEERS for publication in the ASME JOURNAL OF APPLIED MECHANICS. Manuscript received by the ASME Applied Mechanics Division, August 8, 2001; final revision, February 8, 2002. Associate Editor: A K. Mal. Discussion on the paper should be addressed to the Editor, Prof. Robert M. McMeeking, Department of Mechanical and Environmental Engineering University of California–Santa Barbara, Santa Barbara, CA 93106-5070, and will be accepted until four months after final publication of the paper itself in the ASME JOURNAL OF APPLIED MECHANICS.

Despite its linear elastic formulation, classical fracture mechanics ([1]) gives rise to displacement gradient singular behavior at the crack edge. Nevertheless, a finite energy release rate exists. Such analyses have been modified (e.g. [6]) by introducing vanishingly thin cohesive zones at the crack edges that serve to relax the singular behavior. The energy dissipation rate obtained is generally of the same order of magnitude as the classical energy release rates. This result and the decay of the singular gradients with distance from the crack edge ([1,10]) lend credibility to the use of classical fracture mechanics.

Therefore, although incorporation of the cohesive zone model poses no additional analytical difficulties, the superposed infinitesimal field is, as a first step, based on the classical fracture approach. This also allows some more direct comparisons with strictly linear results, e.g. ([1–4]). Moreover, the insights gained into the effects of pre-stress on wave speeds follow from the field equations, not the conditions imposed at the crack edge. The aforementioned spatial decay is seen in the static analysis of indentation by a rigid conical indentor ([9]): The effects of singular behavior in the superposed field die out rapidly away from the indentor apex.

The results developed in this article show that friction enhances the energy release rate, and that the compressive pre-stress noticeably affects that rate and solution behavior in general. As expected ([11]), pre-stress is manifest in the superposed deformations as a de facto anisotropy. Moreover, pre-stress causes the dilatational, rotational, and Rayleigh wave speeds in the crack plane to increase from their classical values ([5]).

For subsonic crack growth, pre-stress generally enhances energy release rate for low crack speeds and when $\nu\rightarrow 1/2$. In the transonic case, pre-stress generates two crack speeds that exhibit positive release rates. Both speeds vary with pre-stress, and exceed the single linear isotropic value ([2]). The higher of the two speeds is associated with release rates that exceed the linear isotropic value, while the rates for the lower speed fall below that value. Moreover, while the linear isotropic rate is actually unbounded when $\nu=0$, a finite rate exists for the lower speed induced by pre-stress. The analysis begins with discussion of the isotropic compressible neo-Hookean material.

Basic Equations

Consider an elastic body $\mathfrak{R}$ that is homogeneous and isotropic relative to an undisturbed reference configuration $\aleph_0$. A smooth motion $\mathbf{x}=\mathbf{x}(\mathbf{X})$ takes $\mathfrak{R}$ to a deformed equilibrium configuration $\aleph$. The Cauchy stress $\mathbf{T}$ in $\aleph$ is

$$\mathbf{T}=\alpha_0\mathbf{1}+\alpha_1\mathbf{B}+\alpha_2\mathbf{B}^2,\quad \mathbf{B}=\mathbf{F}\mathbf{F}^T,\quad \mathbf{F}=\frac{\partial\mathbf{x}}{\partial\mathbf{X}} \tag{1}$$

where $(\alpha_0,\alpha_1,\alpha_2)$ are scalar functions of the principal invariants (I, II, III) of $\mathbf{B}$, and body forces are neglected. Experimentally based inequalities ([12]) tend to support the restrictions

$$\alpha_0-II\alpha_2\leqslant 0,\quad \alpha_1+I\alpha_2>0,\quad \alpha_2\leqslant 0. \tag{2}$$

An adjacent nonequilibrium deformed configuration $\aleph^*$ is obtained by superposing a displacement $\mathbf{u}$ that is infinitesimal almost everywhere and depends on $\mathbf{x}$ and time. This requires an incremental Cauchy stress $\mathbf{T}'=\mathbf{T}^*-\mathbf{T}$, where $\mathbf{T}^*$ is the Cauchy stress in $\aleph^*$. To the first order in $\mathbf{H}=\partial\mathbf{u}/\partial\mathbf{x}$ its components in the principal reference system, i.e., $\mathbf{B}=\mathrm{diag}\{\lambda_1^2,\lambda_2^2,\lambda_3^2\}$ where λ_k are the principal stretches, are

$$T'_{ik}=\lambda'_{ij}H_{ij}\delta_{ik}+\mu'_{ik}H_{ik}+\mu'_{ki}H_{ki}, \tag{3a}$$

$$\lambda'_{ik}=\lambda_{ik}\lambda_k^2, \tag{3b}$$

$$\mu'_{ik}=\mu_{ik}\lambda_k^2 \tag{3c}$$

Here $(\lambda'_{ik},\mu'_{ik})$ are the generalized Lame' constants, i.e., they are independent of time and position, δ_{ik} is the Kronecker delta, $(i,k)=(1,2,3)$ and the summation convention does not apply, and

$$\frac{1}{2}\lambda_{ik}=\frac{\partial\alpha_0}{\partial\lambda_k^2}+\lambda_i^2\frac{\partial\alpha_1}{\partial\lambda_k^2}+\lambda_i^4\frac{\partial\alpha_2}{\partial\lambda_k^2},\quad \mu_{ik}=\mu_{ki}=\alpha_1+\alpha_2(\lambda_i^2+\lambda_k^2). \tag{4}$$

In $\aleph$ incremental traction conditions on a surface with outwardly directed normal $\mathbf{n}$ can be written in terms of the vector

$$\mathbf{t}^{(n)}=\mathbf{T}'\mathbf{n}+\mathbf{T}\mathbf{n}(\mathbf{n.Hn})-\mathbf{T}\mathbf{H}^T\mathbf{n} \tag{5}$$

Because $\aleph_0$ is a homogeneous configuration, the incremental balance of linear momentum reduces to ([8])

$$\mathrm{div}\,\mathbf{T}'=\rho\ddot{\mathbf{u}} \tag{6}$$

where ρ is the mass density, $(\cdot)$ denotes time differentiation, and a Cartesian basis is understood. Finally, in terms of the principal stretches,

$$I=\lambda_1^2+\lambda_2^2+\lambda_3^2,\quad II=\lambda_1^2\lambda_2^2+\lambda_3^2\lambda_1^2+\lambda_2^2\lambda_3^2,\quad III=\lambda_1^2\lambda_2^2\lambda_3^2. \tag{7}$$

A Hadamard material can, in view of (1), be characterized by

$$\alpha_0=2\sqrt{III}\frac{dG(III)}{dIII},\quad \alpha_1=\frac{1}{\sqrt{III}}(a_0-b_0I),\quad \alpha_2=\frac{b_0}{\sqrt{III}} \tag{8}$$

where (a_0,b_0) are material constants such that $a_0-b_0=\mu$, μ is the shear modulus, and $G(1)=0$. Setting $b_0=0$ produces the subclass of compressible isotropic neo-Hookean materials ([9]) and, as a generalization of a form used in ([13–15]), we consider

$$\frac{1}{\mu}G=m_0\left(\frac{1}{\sqrt{III}}-1\right)+m\left(\frac{1}{\sqrt{III}}-1\right)^2. \tag{9}$$

This reduces (8) to the two-parameter model

$$\alpha_0=\frac{\mu}{III}(2m-m_0)-\frac{2m\mu}{III^{3/2}},\quad \alpha_1=\frac{\mu}{\sqrt{III}},\quad \alpha_2=0. \tag{10}$$

The dimensionless constants (m_0,m) are determined as follows: Take $\mathfrak{R}$ in $\aleph_0$ to be a cylindrical bar of cross-sectional area A_0, and place it in a deformed equilibrium state $\aleph$ under uniaxial load P. If the bar axis is aligned with the X_1-direction, the Cauchy stresses are

$$T_{11}=\frac{P}{A},\quad T_{22}=T_{33}=0,\quad T_{ik}=0\quad (i\neq k) \tag{11}$$

where A is the cross-sectional area in $\aleph$, and uniform stress is assumed. Because $\mathbf{X}$ define the principal directions with stretches λ_1 and $\lambda_2=\lambda_3=\lambda_T$, $A=\lambda_r^2A_0$ for homogeneous deformations, and $\lambda_1=1+e_1$, where e_1 is the axial unit extension, Eq. (1), (7), (10), and (11) combine to give

$$\frac{1}{\mu}\frac{P}{A_0}=1+e_1-\frac{\lambda_T^2}{1+e_1},\quad \lambda_T^6+\left(\frac{2m-m_0}{1+e_1}\right)\lambda_T^2-\frac{2m}{(1+e_1)^2}=0. \tag{12}$$

These formulas relate a Piola-Kirchoff stress to unit extension, i.e., the result of the simple extension test ([16]). Replication of a homogeneous linear isotropic solid for small deformations requires that

$$\frac{P}{A_0}=0,\quad \frac{d}{de_1}\left(\frac{P}{A_0}\right)=2\mu(1+\nu)\quad (e_1=0,\lambda_T=1) \tag{13}$$

where ν is Poisson's ratio $(0<\nu<1/2)$. This is accomplished when

$$m_0=1,\quad 2m=\frac{1-4\nu}{2\nu-1}. \tag{14}$$

It can be shown that (2) is automatically satisfied when $1/3<\nu<1/2$, but the condition

$$\sqrt{III}>\frac{2m}{2m-1} \tag{15}$$

arises for $0<\nu<1/3$. This implies a critical compressive $(P<0)$ state, but it is noted that even such a state is highly elastic, e.g., $\sqrt{III}>1/2$ $(\nu=0)$.

Rapid Fracture: Superposed Infinitesimal Deformations

Now take $\mathfrak{R}$ in $\aleph_0$ to be an unbounded solid with a closed semi-infinite slit described in the fixed Cartesian basis by $X_2=0$, $X_1<0$. The smooth motion

$$x_1=\lambda_1X_1,\quad x_2=\lambda_2X_2,\quad x_3=X_3 \tag{16}$$

takes $\mathfrak{R}$ to the plane-strain equilibrium state $\aleph$ where

$$T_{11}=0,\quad T_{22}=\sigma,\quad \lambda_3=1. \tag{17}$$

Here $o<0$ is a specified uniform compressive stress. Now $\mathfrak{R}$ occupies an unbounded region with closed slit $x_2=0$, $x_1<0$ and (x_k,λ_k) are principal directions and stretches. For the compressible neo-Hookean model (1), (7), (10), (14), (16), and (17) combine to give the formulas

$$\lambda_2=\omega\lambda_1,\quad \omega=\frac{\sigma}{2\mu}+\sqrt{1+\left(\frac{\sigma}{2\mu}\right)^2},\quad \lambda_1\lambda_2=\sqrt{III} \tag{18a}$$

$$T_{33}=\mu\left(\frac{1}{\sqrt{\omega}}-\frac{1}{\omega}\right),\quad T_{ik}=0\quad (i\neq k) \tag{18b}$$

that complete the description of $\mathfrak{R}$ in $\aleph$. In $(18a)$

$$\sqrt{III}=(m\omega)^{1/3}\left[\left(1+\sqrt{1-\frac{\omega}{\omega_c}}\right)^{1/3}+\left(1-\sqrt{1-\frac{\omega}{\omega_c}}\right)^{1/3}\right] \tag{19a}$$

for $(1/4<\nu<1/3, 0<\omega<\omega_c)$ and $(1/3<\nu<1/2, 2m-1>0)$, while

$$\sqrt{III}=2\sqrt{\omega}\sqrt{\frac{1}{3}(1-2m)}\cos\frac{1}{3}\tan^{-1}\sqrt{\frac{\omega}{\omega_c}-1} \tag{19b}$$

governs for $(1/4<\nu<1/3, \omega>\omega_c)$ and

$$\sqrt{III}=2\sqrt{\omega}\sqrt{\frac{1}{3}(1-2m)}\cos\frac{1}{3}\left(\pi-\tan^{-1}\sqrt{\frac{\omega}{\omega_c}-1}\right) \tag{19c}$$

holds when $(0<\nu<1/4, \omega>\omega_c)$, where

$$\omega_c=m^2\left(\frac{3}{1-2m}\right)^3=2\left(\frac{3}{4}\right)^3\frac{(1-4\nu)^2(2\nu-1)}{(3\nu-1)^3}. \tag{20}$$

Equations (19) give for the typical values $\nu=(0,1/4,1/3,1/2)$, respectively,

$$\sqrt{III}=(\omega^{1/3},\sqrt{\omega},\omega^{1/3},1). \tag{21}$$

These results show that this neo-Hookean compressible model preserves as a limit case for all deformations the incompressibility that arises in a linear isotropic solid when $\nu=1/2$. It is noted that (18)–(21) are valid for $\sigma>0$ as well.

In view of (2)–(4) and (18), the generalized Lame' constants for any superposed infinitesimal deformation are

$$\lambda'_{1k}=\mu\left(\chi-\frac{1}{\omega}\right),\quad \lambda'_{2k}=\mu(\chi-\omega),\quad \lambda'_{3k}=\mu\left(\chi-\frac{1}{\sqrt{III}}\right) \tag{22a}$$

$$\mu'_{k1}=\frac{\mu}{\omega},\quad \mu'_{k2}=\mu\omega,\quad \mu'_{k3}=\frac{\mu}{\sqrt{III}},\quad \chi=2\left(\frac{1}{\omega}+\frac{m}{III^{3/2}}\right) \tag{22b}$$

where $k=(1,2,3)$. Some λ'_{ik} take on negative values unless a restriction on pre-stress is imposed, e.g.,

$$\sigma<0(\nu=0),\quad \sigma<\frac{\mu}{\sqrt{2}}\left(\nu=\frac{1}{4}\right),$$

$$\sigma<\frac{2\mu}{\sqrt{3}}\left(\nu=\frac{1}{3}\right),\quad \sigma<\infty\left(\nu=\frac{1}{2}\right). \tag{23}$$

The most severe restriction, for $\nu=0$, is of no consequence in this analysis. Setting $\omega=1$ $(\sigma=0)$ in (22) in view of $(18a)$ appropriately yields the isotropic result ([7])

$$\mu'_{ik}=\mu,\quad \lambda'_{ik}=\frac{2\mu\nu}{1-2\nu}\left(0<\nu<\frac{1}{2}\right). \tag{24}$$

The superposed infinitesimal deformation is triggered when shear forces $S>0$ (line loads in the x_3-direction) are applied to both slit surfaces. They translate in the positive x_1-direction at a constant speed v, and cause the slit to extend as a shear crack in that direction. A steady-state dynamic situation is achieved in which the crack speed is also v, and the forces S remain a fixed distance L from the edge. This is depicted schematically in Fig. 1, where it is noted that, for simplicity, the coordinates (x, y, z) replace (x_1, x_2, x_3), respectively, and translate with the crack edge. The superposed deformation is one of plane strain and antisymmetry. Therefore, only the half-space $y>0$ need be considered, subject to, in light of (5), the conditions

$$T'_{22}=0; \tag{25a}$$

$$T'_{21}=-S\delta(x+L)\quad (x<0), \tag{25b}$$

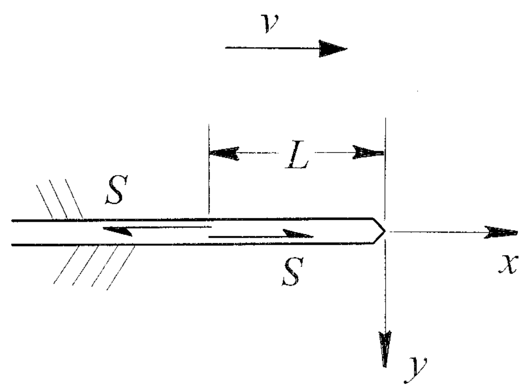

Fig. 1 Schematic of growing shear crack

$$u_1=0\quad (x>0) \tag{25c}$$

for $y=0$. Here $\delta(\ )$ is the Dirac function. In light of (2) and (22), the relevant stress-strain equations are

$$\frac{1}{\mu}T'_{11}=(\chi+\omega)u_{1,x}+(\chi-\omega)u_{2,y} \tag{26a}$$

$$\frac{1}{\mu}T'_{22}=\left(\chi-\frac{1}{\omega}\right)u_{1,x}+\left(\chi+\frac{1}{\omega}\right)u_{2,y} \tag{26b}$$

$$\frac{1}{\mu}T'_{21}=\frac{1}{\mu}T'_{12}=\omega u_{1,y}+\frac{1}{\omega}u_{2,x}. \tag{26c}$$

Here $(\ )_{,\alpha}$ signifies differentiation with respect to α. In the steady state the superposed displacements (u_1, u_2) depend on (x, y) only, and time derivatives in the inertial frame can be written as $-v(\ )_{,x}$. In view of (6) and (26), then, the field equations in $y>0$ are

$$\left(\chi+\frac{1}{\omega}-c^2\right)u_{1,xx}+\omega u_{1,yy}+\chi u_{2,xy}=0 \tag{27a}$$

$$\chi u_{1,xy}+\left(\frac{1}{\omega}-c^2\right)u_{2,xx}+\frac{1}{\omega}u_{2,yy}=0 \tag{27b}$$

where c is the dimensionless crack speed

$$c=\frac{v}{v_r},\quad v_r=\sqrt{\frac{\mu}{\rho}}. \tag{28}$$

Equations (26) and (27) exhibit the typical ([8,9]) anisotropy induced in $\Re$ by pre-stress. In addition, u_k should be bounded as $\sqrt{x^2+y^2}\to\infty$, and should be finite and continuous everywhere except perhaps at $y=0$, $x=-L$.

Solution to Related Problem

Consider now the related problem of an unbounded solid governed by (26)–(28), but with the slit replaced by an extending line of displacement discontinuities. Thus, two half-spaces $(y>0, y<0)$ are treated, subject to the unmixed matching conditions

$$[T'_{21}]=[T'_{22}]=0,\quad [u_1]=U(x),\quad [u_2]=V(x) \tag{29}$$

for $y=0$, where [ ] signifies a discontinuity as the x-axis is crossed from $y=0-$ to $y=0+$. The functions $(U,V)\equiv 0$ for $x>0$ and vanish continuously at $x=0$. The system (26)–(29) can be solved by use of the bilateral Laplace transform ([17]) and, by following the procedure of [13,15], the results

$$u_1=\frac{1}{\pi}\int_C \frac{U(t)dt}{c^2+e}\left[\frac{\omega a y}{(t-x)^2+a^2y^2}-\frac{K}{2}\frac{by}{(t-x)^2+b^2y^2}\right]$$
$$+\frac{1}{2\pi}\int_C \frac{V(t)dt}{c^2+e}\left[\frac{K_+}{a}\frac{t-x}{(t-x)^2+a^2y^2}\right.$$
$$\left.-b\left(\omega+\frac{1}{\omega}\right)\frac{t-x}{(t-x)^2+b^2y^2}\right] \quad (30a)$$
$$u_2=\frac{1}{\pi}\int_C \frac{U(t)dt}{c^2+e}\left[\frac{\omega a(t-x)}{(t-x)^2+a^2y^2}-\frac{K}{2b}\frac{t-x}{(t-x)^2+b^2y^2}\right]$$
$$+\frac{1}{\pi}\int_C \frac{V(t)dt}{c^2+e}\left[\left(\omega+\frac{1}{\omega}\right)\frac{by}{(t-x)^2+b^2y^2}-\frac{K_+ay}{(t-x)^2+a^2y^2}\right] \quad (30b)$$

are obtained for $y>0$ for subsonic values of c. In (30) the definitions

$$e=\frac{\sigma}{\mu}=\omega-\frac{1}{\omega},\quad K=\omega+\frac{1}{\omega}-c^2,\quad K_+=\frac{2}{\omega}-c^2 \quad (31a)$$
$$b=\frac{1}{\sqrt{\omega}}\sqrt{c_b^2-c^2},\quad a=\frac{1}{\sqrt{\chi+\omega}}\sqrt{c_a^2-c^2},\quad c_b=\frac{1}{\sqrt{\omega}},$$
$$c_a=\sqrt{\chi+\frac{1}{\omega}}>c_b \quad (31b)$$

hold, and C denotes integration over the real interval $(-\infty,0)$. The quantities (c_b,c_a) are, respectively, the rotational and dilatational wave speeds associated with the x-direction, nondimensionalized with respect to v_r. The dimensionless parameters (a, b) are real and positive, and indicate, therefore, that the subsonic case corresponds to $0<c<c_b$.

For the transonic and supersonic cases $c_b<c<c_a$ and $c>c_a$, respectively, b and (b, a) are imaginary. Therefore, the branch cuts $\mathrm{Im}(c)=0, |\mathrm{Re}(c)|>c_b$ and $\mathrm{Im}(c)=0, |\mathrm{Re}(c)|>c_a$ are introduced for (b,a), respectively, such that $\mathrm{Re}(b,a)\geqslant 0$ in the cut c-plane. Then, for the transonic case, (30) are replaced for $y>0$ by

$$u_1=\frac{1}{\pi}\int_C \frac{dt}{c^2+e}\left[U(t)\omega a y+\frac{K_+}{2a}V(t)(t-x)\right]\frac{1}{(t-x)^2+a^2y^2}$$
$$-\frac{1}{2(c^2+e)}\left[KU(x_\beta)+\beta\left(\omega+\frac{1}{\omega}\right)V(x_\beta)\right] \quad (32a)$$
$$u_2=\frac{1}{\pi}\int_C \frac{dt}{c^2+e}\left[\omega a U(t)(t-x)-\frac{K_+}{2}V(t)ay\right]\frac{1}{(t-x)^2+a^2y^2}$$
$$+\frac{1}{2(c^2+e)}\left[\frac{K}{\beta}U(x_\beta)-\left(\omega+\frac{1}{\omega}\right)V(x_\beta)\right] \quad (32b)$$

For the supersonic case, finally, the results

$$u_1=\frac{1}{c^2+e}\left[\omega U(x_\alpha)-\frac{K}{2}U(x_\beta)\right]$$
$$-\frac{1}{2(c^2+e)}\left[\frac{K_+}{\alpha}V(x_\alpha)+\beta V(x_\beta)\right] \quad (33a)$$
$$u_2=\frac{1}{c^2+e}\left[\omega\alpha U(x_\alpha)+\frac{K}{2\beta}U(x_\beta)\right]$$
$$+\frac{1}{2(c^2+e)}\left[\left(\omega+\frac{1}{\omega}\right)V(x_\beta)-K_+V(x_\alpha)\right] \quad (33b)$$

hold. In (32) and (33),

$$\beta=\frac{1}{\sqrt{\omega}}\sqrt{c^2-c_b^2},\quad \alpha=\frac{1}{\sqrt{\chi+\omega}}\sqrt{c^2-c_a^2} \quad (34a)$$
$$x_\beta=x+\beta y\in(-\infty,0),\quad x_\alpha=x+\alpha y\in(-\infty,0) \quad (34b)$$

and it is understood that nonintegral terms do not appear unless their arguments lie in the intervals specified by $(34b)$. These terms, therefore, represent signals with plane fronts that radiate from the displacement discontinuity region $y=0$, $x<0$.

Analogous expressions for $y<0$ can be obtained, and it is noted that when $V\equiv 0$, these counterparts and (30), (32), and (33) exhibit antisymmetry with respect to $y=0$, and satisfy $(25a,c)$. Thus, if U is interpreted as the slip (relative tangential displacement) of the crack faces, and chosen so that $(25b)$ is also satisfied, then (30)–(34) comprise the solutions for the superposed infinitesimal deformations in the crack problem. The subsonic case is considered first.

Subsonic Case

Application of $(26b)$ to (30) with $V\equiv 0$ and use of the standard ([18]) result

$$\frac{k}{(t-x)^2+k^2}\to\pi\delta(t-x)(k=0+) \quad (35)$$

give the formulas

$$\frac{1}{\mu}T'_{21}=\frac{R}{2b(c^2+e)}\frac{1}{\pi}\int_C \frac{dU}{dt}\frac{dt}{t-x}, \quad (36a)$$
$$R=2(\omega^2+1)ab-K_+K \quad (36b)$$

for $y=0$ in the subsonic $(0<c<c_h)$ case. The dimensionless quantity R is similar in form to a standard Rayleigh function ([5,13,14]) for the linear isotropic solid and reduces to that form when $\omega=1$ $(\sigma=0)$. It can be shown that R has the roots $c=\pm c_R$, where $0<c_R<c_b$, for any $0<\omega<1$ $(\sigma<0)$. That is, c_Rv_r is the Rayleigh wave speed associated with the x-axis. The quantity R also vanishes when $a=b$, i.e., $c^2+e=0$, but $(36a)$ remains finite because the term c^2+e also appears in its denominator. Indeed, it can be shown that $(30a,b)$ for $y>0$ exhibit no roots or singular behavior when $a=b$ due to the same cancellation effect.

For simplification, therefore, [14] is followed and the factorizations

$$R=\left(1+\frac{\omega}{\chi}\right)\omega(a-b)R', \quad (37a)$$
$$a-b=\frac{\chi(c^2+e)}{\omega(\chi+\omega)(a+b)} \quad (37b)$$

introduced, where the dimensionless quantity

$$R'=c^2(a+b)-\frac{2(\omega^2+1)\chi}{\omega(\chi+\omega)}b \quad (38)$$

has only the roots $c=\pm c_R$. It is, therefore, the effective Rayleigh function, and c_R can be obtained by rationalizing the equation $R'=0$ into a cubic in c^2 and then discarding the extraneous roots. An alternative approach ([19]) gives a formula that is analytic to within a simple quadrature:

$$c_R=\frac{1}{\omega G_0}\sqrt{\frac{2(\omega^2+1)\chi\sqrt{\omega}}{(\chi+\omega)(\sqrt{\omega}+\sqrt{\chi+\omega})}} \quad (39a)$$
$$\ln G_0=\frac{1}{\pi}\int_{c_b}^{c_a}\frac{dt}{t}\tan^{-1}\sqrt{1+\frac{\omega}{\chi}}\sqrt{\frac{t^2-c_b^2}{c_a^2-t^2}}$$
$$\times\left[\frac{2}{t^2}\left(\omega+\frac{1}{\omega}\right)\frac{\chi}{\chi+\omega}-1\right]. \quad (39b)$$

Use of $(36a)$ and (37) in $(25b)$ produces the singular integral equation

$$\frac{R'}{2b(a+b)}\frac{1}{\pi}(P)\int_C \frac{dU}{dt}\frac{dt}{t-x}=-\frac{S}{\mu}\delta(x+L)\quad(x<0). \tag{40}$$

Here (P) denotes Cauchy principal value integration. That (40) defines the gradient of U is of no consequence; the steady-state analysis gives displacements only to within an arbitrary rigid-body motion. Solutions to equations of the form (40) are well known ([20]), and, in particular, the procedure used in [21] gives

$$\frac{dU}{dx}=\frac{2b(a+b)}{\pi R'}\frac{S}{\mu}\frac{\sqrt{L}}{\sqrt{-x}(x+L)}\quad(x<0). \tag{41}$$

It can be shown that the integration of (41) appropriately vanishes as $x\to-\infty$. Substitution of (41) into (36a) and use of (37) and Cauchy residue theory ([21]) gives

$$T'_{21}=\frac{S}{\pi}\frac{\sqrt{L}}{\sqrt{x}(x+L)}\quad(x>0) \tag{42}$$

as the shear traction on the crack plane ahead of the crack. With (41) and (42) available, the fracture energy release rate (per unit of length in the z-direction) $\dot{E}_\omega$ can be, after [1], derived as

$$\frac{\mu}{v_r}\dot{E}_\omega=-\frac{2cb(a+b)}{\pi LR'}S^2. \tag{43}$$

It can be shown that $R'<0$ only for $0<c<c_R$; that is, a positive release rate arises only in this speed range. Thus, the Rayleigh speed $c_R v_r$ emerges, as in a linear isotropic solid ([1]), as a limit speed for subsonic nonbranching shear crack growth.

Transonic/Supersonic Cases

Use of (32), $(26b)$, and (35) reduces $(25b)$ to the equation

$$\frac{\omega^2+1}{c^2+e}\frac{a}{\pi}(P)\int_C\frac{dU}{dt}\frac{dt}{t-x}+\frac{K_+K}{2\beta(c^2+e)}\frac{dU}{dx}=-\frac{S}{\mu}\delta(x+L)\quad(x<0) \tag{44}$$

for the transonic range $c_b<c<c_a$. In this instance, two cases emerge: For $c_b<c<c_-$ or $c_+<c<c_a$, where

$$c_-=\sqrt{\omega+\frac{1}{\omega}},\quad c_+=\sqrt{\frac{2}{\omega}},$$
$$\sqrt{2}<c_-<c_+(\sigma<0),\quad c_\pm=\sqrt{2}(\sigma=0) \tag{45}$$

use of (37b) and the procedure in [21] give

$$\frac{dU}{dx}=-\frac{2\beta\omega}{D}\frac{S}{\mu}\left[K_+K\delta(x+L)+2(\omega^2+1)\frac{a\beta}{\pi}\left(\frac{-x}{L}\right)^{\upsilon}\frac{1}{x+L}\right]\quad(x<0) \tag{46a}$$

$$T'_{21}=\frac{2}{\pi}(\omega^2+1)a\beta\sqrt{\frac{\omega}{(c^2+e)D}}S\left(\frac{x}{L}\right)^{\upsilon}\frac{1}{x+L}\quad(x>0). \tag{46b}$$

The dimensionless eigenvalue υ and dimensionless positive quantity D are given by

$$\upsilon=\frac{1}{\pi}\tan^{-1}\frac{K_+K}{2(\omega^2+1)a\beta}-\frac{1}{2}\left(-\frac{1}{2}<\upsilon<0\right) \tag{47a}$$

$$D=1+\left[\frac{4\chi(\omega^2+1)^2}{\chi+\omega}-3-2\omega^2\right]\beta^2-\omega^2(2+3\omega^2)\beta^4-\omega^4\beta^6 \tag{47b}$$

For $c_-<c<c_+$, however, the signs of (46) are reversed, and

$$\upsilon=\frac{1}{2}+\frac{1}{\pi}\tan^{-1}\frac{K_+K}{2(\omega^2+1)a\beta}\left(0<\upsilon<\frac{1}{2}\right). \tag{48}$$

It is known ([2]) that standard singular (brittle) crack edge behavior—and therefore, a finite fracture energy release rate—in a linear isotropic solid occur for transonic crack growth only when $v=\sqrt{2}v_r$. The results (45)–(48) show that the compressive pre-stress produces two such speeds. When $v=c_-v_r$, $(46b)$ reduces to the subsonic form (42) and

$$\frac{dU}{dx}=-\frac{2\omega}{\omega^2+1}\sqrt{\frac{\chi+\omega}{\chi-\omega}}\frac{S}{\mu\pi}\frac{\sqrt{L}}{\sqrt{-x}(x+L)}\quad(x<0) \tag{49a}$$

$$\frac{\mu}{v_r}\dot{E}_\omega=\frac{2\sqrt{\omega}}{\pi\sqrt{\omega^2+1}}\sqrt{\frac{\chi+\omega}{\chi-\omega}}\frac{S^2}{L}>0. \tag{49b}$$

For $v=c_+v_r$, (42) again arises but now

$$\frac{dU}{dx}=-\frac{1}{\sqrt{\omega}}\sqrt{\frac{\chi+\omega}{\omega\chi-1}}\frac{S}{\mu\pi}\frac{\sqrt{L}}{\sqrt{-x}(x+L)}\quad(x<0) \tag{50a}$$

$$\frac{\mu}{v_r}\dot{E}_\omega=\frac{\sqrt{2}}{\pi\omega}\sqrt{\frac{\chi+\omega}{\omega\chi-1}}\frac{S^2}{L}>0. \tag{50b}$$

For the supersonic case $c>c_a$, (33) indicates that there will be no stress ahead of the crack, and no energy release rate. Thus, this case will not be considered further; a study of the case in a transient situation is given in [22].

Crack Surface Friction

When fracture occurs, frictional resistance can arise on the newly formed surfaces. To incorporate this effect, we assume that, while frictionless slip occurs generally, a finite region governed by Coulomb friction trails the crack edge. Because the superposed infinitesimal deformation is antisymmetric, only the compressive pre-stress $\sigma<0$ provides a normal force on the crack faces. The governing equations for the deformations remain unchanged upon introduction of the friction zone, except that $(25b)$ is replaced by

$$T'_{21}=-S\delta(x+L)-\gamma\sigma H(x+l)(x<0). \tag{51}$$

Here $H(\ )$ is the step function, $0<l<L$ and $\gamma(0<\gamma<1)$ is the dimensionless friction coefficient. When $x<0$, it is noted that the step function in (51) is, in fact, the integral of the Dirac function with respect to L over the interval $(0,l)$. This implies that the solutions for (51) can be obtained by adding to the frictionless results just presented a second set of expressions that follow from those results by replacing S with $\gamma\sigma$, and performing the aforementioned integration. Thus, for allowable $(0<c<c_R)$ subsonic crack growth, (41) and (42) for $y=0$ become

$$\frac{dU}{dx}=\frac{2b(a+b)}{\pi R'\mu}\left[\left(\frac{S\sqrt{L}}{x+L}-2\gamma\sigma\sqrt{l}\right)\frac{1}{\sqrt{-x}}+\gamma\sigma\ln\left|\frac{\sqrt{l}+\sqrt{-x}}{\sqrt{l}-\sqrt{-x}}\right|\right]\quad(x<0) \tag{52a}$$

$$T'_{21}=\frac{1}{\pi}\left[\left(\frac{S\sqrt{L}}{x+L}-2\gamma\sigma\sqrt{l}\right)\frac{1}{\sqrt{x}}+2\gamma\sigma\tan^{-1}\sqrt{\frac{l}{x}}\right]\quad(x>0) \tag{52b}$$

and (43) is replaced with

$$\frac{\mu}{v_r}\dot{E}_\omega=-\frac{2cb(a+b)}{\pi R'}\left(\frac{S}{\sqrt{L}}-2\gamma\sigma\sqrt{l}\right)^2. \tag{53}$$

Because $(S,\sigma)<0$, (52) and (53) show that friction enhances crack edge fields and the energy release rate. Although the $\gamma\sigma$-terms do not decay as strongly as the S-terms, the integral of $(52a)$ still vanishes as $x\to-\infty$. Analogous results hold for the two transonic cases $(c=c_\pm)$; in particular,

$$\frac{\mu}{v_r}\dot{E}_\omega = \frac{2\sqrt{\omega}}{\pi\sqrt{\omega^2+1}}\sqrt{\frac{\chi+\omega}{\chi-\omega}}\left(\frac{S}{\sqrt{L}} - 2\gamma\sigma\sqrt{l}\right)^2 (c=c_-) \tag{54a}$$

$$\frac{\mu}{v_r}\dot{E}_\omega = \frac{\sqrt{2}}{\pi\omega}\sqrt{\frac{\chi+\omega}{\omega\chi-1}}\left(\frac{S}{\sqrt{L}} - 2\gamma\sigma\sqrt{l}\right)^2 (c=c_+). \tag{54b}$$

Full Fields

Differentiation of (30) and (32), substitution of (52) and its transonic counterpart, and use of Cauchy residue theory in the manner of [13,15,21] gives for $y>0, 0<c<c_R$

$$u_{1,x} = \frac{2b(a+b)}{(c^2+e)R'}\frac{\sqrt{2}S}{\mu\pi}\left[\omega\frac{S_a(x+L)+C_a ay}{(x+L)^2+a^2y^2} - \frac{K}{2}\frac{S_b(x+L)+C_b by}{(x+L)^2+b^2y^2}\right] - \frac{2b(a+b)}{(c^2+e)R'}\frac{\sqrt{2}\gamma\sigma}{\mu\pi}\left[\omega(S_a\xi_a + C_a\phi_a) - \frac{K}{2}(S_b\xi_b + C_b\phi_b)\right] \tag{55a}$$

$$u_{2,x} = \frac{2b(a+b)}{(c^2+e)R'}\frac{\sqrt{2}S}{\mu\pi}\left[a\omega\frac{S_a ay - C_a(x+L)}{(x+L)^2+a^2y^2} + \frac{K}{2b}\frac{C_b(x+L)-S_b by}{(x+L)^2+b^2y^2}\right] - \frac{2b(a+b)}{(c^2+e)R'}\frac{\sqrt{2}\gamma\sigma}{\mu\pi} \times\left[a\omega(S_a\phi_a - C_a\xi_a) + \frac{K}{2b}(C_b\xi_b - S_b\phi_b)\right]. \tag{55b}$$

Here the definitions (31) and

$$(C_q, S_q) = \frac{\sqrt{\sqrt{x^2+q^2y^2}\pm x}}{\sqrt{x^2+q^2y^2}} \tag{56a}$$

$$\xi_q = \ln\sqrt{\frac{(x+l)^2+q^2y^2}{x^2+q^2y^2}}, \quad \phi_q = \tan^{-1}\frac{x+l}{qy} - \tan^{-1}\frac{x}{qy} \tag{56b}$$

hold, where $q=(a,b)$. For the transonic case $c=c_-$ the results for $y>0$ are

$$u_{1,x} = \frac{\omega}{\omega^2+1}\frac{\sqrt{2}}{\mu\pi a}\left[\gamma\sigma(S_a\xi_a + C_a\phi_a) - S\frac{S_a(x+L)+C_a ay}{(x+L)^2+a^2y^2}\right] \tag{57a}$$

$$u_{2,x} = \frac{\omega}{\omega^2+1}\frac{\sqrt{2}}{\mu\pi a}\left[S\frac{C_a(x+L)-S_a ay}{(x+L)^2+a^2y^2} + \gamma\sigma(S_a\phi_a - C_a\xi_a)\right] \tag{57b}$$

$$a = \sqrt{\frac{\chi-\omega}{\chi+\omega}}. \tag{57c}$$

For the transonic case $c=c_+$ the results for $y>0$ are

$$u_{1,x} = \frac{\omega}{\omega^2+1}\frac{\sqrt{2}}{\mu\pi a}\left[\gamma\sigma(S_a\xi_a + C_a\phi_a) - S\frac{S_a(x+L)+C_a ay}{(x+L)^2+a^2y^2}\right] + \frac{e}{2(\omega^2+1)}\frac{1}{\mu\pi a}\left[\left(\frac{S\sqrt{L}}{x_\beta+L} - \gamma\sigma\sqrt{l}\right)\frac{1}{\sqrt{-x_\beta}} + \gamma\sigma\ln\left|\frac{\sqrt{l}+\sqrt{-x_\beta}}{\sqrt{l}-\sqrt{-x_\beta}}\right|\right] \tag{58a}$$

$$u_{2,x} = \frac{\omega}{\omega^2+1}\frac{\sqrt{2}}{\mu\pi a}\left[\gamma\sigma(S_a\phi_a - C_a\xi_a) + S\frac{C_a(x+L)-S_a ay}{(x+L)^2+a^2y^2}\right] - \frac{e}{2(\omega^2+1)}\frac{1}{\mu\pi a}\left[\left(\frac{S\sqrt{L}}{x_\beta+y} - \gamma\sigma\sqrt{l}\right)\frac{1}{\sqrt{-x_\beta}} + \gamma\sigma\ln\left|\frac{\sqrt{l}-\sqrt{-x_\beta}}{\sqrt{l}+\sqrt{-x_\beta}}\right|\right] \tag{58b}$$

$$a = \sqrt{\frac{\omega\chi-1}{\omega(\chi+\omega)}}, \quad \beta = \frac{1}{\omega}, \quad x_\beta = x+\beta y \in (-\infty, 0). \tag{58c}$$

It is understood that the terms in (58a,b) with coefficient e appear only when the argument x_β lies in the range specified by (58c). In view of the general form (32) and discussions of the linear isotropic case ([1,2]), such behavior might be expected. However, such terms do not appear in (57), nor do they arise when (57) and (58) coalesce to the linear isotropic case ($c=\sqrt{2}$) in the limit $\omega=1(\sigma=0)$. That is, only in the transonic case $c=c_+$ under pre-stress does a signal with a plane front actually radiate from the growing crack.

Pre-stress Effects: Some Calculations

The prominence of the dimensionless stretch ratio ω in the expressions for the superposed infinitesimal deformations by itself suggests the influence of the compressive pre-stress on shear crack growth. To lend some quantitative aspect to this observation, nondimensionalized rotational (c_b) and dilatational (c_a) speeds defined in (31b) are given in Table 1 for various values of $e=\sigma/\mu\leqslant 0$ and Poisson's ratio $\nu=(0,1/4,1/3,1/2)$. In Table 2, values of the nondimensionalized Rayleigh speed (c_R) defined in (39) are given. As already noted, the compressible neo-Hookean model preserves as a limit case the small-strain incompressibility that occurs when $\nu=1/2$, so c_a is unbounded at this value. Both

Table 1 Dimensionless wave speeds for different pre-stress levels

σ/μ	c_b	c_a ($\nu=0$)	c_a ($\nu=1/4$)	c_a ($\nu=1/3$)	c_a ($\nu=1/2$)
−1.0	1.2721	1.799	2.2033	2.5442	∞
−0.5	1.1317	1.6005	1.9602	2.2634	”
−0.3	1.0776	1.5239	1.8664	2.1552	”
−0.1	1.0253	1.45	1.7759	2.0506	”
−0.05	1.0126	1.432	1.7538	2.0252	”
0	1.0	1.4142	1.6818	2.0	”

Table 2 Dimensionless Rayleigh speeds for different pre-stress levels

σ/μ	c_R ($\nu=0$)	c_R ($\nu=1/4$)	c_R ($\nu=1/3$)	c_R ($\nu=1/2$)
−1.0	1.1623	1.1901	1.1984	1.2124
−0.5	1.0114	1.0481	1.0588	1.0773
−0.3	0.9543	0.9947	1.0063	1.0266
−0.1	0.9001	0.9373	0.9568	0.9785
−0.05	0.887	0.9315	0.9444	0.9668
0	0.874	0.9194	0.9325	0.9553

tables show that all three speeds increase with both compressive pre-stress level and Poisson's ratio. The Rayleigh speed increases imply that subsonic planar nonbranching crack growth can occur at higher rates under compressive pre-stress.

While the effects are small in Tables 1 and 2 for pre-stress levels that would be considered critical ([7]) in a linear elastic body, *e.g.*, c_R for $\nu=0$ increases from 0.874 to 0.887 at 5% of the shear modulus, they are, nonetheless, clear-cut.

For insight into fracture mechanics, we examine the dimensionless ratio

$$r=\frac{\dot{E}_\omega}{\dot{E}_1} \tag{59}$$

of the release rate when pre-stress is present to the rate when it is absent $(\omega=1)$. For allowable $(0<c<c_R)$ subsonic crack growth, (53) governs and, as already noted, friction enhances this rate. To focus on pre-stress, we set $\gamma=0$ so that r now depends only on (ω,c), *i.e.*, (σ,ν). Tables 3(a–d) give r for Poisson's ratio $\nu=(0,1/4,1/3,1/2)$ for values of c at different compressive pre-stress levels. The c-values are sub-Rayleigh for all the pre-stresses. At low subsonic crack speeds, the release rate is generally greater $(r>1)$ when compressive pre-stress is accounted for. For speeds near the Rayleigh levels (Table 1), however, pre-stress actually decreases $(r<1)$ the release rate.

Table 3 (*a*) Ratio of energy release rates with no friction and $\sigma/\mu=-1.0$

c	$r(\nu=0)$	$r(\nu=1/4)$	$r(\nu=1/3)$	$r(\nu=1/2)$
0.05	1.2608	0.9726	1.0226	1.1707
0.1	1.2587	0.9711	1.0215	1.17
0.3	1.2339	0.9548	1.008	1.1615
0.5	1.173	0.9121	0.9724	1.1383
0.7	1.63	0.7927	0.8749	1.0699
0.9	0.4551	0.2036	0.354	0.6731

Table 3 (*b*) Ratio of energy release rates with no friction and $\sigma/\mu=-0.5$

c	$r(\nu=0)$	$r(\nu=1/4)$	$r(\nu=1/3)$	$r(\nu=1/2)$
0.05	1.1612	0.9926	1.0213	1.1063
0.1	1.1594	0.9918	1.0206	1.106
0.3	1.1373	0.9823	1.0131	1.1021
0.5	1.0833	0.9558	0.9923	1.0905
0.7	0.9573	0.875	0.927	1.0504
0.9	0.4398	0.2658	0.4323	0.7259

Table 3 (*c*) Ratio of energy release rates with no friction and $\sigma/\mu=-0.1$

c	$r(\nu=0)$	$r(\nu=1/4)$	$r(\nu=1/3)$	$r(\nu=1/2)$
0.05	1.036	0.9997	1.0058	1.0244
0.1	1.0342	0.9994	1.0057	1.0243
0.3	1.0129	0.9974	1.0041	1.0237
0.5	0.9618	0.9911	0.9994	1.0215
0.7	0.8488	0.9683	0.9821	1.0123
0.9	0.4183	0.534	0.7011	0.8789

Table 3 (*d*) Ratio of energy release rates with no friction and $\sigma/\mu=-0.05$

c	$r(\nu=0)$	$r(\nu=1/4)$	$r(\nu=1/3)$	$r(\nu=1/2)$
0.05	1.0178	0.9999	1.003	1.0123
0.1	1.016	0.9998	1.003	1.0123
0.3	0.9948	0.9988	1.0022	1.012
0.5	0.9437	0.9956	0.9998	1.0109
0.7	0.8319	0.9836	0.9907	1.0061
0.9	0.4176	0.6792	0.8118	0.929

Table 4 (*a*) Ratio of energy release rates when $c=c_->\sqrt{2}$

σ/μ	c_-	$r(\nu=1/4)$	$r(\nu=1/3)$	$r(\nu=1/2)$
−1.0	1.4954	0.6625	0.7601	0.9457
−0.5	1.4358	0.7791	0.8559	0.985
−0.3	1.4221	0.8475	0.9051	0.9945
−0.1	1.4151	0.7395	0.9647	0.9993
−0.05	1.4144	0.9683	0.9818	0.9998

Table 4 (*b*) Ratio of energy release rates when $c=c_+>\sqrt{2}$

σ/μ	c_+	$r(\nu=1/4)$	$r(\nu=1/3)$	$r(\nu=1/2)$
−1.0	1.799	1.8341	1.8927	2.0583
−0.5	1.6006	1.3518	1.3769	1.4494
−0.3	1.5239	1.1901	1.2102	1.2512
−0.1	1.45	1.0607	1.065	1.0779
−0.05	1.432	1.0247	1.0319	1.0382

In the transonic cases, (54) governs, and (62) with $\gamma=0$ must now be interpreted as a ratio of rates at different crack speeds. Insight is still possible: Tables 4(a,b) give r for $\nu=(1/4,1/3,1/2)$ for (54) and the limit case $(\omega=1,c=\sqrt{2})$ and various compressive pre-stresses. The release rates for the lower crack speed $(c=c_-)$ are seen to be less than the limit case rates. The higher $(c=c_+)$ speed release rates, however, exceed them. In both tables, the pre-stress effect generally increases with ν.

The case $\nu=0$ is somewhat different: In view of (18)–(20) and (22), (54) blows up when $\omega=1$, $\nu=0$. That is, the single transonic crack speed in linear isotropic solid ([1]) is associated with an unbounded energy release rate. For $0<\omega<1(\sigma<0)$, $(54b)$ gives the same result, i.e., the higher transonic crack speed $(c=c_+)$ has an unbounded release rate when $\nu=0$. However, when $\nu=0$ in $(54a)$,

$$\frac{\mu}{\nu_r}\dot{E}_\omega=2\sqrt{-\frac{\mu}{\sigma}\omega}\left(\frac{S}{\sqrt{L}}-2\gamma\sigma\sqrt{l}\right)^2(c=c_-). \tag{60}$$

In this case, the compressive pre-stress allows a finite energy release rate.

Some Observations

This article considered dynamic fracture under shear of an unbounded isotropic compressible neo-Hookean material initially subjected to a uniform compressive pre-stress. The material replicated linear isotropic response at small deformations, but preserved as a limit case for all deformations the incompressibility that arises in the linear case when Poisson's ratio $\nu=1/2$. The crack was semi-infinite, and fracture-driven by shear forces moving at a constant speed on both surfaces. A dynamic steady-state and plane strain were assumed, so that the crack edge moved at the same speed, with the forces at a fixed distance from the edge.

The problem was treated as the superposition of (essentially) infinitesimal deformations triggered by fracture upon the finite deformations due to the compressive pre-stress. Exact analytical solutions were obtained for both fields. The infinitesimal results displayed the expected anisotropy induced by pre-stress, and were valid for any constant crack/load speed—subsonic, transonic, supersonic. These speed ranges varied with pre-stress: the rotational and dilatational speeds, as well as the Rayleigh speed, increased from their classical values. A smooth crack surface was treated in detail, and the corresponding results for a finite zone of Coulomb sliding friction at the crack edge were obtained by simple quadrature. These two cases showed that friction enhances the fracture energy release rate.

For subsonic crack growth, the Rayleigh speed served, as in the linear isotropic case, as a limiting speed for planar nonbranching shear crack growth. To examine the effects of pre-stress, friction was neglected, and ratios of energy release rates with and in the absence of pre-stress calculated for a given crack speed at various values of Poisson's ratio. Pre-stress was found, in general, to enhance release rates at low crack speeds, but to decrease it at near-critical (Rayleigh) values. The results indicated that a finite energy release rate does not, in general, arise for supersonic crack speeds.

In a linear isotropic body, an energy release rate exists only at one transonic crack speed. The results presented here showed that two such speeds exist under pre-stress: both speeds exceed the isotropic value, vary with pre-stress, and take on that value when pre-stress vanishes. It was also found that only the higher allowable transonic speed under pre-stress do signals with plane fronts actually radiate from the growing crack.

The energy release rates at the two transonic speeds possible under pre-stress were compared with those for the single linear isotropic limit case. For Poisson's ratio (1/4, 1/3, 1/2) the rates for the larger transonic speed under pre-stress exceeded the isotropic values, while the lower possible speed rates lay below them. When Poisson's ratio vanishes, the linear isotropic limit case gave, in fact, an unbounded energy release rate, and the same result occurs at the higher transonic crack speed possible with pre-stress. However, the lower possible transonic speed gave finite values that became unbounded only in the limit when pre-stress vanished.

In summary, then, these results suggest that dynamic shear crack growth can be noticeably affected by a compressive pre-stress when the material is highly elastic. The existence of two possible transonic crack speeds under pre-stress suggests a bifurcation. That said, the lower-speed result is more similar to the linear isotropic limit case in some respects, and allows a finite energy release rate when Poisson's ratio vanishes. However, the present results are a first step that allows a direct comparison with dynamic fracture results based on classical fracture mechanics ([1]). The present analysis, indeed, serves as the basis for a cohesive zone model ([6]), that allows, of course, the superposed deformations to be infinitesimal everywhere. Moreover, results of the use of nonlinear stress strain laws in such zones ([23,24]) are being included.

References

[1] Freund, L. B., 1993, *Dynamic Fracture Mechanics*, Cambridge University Press, New York.

[2] Freund, L. B., 1979, "The Mechanics of Shear Crack Propagation," J. Geophys. Res., **84**, pp. 2199–2209.

[3] Rosakis, A. J., 2001, "Intersonic Shear Crack Growth Along Weak Paths," *2001 Mechanics and Materials Conference*, UCSD, San Diego, CA.

[4] Huang, Y., and Gao, H., 2001, "Intersonic Crack Propagation," *2001 Mechanics and Materials Conference*, UCSD, San Diego, CA.

[5] Achenbach, J. D., 1973, *Wave Propagation in Elastic Solids*, North-Holland, Amsterdam.

[6] Broberg, K. B., 1999, "Intersonic Crack Propagation in an Orthotropic Material," Int. J. Fract., **99**, pp. 1–11.

[7] Sokolnikoff, I. S., 1956, *Mathematical Theory of Elasticity*, McGraw-Hill, New York.

[8] Green, A. E., and Zerna, W., 1968, *Theoretical Elasticity*, 2nd Ed., Oxford University at the Clarendon Press, London.

[9] Beatty, M. F., and Usmani, S. A., 1975, "On the Indentation of a Highly Elastic Half-Space," Q. J. Mech. Appl. Math., **28**, pp. 47–62.

[10] Ewalds, H. L., and Wanhill, R. J. H, 1985, *Fracture Mechanics*, Edward Arnold, London.

[11] Pao, Y.-H., 1987, "Theory of Acoustoelasticity and Acoustoplasticity," *Solid Mechanics Research for Quantitative Non-Destructive Evaluation*, J. D. Achenbach and Y. Rajapakse, eds., Martinus Nijhoff, Dordrecht.

[12] Truesdell, C., and Noll, W., 1965, "The Non-linear Field Theories of Mechanics," *Handbuch der Physik*, Vol. III/3a, W. Flugge, ed., Springer-Verlag, Berlin.

[13] Brock, L. M., 2001, "Rapid Sliding Contact on a Highly Elastic Pre-stressed Material," Int. J. Non-Linear Mech., **36**, pp. 433–442.

[14] Brock, L. M., 2001, "Transient Green's Function Behavior for a Pre-stressed Elastic Half-Space," ASME J. Appl. Mech., **68**, pp. 162–168.

[15] Brock, L. M., 2001, "Rapid Indentation of a Pre-Stressed Hyper-elastic Half-Space," Int. J. Solids Struct., **38**, pp. 5527–5534.

[16] Hibbeler, R. C., 1997, *Mechanics of Materials*, 3rd Ed., Prentice-Hall, Englewood Cliffs, NJ.

[17] van der Pol, B., and Bremmer, H., 1950, *Operational Calculus Based on the Two-Sided Laplace Integral*, Cambridge University Press, Cambridge, UK.

[18] Carrier, G. F., and Pearson, C. E., 1988, *Partial Differential Equations*, 2nd Ed Academic Press, San Diego, CA.

[19] Brock, L. M., 1998, "Analytical Results for Roots of Two Irrational Functions in Elastic Wave Propagation," J. Aust. Math. Soc. B, Appl. Math., **B40**, pp. 72–79.

[20] Erdogan, F., 1976, "Mixed Boundary Value Problems in Mechanics," *Mechanics Today*, Vol. 4, S. Nemat-Nasser, ed., Pergamon Press, New York.

[21] Brock, L. M., 1999, "Rapid Sliding Indentation With Friction of a Pre-stressed Thermoelastic Material," J. Elast., **53**, pp. 161–188.

[22] Brock, L. M., 1977, "Two Basic Problems of Plane Crack Extension: A Unified Treatment," Int. J. Eng. Sci., **15**, pp. 527–536.

[23] Brock, L. M., 1995, "Wave Diffraction Induced Crack/Cohesive Strip Growth Based on Rudimentary Non-linear Models," J. Elast., **38**, pp. 41–67.

[24] Brock, L. M., and Georgiadis, H. G., 1995, "Rudimentary Non-linear Effects Near Crack Edges in Dynamic Crack Propagation," Indian J. Pure Appl. Math., **26**, pp. 705–724.

On an Elastic Circular Inhomogeneity With Imperfect Interface in Antiplane Shear

P. Schiavone
Department of Mechanical Engineering,
University of Alberta,
Edmonton, AB T6G 2G8
Canada

We develop a rigorous solution to the antiplane problem of a circular inhomogeneity embedded within an infinite isotropic elastic medium (matrix) under the assumption of nonuniform remote loading. The bonding at the inhomogeneity/matrix interface is assumed to be homogeneously imperfect. We examine both the case of a single circular inhomogeneity and the more general case of a three-phase circular inhomogeneity. General expressions for the corresponding complex potentials are derived explicitly in both the inhomogeneity and in the surrounding matrix. The analysis is based on complex variable methods. The solutions obtained demonstrate the effect of the prescribed nonuniform remote loading on the stress field within the inhomogeneity. Specific solutions are derived in closed form which are verified by comparison with existing solutions.
[DOI: 10.1115/1.1488936]

1 Introduction

Problems involving elastic inhomogeneities with imperfect bonding at the inhomogeneity/matrix interface (imperfect interface) are receiving an increasing amount of attention in the literature (see, for example, Ru and Schiavone [1] for an extensive literature review). Interest in these problems is motivated mainly by a desire to study interface damage in composites (for example, debonding, sliding, and/or cracking across an interface) and its subsequent effect on the effective properties of composites.

One of the more widely used models of an imperfect interface (often referred to as the homogeneously imperfect interface) is based on the assumption that tractions are continuous but displacements are discontinuous across the interface. More precisely, jumps in the displacement components are assumed to be proportional (in terms of ''spring-factor-type'' interface parameters) to their respective interface traction components. Under these assumptions, Hashin [2] has examined the case of a spherical inhomogeneity imperfectly bonded to a three-dimensional matrix. The analogous problem for plane deformations has been investigated by Gao [3]. In both these cases, the remote loading is assumed to be uniform. This assumption allows the authors to draw direct comparisons between their results and the classical results derived for analogous problems under the perfect bonding assumption (see, for example, Eshelby [4,5] and Ru and Schiavone [6]).

In this paper we derive rigorous solutions of the problem associated with a circular elastic inhomogeneity embedded within an infinite matrix in antiplane shear when the interface is homogeneously imperfect, under the more general assumption of nonuniform remote loading. Specifically, we consider the case in which the remote loading is an arbitrary-order polynomial in the complex variable describing the matrix. The solution of this problem is extremely important in that, essentially, it leads to the solution of the case where the remote loading is characterized by any continuous, yet otherwise arbitrary function of the complex variable in the matrix. This statement is based on the well-known result from the theory of functions (Weierstrass) which states that any continuous function in a bounded domain can be uniformly approximated by a polynomial. This result applies here since, in practice, the matrix is a bounded domain with the remote loading corresponding to the exterior (to the inhomogeneity) field some ''relatively large'' distance from the inhomogeneity. Consequently, the remote loading is always prescribed in a bounded domain even though, mathematically, this is usually modeled as an inhomogeneity/infinite matrix system with remote loading prescribed ''at infinity.'' Hence, the results in this paper will allow for the approximate calculation of stress fields corresponding to a prescribed non-uniform remote loading characterized by any continuous, yet otherwise arbitrary, function in the presence of an *imperfect* inhomogeneity-matrix interface.

Applications of the results in this paper are numerous. For example, the single inhomogeneity/matrix model with imperfect interface can be used to predict the mechanical properties of fibre-reinforced composites (see, for example, Hashin [2], Jun and Jusiuk [7], and Gao [3]). The three-phase elastic inhomogeneity model is also of great interest in composite mechanics. For example, it arises directly from the study of the interphase layer between the inhomogeneity and its surrounding matrix and it offers the fundamental solution for the generalized self-consistent method (see, for example, Christensen and Lo [8], Luo and Weng [9], Hashin [10], and Jun and Jusiuk [7]). In addition, in the nuclear industry, various fuels and claddings have oxide coatings (Zirconium oxide on Zirconia) and often the oxide coatings can be subjected to cracking from residual or imposed stresses. Similarily, the design of fuel cells may involve the use of Yttria-Sirconium-oxide layers. In each case, the model of an inhomogeneity surrounded by an imperfect interface or interphase layer (the three-phase inhomogeneity problem) is an appropriate starting point in the corresponding mechanical analysis. An example of current interest in electrical engineering is that related to passivated interconnects in large scale integrated circuits (see Okabayashi [11]). Here, the major cause of voiding and failure has been attributed to the residual stresses induced within the interconnect by thermal mismatch between the line and the surrounding passivation and substrate. In this case, an inhomogeneity-matrix model can be used to model the interconnects (see, for example, Niwa et al. [12]).

The formulation of the basic boundary value problem describing the antiplane deformation of an elastic inhomogeneity with homogeneously imperfect interface is presented in Section 2. The case of a single circular inhomogeneity is discussed in Section 3. Here, we find closed-form solutions which demonstrate the effect of the nonuniform remote loading on the stress field within the

Contributed by the Applied Mechanics Division of THE AMERICAN SOCIETY OF MECHANICAL ENGINEERS for publication in the ASME JOURNAL OF APPLIED MECHANICS. Manuscript received by the Applied Mechanics Division, June 20, 2001; final revision, November 19, 2001. Associate Editor: H. Gao. Discussion on the paper should be addressed to the Editor, Prof. Robert M. McMeeking, Chair, Department of Mechanics and Environmental Engineering, University of California–Santa Barbara, Santa Barbara, CA 93106-5070, and will be accepted until four months after final publication in the paper itself in the ASME JOURNAL OF APPLIED MECHANICS.

inhomogeneity. In the special case when the remote loading is assumed to be uniform, we reproduce the result first presented in Ru and Schiavone [1], which reports a uniform stress field inside the inhomogeneity, despite the presence of the imperfect interface. In Section 4, we derive closed-form solutions for the analogous, but more general, case involving a three-phase circular inhomogeneity. These simple results are significant in that they establish, *in the presence of a homogeneously imperfect interface*, direct relationships between the stress field inside the inhomogeneity and the prescribed nonuniform remote loading.

2 Formulation

Consider a domain in $\mathbb{R}^2$, infinite in extent, containing a single internal elastic inhomogeneity, with elastic properties different from the surrounding matrix. The linearly elastic materials occupying the matrix and the inhomogeneity are assumed to be homogeneous and isotropic with associated shear moduli μ_1 and μ_2, respectively. At infinity, the prescribed deformation is such that the elastic antiplane deformation $u(x,y)$ in the matrix satisfies

$$u(x,y)=\mathrm{Re}(P_N^\infty(z))+o(1),\quad |z|=x^2+y^2\to\infty,\quad N=1,2,\ldots,$$

where $P_N^\infty(z)\equiv\Sigma_{n=0}^N a_n z^N$, the a_n are given complex constants (remote stress parameters), $(x,\,y)$ is a generic point in $\mathbb{R}^2$ and $z=x+iy\in\mathbb{C}$. We represent the matrix by the domain S_1 and assume that the inhomogeneity occupies a circular region S_2 with center at the origin and radius R. The inhomogeneity-matrix interface will be denoted by the curve Γ. In what follows, the subscripts 1 and 2 will refer to the regions S_1 and S_2, respectively, and $u_\alpha(x,y)$, $\alpha=1$, 2 will denote the elastic (antiplane) deformation at the point $(x,\,y)$ in S_α, respectively.

It is assumed that the circular inhomogeneity is imperfectly bonded to the matrix along Γ by the ‘‘spring-layer type’’ interface referred to in Section 1. The interface condition on Γ is therefore given by

$$\beta[u_1-(u_2+u^*)]=\mu_2\frac{\partial u_2}{\partial n}=\mu_1\frac{\partial u_1}{\partial n},\ \text{ on }\ \Gamma \tag{2.1}$$

where n is the outward unit normal to Γ, β is the imperfect interface parameter and $u^*(x,y)$ represents the additional displacement induced within the inhomogeneity by a uniform (stress-free) eigenstrain specified below. In accordance with Hashin [2], we note that if $\beta=0$, the condition (2.1) reduces to the case of a traction-free interface while if β is infinite, (2.1) corresponds to a perfectly bonded interface. Consequently, the following boundary value problem describes the antiplane deformation of a circular inhomogeneity with imperfect interface of the form (2.1) (see Ru and Schiavone [6]).

$$\nabla^2 u_1=0\quad\text{in }\ S_1$$

$$\nabla^2 u_2=0\quad\text{in }\ S_2$$

$$\beta(u_1-u_2)=\mu_2\frac{\partial u_2}{\partial n}+\beta u^*(x,y),\quad \mu_1\frac{\partial u_1}{\partial n}=\mu_2\frac{\partial u_2}{\partial n}\quad\text{on }\ \Gamma \tag{2.2}$$

$$u_1(x,y)=\mathrm{Re}(P_N^\infty(z))+o(1),\quad x^2+y^2\to\infty$$

Denote by $v_i(x,y)$ the harmonic functions conjugate to $u_i(x,y)$. Since the external loading is self-equilibrated, $v_i(x,y)$ are single-valued and uniquely determined to within an integration constant and the corresponding complex potentials $\phi_1(z)$ and $\phi_2(z)$ are analytic within S_1 and S_2, respectively. Thus,

$$2u_i(z)=\phi_i(z)+\overline{\phi_i(z)},\quad \sigma_{13}-i\sigma_{23}=\mu_i\phi_i'(z),\quad z\in S_i(i=1,2). \tag{2.3}$$

Noting that

$$2\,\frac{\partial u_2}{\partial n}=\phi_2'(z)e^{in(z)}+\overline{\phi_2'(z)}e^{-in(z)},\quad z\in\Gamma \tag{2.4}$$

where $e^{in(z)}$ represents (in complex form) the outward normal to Γ at z, the boundary value problem (2.2) can be written in the following form:

$$\phi_1(z)=\delta\phi_2(z)+(1-\delta)\overline{\phi_2(z)}+\alpha[\phi_2'(z)e^{in(z)}+\overline{\phi_2'(z)}e^{-in(z)}]+u^*(z),\quad z\in\Gamma \tag{2.5}$$

$$\phi_1(z)=P_N^\infty(z)+o(1),\quad |z|\to\infty.$$

Here

$$\alpha\equiv\frac{\mu_2}{2\beta}\geqslant0,\quad \delta\equiv\frac{\mu_1+\mu_2}{2\mu_1}>\frac{1}{2},\quad u^*=\omega z+\overline{\omega z} \tag{2.6}$$

and ω is a known (complex) constant determined by the uniform eigenstrain given in the circular inhomogeneity. Without loss of generality, we have assumed that the origin of coordinates has been chosen such that the rigid-body displacement at infinity is zero.

3 Single Circular Inhomogeneity With Homogeneously Imperfect Interface

Consider then, a single circular inhomogeneity with homogeneously imperfect interface characterized by the parameter α (or β). In this case, we have

$$\mathrm{R}e^{in(z)}=z,\quad z\in\Gamma$$

so that the interface condition (2.5) can be written as

$$\phi_1(z)+(\delta-1)\overline{\phi_2}\left(\frac{R^2}{z}\right)-\alpha\,\frac{R}{z}\overline{\phi_2'}\left(\frac{R^2}{z}\right)-\frac{\bar{\omega}}{z}R^2=\delta\phi_2(z)+\alpha\,\frac{z}{R}\,\phi_2'(z)+\omega z,\quad z\in\Gamma. \tag{3.1}$$

Since S_2 is a circular region, by symmetric continuation (see, for example, England [13]), $\overline{\phi_2}(R^2/z)$ and $\overline{\phi_2'}(R^2/z)$ are analytic in S_1. Consequently, the right-hand side of (3.1) is analytic in S_2 and the left-hand side of (3.1) is analytic in S_1, except at infinity where the left-hand side of (3.1) has the asymptotic behavior

$$P_N^\infty(z)+(\delta-1)\overline{\phi_2(0)},\quad |z|\to\infty.$$

Define the function $f(z)$ as follows:

$$f(z)=\begin{cases} f_1(z)=\delta\phi_2(z)+\alpha\,\dfrac{z}{R}\,\phi_2'(z)+\omega z, & z\in S_2\\ f_1(z)=f_2(z), & z\in\Gamma,\\ f_2(z)=\phi_1(z)+(\delta-1)\overline{\phi_2}\left(\dfrac{R^2}{z}\right)-\alpha\,\dfrac{R}{z}\overline{\phi_2'}\left(\dfrac{R^2}{z}\right)-\dfrac{\bar{\omega}}{z}R^2, & z\in S_1.\end{cases}$$

It is clear that $f(z)$ is entire in the domain $D=S_1\cup\Gamma\cup S_2$ (which does not include the point at infinity). It follows from Liouville's theorem and the asymptotic behavior of $f_2(z)$ that $f(z)=P_N^\infty(z)+(\delta-1)\overline{\phi_2(0)}$, $z\in D$. In particular,

$$\delta\phi_2(z)+\alpha\frac{z}{R}\phi_2'(z)+\omega z=P_N^\infty(z)+(\delta-1)\overline{\phi_2(0)},\quad z\in S_2.$$

Solving this first-order ordinary differential equation for ϕ_2 and using the notation $\phi_2^{(N)}$ to denote the stress function ϕ_2 for each $N=1,2,3,\ldots,$ leads to

$$\phi_2^{(N)}(z)=\frac{\delta-1}{\delta}\left[\frac{a_0(\delta-1)+\overline{a}_0\delta}{2\delta-1}\right]-\frac{z\omega}{\delta+\frac{\alpha}{R}}+\frac{R}{\alpha}\sum_{i=0}^{N}\frac{(-1)^i z^i}{\left(\frac{\delta R}{\alpha}\right)\cdots\left(\frac{\delta R}{\alpha}+i\right)}\frac{d^iP_N^\infty(z)}{dz^i},\quad z\in S_2 \tag{3.2}$$

$$=\frac{\delta-1}{\delta}\left[\frac{a_0(\delta-1)+\overline{a}_0\delta}{2\delta-1}\right]-\frac{z\omega}{\delta+\frac{\alpha}{R}}+\frac{R}{\alpha}\sum_{i=0}^{N}\frac{(-1)^i z^i}{\left(\frac{\delta R}{\alpha}\right)\cdots\left(\frac{\delta R}{\alpha}+i\right)}\sum_{j=0}^{N-i}a_{N-j}\times\frac{(N-j)!}{(N-j-i)!}z^{N-i-j}$$

which demonstrates the variation of the stress function $\phi_2^{(N)}$ (and hence, through (2.3), the stress field) inside the inhomogeneity with the prescribed remote loading of order N. More precisely, the stress field inside the inhomogeneity is of the same order ($N-1$) as the prescribed remote loading.

For example, in the case $N=1$ (which, from (2.3), corresponds to uniform remote loading), we obtain

$$\phi_2^{(1)}(z)=\frac{a_0\delta+\overline{a}_0(\delta-1)}{2\delta-1}+\frac{(a_1-\omega)z}{\delta+\frac{\alpha}{R}},\quad z\in S_2, \tag{3.3}$$

which, from (2.3), agrees with the result established in Ru and Schiavone [1] that the stress field inside the inhomogeneity is uniform. (The author notes that the result in Ru and Schiavone [1] mistakenly omits the contribution of the constant a_0 to $\phi_2^{(1)}(z)$. This, however, does not affect the expression for the stress field inside the inhomogeneity.) This result is in sharp contrast to the results obtained by Hashin [2] and Gao [3] for the corresponding problems in three-dimensional and plane elasticity, respectively, where, in each case, it was shown that, in the case of a homogeneously imperfect interface, under the assumption of uniform remote loading, the stress field inside the inhomogeneity is nonuniform.

In the case $N=2$ (which, from (2.3) corresponds to linear remote loading), we obtain from (3.2) that

$$\phi_2^{(2)}(z)=\phi_2^{(1)}(z)+a_2z^2\frac{R}{\alpha\left(\frac{\delta R}{\alpha}+2\right)},\quad z\in S_2,$$

which corresponds to a linear stress field inside the inhomogeneity.

The stress field in the surrounding matrix S_1 can be calculated for any value of N from the equation

$$f(z)=P_N^\infty(z)+(\delta-1)\overline{\phi_2(0)},\quad z\in S_1$$

or

$$\phi_1(z)=(1-\delta)\overline{\phi_2}\left(\frac{R^2}{2}\right)+\alpha\frac{R}{z}\overline{\phi_2'}\left(\frac{R^2}{z}\right)+\frac{\overline{\omega}}{z}R^2+P_N^\infty(z)+(\delta-1)\overline{\phi_2(0)},\quad z\in S_1. \tag{3.4}$$

It should be noted that (3.2) and (3.4) can also be derived using the method of series.

4 A Three-Phase Circular Inhomogeneity

The results obtained in Section 3 for a single circular inhomogeneity are easily extended to the case of a three-phase circular inhomogeneity with homogeneously imperfect interface leading to a much stronger result (The solution of the three-phase elastic inhomogeneity problem provides the "fundamental solution" for the generalized self-consistent method (see, for example, Christensen and Lo [8] Luo and Weng [9], Hashin [10], and Jun and Jusiuk [7]) in the mechanics of composite materials). To see this, consider the following.

Suppose there is an intermediate annular region S_0 (with shear modulus μ_0 and outer radius R_1) between the circular region S_2 and the matrix S_1. Assume that S_0 is perfectly bonded to S_1 but imperfectly bonded to S_2 with interface parameter β. Define the following quantities:

$$\delta_1\equiv\frac{\mu_1+\mu_0}{2\mu_0}>\frac{1}{2},\quad \delta_2\equiv\frac{\mu_0+\mu_2}{2\mu_0}>\frac{1}{2},\quad \alpha\equiv\frac{\mu_2}{2\beta}. \tag{4.1}$$

The corresponding antiplane problem requires that we find three analytic functions $\phi_i(z)(i=0,1,2)$ in the domains S_i, respectively, satisfying the following conditions:

$$\phi_0(z)=\delta_1\phi_1(z)+(1-\delta_1)\overline{\phi_1(z)},\quad |z|=R_1$$

$$\phi_0(z)=\delta_2\phi_2(z)+(1-\delta_2)\overline{\phi_2(z)}+\alpha\left[\frac{z}{R}\phi_2'(z)+\frac{R}{z}\overline{\phi_2'(z)}\right]+u^*,\quad |z|=R \tag{4.2}$$

$$\phi_1(z)=P_N^\infty(z)+o(1),\quad |z|\to\infty.$$

To solve this problem, let

$$\phi_1(z)=P_N^\infty(z)+\sum_{n=1}^{\infty}X_nz^{-n},\quad \phi_2(z)=Y_0+\sum_{n=1}^{\infty}Y_nz^n \tag{4.3}$$

where X_n, Y_n ($n=1,2\cdots$) and Y_0 are complex coefficients to be determined. From the first interface condition (4.2), we obtain $\phi_0(z)$ in terms of $\phi_1(z)$ as follows:

$$\phi_0(z)=\delta_1\left[P_N^\infty(z)+\sum_{n=1}^{\infty}X_nz^{-n}\right]+(1-\delta_1)\left[\overline{P_N^\infty}\left(\frac{R_1^2}{z}\right)+\sum_{n=1}^{\infty}\frac{\overline{X_n}z^n}{R_1^{2n}}\right]. \tag{4.4}$$

Substituting (4.3) and (4.4) into the second interface condition (4.2), and equating coefficients of like powers of z, the coefficients X_n and Y_n are found to be

$$Y_0=\frac{\delta_1a_0+(1-\delta_1)\overline{a}_0-\frac{(1-\delta_2)}{\delta_2}[\delta_1\overline{a}_0+(1-\delta_1)a_0]}{\delta_2-\frac{(1-\delta_2)^2}{\delta_2}}, \tag{4.5}$$

$$X_n=\frac{\dfrac{\delta_1\overline{a_n}}{\delta_2+\dfrac{\alpha n}{R}}[(1-\delta_2)R^{2n}+\alpha nR^{2n-1}]-(1-\delta_1)\overline{a_n}R_1^{2n}}{\delta_1-\dfrac{(1-\delta_1)}{R_1^{2n}}\dfrac{[(1-\delta_2)R^{2n}+\alpha nR^{2n-1}]}{\delta_2+\dfrac{\alpha n}{R}}},\tag{4.6}$$

$$Y_n=\frac{1}{\left(\delta_2+\dfrac{\alpha n}{R}\right)}\left[\delta_1 a_n+(1-\delta_1)\frac{\overline{X_n}}{R_1^{2n}}\right],\quad n=2,\ldots,N,\tag{4.7}$$

$$X_n=Y_n=0,\quad n>N.\tag{4.8}$$

The remaining two nonzero constants X_1 and Y_1 are determined by the equations:

$$\delta_1 a_1+(1-\delta_1)\frac{\overline{X_1}}{R_1^2}=\left(\delta_2+\frac{\alpha}{R}\right)Y_1+\omega$$

$$\delta_1X_1+(1-\delta_1)R_1^2\overline{a_1}=[(1-\delta_2)R+\alpha]\overline{Y_1}R+R^2\overline{\omega}.\tag{4.9}$$

The stress functions ϕ_0, ϕ_1, and ϕ_2 are now determined from (4.3)–(4.9) and again demonstrate the direct relationship between the stress field inside the inhomogeneity (characterized by ϕ_2) and the prescribed remote loading of order $N-1$.

In particular, in the case $N=1$,

$$\begin{aligned}\phi_2'&=\frac{\sigma_{13}-i\sigma_{23}}{\mu_2}\\&=Y_1\\&=\frac{(2\delta_1-1)a_1+\left[(1-\delta_1)\dfrac{R^2}{R_1^2}-\delta_1\right]\omega}{(\delta_1+\delta_2-1)\dfrac{R^2}{R_1^2}+\delta_1\delta_2\left(1-\dfrac{R^2}{R_1^2}\right)+\alpha\dfrac{R}{R_1^2}\left[\delta_1\left(1+\dfrac{R_1^2}{R^2}\right)-1\right]}\end{aligned}\tag{4.10}$$

which is the result first presented in Ru and Schiavone [1], i.e., that the stress field inside a three-phase circular inhomogeneity with homogeneously imperfect interface is uniform. Note that (4.10) reduces to ϕ_2' obtained from (3.3) when $\delta_1=1$.

Acknowledgments

The work is supported by the Natural Science and Engineering Research Council of Canada through Grant NSERC OGP 115112. The author would like to thank Dave Barnett for useful discussions.

References

[1] Ru, C. Q., and Schiavone, P., 1997, ''A Circular Inhomogeneity With Circumferentially Inhomogeneous Interface in Antiplane Shear,'' Proc. R. Soc. London, Ser. A, **453**, pp. 2551–2572.
[2] Hashin, Z., 1991, ''The Spherical Inhomogeneity With Imperfect Interface,'' ASME J. Appl. Mech., **58**, pp. 444–449.
[3] Gao, J., 1995, ''A Circular Inhomogeneity With Imperfect Interface: Eshelby's Tensor and Related Problems,'' ASME J. Appl. Mech., **62**, pp. 860–866.
[4] Eshelby, J. D., 1957, ''The Determination of the Elastic Field of an Ellipsoidal Inhomogeneity and Related Problems,'' Proc. R. Soc. London, Ser. A, **241**, pp. 376–396.
[5] Eshelby, J. D., 1959, ''The Elastic Field Outside an Ellipsoidal inhomogeneity,'' Proc. R. Soc. London, Ser. A, **252**, pp. 561–569.
[6] Ru, C. Q., and Schiavone, P., 1996, ''On the Elliptic Inhomogeneity in Antiplane Shear,'' Math. Mech. Solids, **1**, pp. 327–333.
[7] Jun, S., and Jasiuk, I., 1993, ''Elastic Moduli of Two-Dimensional Composites With Sliding Inhomogeneitys—A Comparison of Effective Medium Theories,'' Int. J. Solids Struct., **30**, pp. 2501–2523.
[8] Christensen, R. M., and Lo, K. H., 1979, ''Solutions for Effective Shear Properties in Three-Phase Sphere and Cylinder Models,'' J. Mech. Phys. Solids, **27**, pp. 315–330.
[9] Luo, H. A., and Weng, G. J., 1989, ''On Eshelby's S-tensor in a Three-Phase Cylindrically Concentric Solid, and the Elastic Moduli of Fibre-Reinforced Composites,'' Mech. Mater., **8**, pp. 77–88.
[10] Hashin, Z., 1990, ''Thermoelastic Properties of Fiber Composites With Imperfect Interface,'' Mech. Mater., **8**, pp. 333–348.
[11] Okabayashi, H., 1993, ''Stress-Induced Void Formation in Metallization for Integrated Circuits,'' Mater. Sci. Eng., R., **R**, pp. 191–241.
[12] Niwa, H., Yagi, H., Tsuchikawa, H., and Kato, M., 1990, ''Stress Distribution in an Aluminum Interconnect of Very Large Scale Integration,'' J. Appl. Phys., **68**, pp. 328–333.
[13] England, A. H., 1971, *Complex Variable Methods in Elasticity*, Wiley-Interscience, London.

Radiation Loading of a Cylindrical Source in a Fluid-Filled Cylindrical Cavity Embedded Within a Fluid-Saturated Poroelastic Medium

S. M. Hasheminejad
Assistant Professor
e-mail: hashemi@iust.ac.ir

H. Hosseini
Graduate Student

Department of Mechanical Engineering,
Iran University of Science and Technology,
Narmak, Tehran 16844, Iran

Radiation loading on a vibrating structure is best described through its radiation impedance. In the present work the modal acoustic radiation impedance load on an infinitely long cylindrical source harmonically excited in circumferentially periodic (axially independent) spatial pattern, while positioned concentrically within a fluid cylinder, which is embedded in a fluid-saturated unbounded elastic porous medium, is computed. This configuration, which is a realistic idealization of an acoustic logging tool suspended in a fluid-filled borehole within a permeable surrounding formation (White, J. E., 1983, Underground Sound Application of Seismic Waves, Elsevier, Amsterdam, Fig. 5.29, p. 183), is of practical importance with a multitude of possible applications in seismo-acoustics and noise control engineering. The formulation utilizes the Biot phenomenological model to represent the behavior of the sound in the porous, fluid-saturated, macroscopically homogeneous and isotropic surrounding medium. Employing the appropriate wave-harmonic field expansions and the pertinent boundary conditions for the given boundary configuration, a closed-form solution in the form of an infinite series is developed and the resistive and reactive components of modal radiation impedances are determined. A numerical example for a cylindrical surface excited in vibrational modes of various order, immersed in a water-filled cavity which is embedded within a water-saturated Ridgefield sandstone environment, is presented and several limiting cases are examined. Effects of porosity, frame stiffness, source size, and the interface permeability condition on the impedance values are presented and discussed. [DOI: 10.1115/1.1488664]

1 Introduction

There has been a progressing interest in acoustics of fluid-saturated porous media due to its important applications in various technical and engineering processes. In particular there is an increasing demand in studying the propagation, attenuation, and dispersion of elastic waves in granular media such as rock formations in petroleum reservoirs, ocean bed sedimentary layers, sound-absorbing (impedance) ground, and in fibrous medium such as biological tissues, polymer networks, and sound-absorbing materials. Gassmann [1] presented the first concise model for harmonic plane wave propagation in an infinite fluid-saturated porous solid. His work is considered to be the first major breakthrough in predicting the elastic moduli of porous media at low frequencies. Gassmann's treatment, however, disregarded the relative viscous fluid/elastic solid motion which is known to be the main cause of energy loss in the high-frequency regime. Approaching the problem in a more unified manner, Biot [2–4] extended Gassman's work and developed a straightforward and efficient two-phase theory for wave propagation, addressing such issues as wave speed, attenuation, dispersion, and anisotropy. He formulated the appropriate constitutive equations and equations of motion in poroelastic media and predicted the existence of two types of dilatational (compressional) waves along with one rotational (shear) wave. Biot's treatment agrees well with Gassmann's results in the low-frequency range [5].

For many years following the development of the Biot theory of dynamic poroelasticity the existence of the Biot slow compressional (type II) wave remained the most controversial of its predictions within the seismology and underwater acoustics communities. Recently the scientific groundwork for Biot's model has been more firmly established through several experimental validations of its most fundamental predictions, leading to a renewed interest in the subject. The first clear experimental observation of the slow bulk waves was reported by Plona [6]. He detected Biot's slow wave under controlled experimental conditions in consolidated porous media consisting of lightly fused glass beads (artificial rock) saturated with water. Subsequently Berryman [7] quantitatively analyzed and confirmed Plona's observations and concluded that Biot's model provides the appropriate basic framework for analysis of general two-component effective-medium systems. Similarly, a rigorous microscale-based asymptotic analysis by Burridge and Keller [8] has also confirmed the validity of Biot's equations under the proper set of assumptions. Further experimental validations are accomplished by van der Grinten et al. [9,10], Rasolofosaon [11], and Kelder and Smeulders [12,13]. Just recently, Gurevich, Kelder, and Smeulders [14] performed accurate dynamic numerical modeling and simulation of three successful ultrasonic experiments, in which the type II wave was observed, to gain insight into the problem and further substantiate the validity of the Biot dynamic theory of poroelasticity.

When an interface separates a saturated porous medium from a second medium, the question of the boundary conditions needs to be examined. The interface conditions relate the field variables on

Contributed by the Applied Mechanics Division of THE AMERICAN SOCIETY OF MECHANICAL ENGINEERS for publication in the ASME JOURNAL OF APPLIED MECHANICS. Manuscript received by the Applied Mechanics Division, July 12, 2000; final revision, June 22, 2001. Associate Editor: D. A. Siginer. Discussion on the paper should be addressed to the Editor, Prof. Robert M. McMeeking, Chair, Department of Mechanics and Environmental Engineering, University of California—Santa Barbara, Santa Barbara, CA 93106-5070, and will be accepted until four months after final publication in the paper itself in the ASME JOURNAL OF APPLIED MECHANICS.

both sides of a surface of discontinuity in the material properties that are involved in the coefficients appearing in Biot's equations. The appropriate set of boundary conditions that are sufficient to produce a unique solution to Biot's equations of motion when an interface separates two poroelastic media was originally derived by Deresiewicz and Skalak [15]. Many researchers have employed these conditions to produce the solution to Biot's equations of motion for various scattering problems involving piecewise homogeneous porous materials such as layered poroelastic medium and porous media with inclusions. A proof of these conditions on the basis of Hamilton's principle is given in the monograph by Bourbie et al. [16].

While most research studies involve reflection and transmission from a planar interface, comparatively little work has been done on acoustic scattering or radiation from (bounded) convex-shaped inclusions within a fluid-saturated porous medium. Applying a boundary layer approximation, Mei et al. [17] studied acoustic scattering by a fluid-filled circular cavity within a fluid-infiltrated poroelastic medium. Berryman [18] and Zimmerman [19] have each employed a distinct analytical method to examine scattering of plane compressional waves by a spherical inclusion in an infinite poroelastic medium. Zimmerman and Stern [20] developed closed-form solutions to several basic problems of harmonic wave propagation in a poroelastic medium including radiation from a harmonically pulsating impermeable spherical inclusion, and scattering of a plane compressional wave by a poroelastic spherical inhomogeneity. Kargl and Lim [21] and Lim [22] formulated the scattering problem using a transition matrix approach and presented some numerical results for the case of scatter by a spherical poroelastic inclusion. Lim [23] developed a transition-matrix formulation of the field scattered by a bounded three-dimensional object in a horizontally plane-stratified poroelastic environment. He numerically implemented his proposed exact solution for an aluminum sphere buried in an ocean sediment half-space and insonified by an acoustic source in an overlying water half-space. Gurevich et al. [24] developed a quantitative model for interaction of an incident plane elastic compressional wave with a poroelastic ellipsoidal inclusion embedded within a fluid-saturated porous elastic medium employing the Born approximation. They obtained relatively simple explicit analytical expressions for a number of common cases under the main assumption of low contrast of inclusion's properties relative to the host medium. The transient response of radially pressurized cylindrical cavity within an unbounded fluid-saturated porous medium has been considered by Senjuntichai and Rajapakse [25]. Employing Biot's equations of poroelastodynamics, they obtained time-domain solutions for radial displacements, stresses, pore pressure, and discharge by direct inversion of Laplace domain solutions using an appropriate numerical scheme. Qi and Geers [26] presented the first formulation of singly and doubly asymptotic approximations (DAAs) for a poroelastic medium. They found good agreement of DAAs with the exact solution by examining the surface response of a step-pressurized spherical shell and spherical cavity embedded in an infinite poroelastic medium. The more related problem of radiation loading on a spherical source freely suspended in a fluid-filled spherical cavity embedded within a fluid-infiltrated elastic porous medium has lately been tackled by Hasheminejad [27].

Problems corresponding to sources immersed in fluid near a permeable interface are of great practical importance with a multitude of possible applications in technical fields, such as seismic prospecting, ocean acoustics, atmospheric acoustics, and noise control engineering. In particular, theoretical and experimental studies on the prediction of an acoustic field of a multipole source near a finite impedance surface are of fundamental interest in mentioned fields ([28–36]). Representing an acoustic logging tool as a uniform circular cylinder of unlimited length suspended in a fluid-filled cylindrical cavity leads to an idealized model which may be looked as the starting point for a more realistic description of the problem ([5,37]). Employing the above embodiment, Poterasu [38] investigated dynamic coupling effects for a pulsating source in a fluid-filled cavity embedded within an (ideal) elastic infinite media by the boundary element method. In doing this, however, he made the unrealistic assumption for the surrounding formation to be nonpermeable. The principal objective of present paper is to employ Biot's theory of wave propagation in fluid-saturated poroelastic media to determine the radiation loading on a cylindrical source undergoing circumferentially periodic harmonic vibrations in a fluid-filled cylindrical cavity embedded within a poroelastic environment.

2 Governing Field Equations

Before proceeding to analyze the full problem, we shall first briefly review salient features of Biot's dynamic theory of poroelasticity. On a microscopic scale, sound propagation in porous materials is generally difficult to study due to the complicated geometries of the frames. In the Biot model the medium is taken to be a macroscopically homogeneous and isotropic two-component solid/fluid system. It is therefore described in terms of averaged parameters. The averaging is performed on a macroscopic scale, on volumes with dimensions sufficiently large for the average to be significant. Denoting the average macroscopic displacement of the solid frame and the saturating fluid on the elementary macroscopic volume (EMV) by the vectors $\mathbf{u}$ and $\mathbf{U}$, respectively, the macroscopic stress tensor σ_{ij} and the mean pore fluid pressure p_p are given by ([16])

$$\begin{aligned} \sigma_{ij} &= (\lambda_f e - \beta M \xi)\delta_{ij} + 2\mu e_{ij} \\ p_p &= M(\xi - \beta e) \end{aligned} \tag{1}$$

where

$$\begin{aligned} \lambda_f &= K_f - \frac{2}{3}\mu \\ K_f &= \frac{\phi_0(1/K_s - 1/K_{fl}) + 1/K_s - 1/K_o}{\phi_0/K_o(1/K_s - 1/K_{fl}) + 1/K_s(1/K_s - 1/K_o)} \\ M &= 1/((\beta - \phi_0)/K_s + \phi_0/K_{fl}) \\ \beta &= 1 - K_o/K_s \\ e_{ij} &= (u_{i,j} + u_{j,i})/2 \\ \xi &= -\nabla\cdot\mathbf{w} = -\phi_0(\varepsilon - e) \\ e &= \nabla\cdot\mathbf{u}, \quad \varepsilon = \nabla\cdot\mathbf{U} \end{aligned} \tag{2}$$

in which μ is the shear modulus of the bare skeletal frame, ϕ_0 is the pore volume fraction (porosity), K_o is the bulk modulus of the dry skeleton (i.e., for the "open" system, $p_p = 0$), K_s is the bulk modulus of the material constituting the elastic matrix, K_{fl} is the bulk modulus of the saturating fluid, K_f is the bulk modulus of the "closed" system, and $\mathbf{w} = \phi_0(\mathbf{U} - \mathbf{u})$ is the filtration displacement vector.

Following the standard methods of continuum mechanics the continua are described by sets of coupled balance equations with additional terms corresponding to the interaction between phases. Accordingly, the equations of motion (linear momentum balance) governing the displacements of the solid matrix and interstitial liquid with dissipation taken into account are written as ([16])

$$\begin{aligned} (\lambda + 2\mu)\nabla\nabla\cdot\mathbf{u} + Q\nabla\nabla\cdot\mathbf{U} - \mu\nabla\times\nabla\times\mathbf{u} &= \rho_{11}\ddot{\mathbf{u}} + \rho_{12}\ddot{\mathbf{U}} + b(\dot{\mathbf{u}} - \dot{\mathbf{U}}) \\ Q\nabla\nabla\cdot\mathbf{u} + R\nabla\nabla\cdot\mathbf{U} &= \rho_{12}\ddot{\mathbf{u}} + \rho_{22}\ddot{\mathbf{U}} - b(\dot{\mathbf{u}} - \dot{\mathbf{U}}) \end{aligned} \tag{3}$$

where

$$\begin{aligned} \lambda &= \lambda_f + \phi_0 M(\phi_0 - 2\beta) \qquad \rho = (1 - \phi_0)\rho_s + \phi_0\rho_{fl} \\ Q &= \phi_0 M(\beta - \phi_0) \qquad \rho_{11} = \rho + \phi_0\rho_{fl}(\alpha - 2) \\ R &= \phi_0^2 M \qquad \rho_{12} = \phi_0\rho_{fl}(1 - \alpha) \end{aligned} \tag{4}$$

$$\rho_{22}=\rho-\rho_{11}-2\rho_{12}=\alpha\phi_0\rho_{fl}$$

in which ρ_s is the density of solid matrix material in a consolidated nonporous state, ρ_{fl} is the density of saturating fluid, ρ is the total mass density of fluid-saturated material, and the effective densities ρ_{11}, ρ_{12}, ρ_{22}, which describe the combined effects of viscous and inertial drag, are frequency-independent parameters relying on the geometry of the porous medium and the density of the saturating fluid. The parameter α, the tortuosity (structure factor) of the porous medium, was originally introduced into the theory of acoustical materials by Zwikker and Kosten [39]. It is an intrinsic geometrical property related to variations in pore shapes and orientations. The structure factor is equal to unity if the pores are straight and uniform and increases as the pores become irregularly constricted and more tortuous (i.e., as they deviate more from the direction of wave propagation). The quantity $b(\omega)$ is a viscous coupling factor that accounts for the combined effects of macroscopic frictional dissipation due to finite fluid viscosity (viscous drag forces) and the interaction between the fluid and solid movements (inertial forces). A common functional form for $b(\omega)$, based on heuristic arguments, is given as ([40])

$$b=\frac{\phi_0^2\eta}{\kappa}F(\omega) \tag{5}$$

where η is the saturating fluid viscosity, and κ is the absolute (dc) permeability of the porous medium. Here the quantity $\phi_0^2\eta/\kappa$ corresponds to a frictional drag coefficient derived assuming Poiseuille (laminar and incompressible) flow of a saturating fluid past the lattice walls at low frequencies. At higher frequencies the complexity of the pore geometry cannot properly be accounted for by the "static" permeability alone and the (dynamic) viscosity correction factor $F(\omega)$ is introduced to correct for deviations from the Poiseuille flow (so that, naturally, $F(0)=1$). Biot [3] treated the pore space as an ensemble of straight circular channels and studied viscous parallel fluid flow under an oscillatory pressure gradient. He developed expressions for $F(\omega)$ for cylindrical and flat side pores in terms of fluid viscosity and pore diameter. Thereafter, many researchers have investigated the frequency dependence of the Biot theory in terms of various fundamentally equivalent parameters (e.g., permeability, tortuosity, and viscous characteristic length). In 1987, Johnson et al. [41] considered a network of straight channels with randomly distributed radii and introduced a very simple and fairly accurate alternative model (JKD model) for description of dynamic permeability at arbitrary frequencies based on energy flux consideration on the microscale. Johnson's et al. description differed slightly from Biot's model, but showed the same general behavior in the low and the high-frequency limits. In the present work we shall adopt the JKD description of dynamic permeability effects. According to Johnson et al. [41], the simplest possible model for $F(\omega)$ is (please see their Eq. (3.3))

$$F(\omega)=\left\{1-j\,\frac{4\alpha^2\kappa^2\rho_{fl}\omega}{\eta\Lambda^2\phi_0^2}\right\}^{1/2} \tag{6}$$

where $\Lambda\approx\sqrt{8\alpha\kappa/\phi_0}$, the viscous characteristic length, is a well-defined parameter relevant to a wide range of transport properties. It depends exclusively on frame geometry and intrinsically describes the dimensions of dynamically interconnected pores ([40]).

The Helmholtz decomposition theorem allows us to resolve the displacement fields as the superposition of longitudinal and transverse vector components

$$\begin{aligned}\mathbf{u}&=\nabla\phi+\nabla\times\psi\\ \mathbf{U}&=\nabla\chi+\nabla\times\Theta.\end{aligned} \tag{7}$$

Substituting the above resolutions into Biots' field equations of motion (3), we obtain two sets of coupled equations (hereafter we shall assume harmonic time variations with $e^{-j\omega t}$ dependence suppressed for simplicity):

$$\begin{bmatrix}\lambda+2\mu & Q\\ Q & R\end{bmatrix}\begin{bmatrix}\nabla^2\phi\\ \nabla^2\chi\end{bmatrix}=\begin{bmatrix}\rho_{11}\omega^2-j\omega b & \rho_{12}\omega^2+j\omega b\\ \rho_{12}\omega^2+j\omega b & \rho_{22}\omega^2-j\omega b\end{bmatrix}\begin{bmatrix}\phi\\ \chi\end{bmatrix} \tag{8}$$

$$\begin{bmatrix}\mu & 0\\ 0 & 0\end{bmatrix}\begin{bmatrix}\nabla^2\psi\\ 0\end{bmatrix}=\begin{bmatrix}\rho_{11}\omega^2-j\omega b & \rho_{12}\omega^2+j\omega b\\ \rho_{12}\omega^2+j\omega b & \rho_{22}\omega^2-j\omega b\end{bmatrix}\begin{bmatrix}\psi\\ \Theta\end{bmatrix}. \tag{9}$$

Using standard methods of wave analysis, the above systems may be manipulated to yield the Helmholtz equations ([16]):

$$\begin{aligned}\nabla^2\phi_{f,s}+k_{f,s}^2\phi_{f,s}&=0\\ \nabla^2\psi+k_t^2\psi&=0\end{aligned} \tag{10}$$

where k_f, k_s, and k_t which designate the complex wave numbers of the fast compressional, slow compressional, and the elastic shear waves, respectively, are given as

$$k_{f,s}^2=\frac{B\mp\sqrt{B^2-4AC}}{2A}\qquad k_t^2=\frac{C}{\mu(\rho_{22}\omega^2+j\omega b)} \tag{11}$$

where

$$\begin{aligned}A&=(\lambda+2\mu)R-Q^2\\ B&=\omega^2[\rho_{11}R+\rho_{22}(\lambda+2\mu)-2\rho_{12}Q]+j\omega b(\lambda+2\mu+2Q+R)\\ C&=\omega^2[\omega^2(\rho_{11}\rho_{22}-\rho_{12}^2)+j\omega\rho b].\end{aligned} \tag{12}$$

Employing Eqs. (8) through (11), with some manipulations, the scalar potentials ϕ, χ, Θ, and ψ may be expressed as

$$\begin{aligned}\phi&=\phi_f+\phi_s\\ \chi&=\mu_f\phi_f+\mu_s\phi_s\\ \Theta&=\alpha_0\psi\end{aligned} \tag{13}$$

where

$$\begin{aligned}\mu_{f,s}&=\frac{\omega^2(\rho_{11}R-\rho_{12}Q)-k_{f,s}^2[(\lambda+2\mu)R-Q^2]+j\omega b(Q+R)}{\omega^2(\rho_{22}Q-\rho_{12}R)+j\omega b(Q+R)}\\ \alpha_0&=-\frac{\omega^2\rho_{12}-j\omega b}{\omega^2\rho_{22}+j\omega b}.\end{aligned} \tag{14}$$

The fluid contained in the cylindrical cavity is assumed to be inviscid and ideally compressible that cannot support shear stresses making the state of stress in the fluid purely hydrostatic. Consequently the field equations may be expressed in terms of the velocity potential of the cavity fluid as ([42])

$$\begin{aligned}\dot{\mathbf{s}}&=\nabla\varphi\\ p&=-\bar{\rho}\dot{\varphi}\\ \nabla^2\varphi+k^2\varphi&=0\end{aligned} \tag{15}$$

where $k(=\omega/c)$ is the wave number for the dilatational wave, $\bar{\rho}$ is the density, $\dot{\mathbf{s}}$ is the velocity vector, and p is the acoustic pressure in the inviscid fluid.

3 Field Expansions and Boundary Conditions

The geometry and the coordinate system used are depicted in Fig. 1, which is a close reproduction of Fig. 5.29 in Ref. [5]. The dynamics of the problem may be expressed in terms of appropriate scalar potentials. The compressional waves that are trapped in the inviscid fluid layer inside the cylindrical cavity may be expressed as

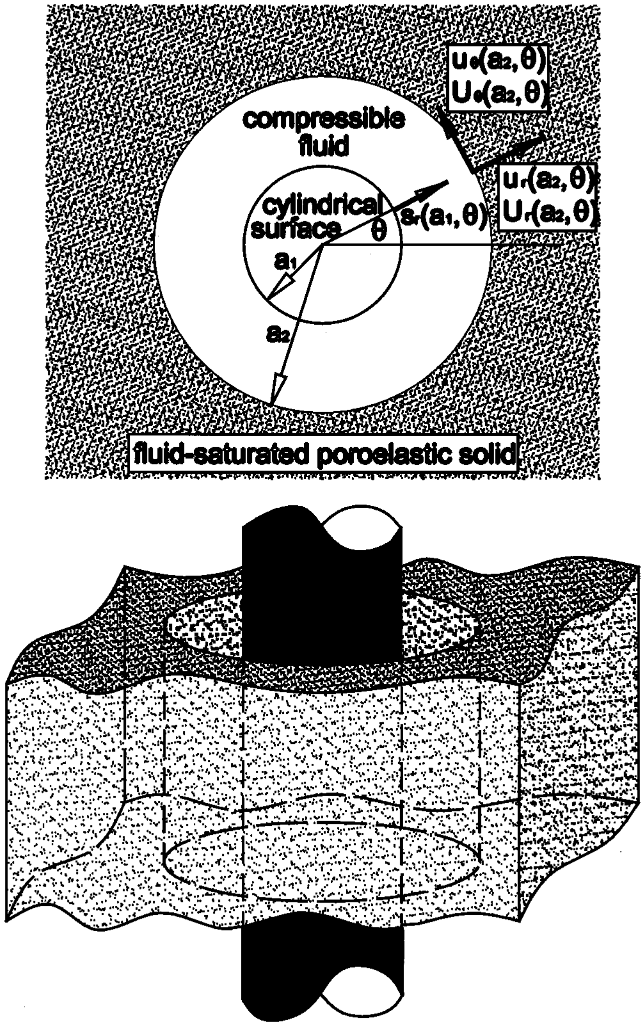

Fig. 1 Problem geometry

$$\varphi=\sum_{n=0}^{\infty}[D_nJ_n(kr)+E_nH_n(kr)]\cos n\theta \tag{16}$$

where J_n are cylindrical Bessel functions, and H_n are the cylindrical Hankel functions ([43]), D_n and E_n are unknown scattering coefficients. Similarly, the transmitted (outgoing) fast dilatational wave, slow dilatational wave, and the shear wave in the poroelastic medium exterior to the cavity are, respectively, represented by

$$\phi_f=\sum_{n=0}^{\infty}A_nH_n(k_fr)\cos n\theta$$

$$\phi_s=\sum_{n=0}^{\infty}B_nH_n(k_sr)\cos n\theta \tag{17}$$

$$\psi=\sum_{n=0}^{\infty}nC_nH_n(k_tr)\sin n\theta.$$

Now considering the basic field equations in cylindrical coordinates, assuming no axial dependence, the solid and liquid displacements in the r and θ-directions in terms of displacement potentials in the poroelastic media are ([42])

$$u_r=\frac{\partial\phi}{\partial r}+\frac{1}{r}\frac{\partial\psi}{\partial\theta}\quad u_\theta=\frac{1}{r}\frac{\partial\phi}{\partial\theta}-\frac{\partial\psi}{\partial r}$$
$$U_r=\frac{\partial\chi}{\partial r}+\frac{1}{r}\frac{\partial\Theta}{\partial\theta}\quad U_\theta=\frac{1}{r}\frac{\partial\chi}{\partial\theta}-\frac{\partial\Theta}{\partial r}. \tag{18}$$

Expressions for the frame and liquid dilatations can be manipulated to yield

$$e=\nabla\cdot\mathbf{u}=\nabla^2\phi=\nabla^2\phi_f+\nabla^2\phi_s=-k_f^2\phi_f-k_s^2\phi_s$$
$$\epsilon=\nabla\cdot\mathbf{U}=\nabla^2\chi=\mu_f\nabla^2\phi_f+\mu_s\nabla^2\phi_s=-\mu_fk_f^2\phi_f-\mu_sk_s^2\phi_s \tag{19}$$

where

$$\nabla^2=\frac{1}{r}\frac{\partial}{\partial r}\left(r\frac{\partial}{\partial r}\right)+\frac{1}{r^2}\frac{\partial^2}{\partial\theta^2}. \tag{20}$$

Utilizing Eqs. (1), (13), (18), and (19), pore fluid pressure, radial and tangential stress components are expressed as

$$\sigma_{rr}=a_fk_f^2\phi_f+a_sk_s^2\phi_s+2\mu(\partial u_r/\partial r) \tag{21}$$

$$p_p=Mb_fk_f^2\phi_f+Mb_sk_s^2\phi_s \tag{22}$$

$$\sigma_{r\theta}=\frac{\mu}{r}\left(\frac{\partial u_r}{\partial\theta}+r\frac{\partial u_\theta}{\partial r}-u_\theta\right) \tag{23}$$

where

$$a_{f,s}=-\lambda_f+\phi_0\beta M(1-\mu_{f,s})$$
$$b_{f,s}=\beta+\phi_0(\mu_{f,s}-1). \tag{24}$$

The unknown scattering coefficients A_n through E_n in Eqs. (16) and (17) must be determined by the application of suitable interface conditions. The only boundary condition at the cylindrical surface (i.e., at $r=a_1$) is the continuity of normal velocity, thus the first of Eqs. (15) leads to

$$\left.\frac{\partial\varphi}{\partial r}\right]_{r=a_1}=v=\sum_{n=0}^{\infty}v_n\cos n\theta \tag{25}$$

where v_n represents the modal radial velocity amplitude of the cylindrical surface.

Microscopically, the boundary conditions at a poroelastic interface are very complicated. This is true particularly at the interface between two poroelastic media of distinct pore size. The situation can be simplified by averaging in a volume sense as discussed by Deresiewicz and Skalak [15]. The appropriate boundary conditions that have to be satisfied at the cavity wall (i.e., at $r=a_2$) to yield a unique solution for the proposed problem are ([16]):

1. compatibility of normal stress in poroelastic media with the acoustic pressure in the cavity fluid

$$\sigma_{rr}=-p \tag{26a}$$

2. vanishing of tangential stress

$$\sigma_{r\theta}=0 \tag{26b}$$

3. continuity of normal component of the filtration velocity

$$\dot{w}_r=\phi_0(\dot{U}_r-\dot{u}_r)=\dot{s}_r-\dot{u}_r \tag{26c}$$

4. consistency of the pressure drop and the normal component of filtration velocity (i.e., satisfaction of Darcy's law which governs the fluid flow across the interface)

$$\dot{w}_r=-\kappa_s(p-p_p) \tag{26d}$$

where the parameter κ_s characterizes the permeability of the interface, i.e., it describes the quality of interconnection between two media. For an open interface, we expect zero pressure drop ($p=p_p$) and hence we let $\kappa_s=\infty$. To characterize a sealed interface (i.e., for $\dot{\mathbf{w}}=0$) we take $\kappa_s=0$. Obviously, acoustic properties involving the interface is expected to be highly sensitive to the state of the surface condition. For clarity, in the present article we do not consider the possibility of a partially sealed boundary condition.

Now the unknown scattering coefficients shall be determined by imposing the stated boundary conditions. Employing expansions (16) and (17) in the field Eqs. (18) through (24), and substituting obtained results into the boundary conditions (25) and (26), we obtain

$$kJ_n'(ka_1)D_n+kH_n'(ka_1)E_n=v_n \tag{27}$$

$$\begin{aligned}&\{k_f^2[a_fH_n(k_fa_2)+2\mu H_n''(k_fa_2)]\}A_n+\{k_s^2[a_sH_n(k_sa_2)\\&\quad+2\mu H_n''(k_sa_2)]\}B_n+\left\{\frac{2\mu n^2}{a_2}\left[k_tH_n'(k_ta_2)-\frac{1}{a_2}H_n(k_ta_2)\right]\right\}\\&\quad\times C_n+\{j\omega\overline{\rho}J_n''(ka_2)\}D_n+\{j\omega\overline{\rho}H_n(ka_2)\}E_n=0\end{aligned} \tag{28}$$

$$\begin{aligned}&\left\{\frac{2\mu}{a_2}\left[\frac{1}{a_2}H_n(k_fa_2)-k_fH_n'(k_fa_2)\right]\right\}A_n+\left\{\frac{2\mu}{a_2}\left[\frac{1}{a_2}H_n(k_sa_2)\right.\right.\\&\quad\left.\left.-k_sH_n'(k_sa_2)\right]\right\}B_n+\frac{\mu}{a_2^2}\{(-n^2)H_n(k_ta_2)+a_2k_tH_n'(k_ta_2)\\&\quad-a_2^2k_t^2H_n''(k_ta_2)\}C_n=0\end{aligned} \tag{29}$$

$$\begin{aligned}&\{j\omega k_fH_n'(k_fa_2)[\phi_0(1-\mu_f)-1]\}A_n\\&\quad+\{j\omega k_sH_n'(k_sa_2)[\phi_0(1-\mu_s)-1]\}B_n\\&\quad+\left\{\frac{n^2}{a_2}j\omega H_n(k_ta_2)[\phi_0(1-\alpha_0)-1]\right\}C_n\\&\quad+\{-kJ_n'(ka_2)\}D_n+\{-kH_n'(ka_2)\}E_n=0\end{aligned} \tag{30}$$

$$\begin{aligned}&\{j\omega\phi_0k_fH_n'(k_fa_2)[1-\mu_f]-\kappa_sMb_fk_f^2H_n(k_fa_2)\}A_n\\&\quad+\{j\omega\phi_0k_sH_n'(k_sa_2)[1-\mu_s]-\kappa_sMb_sk_s^2H_n(k_sa_2)\}B_n\\&\quad+\left\{\frac{n^2}{a_2}j\omega\phi_0H_n(k_ta_2)[1-\alpha_0]\right\}C_n+\{j\omega\overline{\rho}\kappa_sJ_n(ka_2)\}D_n\\&\quad+\{j\omega\overline{\rho}\kappa_sH_n(ka_2)\}E_n=0\end{aligned} \tag{31}$$

where $n=0,1,2,\ldots$, except for Eq. (29) where $n=1,2,\ldots$.

The fluctuating acoustic pressure on the surface of a vibrating structure constitutes its radiation loading. The radiation loading on a cylindrical surface excited in vibrational modes of various order (i.e., monopole, dipole, quadrupole, and multipole-like radiators) is best described through its acoustic radiation impedance. For a unique review on the subject one should consider Ref. [44]. At this point we may favorably express the system of Eqs. (27) through (31) in matrix form as

$$\mathbf{u}_0=\mathbf{R}_0\mathbf{c}_0,\quad \mathbf{u}_n=\mathbf{R}_n\mathbf{c}_n\quad n\geqslant 1 \tag{32}$$

where

$$\begin{aligned}\mathbf{c}_0&=[A_0,B_0,D_0,E_0]^T\quad \mathbf{c}_n=[A_n,B_n,C_n,D_n,E_n]^T\\ \mathbf{u}_0&=[v_0,0,0,0]^T\quad \mathbf{u}_n=[v_n,0,0,0,0]^T.\end{aligned} \tag{33}$$

Fluid pressure on the vibrating cylindrical surface is determined from the second of Eqs. (15) and Eq. (16) as

$$p_n(r=a_1)=\{j\omega\overline{\rho}J_n(ka_1)\}D_n+\{j\omega\overline{\rho}H_n(ka_1)\}E_n \tag{34}$$

which can also readily be put in matrix form as

$$p_0=S_0c_0,\quad p_n=S_nc_n\quad n\geqslant 1. \tag{35}$$

Using Eqs. (32) and (35), modal pressure may be stated as

$$p_0=\mathbf{Z}_0\mathbf{u}_0,\quad p_n=\mathbf{Z}_n\mathbf{u}_n\quad n\geqslant 1 \tag{36}$$

where

$$\mathbf{Z}_0=\mathbf{S}_0\mathbf{R}_0^{-1},\quad \mathbf{Z}_n=\mathbf{S}_n\mathbf{R}_n^{-1}\quad n\geqslant 1. \tag{37}$$

Table 1 Input parameter values used in Biot's model

Parameter	Water-Saturated Sandstone
ϕ_0	0.37
α	1.58
κ (cm^2)	27.7×10^{-8}
ρ_s (g/cm^3)	2.48
K_s (dyn/cm^2)	4.99×10^{11}
K_o (dyn/cm^2)	5.24×10^{10}
μ (dyn/cm^2)	3.26×10^{10}
ρ_{fl} (g/cm^3)	1.00
K_{fl} (dyn/cm^2)	2.25×10^{10}
η (g/cm·sec)	0.01
Λ (cm)	19.4×10^{-4}

Finally, noting the structure of the vectors u_0 and u_n, we identify the acoustic impedance for modal vibrations of the cylindrical surface inside the cavity, z_n, as the first element of the "**Z**" (impedance) matrix ([45]). Moreover, modal acoustic impedance can be expressed in terms of its resistive and reactive components as ([44])

$$z_n(\omega)=\overline{\rho}cr_n(\omega)-i\omega\overline{\rho}a_1m_n(\omega). \tag{38}$$

4 Numerical Results

In order to illustrate the nature and general behavior of the solution, we consider a numerical example in this section. Realizing the large number of parameters involved here, no attempt is made to exhaustively evaluate the effect of varying each of them. The intent of the collection of data presented here is merely to illustrate the kinds of results to be expected from some representative and physically realistic choices of values for these parameters. From these data some trends are noted and general conclusions made about the relative importance of certain parameters.

Accurate computation of cylindrical Bessel functions of complex argument is a challenging task. To achieve this, FORTRAN subroutines CBESH and CBESJ were first employed ([46]). The precision of calculated values were checked against MATLAB(5.3) specialized math functions "besselh" and "besselj," and also the printed tabulations in the handbook by Abramowitz and Stegun [43]. Performing computations over a wide range of (complex) arguments and (integer) orders on a Pentium personal computer, it was concluded that MATLAB results are more dependable especially for large arguments and high orders. Subsequently, a MATLAB code for computing $\mathbf{Z}=\mathbf{SR}^{-1}$ was constructed to calculate modal acoustic impedance values as functions of nondimensional frequency $ka_1=\omega a_1/c$. Accurate computations for derivatives of cylindrical Bessel functions of complex argument were accomplished by utilizing Eq. (9.1.27) in Ref. [43].

Noting the crowd of parameters that enter into the final expressions and keeping in view the availability of numerical data, we shall confine our attention to a particular model. Johnson et al. [47,48] reported the first instance in which all the input parameters necessary for a complete description of acoustic material properties within the context of Biot theory have been measured independently over the entire frequency spectrum. The input parameter values for water-saturated Ridgefield sandstone, which are used in the calculations, are compiled in Table 1.

Figures 2 and 3 each displays the inertial and the resistive components of the modal acoustic impedance, for a radii ratio of $a_2/a_1=20$ cm/10 cm, and 200 cm/100 cm, respectively, with open interface condition (i.e., $\kappa_s=\infty$) and basic material properties as given in Table 1. Here we note the high-frequency oscillations of modal impedance curves, which is due to boundary interference and rebeveration effects, as it is discussed in detail by Hasheminejad and Geers [49]. To assess the effects of interface condition, porosity, and frame stiffness on modal impedance re-

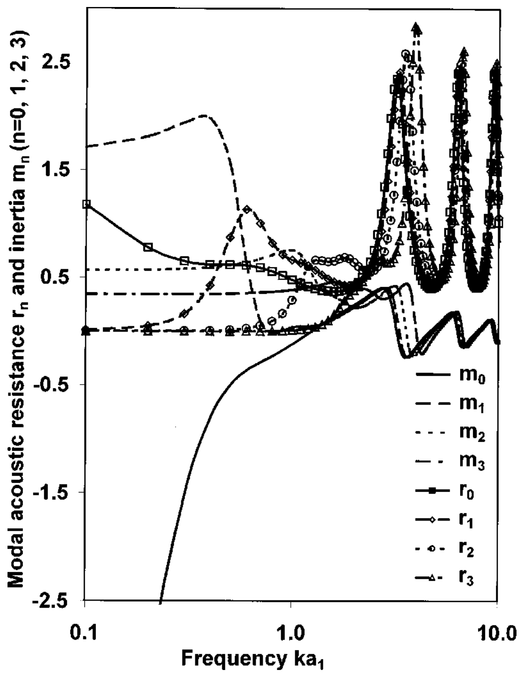

Fig. 2 Modal acoustic impedance curves (a_2/a_1 =20 cm/10 cm, $\kappa_s=\infty$)

sults, several computer program runs were made using various source and cavity sizes. It was concluded that the most pronounced overall effects occur for a radii ratio near unity (i.e., small gap size). Figures 4 to 6 display such effects for the selected radii ratio of $a_2/a_1=12.\text{cm}/10\,\text{cm}$.

In regard to the borehole condition, obviously the creation of a borehole may drastically change the properties of the surrounding medium in the vicinity of the well-hole wall. As most of the acoustic experimental techniques are highly sensitive to the permeability of the interface, it seems logical to investigate the effect

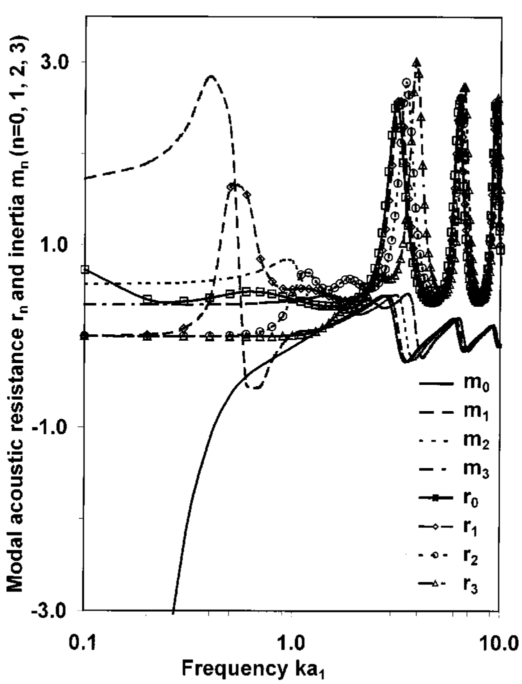

Fig. 3 Modal acoustic impedance curves (a_2/a_1 =200 cm/100 cm, $\kappa_s=\infty$)

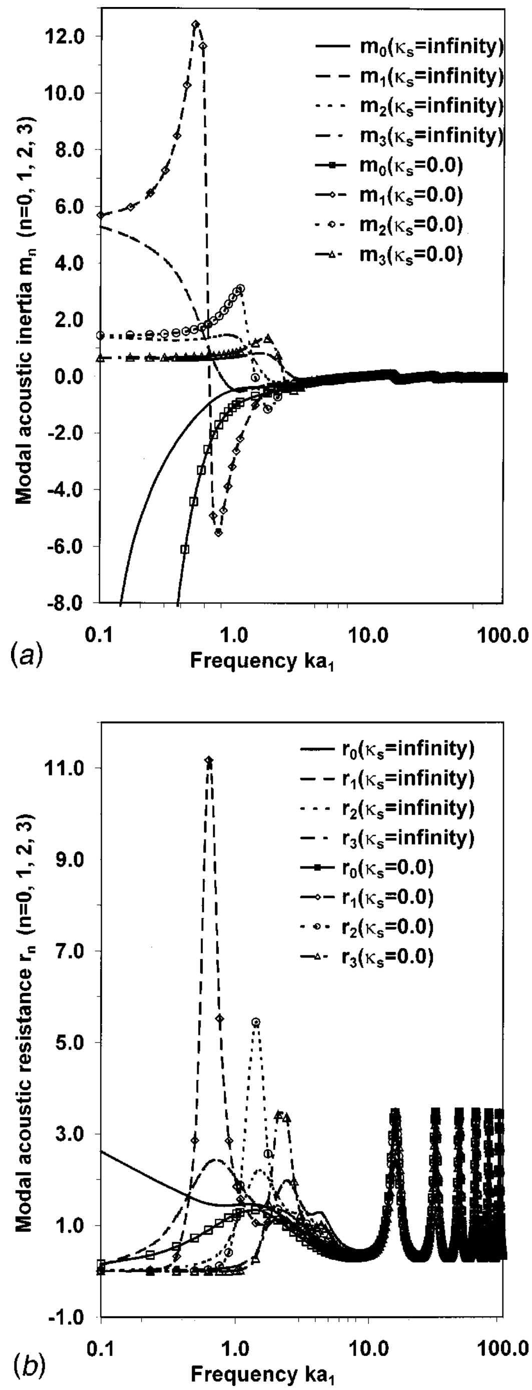

Fig. 4 (*a*) Effect of interface condition on modal acoustic reactance values (a_2/a_1=12 cm/10 cm); (*b*) effect of interface condition on modal acoustic resistance values (a_2/a_1 =12 cm/10 cm)

of an interface condition on radiation loading of the cylindrical source. This effect may be studied through the parameter $0\leq\kappa_s<\infty$, which, as explained before, characterizes the permeability of the interface. For simplicity we have only considered two limiting cases of $\kappa_s=\infty$ (fully open interface) and $\kappa_s=0$ (completely sealed interface). The relevant results are compared in Figs. 4(*a*) and 4(*b*). As expected, the modal impedance values increase as the quality of interconnection weakens. Note the extremely high reactance value obtained for the $n=0$ ("breathing") mode in the sealed interface case. In this instance, fluid exchange through the

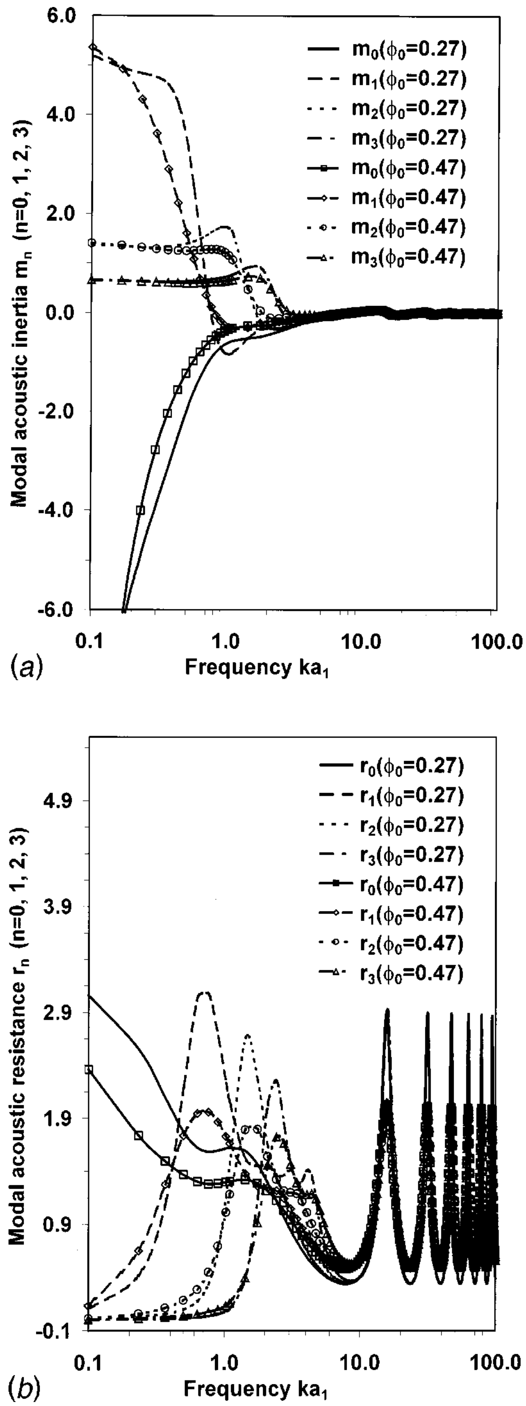

Fig. 5 (***a***) **Influence of porosity on modal acoustic reactance values** (a_2/a_1=**12 cm/10 cm,** $\kappa_s=\infty$)**;** (***b***) **influence of porosity on modal acoustic resistance values** (a_2/a_1=**12 cm/10 cm,** $\kappa_s=\infty$)

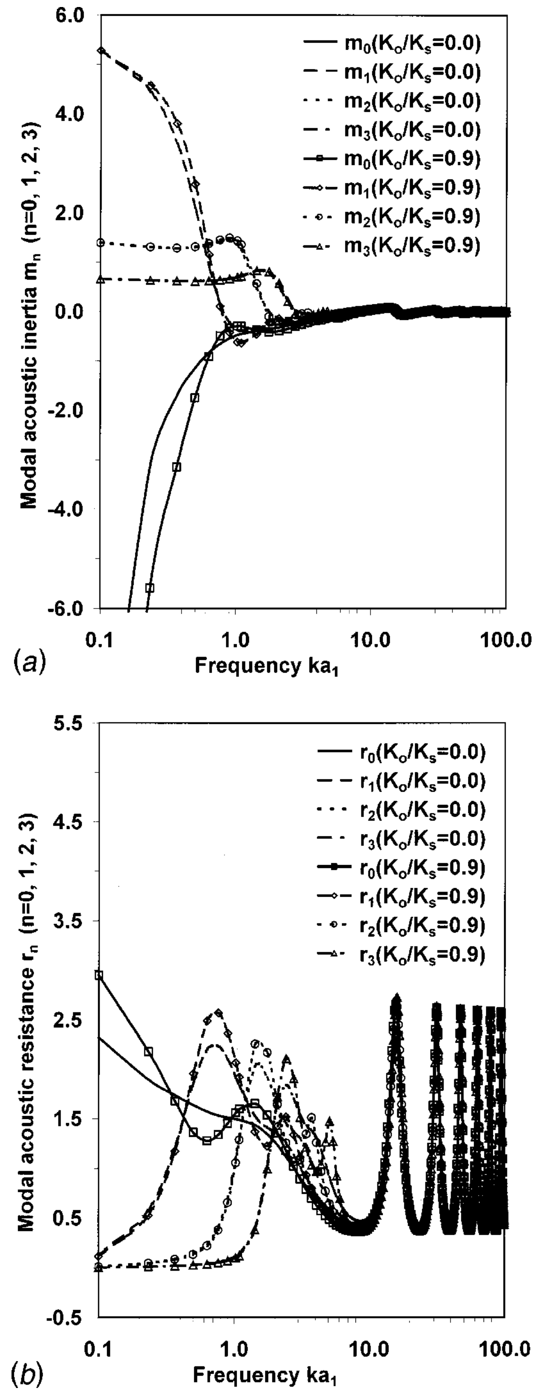

Fig. 6 (***a***) **Effect of frame stiffness on modal acoustic reactance values** (a_2/a_1=**12 cm/10 cm,** $\kappa_s=\infty$)**;** (***b***) **effect of frame stiffness on modal acoustic resistance values** (a_2/a_1=**12 cm/10 cm,** $\kappa_s=\infty$)

interface is impossible so we expect the Biot dissipation mechanism to become negligible as in the case of wave propagation in an infinite elastic medium.

The influence of porosity on modal impedance curves is shown in Figs. 5(a) and 5(b). For the reason of clarity only two porosity values are examined, namely $\phi_0=0.27$ and $\phi_0=0.47$. The related tortuosity and Λ values are obtained by scaling the experimental values given in Table 1 according to the following approximations:

$$\alpha\approx 1/\sqrt{\phi_0} \quad \text{(Berryman [50])}$$
$$\Lambda\approx\sqrt{8\alpha\kappa/\phi_0} \quad \text{(Allard [40])}. \tag{39}$$

Table 2 displays the input parameter values for α, and Λ which are utilized in numerical computations. The main outcome is the increase in impedance values as the porosity (tortuosity) decreases (increases). This result is readily conceivable, since as the porosity decreases (tortuosity increases) we anticipate higher force opposing modal vibrations of the cylindrical surface inside the cavity.

Table 2 Estimated values for tortousity, characteristic viscous length, and frequency. (Note: values listed in the first row are experimental, taken from Table 1.)

ϕ_0	α	Λ	ω_c
0.37	1.58	19.4×10^{-4}	8.36×10^{3}
0.27	1.85	24.7×10^{-4}	5.18×10^{3}
0.47	1.40	16.2×10^{-4}	12.02×10^{3}

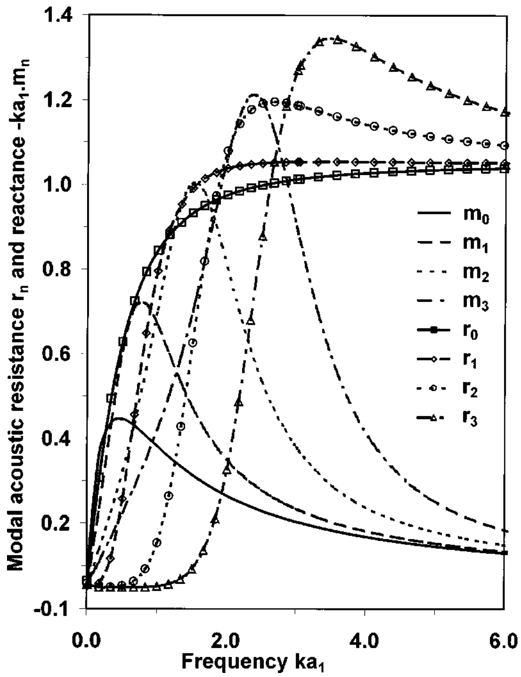

Fig. 7 Modal impedance curves for the "all-fluid" medium approximation ($a_2/a_1=12$ cm/10 cm, $\kappa_s=\infty$, $\phi_0=\alpha=1$, $K_0=\mu=\eta=0$)

Figures 6(*a*) and 6(*b*) analyze the effect of frame stiffness by considering two K_o/K_s ratios, namely $K_o/K_s\cong0$ and $K_o/K_s=0.9$. Increasing K_o/K_s at constant porosity corresponds to the existence of increasingly finer pore channels. Here as the frame stiffens, the opposing acoustic force grows which is the precisely expected outcome as displayed in the figures. Finally, to check the overall validity of our work we consider the "all-fluid" surrounding medium case ([16]), i.e., we make the computations for $\phi_0=\alpha=1$, and $K_0=\mu=\eta\cong0$ as shown in Fig. 7. Evidently, our results reduce to those for modal vibrations of a cylindrical surface in an ideal infinite acoustic fluid (e.g., Fig. 21.4, p. 437, Ref. [51]). This simply implies that when there is no impedance mismatch at the interface, we get no wave reflections (interference) from the borehole boundary.

Clearly the overall displayed trends are somewhat anticipated. The most surprising observation is the general low-frequency behavior of $n=0$ (breathing mode) modal acoustic resistance curves. Inasmuch as acoustic resistance is directly proportional to the radiated power, the notable low-frequency $r_0(\omega)$ values simply imply that the pulsating cylindrical source (i.e., the expander type acoustic device) is expected to be an efficient sound projector even in the low-frequency range for the studied configuration.

5 Conclusions

Modal acoustic impedance curves have been generated for a cylindrical radiator in a fluid-filled cylindrical cavity embedded within a fluid-infiltrated unbounded poroelastic medium. These curves are the product of an exact treatment of the fluid/structure interaction that involves utilizing Biot's dynamic model and the appropriate boundary conditions of poroelasticity. The numerical results reveal the important effects of the interface condition, porosity (tortuosity), and frame stiffness on the computed modal acoustic impedance values. They also show that for the given arrangement the pulsating (expander-type) cylindrical source is expected to be an efficient sound projector even at the low-frequency limit. The presented formulation can lead to a better understanding of dynamic response of downhole sources (acoustic logging tools) which are commonly applied in seismic prospecting. Moreover, the proposed model is equally applicable in noise control engineering situations in which the surrounding medium consists of rigid (elastic) frame porous materials. Therefore it is hoped that this work may initiate further studies, both theoretical and observational, in the acoustics of fluid-saturated porous media.

Acknowledgments

The authors wish to sincerely thank Profs. G. Degrande, O. Kelder, M. Kaczmarek, J. Dvorkin, J. S. Bolton, D. L. Johnson, J. F. Allard, J. L. Auriault, M. D. Sharma, and P. N. J. Rasolofosaon for valuable and productive consultations on the Biot dynamic theory of poroelasticity. They are also indebted to Dr. D. E. Amos at Sandia National Laboratories, Albuquerque, NM, for providing FORTRAN subroutines for computation of cylindrical Bessel functions of complex arguments and non-negative order.

References

[1] Gassmann, F., 1951, "Uber die elastizitat poroser medien," Vieteljahrsschrift d Naturforsch. Gesell. Zurich, **96**, pp. 1–23.
[2] Biot, M. A., 1956, "Theory of Propagation of Elastic Waves in a Fluid-Saturated Porous Solid, I: Low-Frequency Range," J. Acoust. Soc. Am., **28**, pp. 168–178.
[3] Biot, M. A., 1956, "Theory of Propagation of Elastic Waves in a Fluid-Saturated Porous Solid, II: Higher Frequency Range," J. Acoust. Soc. Am., **28**, pp. 179–191.
[4] Biot, M. A., 1962, "Mechanics of Deformation and Acoustic Propagation in Porous Media," J. Appl. Phys., **23**, pp. 1482–1498.
[5] White, J. E., 1983, *Underground Sound: Application of Seismic Waves*, Elsevier, Amsterdam.
[6] Plona, T. J., 1980, "Observation of the Second Compressional Wave in a Porous Medium at Ultrasonic Frequencies," Appl. Phys. Lett., **36**, pp. 259–261.
[7] Berryman, J. G., 1980, "Confirmation of Biot's Theory," Appl. Phys. Lett., **73**, pp. 382–384.
[8] Burridge, R., and Keller, J. B., 1981, "Poroelasticity Equations Derived From Microstructure," J. Acoust. Soc. Am., **70**, p. 1140.
[9] Van der Grinten, J. G. M., Van Dongen, M. E. H., and Van der Kogel, H., 1985, "A Hock-Tube Technique for Studying Pore-Pressure Propagation in a Dry and Water-Saturated Porous Medium," J. Appl. Phys., **58**, pp. 2937–2942.
[10] Van der Grinten, J. G. M., Van Dongen, M. E. H., and Van der Kogel, H., 1987, "Strain and Pore Pressure Propagation in a Water-Saturated Porous Medium," J. Appl. Phys., **62**, pp. 4682–4687.
[11] Rasolofosaon, P. N. J., 1988, "Importance of the Interface Hydraulic Condition on Generation of Second Bulk Compressional Wave in Porous Media," Appl. Phys. Lett., **52**, pp. 780–782.
[12] Kelder, O., and Smeulders, D. M. J., 1995, "Propagation and Damping of Compressional Waves in Porous Rocks: Theory and Experiments," *Ann. Internat. Mtg., 64th Annual Meeting*, Society of Exploration Geophysicists, expanded abstracts, pp. 675–678.
[13] Kelder, O., and Smeulders, D. M. J., 1997, "Observation of the Biot Slow Wave in Water-Saturated Nivelsteiner Sandstone," Geophysics, **62**, pp. 1794–1796.
[14] Gurevich, B., Kelder, O., and Smeulders, D. M. J., 1999, "Validation of the Slow Compressional Wave in Porous Media: Comparison of Experiments and Numerical Simulations," Transp. Porous Media, **36**, pp. 149–160.
[15] Deresiewicz, H., and Skalak, R., 1963, "On Uniqueness in Dynamic Poroelasticity," Bull. Seismol. Soc. Am., **53**, pp. 783–788.
[16] Bourbie, T., Coussy, O., and Zinszner, B. E., 1987, *Acoustics of Porous Media*, Gulf Publishing, Houston.
[17] Mei, C. C., and Si, B. I., 1984, "Scattering of Simple Harmonic Waves by a Circular Cavity in a Fluid-Infiltrated Poro-elastic Medium," Wave Motion, **6**, pp. 265–278.
[18] Berryman, J. G., 1985, "Scattering by a Spherical Inhomogeneity in a Fluid-Saturated Porous Medium," J. Math. Phys., **26**, pp. 1408–1419.
[19] Zimmerman, C., 1993, "Scattering of Plane Compressional Waves by a

Spherical Inclusions in a Poroelastic Medium,'' J. Acoust. Soc. Am., **94**, pp. 527–536.
[20] Zimmerman, C., and Stern, M., 1994, ''Analytical Solutions for Harmonic Wave Propagation in Poroelastic Media,'' J. Eng. Mech., **120**, pp. 2154–2178.
[21] Kargl, S. G., and Lim, R., 1993, ''A Transition-Matrix Formulation of Scattering in Homogeneous, Saturated, Porous Media,'' J. Acoust. Soc. Am., **94**, pp. 1527–1550.
[22] Lim, R., 1993, ''Scattering by a Layered Poroelastic Obstacle Embedded in a Poroelastic Host,'' *ASA 126th Meeting*, Denver, Acoustical Society of America, pp. 160–175.
[23] Lim, R., 1994, ''Scattering by an Obstacle in a Plane-Startified Poroelastic Medium: Application to an Obstacle in Ocean Sediments,'' J. Acoust. Soc. Am., **95**, pp. 1223–1244.
[24] Gurevich, B., Sadovnichaja, A. P., Lopatnikov, S. L., and Shapiro, S. A., 1998, ''Scattering of a Compressional Wave in a Poroelastic Medium by an Ellipsoidal Inclusion,'' Geophys. J. Int., **133**, pp. 91–103.
[25] Senjuntichai, T., and Rajapakse, R. K. D., 1993, ''Transient Response of a Circular Cavity in a Poroelastic Medium,'' Int. J. Numer. Analyt. Meth. Geomech., **17**, pp. 357–383.
[26] Qi, Q., and Geers, T. L., 1997, ''Doubly Asymptotic Approximations for Transient Poroelastodynamics,'' J. Acoust. Soc. Am., **102**, pp. 1361–1371.
[27] Hasheminejad, M., 1998, ''Modal Impedances for a Spherical Source in a Fluid-Filled Spherical Cavity Embedded Within a Fluid-Infiltrated Elastic Porous Medium,'' Int. J. Solids Struct., **35**, pp. 129–148.
[28] Hasheminejad, M., 2001, ''Modal Acoustic Force on a Spherical Radiator in an Acoustic Half-Space With Locally Reacting Boundary,'' Acta Acust. (Beijing), Acta Acustica/Acustica, to appear.
[29] Stinson, M. R., 1995, ''A Note on the Use of an Approximate Formula to Predict Sound Fields Above an Impedance Plane due to a Point Source,'' J. Acoust. Soc. Am., **98**, pp. 1810–1812.
[30] Li, K. M., Taherzadeh, S., and Attenborough, K., 1997, ''Sound Propagation From a Dipole Source Near an Impedance Plane,'' J. Acoust. Soc. Am., **101**, pp. 3343–3352.
[31] Li, K. M., and Taherzadeh, S., 1997, ''The Sound Field of an Arbitrarily Oriented Quadrupole Near Ground Surface,'' J. Acoust. Soc. Am., **102**, pp. 2050–2057.
[32] Attenborough, K., and Richards, T. L., 1989, ''Solid Particle Motion Induced by a Point Source Above a Poroelastic Half-Space,'' J. Acoust. Soc. Am., **86**, pp. 1085–1092.
[33] Richards, T. L., Attenborough, K., Heap, N. W., and Watson, A. P., 1985, ''Penetration of Sound From a Point Source Into a Rigid Porous Medium,'' J. Acoust. Soc. Am., **78**, pp. 956–963.
[34] Tooms, S., Taherzadeh, S., and Attenborough, K., 1993, ''Sound Propagation in a Refracting Fluid Above a Layered Fluid-Saturated Porous Elastic Material,'' J. Acoust. Soc. Am., **93**, pp. 173–181.
[35] Sabatier, J. M., Bass, H. E., Bolen, L. N., Attenborough, K., and Sastry, V. V. S. S., 1986, ''The Interaction of Airborne Sound With the Porous Ground: The Theoretical Formulation,'' J. Acoust. Soc. Am., **79**, pp. 1345–1352.
[36] Hu, Z., and Bolton, J. S., 1994, ''Sound Propagation From an Arbitrary Oriented Multipole Placed Near a Plane, Finite Impedance Surface,'' J. Sound Vib., **170**, pp. 637–699.
[37] White, J. E., 1984, ''Radiation From a Borehole,'' Colo. School Mines Q., **2**, pp. 46–50.
[38] Poterasu, V. F., 1993, ''Coupled Vibrations of a Cavity Filled With a Pulsating Fluid in Elastic Infinite Media by the Boundary Element Method,'' Comput. Methods Appl. Mech. Eng., **106**, pp. 285–296.
[39] Zwikker, C., and Kosten, C. W., 1949, *Sound Absorbing Materials*, Elsevier, Amsterdam.
[40] Allard, J. F., 1993, *Propagation of Sound in Porous Media, Modelling Sound Absorbing Materials*, Elsevier Applied Science, London.
[41] Johnson, D. L., Koplik, J., and Dashen, R., 1987, ''Theory of Dynamic Permeability and Tortuosity in Fluid-Saturated Porous Media,'' J. Fluid Mech., **76**, pp. 379–402.
[42] Achenbach, J. D., 1976, *Wave Propagation in Elastic Solids*, North-Holland, New York.
[43] Abramovitz, M., and Stegun, I. A., 1964, *Handbook of Mathematical Functions*, National Bureau of Standards, Washington, DC.
[44] Junger, M. C., and Feit, D., 1972, *Sound, Structures, and Their Interaction*, M. I. T. Press, Cambridge, MA.
[45] Hasheminejad, M., and Geers, T. L., 1993, ''Modal Impedances for Two Spheres in a Thermoviscous Fluid,'' J. Acoust. Soc. Am., **94**, pp. 2205–2214.
[46] Amos, D. E., 1986, ''A Portable Package for Bessel Functions of Complex Argument and Non-negative Order,'' Trans. Math. Software, **97**, pp. 121–133.
[47] Johnson, D. L., Hemmick, D. L., and Kojima, H., 1994, ''Probing Porous Media With First and Second Sound, I. Dynamic Permeability,'' J. Appl. Phys., **76**, pp. 104–114.
[48] Johnson, D. L., Plona, T. J., and Kojima, H., 1994, ''Probing Porous Media With First and Second Sound, II. Acoustic Properties of Water-Saturated Porous Media,'' J. Appl. Phys., **76**, pp. 115–125.
[49] Hasheminejad, M., and Geers, T. L., 1992, ''The Accuracy of Doubly Asymptotic Approximations for an Acoustic Half-Space,'' ASME J. Vibr. Acoust., **114**, pp. 555–563.
[50] Berryman, J. G., 1982, ''Elastic Waves in Fluid-Saturated Porous Media,'' *Macroscopic Properties of Disordered Media* (Lecture Notes in Physics, 154), R. Burridge, et al., eds., Springer-Verlag, Berlin, pp. 39–49.
[51] Skudrzyk, E., 1971, *The Foundations of Acoustics*, Springer-Verlag, New York.

Buckling of Laminated Composite Rectangular Plates Under Transient Thermal Loading

K. K. Shukla
Applied Mechanics Department,
M.N.R. Engineering College,
Allahabad 211004, India

Y. Nath
Applied Mechanics Department,
I.T.T.,
Delhi 110016, India

This paper deals with the nonlinear dynamic buckling of laminated composite rectangular plates subjected to uniform time-dependent in-plane temperature-induced loading. The dynamic post-buckling deflection response is obtained and dynamic critical temperatures are estimated. The nonlinear governing equations of motion are solved analytically using fast Chebyshev series technique. The numerical results for CCCC, CCCS, CCSS, CSCS, CSSS and SSSS boundary conditions are presented. [DOI: 10.1115/1.1485755]

1 Introduction

The structural elements of certain advanced engineering structures are subjected to a periodic, intense thermal input, which generates a high level of structural vibrations and instability. Large stresses due to dynamic instability lead to structural failure. Thermal buckling problems of laminated composite structures have been the interest of the researchers for the last several years. A majority of the published literature is concerned with time-independent temperature fields and application of numerical approaches. The dynamic instability behavior of composite laminates subjected to harmonically varying uniform mechanical edge loading has been investigated by several researchers (Bert and Birman [1], Moorthy and Reddy [2] Ganapathi et al. [3], and Liao and Cheng [4]) and still has an interest. A review of the literature reveals that the nonlinear transient response and post-buckling of laminated composite plates under transient thermal loading have received little attention.

Nonlinear random response of antisymmetric angle-ply laminated composite rectangular plates subjected to thermal and acoustic loads was investigated by Locke [5]. He used a single-mode Galerkin approach in conjunction with the method of equivalent linearization. Abbas et al. [6] carried out nonlinear flutter analysis of an orthotropic composite panel under aerodynamic heating. They estimated the nonlinear dynamic deflection for different aerodynamic pressures and obtained the Poincare sections. Lee and Lee [7] studied the vibration behavior of thermally post-buckled anisotropic plates, using the finite element method. Their model was based on the first-order shear deformation theory and von Karman strain displacement relations. They investigated the effects of fiber orientation angle and aspect ratio on the post-buckling and vibration behaviors for a simply supported laminated plate subjected to steady-state in-plane uniform temperature field. The geometrically nonlinear supersonic flutter characteristics of laminated composite thin plate structures subjected to thermal loads were investigated by Liaw [8], using a 48-degree-of-freedom rectangular laminated thin finite element. The influence of the amplitude of vibration on the dynamic stability regions of composite laminates exposed to temperature field was carried out by Ganapathy and Touratier [9] using the finite element method. They evaluated the instability boundaries from the nonlinear governing equations using a direct iteration technique. Tylikowaski and Hetnarski [10] presented an investigation of dynamic stability for linear elastic structures due to nonuniform time and space-dependent stochastic temperature field. They used the Liapunov method for solving the stability problems of laminated plates. Librescu and Souza [11] investigated the effects of nonlinearities on the dynamics of orthogonal stiffened simply supported flat panels having initial geometric imperfections and subjected to lateral pressure and uniform temperature field through thickness.

In the present study, the nonlinear dynamic analysis of laminated composite plates subjected to uniform in-plane temperature is carried out using Chebyshev series (Fox and Parker [12]) and the Houbolt time marching technique (Houbolt [13]). An iterative incremental approach (Shukla and Nath [14]) is used for the solution. The dynamic post-buckling temperature-deflection response is obtained and the dynamic critical temperatures are estimated. Discontinuous jump in the characteristics parameter (central deflection) or the point of inflexion of the maximum displacement response or convergence failure in 300 iterations due to a small increment in the marching variable (load) is adopted as a criteria for the estimation of buckling load (Budiansky and Roth [15], Stephens and Fulton [16], and Jain and Nath [17]).

2 Formulation

Perfect bonding between the orthotropic layers and temperature-independent mechanical and thermal properties are assumed. The displacement field at a point in the laminate shown in Fig. 1 is expressed as

$$\begin{aligned} U(X,Y,Z,t) &= u_0(X,Y,t) + z\psi_x(X,Y,t) \\ V(X,Y,Z,t) &= v_0(X,Y,t) + z\psi_y(X,Y,t) \\ W(X,Y,Z,t) &= w_0(X,Y,t) \end{aligned} \tag{1}$$

where u_0, v_0, and w_0 are displacements at a point on the mid-plane of the plate. ψ_x, ψ_y are rotations of xz and yz-plane, respectively.

The strain-displacement relations due to von karman-type nonlinearity become

$$\begin{Bmatrix} \varepsilon_X \\ \varepsilon_Y \\ \gamma_{XY} \\ \gamma_{XZ} \\ \gamma_{YZ} \end{Bmatrix} = \begin{Bmatrix} u_{0,X} + \dfrac{1}{2}(w_{0,X})^2 \\ v_{0,Y} + \dfrac{1}{2}(w_{0,Y})^2 \\ u_{0,Y} + v_{0,X} + w_{0,X}w_{0,Y} \\ w_{0,X} + \psi_X \\ w_{0,Y} + \psi_Y \end{Bmatrix} + z\begin{Bmatrix} \psi_{X,X} \\ \psi_{Y,Y} \\ \psi_{X,Y} + \psi_{Y,X} \\ 0 \\ 0 \end{Bmatrix}. \tag{2}$$

Contributed by the Applied Mechanics Division of THE AMERICAN SOCIETY OF MECHANICAL ENGINEERS for publication in the ASME JOURNAL OF APPLIED MECHANICS. Manuscript received by the ASME Applied Mechanics Division, February 1, 2001; final revision, November 15, 2001. Associate Editor: R. C. Benson. Discussion on the paper should be addressed to the Editor, Prof. Robert M. McMeeking, Department of Mechanical and Environmental Engineering University of California–Santa Barbara, Santa Barbara, CA 93106-5070, and will be accepted until four months after final publication of the paper itself in the ASME JOURNAL OF APPLIED MECHANICS.

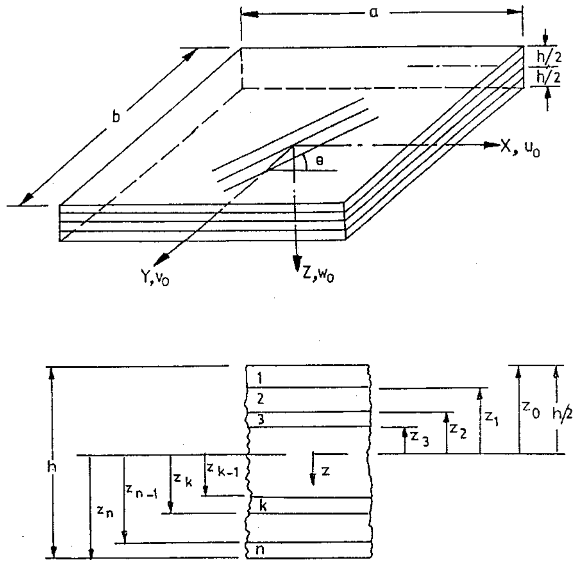

Fig. 1 Geometry of laminated plate

The stress and moment resultants of laminated composite rectangular plates having n layers of orthotropic lamina, subjected to thermal loading due to uniform in-plane temperature can be expressed as

$$\begin{Bmatrix} N_X \\ N_Y \\ N_{XY} \\ M_X \\ M_Y \\ M_{XY} \end{Bmatrix} = \begin{bmatrix} A_{11} & A_{12} & A_{16} & B_{11} & B_{12} & B_{16} \\ A_{12} & A_{22} & A_{26} & B_{12} & B_{22} & B_{26} \\ A_{16} & A_{26} & A_{66} & B_{16} & B_{26} & B_{66} \\ B_{11} & B_{12} & B_{16} & D_{11} & D_{12} & D_{16} \\ B_{12} & B_{22} & B_{26} & D_{12} & D_{22} & D_{26} \\ B_{16} & B_{26} & B_{66} & D_{16} & D_{26} & D_{66} \end{bmatrix}$$
$$\times \begin{Bmatrix} u_{0,X}+\frac{1}{2}(w_{0,X})^2 \\ v_{0,Y}+\frac{1}{2}(w_{0,Y})^2 \\ u_{0,Y}+v_{0,x}+w_{0,X}w_{0,Y} \\ \psi_{X,X} \\ \psi_{Y,Y} \\ \psi_{X,Y}+\psi_{Y,X} \end{Bmatrix} - \begin{Bmatrix} N_X^T \\ N_Y^T \\ N_{XY}^T \\ M_X^T \\ M_Y^T \\ M_{XY}^T \end{Bmatrix} \tag{3}$$

$$\begin{Bmatrix} Q_Y \\ Q_X \end{Bmatrix} = \begin{bmatrix} A_{44} & A_{45} \\ A_{45} & A_{55} \end{bmatrix} \begin{Bmatrix} \gamma_{YZ} \\ \gamma_{XZ} \end{Bmatrix}. \tag{4}$$

Thermal force and moment resultants are

$$\begin{Bmatrix} N_x^T, M_x^T \\ N_y^T, M_y^T \\ N_{xy}^T, M_{xy}^T \end{Bmatrix} = \sum_{k=1}^{n} \int_{z_{k-1}}^{z_k} \begin{bmatrix} \bar{Q}_{11} & \bar{Q}_{12} & \bar{Q}_{16} \\ \bar{Q}_{12} & \bar{Q}_{22} & \bar{Q}_{26} \\ \bar{Q}_{16} & \bar{Q}_{26} & \bar{Q}_{66} \end{bmatrix}_k \begin{Bmatrix} \alpha_x \\ \alpha_y \\ \alpha_{xy} \end{Bmatrix}_k \times \Delta T(t)(1,z)dz \tag{5}$$

where ΔT = applied temperature − reference temperature.

The laminate stiffness coefficients (A_{ij}, B_{ij}, D_{ij}) defined in terms of the reduced stiffness coefficients $(\bar{Q}_{ij})_k$ for the layers $k = 1,2,\text{—}n$ (Jones [18]) are

$$(A_{ij},\ B_{ij},\ D_{ij}) = \sum_{k=1}^{n} \int_{z_{k-1}}^{z_k} (1,z,z^2)(\bar{Q}_{ij})_k\ dz \qquad (i,j=1,2,6) \tag{6}$$

$$A_{ij} = \sum_{k=1}^{n} k_i k_j \int_{z_{k-1}}^{z_k} (\bar{Q}_{ij})_k\ dz \qquad (i,j=4,5) \tag{7}$$

where $k_4^2 = 5/6$, $k_5^2 = 5/6$ are shear correction factors (Whitney [19]).

Neglecting the body forces and surface shearing forces, the equations of motion along with the admissible domain conditions can be derived using Hamilton's principle.

The equations of motion (Yang, Norris, and Stavsky [20]) are

$$N_{X,X} + N_{XY,Y} = Ru_{0,u} + S\psi_{X,u} \tag{8}$$

$$N_{XY,X} + N_{Y,Y} = Rv_{0,tt} + S\psi_{Y,tt} \tag{9}$$

$$Q_{X,X} + Q_{Y,Y} + \mathfrak{R}(N_i, w) + q = Rw_{0,tt} \tag{10}$$

$$M_{X,X} + M_{XY,Y} - Q_X = Su_{0,tt} + I\psi_{X,tt} \tag{11}$$

$$M_{XY,X} + M_{Y,Y} - Q_Y = Sv_{0,tt} + I\psi_{Y,tt} \tag{12}$$

where in-plane (R), coupled normal-rotary (S), and rotary (I) inertia are

$$(R,S,I) = \int_{-h/2}^{h/2} \rho(1,z,z^2)dz = \sum_{k=1}^{n} \int_{z_{k-1}}^{z_k} \rho^{(k)}(1,z,z^2)dz. \tag{13}$$

The nonlinear operator in Eq. (10) is

$$\mathfrak{R} = \frac{\partial}{\partial x}\left(N_X \frac{\partial w}{\partial X}\right) + \frac{\partial}{\partial Y}\left(N_{XY}\frac{\partial w}{\partial X}\right) + \frac{\partial}{\partial X}\left(N_{XY}\frac{\partial w}{\partial Y}\right) + \frac{\partial}{\partial Y}\left(N_Y \frac{\partial w}{\partial Y}\right). \tag{14}$$

Substituting Eqs. (2)–(7) in the equations of motion (8)–(12), the governing differential equations are transformed in terms of the displacement components and are expressed in nondimensional form as

$$L_1u_{,xx} + L_2u_{,yy} + L_3u_{,xy} + L_4v_{,xx} + L_5v_{,yy} + L_6v_{,xy} + L_7\psi_{x,xx} + L_8\psi_{x,yy} + L_9\psi_{x,xy} + L_{10}\psi_{y,xx} + L_{11}\psi_{y,yy} + L_{12}\psi_{y,xy}$$
$$+ (L_{13}w_{,xx} + L_{14}w_{,yy} + L_{15}w_{,xy})w_{,x} + (L_{16}w_{,xx} + L_{17}w_{,yy} + L_{18}w_{,xy})w_{,y} - L_{19}\bar{N}_{x,x}^T - L_{20}\bar{N}_{xy,y}^T = R_1u_{,\tau\tau} + R_2\psi_{x,\tau\tau} \tag{15}$$

$$L_{21}u_{,xx} + L_{22}u_{,yy} + L_{23}u_{,xy} + L_{24}v_{,xx} + L_{25}v_{,yy} + L_{26}v_{,xy} + L_{27}\psi_{x,xx} + L_{28}\psi_{x,yy} + L_{29}\psi_{x,xy} + L_{30}\psi_{y,xx} + L_{31}\psi_{y,yy} + L_{32}\psi_{y,xy}$$
$$+ (L_{33}w,_{xx} + L_{34}w,_{yy} + L_{35}w,_{xy})w,_x + (L_{36}w,_{xx} + L_{37}w,_{yy} + L_{38}w,_{xy})w,_y - L_{39}\bar{N}_{xy,x}^T - L_{40}\bar{N}_{y,y}^T = R_3v,_{\tau\tau} + R_4\psi_{y,\tau\tau} \tag{16}$$

$$L_{41}w,_{xx}+L_{42}w,_{yy}+L_{43}w,_{xy}+L_{44}\psi_{x,x}+L_{45}\psi_{x,y}+L_{46}\psi_{y,x}+L_{47}\psi_{y,y}+(L_{48}u,_x+L_{49}u,_y+L_{50}v,_x+L_{51}v,_y+L_{52}\psi_{x,x}+L_{53}\psi_{x,y}$$
$$+L_{54}\psi_{y,x}+L_{55}\psi_{y,y})w,_{xx}+(L_{56}u,_x+L_{57}u,_y+L_{58}v,_x+L_{59}v,_y+L_{60}\psi_{x,x}+L_{61}\psi_{x,y}+L_{62}\psi_{y,x}+L_{63}\psi_{y,y})w,_{yy}$$
$$+(L_{64}u,_x+L_{65}u,_y+L_{66}v,_x+L_{67}v,_y+L_{68}\psi_{x,x}+L_{69}\psi_{x,y}+L_{70}\psi_{y,x}+L_{71}\psi_{y,y})w,_{xy}+(L_{72}w,_{xx}+L_{73}w,_{yy}+L_{74}w,_{xy})(w,_x)^2$$
$$+(L_{75}w,_{xx}+L_{76}w,_{yy}+L_{77}w,_{xy})(w,_y)^2+(L_{78}w,_{xx}+L_{79}w,_{yy}+L_{80}w,_{xy})w,_xw,_y+(L_{81}u,_{\tau\tau}+L_{82}\psi_{x,\tau\tau})w,_x$$
$$+(L_{83}v,_{\tau\tau}+L_{84}\psi_{y,\tau\tau})w,_y-L_{85}\bar{N}_x^Tw,_{xx}-L_{86}\bar{N}_y^Tw,_{yy}-L_{87}\bar{N}_{xy}^Tw,_{xy}+q^*=R_5w,_{\tau\tau} \tag{17}$$

$$L_{88}u,_{xx}+L_{89}u,_{yy}+L_{90}u,_{xy}+L_{91}v,_{xx}+L_{92}v,_{yy}+L_{93}v,_{xy}+L_{94}\psi_{x,xx}+L_{95}\psi_{x,yy}+L_{96}\psi_{x,xy}+L_{97}\psi_{y,xx}+L_{98}\psi_{y,yy}+L_{99}\psi_{y,xy}$$
$$+L_{100}w,_x+L_{101}w,_y+L_{102}\psi_x+L_{103}\psi_y+(L_{104}w,_{xx}+L_{105}w,_{yy}+L_{106}w,_{xy})w,_x+(L_{107}w,_{xx}+L_{108}w,_{yy}+L_{109}w,_{xy})w,_y$$
$$-L_{110}\bar{M}_{x,x}^T-L_{111}\bar{M}_{xy,y}^T=R_6u,_{\tau\tau}+R_7\psi_{x,\tau\tau} \tag{18}$$

$$L_{112}u,_{xx}+L_{113}u,_{yy}+L_{114}u,_{xy}+L_{115}v,_{xx}+L_{116}v,_{yy}+L_{117}v,_{xy}+L_{118}\psi_{x,xx}+L_{119}\psi_{x,yy}+L_{120}\psi_{x,xy}+L_{121}\psi_{y,xx}+L_{122}\psi_{y,yy}$$
$$+L_{123}\psi_{y,xy}+L_{124}w,_x+L_{125}\psi,_y+L_{126}\psi_x+L_{127}\psi_y+(L_{128}w,_{xx}+L_{129}w,_{yy}+L_{130}w,_{xy})w,_x$$
$$+(L_{131}w,_{xx}+L_{132}w,_{yy}+L_{133}w,_{xy})w,_y-L_{134}\bar{M}_{xy,x}^T-L_{135}\bar{M}_{y,y}^T=R_8v,_{\tau\tau}+R_9\psi_{y,\tau\tau}. \tag{19}$$

The nondimensional parameters, $L_1,\ L_2,\ \ldots$ and $R_1,\ R_2\ \ldots$ and nondimensional time τ are given in the Appendix.

Boundary Conditions.

(a) simple supported (S):

$$u,N_{xy},w,M_x,\psi_y=0 \quad \text{at} \quad x=-1 \quad \text{and} \quad 1$$

$$N_{xy},v,w,\psi_x,M_y=0 \quad \text{at} \quad y=-1 \quad \text{and} \quad 1$$

(b) clamped (C):

$$u,N_{xy},w,\psi_x,\psi_y=0 \quad \text{at} \quad x=-1 \quad \text{and} \quad 1$$

$$N_{xy},v,w,\psi_x,\psi_y=0 \quad \text{and} \quad y=-1 \quad \text{and} \quad 1$$

3 Method of Solution

A general function $\phi(x,y)$ can be approximated in the space domain by the finite degree double Chebyshev polynomial (Fox and Parker [12]) as

$$\phi(x,y)=\delta\sum_{i=0}^{M}\sum_{j=0}^{N}\phi_{ij}T_i(x)T_j(y) \tag{20}$$

where

$$\delta=\frac{1}{4} \quad \text{if} \quad i=0 \quad \text{and} \quad j=0$$

$$\delta=\frac{1}{2} \quad \text{if} \quad i=0 \quad \text{and} \quad j\neq 0 \quad \text{or} \quad i\neq 0 \quad \text{and} \quad j=0$$

$$\delta=1 \quad \text{otherwise.}$$

The spatial derivative of a general function $\phi(x,y)$ can be expressed as

$$\phi_{,xy}^{rs}=\delta\sum_{i=0}^{M-r}\sum_{j=0}^{N-s}\phi_{ij}^{rs}T_i(x)T_j(y) \tag{21}$$

Here, r and s are the order of derivatives with respect to x and y, respectively.

The derivative function ϕ_{ij}^{rs} is evaluated, using the recurrence relations given by Fox and Parker [12]

$$\begin{aligned}\phi_{(i-1)j}^{rs}&=\phi_{(i+1)j}^{rs}+2i\,\phi_{ij}^{(r-1)s}\\ \phi_{i(j-1)}^{rs}&=\phi_{i(j+1)}^{rs}+2j\,\phi_{ij}^{r(s-1)}.\end{aligned} \tag{22}$$

The nonlinear terms are linearized at any step-marching variable using the quadratic extrapolation technique. A typical nonlinear function G at step J is expressed as

$$G_j=\left[\delta\sum_{i=0}^{M-r}\sum_{j=0}^{N}\phi_{ij}^{r}T_i(x)T_j(y)\right]_j*\left[\delta\sum_{i=0}^{M}\sum_{j=0}^{N-s}\phi_{ij}^{s}T_i(x)T_j(y)\right]_J \tag{23}$$

where

$$(\phi_{ij})_J=A(\phi_{ij})_{J-1}+B(\phi_{ij})_{J-2}+C(\phi_{ij})_{J-3}. \tag{24}$$

During initial steps-marching variables, the coefficients A, B, C of the quadratic extrapolation scheme of linearization (Nath and Sandeep [21]) take the following values:

$$1,0,0 \quad (J=1); \quad 2,-1,0\,(J=2); \quad 3,-3,1 \quad (J\geqslant 3).$$

The product of two Chebyshev polynomials is expressed as

$$\begin{aligned}T_i(x)T_j(y)T_k(x)T_l(y)=[&T_{i+k}(x)T_{j+1}(y)+T_{i+k}(x)T_{j-1}(y)\\ &+T_{i-k}(x)T_{j+1}(y)+T_{i-k}(x)T_{j-1}(y)]/4.\end{aligned} \tag{25}$$

The displacement functions and loading are approximated by finite degree Chebyshev polynomials as

$$\begin{aligned}&(u,v,w,\psi_x,\psi_y,Q)\\ &\quad=\delta\sum_{i=0}^{M}\sum_{j=0}^{N}(u_{ij},v_{ij},w_{ij},\psi_{xij},\psi_{yij},Q_{ij})T_i(x)T_j(y);\\ &\qquad -1\leqslant x\leqslant 1\\ &\qquad -1\leqslant y\leqslant 1.\end{aligned} \tag{26}$$

The implicit Houbolt time-marching scheme (Houbolt [13]) is used to evaluate the acceleration terms $(u_{,\tau\tau})_J$, $(v_{,\tau\tau})_J$, $(w_{,\tau\tau})_J$, $(\psi_{x,\tau\tau})_J$, and $(\psi_{y,\tau\tau})_J$ in the governing equations of motion. The expression for general acceleration $(\phi_{,\tau\tau})_J$ is evaluated as

$$(\phi_{,\tau\tau})_J=(\beta_1\phi_J+\beta_2\phi_{J-1}+\beta_3\phi_{J-2}+\beta_4\phi_{J-3}+\beta_5)/(\Delta\tau^2) \tag{27}$$

where τ is nondimensional time and β_{i} are coefficients of the time-marching scheme.

Making use of the above procedure of spatial and temporal discretizations and linearization, the nonlinear differential Eq. (15)–(19) are discretized in space and time domains, respectively. A set of generating linear algebraic equation can be expressed as

Table 1 Convergence study for four layers antisymmetric cross-ply [0/90/0/90] square CSCS plate ($a/h=10$, $qa^4/E_2h^4=50$, Material A)

M,N	Center ($\Delta\tau=0.1$)			
	w_c (max.)	τ	$\bar{M}_x$ (max)	τ
5	0.516899	12.6	2.46606	9.6
6	0.498366	11.2	2.52769	9.7
7	0.493602	11.2	2.39125	9.8
8	0.499053	11.4	2.29421	10.4
9	0.497812	11.4	2.28463	10.3
10	0.492611	11.1	2.36994	9.9
11	0.492311	11.1	2.35379	9.9
12	0.493070	11.1	2.32018	9.9
	Center (M=N=9)			
$\Delta\tau$	w_c (max.)	τ	$\bar{M}_x$ (max)	τ
0.2	0.474231	11.6	2.28616	10.4
0.1	0.497812	11.4	2.28463	10.3
0.05	0.497660	11.3	2.27933	10.6

Table 2 Comparison of uniaxial nondimensional static critical loads $\lambda_{cr}(=N_xb^2/E_2h^3)$ for symmetrically laminated cross-ply simply supported square plate ($a/h=10$, Material A)

Number of Layers	E_1/E_2	λ_{cr}		
		Present	Noor [22]	Owen and Li [23]
3	40	22.7273	22.8807	23.3330
	30	19.2300	19.3040	19.6872
	20	15.1563	15.0191	15.3201
	10	9.8920	9.7621	9.9590
	3	5.3754	5.3044	5.4026
5	40	24.8322	25.2150	24.5929
	30	20.8000	20.9518	20.4663
	20	15.8696	15.9976	15.6527
	10	10.1712	10.1609	9.9603
	3	5.4487	5.4208	5.3255
9	40	25.6957	25.7093	25.3436
	30	21.2281	21.2697	20.9614
	20	16.1403	16.1560	15.9153
	10	10.2344	10.1990	10.0417
	3	5.4281	5.4187	5.3352

$$\sum_{k=1}^{5}\sum_{i=0}^{M-2}\sum_{j=0}^{N-2} F_k(u_{ij},v_{ij},w_{ij},\psi_{xij},\psi_{yij},Q_{ij})T_i(x)T_j(y)=\mathbf{0}. \tag{28}$$

Similarly the appropriate sets of boundary conditions are also discretized.

The total number of unknown coefficients are 5(M+1)(N+1). Collocating the zeroes of Chebyshev polynomials, 5(M–1)(N–1) algebraic equations are generated from the governing differential equations. Similarly the CCCC (all edges clamped), CCCS (three edges clamped and one simply supported), CCSS (two opposite edges clamped and two simply supported), CSCS (two adjacent edges clamped and two simply supported), CSSS (one edge clamped and three simply supported), and SSSS (all edges simply supported) boundary conditions generate (10M+10N+16), (10M+10N+15), (10M+10N+14), (10M+10N+14), (10M+10N+13), and (10M+10N+12) algebraic equations, respectively. It is clear that the total number of equations is more than the unknown coefficients. In order to have a compatible solution, the multiple regression analysis (Nath and Sandeep [21]) based on the least-square error norms is used. The nonlinear terms are transferred to the right side and computed at each step of the marching variable. The left side matrix consists of linear terms and hence remains invariant with respect to the marching variable. The set of linear equations are expressed in matrix form as

$$[A]\{a\}=\{Q\} \tag{29}$$

where $[A]$ is the (m*n) coefficient matrix, $\{a\}$ is the (n*1) displacement vector, and $\{Q\}$ is the (m*1) load vector. Multiple regression analysis gives

$$\{a\}=([A]^T[A])^{-1}[A]^T\{Q\}$$

or

$$\{a\}=[B]\{Q\}. \tag{30}$$

The matrix $[B]$ is evaluated once and retained for subsequent usage.

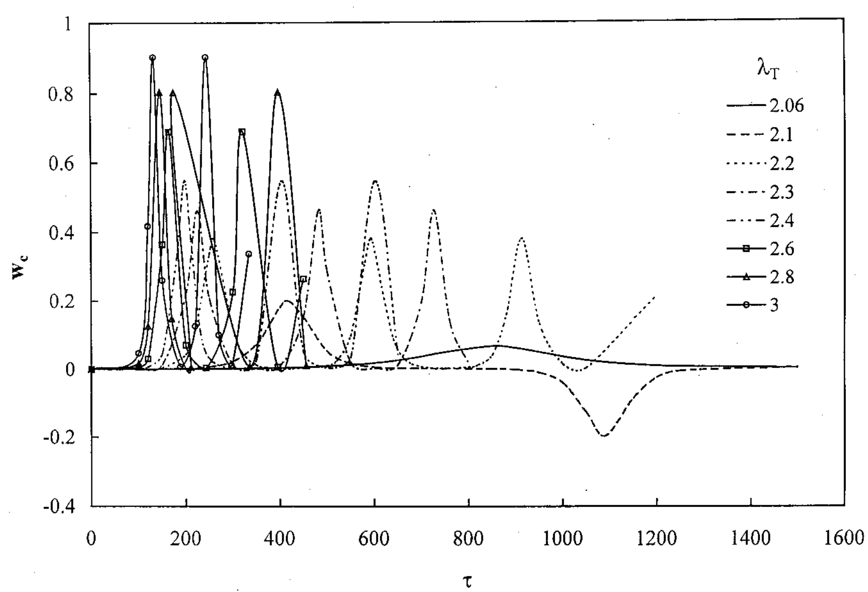

Fig. 2 Central displacement response for antisymmetric angle-ply [45/-45/45/-45] square SSSS plate ($a/h=20$, Material B) under in-plane uniform thermal loading

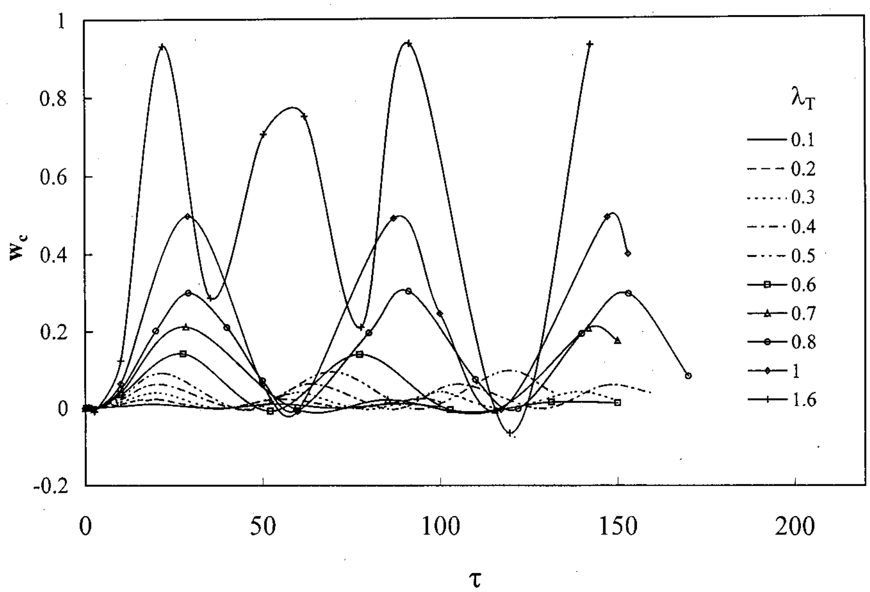

Fig. 3 Central displacement response for unsymmetric angle-ply [0/15/30/45] square SSSS plate ($a/h=20$, Material B) under in-plane uniform thermal loading

4 Results and Discussions

The nonlinear governing equations of motion for a laminated composite rectangular plate subjected to transient thermal loading are solved, analytically using fast converging double Chebyshev series approximations. In order to check the accuracy and stability of the method a convergence study is carried out. Table 1 reveals that the nine-term expansion of Chebyshev series and an increment of 0.1 for nondimensional time τ are sufficient to yield quite accurate results. An iterative incremental approach with relative convergence criteria of 0.01% of each coefficient at every step of the marching variable is adopted. The in-plane uniform temperature is incremented in small steps. The transient thermal post-buckling responses are obtained and dynamic critical temperatures are estimated. The numerical results for cross-ply and angle-ply rectangular plates with SSSS, CCCS, CCSS, CSCS, CSSS, and CCCC boundary conditions are presented. Two materials considered for the analyses are:

Material A: $E_1/E_2=25$, $G_{12}=0.5E_2$, $G_{23}=0.2E_2$, $G_{13}=G_{12}$, and $\nu_{12}=0.25$,

$$\alpha_1=\alpha_0, \quad \alpha_2=10\ \alpha_0, \quad \alpha_0=10^{-06}\ {}^0/c,$$

$$\rho=8\times10^{-06}\ \text{Kg-Sec}^2/\text{cm}^4.$$

Material B: $E_1=181.0$ Gpa, $E_2=10.3$ GPa, $\nu_{12}=0.28$, $G_{12}=G_{13}=7.17$ Gpa,

$$G_{23}=2.39\ \text{Gpa}, \quad \alpha_1=0.02\alpha_0, \quad \alpha_2=22.5\ \alpha_0,$$

$$\alpha_0=10^{-06}\ {}^0/c, \quad \rho=8\times10^{-06}\ \text{Kg-Sec}^2/\text{cm}^4.$$

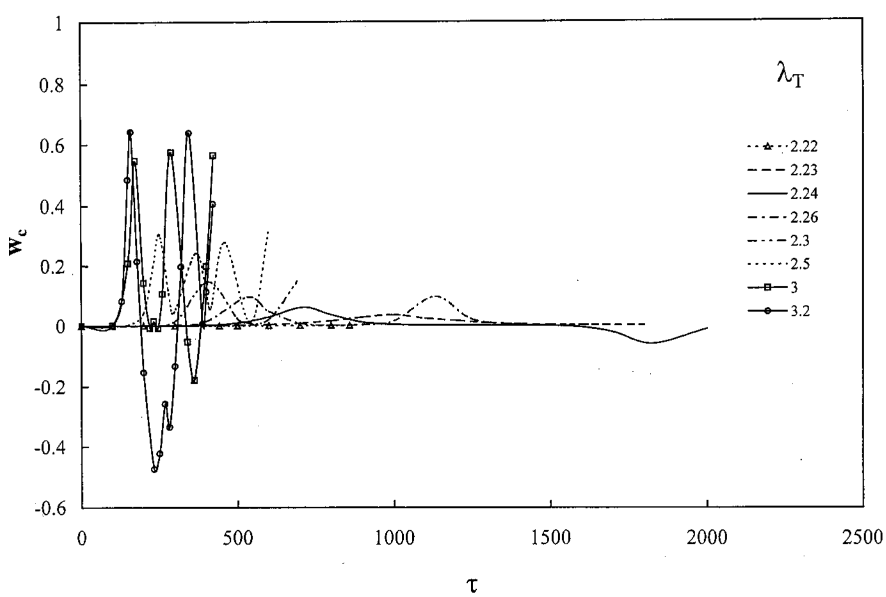

Fig. 4 Central displacement response for symmetric cross-ply [0/90/90/0] square CSCS plate ($a/h=20$, Material A) under in-plane uniform thermal loading

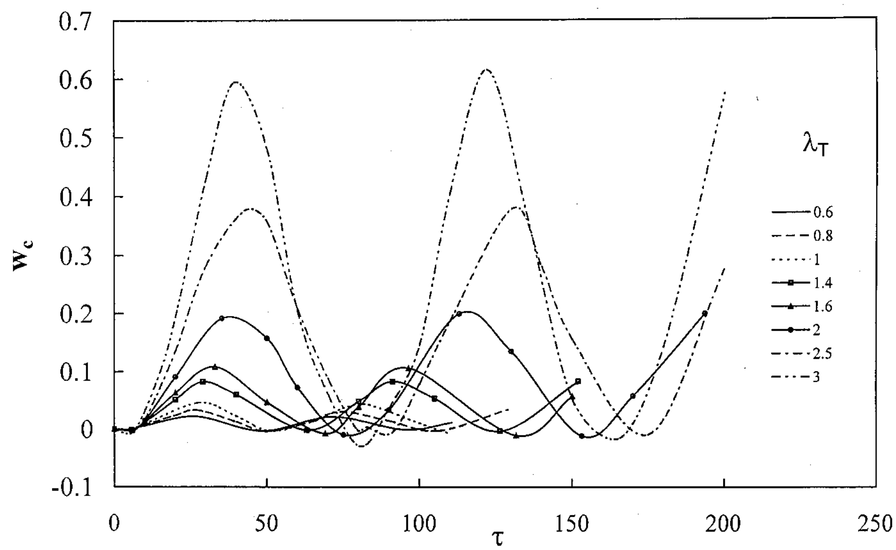

Fig. 5 Central displacement response for antisymmetric cross-ply [0/90/0/90] square CCSS plate ($a/h=20$, Material A) under in-plane uniform thermal loading

The nondimensional temperature parameters are defined as

$$\lambda_T = \alpha_0 \Delta T \times 10^3 \qquad \text{and} \qquad \lambda_{T_{cr}} = \alpha_0 \Delta T_{cr} \times 10^3.$$

The present methodology of solution is validated by comparing the results of nondimensional static critical loads obtained by Noor [22] and Owen and Li [23] using the three-dimensional linear elasticity solution and finite element method, respectively. The comparison of the results is shown in Table 2. It is observed that results are in good agreement and have a maximum difference of less than 3%.

The central displacement (w_c) response for antisymmetric [45/-45/45/-45] and unsymmetric [0/15/30/45] angle-ply square SSSS plates for ($a/h=20$ and Material B) are shown in Figs. 2 and 3, respectively. From these plots it is clear that the maximum peak displacement increases with increase in the in-plane temperature and at a certain temperature level there may be a sudden jump in the deflection but is not observed distinctly.

The central displacement response for four-layer symmetric cross-ply CSCS plate ($a/h=20$, Material A) is plotted in Fig. 4. The deflection response for $\lambda_T \leqslant 2.22$ do not show discontinuous jump but for the response at $\lambda_T = 2.23$, there is a sudden jump in the deflection at approximately τ equal to 1000. In fact the jump in the deflection is not distinct in the plots as the amplitude is very small. The displacement response for antisymmetric cross-ply CCSS and CSSS plates ($a/h=20$, Material A) are shown in Figs. 5 and 6, respectively, and similar conclusions can be deduced.

It is difficult to estimate dynamic critical temperatures from the displacement response. In order to estimate the dynamic critical

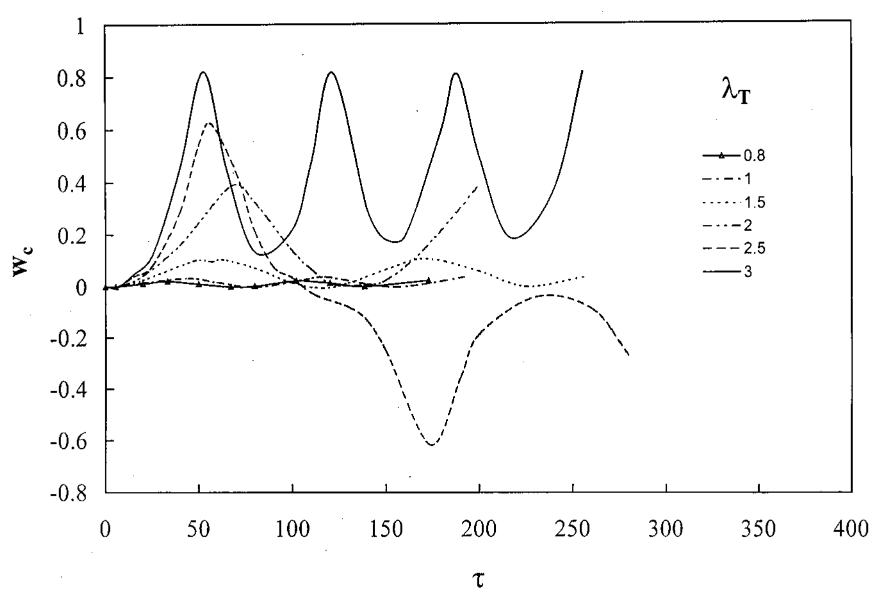

Fig. 6 Central displacement response for antisymmetric cross-ply [0/90/0/90] square CSSS plate ($a/h=20$, Material A) under in-plane uniform thermal loading

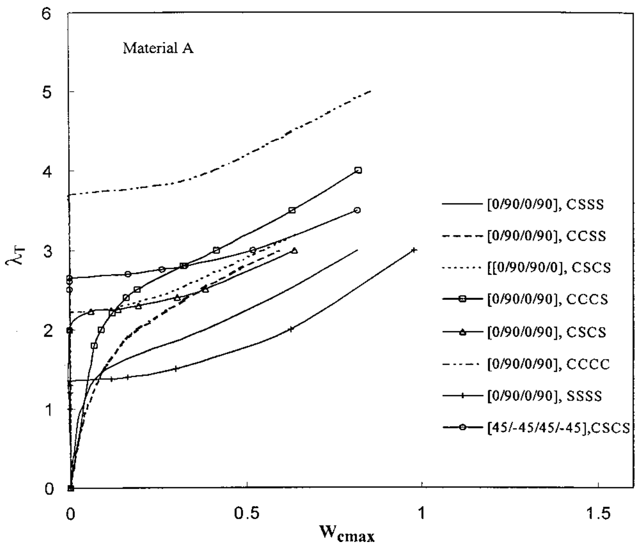

Fig. 7 Dynamic thermal post-buckling response of laminated composite plates ($a/h=20$) under in-plane uniform thermal loading

Table 3 Nondimensional dynamic critical temperatures for laminated composite square plates ($a/h=20$)

Lamination Scheme	Boundary Conditions	Nondimensional Dynamic Critical Temperature $\lambda_{T_{cr}}$
	Material A	
[0/90/0/90]	SSSS	1.35
	CSSS	1.41
	CCSS	1.65
	CSCS	2.15
	CCCS	2.29
	CCCC	3.7
[0/90/90/0]	CSCS	2.22
[45/-45/45/-45]	CSCS	2.64
	Material B	
[45/-45/45/-45]	SSSS	2.06
[45/-45/45/-45]	CCCS	3.32
[0/15/30/45]	SSSS	0.57

temperature, maximum peak deflections versus in-plane temperature are plotted for cross-ply and angle-ply plates with different boundary conditions and is shown in Fig. 7. Dynamic critical temperatures are estimated and are given in Table 3. Dynamic critical temperature and post-buckling strength are higher for an antisymmetric cross-ply [0/90/0/90] CCCC plate and the post-buckling strength is lower for a [0/90/0/90] SSSS plate. Dynamic critical temperature and reserve strength (load carrying capacity after buckling) for a four layers antisymmetric angle-ply [45/-45/45/-45] CSCS plate are higher than for four layers symmetric [0/90/90/0] and antisymmetric [0/90/0/90] cross-ply CSCS plates. A symmetric cross-ply [0/90/90/0] CSCS plate has higher dynamic critical temperature than an antisymmetric cross-ply [0/90/0/90] CSCS plate.

5 Conclusions

The displacement response for laminated composite plates subjected to uniform in-plane dynamic thermal loading is obtained. Dynamic critical temperatures are estimated from the plot between maximum peak deflection and thermal loading. It is observed that lamination scheme and boundary conditions have significant effects on dynamic critical temperature and reserve strength of the plate. Dynamic critical temperature is higher for an antisymmetric angle-ply laminated plate than for symmetric or antisymmetric cross-ply laminated plates. It is lower for an unsymmetrically laminated plate. The dynamic critical temperature and post-buckling strength for an antisymmetric cross-ply plate are less than for a symmetric cross-ply plate.

Acknowledgment

The research is partially supported by the Council of Scientific and Industrial Research, New Delhi, Grant No. 22(0315)/00/EMR-II. The support is gratefully acknowledged.

Appendix

Nondimensional parameters and coefficients are

$$u=\frac{u_o}{h},\quad v=\frac{v_o}{h},\quad w\frac{=w_o}{h},\quad x=\frac{2X}{a},\quad y=\frac{2Y}{b},$$

$$\lambda=\frac{a}{b},\quad \beta=\frac{a}{h},\quad (\bar{N}_x,\bar{N}_x^T)=\frac{(N_x,N_x^T)\beta}{A_{11}},$$

$$(\bar{N}_y,\bar{N}_y^T)=\frac{(N_y,N_y^T)\beta}{A_{22}},$$

$$(\bar{N}_{xy},\bar{N}_{xy}^T)=\frac{(N_{xy},N_{xy}^T)\beta}{A_{66}},\quad (\hat{M}_x,\hat{M}_x^T)=\frac{(M_x,M_x^T)h\beta^2}{D_{11}},$$

$$(\bar{M}_y,\bar{M}_y^T)=\frac{(M_y,M_y^T)h\beta^2}{D_{22}},\quad (\bar{M}_{xy},\bar{M}_{xy}^T)=\frac{(M_{xy},M_{xy}^T)h\beta^2}{D_{66}}$$

$$q^*=\frac{qa^2}{4A_{22}h},\quad \lambda_T=\alpha_0\Delta T\times 10^3,\quad \lambda_{T_{cr}}=\alpha_0\Delta T_{cr}\times 10^3,$$

$$\tau=t\times\sqrt{\frac{4A_{22}}{h^2\beta^2R}}$$

$$L_1=1,\quad L_2=\frac{A_{66}}{A_{11}}\lambda^2,\quad L_3=2\frac{A_{16}}{A_{11}}\lambda,\quad L_4=\frac{A_{16}}{A_{11}},$$

$$L_5=\frac{A_{26}}{A_{11}}\lambda^2,\quad L_6=\frac{(A_{12}+A_{66})}{A_{11}}\lambda$$

$$L_7=\frac{B_{11}}{A_{11}h},\quad L_8=\frac{B_{66}}{A_{11}h}\lambda^2,\quad L_9=2\frac{B_{16}}{A_{11}h}\lambda,\quad L_{10}=\frac{B_{16}}{A_{11}h},$$

$$L_{11}=\frac{B_{26}}{A_{11}h}\lambda^2,\quad L_{12}=\frac{(B_{12}+B_{66})\lambda}{A_{11}h}$$

$$L_{13}=\frac{2}{\beta},\quad L_{14}=2\frac{A_{66}}{A_{11}}\frac{\lambda^2}{\beta},\quad L_{15}=4\frac{A_{16}}{A_{11}}\frac{\lambda}{\beta},$$

$$L_{16}=2\frac{A_{16}}{A_{11}}\frac{\lambda}{\beta},\quad L_{17}=2\frac{A_{26}}{A_{11}}\frac{\lambda^3}{\beta},\quad L_{18}=2\frac{(A_{12}+A_{66})}{A_{11}}\frac{\lambda^2}{\beta}$$

$$L_{19}=0.5,\quad L_{20}=0.5\frac{A_{66}}{A_{11}}\lambda,\quad L_{21}=\frac{A_{16}}{A_{22}},\quad L_{22}=\frac{A_{26}}{A_{22}}\lambda^2,$$

$$L_{23}=\frac{(A_{12}+A_{66})}{A_{22}}\lambda,\quad L_{24}=\frac{A_{66}}{A_{22}}$$

$$L_{25}=\lambda^2,\quad L_{26}=2\frac{A_{26}}{A_{22}},\quad L_{27}=\frac{B_{16}}{A_{22}h},\quad L_{28}=\frac{B_{26}}{A_{22}h}\lambda^2,$$

$$L_{29}=\frac{(B_{12}+B_{66})}{A_{22}h}\lambda,\quad L_{30}=\frac{B_{66}}{A_{22}h}$$

$$L_{31}=\frac{B_{22}}{A_{22}h}\lambda^2,\quad L_{32}=2\frac{B_{26}}{A_{22}h}\lambda,\quad L_{33}=2\frac{A_{16}}{A_{22}\beta},$$

$$L_{34}=2\frac{A_{26}}{A_{22}}\frac{\lambda^2}{\beta},\quad L_{35}=2\frac{(A_{12}+A_{66})}{A_{22}}\frac{\lambda}{\beta}$$

$$L_{36}=2\frac{A_{66}}{A_{22}}\frac{\lambda}{\beta},\quad L_{37}=2\frac{\lambda^3}{\beta},\quad L_{38}=4\frac{A_{26}}{A_{22}}\frac{\lambda^2}{\beta},$$

$$L_{39}=0.5\frac{A_{66}}{A_{22}},\quad L_{40}=0.5\lambda$$

$$L_{41}=\frac{A_{55}}{A_{22}},\quad L_{42}=\frac{A_{44}}{A_{22}}\lambda^2,\quad L_{43}=2\frac{A_{45}}{A_{22}}\lambda,$$

$$L_{44}=0.5\frac{A_{55}}{A_{22}}\beta,\quad L_{45}=0.5\frac{A_{45}}{A_{22}}\lambda\beta$$

$$L_{46}=0.5\frac{A_{45}}{A_{22}}\beta,\quad L_{47}=0.5\frac{A_{44}}{A_{22}}\lambda\beta,\quad L_{48}=2\frac{A_{11}}{A_{22}\beta},$$

$$L_{49}=2\frac{A_{16}}{A_{22}}\frac{\lambda}{\beta},\quad L_{50}=2\frac{A_{16}}{A_{22}\beta}$$

$$L_{51}=2\frac{A_{12}}{A_{22}}\frac{\lambda}{\beta},\quad L_{52}=2\frac{B_{11}}{A_{22}h\beta},\quad L_{53}=2\frac{B_{16}}{A_{22}h}\frac{\lambda}{\beta},$$

$$L_{54}=2\frac{B_{16}}{A_{22}h\beta},\quad L_{55}=2\frac{B_{12}}{A_{22}h}\frac{\lambda}{\beta}$$

$$L_{56}=2\frac{A_{12}}{A_{22}}\frac{\lambda^2}{\beta},\quad L_{57}=2\frac{A_{26}}{A_{22}}\frac{\lambda^3}{\beta},\quad L_{58}=2\frac{A_{26}}{A_{22}}\frac{\lambda^2}{\beta},$$

$$L_{59}=2\frac{\lambda^3}{\beta},\quad L_{60}=2\frac{B_{12}}{A_{22}h}\frac{\lambda^2}{\beta}$$

$$L_{61}=2\frac{B_{26}}{A_{22}h}\frac{\lambda^3}{\beta},\quad L_{62}=2\frac{B_{26}}{A_{22}h}\frac{\lambda^2}{\beta},\quad L_{63}=2\frac{B_{22}}{A_{22}h}\frac{\lambda^3}{\beta},$$

$$L_{64}=4\frac{A_{16}}{A_{22}}\frac{\lambda}{\beta},\quad L_{65}=4\frac{A_{66}}{A_{22}}\frac{\lambda^2}{\beta}$$

$$L_{66}=4\frac{A_{66}}{A_{22}}\frac{\lambda}{\beta},\quad L_{67}=4\frac{A_{26}}{A_{22}}\frac{\lambda^2}{\beta},\quad L_{68}=4\frac{B_{16}}{A_{22}h}\frac{\lambda}{\beta},$$

$$L_{69}=4\frac{B_{66}}{A_{22}h}\frac{\lambda^2}{\beta},\quad L_{70}=4\frac{B_{66}}{A_{22}h}\frac{\lambda}{\beta}$$

$$L_{71}=4\frac{B_{26}}{A_{22}h}\frac{\lambda^2}{\beta},\quad L_{72}=2\frac{A_{11}}{A_{22}\beta^2},\quad L_{73}=2\frac{A_{12}}{A_{22}}\frac{\lambda^2}{\beta^2},$$

$$L_{74}=4\frac{A_{16}}{A_{22}}\frac{\lambda}{\beta^2},\quad L_{75}=2\frac{A_{12}}{A_{22}}\frac{\lambda^2}{\beta^2}$$

$$L_{76}=2\frac{\lambda^4}{\beta^2},\quad L_{77}=4\frac{A_{26}}{A_{22}}\frac{\lambda^3}{\beta^2},\quad L_{78}=4\frac{A_{16}}{A_{22}}\frac{\lambda}{\beta^2},$$

$$L_{79}=4\frac{A_{26}}{A_{22}}\frac{\lambda^3}{\beta^2},\quad L_{80}=8\frac{A_{66}}{A_{22}}\frac{\lambda^2}{\beta^2},\quad L_{81}=\frac{2}{\beta}$$

$$L_{82}=\frac{2}{\beta}\frac{S}{Rh},\quad L_{83}=\frac{2\lambda}{\beta},\quad L_{84}=\frac{2\lambda}{\beta}\frac{S}{Rh},\quad L_{85}=\frac{A_{11}}{A_{22}\beta},$$

$$L_{86}=\frac{\lambda^2}{\beta},\quad L_{87}=2\frac{A_{66}}{A_{22}}\frac{\lambda}{\beta},\quad L_{88}=\frac{B_{11}h}{D_{11}}$$

$$L_{89}=\frac{B_{66}h}{D_{11}}\lambda^2,\quad L_{90}=2\frac{B_{16}h}{D_{11}}\lambda,$$

$$L_{91}=\frac{B_{16}h}{D_{11}},\quad L_{92}=\frac{B_{26}h}{D_{11}}\lambda^2,\quad L_{93}=\frac{(B_{12}+B_{66})h}{D_{11}}\lambda$$

$$L_{94}=1,\quad L_{95}=\frac{D_{66}}{D_{11}}\lambda^2,\quad L_{96}=2\frac{D_{16}}{D_{11}}\lambda,\quad L_{97}=\frac{D_{16}}{D_{11}},$$

$$L_{98}=\frac{D_{26}}{D_{11}}\lambda^2,\quad L_{99}=\frac{(D_{12}+D_{66})}{D_{11}}\lambda$$

$$L_{100}=-0.5\frac{A_{55}h^2}{D_{11}}\beta,\quad L_{101}=-0.5\frac{A_{45}h^2}{D_{11}}\lambda\beta,$$

$$L_{102}=-0.25\frac{A_{55}h^2}{D_{11}}\beta^2,\quad L_{103}=-0.25\frac{A_{45}h^2}{D_{11}}\beta^2$$

$$L_{104}=2\frac{B_{11}h}{D_{11}\beta},\quad L_{105}=2\frac{B_{66}h}{D_{11}}\frac{\lambda^2}{\beta},\quad L_{106}=4\frac{B_{16}h}{D_{11}}\frac{\lambda}{\beta},$$

$$L_{107}=2\frac{B_{16}h}{D_{11}}\frac{\lambda}{\beta},\quad L_{108}=2\frac{B_{26}h}{D_{11}}\frac{\lambda^3}{\beta}$$

$$L_{109}=2\frac{(B_{12}+B_{66})h}{D_{11}}\frac{\lambda^2}{\beta},\quad L_{110}=\frac{1}{2\beta},\quad L_{111}$$

$$=0.5\frac{D_{66}}{D_{11}}\frac{\lambda}{\beta},\quad L_{112}=\frac{B_{16}h}{D_{22}}$$

$$L_{113}=\frac{B_{26}h}{D_{22}}\lambda^2,\quad L_{114}=\frac{(B_{12}+B_{66})h}{D_{22}}\lambda,\quad L_{115}=\frac{B_{66}h}{D_{22}},$$

$$L_{116}=\frac{B_{22}h}{D_{22}}\lambda^2,\quad L_{117}=2\frac{B_{26}h}{D_{22}}\lambda$$

$$L_{118}=\frac{D_{16}}{D_{22}},\quad L_{119}=\frac{D_{26}}{D_{22}}\lambda^2,\quad L_{120}=\frac{(D_{12}+D_{66})}{D_{22}}\lambda,$$

$$L_{121}=\frac{D_{66}}{D_{22}},\quad L_{122}=\lambda^2$$

$$L_{123}=2\frac{D_{26}}{D_{22}}\lambda,\quad L_{124}=-0.5\frac{A_{45}h^2}{D_{22}}\beta,\quad L_{125}=$$

$$-0.5\frac{A_{44}h^2}{D_{22}}\lambda\beta,\quad L_{126}=-0.25\frac{A_{45}h^2}{D_{22}}\beta^2$$

$$L_{127}=-0.25\frac{A_{44}h^2}{D_{22}}\beta^2,\quad L_{128}=2\frac{B_{16}h}{D_{22}\beta},\quad L_{129}$$

$$=2\frac{B_{26}h}{D_{22}}\frac{\lambda^2}{\beta},\quad L_{130}=2\frac{(B_{12}+B_{66})h}{D_{22}}\frac{\lambda}{\beta}$$

$$L_{131}=2\frac{B_{66}h}{D_{22}}\frac{\lambda}{\beta},\quad L_{132}=2\frac{B_{22}h}{D_{22}}\frac{\lambda^3}{\beta},\quad L_{133}=4\frac{B_{26}h}{D_{22}}\frac{\lambda^2}{\beta},$$

$$L_{134}=0.5\frac{D_{66}}{D_{22}\beta},\quad L_{135}=0.5\frac{\lambda}{\beta}$$

$$R_1=\frac{A_{22}}{A_{11}},\quad R_2=\frac{A_{22}}{A_{11}}\frac{S}{Rh},\quad R_3=1,\quad R_4=\frac{S}{Rh},\quad R_5=1,$$

$$R_6=\frac{A_{22}h}{D_{11}}\frac{S}{R}$$

$$R_7=\frac{A_{22}}{D_{11}}\frac{I}{R},\quad R_8=\frac{A_{22}h}{D_{22}}\frac{S}{R},\quad R_9=\frac{A_{22}}{D_{22}}\frac{I}{R}.$$

References

[1] Bert, C. W., and Birman, V., 1987, ‘‘Dynamic Stability of Shear Deformable Antisymmetric Angle-Ply Plates,’’ Int. J. Solids Struct., **23**, pp. 1053–1061.
[2] Moorthy, J., and Reddy, J. N., 1990, ‘‘Parametric Stability of Laminated Composite Plates With Transverse Shear Deformation,’’ Int. J. Solids Struct., **26**, pp. 801–811.
[3] Ganapathi, M., Vardan, T. K., and Balamurugan, V., 1994, ‘‘Dynamic Instability of Laminated Composite Curved Panels Using Finite Element Method,’’ Comput. Struct., **53**, pp. 335–342.
[4] Liao, C.-L., and Cheng, C.-R., 1994, ‘‘Dynamic Stability of Stiffened Lami-

nated Composite Plates and Shells Subjected to In-Plane Pulsating Forces,'' Int. J. Numer. Methods Eng., **37**, pp. 4167–4183.
[5] Locke, J., 1990, ''Nonlinear Random Response of Angle-Ply Laminates With Static and Thermal Preloads,'' AIAA J., **29**(9), pp. 1480–1487.
[6] Abbas, J. F., Ibrahim, R. A., and Gibson, R. F., 1993, ''Nonlinear Flutter of Orthotropic Composite Panel Under Aerodynamic Heating,'' AIAA J., **31**(8), pp. 1478–1488.
[7] Lee, D. M., and Lee, I., 1997, ''Vibration Behaviors of Thermally Postbuckled Anisotropic Plates Using First-Order Shear Deformation Theory,'' Comput. Struct., **71**, pp. 617–626.
[8] Liaw, D. G., 1997, ''Nonlinear Supersonic Flutter of Laminated Composite Plates Under Thermal Loads,'' Comput. Struct., **65**(5), pp. 733–746.
[9] Ganapathi, M., and Touratier, M., 1999, ''Dynamic Instability of Laminates Subjected to Temperature Field,'' J. Eng. Mech., ASCE, **124**(10), pp. 1166–1168.
[10] Tylikowski, A., and Hetnarski, R. B., 1996, ''Thermally Induced Instability of Laminated Beams and Plates,'' ASME J. Appl. Mech., **63**, pp. 884–890.
[11] Librescu, L., and Souza, M. A., 2000, ''Nonlinear Dynamics of Stiffened Flat Panels Under Thermomechanical Loads,'' J. Aerospace Engg., ASCE., **13**(3), pp. 78–84.
[12] Fox, L., and Parker, I. B., 1968, *Chebyshev Polynomials in Numerical Analysis*, Oxford University Press, London.
[13] Houbolt, J. C., 1950, ''A Recurrence Matrix Solution for the Dynamic Response of Elastic Aircraft,'' J. Aerosp. Sci., **17**, pp. 540–550.
[14] Shukla, K. K., and Nath, Y., 2000, ''Non-linear Analysis of Moderately Thick Laminated Rectangular Plates,'' J. Eng. Mech., ASCE, **126**(8), pp. 831–838.
[15] Budiansky, B., and Roth, R. S., 1962, ''Axisymmetric Dynamic Buckling of Clamped Shallow Spherical Shells,'' NASA, TND 1510, pp. 597–606.
[16] Stephens, W. B., and Fulton, R. E., 1967, ''Axisymmetric Static and Dynamic Buckling of Spherical Caps due to Centrally Distributed Pressure,'' AIAA J., **8**, pp. 2120–2126.
[17] Jain, R. K., and Nath, Y., 1987, ''Dynamic Buckling of Orthotropic Caps Supported by Elastic Media,'' AIAA J., **25**(4), pp. 630–633.
[18] Jones, R. M., 1998, *Mechanics of Composite Materials*, Taylor & Francis, Philadelphia.
[19] Whitney, J. M., 1973, ''Shear Correction Factors for Orthotropic Laminates Under Static Loads,'' ASME J. Appl. Mech., **40**, pp. 302–304.
[20] Yang, P. C., Norris, C. H., and Stavsky, Y., 1966, ''Elastic Wave Propagation in Heterogeneous Plates,'' Int. J. Solids Struct., **2**, pp. 665–684.
[21] Nath, Y., and Sandeep, K., 1995, ''Chebyshev Series Solution to Non-Linear Boundary Value Problems in Rectangular Domain,'' Comput. Methods Appl. Mech. Eng., **125**, pp. 41–52.
[22] Noor, A. K., 1975, ''Stability of Multilayered Composite Plates,'' Fibre Sci. Technol., **8**, pp. 81–89.
[23] Owen, D. R. J., and Li, Z. H., 1987, ''A Refined Analysis of Laminated Plates by Finite Element Displacement Methods—II, Vibration and Stability,'' Comput. Struct., **26**(6), pp. 915–923.

Journal of Applied Mechanics

Brief Notes

A Brief Note is a short paper that presents a specific solution of technical interest in mechanics but which does not necessarily contain new general methods or results. A Brief Note should not exceed 2500 words *or equivalent* (a typical one-column figure or table is equivalent to 250 words; a one line equation to 30 words). Brief Notes will be subject to the usual review procedures prior to publication. After approval such Notes will be published as soon as possible. The Notes should be submitted to the Editor of the JOURNAL OF APPLIED MECHANICS. Discussions on the Brief Notes should be addressed to the Editorial Department, ASME International, Three Park Avenue, New York, NY 10016-5990, or to the Editor of the JOURNAL OF APPLIED MECHANICS. Discussions on Brief Notes appearing in this issue will be accepted until two months after publication. Readers who need more time to prepare a Discussion should request an extension of the deadline from the Editorial Department.

Crack-Tip Field of a Supersonic Bimaterial Interface Crack

J. Wu

Conexant Systems, Inc., 4311 Jamboree Road, Newport Beach, CA 92561. Assoc. Mem. ASME

The sextic approach was used to investigate the asymptotic field of a bimaterial interface crack in the entire supersonic regime and extended to include the combination of isotropic and homogeneous materials, where the sextic method had been considered difficult. Application to typical systems was demonstrated.
[DOI: 10.1115/1.1427338]

Introduction

The crack-tip field of a static interface crack between two isotropic or anisotropic materials has been well understood ([1–3]). In the lower part of the supersonic regime, the experimental and theoretical progress in interface dynamic fracture mechanics of isotropic bimaterial systems is represented by the work of Tippur et al. [4], Liu et al. [5], Lambros et al. [6], and Huang et al. [7]. However, the crack-tip behavior of isotropic bimaterial systems in the upper supersonic regime and that of anisotropic bimaterial systems in the entire supersonic regime had not yet been solved by the time of this work, which is the major focus of this brief note. Based on an early mathematical formulation ([8]), this problem was solved using a sextic approach for a given bimaterial interface crack composed of any combination of anisotropic and isotropic materials with the crack tip moving at an arbitrary constant speed. Application to typical systems was demonstrated.

Eigenvalue Problem for the Crack-Tip Field in the Supersonic Regime

For a bimaterial interface crack shown in Fig. 1, Materials I and II occupy the upper and the lower half-planes, respectively. The constant crack-tip speed v is measured with respect to a quiescent coordinate system $x'-o'-y'$. The moving coordinate system $x-o-y$ is attached to the crack tip.

Contributed by the Applied Mechanics Division of for publication in the ASME JOURNAL OF APPLIED MECHANICS. Manuscript received by the ASME Applied Mechanics Division, September 26, 2000; final revision, July 30, 2001. Associate Editor: H. Gao.

The general solution to the stress field for an anisotropic material in the subsonic regime is obtained using the Stroh formalism ([9]). For a complete description of the mathematical procedures leading to the results in this work, the reader is referred to [8]. The special feature in the supersonic regime is that some or all of the six Stroh eigenvalues $p_i (i=1, \ldots ,6)$ become real, of which only these three representing upward energy flow (in the positive y-direction) in the upper half-plane and these three representing the downward energy flow in the lower half plane should be selected for the current interface crack problem. A good discussion on the selection of the proper eigenvalues is given in [10]. Mathematically, Stroh showed that the energy flow direction with respect to the y-axis has the same algebraic sign as $A_{i\alpha}L_{i\alpha}$ ([9]), where A is the polarization matrix and L the traction matrix. Physically, the energy flow is associated with the group velocity. It should also be noted that, when an eigenvalue p is real, the phase velocity of the plane wave associated with p has a direction (x, y) that can be explicitly expressed in terms of p as $p=y/x$ ([9]). Generally, the phase velocity and the group velocity do not necessarily have the same direction. However, in cases where the two velocities do have the same direction, the selection of the real eigenvalue p can be made directly based on the algebraic sign of the eigenvalue itself.

For the problem stated above, the eigenvalue problem for the oscillatory index ϵ and the eigenvector $\mathbf{w}$ can be expressed in terms of the bimaterial matrix H as

$$\begin{cases} H^{*}\mathbf{w}=\lambda H\mathbf{w}, \\ \lambda=e^{2\pi\epsilon} \end{cases}. \tag{1}$$

In each half-plane, the displacement and the stress fields are obtained in terms of the stress potential vector ϕ as

$$\begin{cases} \mathbf{u}=2\,\mathrm{Im}(B\phi), \\ \{\sigma_{12} \quad \sigma_{22} \quad \sigma_{23}\}^T=2\,\mathrm{Re}\left(\dfrac{\partial\phi}{\partial z}\right), \\ \{\sigma_{11} \quad \sigma_{12} \quad \sigma_{13}\}^T=2\,\mathrm{Re}\left(M\,\dfrac{\partial\phi}{\partial z}\right), \end{cases} \tag{2}$$

where B is as defined in [2]. The matrix M is introduced here for the first time to write the results in a compact form, which is defined in terms of the material density ρ and traction matrix L as

$$M=-i\rho v^2 B-LPL^{-1}, \qquad \text{and} \qquad P=dia[p_1,p_2,p_3],$$

where p_i, $i=1, 2, 3$, are the three Stroh eigenvalues used in constructing the general solution in the corresponding half-plane.

The Stroh eigenvalue problem is degenerate in case of a system with high symmetry. For example, it has only one independent eigenvector in the case of an isotropic material, so special

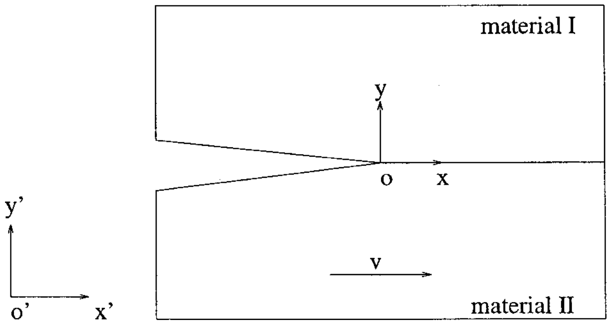

Fig. 1 A half-space crack with its tip moving at a constant speed *v* with respect to the quiescent coordinate system $x'-o'-y'$

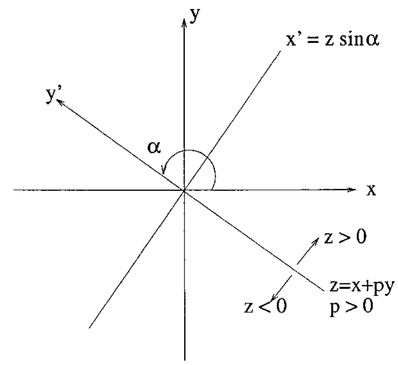

Fig. 2 A singular characteristic line corresponding to a real eigenvalue in the Stroh eigenvalue problem Eq. (1)

schemes were used to set up the proper eigensystems ([9,11]). Besides, it has been argued that the formulation for a bimaterial interface crack does not converge to that for a homogeneous material ([2]). This work showed that both problems could be solved elegantly if the following six-dimensional polarization matrix is set up for an isotropic material

$$A=\begin{bmatrix} 1 & -p_2 & 0 & 1 & p_2 & p_2 \\ p_1 & 1 & 0 & -p_1 & 1 & 1 \\ 0 & 0 & 1 & 0 & -1 & 1+p_2^2 \end{bmatrix} \tag{3}$$

where the Stroh eigenvalues p_1 and p_2 are given by

$$p_1=\sqrt{\left[\frac{v}{c_L}\right]^2-1},\quad p_2=\sqrt{\left[\frac{v}{c_T}\right]^2-1}$$

and c_L and c_T are the dilatational and transverse shear wave speeds, respectively. Eq. (3) defines six independent eigenvectors that span the proper eigenspace of the sextic problem for the isotropic material.

In the case of homogeneous systems, it was proposed here that if the homogeneous material is divided into two half-spaces along a plane containing the crack, then the formulation for a bimaterial interface crack developed above can be applied directly with the two materials having identical properties. Moreover, there is no difficulty with the convergence of results for the bimaterial systems to that of the homogeneous ones. The example in the following sections will show that this treatment gives the correct results.

Discussions on the Solutions

If λ is an eigenvalue of Eq. (1), $1/\lambda^*$ must satisfy the equation, too. Therefore, two types of solutions are obtained.

1 Type I Field
When the eigenvalue is not equal to the reciprocal of its complex conjugate, i.e., $\lambda \neq 1/\lambda^*$, there are three sets of solutions:

$$(\epsilon,\mathbf{w}),\quad (-\epsilon^*,\mathbf{w}^*),\quad \text{and}\quad (\epsilon_3,\mathbf{w}_3), \tag{4}$$

where the oscillatory index $\epsilon=\epsilon_r+i\epsilon_m$ is complex and so is its corresponding eigenvector $\mathbf{w}$, ϵ_3 is a purely imaginary number, with a corresponding real eigenvector $\mathbf{w}_3$. For the convenience of discussion, the stress field associated with this solution is called the Type I field, and is oscillatory. The three eigenvalues in this paper are referred to as the *branches*, because in general they do not correspond to the three fracture modes.

2 Type II Field
When all the three eigenvalues satisfy $\lambda=1/\lambda^*$, they are purely imaginary and result in three real eigenvectors. The solution in this case can thus be expressed as

$$(i\epsilon_{m1},\mathbf{w}_1)\quad (i\epsilon_{m2},\mathbf{w}_2)\quad (i\epsilon_{m3},\mathbf{w}_3). \tag{5}$$

These eigenvalues can be degenerate. All the three branches are decoupled from each other in this case, and correspond to the mode I, mode II, and mode III crack-tip fields, respectively. This solution is designated as the Type II, and is nonoscillatory.

3 Singular Characteristics
For a real Stroh eigenvalue p, the independent variable $z=x+py$ becomes real. The corresponding characteristic line makes an angle of $\alpha=\pi-\tan^{-1}(1/p)$ with the positive x-axis. There are maximum three singular characteristic lines in each half-plane. Consider Type I crack-tip field in material I as an example. Using a rectangular coordinate system $x'-y'$ attached to the singular line (Fig. 2), it can be shown that $\sigma_{2i}=0$, $i=1,2,3$, for $z,x'<0$. However, σ_{2i} approach infinity on the other side $(z,x'>0)$ of this singular line, according to $|x'|^{-1/2+i\epsilon}$, $|x'|^{-1/2-i\epsilon^*}$, and $|x'|^{-1/2+i\epsilon_3}$, for the three branches of the oscillatory index, respectively.

Application to Typical Bimaterial Systems

In the following cases, only the singularity exponent q was plotted, which is related to the oscillatory index $\epsilon=\epsilon_r+i\epsilon_m$ by $q=\frac{1}{2}+\epsilon_m$, and the crack-tip deformation field is proportional to $r^{-q+i\epsilon_r}$. The physically meaningful value is limited to $0<q\leq\frac{1}{2}$ considering the requirement for a finite strain energy and the con-

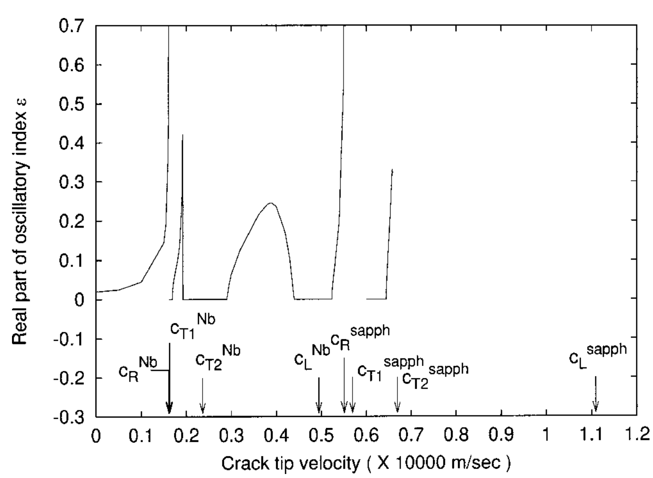

Fig. 3 The real part of the two coupled branches of the oscillatory index as a function of the crack-tip speed for the anisotropic niobium-basal sapphire system. The two branches have identical real parts but with opposite sign. The third branch always has a zero real part.

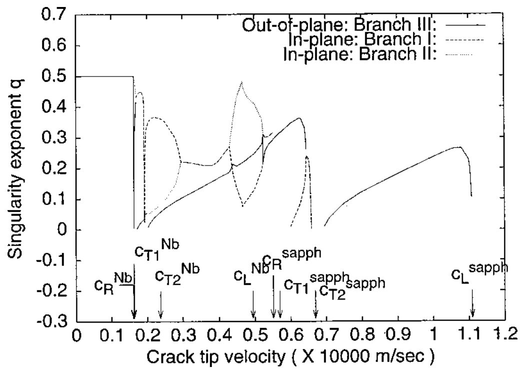

Fig. 4 Crack-tip singularity exponent *q* as a function of the crack-tip speed for the anisotropic niobium-basal sapphire system. Note, $q=1/2+\varepsilon_m$, where ε_m is the imaginary part of the oscillatory index ε.

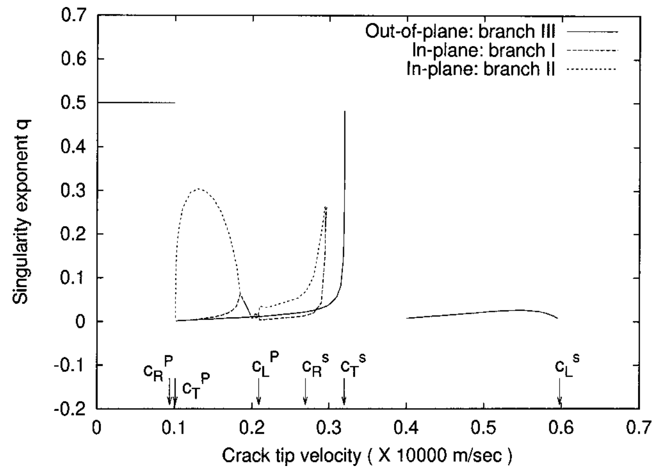

Fig. 6 Crack-tip singularity exponent *q* as a function of the crack-tip speed for the isotropic PMMA-steel system. Note, $q=1/2+\varepsilon_m$, where ε_m is the imaginary part of the oscillatory index ε.

vergence of the volume integral for the strain energy along the singular characteristic lines in addition to those around the point of the crack tip.

Anisotropic-Anisotropic Bimaterial Systems. The singularities are calculated for a crack growing along an anisotropic Nb/sapphire interface, having an orientation relationship $(111)_{\mathrm{Nb}}\|(0001)_{\mathrm{sapphire}}$ and $[110]_{\mathrm{Nb}}\|[2\bar{1}\bar{1}0]_{\mathrm{sapphire}}$, which occurs in the growth of single crystal niobium thin films on basal sapphire substrates by molecular beam epitaxy [12]. The coordinates are chosen such that *x* and *y*- axes are aligned with the basal plane crystal axis and the *c*-axis of the sapphire, respectively. The crack is oriented with its face in the $x-z$ plane, and its tip propagating in the *x*-direction, at an arbitrary constant speed v. The elastic constants were cited from [13] and [14]. The Rayleigh wave speed (c_R), the transverse shear wave speed (c_T), and the longitudinal wave speed (c_L) of sapphire and niobium in the crack propagation direction were calculated. The oscillatory index was computed using the above formulas and summarized in Figs. 3 and 4.

Isotropic Bimaterial Systems. An example of isotropic bimaterial systems is the PMMA-steel system that has been studied extensively. The results are shown in Figs. 5 and 6. Huang et al. [7] investigated one section of the supersonic regime between the two shear wave speeds for the out-of-plane and in-plane cases by directly solving the wave equations. As compared with their work, the above results are numerically identical to that. This proves that the above approach is mathematically correct.

Homogeneous Anisotropic Systems. The single crystal basal sapphire is used to demonstrate the application to a homogeneous

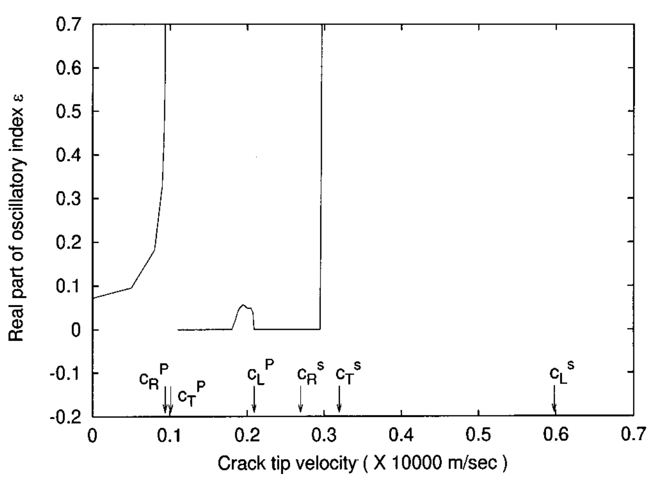

Fig. 5 The real part of the two coupled branches of the oscillatory index as a function of the crack-tip speed for the isotropic PMMA-steel system. The two branches have identical real parts but with opposite sign. The third branch always has a zero real part.

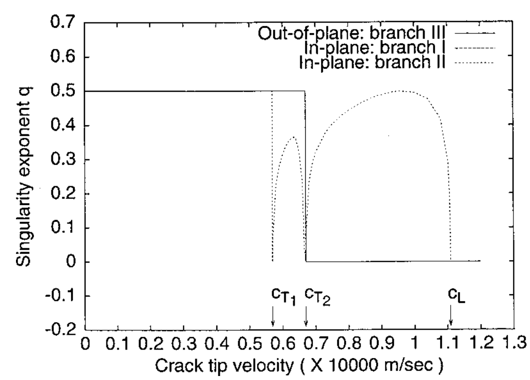

Fig. 7 Crack-tip singularity exponent *q* as a function of the crack-tip speed for the homogeneous anisotropic basal sapphire system. Note, $q=1/2+\varepsilon_m$, where ε_m is the imaginary part of the oscillatory index ε.

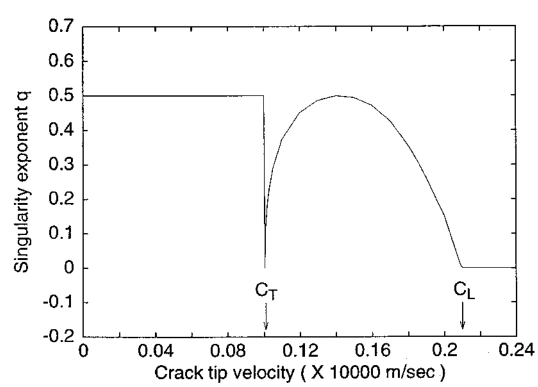

Fig. 8 Crack-tip singularity exponent *q* as a function of the crack-tip speed for the homogeneous isotropic PMMA system. Note, $q=1/2+\varepsilon_m$, where ε_m is the imaginary part of the oscillatory index ε.

anisotropic system. Using the formulation for a homogeneous system proposed above, the material properties for the upper and lower half-planes are set identical. The results are shown in Fig. 7. As well expected, the homogeneous system is nonoscillatory, and there are at most two distinct values for the singularity exponent q at a particular crack speed. It is interesting to note that the crack-tip singularity exponent q reaches a maximum of 0.5 at $v=\sqrt{2}c_{T_2}$, where c_{T_2} is the second (larger) transverse shear wave speed. Obviously, the singularity behavior is sharply different from that of the inhomogeneous systems (Figs. 3–6). Unfortunately, there has been no analytical solution for such a system to compare with.

Homogeneous Isotropic Systems. The homogeneous system of PMMA was used to demonstrate the homogeneous isotropic systems. The results are shown in Fig. 8. In fact, the system of a homogeneous isotropic material had been solved analytically for the out-of-plane and in-plane cases separately in the 1960s [15]. The results in the present work match numerically with theirs. For instance, the singularity exponent q reaches a maximum of 0.5 at $\sqrt{2}c_T$, where c_T is the shear wave speed. The purpose of including this section here is simply to validate the eigensystem established in this work.

Discussions

The sextic approach as described in this work is convenient to treat the asymptotic problem at an arbitrary crack speed for any homogeneous or bimaterial system with either isotropic or anisotropic component materials in the linear elastic regime. The crack-tip field has a weak singularity in most of the supersonic regime, and singularity is absent within some small crack speed intervals in the case of bimaterial systems, while homogeneous systems have singularity for all crack speed up to the dilatational wave speed. When the singularity does not exist, it implies that an energy equal or above the materials' intrinsic interface adhesive energy is required to sustain the interface crack propagation for the ideally linear elastic materials under consideration, that is, it is equivalent to debonding. In the supersonic regime, anisotropy aggravates crack-tip singularity, while inhomogeneity alleviates the singularity significantly. The conclusions are practically important in designing material systems containing interfaces.

From the point of view of energy balance, a crack propagates due to a finite energy release rate. However, for the linear elasticity considered here, the crack has a weak singularity, which results in a zero energy release rate if it is carried out in terms of the conventional definition ([4,5]). Here it simply assumes that the weak singularity would still augment the remote loading such that it is strong enough at the crack tip to propagate it. Besides, it should be noted that the oscillatory crack-tip field has the problem of crack-face contact, which is not covered here.

References

[1] Rice, J. R., 1988, "Elastic Fracture Mechanics Concepts for Interfacial Cracks," ASME J. Appl. Mech., **55**, pp. 98–103.
[2] Zhigang, Suo, 1990, "Singularities, Interfaces and Cracks in Dissimilar Anisotropic Media," Proc. R. Soc. London, Ser. A, **A427**, pp. 331–358.
[3] Ting, T. C. T., and Chadwick, P., 1988, "Harmonic Waves in Periodically Layered Anisotropic Elastic Composites," *Wave Propagation in Structural Composites*, A. X. Mal and T. C. T., eds., ASME, New York, pp. 69–79.
[4] Tippur, H. V., and Rosakis, A. J., 1991, "Quasi-Static and Dynamic Crack Growth Along Bimaterial Interfaces: A Note on Crack-Tip Field Measurement Using Coherent Gradient Sensing," Exp. Mech., **31**, No. 3, pp. 243–251.
[5] Liu, C., Lambros, J., and Rosakis, A. J., 1993, "Highly Transient Elasto-Dynamic Crack Growth in a Bimaterial Interface: Higher Order Asymptotic Analysis and Optical Experiment," J. Mech. Phys. Solids, **41**, No. 12, pp. 1887–1954.
[6] Lambros, J., and Rosakis, A. J., 1995, "Shear Dominated Transonic Crack Growth in a Bimaterial—Experimental Observations," J. Mech. Phys. Solids, **43**, No. 2, pp. 169–188.
[7] Huang, Y., Liu, C., and Rosakis, A. J., 1996, "Transonic Crack Growth Along a Bimaterial Interface: An Investigation of the Asymptotic Structure of Near-Tip Fields," Int. J. Solids Struct., **33**, No. 18, pp. 2625–2645.
[8] Wu, Jianxin, 2000, "Asymptotic Analysis of Supersonic Bimaterial Interface Cracks Using the Sextic Approach," *Seismic Engineering*, ASME, New York, pp. 81–88.
[9] Stroh, A. N., 1962, "Steady-State Problems in Anisotropic Elasticity," J. Math. Phys., **XLI**, No. 2, pp. 77–102.
[10] Yu, H. H., and Suo, Z., 2000, "Intersonic Crack Growth on an Interface," Proc. R. Soc. London, Ser. A, **A45b**, pp. 223–246.
[11] Bacon, D. J., Barnett, D. M., and Scattergood, R. O., 1980, "Anisotropic Continuum Theory of Lattice Defects," Prog. Mater. Sci., **23**, pp. 51–262.
[12] Gutekunst, G., Mayer, J., and Rühle, M., 1994, "The Niobium/Sapphire Interface: Structural Studies by HREM," Scripta Metall., **31**(8), pp. 1097–1102.
[13] Bernstein, T. B., 1963, "Elastic Constants of Synthetic Sapphire at 27°C," J. Appl. Phys., **34**, No. 1, pp. 169–172.
[14] Bolef, D. I., 1961, "Elastic Constants of Single Crystals of the bcc Transition Elements V, Nb, and Ta," J. Appl. Phys., **32**, pp. 100–105.
[15] Freund, L. B., *Dynamic Fracture Mechanics*, 1990, Cambridge University Press, Cambridge, UK.

Effective Antiplane Dynamic Properties of Fiber-Reinforced Composites

X. D. Wang
Mem. ASME
e-mail: xiaodong.wang@ualberta.ca

S. Gan

Department of Mechanical Engineering, University of Alberta, Edmonton, Alberta T6G 2G8, Canada

This paper provides an theoretical analysis of the properties of fiber-reinforced composite materials under antiplane waves. A self-consistent scheme is adopted in calculating the effective material constants. A new averaging technique is developed to account for the effects of the waveform. The model is then used to evaluate the effective dynamic properties of composites with randomly distributed fibers. Typical examples are presented to show the effects of different pertinent parameters upon the effective wave speed and the attenuation. [DOI: 10.1115/1.1480819]

1 Introduction

Fiber-reinforced composites are increasingly used in situations involving dynamic loading, where the evaluation of wave propagation will be a main concern ([1]). Because the interaction between fibers decays slowly with the distance between them, a large number of fibers need to be considered simultaneously in the determination of the average properties of fiber-reinforced composites. Simplified models, such as multiple scattering method ([2–4]) and self-consistent method ([5–7]) are usually used to study the effective dynamic mechanical properties of composites. Because of the difficulties in approximating the multiple scattering from the inhomogeneities, high-order scattering effects are usually neglected in multiple scattering method. This method has been rigorously modified in [8] by introducing more realistic pair-correlation functions to evaluate the average of scattering waves accurately. In the self-consistent model ([5]), the determination of the effective property is based on the use of direct volume average of field parameters. The model will, therefore, be suitable for the cases where the wavelength is much longer than the size of the reinforcements.

Contributed by the Applied Mechanics Division of THE AMERICAN SOCIETY OF MECHANICAL ENGINEERS for publication in the ASME JOURNAL OF APPLIED MECHANICS. Manuscript received by the ASME Applied Mechanics Division, June 19, 2001; final revision, February 25, 2002. Associate Editor: M.-J. Pindera.

The current study proposed a new volume average process in evaluating the effective dynamic properties of fiber-reinforced composites by considering the effect of the waveform, which enables the treatment of the variation of field parameters in the reinforcements. The results are then implemented into a self-consistent scheme to determine the effective dynamic properties of fiber-reinforced composites. Numerical examples are provided to show the effect of the volume fraction of the fibers, the material constants, and the loading frequency upon the dispersion and attenuation properties of the composites.

2 Formulation of the Problem

Consider the antiplane problem of a fiber-reinforced composite containing randomly distributed circular fibers of radius R with volume fraction ϕ, subjected to a harmonic incident wave of frequency ω, as shown in Fig. 1. For the steady-state dynamic solution of the problem, the time factor $e^{-i\omega t}$ applying to all the field parameters will be suppressed.

It is assumed that the composite can be modeled as an effective homogeneous, isotropic medium, which is governed by the following equations:

$$\nabla\sigma=-i\omega p \tag{1}$$

$$\sigma=\mu_e\gamma, \quad p=-i\omega\rho_e w \tag{2}$$

where $\nabla=(\partial/\partial x,\partial/\partial y)$, σ and p are the stress and momentum density, respectively, with $\sigma=(\tau_{xz},\tau_{yz})^T$, $\gamma=(\gamma_{xz},\gamma_{yz})^T$, w being the antiplane displacement, and μ_e and ρ_e the effective elastic modulus and effective mass density of the composite.

Attention will be focussed on a harmonic antiplane wave in the effective medium of the form

$$w^{in}(x,y)=w^0e^{ik_ex} \tag{3}$$

which represents a wave propagation in the x-direction, with $k_e=\omega\sqrt{\rho_e/\mu_e}$ being the wave number of the effective medium. Equation (3) represents the approximate (effective) displacement field in the composite medium, i.e.,

$$w(x,y)\approx w^0e^{ik_ex}. \tag{4}$$

The effective wave field can be related to the real displacement field $w(x,y)$ using a Fourier integration. Multiplying both sides of Eq. (4) with e^{-ik_ex} and integrating over a representative volume V, the volume average of w^{in} can be obtained

$$\langle w^{in}\rangle=w^0=\frac{1}{V}\int_V w(x,y)e^{-ik_ex}dV. \tag{5}$$

The averages of other field parameters can be obtained similarly. Accordingly, the average stress $\langle\sigma\rangle$, strain $\langle\gamma\rangle$, momentum density $\langle p\rangle$ and particle velocity $\langle -i\omega w\rangle$ can be expressed in terms of average values in the matrix and the fiber as

$$\langle f\rangle=(1-\phi)\langle f\rangle_m+\phi\langle f\rangle_f \tag{6}$$

with f representing the stress, strain, momentum density and particle velocity, with subscripts m and f refering to matrix and fiber, respectively. Using the constitutive relations of the matrix and the fiber to eliminate $\langle\gamma\rangle_m$ and $\langle -i\omega w\rangle_m$ from the above equations, following results can be obtained:

$$\langle\sigma\rangle=\mu_m\langle\gamma\rangle+\phi(\mu_f-\mu_m)\langle\gamma\rangle_f \tag{7}$$

$$\langle p\rangle=\rho_m\langle -i\omega w\rangle+\phi(\rho_f-\rho_m)\langle -i\omega w\rangle_f. \tag{8}$$

The average strain and particle velocity in the fibers $\langle\gamma\rangle_f$ and $\langle -i\omega w\rangle_f$ can be expressed in terms of that of the effective field, i.e.,

$$\langle\gamma\rangle_f=N\langle\gamma\rangle, \quad \langle -i\omega w\rangle_f=M\langle -i\omega w\rangle \tag{9}$$

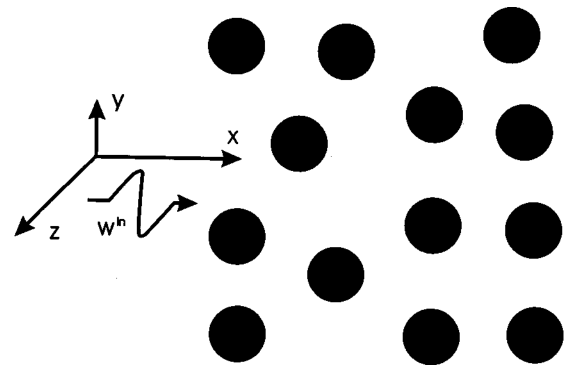

Fig. 1 Antiplane wave propagation in fiber-reinforced composites

with N and M being in terms of the material constants, geometry and frequency. The effective constitutive relation of the composite can then be determined, such that

$$\langle\sigma\rangle=\mu_e\langle\gamma\rangle, \quad \langle p\rangle=\rho_e\langle -i\omega w\rangle \tag{10}$$

with

$$\mu_e=\mu_m+\phi(\mu_f-\mu_m)N, \quad \rho_e=\rho_m+\phi(\rho_f-\rho_m)M. \tag{11}$$

N and M are in terms of the effective material constants μ_e and ϵ_e and will be determined using a self-consistent model.

3 Self-Consistent Method

To determine N and M in (9), the self-consistent scheme developed by Sabina and Willis [5] will be used in the current analysis. The strain and velocity fields around a fiber can be approximately evaluated by assuming that the effects of other fibers can be represented by an effective medium. This will then necessitate the solution of a problem that a single fiber is embedded in the effective medium with material constants μ_e and ρ_e.

Consider now the problem of a single fiber embedded in the effective medium subjected to an incident wave given by (3). Following the idea of Willis [9], the stress and momentum density can be generally expressed as

$$\sigma=\mu_e\gamma+\tau, \quad p=-i\omega\rho_e w+\pi \tag{12}$$

where τ and π are caused by the existence of the fiber. The resulting displacement field is equivalent to that of a uniform effective medium subjected to body forces and can be represented in terms of a convolution integral using Green's function for the effective medium,

$$w=w^{in}+G*F, \tag{13}$$

where $F=-1/\mu_e(\nabla\tau+i\omega\pi)$ and $G=-i/4H_0^{(1)}(k_er)$ is the Green's function satisfying $\nabla^2w+k_e^2w=\delta(r)$ with $H_0^{(1)}$ being the zeroth-order Hankel function of the first kind.

Using the constitutive relations of the fiber and the effective medium, the strain and the particle velocity in the fiber can be expressed in terms of τ and π as

$$\gamma=(\mu_f-\mu_e)^{-1}\tau, \quad -i\omega w=(\rho_f-\rho_e)^{-1}\pi. \tag{14}$$

Making use of Eqs. (13) and (14), the following relations are obtained within the fiber,

$$(\rho_f-\rho_e)^{-1}\pi+i\omega G*F=-i\omega w^{in} \tag{15}$$

$$(\mu_f-\mu_e)^{-1}\tau-G^{\gamma}*F=\gamma^{in}, \tag{16}$$

where $G^{\gamma}=[\partial G/\partial x,\partial G/\partial y]^T$. From this equation, $\tau=[\tau_{xz},\tau_{yz}]$ and π can be determined.

To obtain an approximate solution including the effect of the waveform τ and π are assumed, in the fiber, to be

$$\tau = \begin{bmatrix} \tau_{xz}^0 \\ \tau_{yz}^0 \end{bmatrix} e^{ik_e x}, \quad \pi = \pi^0 e^{ik_e x}. \tag{17}$$

Since the average displacement and strain of the effective medium are given by $\langle w^{in}\rangle = w^0, \langle \gamma_{zx}^{in}\rangle = \gamma_{xz}^0, \langle \gamma_{yz}^{in}\rangle = \gamma_{yz}^0$, substituting (17) into (15)–(16) and taking the average defined by (5), the following algebraic equations can be obtained:

$$[(\rho_f - \rho_e) + \omega^2 I/\mu_e]\pi^0 + i\omega(ik_e I + I_1)/\mu_e \tau_{xz}^0 + i\omega I_2/\mu_e \tau_{yz}^0 = -i\omega w^0 \tag{18}$$

$$i\omega J/\mu_e \pi^0 + [1/(\mu_f - \mu_e) - (ik_e J + J_1)/\mu_e]\tau_{xz}^0 - J_2/\mu_e \tau_{yz}^0 = \gamma_{xz}^0 \tag{19}$$

$$i\omega K/\mu_e \pi^0 - (ik_e K + K_1)/\mu_e \tau_{xz}^0 + [1/(\mu_f - \mu_e) - K_2/\mu_e]\tau_{yz}^0 = \gamma_{yz}^0 \tag{20}$$

from which π^0, τ_{xz}^0, and τ_{yz}^0 can be obtained. In these equations, I, I_i, J, J_i, K, and K_i are given by

$$I = \frac{1}{A}\int_{A(x)}\int_{A(\xi)} G(x-\xi) e^{ik_e(x_1-\xi_1)} d\xi dx \tag{21}$$

$$I_i = \frac{1}{A}\int_{A(x)}\int_{S(\xi)} G(x-\xi) e^{ik_e(x_1-\xi_1)} n_i(\xi) ds dx \tag{22}$$

$$J = \frac{1}{A}\int_{A(x)}\int_{A(\xi)} G_{,x_1}(x-\xi) e^{ik_e(x_1-\xi_1)} d\xi dx \tag{23}$$

$$J_i = \frac{1}{A}\int_{A(x)}\int_{S(\xi)} G_{,x_1}(x-\xi) e^{ik_e(x_1-\xi_1)} n_i(\xi) ds dx \tag{24}$$

$$K = \frac{1}{A}\int_{A(x)}\int_{A(\xi)} G_{,x_2}(x-\xi) e^{ik_e(x_1-\xi_1)} d\xi dx \tag{25}$$

$$K_i = \frac{1}{A}\int_{A(x)}\int_{S(\xi)} G_{,x_2}(x-\xi) e^{ik_e(x_1-\xi_1)} n_i(\xi) ds dx \tag{26}$$

with n_j representing the normal direction of the surface (interface) of the fiber, $A(x)$ and $S(\xi)$ being the area of integration and its boundary, defined by $x_1^2 + x_2^2 \leqslant R^2$.

According to (9) and (14), N and M used in (11) can be determined:

$$N = (\mu_f - \mu_e)^{-1}\frac{\tau_{xz}^0}{\gamma_{xz}^0}, \quad M = (\rho_f - \rho_e)^{-1}\frac{\pi^0}{-i\omega w^0}. \tag{27}$$

The effective material constants can then be calculated as

$$\mu_e = \mu_m + \phi\frac{(\mu_f - \mu_m)}{(\mu_f - \mu_e)}\frac{\tau_{xz}^0}{\gamma_{xz}^0}, \quad \rho_e = \rho_m + \phi\frac{(\rho_f - \rho_m)}{(\rho_f - \rho_e)}\frac{\pi^0}{-i\omega w^0}. \tag{28}$$

The integrals (21)–(26) are very important in obtaining reliable solutions. Efforts have been made in evaluating these integrations to ensure accuracy and efficiency. It should be mentioned that by considering the effect of the waveform in the average process as given by Eq. (5), the current model provides a consistent solution of the average field parameters by avoiding the usage of extra average process over fiber distribution, which was used in [5] to deal with the variation of averaged field parameters with the position of the fiber.

4 Results and Discussion

Numerical simulation is conducted to simulate the effective antiplane dynamic properties of fiber-reinforced composites. As expected, the solution predicts the existence of complex material constants ρ_e and μ_e, which result in a complex wave number $k_e = k_r + ik_i$. The antiplane wave in the effective medium given by (3) can then be expressed as

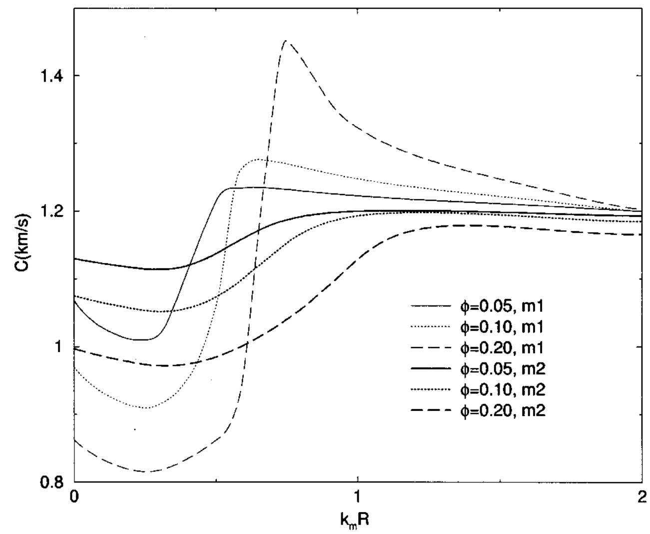

Fig. 2 Phase velocity for material combinations 1 and 2

$$w^{in} = w^0 e^{-k_i x} e^{ik_r x} \tag{29}$$

with the real part of the effective wave number k_r corresponding to the phase velocity $C = \omega/k_r$ of the elastic wave propagating in the effective medium and the imaginary part k_i corresponding to the attenuation of the wave.

The material constants used in the simulation are

$$\mu_m = 1.73(\text{GPa}), \quad \rho_m = 1200(\text{kg/m}^3)$$

$$\text{Fiber 1}, \ \mu_f = 8.36(\text{GPa}), \quad \rho_f = 11300(\text{kg/m}^3);$$

$$\text{Fiber 2}, \ \mu_f = 4.18(\text{GPa}), \quad \rho_f = 5650(\text{kg/m}^3);$$

$$\text{Fiber 3}, \ \mu_f = 1.05(\text{GPa}), \quad \rho_f = 1410(\text{kg/m}^3)$$

corresponding to material combinations 1, 2, and 3 (m1, m2, and m3), respectively.

Figure 2 shows the variation of phase velocity C with normalized loading frequency $k_m R$ with different volume fraction (ϕ) for material combinations 1 and 2 in which $k_m = \omega\sqrt{\rho_m/\mu_m}$ is the wave number in the matrix. Figure 3 shows the attenuation of the composite for different frequencies and volume fractions. A noteworthy feature of the attenuation curves is the presence of a

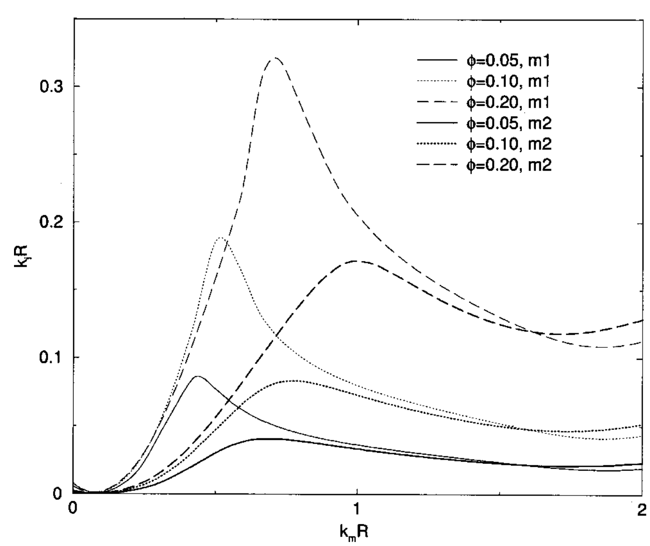

Fig. 3 Attenuation for material combinations 1 and 2

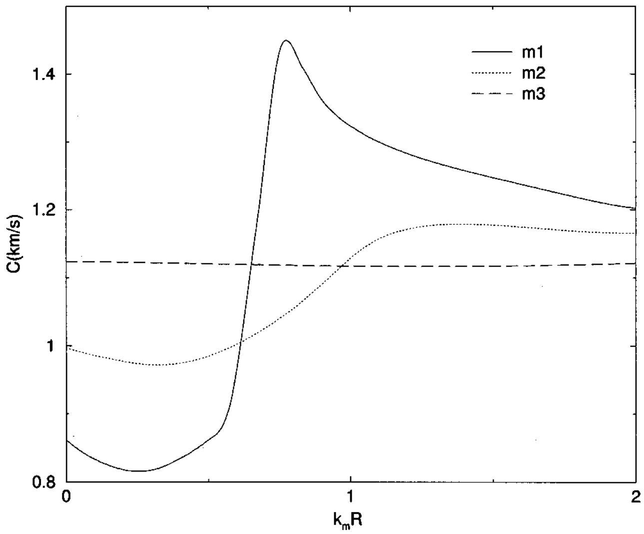

Fig. 4 Phase velocity for $\phi=0.2$

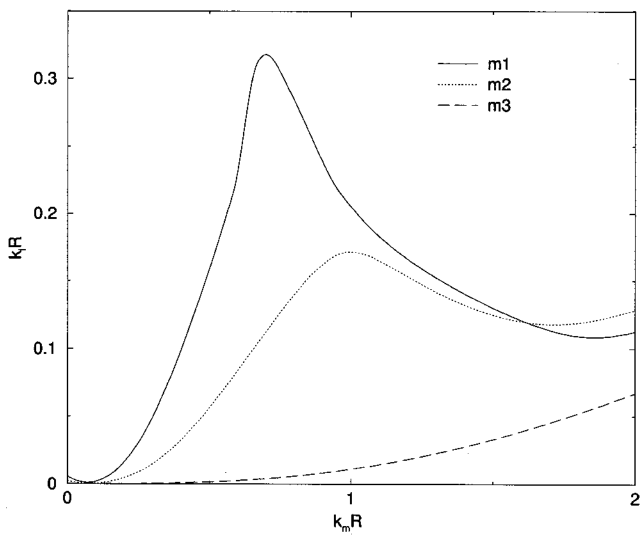

Fig. 5 Attenuation for $\phi=0.2$

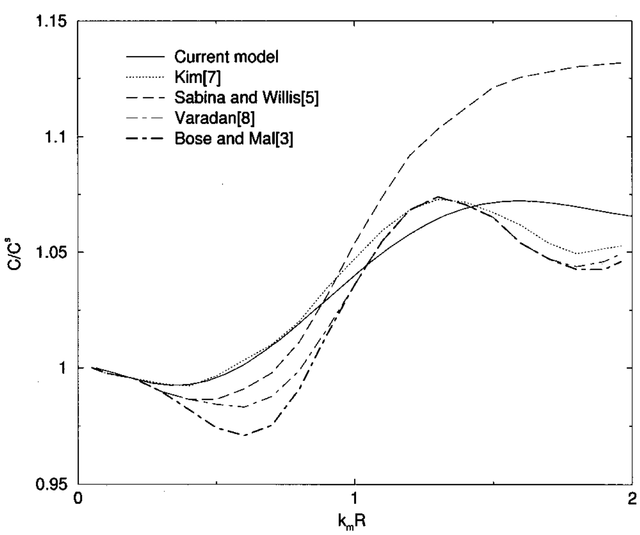

Fig. 6 Normalized phase velocity for $\phi=0.27$

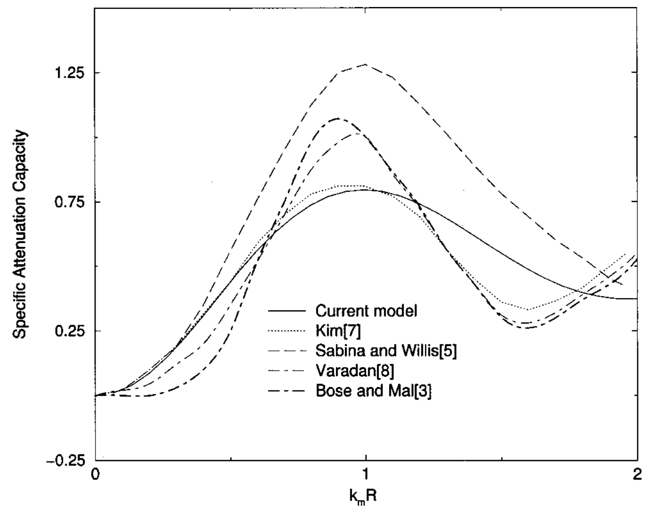

Fig. 7 Specific attenuation capacity for $\phi=0.27$

"resonance" effect at specific frequencies. With the increase of volume fraction the effective medium shows stronger dispersion and attenuation properties.

To evaluate the effect of material combination directly, the phase velocity and attenuation of the composite for material combinations 1, 2, and 3 are depicted in Figs. 4 and 5 for $\phi=0.2$. As the material mismatch becomes smaller, the dispersion and attenuation of the composite decrease, as evidenced by the fact that for material combination 3 the phase velocity is almost frequency-independent and the attenuation is much lower than that of material combinations 1 and 2.

The prediction from the current method has been compared with results from other existing techniques for steel(fibre)/aluminum(matrix) composites ([7]). The normalized phase velocity and the specific attenuation capacity for $\phi=0.27$ are depicted in Figs. 6 and 7, respectively, where C is normalized by the phase velocity corresponding to zero-frequency, C^s, and the specific attenuation capacity is defined as $4\pi k_i/k_r$. It is interesting to mention that the current result is similar to that given by Kim [7] for low frequencies ($k_mR<1$). Significant difference, however, can be observed for higher frequencies ($k_mR>1$).

Acknowledgments

This work was supported by the Natural Sciences and Engineering Research Council of Canada (NSERC).

References

[1] Wang, X. D., and Meguid, S. A., 1997, "Diffraction of SH-Wave by Interacting Matrix Crack and an Inhomogeneity," ASME J. Appl. Mech., **64**, pp. 558–574.
[2] Waterman, P. C., and Truell, R., 1960, "Multiple Scattering of Waves," J. Math. Phys., **2**, pp. 512–537.
[3] Bose, S. K., and Mal, A. K., 1973, "Longitudinal Shear Waves in a Fiber-Reinforced Composite," Int. J. Solids Struct., **9**, pp. 1075–1085.
[4] Datta, S. K., Ledbetter, H. M., and Kriz, R. D., 1984, "Calculated Elastic Constants of Composites Containing Anisotropic Fibers," Int. J. Solids Struct., **20**, pp. 429–438.
[5] Sabina, F. J., and Willis, J. R., 1988, "A Simple Self-Consistent Analysis of Wave Propagation in Particulate Composite," Wave Motion, **10**, pp. 127–142.
[6] Yang, R. B., and Mal, A. K., 1996, "Elastic Waves in a Composite Containing Inhomogeneous Fibers," Int. J. Eng. Sci., **34**, pp. 67–79.
[7] Kim, J. Y., 1996, "Dynamic Self-Consistent Analysis for Elastic Wave Propagation in Fiber Reinforced Composites," J. Acoust. Soc. Am., **100**(4), pp. 2002–2010.
[8] Varadan, V. K., Varadan, V. V., and Ma, Y., 1985, "Multiple Scattering of Elastic Waves by Cylinders of Arbitrary Cross Section. II. Pair-Correlated Cylinders," J. Acoust. Soc. Am., **78**, pp. 1874–1878.
[9] Willis, J. R., 1980, "A Polarization Approach to the Scattering of Elastic Waves—I. Scattering by a Single Inclusion," J. Mech. Phys. Solids, **28**, pp. 287–305.

Elasticity Solution for a Laminated Orthotropic Cylindrical Shell Subjected to a Localized Longitudinal Shear Force

K. Bhaskar
e-mail: kbhas@aero.iitm.ernet.in

N. Ganapathysaran

Department of Aerospace Engineering, Indian Institute of Technology, Madras, Chennai, 600 036, India

A three-dimensional elasticity solution is presented for the title problem. The solution is in terms of a double Fourier series in the surface-parallel directions and a power series in the thickness direction. On the basis of this solution, it is shown that the classical lamination theory is inadequate for this problem because the steep displacement and stress gradients near the load cannot be captured by it correctly even if the shell is thin.
[DOI: 10.1115/1.1480823]

Introduction

Of late, there has been considerable interest in the development of three-dimensional elasticity solutions for laminated composite shells. Confining attention to cylindrical shells under static mechanical loading, one finds that such solutions have been obtained for the cases of cylindrical bending due to sinusoidal surface tractions ([1,2]), axisymmetric deformation due to sinusoidal as well as band loading ([3,4]); and general deformation due to sinusoidally varying tractions ([5,6]), pinching loads ([7]), and a single patch radial load ([8]). This sort of rigorous analysis, albeit for certain specific boundary conditions, layups, and loading, is justified because it is now well known that nonclassical influences like thickness-shear and thickness-normal strain are significant for composite structures and that there is a need to quantify the errors of classical shell theories against some three-dimensional benchmark solutions which automatically account for the nonclassical effects.

A look at the literature cited above reveals that all the available elasticity solutions are for smoothly varying or localized radial loads. Localized loading transmitted through attachments like support brackets, lifting lugs, nozzles, etc., can result in significant shear forces besides radial forces, and such forces are often accounted for, as for instance in pressure vessel design ([9]). The objective of this note is to provide a baseline elasticity solution for the case of a localized longitudinal shear force and to examine the errors of classical lamination theory when applied to this problem.

Formulation and Solution

An N-layered cylindrical shell is subjected to a shear force P, applied in the longitudinal direction, on a small rectangular patch on the outer surface as shown in Fig. 1. The material axes of any layer coincide with the geometric r-θ-z axes, so that the stress-strain law is given by

Contributed by the Applied Mechanics Division of THE AMERICAN SOCIETY OF MECHANICAL ENGINEERS for publication in the ASME JOURNAL OF APPLIED MECHANICS. Manuscript received by the ASME Applied Mechanics Division, August 24, 2001; final revision, December 15, 2001. Associate Editor: A. K. Mal.

$$\sigma_i=\Sigma C_{ij}\varepsilon_j\,,\quad i,j=1(r),2(\theta),3(z);$$
$$\tau_k=C_{kk}\gamma_k\,,\quad k=4(rz),5(r\theta),6(\theta z). \tag{1}$$

The ends are axially restrained but otherwise free to move, i.e.,

$$\text{at } z=0,L:\ \ u_z=\tau_{zr}=\tau_{z\theta}=0. \tag{2}$$

The boundary conditions at the lateral surfaces and the interfaces are

$$\text{at } r=R_{\max}:\quad \sigma_r=\tau_{r\theta}=0 \ \text{ and }\ \tau_{rz}=q_z$$
$$\text{at } r=R_{\min}:\quad \sigma_r=\tau_{r\theta}=\tau_{rz}=0$$
$$\text{across any interface:}$$
$$u_r,u_\theta,u_z,\sigma_r,\tau_{rz},\tau_{r\theta}\ \text{ are continuous} \tag{3}$$

where q_z stands for the shear force per unit area corresponding to the applied local load P. For later use, q_z is written in the form of the following double Fourier series:

$$q_z=\sum_{m=1,3,\ldots}\ \sum_{n=0,1,2,\ldots} q_{mn}\sin(m\pi z/L)\cos n\theta \tag{4}$$

where

$$q_{m0}=(2P/\pi^2 mL_pR_{\max})\sin(m\pi L_p/2L)\sin(m\pi/2);$$
$$q_{mn}=(8P/\pi^2 mnL_PR_{\max}\theta_p)\sin(m\pi L_p/2L)\sin(m\pi/2)\sin(n\theta_P/2)$$
$$\text{for } n\geqslant 1$$

and L_P and θ_P are as shown in Fig. 1.

The above three-dimensional boundary value problem can be solved by using the displacement approach as follows. The three equilibrium equations with respect to r-θ-z coordinates are first expressed in terms of the displacements u_r, u_θ, and u_z to yield three coupled partial differential equations. Then the displacements are assumed to vary harmonically in the θ and z-directions as

$$(u_r,u_\theta,u_z)=h[\phi_r\cos(m\pi z/L)\cos n\theta,$$
$$\phi_\theta\cos(m\pi z/L)\sin n\theta,\ \ \phi_z\sin(m\pi z/L)\cos n\theta] \tag{5}$$

corresponding to one harmonic (i.e., m,n combination) of q_z. It can easily be verified that the above displacement variations automatically satisfy the end conditions (Eq. (3)). They also reduce the system of partial differential equations to the following ordinary differential equations:

$$[C_{11}(\xi+t)^2D_2+C_{11}(\xi+t)D_1-C_{55}n^2-C_{22}-C_{44}s^2(\xi+t)^2]\phi_r$$
$$+[(C_{55}+C_{12})n(\xi+t)D_1-(C_{55}+C_{22})n]\phi_\theta$$
$$+[(C_{13}+C_{44})s(\xi+t)^2D_1+[(C_{13}-C_{23})(\xi+t)s]\phi_z=0$$
$$-[(C_{55}+C_{12})n(\xi+t)D_1+(C_{55}+C_{22})n]\phi_r+[C_{55}(\xi+t)^2D_2$$
$$+C_{55}(\xi+t)D_1-C_{22}n^2-C_{55}-C_{66}s^2(\xi+t)^2]\phi_\theta$$
$$-[(C_{23}+C_{66})ns(\xi+t)]\phi_z=0$$
$$-[(C_{13}+C_{44})s(\xi+t)^2D_1+[(C_{44}+C_{23})(\xi+t)s]\phi_r$$
$$-[(C_{23}+C_{66})ns(\xi+t)]\phi_\theta+[C_{44}(\xi+t)^2D_2$$
$$+C_{44}(\xi+t)D_1-C_{66}n^2-C_{33}s^2(\xi+t)^2]\phi_z=0 \tag{6}$$

where $D_2=d^2/d\xi^2$; $D_1=d/d\xi$; $s=m\pi h/(2L)$; $t=2R_0/h$, where R_0 is the mean radius of the shell as shown in Fig. 1; ξ is a nondimensional radial coordinate given by $\xi=2(r-R_0)/h$.

The above equations have variable coefficients and hence have to be solved by using power series. The only associated singular point is at $r=0$ (i.e., $\xi=-2R_0/h$), and hence a power series solution about $\xi=0$ as given by

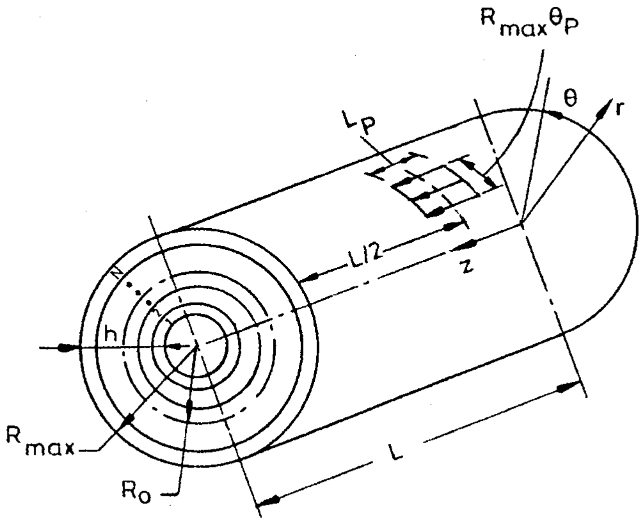

Fig. 1 Geometry and loading

Table 1 Axial and circumferential variations of the surface-parallel stresses

S	z/L	$\sigma_z^*(\theta=0)$	$\sigma_\theta^*(\theta=0)$	$\tau_{\theta z}^*(\theta=0.02\pi)$
20	0.48	391.4(0.46)	-100.7(0.07)	-42.76(0.30)
	0.49	214.1(0.43)	-61.13(0.06)	-77.23(0.20)
	0.50	0.0	0.0	-79.66(0.21)
50	0.48	889.6(0.52)	-219.9(0.10)	-60.13(0.53)
	0.49	380.0(0.61)	-129.1(0.10)	-102.1(0.39)
	0.50	0.0	0.0	-103.3(0.41)
100	0.48	1626.(0.57)	-383.6(0.14)	-88.10(0.72)
	0.49	578.1(0.80)	-214.8(0.14)	-135.9(0.59)
	0.50	0.0	0.0	-137.0(0.61)
500	0.48	6739.(0.70)	-1094.(0.40)	-307.0(0.99)
	0.49	2158.(1.10)	-743.7(0.33)	-378.3(1.00)
	0.50	0.0	0.0	-392.3(1.01)
S	**θ/π**	**$\sigma_z^*(z=0.48L)$**	**$\sigma_\theta^*(z=0.48L)$**	**$\tau_{\theta z}^*(z=0.5L)$**
20	0.00	391.4(0.47)	-100.7(0.07)	0.0
	0.01	362.0(0.48)	-88.45(0.07)	-18.88(0.32)
	0.02	241.9(0.42)	-47.54(0.08)	-79.66(0.21)
50	0.00	889.6(0.52)	-219.9(0.10)	0.0
	0.01	837.9(0.52)	-203.7(0.10)	-18.92(0.80)
	0.02	535.1(0.48)	-93.46(0.14)	-103.3(0.41)
100	0.00	1626.(0.57)	-383.6(0.14)	0.0
	0.01	1528.(0.57)	-340.9(0.15)	-30.61(0.93)
	0.02	939.9(0.55)	-137.1(0.23)	-137.0(0.72)
500	0.00	6739.(0.70)	-1094.(0.40)	0.0
	0.01	6279.(0.71)	-940.5(0.41)	-125.4(1.12)
	0.02	3462.(0.71)	-90.32(2.27)	-392.3(1.01)

σ_z^* at $\xi = 1/3(0^0$ layer); σ_θ^* at $\xi = -1$; $\tau_{\theta z}^*$ at $\xi = 1$. Values in brackets are CST results normalized with respect to corresponding elasticity results, i.e. (CST result/Elasticity result).

$$\phi_i = \sum_{j=0,1,2\ldots}^{\infty} \xi^j H_i(j) \quad \text{for } i=r,\theta,z \tag{7}$$

would be convergent at every point in the shell domain $-1 \leqslant \xi \leqslant 1$. The methodology for finding out the coefficients $H_r(j)$, $H_\theta(j)$, and $H_z(j)$ is straightforward ([10])—substitution of Eq. (7) in Eqs. (6) and equating the coefficient of each power of ξ to zero yields the coefficients as

$$H_r(j),H_\theta(j),H_z(j) = \sum_{k=1}^{6} G(k)[d_r(j,k),d_\theta(j,k),d_z(j,k)] \tag{8}$$

where $G(k)$ are six undetermined constants and $d_r(j,k)$, etc., are known quantities obtained using recurrence relations ([11]). For the sake of brevity, the recurrence relations are not given here.

Equation (8) is applicable for any particular layer, and hence, for the N-layered shell, there would be $6N$ unknowns. These are determined by enforcing the $6N$ lateral surface and interface conditions (Eq. (3)).

Results and Discussion

A (90 deg/0 deg/90 deg) shell with $L/R_0=4$ is considered for numerical studies. The material properties, typical of high-modulus graphite-epoxy, are taken as

$$E_l/E_T=25 \qquad G_{LT}/E_T=0.5 \qquad G_{TT}/E_T=0.2$$

$$\nu_{LT}=\nu_{TT}=0.25.$$

The patch size is taken to be $L_p=0.04L$ and $\theta_p=0.04\pi$. The results are presented in terms of the following nondimensional parameters:

$$U_i^* = E_L R_0 u_i/P \qquad \text{for } i=r,z$$

$$(\sigma_i^*, \tau_{ij}^*) = R_0^2(\sigma_i, \tau_{ij})/P \quad \text{for } i,j=r,\theta,z.$$

For any harmonic, the number of terms taken in the Taylor's series is such as to obtain four-digit convergence of the results; the number of harmonics considered is such that an increase of $m_{\max}$ or $n_{\max}$ by 10 does not affect the final results by more than 0.5%.

Table 1 presents the variation of the surface-parallel stresses in the close neighborhood of the patch in both the axial and circumferential directions. These are presented at critical ξ values at which the stresses reach high magnitudes. It should be noted that σ_z and σ_θ are antisymmetric about $z=L/2$ while $\tau_{\theta z}$ is symmetric; similarly about $\theta=0$, σ_z and σ_θ are symmetric while $\tau_{\theta z}$ is antisymmetric. Table 1 also includes values calculated using the classical lamination theory based on Love-Kirchhoff hypothesis—the actual shell theory employed is that in which no further assumptions besides Love-Kirchhoff hypothesis are made, commonly referred to as generalized Langhaar-Boresi theory ([12]). The corresponding solutions are based on the well-known Navier approach with assumed harmonic variations of the displacements for each harmonic of the load, leading to simple algebraic equations which directly yield the displacements. The harmonic variations in the axial and circumferential directions are the same as in Eq. (5). Results convergent upto four significant digits are obtained by summing the harmonics; in Table 1 they are presented in normalized form with respect to the corresponding elasticity values.

From Table 1, it can be seen that σ_z is predominant compared to the other two surface-parallel stresses, which are, however, not

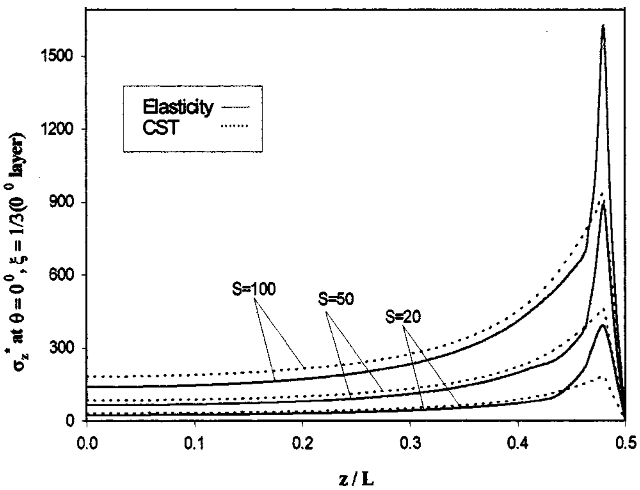

Fig. 2 Axial variation of longitudinal stress

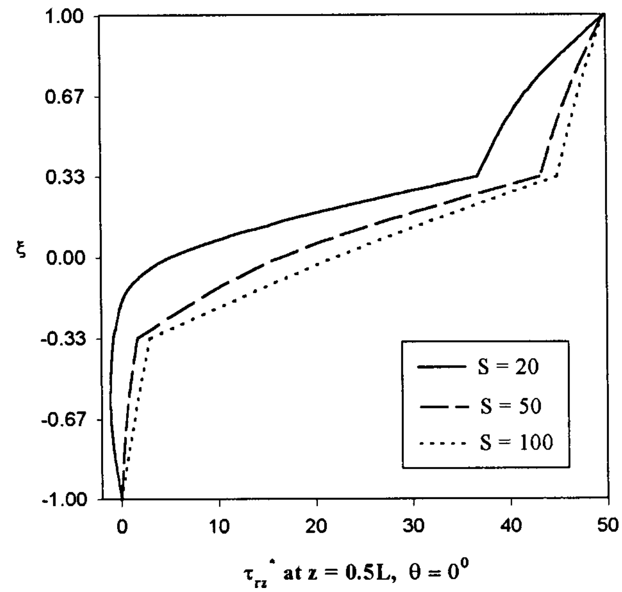

Fig. 5 Thickness-wise variation of τ_{rz}

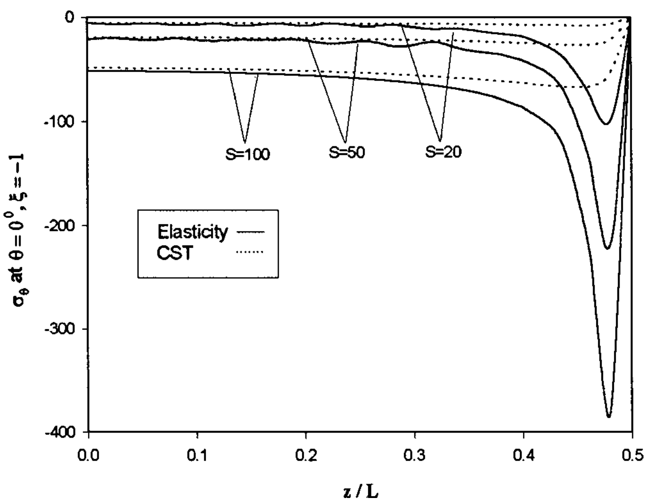

Fig. 3 Axial variation of circumferential stress

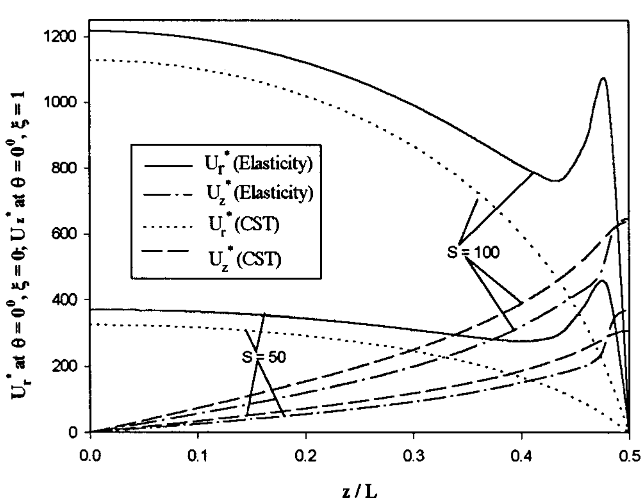

Fig. 4 Axial variations of u_r and u_z

negligible. CST errors decrease with increasing R_0/h (denoted by S hereafter) as can be expected, but the errors are significant even for thin shells with $S=500$. Further, CST predictions are much worse for σ_θ compared to the other two stresses. Plots of the axial variations of σ_z and σ_θ are presented in Figs. 2 and 3, which show that steep stress gradients occur close to the load patch as can be expected. The CST predictions are close to the elasticity values away from the load patch, but start diverging as one approaches the load.

Axial variations of the displacements u_r and u_z are presented in Fig. 4. These displacements are antisymmetric and symmetric, respectively, with respect to midspan. One can notice sudden steep gradients of both the displacements near the load, which are not captured by CST. This can be explained as follows. The applied loading—a shear stress τ_{rz}—results in nonzero shear strain γ_{rz}, a strain totally neglected in CST. This strain depends on two displacement gradients—$u_{z,r}$ and $u_{r,z}$—and hence, it should be expected that both u_z and u_r cannot be accurately predicted by CST. The displacement errors directly translate into erroneous predictions of the various stresses.

Finally, Fig. 5 presents the decay of τ_{rz} through the thickness at the center of the load patch. This shows that the decay pattern is more or less identical for all values of S, and that significant transverse shear occurs in the top two layers.

Conclusion

A baseline elasticity solution has been obtained for a cross-ply cylindrical shell subjected to a localized longitudinal shear force. The results presented show that steep stress-gradients occur close to the load and that a classical shell theory based on Love-Kirchhoff hypothesis is inadequate to capture these gradients correctly.

References

[1] Ren, J. G., 1987, "Exact Solutions for Laminated Cylindrical Shells in Cylindrical Bending," Compos. Sci. Technol., **29**, pp. 169–187.
[2] Bhaskar, K., and Varadan, T. K., 1993, "Exact Elasticity Solution for Laminated Anisotropic Cylindrical Shells," ASME J. Appl. Mech., **60**, pp. 41–47.
[3] Bhaskar, K., and Varadan, T. K., 1993, "A Benchmark Elasticity Solution for an Axisymmetrically Loaded Angle-Ply Cylindrical Shell," Composites Eng., **3**, pp. 1065–1073.
[4] Chandrasekhara, K., and Kumar, B. S., 1993, "Static Analysis of a Thick Laminated Circular Cylindrical Shell Subjected to Axisymmetric Load," Compos. Struct. **23**, pp. 1–9.

[5] Varadan, T. K., and Bhaskar, K., 1991, "Bending of Laminated Orthotropic Cylindrical Shells—An Elasticity Approach," Compos. Struct. **17**, pp. 141–156.

[6] Bhimaraddi, A., and Chandrasekhara, K., 1992, "Three-Dimensional Elasticity Solution for Static Response of Simply Supported Orthotropic Cylindrical Shells," Compos. Struct. **20**, pp. 227–235.

[7] Bhaskar, K., and Varadan, T. K., 1994, "Benchmark Elasticity Solution for Locally Loaded Laminated Orthotropic Cylindrical Shells," AIAA J., **32**, pp. 627–632.

[8] Chandrasekhara, K., and Kumar, B. S., 1993, "Static Analysis of Thick Laminated Circular Cylindrical Shells," ASME J. Pressure Vessel Technol., **115**, pp. 193–200.

[9] Gill, S. S., 1970, *The Stress Analysis of Pressure Vessels and Pressure Vessel Components*, Pergamon Press, Oxford, UK.

[10] Ince, E. L., 1956, *Ordinary Differential Equations*, Dover, New York.

[11] Ganapathysaran, N., 2001, "Three-Dimensional Analysis of Cross-Ply Cylindrical Shells Under Localized Forces and Moments," M.S. thesis, Indian Institute of Technology, Madras, India.

[12] Bert, C. W., 1975, "Analysis of Shells," *Composite Materials*, **7**, Academic Press, San Diego, CA.

Bubble Shape in Non-Newtonian Fluids

D. De Kee and C. F. Chan Man Fong
Department of Chemical Engineering, Tulane University, New Orleans, LA 70118

J. Yao
Department of Physics and Reengineering, Xavier University of Louisiana and Tulane/Xavier Center for Bioenvironmental Research

The study of the behavior of bubbles in complex fluids is of industrial as well as of academic importance. Bubble velocity-volume relations, bubble shapes, as well as viscous, elastic, and surfactant effects play a role in bubble dynamics. In this note we extend the analysis of Richardson to a non-Newtonian fluid.

[DOI: 10.1115/1.1480822]

Introduction

The motion of bubbles in non-Newtonian fluids is of considerable importance and has attracted a lot of interest in the past few decades. De Kee et al. [1] have recently reviewed this topic. One of the outstanding problems in this area is the experimental observation of an abrupt jump in the terminal velocity of a rising bubble in some non-Newtonian fluids at a certain critical volume. It is now generally accepted that viscoelastic effects as well as surface tension are among the factors that contribute to this jump discontinuity. Rodrigue et al. [2,3] have proposed a few criteria, based mainly on dimensional analysis, that have successfully predicted the existence of the jump discontinuity.

This jump discontinuity has also been associated with the shape of the bubble. Liu et al. [4] have proposed that the jump discontinuity occurs at a critical capillary number when a cusp is suddenly formed at the tail end of the bubble. The sudden transition from rounded to pointed end of a bubble rising in a fluid was observed by Rumscheidt and Mason [5] but no jump discontinuity in the velocity was reported. Further comments on the criterion proposed by Liu et al. [4] are given in Rodrigue et al. [3].

The formation of a cusp on the free surface in flows at low Reynolds number has been investigated by various authors ([6–9]). Noh et al. [10] have computed the deformation of a bubble rising in a non-Newtonian fluid and have observed a tendency towards the formation of a cusp at the tail end as the capillary number increases. Analytical models are appropriate for demonstrating the existence of such a singular point. The models employed by Richardson [6] and by Jeong and Moffat [9] are particularly appropriate for resolving such difficult free surface problems. However, it should be pointed out that analytical models are applicable to idealized problems. In the case of a rising bubble we need to consider the bubble to be two dimensional. Solving an idealized problem is usually the first step towards solving a complex problem. Here, we extend the analysis of Richardson [6] to a non-Newtonian fluid.

Contributed by the Applied Mechanics Division of THE AMERICAN SOCIETY OF MECHANICAL ENGINEERS for publication in the ASME JOURNAL OF APPLIED MECHANICS. Manuscript received by the ASME Applied Mechanics Division, August 29, 2001; final revision, March 4, 2002. Associate Editor: D. A. Siginer.

Mathematical Model

The present flow is a steady slow flow and the constitutive equation considered by Chan Man Fong and De Kee [11] is appropriate. The chosen constitutive equation can be written as

$$\tau = -\eta_0(1-\alpha_0 \mathrm{II})\gamma_{(1)} - \alpha_1 \gamma_{(1)} \cdot \gamma_{(1)} - \alpha_2 \gamma_{(2)} \tag{1}$$

where τ is the extra stress tensor, $\gamma_{(1)}$ and $\gamma_{(2)}$ are the first and second rates of deformation tensors, respectively, as defined in Bird et al. [12]; η_0, α_0, α_1, and α_2 are constants and $\mathrm{II} = \mathrm{tr}\gamma_{(1)}^2$.

We consider a two-dimensional flow in the usual (x, y) plane with velocity components (u, v). The fluid is incompressible and we introduce a stream function $\psi(x,y)$ defined as

$$u = \frac{\partial \psi}{\partial y}, \quad v = -\frac{\partial \psi}{\partial x}. \tag{2}$$

Combining Eqs. (1) and (2) yields the stress components τ_{xx}, τ_{xy}, and τ_{yy} and they are given by

$$\tau_{xx} = -2\eta_0(1-\alpha_0 \mathrm{II})\frac{\partial^2\psi}{\partial x \partial y} - \alpha_1(\nabla^2\psi)^2 - \alpha_2\left[2\frac{\partial\psi}{\partial y}\frac{\partial^3\psi}{\partial x^2\partial y} - 2\frac{\partial\psi}{\partial x}\frac{\partial^3\psi}{\partial x\partial y^2} - 4\left(\frac{\partial^2\psi}{\partial x\partial y}\right)^2 - 2\frac{\partial^2\psi}{\partial y^2}\left(\frac{\partial^2\psi}{\partial y^2} - \frac{\partial^2\psi}{\partial x^2}\right)\right] \tag{3a}$$

$$\tau_{xy} = -\eta_0(1-\alpha_0 \mathrm{II})\left(\frac{\partial^2\psi}{\partial y^2} - \frac{\partial^2\psi}{\partial x^2}\right) - \alpha_2\left[\frac{\partial\psi}{\partial y}\left(\frac{\partial^3\psi}{\partial x\partial y^2} - \frac{\partial^3\psi}{\partial x^3}\right) - \frac{\partial\psi}{\partial x}\left(\frac{\partial^3\psi}{\partial y^3} - \frac{\partial^3\psi}{\partial x^2\partial y}\right) + 2\frac{\partial^2\psi}{\partial x\partial y}(\nabla^2\psi)\right] \tag{3b}$$

$$\tau_{yy} = 2\eta_0(1-\alpha_0 \mathrm{II})\frac{\partial^2\psi}{\partial x \partial y} - \alpha_1(\nabla^2\psi)^2 - \alpha_2\left[2\frac{\partial\psi}{\partial x}\frac{\partial^3\psi}{\partial x\partial y^2} - 2\frac{\partial\psi}{\partial y}\frac{\partial^3\psi}{\partial x^2\partial y} + 2\frac{\partial^2\psi}{\partial x^2}\left(\frac{\partial^2\psi}{\partial y^2} - \frac{\partial^2\psi}{\partial x^2}\right) - 4\left(\frac{\partial^2\psi}{\partial x\partial y}\right)^2\right] \tag{3c}$$

$$\mathrm{II} = 2(\nabla^2\psi)^2 \tag{3d}$$

where ∇^2 is the Laplacian.

The equations governing creeping flows can be written as

$$\frac{\partial p}{\partial x} = -\left(\frac{\partial \tau_{xx}}{\partial x} + \frac{\partial \tau_{xy}}{\partial y}\right) \tag{4a}$$

$$\frac{\partial p}{\partial y} = -\left(\frac{\partial \tau_{xy}}{\partial x} + \frac{\partial \tau_{yy}}{\partial y}\right) \tag{4b}$$

where p is the pressure.

Combining Equations (3a)–(4b) and eliminating p yields

$$\eta_0\left\{(1-\alpha_0\mathrm{II})\nabla^4\psi-\alpha_0\left[2\frac{\partial\mathrm{II}}{\partial y}\frac{\partial}{\partial y}(\nabla^2\psi)+2\frac{\partial\mathrm{II}}{\partial x}\frac{\partial}{\partial x}(\nabla^2\chi)\right.\right.$$
$$\left.\left.+4\frac{\partial^2\mathrm{II}}{\partial x\partial y}\frac{\partial^2\psi}{\partial x\partial y}+\left(\frac{\partial^2\mathrm{II}}{\partial y^2}-\frac{\partial^2\mathrm{II}}{\partial x^2}\right)\left(\frac{\partial^2\psi}{\partial y^2}-\frac{\partial^2\psi}{\partial x^2}\right)\right]\right\}$$
$$-\alpha_2\left[\frac{\partial\psi}{\partial y}\frac{\partial}{\partial x}\nabla^4\psi-\frac{\partial\psi}{\partial x}\frac{\partial}{\partial y}\nabla^4\psi\right]=0. \tag{5}$$

In the case of a Newtonian fluid ($\alpha_0=\alpha_1=\alpha_2=0$), Eq. (5) reduces to a biharmonic equation and ψ is given by Richardson [6]

$$\psi=\mathrm{Re}(\bar{z}\phi(z)+\chi(z)) \tag{6}$$

where Re denotes the real part, $z(=x+iy)$ is the complex variable, the bar denotes the complex conjugate; ϕ and χ are analytic functions of z.

Equation (5) is a nonlinear equation and is difficult to solve. We consider the simpler case of $\alpha_0=0$. This implies that the viscosity of the fluid is constant.

De Kee et al. [13] have shown that the jump discontinuity cannot be attributed to the shear thinning effect. Thus putting $\alpha_0=0$ is probably not a serious limitation. It can be seen that in this case, ψ as given by Eq. (6) is also a solution. Further, using the theorem of Tanner and Pipkin ([12]) gives the pressure p as

$$p=p_N+\frac{\alpha_2}{\eta_0}\frac{D}{Dt}p_N+\left(\frac{\alpha_1}{2}-\frac{\alpha_2}{4}\right)\mathrm{II} \tag{7}$$

where p_N is the pressure for a Newtonian fluid and D/Dt is the material derivative.

The pressure p_N is given in Richardson [6] and can in our notation be written as

$$p_N=-4\eta_0\,\mathrm{Im}[\phi'(z)] \tag{8}$$

where Im denotes the imaginary part and the prime denotes the derivative with respect to the argument.

Noting that ϕ and χ are analytic functions, we can deduce that

$$\nabla^2\psi=2\phi'; \tag{9a}$$

$$\frac{\partial^2\psi}{\partial y^2}-\frac{\partial^2\psi}{\partial x^2}=-(2\phi'+\bar{z}\phi''+\chi'') \tag{9b}$$

$$\frac{\partial^2\psi}{\partial x\partial y}=\mathrm{Im}(z\overline{\phi''}-\chi''). \tag{9c}$$

The stress components and p can be expressed in terms of ϕ, χ, and z.

If (Xds, Yds) are the (x, y) components of the force exerted across a line element ds,

$$(X+iY)ds=ip(dx+idy)-(\tau_{xy}+i\tau_{yy})dx+(\tau_{xx}+i\tau_{xy})dy. \tag{10}$$

The boundary condition on the surface of the bubble is given by ([6])

$$(X+idY)ds=\sigma d\left(\frac{dz}{ds}\right) \tag{11}$$

where σ is the surface tension.

Equation (11) can be expressed in term of ϕ, χ, and z and following the analysis given in Richardson, we may conclude that a cusp might exist at the tail end of the bubble.

Discussion

In the present analysis it is assumed that the surface tension σ is constant. In reality it is a function of (x, y), especially if contaminants and polymer molecules are present. Thus we are still not definitely certain that a cusp is formed at the rear end of the bubble. Experimentally it is not possible to verify that a pointed end is a true cusp. However, it is beyond doubt that the jump discontinuity is related to the existence of a pointed end (true cusp or not) and any attempt at explaining the jump discontinuity needs to take into account the nonspherical shape of the bubble. As stated earlier the existence of a pointed end is a necessary but not sufficient condition for the occurrence of a jump discontinuity.

Joseph [14] reported that in non-Newtonian fluids cusping occurs suddenly whereas in Newtonian fluids the transition to cusping is gradual. This observation may partly explain the jump discontinuity. De Kee and Chhabra [14] did not observe a sudden cusp formation and from their figures we are led to believe that the change of shape is gradual.

The role of shear thinning on the shape of the bubble needs further examination. Based on a qualitative analysis, Chan Man Fong and De Kee [11] concluded that elasticity will deform a spherical bubble into a tear drop shape whereas shear thinning will deform it to an ellipsoidal shape. We need to extend the present analysis to include α_0.

Hassager [15] has observed a negative wake behind bubbles in non-Newtonian fluids. This implies that there is a considerable element of extensional flow around the bubble and this will enhance the formation of a cusp. It is also relevant to note that in Richardson's analysis, the flow is in the negative x-direction which corresponds to a negative wake.

At present the empirical criteria proposed by Rodrigue et al. [2,3] seem to be the most appropriate to use to determine the existence of the jump discontinuity. The jump discontinuity is a stability and bifurcation problem and it is not easy to solve such a complex free-surface problem.

The above analysis shows that the formation of a genuine cusp is possible for both Newtonian and second-order fluids. It seems very unlikely that the jump discontinuity in the bubble velocity can be attributed to the cusp formation. It is most likely due to a discontinuity in the surface forces, as pointed out recently by Rodrigue and De Kee [16]. A study of the convection of adsorbed surfactants at the surface would also be desirable.

References

[1] De Kee, D., Chhabra, R. P., and Rodrigue, D., 1996, ''Hydrodynamics of Free Rise of Bubbles in Non-Newtonian Polymer Solutions,'' *Handbook of Applied Polymer Processing Technology*, N. P. and P. N. Cheremisinoff, eds., Marcel Dekker, New York, p. 87.

[2] Rodrigue, D., De Kee, D., and Chan Man Fong, C. F., 1996, ''An Experimental Study of the Effect of Surfactants on the Free Rise Velocity of Gas Bubbles,'' J. Non-Newtonian Fluid Mech., **66**(2–3), pp. 213–232.

[3] Rodrigue, D., De Kee, D., and Chan Man Fong, C. F., 1998, ''Bubble Velocities: Further Developments on the Jump Discontinuity,'' J. Non-Newtonian Fluid Mech., **79**(1), pp. 45–55.

[4] Liu, Y., Liao, T., and Joseph, D., 1995, ''A Two-Dimensional Cusp at the Trailing Edge of an Air Bubble Rising in a Viscoelastic Liquid,'' J. Fluid Mech., **304**, pp. 321–342.

[5] Rumscheidt, F., and Mason, S., 1961, ''Particle Motions in Sheared Suspensions. XII. Deformation and Burst of Fluid Drops in Shear and Hyperbolic Flow,'' J. Colloid Sci., **16**, pp. 238–261.

[6] Richardson, S., 1968, ''Two-Dimensional Bubbles in Slow Viscous Flows,'' J. Fluid Mech., **33**, pp. 476–493.

[7] Joseph, D., Nelson, J., Renardy, M., and Renardy, Y., 1991, ''Two-Dimensional Cusped Interfaces,'' J. Fluid Mech., **223**, pp. 383–409.

[8] Joseph, D., 1992, ''Understanding Cusped Interfaces,'' J. Non-Newtonian Fluid Mech., **44**, pp. 127–148.

[9] Jeong, J. T., and Moffat, H. K., 1992, ''Free-Surace Cusps Associated With Flow at Low Reynolds Number,'' J. Fluid Mech., **241**, pp. 1–22.

[10] Noh, D., Kang, I., and Leal, L., 1983, ''Numerical Solutions for the Deformation of a Bubble Rising in Dilute Polymeric Fluids,'' Phys. Fluids A, **5**(6), pp. 1315–1332.

[11] Chan Man Fong, C. F., and De Kee, D., 1994,''The Effect of a Thermal Gradient on the Motion of a Bubble in a Viscoelastic Fluid,'' J. Non-Newtonian Fluid Mech., **53**, pp. 165–174.

[12] Bird, R. B., Armstrong, R. C., and Hassager, O., 1987, *Dynamics of Polymeric Liquids* (Fluid Mechanics **1**), Second Ed., John Wiley and Sons, New York.

[13] De Kee, D., Rodrigue, D., and Chan Man Fong, C. F., 1996, *Rheology and Fluid Mech. of Nonlinear Materials*, D. A. Siginer and S. G. Advani, eds., ASME, New York, AMD-Vol. 217, p. 37.

[14] De Kee, D., and Chhabra, R. P., 1998, ''A Photographic Study of Shapes of Bubbles and Coalescence in Non-Newtonian Polymer Solutions,'' Rheol. Acta, **27**(6), pp. 656–660.

[15] Hassager, O., 1976, "Negative Wake Behind Bubbles in Non-Newtonian Liquids," Nature (London), **279**, pp. 402–403.
[16] Rodrigue, D., and De Kee, D., 1999, "Bubble Velocity Jump Discontinuity in Polyacrylamide Solutions: A Photographic Study," Rheol. Acta, **38**(2), pp. 177–182.

Dynamic Stability of a Rotor Partially Filled With a Viscous Liquid

M. Tao
Professor

W. Zhang
Professor, Mem. ASME

Department of Mechanics and Engineering Science,
Fudan University, Shanghai 200433, P. R. China

By means of the obtained explicit expressions of dynamic forces acting on a rotor partially filled with a viscous liquid, the equations of motion are derived. The corresponding eigenvalue problem is solved accurately in correcting to the first order of magnitude of $\mathrm{Re}^{-1/2}$. *Dynamic stability of the rotor is studied in detail and some valuable results are obtained. We can regulate the stable interval so long as we properly choose the value of external damping.* [DOI: 10.1115/1.1458553]

1 Introduction

Here the perturbed motion of a spinning rigid rotor filled partially with a viscous liquid is studied. The problem is of technical importance to fluid-cooled turbines as well as to spin-stabilized satellites or rockets containing liquid fuels.

Unfortunately, the above-mentioned perturbed motion of the fluid-structure coupled system is somewhat unstable over some spinning ranges. Stability of a rotor partially filled with an inviscous liquid has already analyzed. Wolf [1] and Kuipers [2] analyzed undamped and damped rotors, respectively. Zhang, Tang, and Tao [3] gave a further general discussion on this topic and obtained some more general results. Up to now, however, a rotor partially filled with a viscous liquid has not been discussed extensively. Hendricks and Morton [4] analyzed a circular whirling motion of the rotor and gave the viscosity correction by means of a procedure introduced by Greenspan, where not all the boundary conditions were satisfied. Holm-Christensen and Träger [5] directly used the full Navier-Stokes equations and solved them numerically, the procedure is rather time-consuming and sensitive to the initial guess.

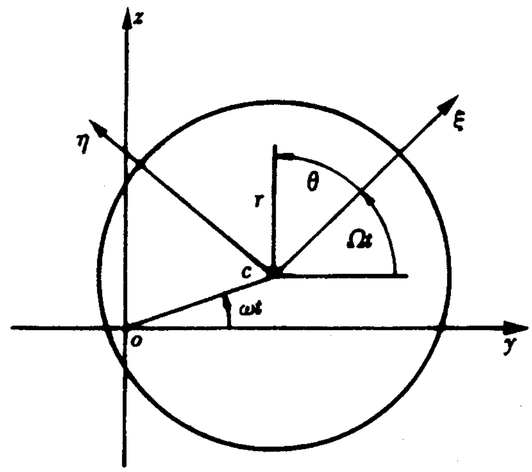

Fig. 1 Analytic model

In this paper, the explicit expressions of dynamic forces acting on a rotor partially filled with the viscous liquid are used and the dynamic stability of the coupled system is discussed. The equations of motion are obtained. The corresponding eigenvalue problem is solved accurately in correcting to the first order of magnitude of $\mathrm{Re}^{-1/2}$.

2 Dynamic Analysis of the Rotor

A rigid cavity rotor is mounted symmetrically in the middle of a massless elastic uniform shaft supported by two identical bearings at the shaft two ends. The rotor spins at a constant rate Ω. The flow in the rotor is assumed to also be of plane motion. The fixed Cartesian coordinate systems $o-yz$ and the spinning Cartesian coordinate systems $c-\xi\eta$ are showed in Fig. 1. The superimposed disturbed motion of the center of the rotor, c, is assumed to be a small whirl motion with angular speed ω. Referred to the fixed coordinate system, the disturbed motion of the point c can be described as

$$y_c=\Delta_1 e^{i\omega t},\quad z_c=\Delta_2 e^{i\omega t} \tag{1}$$

where Δ_1 and Δ_2 are complex parameters and may be unequal. Supposing F_y and F_z are the dynamic forces acting on the rotor by the perturbed liquid, we have (Tao and Zhang [6], also see the Appendix)

$$\begin{bmatrix}F_y\\F_z\end{bmatrix}=\frac{1}{2}\rho a^2\omega^2\pi\begin{bmatrix}M_1+M_2+\varepsilon(1-i)(K_1+K_2) & -i(M_1-M_2)-\varepsilon(1+i)(K_1-K_2)\\ i(M_1-M_2)+\varepsilon(1+i)(K_1-K_2) & M_1+M_2+\varepsilon(1-i)(K_1+K_2)\end{bmatrix}\begin{bmatrix}\Delta_1\\\Delta_2\end{bmatrix}e^{i\omega t} \tag{2}$$

where both F_y and F_z are complex, and

$$M_{1,2}=\frac{2(\omega\pm\Omega)^2-\omega^2}{(1+\gamma)(\omega\pm\Omega)-\omega^2},$$

$$K_{1,2}=\sqrt{\frac{2}{\omega\pm\Omega}}(\omega\pm\Omega)^2\frac{\omega^2+\frac{3}{b^2}(2(\omega\pm\Omega)^2-\omega^2)}{\left[\omega^2+\frac{1}{b^2}(2(\omega\pm\Omega)^2-\omega^2)\right]^2},$$

$$\varepsilon=(\mathrm{Re})^{-1/2},\quad \mathrm{Re}=\frac{a^2\omega_0}{v},\quad \omega_0=(k/m_R)^{1/2},\quad \gamma=\frac{a^2+b^2}{a^2-b^2}.$$

Contributed by the Applied Mechanics Division of THE AMERICAN SOCIETY OF MECHANICAL ENGINEERS for publication in the ASME JOURNAL OF APPLIED MECHANICS. Manuscript received by the ASME Applied Mechanics Division, Apr. 18, 2000; final revision, Sept. 26, 2001. Associate Editor: D. A. Siginer.

Even if $\omega-\Omega=0$, K_2 can also be determined as zero. m_R and k are the mass of the rotor and the rigidity of the flexible shaft. If $\nu\rightarrow 0$, then $\mathrm{Re}\rightarrow\infty$, therefore (2) will degenerate into the result of the inviscid case.

Taking the external damping C_e into account, the equation of motion of the rotor, in the fixed coordinate system, is

$$\begin{bmatrix} m_R & \\ & m_R \end{bmatrix}\begin{bmatrix} \ddot{y}_c \\ \ddot{z}_c \end{bmatrix}+\begin{bmatrix} C_e & \\ & C_e \end{bmatrix}\begin{bmatrix} \dot{y}_c \\ \dot{z}_c \end{bmatrix}+\begin{bmatrix} k & \\ & k \end{bmatrix}\begin{bmatrix} y_c \\ z_c \end{bmatrix}=\begin{bmatrix} F_y \\ F_z \end{bmatrix}. \quad (3)$$

Substituting (1) and (2) into (3), we get the characteristic equations as

$$\{m_c[M_j+\varepsilon(1-i)K_j]+m_R\}\omega^2-iC_e\omega-k=0 \quad (4)$$

$$(j=1,2) \quad (5)$$

where $m_c=\rho a^2\pi$ denotes the mass of the liquid needed to fully fill the cavity. Introducing the following nondimensional parameters

$$m=\frac{m_c}{m_R},\ \lambda=\frac{\omega}{\omega_0},\ S=\frac{\Omega}{\omega_0},\ C=\frac{C_e}{2m_R\omega_0},$$

(4) and (5) can be reduced to the follow characteristic equations of λ:

$$\left\{ m\left[\varepsilon(1-i)\sqrt{\frac{2}{\lambda\pm S}}\frac{(S\pm\lambda)^2\left(\lambda^2+\frac{3}{b^3}(2(S\pm\lambda)^2-\lambda^2)\right)}{\left(\lambda^2+\frac{1}{b^3}(2(S\pm\lambda)^2-\lambda^2)\right)^2}((1+\gamma)(S\pm\lambda)^2-\lambda^2)\right]\right.$$
$$\left. +2(S\pm\lambda)^2-\lambda^2+((1+\gamma)(S\pm\lambda)^2-\lambda^2)\right\}\lambda^2-(2iC\lambda+1)((1+\gamma)(S\pm\lambda)^2-\lambda^2)=0 \quad (6)$$

where the positive and negative sign correspond with (6) and (7), respectively.

All the discussions in the paper are based only on the first order of magnitude of ε (Tao and Zhang [6]), therefore the λ in (9) can be written as

$$\lambda=\lambda_0+\varepsilon\lambda_1. \quad (7)$$

Substituting (7) into (6), we get

$$(m+\gamma)\lambda_0^4+(\pm 2S(2m+\gamma+1)-2iC\gamma)\lambda_0^3+((2m+\gamma+1)S^2-\gamma$$
$$\mp 4iCS(1+\gamma))\lambda_0^2-2(1+\gamma)S(iCS\pm 1)\lambda_0-(1+\gamma)S^2=0 \quad (8)$$

and

$$[(2m+\gamma+1)(\pm S+\lambda_0)^2-(m+1)\lambda_0^2]2\lambda_0\lambda_1$$
$$+[2(2m+\gamma+1)(\pm S+\lambda_0)\lambda_1-2(m+1)\lambda_0\lambda_1]\lambda_0^2$$
$$+(1-i)mF-(2iC\lambda_0+1)(2\gamma\lambda_0\lambda_1\pm 2S(1+\gamma)\lambda_1)$$
$$-2iC\lambda_1[(1+\gamma)(\pm S+\lambda_0)^2-\lambda_0^2]=0 \quad (9)$$

corresponding the power ε^0 and ε, respectively, in which

$$F=\sqrt{\frac{2}{\lambda_0\pm s}}\frac{(\lambda_0\pm s)^2\left(\lambda_0^2+\frac{3}{b^3}(2(\pm S+\lambda_0)^2-\lambda_0^2)\right)}{\left(\lambda_0^2+\frac{1}{b^3}(2(\pm S+\lambda_0)^2-\lambda_0^2)\right)^2}$$
$$\times[(1+\gamma)(\pm S+\lambda_0)^2-\lambda_0^2].$$

There are two algebraic characteristic equations with fourth order in (8) and (8) has eight eigenvalues $\lambda_{0,j}(j=1,2\ldots 8)$ in all. $\lambda_{1,j}$ then can be obtained from (9). For any given S, if the $\alpha_{\max}=\max_j[\mathrm{Re}(i\lambda_j)]\leqslant 0$, the rotor with spinning rate S is stable.

3 Results

For comparing with previous results (Hendricks and Morton, [4] and Christenson and Träger, [5]), the same values of parameters $m=0.206$, $b=0.67$, $\mathrm{Re}=2.5\times 10^5$ are used. The damping values are taken as $C=0.01$, 0.02, 0.05, 0.1, 0.2, 0.4, 0.6 successively. Figure 2 shows the numerical results of $\alpha_{\max}\sim S$. The value $S=S_0$ is corresponding to $\alpha_{\max}=0$. It is obvious that the lower spin region $S<S_0$ is the stable region. The smaller the external damping C, the larger the stable region. However, there is no stable region when the Re is beyond the value 2.5×10^5.

It is worth showing the results of $\mathrm{Re}=2.5\times 10^4$. First, taking $C=0.005$, 0.01, there are two stable intervals in the low and high spinning regions separately. Figure 3 shows the high cases. When $C\leqslant 0.002$, however, the stable interval in the high-spin region disappears. while $C=0.45$, however, the stable interval in the low-spin region is minimum $(S_0=0.938)$. This means that if the value of C increases or decreases, the stable interval will always extend (Fig. 4). However, it extends when C decreases in the result of Hendricks and Morton [4] and the case is on the contrary in the result of Christenson and Träger [5].

The characteristic Eqs. (6) can be derived, and it becomes very easy to discuss the dynamic stability of a spinning rotor partially filled with viscous liquid.

1. The form of the characteristic Eqs. (9) seems rather complex, there are only two fourth-order algebraic equations and they only have eight eigenvalues to evaluate in connecting with the first order of ε.

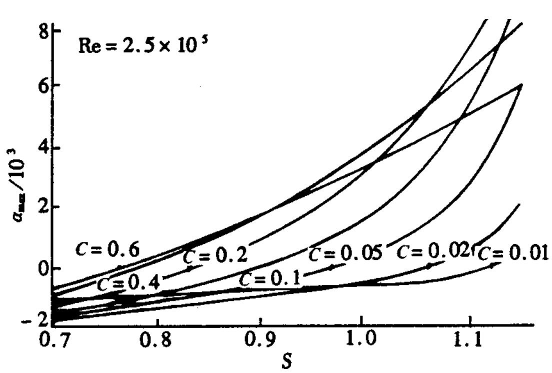

Fig. 2 When $\mathrm{Re}=2.5\times 10^5$, $\alpha_{\max}$ varies with S. The stable intervals in the lower span speeds are shown.

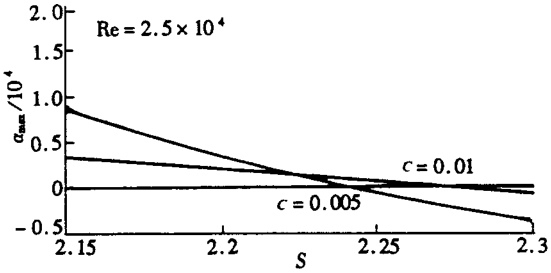

Fig. 3 When Re=2.5×10^4, α_{max} varies with *S*. The stable intervals in the lower span speeds are shown, but those in the higher speeds are not shown.

2. Taking the larger Reynolds number Re$=2.5\times10^5$, the liquid appears almost inviscid. In this case there is only one stable interval in the low spin region. While Re$=2.5\times10^4$, however, the liquid appears somewhat viscous and another stable interval in the high spin region occurs.
3. When Re$=2.5\times10^4$, the stable interval in the low spin region can be at minimum if the value of the external damping is properly chosen.

Acknowledgment

The project is supported by National Key Basic Research Special Fund (No. G1998020316) and the Foundation of the Ministry of Education (No. 1999024624).

Appendix

A Brief Derivation of Eq. (2). Consider the transverse motion of the rotor in the y-direction only, i.e.,

$$y_c=\Delta_1 e^{i\omega t}, \quad z_c=0$$

and nondimensionalize the velocity by $\Delta_1\omega$, the time by $1/\omega$, the angular speed by ω, the length by a, the pressure by $\rho a\Delta_1\omega^2$, where ρ is the density of the fluid, and a is the inner radius of the rotor. Introducing a perturbed stream function ψ, then the equation of motion of the viscous fluid in the rotor is

$$\frac{\partial(\Delta\psi)}{\partial t}-\frac{1}{\mathrm{Re}}\Delta\Delta\psi=0 \quad \left(\Delta=\frac{\partial^2}{\partial r^2}+\frac{1}{r}\frac{\partial}{\partial r}+\frac{1}{r^2}\frac{\partial^2}{\partial\theta^2}\right). \tag{A1}$$

Stokes numbers is Re$=a^2\omega/\nu$. The kinematic boundary conditions are taken as

$$\psi=0, \quad \frac{\partial\psi}{\partial r}=0 \tag{A2}$$

$$(r=1) \tag{A3}$$

$$\frac{1}{b}\frac{\partial\psi}{\partial\theta}=\frac{\partial\eta}{\partial t} \tag{A4}$$

$$(r=b) \tag{A5}$$

where η is the deviation of free surface. The pressure boundary conditions are taken as

$$p_{r\theta}=\frac{1}{\mathrm{Re}}\left(\frac{1}{r}\frac{\partial u}{\partial\theta}+\frac{\partial v}{\partial r}-\frac{v}{r}\right)=0, \quad p_{rr}=-p+\frac{2}{\mathrm{Re}}\frac{\partial u}{\partial r}=0. \tag{A6}$$

p in (A6) can be eliminated with the equation of circumferential motion. Finally, we obtain

$$-\frac{\partial^2\psi}{\partial t\partial r}+\frac{2\Omega}{b}\frac{\partial\psi}{\partial\theta}=-\frac{\partial\Pi}{b\partial\theta}+\frac{1}{\mathrm{Re}}\left(-\frac{\partial^3\psi}{\partial r^3}-\frac{1}{b}\frac{\partial^2\psi}{\partial r^2}-\frac{3}{b^2}\frac{\partial^3\psi}{\partial\theta^2\partial r}+\frac{4}{b^3}\frac{\partial^2\psi}{\partial\theta^2}+\frac{1}{b^2}\frac{\partial\psi}{\partial r}\right) \tag{A7}$$

where Π is the potential of the inertial force taken as

$$\Pi=-\tfrac{1}{4}r\left[e^{i(t+\theta+\Omega t)}+e^{-i(t+\theta+\Omega t)}+e^{i(t-\theta-\Omega t)}+e^{-i(t-\theta-\Omega t)}\right]. \tag{A8}$$

η in (A7) can also be eliminated by (A4).

Corresponding to the first term of the right-hand side of (A8), ψ can be taken as

$$\psi_1=\varphi(r)e^{i(t+\theta+\Omega t)}.$$

With the boundary conditions (A2, A3, A4, A5, and A7), ψ_1 can be obtained as

$$\psi_1=\frac{1-i}{4N_+M_+}\left(1-\frac{A_+}{N_+}\right)\left[-\frac{1}{2}\left((1+i)N_++\frac{1}{2}\right)r+\frac{1}{2}\left((1+i)N_+-\frac{3}{2}\right)\frac{1}{r}+r^{-1/2}E_-(1)E_+(r)\right]e^{i(t+\theta+\Omega t)}$$

where

$$E_\pm(r)=e^{\pm N_+r\pm i(N_+r-\pi/4)}$$

Carrying the same procedures for the remaining terms on the right-hand side of (A8), ψ_2, ψ_3, and ψ_4 can also be obtained, respectively. The stream function is then taken as

$$\psi=\psi_1+\psi_2+\psi_3+\psi_4.$$

Next, consider the transverse motion of the rotor in the z direction:

$$y_c=0, \quad z_1=\Delta_2 e^{i\omega t}$$

after a rather lengthy deduction, formula (2) is derived.

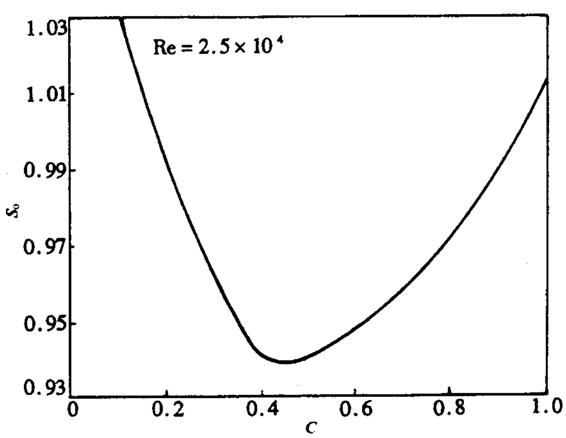

Fig. 4 When Re=2.5×10^4, S_0 varies with *C*. A minimum sable interval exists.

References

[1] Wolf, I. A., 1968, "Whirl Dynamics of a Rotor Partially Filled With Liquid," ASME J. Appl. Mech., **35**, pp. 676–682.
[2] Kuipers, M., 1966, "Die Instabilität eines ferdend gelagerten und teilweise mit flüssigkeit gefü llten umlaufeuden Hohlzylinders," Forsch. Geb. Ingenieurwes., **32**, No. 6, pp. 194–195.
[3] Zhang, W., Tang, J., and Tao, M. D., 1996, "Dynamic Stability of a Rotor Filled or Partially Filled With Liquid," ASME J. Appl. Mech., **63**, pp. 101–105.
[4] Hendricks, S. L., and Morton, J. B., 1979, "Stability of a Rotor Partially Filled With Viscous Incompressible Fluid," ASME J. Appl. Mech., **46**, pp. 913–918.
[5] Holm-Christenson, G., and Träger, K., 1991, "A Note on Rotor Instability Caused by Liquid Motions," ASME J. Appl. Mech., **58**, pp. 804–811.
[6] Tao, M. D., and Zhang, W., 1995, "Forced Vibrations of a Rotor Partially Filled With a Viscous Liquid," J. Fudan Univ. (Nat. Sci.), **34**, pp. 661–670 (in Chinese).

Dynamic Stability of a Flexible Spinning Cylinder Partially Filled With Liquid

M. Tao
Professor

W. Zhang
Professor, Mem. ASME

Department of Mechanics and Engineering Science,
Fudan University, Shanghai 200433, P. R. China

Dynamic stability of a flexible spinning cavity cylinder partially filled with liquid is discussed in the paper. The cylinder is assumed to be slender. Choosing characteristic quantities and estimating the orders of magnitude of all terms in the governing equations and boundary conditions, the three-dimensional flow in the slender cylinder is reduced to a quasi-two-dimensional flow. Using the known formulas of a two-dimensional dynamic force acting on the rotor and regarding the slender cylinder as a Bernoulli-Euler beam, the perturbed equations of the liquid-filled beam-wise cylinder are derived. The analytical stability criteria as well as the stability boundaries are obtained. The results further the study of this problem. [DOI: 10.1115/1.1458554]

1 Introduction

Dynamic stability of a rotor partially filled with liquid has already been discussed extensively, however, there are few papers in the literature dealing with flexible spinning cylinders. The reason is that the flow in the deformed cylinder is three dimensional. Dynamic pressure of the liquid is effected by the cylinder deflection. It is difficult to obtain analytical formulas of the dynamic force acted on a cylinder by a liquid. Crandall [1] discussed the problem first by giving an outline of the problem only. Zhang [2] studied the problem in greater detail, but the cylinder is completely filled with liquid and then no free surface should be considered. In this paper a fresh start is made. By virtue of the estimation of the order of magnitude of all the terms in the equations, the three-dimensional flow is then reduced to the quasi-two-dimensional flow mathematically because of the slender feature of the cylinder and its small deflection in practice. Thus the problem is greatly simplified and a series of analytical results are obtained in this paper.

2 Simplification of the Problem

A uniform slender cylindrical cavity rotor is simply supported at its two ends as shown in Fig. 1. The length and inner radius of the cylinder are $2L$ and a, respectively. The cylindrical rotor is partially filled with liquid in the cavity. The rotor spins at a constant speed Ω without perturbation. The contained liquid is uniformly attached to an inner wall under the action of centrifugal force and synchronously spins as a rigid body with the same Ω. The inner radius of the steady spinning motion of the solid-fluid coupled system. Thus a small perturbed whirl motion of the rotor with whirl speed ω is superimposed on it. Introducing the fixed Cartesian coordinate system $o'-x'y'z'$, the rotating Cartesian coordinate system $o-xyz$ with spinning speed Ω around z'-axis and the corresponding cylindrical coordinate system $o-roz$, where z and z'-axes coincide with the undisturbed spinning direction and o is the middle point of the cylinder. During the whirling, liquid also undergoes a perturbed motion. Let u, v, and w be the relative perturbed velocities of the liquid in the r, θ, z-directions, respectively; in the cylindrical coordinate system $o-roz$, F_r, F_θ, and F_z are the inertial forces in the r, θ and z-directions, respectively.

$$F_r=\omega^2\delta\cos[(\Omega-\omega)t+\theta],$$

$$F_\theta=\omega^2\delta\sin[(\Omega-\omega)t+\theta],\quad F_z=0$$

where the whirl deflexion curve of the cylinder is denoted as $\delta(z)$ $(\delta\ll a)$.

The problem of three-dimensional flow in the cylinder should be simplified because it is very difficult to solve exactly. Let us first estimate the order of magnitudes of every term in the equations by nondimensional procedure. The order of magnitude of u, v is the same as that of cylinder perturbed motion, $\Delta\omega$, where Δ is a typical value of $\delta(z)$. The order of magnitudes of w, on the other hand, is the order of $\Delta\omega a/L$. This is due to the fact that the order of magnitude of the longitudinal displacement of the liquid is the same as that of the longitudinal displacement of the cylinder. We introduce the following dimensionless quantities denoted by an overbar:

$$(\bar{u},\bar{v})=(u,v)/\Delta\omega,\quad \bar{w}=w/\frac{a\Delta\omega}{L},\quad (\bar{r},\bar{b})=(r,b)/a,\quad \bar{z}=z/L$$

$$(\bar{\delta},\bar{\eta})=(\delta,\eta)/\Delta,\quad \bar{t}=t\omega,\quad \bar{\Omega}=\Omega/\omega,\quad \bar{p}=p/\rho a\Delta\omega^2$$

$$(\bar{F}_r,\bar{F}_\theta)=(F_r,F_\theta)/\Delta\omega^2,\quad \bar{F}_z=F_z/\frac{a\Delta\omega^2}{L}.$$

Substituting the above expressions into the related equations, we have

$$\frac{\partial\bar{u}}{\partial\bar{t}}+\frac{\Delta}{a}\left(\bar{u}\frac{\partial\bar{u}}{\partial\bar{r}}+\bar{v}\frac{\partial\bar{u}}{\bar{r}\partial\theta}-\frac{\bar{v}^2}{\bar{r}}\right)+\frac{a\Delta}{L^2}\bar{w}\frac{\partial\bar{u}}{\partial\bar{z}}-2\bar{\Omega}\bar{v}=\bar{F}_r-\frac{\partial\bar{p}}{\partial\bar{r}}\tag{1}$$

$$\frac{\partial\bar{v}}{\partial\bar{t}}+\frac{\Delta}{a}\left(\bar{u}\frac{\partial\bar{v}}{\partial\bar{r}}+\bar{v}\frac{\partial\bar{v}}{\bar{r}\partial\theta}+\frac{\overline{uv}}{\bar{r}}\right)+\frac{a\Delta}{L^2}\bar{w}\frac{\partial\bar{v}}{\partial\bar{z}}+2\bar{\Omega}\bar{u}=\bar{F}_\theta-\frac{\partial\bar{p}}{\bar{r}\partial\theta}\tag{2}$$

$$\frac{\partial\bar{w}}{\partial\bar{t}}+\frac{\Delta}{a}\left(\bar{u}\frac{\partial\bar{w}}{\partial\bar{r}}+\bar{v}\frac{\partial\bar{w}}{\bar{r}\partial\theta}\right)+\frac{a\Delta}{L^2}\bar{w}\frac{\partial\bar{w}}{\partial\bar{z}}=\bar{F}_z-\frac{\partial\bar{p}}{\partial\bar{z}}\tag{3}$$

$$\frac{\partial\bar{u}}{\partial\bar{r}}+\frac{\bar{u}}{\bar{r}}+\frac{\partial\bar{v}}{\bar{r}\partial\theta}+\frac{a^2}{L^2}\frac{\partial\bar{w}}{\partial\bar{z}}=0.\tag{4}$$

Then the following conclusions are obtained from (1)–(4):

1 If the cylinder is slender, the ratio $a^2/L^2\ll1$, all the terms including derivatives of z in (8), (9), and (11) can be omitted compared with the other terms. Only $\bar{u}$, $\bar{v}$, and $\bar{p}$ remain in Eqs. (8), (9), and (11) and the problem is reduced to a plane one. After $\bar{u}$, $\bar{v}$, and $\bar{p}$ are solved, $\bar{w}$ can then be obtained from Eq. (10).

2 For a small perturbed motion, $S=\Delta/a\ll1$, all the nonlinear terms in the above equations can be neglected, and the problem is reduced further to a linear problem.

The next step is to simplify the boundary conditions. During the whirl motion, the equation of the deformed side surface of the cylinder partially filled with an inviscid liquid can be written as $r=a+\xi(\theta,z,t)$. Its normal vector is

$$\mathbf{n}=\left(-1,\frac{\partial\xi}{r\partial\theta},\frac{\partial\xi}{\partial z}\right).$$

Contributed by the Applied Mechanics Division of THE AMERICAN SOCIETY OF MECHANICAL ENGINEERS for publication in the ASME JOURNAL OF APPLIED MECHANICS. Manuscript received by the ASME Applied Mechanics Division, Apr. 18, 2000; final revision, Sept. 26, 2001. Associate Editor: D. A. Siginer.

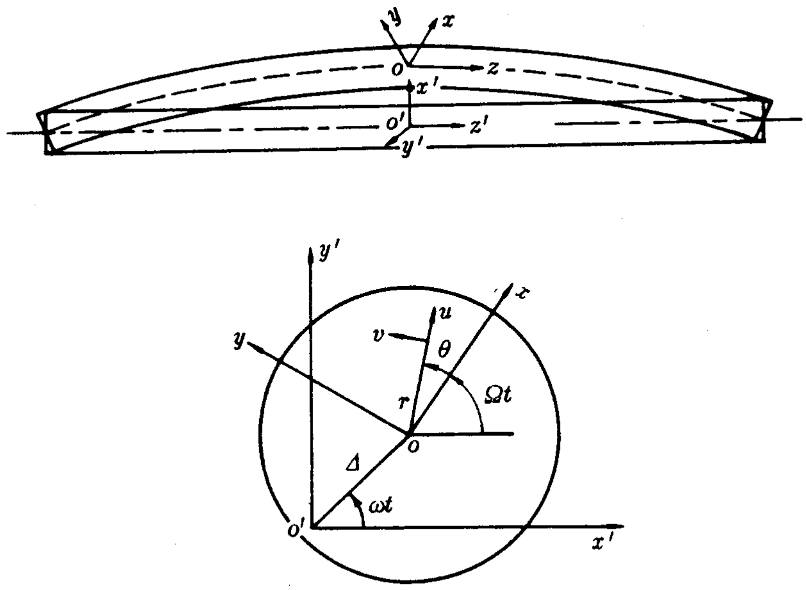

Fig. 1 Analytic model

Hence the boundary condition on the surface is

$$-u+v\frac{\partial\xi}{r\partial\theta}+w\frac{\partial\xi}{\partial z}=V_n$$

where V_n is the normal velocity component of the corresponding point of the cylinder. The corresponding nondimensional boundary condition is

$$-\bar{u}+\frac{\Delta}{a}\bar{v}\frac{\partial\bar{\xi}}{\bar{r}\partial\theta}+\frac{a\Delta}{L^2}\bar{w}\frac{\partial\bar{\xi}}{\partial\bar{z}}=V_n/\Delta\omega \tag{5}$$

where $\bar{\xi}=\xi/\Delta$. The third term of the left side can be omitted compared with the other terms because $a^2/L^2\ll 1$. And V_n can also be substituted with velocity projection on the $o-xy$ plane. Then (5) is altered to the boundary condition of a plane problem. The boundary conditions the inner free surface and the two end faces are discussed in like manner.

Summarily speaking, the flow pattern of the liquid in the cylinder with small deflexion can be described as a quasi-two-dimensional flow on any section of the cylinder. Thus we can use the formulas of two-dimensional dynamic force of a liquid (Zhang, Tang, and Tao [3]) to analyze the dynamic stability problem of the flexible spinning cylinder partially filled with an inviscid liquid.

3 Dynamic Stability

Assume the components of the dynamic force density of the liquid acting on the cylinder are F'_x and F'_y, respectively, in the fixed Cartesian coordinate system $o'-x'y'z'$. Thus we have (Zhang, Tang, and Tao [3])

$$F'_x=m_c\omega^2M_2\delta(z')\cos\omega t \quad F'_y=m_c\omega^2M_2\delta(z')\sin\omega t$$

where

$$m_c=\rho\pi a^2 \quad M_2=\frac{2(\Omega-\omega)^2-\omega^2}{(1+\gamma)(\Omega-\omega)^2-\omega^2} \quad \left(\gamma=\frac{a^2+b^2}{a^2-b^2}\right). \tag{6}$$

The resultant force density is

$$P(z')=\sqrt{F^2_{x'}+F^2_{y'}}=m_c\omega^2M_2\delta(z').$$

In a stable case, this force and the centrifugal force caused by whirling motion of the flexible cylinder together balance the elastic force of the flexible cylinder, i.e.,

$$EI\delta^{(4)}=\rho_RA_R\omega^2\delta+m_cM_2\omega^2\delta \tag{7}$$

where ρ_R and A_R are the density and sectional area of the cylinder, respectively. Equation (16) is a linear ordinary differential equation of δ rather than a complex nonlinear equation (Crandall [1] and Zhang [2]). This is due to the simplification of the quasi-two-dimensional model.

The boundary conditions of the bending curve are

$$\delta(\pm L)=\delta''(\pm L)=0. \tag{8}$$

Only for some special values (eigenvalues), (7) has nonvanish solutions (eigenfunctions). Equation (7) has a general solution

$$\delta(z')=c_1\cos Kz'+c_2\sin Kz'+c_3\cosh Kz'+c_4\sinh Kz'$$

where

$$K^4=\frac{\rho_RA_R+m_cM_2}{EI}\omega^2. \tag{9}$$

Substituting the above general solution into (8), we have

$$\begin{pmatrix}\cos KL & \sin KL & \cosh KL & \sinh KL\\ \cos KL & -\sin KL & \cosh KL & -\sinh KL\\ \cos KL & \sin KL & -\cosh KL & -\sinh KL\\ \cos KL & -\sin KL & -\cosh KL & \sinh KL\end{pmatrix}\begin{pmatrix}c_1\\ c_2\\ c_3\\ c_4\end{pmatrix}=0. \tag{10}$$

After some simplification, it is

$$\text{Sin}\,2KL=0.$$

Hence

$$K_nL=\frac{n\pi}{2} \quad (n=1,2,\ldots).$$

If $n=1$, $K_1L=\pi/2$. From (19) we have $c_2=c_3=c_4=0$. The corresponding eigenfunction is

$$\varphi_1(z')=\cos\frac{\pi}{2L}z'.$$

This is a symmetrical whirl mode, and the flexible cylinder is deflected as a bow. If $n=2$, $K_2L=\pi$. We have $c_1=c_3=c_4=0$. The corresponding eigenfunction is

$$\varphi_2(z')=\sin\frac{\pi}{L}z'.$$

This is an antisymmetrical whirl mode, and the flexible cylinder is as an S-form. Its middle point is a nodal point.

For the symmetrical mode, from (9) we have

$$\left(\frac{\pi}{2L}\right)^4=\frac{\rho_RA_R+m_cM_2}{EI}\omega_1^2.$$

In order to compare this with the result of Wolf [4]. The total length of the flexible cylinder should be taken alternatively as $2L$. The above expression thus should be rewritten as

$$2L(\rho_RA_R+m_cM_2)\omega_1^2=2\left(\frac{\pi}{2L}\right)^4EIL. \tag{11}$$

For a rotor, Wolf's result is

$$(M_R+M_Cf)\omega^2=k \tag{12}$$

where f equals M_2 in (6), and k is the rigidity of the shaft on which the rotor is mounted. M_R and M_C are the mass of a solid rotor and the mass of liquid fully filled, respectively. Comparing (11) and (12), we have

$$2L\rho_RA_R=M_R,\quad 2Lm_c=M_C,\quad k=2\left(\frac{\pi}{2L}\right)^4EIL. \tag{13}$$

Thus the result of the flexible cylinder can correspond to Wolf's result of the rotor.

Assume

$$F=\frac{\omega}{\omega_0},\quad S=\frac{\Omega}{\omega_0},\quad \omega_0^2=2\left(\frac{\pi}{2L}\right)^4\frac{EIL}{M_R},\quad \mu=\frac{M_C}{M_R}=\frac{Lm_c}{\rho_RA_R}.$$

The characteristic Eq. (11) can be written as

$$(\gamma+\mu)F^4-2\alpha SF^3+(\alpha S^2-\gamma)F^2+2(\gamma+1)SF-(1+\gamma)S^2=0 \tag{14}$$

where $\alpha=\gamma+2\mu+1$. Assuming $F=S$, it corresponds to synchronous whirl motion. From (14), the first critical speed is obtained as

$$S_1^2=\frac{1}{1+\mu}\ \text{ or }\ \Omega_{cr,1}=\left(\frac{\pi}{2L}\right)^2\sqrt{\frac{2EIL}{M_R+M_C}}.$$

For asynchronous whirling, curve $F\sim S$ of the flexible cylinder can directly be referred to the Wolf's results ([4]). The instability region of a spinning speed is $B_1<S<B_2$. The lowest threshold speed of the system is $\Omega_1=B_1\omega_0=B_1(\pi/2L)^2\sqrt{2EIL/M_R}$. By values of μ and γ, the liquid influences the value of B_1, and therefore the value of Ω_1, too.

4 Conclusion

We came to the following conclusions:

1. When the slender ratio $a^2/L^2\ll 1$, the three-dimensional flow in the cylinder can be approximated by a two-dimensional flow.
2. Using this model, the dynamic stability of a thin cylinder partially filled with a viscous fluid can also be discussed analytically on the basis that the two-dimensional dynamic force of the viscous fluid acting on the cylinder has been obtained.

Acknowledgment

The project is supported by the National Key Basic Research Special Fund (No. G1998020316) and the Foundation of the Ministry of Education (No. 1999024624).

References

[1] Crandall, S. H., and Mroszczyk, J., 1986, "Whirling of a Flexible Cylinder Filled With Liquid," *Proc. of International Conference on Rotordynamics*, Tokyo, pp. 449–452.

[2] Zhang, W., 1990, *Theory of Rotordynamics*, Science Press, Beijing (in Chinese).

[3] Zhang, W., Tang, J., and Tao, M. D., 1996, "Dynamic Stability of a Rotor Filled or Partially Filled With Liquid," ASME J. Appl. Mech., **63**, pp. 101–105.

[4] Wolf Jr., J. A., 1968, "Whirl Dynamics of a Rotor Partially Filled With Liquid," ASME J. Appl. Mech., **35**, pp. 678–682.

Journal of Applied Mechanics

Discussion

Discussion: "On the Relationship Between the L-Integral and the Bueckner Work-Conjugate Integral" (Shi, J. P., Liu, X. H., and Li, J., 2000 ASME J. Appl. Mech., 67, pp. 828–829)

Y. Z. Chen
Division of Engineering Mechanics, Jiangsu University, Zhenjiang, Jiangsu 212013, P.R. China

K. Y. Lee
Department of Mechanical Engineering, Yonsei University, Seoul 120-749, South Korea

Three wrong expressions in the paper ([1]) have been found. Equations (4) and (5) in the paper are written in the forms

$$\varphi^{(\mathrm{II})}(z) = -i\varphi'(z), \quad \psi^{(\mathrm{II})}(z) = -iz\psi'(z) + 2i\bar{z}\varphi'(z), \tag{1}$$

$$u_i^{(\mathrm{II})} = yu_{i,x} - xu_{i,y} \tag{2}$$

$$\sigma_{ij}^{(\mathrm{II})} = y\sigma_{ij,x} - x\sigma_{ij,y} + \frac{1}{2}\int \sigma_{ij,x}dy - \frac{1}{2}\int \sigma_{ij,y}dx \quad (i,j=1,2). \tag{3}$$

1 Complex potentials suggested by Muskhelishvili should be an analytic function ([2]). However, since the argument $\bar{z}$ is involved in the second term of $\psi^{(\mathrm{II})}(z)$ in Eq. (1), $\psi^{(\mathrm{II})}(z)$ cannot be an analytic function. Therefore, $\psi^{(\mathrm{II})}(z)$ in Eq. (1) is a wrong expression.

2 In the complex variable function method, the displacement components can be expressed as ([2])

$$\begin{aligned} 2G(u+iv) &= \kappa\varphi(z) - z\overline{\varphi'(z)} - \overline{\psi(z)} \\ &= \kappa\varphi(z) + z\{-\overline{\varphi'(z)}\} - \overline{\psi(z)} \end{aligned} \tag{4}$$

where G is the shear modulus of elasticity, $\kappa=(3-\nu)/(1+\nu)$ is for the plane stress problem, $\kappa=3-4\nu$ is for the plane strain problem, and ν is the Poisson's ratio, and $\varphi(z)$ and $\psi(z)$ are two analytic functions.

Equation (4) reveals a rule that in a real displacement expression of plane elasticity, if the function after the elastic constant κ is $\varphi(z)$, the term after z in Eq. (4) should be $-\overline{\varphi'(z)}$.

On the other hand, from Eq. (4) we have

$$2G\left(\frac{\partial u}{\partial x} + i\frac{\partial v}{\partial x}\right) = (\kappa\varphi'(z) - \overline{\varphi'(z)}) - (z\overline{\varphi''(z)} + \overline{\psi'(z)})$$

$$2G\left(\frac{\partial u}{\partial y} + i\frac{\partial v}{\partial y}\right) = i\{(\kappa\varphi'(z) - \overline{\varphi'(z)}) + (z\overline{\varphi''(z)} + \overline{\psi'(z)})\}. \tag{5}$$

Therefore, from Eqs. (2) and (5), the displacement components in Eq. (2) can be expressed as

$$\begin{aligned} 2G(u^{(\mathrm{II})} + iv^{(\mathrm{II})}) &= 2G\left(y\left(\frac{\partial u}{\partial x} + i\frac{\partial v}{\partial x}\right) - x\left(\frac{\partial u}{\partial y} + i\frac{\partial v}{\partial y}\right)\right) \\ &= \kappa\{-iz\varphi'(z)\} + z\{i(\overline{\varphi'(z)} - \bar{z}\overline{\varphi''(z)})\} \\ &\quad - i\bar{z}\overline{\psi'(z)}. \end{aligned} \tag{6}$$

From the fact that

$$-\overline{\frac{d}{dz}\{-iz\varphi'(z)\}} = -i(\overline{\varphi'(z)} + \bar{z}\overline{\varphi''(z)}) \neq i(\overline{\varphi'(z)} - \bar{z}\overline{\varphi''(z)}) \tag{7}$$

and the rule mentioned above, the displacements $u^{(\mathrm{II})}$ and $v^{(\mathrm{II})}$ shown in Eq. (2) are not an elasticity solution. Therefore, the displacement shown in Eq. (2) is also a wrong expression.

3 In Eq. (3) an indefinite integral is used to express the stress components. In the continuum medium of elastic body, the integral should be path-independent. Also, it is well known that if a function $F(x,y)$

$$F(x,y) = \int_{(x_o,y_o)}^{(x,y)} p(x,y)dx + q(x,y)dy \tag{8}$$

is a path independent integral, the following condition must be satisfied:

$$\frac{\partial p(x,y)}{\partial y} = \frac{\partial q(x,y)}{\partial x} \quad \text{or} \quad \frac{\partial q(x,y)}{\partial x} - \frac{\partial p(x,y)}{\partial y} = 0. \tag{9}$$

If Eq. (3) were true, substituting $p(x,y) = -\sigma_{ij,y}/2$ and $q(x,y) = \sigma_{ij,x}/2$ into Eq. (9) yields the following:

$$\frac{\partial^2\sigma_{ij}}{\partial x^2} + \frac{\partial^2\sigma_{ij}}{\partial y^2} = 0. \tag{10}$$

However, the stress components σ_{ij} are not a harmonic function in general. Thus, the $\sigma_{ij}^{(\mathrm{II})}$ shown by Eq. (3) is also a wrong expression.

References

[1] Shi, J. P., Liu, X. H., and Li, J. M., 2000, "On the Relation Between the L-integral and the Bueckner Work-Conjugate Integral," ASME J. Appl. Mech., **67**, pp. 828–829.
[2] Muskhelishvili, N. I., 1953, *Some Basic Problems of Mathematical Theory of Elasticity*, Noordhoof, Dordrecht, The Netherlands.

Discussion: "A Critical Reexamination of Classical Metal Plasticity" (Wilson, C. D., 2002, ASME J. Appl. Mech., 69, pp. 63–68)

C. J. Lissenden
Department of Engineering Science and Mechanics,
The Pennsylvania State University, 212 Earth-Engineering
Sciences Building, University Park, PA 16802

The author correctly identifies the backbone of metal plasticity as the Mises yield criterion, the Prandtl-Reuss flow law, and isotropic/kinematic hardening. However, there has always been the qualification that these simplifications of plasticity work well for "most metals" or "some metals." It is noteworthy that while the author has devoted a section of his paper to Richmond's work refuting the widespread use of the assumption of pressure-independent flow in metals, he did not reference the keystone work of Spitzig and Richmond [1], where they provide additional results for 1100 aluminum. This would have further reinforced his point. Spitzig and Richmond found 1100 aluminum to exhibit pressure-dependence but not a strength-differential. Here the term strength-differential means a tension-compression asymmetry (e.g., compressive yield strength larger than tensile yield strength), which is different from a Bauschinger effect. The yield function that Spitzig and Richmond used can be written in the forms

$$f=aI_1+\sqrt{3J_2}-c$$

$$f=\alpha I_1+\frac{\sqrt{3J_2}}{c}-1$$

where I_1 and J_2 are the usual stress invariants and $\alpha=a/c$, a is the pressure coefficient, and c is the strength coefficient. The strength-differential depends only on the parameter a, but pressure-dependence is affected by both a and c. While a and c were shown to be strain-dependent, α was not ([1]). In fact, $\alpha=a/c$ for aluminum was approximately three times that of iron-based materials.

Based on the tensile and compressive yield strengths reported by Wilson for 2024-T351 aluminum, presumably using the 0.2% offset strain definition; the yield function parameters can be calculated and compared with results from Spitzig and Richmond in Table 1.

Table 1 Yield function parameters

Material	a	c (MPa)	$\alpha=a/c$ (TPa)
2024-T351 aluminum	0.0296	791	37
1100 aluminum ([1])	0.0014	25	56
Aged maraging steel ([1])	0.037	1833	20

The pressure-dependence of 1100 and 2024-T351 is similar, but 2024-T351 exhibits a strength-differential $(2a)$ of 5.9%, while 1100 does not exhibit an appreciable strength-differential. While Wilson did not measure volume change, Spitzig and Richmond did, and found there to be no significant dilation; indicating that an associated flow rule will not correctly predict plastic strain. This is also the case for frictional materials, where it is common to employ a nonassociated flow rule.

We have observed strength-differential in laboratory experiments using aged Inconel 718 (a precipitation strengthened nickel-base alloy) ([2,3]), 6061-T6 aluminum and 6092/SiC/17.5-T6 (a particulate reinforced aluminum alloy) ([4]). The Mises yield criterion does not apply well to these materials either. Our work on Inconel 718 ([3]) indicates that a J_2-J_3 yield function, which we called a threshold function because we were working in the realm of viscoplasticity, along the lines of that proposed by Drucker [5] for an aluminum alloy was most suitable.

Finally, while it is fairly obvious, it is worth pointing out that the Drucker-Prager yield criterion predicts more flow for the same tensile stress than the Mises yield criterion simply due to the presence of the positive I_1 term. Thus, the finite element results of Wilson for Mises and Drucker-Prager yield criteria are self-consistent. It would be interesting to know the range of I_1 for a particular notch geometry.

References

[1] Spitzig, W. A., and Richmond, O., 1984, "The Effect of Pressure on the Flow Stress of Metals," Acta Metall., **32**, pp. 457–463.
[2] Gil, C. M., Lissenden, C. J., and Lerch, B. A., 1999, "Yield of Inconel 718 by Axial-Torsional Loading at Temperatures Up to 649C," J. Test. Eval., **27**, pp. 327–336.
[3] Iyer, S. K., and Lissenden, C. J., 2002, "Viscoplastic Model Accounting for the Strength-Differential in Inconel 718," submitted for publication.
[4] Lissenden, C. J. and Lei, X., 2002, "A More Comprehensive Method for Yield Locus Construction for Metallic Alloys," submitted for publication.
[5] Drucker, D. C., 1949, "Relation of Experiments to Mathematical Theories of Plasticity," ASME J. Appl. Mech., **16**, pp. 349–357.

Journal of Applied Mechanics

Erratum

Erratum: "On Some Issues in Shakedown Analysis" [ASME J. Appl. Mech., 2001, 68, pp. 799–808]

G. Maier

In this paper, on page 800, $D=$ should be deleted from Eq. (2.4).

